

Introduction	
Quantum Information Processing	
Superconducting Qubits and Circuit QED	
Circuit QED: Quantum Information Processing with a Photon Bus	
Experimental Setup and Details	
Initialization and Benchmarking of Single-Qubit Gates	
Two-Qubit Circuit QED: Riding the Quantum Bus	
Entanglement On-Demand and Joint Readout	
Two-Qubit Algorithms	
Conclusions and Future Work	
Bibliography	

© 2010 by Jerry Moy Chow
All rights reserved.

Quantum Information Processing with Superconducting Qubits

A Dissertation
Presented to the Faculty of the Graduate School
of
Yale University
in Candidacy for the Degree of
Doctor of Philosophy

by
Jerry Moy Chow

Dissertation Director: Professor Robert J. Schoelkopf

May 2010

Abstract
Quantum Information Processing with Superconducting Qubits
Jerry Moy Chow
2010

This thesis describes the theoretical framework, implementation, and measurements of a quantum processor comprised of superconducting qubits coupled in the circuit quantum electrodynamics (QED) architecture. In the realization of circuit QED, two superconducting ‘transmon’ charge qubits are capacitively coupled to a one-dimensional microwave transmission line resonator which serves as a quantum bus. Single-qubit rotations can be applied through the resonator and their operation is characterized using various benchmarking techniques. Through a virtual photon interaction via the quantum bus, the two qubits can coherently swap a single excitation. A separate two-qubit conditional phase interaction is also observed which is attributable to an interaction in the two-excitation manifold of the transmons. Furthermore, the same quantum bus which couples the qubits can be used as a joint detector of the full two-qubit quantum state. Entanglement witnesses and a violation of a Bell-type inequality are found using this joint detector on highly entangled states. Finally, combining the single-qubit rotations, conditional phase interaction, and joint readout, allows the realization and characterization of simple quantum algorithms, specifically the Deutsch-Jozsa and Grover’s search algorithms.

Contents

Contents	v
List of Figures	xi
List of Tables	xv
Acknowledgements	xvii
Publication list	xix
Nomenclature	xxi
1 Introduction	1
1.1 Computing with quantum mechanics	2
1.2 Experimental implementations of quantum processors	4
1.3 Overview of thesis	6
2 Quantum Information Processing	9
2.1 Universal quantum computing	10
2.2 Single-qubit gates	11
2.3 Two-qubit entanglement gates	14
2.3.1 c NOT gate	14
2.3.2 c -Phase gate (cU_{ij})	16
2.3.3 i SWAP and \sqrt{i} SWAP gates	18
2.4 Quantum algorithms	20
2.4.1 Quantum parallelism in an algorithm	21
2.4.2 Deutsch-Jozsa algorithm	23

2.4.3	Grover's search algorithm	25
2.4.4	Shor's and other quantum algorithms	29
2.5	Quantum measurement	30
2.5.1	Density matrix	31
2.5.2	State tomography	33
2.6	Entanglement metrics	35
2.6.1	Concurrence	36
2.6.2	Entanglement witnesses	38
2.7	Bell tests	40
2.7.1	Cluser-Horne-Shimony-Holt inequality	40
2.7.2	CHSH entanglement witness	43
2.8	Chapter summary	43
3	Superconducting Qubits and Circuit QED	45
3.1	Superconducting qubits	46
3.1.1	Josephson junction as a non-linear inductor	46
3.1.2	The Cooper-pair box qubit	47
3.1.3	The transmon qubit	50
3.2	Coupling superconducting qubits	53
3.2.1	Fixed capacitive coupling	53
3.2.2	Tunable inductive coupling	54
3.2.3	Quantum bus coupling	56
3.3	Cavity quantum electrodynamics	58
3.3.1	Strong coupling regime	60
3.3.2	Dispersive coupling regime	60
3.4	Circuit QED	61
3.4.1	Coupling a transmon to a coplanar waveguide resonator	61
3.4.2	Dispersive regime of circuit QED	65
3.4.3	Strong dispersive regime	66
3.5	Qubit decoherence	66
3.5.1	Relaxation and the Purcell effect	68
3.5.2	Dephasing	70
3.6	Chapter summary	74
4	Circuit QED: Quantum Information Processing with a Photon Bus	75
4.1	Initialization	76
4.2	Single-qubit gates in circuit QED	77
4.2.1	Introducing a drive	77
4.2.2	X-Y gates for a qubit	79
4.2.3	X-Y gates for a transmon multi-level atom	80
4.2.4	Z (phase) gates	85
4.3	Two-qubit gates in circuit QED	87

4.3.1	Two-qubits in the dispersive regime	88
4.3.2	Virtual qubit-qubit interaction	89
4.3.3	$\sigma_z \otimes \sigma_z$ higher level transmon interaction	92
4.4	Multiplexed joint qubit readout	97
4.4.1	Deriving the measurement operator	97
4.4.2	State tomography in circuit QED	101
4.4.3	Entanglement by joint measurement	103
4.5	Chapter summary	104
5	Experimental Setup and Details	105
5.1	Experimental test samples	106
5.2	Resonator Fabrication	106
5.2.1	Resonator parameters	106
5.2.2	Optical lithography	108
5.3	Transmon fabrication	109
5.3.1	‘Traditional’ transmon	110
5.3.2	Balanced design	112
5.3.3	Flux-bias transmon design	112
5.4	Sample boards and holders	120
5.4.1	Coffin design	121
5.4.2	Octobox design	121
5.5	Cryogenic setup	123
5.6	Room temperature control	127
5.7	Pulse control and modulation	129
5.8	Chapter summary	129
6	Initialization and Benchmarking of Single-Qubit Gates	131
6.1	Initializing pure states	132
6.1.1	Nonlinear vacuum Rabi	133
6.1.2	Cavity temperature	139
6.1.3	Vacuum Rabi summary	139
6.2	Characterizing single-qubit gates	141
6.3	Single-qubit gate error experiments	142
6.3.1	Microwave pulse shaping	143
6.3.2	Calibration of single-qubit gates	145
6.3.3	Single qubit readout calibration	145
6.3.4	Double π metric	146
6.3.5	Quantum process tomography	149
6.3.6	Randomized benchmarking	153
6.3.7	Summary of error metrics	156
6.4	Derivative-based pulse shaping	159
6.4.1	Experimental details	159

6.4.2	Results with standard pulse shaping	160
6.4.3	Experimentally implementing derivative pulse shaping	162
6.4.4	Summary of DPS	166
6.5	Chapter summary	168
7	Two-Qubit Circuit QED: Riding the Quantum Bus	169
7.1	Experimental details	170
7.2	Two-qubit spectroscopy	172
7.2.1	Qubit-qubit avoided crossing	175
7.2.2	The dark state	175
7.3	Multiplexed joint qubit readout	178
7.4	Coherent state transfer: Stark swap	180
7.5	Chapter summary	185
8	Entanglement On-Demand and Joint Readout	187
8.1	Experimental setup	189
8.2	Virtual swap interaction via flux bias	192
8.3	Higher-level transmon interaction	194
8.3.1	Tuning up a c-Phase gate	196
8.3.2	Generating Bell states	199
8.4	Joint readout of two qubits	199
8.5	Calibrating the measurement model	201
8.6	Quantum state tomography and the Pauli set	204
8.6.1	The density matrix representation	205
8.6.2	Biasing of metrics by maximum-likelihood estimation	208
8.6.3	The Pauli set representation	209
8.7	Characterizing the quantum states	212
8.7.1	Fidelity to targeted states	212
8.7.2	Entanglement witnesses	213
8.7.3	Clouser-Horne-Shimony-Holt inequality violation	214
8.8	Chapter summary	216
9	Two-Qubit Algorithms	219
9.1	Experimental details	220
9.2	Deutsch-Jozsa algorithm	221
9.2.1	Breaking down the algorithm	221
9.2.2	Deutsch-Jozsa results	223
9.3	Grover search algorithm	225
9.3.1	The oracle	225
9.3.2	Breaking down the algorithm	226
9.3.3	Grover results and debugger	227
9.4	Chapter summary	231

10 Conclusions and Future Work	233
10.1 Improving one and two-qubit operations	234
10.1.1 Longer coherence times	234
10.1.2 Better qubit operations	235
10.2 More qubits in circuit QED	237
10.3 Quantum information outlook	240
 Bibliography	 243
 Appendices	 258
A Mathematica code for microwave pulse generation	259
B Mathematica code for tomography	281
 Copyright Permissions	 297

List of Figures

2.1	The Bloch sphere	12
2.2	Circuit representation for the controlled NOT gate	15
2.3	Circuit representation for the conditional phase gate	17
2.4	Circuit form for constructing a c NOT from c -Phase	18
2.5	Circuit form for constructing a c NOT from $\sqrt{i$ SWAP or i SWAP	19
2.6	Anatomy of a quantum algorithm	22
2.7	Deutsch-Jozsa algorithm	25
2.8	Grover's search algorithm	27
2.9	Cartoon state illustration of the Grover iteration	28
2.10	Entanglement of formation versus concurrence	37
2.11	State space and entanglement witnesses	39
2.12	Schematic for the CHSH test	41
3.1	The Cooper pair box	48
3.2	Charge dispersion	50
3.3	Schemes for coupling charge qubits	54
3.4	Charge-qubit coupling networks	57
3.5	Charge-qubit quantum bus	58
3.6	Illustration of Cavity QED	59
3.7	Illustration of circuit QED	62
3.8	Reduced transmon coupling to CPW network	63
3.9	Strong dispersive regime of circuit QED	67
3.10	Environmental coupling of a transmon	70
3.11	Flux noise contribution to dephasing	73
4.1	Frequency bandwidth of Gaussian pulse shapes	83
4.2	Error per gate with and without DRAG	84

4.3	Virtual Swap	90
4.4	Two excitation manifold	93
4.5	Level scheme for c-Phase	94
4.6	Transmission in strong dispersive regime for two qubits	98
4.7	Measurement model coefficients versus drive frequency	101
4.8	Dispersive peaks for generating Bell states by measurement	104
5.1	Coplanar waveguide geometry	107
5.2	Optical images of resonator topologies	108
5.3	Optical images of different transmon designs	110
5.4	The capacitance network for the transmon in a coplanar waveguide resonator	111
5.5	The flux-bias line	114
5.6	FBL schematic for Sonnet simulations	115
5.7	Sonnet simulations of resonators with and without FBLs	116
5.8	Current density simulations of resonators with FBLs	117
5.9	Pushing up the wiggle-waggle with bondwires	118
5.10	Optical image of an on-chip wirebond	119
5.11	Experimental transmission spectrum with and without wirebond	120
5.12	Coffin box holder	122
5.13	Octobox holder	123
5.14	Resonator with FBL in octobox	124
5.15	Schematic of cryogenic circuitry	126
5.16	Room temperature control schematic	128
6.1	Vacuum Rabi splitting	134
6.2	Jaynes-Cummings ladder	134
6.3	Transmission versus magnetic field and drive frequency	136
6.4	Emergence of \sqrt{n} peaks under strong driving of the vacuum Rabi transition	137
6.5	Strongly driven vacuum Rabi at elevated temperature	140
6.6	Microwave pulse shapes	143
6.7	Sample sequence of concatenated pulses	144
6.8	Bang-bang gate characterization and visibility	147
6.9	Schematic for quantum process tomography	149
6.10	Quantum process tomography experimental results	151
6.11	Gate errors from QPT	152
6.12	Pulse sequence schematic for randomized benchmarking	155
6.13	Randomized benchmarking 3 ns pulse width	156
6.14	Trace by trace randomized benchmarking	157
6.15	Error per gate versus pulse width	158
6.16	Clifford averaged RB for cQED222 with standard pulse shaping	160
6.17	Error per gate with normal pulse shaping	161
6.18	Composite x and y rotations with standard Gaussian pulse shaping	162

6.19	Gaussian and derivative on I and Q quadratures	163
6.20	Composite x and y rotations with derivative pulse shaping	164
6.21	Randomized benchmarking for various pulse widths using derivative pulse shaping	165
6.22	Trace by trace with and without derivative pulse shaping	167
6.23	Error per gate with derivative pulse shaping	168
7.1	Sample and scheme used to couple two qubits to an on-chip microwave cavity	171
7.2	Strong coupling of two superconducting qubits	173
7.3	Two qubit dispersive cavity shifts	173
7.4	Scheme of the virtual photon swap interaction	174
7.5	Two qubit spectroscopy	176
7.6	Independent Rabi driving of two qubits	179
7.7	Two qubit multiplexed readout	180
7.8	Two qubit Stark shift spectroscopy	181
7.9	Coherent swap protocol	182
7.10	Coherent state exchange	183
7.11	Stark swap frequency	184
8.1	Schematic for two-qubit quantum bus with on-chip flux bias lines	190
8.2	Single excitation spectroscopy	191
8.3	Flux bias swap experiments	193
8.4	Two excitation spectroscopy	195
8.5	Agreement of the splitting between experiment and theory	197
8.6	Conditional phase gate tune-up sequences	198
8.7	Experimental protocols for generating Bell states	200
8.8	Measurement transients for joint readout	201
8.9	Rabi oscillations for readout characterization	202
8.10	Fourier transforms of Rabi oscillations	203
8.11	Density matrix representation of Bell states	206
8.12	Bias of entanglement metrics from MLE	209
8.13	Pauli set representation of two-qubit states	211
8.14	Pauli set for separable and entangled states differing only by a single-qubit rotation	212
8.15	Entanglement witness for separable states	214
8.16	Entanglement witness for entangled states	215
8.17	CHSH for separable states	216
8.18	CHSH for entangled states	217
9.1	Quantum circuit for DJ algorithm	222
9.2	Results for four cases in DJ algorithm	224
9.3	Two-qubit Grover algorithm schematic	226

9.4	Microwave and flux pulses for Grover algorithm	228
9.5	Implementing Grover's algorithm	230
9.6	Grover fidelity for all choice of oracles	231
10.1	Four qubit sample	238
10.2	Three qubit protocols	239

List of Tables

5.1	Summary of measured sample parameters	130
6.1	Gate errors for the three metrics	158
8.1	The 30 raw measurements	207

for James

Acknowledgements

FIRST I would like to thank my advisor ROB SCHOELKOPF for giving me the amazing opportunity to work on superconducting quantum computing in RSL. From late nights in the lab to phone calls while he is driving to work, he has taught me countless things to become a better scientist. I'm very grateful for his patience for those times when I have scurried onto some experimental tangent, and even more thankful for his unique quantum engineer's perspective.

I have always been amazed by how STEVE GIRVIN could step into a complicated discussion, get caught up within five minutes, and immediately begin to make experimental suggestions which we might never have considered. MICHEL DEVORET has shown me multiple times how broad and how beautiful physics can be, through innocent experimental discussions that blossom into philosophical treatises. Another very important individual and mainstay of RSL has been LUIGI FRUNZIO. Much thanks goes to him for the fabrication of the samples which I have worked with. Furthermore, I have deeply appreciated his accessibility for discussions and enthusiasm for new ideas and results.

Through my graduate career at Yale, I have also had the pleasure to work with a number of truly remarkable experimental postdoctoral associates. The day-to-day interactions with them, and team-bonding have helped shape my development as a scientist. First, there was JOHANNES MAJER, with whom I first plunged into the exciting experiments presented in this thesis. I found it amazing that any given night in the lab with him could quickly transition from taking critical experimental data to reveling and socializing at GPSCY. ANDREW HOUCK was ever the happy-go-lucky physicist, with a knack for always pointing me towards the most efficient data set, so as to make time to go outside and fit in a round of wiffleball. Finally, LEONARDO DICARLO has helped fill these final few years with some of the most productive

and ground-breaking science. He has shown me what true passion in science means and I am very grateful for that.

On the theory side, the work and advice of postdocs JAY GAMBETTA and JENS KOCH have been immeasurable. From completing the J^4 team on the original cavity bus with myself and Johannes, to going out for beers and working out at the gym, to always helping me understand the gigabytes of data I've taken, they have rounded-out my scientific experience at Yale by blurring the line between theorists and experimentalists.

The camaraderie and success of the fourth floor of Becton are truly remarkable. I especially want to thank LEV BISHOP, for always being there for me, from helping understand the vacuum Rabi data of chapter 6, to being patient and waiting whenever I ask him to 'hold on.' I have never met anyone quite like the 'idea-machine' DAVID SCHUSTER, with whom I have enjoyed playing basketball and discussing zany start-up projects. Then, there are also the grad students with whom I entered the Yale physics department. Since day one, they have always been accessible for hanging out and it has been absolutely wonderful to have shared the grad school experience and developed life friendships with them.

Words cannot simply describe the bond and all the shared experiences between myself and BLAKE JOHNSON while chugging through graduate school together. Blake has become like a brother to me and his constant presence and cool demeanor have kept me grounded through some of the most stressful periods. I also definitely have to thank him and his wife PHYLLIS for providing me with so many excellent meals and truly helping me mature as a person.

Finally, there are my friends and family back home, who have been a constant source of support and love. I am very grateful to have been able to be so physically close to them, so that I could visit on a whim and have some of my MOTHER's home cooked meals. I need to especially thank my FATHER, who's confidence and teaching have guided me towards this degree. From my brother JAMES, to my aunts, and to all my cousins who check up on me, the connection to family has been an absolute driving force of my desire to learn and to achieve. I have to also thank my dear CHARLOTTE for giving me perspective and connecting with my heart at all times, apart and together.

Publication list

This thesis is based in part on the following published articles:

1. J. Majer, J. M. Chow, J. M. Gambetta, J. Koch, B. R. Johnson, J. A. Schreier, L. Frunzio, D. I. Schuster, A. A. Houck, A. Wallraff, A. Blais, M. H. Devoret, S. M. Girvin, and R. J. Schoelkopf, “Coupling superconducting qubits via a cavity bus,” *Nature* **449**, 443–447 (2007).
2. J. M. Chow, J. M. Gambetta, L. Tornberg, J. Koch, L. S. Bishop, A. A. Houck, B. R. Johnson, L. Frunzio, S. M. Girvin, and R. J. Schoelkopf, “Randomized benchmarking and process tomography for gate errors in a solid-state qubit,” *Phys. Rev. Lett.* **102**, 090502 (2009).
3. L. S. Bishop, J. M. Chow, J. Koch, A. A. Houck, M. H. Devoret, E. Thuneberg, S. M. Girvin, and R. J. Schoelkopf, “Nonlinear response of the vacuum Rabi resonance,” *Nature Phys.* **5**, 105–109 (2009).
4. L. DiCarlo, J. M. Chow, J. M. Gambetta, L. S. Bishop, B. R. Johnson, D. I. Schuster, J. Majer, A. Blais, L. Frunzio, S. M. Girvin, and R. J. Schoelkopf, “Demonstration of two-qubit algorithms with a superconducting quantum processor,” *Nature* **460**, 240–244 (2009).
5. J. M. Chow, L. DiCarlo, J. M. Gambetta, A. Nunnenkamp, L. S. Bishop, L. Frunzio, M. H. Devoret, S. M. Girvin, and R. J. Schoelkopf, “Entanglement metrology using a joint readout of superconducting qubits,” arXiv:0908.1955 [cond-mat].

Nomenclature

Abbreviations:

CHSH	Clauser-Horne-Shimony-Holt, see section 2.7.
CPB	Cooper-pair box, see section 3.1.2.
c-Phase	conditional-phase gate, see section 2.3.2.
cNOT	controlled-NOT, see section 2.1.
DJ	Deutsch-Jozsa, see section 2.4.2.
FBL	flux-bias line, see section 5.3.3.
IC	integrated circuit, see chapter 1.
JC	Jaynes-Cummings, see section 3.3.
NMR	nuclear magnetic resonance, see section 1.2.
PCB	printed circuit board, see section 5.4.1.
POVM	positive operator-valued measure, see section 2.5.
QED	quantum electrodynamics, see section 1.3.
QFT	quantum fourier transform, see section 2.4.4.
QIP	quantum information processing, see section 1.3.
RF	radio-frequency, see section 1.2.
RSA	Rivest, Shamir, and Adleman, see section 1.1.
RWA	rotating wave approximation, see section 3.3.

SQUID superconducting quantum interference device, see section 3.1.2.



Latin Letters:

- \mathcal{B} bound to concurrence, see section 2.6.2.
- C_g qubit-cavity coupling capacitance, see (3.34).
- \mathbb{C} Clauser-Horne-Shimony-Holt operator, see section 2.7.
- C concurrence, see section 2.6.1.
- cU_{ij} conditional-phase gate, conditioned on state ij , see section 2.3.2.
- C_Σ total capacitance to ground of charge qubit, see section 3.1.2.
- D derivative pulse-shape amplitude scale factor, see section 6.4.3.
- E_C electrostatic charging energy, see section 3.1.2.
- E_J Josephson energy, see section 3.1.2.
- E_m energy of m -th transmon level, see section 4.2.4.
- \mathcal{F} state fidelity, see (2.42).
- G Grover iteration, see section 2.4.3.
- g_{ij} transmon dipole coupling energy between charge levels i and j , see (3.36).
- g vacuum Rabi coupling frequency, see (3.27).
- $H^{(i)}$ Hadamard gate on qubit i , see section 2.2.
- $H^{\otimes n}$ n -qubit simultaneous Hadamard gate, see section 2.4.1.
- I single-qubit identity operator, also defined as $\mathbb{1}$, see section 2.2.
- i SWAP i -swap gate, see section 2.3.3.
- $\mathbb{1}$ single-qubit identity operator, also defined as I , see section 2.2.
- J virtual photon qubit-qubit swap interaction strength, see (4.34).
- M measurement operator, see sections 2.5 and 4.4.1.
- \hat{n} integer-valued Cooper pair number operator, see section 3.1.2.
- \bar{n} mean number of photons in the cavity, also defined as $\langle n \rangle$, see section 3.4.3.
- n_g gate charge, see section 3.1.2.

P_1	qubit excited state population, see ??.
\mathcal{P}	state purity, see section 2.6.
RQ	two-qubit Pauli operators, where $R, Q \in I, X, Y, Z$, and also referred to as $R \otimes Q$, see section 2.5.2.
Q	quality factor of cavity, see section 5.2.
$R_i(\theta)$	rotation around the axis i by angle θ , also defined as R_i^θ , see (2.3).
$\sqrt{i\text{SWAP}}$	square-root of i -swap gate, see section 2.3.3.
T_1	qubit relaxation time, see section 3.5.1.
T_ϕ	qubit dephasing time, see section 3.5.2.
T_2	qubit decoherence time, see section 3.5.2.
V_0	zero point root mean squared voltage in the cavity, see (3.34).
\mathcal{W}	entanglement witness, see section 2.6.2.
X, Y, Z	single-qubit Pauli operator, also defined as $\sigma_{x,y,z}$, see (2.2).
z -cNOT	zero controlled-NOT gate, see section 2.4.2.



Greek Letters:

α_m	absolute anharmonicity of the m -th transmon level, see (3.18).
α_m^r	relative anharmonicity of the m -th transmon level, see (3.19).
β	voltage division ratio, see (3.34).
β_i	sensitivity of the measurement to a specific Pauli operator indexed by i , see section 4.4.1.
ϵ_m	charge dispersion of the m -th transmon level, see (3.15).
χ	state dependent cavity shift, see (3.45).
χ_{mn}	positive superoperator process determined by quantum process tomography, see section 6.3.5.
$\tilde{\Phi}$	external magnetic flux, see section 3.1.2.
$\hat{\phi}$	Josephson phase operator, see section 3.1.2.
Φ_0	magnetic flux quantum, see section 3.1.2.

θ_z	z -rotation phase of the qubit, see (4.30).
ρ	density matrix, see section 2.5.
$\sigma_{x,y,z}$	single-qubit Pauli operator, also defined as X, Y, Z , see (2.2).
ω_C	cavity excitation frequency, see (3.27).
ω_k	transmon transition frequency to level k , see (3.21).
ω_q	qubit transition frequency, see (3.20).
ω_d	qubit drive frequency, see section 7.2.2.
ζ	two-qubit $\sigma_z \otimes \sigma_z$ interaction strength, see section 4.3.3.

CHAPTER 1

Introduction

THE ubiquity of computers and other devices with microprocessors reflects one of the more successful technological developments over the past few decades. When the first solid-state transistor was made in 1947 by John Bardeen, Walter Brittain, and William Shockley at Bell Laboratories, it is fair to say that not even they would have imagined the proliferation of and extent to which computing has reached. Yet, science and society continue to march forward, looking for ever more computational power and faster processors. Before considering the future of computing however, we can obtain some perspective about the scope of computers today through looking at the historical development of information processors.

Computers were not always silicon based nor made up of transistors. Rather, the earliest processors were made up of vacuum tubes and electromechanical relays, physically taking up large amounts of space. Arguably the first critical implementation of computers was during World War II, with the British Colossus computers [1] used to break German wartime codes. The war stimulated the scientific progression of digital computing and fortunately, scientists responded to the challenge, helping decrypt intercepted Nazi transmissions.

Subsequently, new technological advances in transistors and integrated circuits changed the classical computing landscape forever. Instead of a single bit of information taking an individual vacuum tube, a solid-state chip only a tiny fraction of the volume of the vacuum tube could hold millions of transistors, each representing a bit. Computers no longer needed

to take up entire floors of a building, but could even begin to become personalized for use in the everyday home.

So how many bits can we fit into a microprocessor and how does information processing scale? The well-known Moore's law has predicted that the number of transistors which can be placed onto an integrated circuit (IC) doubles approximately every two years [2]. The trend has been traced for the past half century and demonstrates the ability of technology to continue improving at exponential levels. Yet, there is a fundamental physical limit to Moore's law because as we continue to increase the density of bits, we eventually reach the level of the individual atoms of silicon. At these scales, standard solid-state physics breaks down, transitioning into the physics of the atomic scale. Specifically, quantum mechanics begins to play a role: interactions between the atoms become no longer negligible, and quantum tunneling between parts of the IC can occur. Already in our smallest present-day processors, quantum mechanics is responsible for substantial gate leakage, resulting in significant heating.

Therefore, in the terms of computing progress moving forward, there are two paths to consider. The first is to understand what will be the fundamental limits to Moore's law and what techniques within classical computation and semiclassical solid-state engineering can be done to continue improvement, even if not at Moore's law levels. The second is to start from quantum mechanics, perhaps even at the atomic level, and think about computing and information processing by *directly employing the quantum effects*. The first path is the task of electrical engineers, materials scientists, and computer engineers to figure out different physical architectures for constructing ICs, improved materials to minimize loss mechanisms while continuing to scale down, and shift towards more parallel processors which will require more efficient and adapted computer programs. The second path has resulted in the burgeoning field of quantum information processing, which we will motivate in the next section. The experimental implementation in a solid-state system is the subject of this thesis.

1.1 Computing with quantum mechanics

Devices which perform quantum information processing are called quantum computers. The concept of quantum computing can be traced back to the early 1980s, first with the suggestion by Richard Feynman for quantum mechanics simulations [3] and then for the solution of a toy problem with a quantum algorithm developed by David Deutsch [4].

Feynman noted that classical computers would not be able to simulate quantum mechanical systems efficiently. The general direction of quantum simulation using classical computers is to describe the mean behavior of a system comprised of more than a million degrees of freedom. However, in nuclear physics, atomic physics and chemistry, it is often important to be able to simulate systems made up of tens to hundreds of quantum objects. In this case, the mean field approach does not give a complete enough picture. Rather, it was suggested that having control over quantum systems would permit the first principles construction of many-body systems.

The first simple quantum algorithm was proposed by David Deutsch in 1985, using quantum mechanics to solve essentially the problem of determining if a coin is fair or biased more efficiently than any classical computing algorithm could [4]. But the proposed problem was very limited in scope, and although Deutsch's algorithm demonstrated a concrete way in which quantum computers could beat a classical computer, it was not yet enough to push forward with a major physical research effort to investigate and implement a quantum computer.

The landscape of quantum information processing quickly changed, however, when Peter Shor introduced an integer factoring algorithm which could exponentially outperform any known classical computational algorithm [5]. The problem of factoring large numbers is in fact very computationally difficult, with even the most complex classical computers requiring the lifetime of the universe to complete the task. Interestingly enough, the factorizing problem in reverse, integer multiplication, is very simply implemented with classical computers. These two features, simplicity to multiply and the difficulty to factor, have led to the public-key encryption scheme developed by Rivest, Shamir, and Adleman (RSA), widely used for electronic business communication and transaction applications [6]. Furthermore, new quantum information based encryption schemes were developed by Charles Bennett and researchers at IBM [7]. Such quantum encrypted systems become unbreakable via classical means, relying on the concepts of quantum entanglement and measurement. The possibility that a quantum computer implementing Shor's algorithm could be used for breaking one of the most powerful classical encryption algorithms stimulated considerable interest in both quantum computing theory and physical implementations to try to implement Shor's or develop new quantum encryption protocols. The combination of intellectual interest from scientists in a variety of disciplines, and the realization that quantum computing might have national security implications in the future, made it a topic of increasing importance.

Subsequently, in addition to a lot more quantum computing theory devoted towards

the development of new algorithms and novel applications of quantum information, there was also a new theoretical emphasis on how to physically and experimentally implement a quantum computer. The basic building block of such a quantum computer is the quantum bit or qubit. It is similar to the classical bit in that it is a system comprised of two discrete states, $|0\rangle$ and $|1\rangle$. However, these states need to be any set of two quantum mechanical levels, such as an electron spin or nuclear spin, or a pair of energy levels in an atom, ion or molecule. We next briefly review some of the experimental realizations of quantum processors.

1.2 Experimental implementations of quantum processors

Building a quantum processor first requires a physical pair of quantum levels which are addressable to form a qubit, the ability to couple multiple qubits, and a way to measure the state of the qubits, all while maintaining quantum coherence, such that the quantum information is not degraded and lost. Details about the various aspects of a quantum information processor will be described later in this thesis in chapter 2.

Shortly following the discovery of Shor's algorithm, the first successful experimental implementation of quantum processors was realized using ensembles of nuclear spins in a single molecule as the qubits [8]. The techniques of nuclear magnetic resonance (NMR), which were already developed at a very high level for other applications such as magnetic resonance imaging for medicine and chemistry, were easily transferred for performing operations on the collection of spins. Another important property of NMR qubits was the ability to have long coherence times (on the timescales of seconds) despite being composed of an ensemble of spins. NMR quantum computers progressed very rapidly, moving from simple two-qubit algorithms [8–10] up to ultimately a seven-qubit quantum computer capable of factoring the number 15 and demonstrating the first experimental instance of Shor's algorithm [11]. However, the scalability past seven qubits became very challenging as a result of increasing complexity of experimental controls along with each qubit not being very 'pure' due to being composed of a statistical distribution of molecular spins [12].

Another quantum computing experiment which matured very rapidly was trapped-ion qubits, first proposed by Cirac and Zoller in 1995 [13]. The qubits are defined in the electron or nuclear energy states of ions which are confined and trapped using electromagnetic fields. Multiple qubits couple with one another through the collective motion of all the ions in the trap, mediated via Coulomb interaction. The controls on each trapped-ion qubit and the coupling of multiple qubits are performed via optical excitation using lasers. Here, again the

progress of trapped-ion quantum computing was very rapid owing to the strong experimental foundations in atomic clocks and long coherence times [14] of ions. Currently, trapped-ion quantum computers have demonstrated the ability to couple up to 8 calcium ions [15, 16]. There are also proposals involving the shuttling of ions between arrays of ion traps, and chip-based trap schemes to scale the system further. Nonetheless, the increasing amount of resources necessary to control a large-scale trapped-ion quantum computer is a daunting challenge which will need to be addressed in its own right moving forward.

Although NMR and trapped ions have been relatively successful quantum processor technologies, as we have alluded, the scalability and controls have still remained an outstanding challenge. Another research approach has been solid-state quantum computing, attempting to define and address the qubits on a chip, much like the transistors which are now packed into an integrated circuit on a silicon microprocessor. In terms of qubits there are solid-state approaches which aim to isolate single electron spins as in GaAs quantum dots [17], nitrogen-vacancy centers in diamond [18, 19], and implanted phosphorous donors in silicon [20] as well as approaches which use the collective quantum coherence of Cooper pairs in superconducting tunnel junctions.

The benefits of solid-state approaches are the flexibility and volume of production which current lithographic fabrication techniques provide. Technological development in electron beam lithography has allowed for circuits to be defined with nanoscale precision. This type of control over circuits allows for tailorable qubit energy levels as well as the possibility for tunability in-situ. This is especially the case for the superconducting qubit architecture, which uses macroscopic sized circuits to define the energy levels and coupling strengths of the qubits. Here, the quantum mechanical states can be discrete Cooper-pair charge states on a type of a superconducting tunnel junction known as a Josephson junction. The energy levels of the superconducting qubit are tunable and tailorable via lithography of the Josephson junctions. Another benefit of the superconducting qubit architecture is the all-electrical control using standard microwave and radio-frequency (RF) engineering techniques. The well-developed fabrication protocols and electrical controls could possibly allow for superconducting qubits to be made in large numbers and have tailored and controllable properties.

Yet, in terms of real quantum processors, the superconducting qubit architecture has lagged behind. The primary issue has been reduced coherence times. When the first superconducting qubits arrived on the scene around ten years ago [21], energy relaxation times were on the order of nanoseconds. Recent progress has increased these times to the order of micro-seconds. One standard goal in practice is for the probability of error when per-

forming a quantum operation to be very small, and below what is called the ‘fault-tolerant threshold.’ Quantum computing theorists have placed this threshold at being able to perform over ten-thousand operations before encountering a single error. When a qubit architecture is capable of reaching this low error rate, there are a number of quantum error correcting codes which can be enacted to make the quantum computer fault-tolerant. Whereas trapped-ions and NMR systems have long coherence times making this threshold within reach, the superconducting qubit architecture is still working to catch up.

Nonetheless, with the current state of the art, we will show, in this thesis, the ability to perform simple quantum information processing on a quantum computer built with two superconducting qubits. To some degree the results presented here help put the superconducting qubit architecture on the same map as other more developed quantum systems. Moving forward, however, reaching the ultimate realization of a scaled-up quantum computer is still a hefty challenge.

1.3 Overview of thesis

This thesis work demonstrates the first solid-state implementation of a quantum processor. The qubits which we will work with are superconducting charge qubits, specifically the transmon, which is a modified version of the Cooper-pair box. Coherence times of the transmon qubit have now reached $1 - 2 \mu\text{s}$ setting up the possibility of the quantum information experiments presented in this thesis. The architecture for the multi-qubit coupling will be circuit quantum electrodynamics (QED), an on-chip version of cavity quantum electrodynamics which is the fundamental interaction between a photon and an atom. We will see that this architecture will allow us to use a separate quantum degree of freedom, namely the photons in the cavity, to act as a quantum bus to mediate interactions between non-local qubits.

To be able to fundamentally understand the requirements of building a rudimentary quantum processor, we will start this thesis with some of the basics of quantum information processing (QIP) in chapter 2. This involves identifying a universal set of quantum gates, including single-qubit and two-qubit gates, and how to concatenate them to construct simple quantum algorithms to run on the processor. Chapter 2 will also describe the general quantum state measurement process, including state tomography and entanglement quantification, such that at the end of a set of quantum operations, we may identify the state of the system and the degree of entanglement contained.

That will be followed by chapter 3, in which we will review superconducting qubits, and especially describe the transmon qubit used in this work. There will also be discussion about some of the basics of coupling to a microwave transmission line cavity in circuit QED. We will be able to associate a number of key concepts from cavity QED, including the strong and dispersive coupling regimes, which will be useful for quantum information processing. Furthermore, there will be a discussion about the transmon qubit decoherence properties in the circuit QED regime. Then, in chapter 4, we will describe how the language and concepts of quantum information processing can be defined in our circuit QED system. We will provide a description of how to build a quantum processor with transmon qubits in a microwave cavity, understanding how to implement a universal set of gates. Details for how to generate two-qubit entangling gates will be given, as well as a discussion which expands the idea of the strong dispersive limit of cavity QED to a joint quantum state readout.

The experimental details about building up the quantum processor will be described in chapter 5. We will review some of the sample fabrication details, including optical and electron-beam lithography procedures, performed with the help of Luigi Frunzio, Blake Johnson, and Joseph Schreier. We will also discuss considerations for designing the transmon qubits and the microwave cavities. There will be a specific emphasis on the design of a qubit with incorporated on-chip magnetic flux biasing (developed together with postdoc Johannes Majer, and implemented with postdoc Leonardo DiCarlo). The whole experimental setup from the chip-level up through the cryogenic circuitry and out to the room temperature control electronics will also be described.

The next four chapters, chapter 6–chapter 9, will highlight experiments which progress towards the implementation of quantum algorithms on our solid-state quantum processor.

First, in chapter 6 we describe experiments which point to a very good initialization of the qubits to the ground state. Through a unique strongly-driven vacuum Rabi experiment, we will characterize the average photon number of our microwave cavity, and translate that to an equilibrium ground-state polarization of our qubit at the 99.99% level. Furthermore, the chapter will also describe a number of metrics for characterizing single-qubit gates, demonstrating gate fidelities of 99%, not yet reaching, but approaching the fault-tolerant threshold. We will also highlight some preliminary work towards optimized pulse-shaping to further reduce certain single-qubit gate errors.

Chapter 7 presents the first two-qubit quantum bus experiment, performed with Johannes Majer, and shows the ability to reach both the strong and dispersive regimes of circuit QED with two qubits. The coupling between two qubits via the cavity is demonstrated

spectroscopically via an avoided crossing and the presence of a ‘dark-state.’ We also describe how this two-qubit coupling, which is a virtual-photon cavity-mediated two-qubit interaction, can be used for coherent oscillations between states of the two qubits. These coherent swaps represent a precursor for an entangling two-qubit gate.

Then, chapter 8 presents a new experiment performed together with Leonardo DiCarlo, exploiting qubits with better coherence times and the ability to tune a novel two-qubit coupling on and off with fast timescales. This new interaction is derived from the presence of higher energy levels in the transmon charge-based qubits. Using on-chip magnetic flux bias lines, the transition energies of the qubits are tunable, such that the two-qubit interaction can be turned on and off at nanosecond timescales. This interaction is used to make an entangling conditional-phase gate, permitting the generation of high fidelity two-qubit states, including highly entangled two-qubit states. We further describe how the circuit QED architecture can be used for determining these two-qubit states and characterizing the degree of entanglement in our system.

Chapter 9 culminates with the implementation of two simple quantum algorithms on our superconducting processor, again in work performed together with Leonardo DiCarlo. Specifically, we describe how we program in the two-qubit Deutsch-Jozsa algorithm as well as the four state Grover’s search algorithm, representing the first-ever solid-state quantum processor.

Finally, chapter 10 will present some future directions for superconducting quantum computing, specifically detailing anticipated experiments on three to four qubits.

Quantum Information Processing

QUANTUM computing, once merely a casual thought by a few notable scientists, including Richard Feynman [3], in the 1980s, has blossomed into an interdisciplinary research field encompassing wide areas of physics, computer science, and mathematics. Practical aspects of realizing a physical quantum computing platform are now the subject of countless research programs, with implementations spanning naturally occurring to man-made quantum systems. As introduced in the previous chapter (chapter 1), this thesis will present in detail the first solid-state demonstration of a simple quantum processor. However, before delving into the physical system of circuit quantum electrodynamics (chapter 3 and chapter 4) in which we realize such a processor, it is useful to review and understand the language of quantum operations and algorithms for the sake of perspective and foundation.

Certainly, one could pick up a standard text on this subject, such as Nielsen and Chuang [12], Mermin [22], or Kaye, Laflamme, and Mosca [23], to learn about all the nuances of quantum information processing, from as simple as single-qubit operations to as complex as Shor's factoring algorithm and quantum error correcting codes. Such texts give a broad scope of both the monumental prospects and challenges for making a quantum computer. Whereas long range dreams of breaking RSA encryption and simulating real quantum systems are worth keeping in the back of one's mind for motivation, the practical quantum experimentalist

has to start with building a quantum processor from the ground up and learn the basic quantum algorithms and measurements for only a few qubits.

This chapter will describe quantum information processing on a more fundamental level of quantum operations of a few qubits, picking relevant parts from the standard texts mentioned previously. This will allow us to have a solid point of reference for the actual experimental implementation to be described later in this thesis. We will start by describing a set of single and two-qubit gates which form a universal set for computing (section 2.1, section 2.2, section 2.3). Then we describe the general quantum computing process in terms of building up simple two-qubit algorithms (section 2.4), including the Deutsch-Jozsa and Grover's search. Next, it is important to overview the quantum measurement problem and how we can characterize a quantum state (section 2.5). Then, we demonstrate how to go from simple state identification to the ability to measure the degree of entanglement in a system (section 2.6). Finally, we end the chapter with a discussion about Bell inequalities and its role in quantifying entanglement (section 2.7).

2.1 Universal quantum computing

In classical computing, the most basic unit of information is the bit, with two discrete states 0 and 1. Computational algorithms are comprised of binary logic operations, such as the AND, OR, and NOT gates. The concept of universality refers to the ability to comprise any computational algorithms with a closed set of simple gates [12]. For example, the NAND gate and the NOR gate are each universal, such that using only combinations of each gate, one can accomplish all basic binary logic operations which may be in an algorithm.

In quantum computing, instead of bits, we have qubits, which can be in not only the discrete quantum states $|0\rangle$ and $|1\rangle$, but in fact arbitrary superposition states. Similar to universal logic operations, there also exists a set of quantum gates which are universal, such that combinations of gates can realize complex quantum algorithms. However, unlike the classical computational case where only a single gate is necessary, in the quantum case universality can only be achieved with the combination of arbitrary single qubit gates and a two-qubit gate such as the controlled-NOT (c NOT). The proof for this universality construction of quantum computing is given in Ref. [24], showing that any unitary operation can be approximated to arbitrary accuracy through a quantum circuit.

One of the key differences between the construction of a quantum computation and a classical computation is reversibility. Classical gates such as the NAND, NOR, AND, and

OR are destructive, or irreversible, in the sense that they take two inputs and return a single output. However, reversible classical computing is certainly possible, and requires only a function which takes an n -bit input to an n -bit output. Understanding reversible classical computing is one way to step towards building a quantum computer, as quantum computing is based upon the action of reversible unitary operations in quantum mechanics. For example, the two-qubit gate c NOT is not only a unitary transformation within a two-qubit Hilbert space, but also a two-bit reversible classical operation. Perhaps one of the most interesting wrinkles is that although the c NOT is part of a universal set of gates for quantum computing, it is not universal for classical reversible computation. Rather, it takes at the least a 3-bit Toffoli gate or a cc NOT [25]. The reason that a quantum computer would require fewer number of qubits per gate is the ability to generate entanglement and superposition between qubits using certain gates, such as the Hadamard gate, or Hadamard combined with a c NOT. These aspects will be explored in detail in the rest of this chapter.

The operations of a quantum computer can thus be summarized as the combination of unitary operations on multiple qubits, and built up in a *quantum circuit* formalism [12]. The operations on an n -qubit quantum circuit will be sequences of quantum gates, all of which will be reversible transformations on the n -qubit register. Next, we build up this model of quantum computing with the introduction of the most basic building blocks, the single-qubit gates.

2.2 Single-qubit gates

Perhaps the simplest quantum operations to consider are those for just a single qubit. A single qubit is comprised of only two quantum states, $|0\rangle$ and $|1\rangle$, and single-qubit gates traverse through the Hilbert space spanned by these two states. We can represent a single qubit by the state vector

$$|\psi\rangle = a|0\rangle + b|1\rangle, \quad (2.1)$$

with complex amplitudes a and b which are normalized $|a|^2 + |b|^2 = 1$. All single-qubit gates can be represented as 2×2 unitary matrices. The space of such matrices are spanned by the

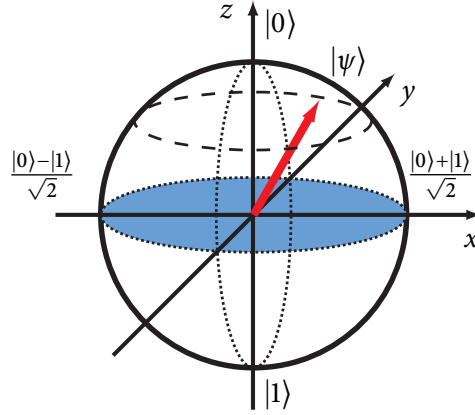


Figure 2.1: The Bloch sphere. Geometrical representation of the state space of a single qubit (two-level quantum system). The state of the qubit is represented by the Bloch vector, which is a unit vector within the sphere, describe by two numbers, θ and ϕ .

identity (referred to as $\mathbb{1}$ or I in this thesis) along with the three Pauli matrices,

$$\sigma_x \equiv X \equiv \begin{pmatrix} 0 & 1 \\ 1 & 0 \end{pmatrix} \quad (2.2a)$$

$$\sigma_y \equiv Y \equiv \begin{pmatrix} 0 & -i \\ i & 0 \end{pmatrix} \quad (2.2b)$$

$$\sigma_z \equiv Z \equiv \begin{pmatrix} 1 & 0 \\ 0 & -1 \end{pmatrix}. \quad (2.2c)$$

These Pauli matrices can be used to generate rotations about the x , y , and z axes to traverse the entire two-qubit space, often pictorially represented by the Bloch sphere (shown in figure 2.1).

The rotation operations, which are also unitary gates, are given by

$$R_x(\theta) \equiv X_\theta \equiv e^{-i\theta\sigma_x/2} = \begin{pmatrix} \cos \frac{\theta}{2} & -i \sin \frac{\theta}{2} \\ -i \sin \frac{\theta}{2} & \cos \frac{\theta}{2} \end{pmatrix} \quad (2.3a)$$

$$R_y(\theta) \equiv Y_\theta \equiv e^{-i\theta\sigma_y/2} = \begin{pmatrix} \cos \frac{\theta}{2} & -\sin \frac{\theta}{2} \\ \sin \frac{\theta}{2} & \cos \frac{\theta}{2} \end{pmatrix} \quad (2.3b)$$

$$R_z(\theta) \equiv Z_\theta \equiv e^{-i\theta\sigma_z/2} = \begin{pmatrix} e^{-i\theta/2} & 0 \\ 0 & e^{i\theta/2} \end{pmatrix}, \quad (2.3c)$$

where θ is the angle of rotation.

We can combine the Pauli operators and the identity to form a generalized rotation about

any axis \hat{n} given by

$$R_{\hat{n}}(\theta) \equiv \exp(-i\theta\hat{n} \cdot \vec{\sigma}/2) = \cos \frac{\theta}{2} \mathbb{1} - i \sin \frac{\theta}{2} (n_x \sigma_x + n_y \sigma_y + n_z \sigma_z). \quad (2.4)$$

Some important single-qubit gates are rotations of $\theta = \pm\pi$ and $\theta = \pm\pi/2$, often referred to as π -pulses and $\pi/2$ -pulses, respectively. We can identify certain rotations with the Pauli matrices, $R_y(\pi) = -i\sigma_y$, $R_x(\pi) = -i\sigma_x$, $R_z(\pi) = -i\sigma_z$. Experimentally, it is often simpler to access rotations about the three Cartesian axes and to use the set of rotation operators to build up the more standard single-qubit gates which are used throughout the theoretical literature and quantum computing texts. Specifically, quantum circuits often feature the single-qubit gates such as the Hadamard, X gate, Z gate, phase gate, and $\pi/8$ gate, given by

$$H = \frac{1}{\sqrt{2}} \begin{pmatrix} 1 & 1 \\ 1 & -1 \end{pmatrix} \quad \text{Hadamard gate} \quad (2.5a)$$

$$X = \begin{pmatrix} 0 & 1 \\ 1 & 0 \end{pmatrix} \quad \text{bit-flip gate} \quad (2.5b)$$

$$Z = \begin{pmatrix} 1 & 0 \\ 0 & -1 \end{pmatrix} \quad \text{phase-flip gate} \quad (2.5c)$$

$$S = \begin{pmatrix} 1 & 0 \\ 0 & i \end{pmatrix} \quad \text{phase gate} \quad (2.5d)$$

$$T = \begin{pmatrix} 1 & 0 \\ 0 & \exp(i\pi/4) \end{pmatrix} \quad \pi/8 \text{ gate.} \quad (2.5e)$$

The Hadamard gate is very significant because it enables the qubit interference which is necessary for many quantum algorithms. As we will show later in section 2.4, the Hadamard gate allows one to access quantum parallelism, such that a single function may be evaluated for a whole set of computational states at once. In terms of single-qubit rotations, the Hadamard reflects a $\pi/4$ rotation around the y axis followed by a π rotation around the z axis.

The X gate, also commonly referred to as the NOT or bit-flip gate changes the computational basis value from one state to the other. It is equivalent to the σ_x Pauli operator, or a rotation around the y axis by π . The Z gate, or the phase-flip gate, is simply the Pauli σ_z operator and represents an azimuthal rotation of the Bloch vector by π . The phase gate can be seen to be the square root of the Z gate, as $S^2 = Z$, and reflects an azimuthal rotation by

$\pi/2$. The T or $\pi/8$ gate is the square root of the phase gate, $T^2 = S$. As noted in Ref. [12], this is quite an unfortunate name given that it is a rotation of $\pi/4$ which enters.

Therefore, although a lot of the literature presents algorithms with a specific library of single-qubit gates, in the end, they are all simply combinations of rotations about x , y and z , which can be more easily accessible in particular experimental architectures. In Ref. [12] the Hadamard, S , and T gates are part of the universal set for quantum computing. Here, we will later show (chapter 4) that we can experimentally access the Cartesian rotation operators, and we will use the appropriate combinations of such gates to eventually build up simple algorithms (chapter 9). Furthermore, the specific set of rotations of $\pi/2$ about x , y , and z generate the single-qubit Clifford group [26]. Later in this thesis we will discuss Clifford group operations with regards to determining the average fidelity of single-qubit operations (chapter 6).

2.3 Two-qubit entanglement gates

The previous section dealt with only single qubit logic. We can now expand to two qubits, and investigate unique gates in this expanded Hilbert space which are not simply products of single-qubit operations. One class of such gates are *controlled* operations. One qubit can be labeled the control qubit and the other the target qubit. Controlled operations involve an action on the target qubit which will change depending on the state of the control qubit. Such two-qubit gates are the basis of generating entanglement and along with arbitrary single-qubit rotations, complete the universal set (section 2.1) for approximating multi-qubit unitary operations.

2.3.1 c NOT gate

The controlled-NOT or c NOT is the “canonical” two-qubit entanglement gate, used throughout theoretical constructions of quantum algorithms as well as described in depth in standard quantum computing texts [12, 22, 23]. The circuit representation for the c NOT gate is shown in figure 2.2, with two inputs corresponding to the control and target qubits and then two outputs. This two-in, two-out operation reflects a difference from a classical computing operation where two-bit gates end with a single output bit. For example, the classical analog of the c NOT is the XOR gate, which takes two bits A and B and returns a single bit corresponding

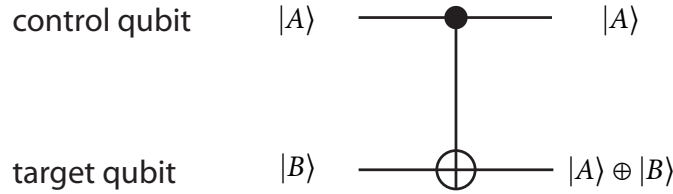


Figure 2.2: Circuit representation for the controlled-*NOT* gate. In the quantum circuit model, operations on different qubits are represented on different horizontal tracks. For the *cNOT* gate, there are two qubits and two tracks, a control qubit along the upper track and a target qubit along the lower track. In the *cNOT* gate, the control qubit is symbolized with a solid black circle and the target qubit is symbolized with an open circle.

to the modulo 2 addition operator \oplus ,

$$\begin{aligned} A \oplus 0 &= A \\ A \oplus 1 &= 1 - A = \bar{A}. \end{aligned} \tag{2.6}$$

Classically, this is an irreversible process. However, the *cNOT* gate achieves a similar result, but is reversible and describable by a unitary matrix. The action of the *cNOT* gate is to leave the target qubit alone if the control qubit is in state $|0\rangle$ and to flip the target qubit if the control qubit is in state $|1\rangle$. We can write this for two qubits as $|A\rangle|B\rangle \rightarrow |A\rangle|B \oplus A\rangle$. Therefore, *cNOT* can be written in a 4×4 unitary matrix representation with the columns and rows being the computational basis states of two-qubits, $|0, 0\rangle$, $|0, 1\rangle$, $|1, 0\rangle$, and $|1, 1\rangle$ as

$$U_{cNOT} = \begin{pmatrix} 1 & 0 & 0 & 0 \\ 0 & 1 & 0 & 0 \\ 0 & 0 & 0 & 1 \\ 0 & 0 & 1 & 0 \end{pmatrix}. \tag{2.7}$$

We can recognize the difference between the *cNOT* and the XOR in that the *cNOT* is a reversible operation, whereas the XOR actually has erased the information in the control bit, leaving only a single bit of information in the target bit. However, it is also the association of the *cNOT* with the classical XOR operation which makes it a ubiquitous reference in quantum circuits, as it permits the possibility of transferring computation schemes written for reversible classical computation over into the quantum language.

Therefore, given single-qubit gates and the *cNOT* two-qubit gate, we can start to explore more complex quantum algorithms through their concatenation in quantum circuits. However, when we try to relate the quantum circuit formalism to a particular experimental

implementation of qubits, the c NOT may or may not be the most natural selection for a two-qubit primitive entangling gate. Rather, as practical quantum engineers, it is critical to recognize the type of qubit interactions present, and then to employ the appropriate gate which makes the most efficient use of resources. The formally solved quantum protocols and algorithms which are simply broken down into single qubit unitaries and c NOT gates can then be *recompiled* into the gates which are most easily accessible in a particular experimental architecture.

2.3.2 c -Phase gate (cU_{ij})

A particular coupling that arises in many experimental architectures such as nuclear magnetic resonance (NMR), as well as flux [27] and charge superconducting qubits [28], is the ZZ -interaction, where the interaction Hamiltonian between qubit 1 and 2 is given by

$$H_{1,2}^{ZZ} = \frac{E_{1,2}^{ZZ}}{4} \sigma_z^{(1)} \otimes \sigma_z^{(2)}, \quad (2.8)$$

where \otimes is the outer product. This interaction thus corresponds to a unitary time-evolution given by $U_{1,2}^{ZZ} = \exp[-iH_{1,2}^{ZZ}t]$. Given the ability to turn on and off this interaction over a time of $t = \hbar\pi/E_{1,2}^{ZZ}$ corresponds to

$$U_{1,2}^{ZZ} = \exp[i\pi/4] \begin{pmatrix} 1 & 0 & 0 & 0 \\ 0 & -i & 0 & 0 \\ 0 & 0 & -i & 0 \\ 0 & 0 & 0 & 1 \end{pmatrix}, \quad (2.9)$$

where we have used the computational basis states $|0, 0\rangle$ [with corresponding vector $(1, 0, 0, 0)$], $|0, 1\rangle$ [with corresponding vector $(0, 1, 0, 0)$], $|1, 0\rangle$ [with corresponding vector $(0, 0, 1, 0)$], and $|1, 1\rangle$ [with corresponding vector $(0, 0, 0, 1)$] where $|n_1, n_2\rangle$ denotes excitation level n_1 on qubit 1 and n_2 on qubit 2. This unitary operation can be combined with rotations around z of each qubit, $R_z^{(1)}(-\pi/2)$ and $R_z^{(2)}(\pi/2)$, so that we arrive (up to a global phase factor) at the

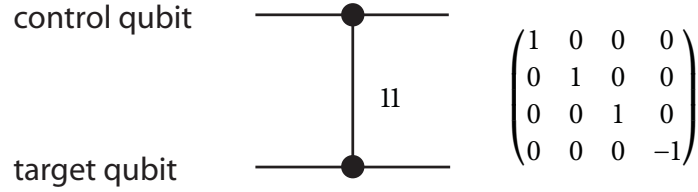


Figure 2.3: Circuit representation for the controlled-Phase gate. In the c -Phase gate, also commonly labeled as cU_{ij} , both the control and target qubit are symbolized with a solid black circle, and the specific computational basis state which picks up the -1 phase shift is written to the side as ij . In the case shown here $ij = 11$.

conditional-phase or c -Phase gate,

$$cU_{11} = \left[R_z^{(i)}(-\pi/2) \otimes R_z^{(j)}(-\pi/2) \right] U_{i,j}^{ZZ} = \exp[i\pi/4] \begin{pmatrix} 1 & 0 & 0 & 0 \\ 0 & 1 & 0 & 0 \\ 0 & 0 & 1 & 0 \\ 0 & 0 & 0 & -1 \end{pmatrix}. \quad (2.10)$$

This particular c -Phase gate corresponds to a phase shift of π on the target qubit excited state when the control qubit is in the excited state $|1\rangle$. The circuit representation is shown in figure 2.3. Through manipulating the rotation around z of either qubit, we can form any of the three other c -Phase gates as well,

$$cU_{10} = \begin{pmatrix} 1 & 0 & 0 & 0 \\ 0 & 1 & 0 & 0 \\ 0 & 0 & -1 & 0 \\ 0 & 0 & 0 & 1 \end{pmatrix}, \quad cU_{01} = \begin{pmatrix} 1 & 0 & 0 & 0 \\ 0 & -1 & 0 & 0 \\ 0 & 0 & 1 & 0 \\ 0 & 0 & 0 & 1 \end{pmatrix}, \quad cU_{00} = \begin{pmatrix} -1 & 0 & 0 & 0 \\ 0 & 1 & 0 & 0 \\ 0 & 0 & 1 & 0 \\ 0 & 0 & 0 & 1 \end{pmatrix}, \quad (2.11)$$

reflecting the control qubit state being $|0\rangle$ and then also swapping the roles of the control and target qubits.

The c NOT gate and c -Phase gate are intimately related, differing by only single-qubit rotations. The c NOT can be built (see figure 2.4) from the c -Phase with Hadamard gates on the target qubit,

$$U_{c\text{NOT}} = H^{(2)} cU_{11} H^{(2)}. \quad (2.12)$$

Therefore, although many quantum algorithms are written in terms of c NOT operations as the two-qubit operation, it is not too difficult to translate these sequences in terms of c -

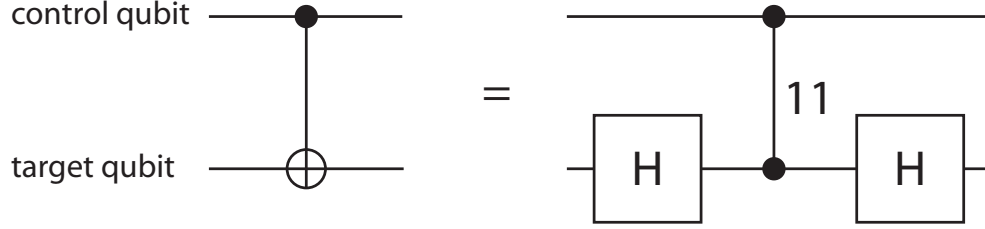


Figure 2.4: Circuit form for constructing a c NOT from a c -Phase gate. A c NOT gate can easily be constructed from the c -Phase gate cU_{11} by performing single-qubit Hadamard gates on the target qubit before and after.

Phase along with single-qubit rotations. Examples are the Grover's search and Deutsch-Jozsa algorithms (section 2.4) discussed later in this chapter. Ref. [22] refers to the c -Phase gate in fact as a more natural and efficient gate compared to c NOT and we will find that in the circuit QED charge qubit architecture which is the experimental focus of this thesis, the c -Phase will be the two-qubit gate of choice (section 4.3.3).

2.3.3 i SWAP and $\sqrt{i$ SWAP gates

Another interaction scheme which arises quite frequently in experimental quantum computing implementations is the XY or transverse qubit-qubit coupling. The relevant interaction Hamiltonian is given by

$$H_{1,2}^{XY} = \frac{E_{1,2}^{XY}}{4} \left(\sigma_x^{(1)} \sigma_x^{(2)} + \sigma_y^{(1)} \sigma_y^{(2)} \right), \quad (2.13)$$

and often written in terms of Pauli raising and lower operators,

$$H_{1,2}^{XY} = \frac{E_{1,2}^{XY}}{2} \left(\sigma_+^{(1)} \sigma_-^{(2)} + \sigma_-^{(1)} \sigma_+^{(2)} \right). \quad (2.14)$$

This type of coupling can be realized in quantum dot spins [17], nuclear spins interacting via a two-dimensional gas [29], as well as Josephson charge qubits coupled either by a transmission line resonator [30] or other Josephson junctions.

The time-evolution of the two-qubit system due to this type of coupling does not simply result in a controlled operation, such as cU_{ij} or c NOT. Instead, it is most suited for generating the i SWAP and $\sqrt{i$ SWAP two-qubit gates, which can also form part of a universal set when combined with appropriate single-qubit rotations.

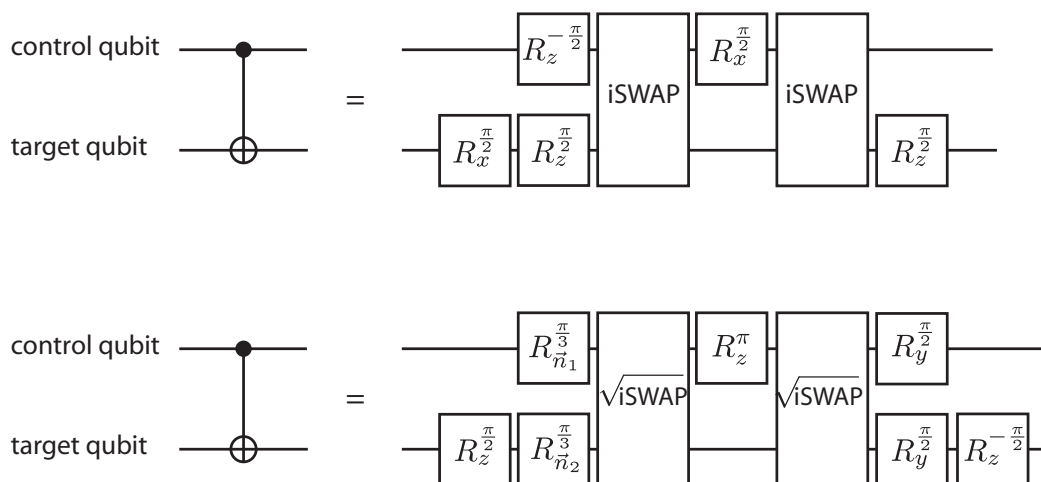


Figure 2.5: Circuit form for constructing a c NOT from an i SWAP or $\sqrt{i$ SWAP gate. When the accessible two-qubit interaction is XY and not ZZ , the natural two-qubit entangling gates are either the i SWAP or $\sqrt{i$ SWAP. Creating a c NOT gate then requires the concatenation of at least two of each of the gates, combined with multiple single-qubit rotations around various directions.

By turning on the XY interaction for a time $t = \pi\hbar/E_{1,2}^{XY}$, we arrive at the i SWAP operation,

$$U_{i\text{SWAP}} = \exp\left[-iH_{1,2}^{XY} \frac{\pi}{E_{1,2}^{XY}}\right] = \begin{pmatrix} 1 & 0 & 0 & 0 \\ 0 & 0 & i & 0 \\ 0 & i & 0 & 0 \\ 0 & 0 & 0 & 1 \end{pmatrix}. \quad (2.15)$$

One cannot construct a c NOT from just simple single-qubit rotations along with a single i SWAP. However, if we are allowed to use two i SWAP gates, then we do have this possibility,

$$U_{c\text{NOT}} = \left[\mathbb{1}^{(1)} \otimes R_x^{(2)}(\pi/2)\right] \left[R_z^{(1)}(-\pi/2) \otimes R_z^{(2)}(\pi/2)\right] U_{i\text{SWAP}} \left[R_x^{(1)}(\pi/2) \otimes \mathbb{1}^{(2)}\right] U_{i\text{SWAP}} \left[\mathbb{1}^{(1)} \otimes R_z^{(2)}(\pi/2)\right], \quad (2.16)$$

and shown in quantum circuit form in figure 2.5.

Similarly, the same XY interaction can be turned on for half of the time $t = \pi\hbar/2E_{1,2}^{XY}$,

which then gives rise to the $\sqrt{i\text{SWAP}}$ gate

$$U_{\sqrt{i\text{SWAP}}} = \begin{pmatrix} 1 & 0 & 0 & 0 \\ 0 & 1/\sqrt{2} & i/\sqrt{2} & 0 \\ 0 & i/\sqrt{2} & 1/\sqrt{2} & 0 \\ 0 & 0 & 0 & 1 \end{pmatrix}. \quad (2.17)$$

Again, just as for the $i\text{SWAP}$, it takes two $\sqrt{i\text{SWAP}}$ gates to construct a $c\text{NOT}$ gate along with single-qubit rotations,

$$U_{c\text{NOT}} = e^{i\pi/4} R_z^{(2)}(\pi/2) R_{\vec{n}_1}^{(1)}(\pi/3) R_{\vec{n}_2}^{(2)}(\pi/3) \sqrt{i\text{SWAP}} \\ R_z^{(1)}(\pi) \sqrt{i\text{SWAP}} [R_y^{(1)}(\pi/2) \otimes R_y^{(2)}(\pi/2)] R_z^{(2)}(-\pi/2)$$

where $\vec{n}_1 = (1, 1, -1)/\sqrt{3}$ and $\vec{n}_2 = (-1, 1, 1)/\sqrt{3}$.

The constructions of $c\text{NOT}$ in terms of $i\text{SWAP}$ and $\sqrt{i\text{SWAP}}$ can get quite expensive in terms of the time it takes to perform all the operations. Although single-qubit rotations are relatively simple to implement, at present they certainly take up a non-trivial fraction of the relaxation lifetime of the qubit. In addition, the recipes above require two copies of either $i\text{SWAP}$ or $\sqrt{i\text{SWAP}}$. The time it takes to perform either gate is dependent on the interaction strength and the ability to turn the interaction on and off very rapidly. Depending on the qubit architecture, implementing longer gate sequences, which is necessary for performing quantum algorithms, will require a careful economy of the total gates used, both single-qubit rotations and entangling gates.

2.4 Quantum algorithms

With access to a universal set of quantum gates, we can now construct algorithms which exploit superposition and entanglement to perform specific computations. Here, we will be able to see how quantum computers can theoretically solve certain problems more efficiently than classical computers. To get a feel for how such quantum algorithms can be built, we can first investigate how a quantum computer can be programmed to evaluate some function $f(x)$ for multiple values of x simultaneously, or what is known as *quantum parallelism*. Then, we move on to discuss a few quantum algorithms which are implementable in the most basic quantum processors made up of only two qubits.

2.4.1 Quantum parallelism in an algorithm

Suppose we start with a register of $n + m$ qubits, where n qubits can be thought of as control qubits on which we can give a specific set of inputs, to then perform a computation on m target qubits which will be the output. The separate registers allow for reversibility of the computation. Now suppose we have an $(n + m) \times (n + m)$ unitary transformation U_f in which we encode a function $f(x)$ such that its action on any computational basis state gives

$$U_f(|x\rangle_n |y\rangle_m) = |x\rangle_n |y \oplus f(x)\rangle_m, \quad (2.18)$$

where x and y are n and m bit integers and \oplus represents bitwise addition mod 2. By starting with the output register of qubits in $|0\rangle$ it is possible to evaluate $f(x)$ and have the result in the output register,

$$U_f(|x\rangle_n |0\rangle_m) = |x\rangle_n |f(x)\rangle_m. \quad (2.19)$$

However, now we can employ the ability to produce superpositions of each qubit to operate U_f only after applying a Hadamard transformation on all the input qubits. The n -qubit Hadamard gives the maximal superposition state of the full register. For example, with two qubits,

$$\begin{aligned} (H^{(1)} \otimes H^{(2)})(|0\rangle|0\rangle) &= \frac{1}{\sqrt{2}}(|0\rangle + |1\rangle) \frac{1}{\sqrt{2}}(|0\rangle + |1\rangle) \\ &= \frac{1}{2}(|00\rangle + |01\rangle + |10\rangle + |11\rangle) \\ &= \frac{1}{2}(|0\rangle_2 + |1\rangle_2 + |2\rangle_2 + |3\rangle_2) \end{aligned} \quad (2.20a)$$

giving a maximal superposition state involving all the computational states in the 2-qubit input register. Therefore, now by applying U_f after the n -qubit Hadamard, $H^{\otimes n} = H^{(1)} \otimes H^{(2)} \otimes \dots \otimes H^{(n)}$, on the ground state of the n -qubit register, we find

$$U_f(H^{\otimes n} \otimes \mathbb{1}_m)|0\rangle_n |0\rangle_m = \frac{1}{\sqrt{2^n}} \sum_x |x\rangle_n |f(x)\rangle_m, \quad (2.21)$$

which now contains all evaluations of the function f , despite having only operated f once by applying U_f .

Note that the problem remains in how to access all this information about f . It is possible to measure in the computational basis states of each of the individual qubits. Yet, to simply

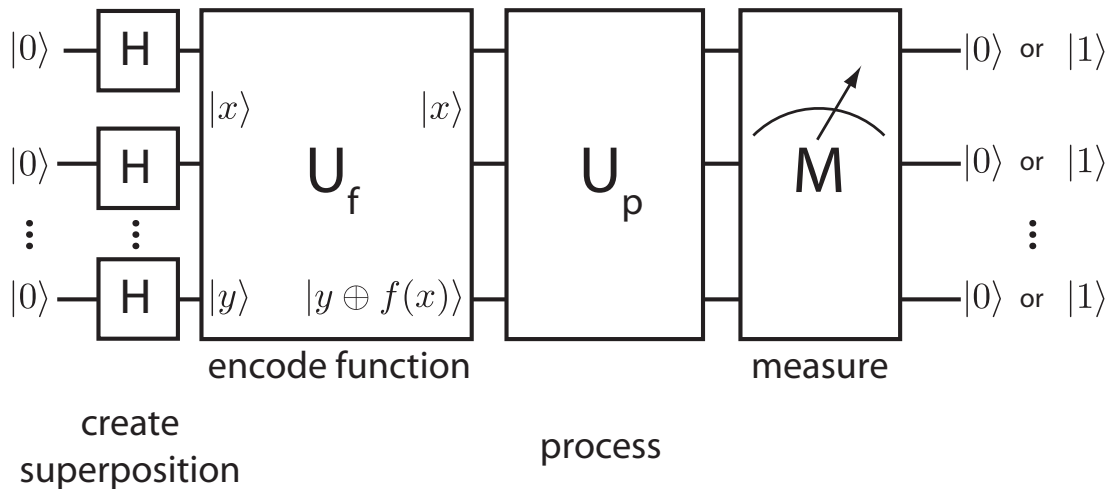


Figure 2.6: Anatomy of a quantum algorithm. The general quantum algorithm can be broken down into four main parts. The first stage takes an initialized register of qubits into a superposition state via single-qubit operations, such as Hadamard gates. Then, a multi-qubit function f is applied through a multi-qubit unitary operation which can be comprised of single-qubit and two-qubit gates. Next, a processing step also made up of single-qubit and two-qubit gates is performed to allow interpretation of the qubit register in the computational basis. Finally, measurements are performed on all or some of the qubits.

measure all of the m qubits in the output register would only randomly reveal with equal probability some choice of $x_0 < 2^n$. Therefore, we would only find out about the function $f(x_0)$ at a particular random x_0 . In this case, we have only performed what a classical computer could easily have done.

However, quantum algorithms often employ a further stage applying additional unitary gates which serve to form relationships between multiple evaluations of f for different values of x . Here, to be able to know the values of certain combinations of f also means losing the ability to know about individual values of $f(x)$. A classical computer could only give the values of relationships by making all of the individual independent evaluations. The advantage gained through quantum algorithms is through the quantum mechanical concept of interference, being able to tradeoff one kind of information for another.

Therefore, we can summarize the general computation structure with primarily four stages of a quantum algorithm: the register of qubits must be placed into a superposition; then a unitary function which encodes a function is applied; next a processing step to transfer relational information into a form which can be readout; and finally a multi-qubit state readout. These steps are summarized in figure 2.6 in a quantum circuit model.

2.4.2 Deutsch-Jozsa algorithm

One of the simplest demonstrations of how a quantum algorithm can outperform a classical computation is with the Deutsch-Jozsa (DJ) algorithm [31]. It represents a situation with a quantum tradeoff of one particular information for a different global information. It is also an example of *quantum phase kick-back*, where the target qubit can be placed in an eigenstate of a controlled unitary such that an eigenvalue can be associated with the state of the control register.

The DJ algorithm solves Deutsch's problem [4] which can be succinctly described as finding out whether a function f which takes a single bit x to a single bit $f(x)$, is constant or balanced. There are only four possible functions that take one bit to one bit, two of which are constant, $f(x) = 0$, $f(x) = 1$, and two of which are balanced, $f(x) = x$, $f(x) = 1 - x$. Another way of motivating the problem is to consider the case of finding out whether a coin is biased (constant) or fair (balanced). There are two possible fair coins, with heads and tails on each side, and two possible biased coins, with two heads or two tails.

Classically Deutsch's problem is solved by querying $f(x)$ for all values of the input bit $x = 0, 1$, or looking at both sides of the coin. However, the DJ algorithm will allow us to avoid finding out the information of specifically $f(x = 0)$ or $f(x = 1)$, in favor of knowledge about the nature of the function, as balanced or constant. This is especially relevant when evaluating f might be very computationally expensive.

Consider a unitary transformation which applies one of the four possible functions, operating on two qubits, one of which serves as a control qubit, and the other as the target qubit,

$$U_f (|x\rangle |y\rangle) = |x\rangle |y \oplus f(x)\rangle. \quad (2.22)$$

The two constant functions are reflected by always giving 0 or always giving 1 regardless of the input bit. These functions are implemented using $U_{f_0} = \mathbb{1} \otimes \mathbb{1}$ and $U_{f_1} = \mathbb{1} \otimes X$, for results 0 and 1, respectively. The two balanced functions are reflected by always returning the same value, such that $f(x) = x$, or always returning the opposite value, where $f(x) = 1 - x$. These functions are applied using $U_{f_2} = \text{cNOT}$, and $U_{f_3} = z\text{-cNOT}$, respectively. The unitary

matrix corresponding to z - c NOT is

$$U_{z-c\text{NOT}} = \begin{pmatrix} 0 & 1 & 0 & 0 \\ 1 & 0 & 0 & 0 \\ 0 & 0 & 1 & 0 \\ 0 & 0 & 0 & 1 \end{pmatrix}, \quad (2.23)$$

where the state of the target qubit is flipped when the control qubit is in the state $|0\rangle$.

The DJ algorithm is given in quantum circuit form as in figure 2.7. The algorithm is very simple. Let qubit 1 be the control and qubit 2 be the target. We first apply rotations around the y axis of $\pi/2$ on the target qubit and $-\pi/2$ on the control qubit to start, placing them into the superpositions $|\psi\rangle_1 = (|0\rangle + |1\rangle)/\sqrt{2}$ and $|\psi\rangle_2 = (|0\rangle - |1\rangle)/\sqrt{2}$. That is then followed by the application of any of the four unitary transformations that implement either a balanced or constant function.

For illustrative purposes, suppose we apply the identity unitary $U_{f_0} = \mathbb{1} \otimes \mathbb{1}$ for one of the constant functions. In this case, the two superpositions remain the same. The processing step consists of applying a $R_y(-\pi/2)$ rotation on the target qubit and a $R_y(\pi/2)$ rotation on the control qubit, which in the case nothing is done in the unitary transformation stage, simply undoes the original superpositions created and return the register to the initial states.

However, suppose we instead have a balanced function, such that the unitary is $U_{f_2} = c\text{NOT}$. An interesting thing occurs in this case, as the superposition state of qubit 2 is actually an eigenstate of $c\text{NOT}$, with an eigenvalue of -1 , no matter the state of qubit 1:

$$c\text{NOT} |x\rangle \left(\frac{|0\rangle - |1\rangle}{\sqrt{2}} \right) = (-1)^x |x\rangle \left(\frac{|0\rangle - |1\rangle}{\sqrt{2}} \right). \quad (2.24)$$

This can be interpreted as the eigenvalue giving a phase ‘kick back’ to the control qubit. Here, an entangled state of the two qubits is not an intermediary step, but rather the entangling gate serves to return a phase onto the control register. Therefore, in the case of the DJ algorithm, the original positive superposition on qubit 1, $|\psi\rangle_1 = (|0\rangle + |1\rangle)/\sqrt{2}$, gets turned into a negative superposition, $|\psi\rangle_1 = (|0\rangle - |1\rangle)/\sqrt{2}$. Then, the final set of rotations in the processing step will place the control qubit into the state $|1\rangle$ and allow the target qubit to return to the state $|0\rangle$.

A final measurement of the state of the control qubit is in fact all which is needed at the end of the algorithm. From the state being either $|0\rangle$ or $|1\rangle$, we are able to discern whether the applied unitary corresponds to a balanced or constant function. Throughout the algorithm,

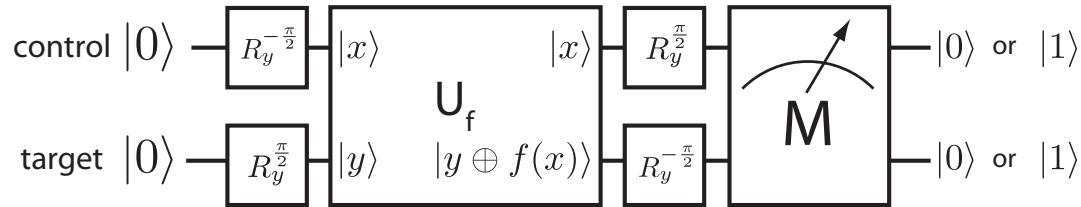


Figure 2.7: Deutsch-Jozsa algorithm. The two qubits are initialized in their ground states. The first superposition step involves only single-qubit rotations. The functions, either constant or balanced, are encoded through applying the appropriate two-qubit unitary. The processing stage involves only single-qubit rotations, serving to rotate the qubits to either $|0\rangle$ or $|1\rangle$ depending on the form of the function. The final measurement need only be performed on the control qubit to determine the nature of the function.

the target qubit simply goes along for the ride, providing the quantum phase kick-back necessary in the case of the balanced functions.

With the DJ algorithm, we thus extract information about $f(0) + f(1)$, instead of finding out specifically what $f(0)$ or $f(1)$ are, which would be necessary for any classical computation process. A classical algorithm would have required two calls to the function to determine the flavor of the function, whereas here we can succeed deterministically with a single call. Note that the DJ algorithm can be extended to more qubits for functions which deal with inputs greater than a single bit. In this case, it also remains a deterministic algorithm requiring a single call to the multi-qubit unitary, so long as the entire space of functions can be split into either balanced or constant functions. Chapter 9 will demonstrate the implementation of the DJ algorithm in our superconducting circuit QED processor.

2.4.3 Grover's search algorithm

Another class of algorithms are for search with a quantum computer. Consider the problem of searching for a specific name in an unordered database of N names. Classically, the best that one can do is to choose names sequentially or at random, a process which takes on average $N/2$ queries. However, Grover's quantum search algorithm [32] can give a polynomial speed-up on the classical case. Specifically, for searching an n -bit integer out of a list of $N = 2^n$ different integers, Grover's algorithm does better than random classical queries by a factor of $1/\sqrt{N}$.

Suppose we start with $\log_2 N$ qubits, and represent each of the database entries with a ket, $\{|1\rangle, |2\rangle, \dots, |N\rangle\}$. Next, we can imagine a quantum *oracle* which will be a black box for

performing the search over the N entries. We can think of the oracle as applying a unitary transformation U_O to the entire qubit register, with the properties that

$$U_O |\alpha\rangle = -|\alpha\rangle \quad (2.25a)$$

$$U_O |x\rangle = |x\rangle, \quad \text{for all } x \neq \alpha. \quad (2.25b)$$

The transformation thus has the effect of marking with a phase the specific entry $|\alpha\rangle$, which is the entry we are searching for from the entire database. The processing of the search is performed with the application of another unitary transformation U_ϕ which induces a conditional phase shift on every single state except for the first state, $|1\rangle$,

$$U_\phi |1\rangle = |1\rangle \quad (2.26a)$$

$$U_\phi |x\rangle = -|x\rangle, \quad \text{for all } x \neq 1. \quad (2.26b)$$

Grover's algorithm is then implemented as follows:

- Create an equal superposition state, by applying the n -qubit Hadamard, $H^{\otimes n}$:

$$|s\rangle = \frac{1}{\sqrt{N}} \sum_{x=1}^N |x\rangle. \quad (2.27)$$

- Perform a Grover iteration $R \approx \pi\sqrt{2^n}/4$ times, where a Grover iteration involves
 1. Apply the oracle transformation U_O .
 2. Apply the n -qubit Hadamard, $H^{\otimes n}$
 3. Apply the conditional phase transformation U_ϕ
 4. Apply the n -qubit Hadamard, $H^{\otimes n}$
- Measure the final qubit register, which should give the computational basis state we are searching for $|\alpha\rangle$.

In terms of the generalized quantum algorithm, the Grover iteration (figure 2.8) contains both the function encoding part as well as the processing. However, it must be repeated multiple times due to the nature of the algorithm, which can be understood as a routine which turns a phase into a detectable amplitude. With only conditional phase transformations and n -qubit Hadamard gates, multiple Grover iterations serve to amplify the amplitude of the target state each time.

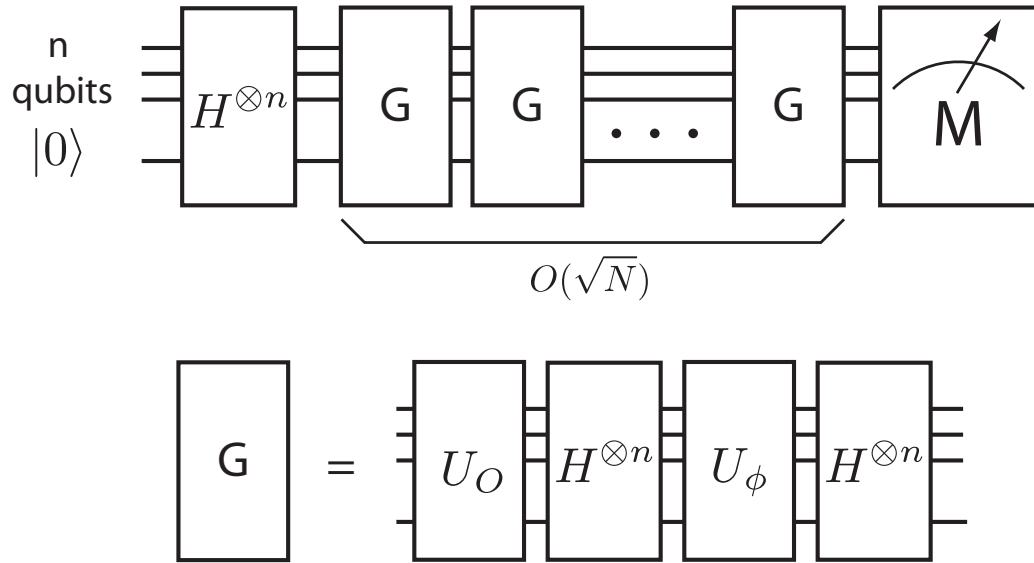


Figure 2.8: Grover’s search algorithm. The algorithm consists of an initial n -qubit Hadamard $H^{\otimes n}$ for generating a full superposition of all the qubit states. The rest of the algorithm requires repeating the Grover iteration G until the amplitude of the searched state is ~ 1 . The Grover iteration consists of the application of an oracle unitary function U_O which performs the search, followed by processing steps involving $H^{\otimes n}$ and a conditional phase transformation U_ϕ , whose properties are discussed in the main text.

The first part of the Grover iterate, the multi-qubit oracle U_O does all of the encoding work, by marking the phase of the searched for target state. If such a phase could easily be detected then the entire search problem would be finished. Unfortunately, to distinguish that phase requires the processing stages of the other three parts of the Grover iterate, which we will call $U_\perp = H^{\otimes n}U_\phi H^{\otimes n}$. This operator can be written as $(2|s\rangle\langle s| - \mathbb{1})$. We can understand what the operator does by applying it to an arbitrary superposition state $|\phi\rangle = \sum_x a_x |x\rangle$ where the mean of the amplitudes is given by $m = \sum_x a_x/N$. In this case,

$$U_\perp |\phi\rangle = \sum_x (m - a_x) |x\rangle, \tag{2.28}$$

which represents returning a superposition state that has mean $(N - 1)m$, by flipping the amplitude of all the states around the mean m .

It is precisely this mean inversion which allows an amplitude amplification of the target state $|a\rangle$ in the Grover iteration. We can use a picture to represent the action of the Grover iteration. In figure 2.9a, we start off with having applied the first $H^{\otimes n}$, taking us to the equal superposition state with all basis states having the same amplitude of $1/\sqrt{N}$. The

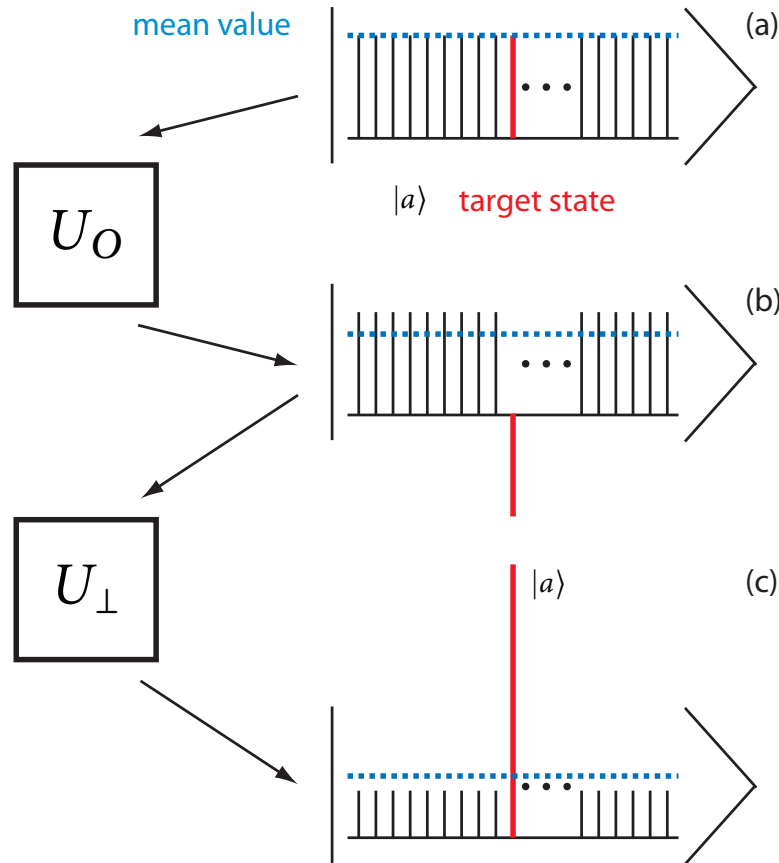


Figure 2.9: Cartoon state illustration of Grover iteration. The search space starts off in an equal superposition of all states in the qubit register Hilbert space as in (a). The appropriate oracle U_O for finding target state $|a\rangle$ is applied, inverting the phase of only $|a\rangle$.

mean amplitude value of all the states here is \sqrt{N} and indicated by the dashed line. Next in figure 2.9b, the oracle U_O has flipped the sign of the target state $|a\rangle$, which slightly lowers the overall mean. Then, applying U_\perp will invert all the states about the mean, increase the size of the amplitude on $|a\rangle$ while diminishing the amplitudes on all the rest of the states (figure 2.9c). Now, repeating the application of U_O followed by U_\perp will continue to push the overall mean down and increasing the size of the amplitude of $|a\rangle$. It can be shown that it then takes $\approx \pi\sqrt{N}/4$ repetitions to obtain an amplitude for $|a\rangle$ of ≈ 1 .

For the simplest search of only 4 entries using a two-qubit register, it is possible to perform the Grover's search algorithm to find the target state through only 1 iteration. This has been implemented in NMR, linear optics, and trapped-ion quantum computer implementations. In chapter 9 of this thesis, we will present the first implementation of such an algorithm with superconducting qubits and go into a step-by-step breakdown of its operation.

2.4.4 Shor's and other quantum algorithms

Besides the DJ and Grover's algorithms, there are a number of other quantum algorithms that similarly exploit properties such as phase kick-back and amplitude amplification. We group the rest of these algorithms in this subsection, without going into detail into any of them, as they represent a class of quantum computing beyond the scope of this experimental thesis. Nonetheless, it is still important to recognize for completeness and future motivation the existence of more complex algorithms which might even lie on the horizon for superconducting quantum processors.

Many of the more complex quantum algorithms are built up from the quantum Fourier transform (QFT), which is defined as the map

$$|x\rangle \rightarrow \frac{1}{\sqrt{2^n}} \sum_{y=0}^{2^n-1} e^{2\pi i \frac{x}{2^n} y} |y\rangle. \quad (2.29)$$

The QFT can be performed on an n -qubit register through a decomposition into only Hadamard gates and conditional-phase gates. By operating the QFT on a superposition of quantum states, we effectively apply the classical discrete Fourier transform to all 2^n input states in parallel. A full treatment of the QFT can be found in Ref. [23]. The QFT is applied in various algorithms for estimating mathematical quantities, providing exponential speed-ups over classical algorithms. For example, it is used for estimating eigenvalues of a unitary operator using the quantum phase estimation algorithm, as well as for finding discrete logarithms [23].

Perhaps the most well-known quantum algorithm which employs the QFT is Shor's algorithm for factorization of a number N into prime numbers. Shor's algorithm consists of two primary phases, the first phase being a translation of the factoring problem into a problem of finding the period of a function, and second phase using the QFT for finding the period. The exponential speed-up occurs during the second quantum phase. Again, details about both of these stages can be found in any of the listed quantum information texts [12, 22, 23].

The discovery of Shor's algorithm in 1994 actually represented a serious historical paradigm shift in regards to experimental efforts for quantum computing. The primary use of factoring large numbers is in fact for breaking the very widely used public-key encryption scheme of RSA. RSA is a very ubiquitous protocol for cryptography which relies on the difficulty for classical computers for factoring large numbers. Shor's algorithm showed that it

could be broken efficiently using a quantum computer. Subsequently, the quantum computers gained a lot of visibility, pushing forward numerous experimental efforts.

Shor's algorithm is in fact the most complex algorithm to have been implemented in an experimental quantum processor. Using an NMR system of seven qubits, researchers at IBM Almaden Laboratory managed to factor 15 into 5×3 [12]. With the superconducting two-qubit processor described in this thesis, we cannot yet implement Shor's algorithm. However, the further development of the superconducting qubit architecture will hopefully lead to this possibility.

2.5 Quantum measurement

At the end of performing the operations which comprise a quantum algorithm on a qubit register, the final step is a quantum measurement of the register, by which we gain access to information about the underlying quantum state, and hence the result of the computation. Measurements can be considered to have an associated observable, which is Hermitian and has real eigenvalues with corresponding eigenkets to span the state space. Historically, the action of measurement has been a sensitive issue, with regards to how a classical macroscopic channel can be used to infer microscopic quantum states.

In the earlier days of quantum mechanics, the Copenhagen interpretation presented quantum measurement as wavefunction collapse. For a single qubit in a superposition state, $|\psi\rangle = \alpha_0 |0\rangle + \alpha_1 |1\rangle$, a measurement of the qubit projection onto state $|0\rangle$, $P = |0\rangle\langle 0|$ will return the qubit in the state $|\psi\rangle = |0\rangle$ with probability $|\alpha_0|^2$ and in the state $|\psi\rangle = |1\rangle$ with probability $|\alpha_1|^2 = 1 - |\alpha_0|^2$. Here, it is the act of measurement which forces the state into one of the two eigenbasis states of P .

Although numerous thought experiments [33] have challenged the ideas of this awkward measurement formalism, actual experimental progress in quantum information has led to real measurements of quantum mechanics. Such experiments do not have perfect projective measurements; rather, there can be statistical noise which results in the incorrect identification of a measurement result. Therefore, it becomes crucial to obtain measurement statistics on starting quantum mechanical states and a completely general framework for describing quantum measurements has been developed, known as the Positive Operator-Valued Measure (POVM) formalism [12]. This takes into account the possibility of weak (non-projective) measurements, as well as statistical noise on the measurement process, allowing for the probability of misidentifying one basis state as another. POVMs are related to the statistical

treatment of the state vector describing a quantum system, which is the density matrix formalism.

For the results presented in this thesis, we only deal with ensemble-averaged measurements, giving a simpler version of measurement theory. Specifically, by repeating the two-step process of preparation of a quantum state and then performing a subsequent measurement, we obtain expectation values of the form $\text{tr}(\rho M)$ where ρ is the density matrix of the quantum state and M is a Hermitian measurement operator. The problem thus becomes one of identifying what is the measurement operator corresponding to the system, and then to use ensemble measurements of the state to identify components of the state in a technique known as quantum state tomography. We first start with a description of representing the state using the density matrix formalism.

2.5.1 Density matrix

The density matrix representation can be a more powerful tool than the standard wavefunction formalism for real experimentally generated quantum states. It is especially useful for describing ensembles of quantum states, for example, a qubit coupled to an environmental bath, or a system of multiple qubits. Furthermore, processes such as relaxation and decoherence can lead to statistical mixtures of pure quantum states, and can be accounted for with non-equilibrium time-evolution of the density matrix through master equations [34].

Suppose a quantum system is comprised of many states $|n\rangle$, with probability p_n of being in each. Then, the most general density matrix of the system is given by

$$\rho \equiv \sum_n p_n |n\rangle \langle n|, \quad (2.30)$$

where the sum is performed over all states n and $\sum_n p_n = 1$. Similar to the state vector, the density matrix evolves under unitary transformations,

$$\rho \rightarrow \sum_n p_n (U|n\rangle)(\langle n|U^\dagger) = U\rho U^\dagger. \quad (2.31)$$

Furthermore, this formalism provides a classification of the types of quantum states produced. If the state of the system is known exactly to be describable by a state vector $|\psi\rangle$, then it is a pure state, with a density matrix given by $\rho = |\psi\rangle \langle \psi|$. If only partial information about the state is known, then the system can be described by a *mixed* state, or a statistical ensemble of the pure states. As the wavefunction formalism is limited to only describing a state which is pure,

in the case of a mixed state we use the density matrix as defined in (2.30). The probabilistic mixing of pure states can arise due to noise processes such as relaxation, decoherence, or heating.

Some properties of the density matrix which are useful to keep in mind are

1. $\text{tr}(\rho) = 1$.
2. ρ is Hermitian.
3. ρ is always a positive operator, such that for any state $|\phi\rangle$, we have $\langle \phi | \rho | \phi \rangle \geq 0$.
4. The full joint density matrix of separable individual systems is the tensor product of the individual density matrices, $\rho_1 \otimes \rho_2 \otimes \dots \otimes \rho_n$.
5. A pure state has $\text{Tr}(\rho^2) = 1$. A mixed state has $\text{Tr}(\rho^2) < 1$.

Specifically with regards to mixed states of single qubits, the density matrix representation allows one to see that there is also a Bloch sphere, described by a Bloch vector \vec{r} , where

$$\rho = \frac{\mathbb{1} + \vec{r} \cdot \vec{\sigma}}{2}, \quad (2.32)$$

and \vec{r} is now a real three-dimensional vector with $|\vec{r}| \leq 1$. A pure state will have $|\vec{r}| = 1$ whereas a mixed state will be a vector within the interior of the Bloch sphere.

The density matrix formalism is also a good way to represent ensemble measurements in a quantum system. For example, the expectation value of the operator A , can be written as

$$\langle A \rangle = \sum_n p_n \langle \psi_n | A | \psi_n \rangle = \text{tr}(\rho A). \quad (2.33)$$

One other feature of the density matrix of composite systems is the ability to describe a subsystem through a partial trace. Namely, if we have a quantum state comprised of two systems A and B , described by ρ_{AB} , then the average properties of subsystem A can be represented by a density matrix,

$$\rho_A = \text{tr}_B(\rho_{AB}) \quad (2.34)$$

where tr_B reflects a partial trace over the elements of subsystem B . This partial density matrix formalism can be especially useful in the case of entangled quantum systems, where there is no way to associate a pure wavefunction state to the subsystem A .

Section 2.5.2 will demonstrate how combinations of ensemble measurements can actually be used to retrieve the density matrix of the quantum system with a technique known as quantum state tomography.

2.5.2 State tomography

Quantum state tomography involves finding the elements of the density matrix which represents an unknown quantum state. Given a single copy of ρ it is impossible to fully determine the state. But we can estimate ρ by preparing ensembles of the same state and then measuring a whole host of observables.

For a single qubit state, the density matrix ρ can be written in terms of the orthonormal set of Pauli operators, $\{\sigma_x, \sigma_y, \sigma_z\}$ along with the identity, $\mathbb{1}$ as

$$\rho = \frac{\text{tr}(\rho)\mathbb{1} + \text{tr}(\sigma_x\rho)\sigma_x + \text{tr}(\sigma_y\rho)\sigma_y + \text{tr}(\sigma_z\rho)\sigma_z}{2}, \quad (2.35)$$

which is simply an expansion of (2.32) using the components of the Bloch vector [12].

The trace expressions, *i.e.* $\text{tr}(\sigma_x\rho)$, are simply the expectation values of the Pauli operators. On any single qubit measurement, the value returned will either be +1 or -1. However, upon looking at the same measurement over and over on N copies of the same state, the expectation can be determined with Gaussian statistics and hence standard deviation given by $1/\sqrt{N}$. Note that the decomposition of ρ into the Pauli basis here is not a unique one. There are in fact an infinite number of choices of bases which span the entire single-qubit state space. However, it is often simpler to think about the decomposition in terms of the Pauli measurements, which are easily attainable in many systems, especially the case for circuit QED to be described later in this thesis. Specifically for a single qubit, only 3 observables are necessary for complete state characterization, since the density matrix has 4 entries along with the constraint $\text{tr}(\rho) = 1$. Therefore, to perform single-qubit state tomography requires the ability to repeat measurements of 3 observables which determine the single-qubit polarization.

Expanding the state tomography to two qubits, there are then 16 matrix elements of the density matrix to be determined. Therefore, we find a set of 15 linearly independent operators $\{M_i\}$ which span the two-qubit density matrix space. Then, ρ can be decomposed as

$$\rho = \sum_i c_i M_i, \quad (2.36)$$

where we can estimate $\{c_i\}$ from measurements of $\{M_i\}$. Obtaining the expectation values $m_i = \text{tr}(M_i\rho)$, we then have

$$m_i = \sum_j \text{tr}(M_i M_j) c_j. \quad (2.37)$$

Analogous to the single-qubit case, one choice we can make for the $\{M_i\}$ is to use all of the two-qubit Pauli operators, which are all pairwise combinations of the Pauli operators on each qubit $R \otimes Q$, where $R, Q \in \{I, X, Y, Z\}$. Then, the density matrix is given by

$$\rho = \sum_{R, Q \in \{I, X, Y, Z\}} \frac{\text{tr}(R^{(1)} \otimes Q^{(2)} \rho) (R^{(1)} \otimes Q^{(2)})}{4}. \quad (2.38)$$

Therefore, the two-qubit quantum state tomography is now reduced to measuring two-qubit correlation terms, such as XX, YY, ZZ , etc., in addition to single-qubit Pauli observables, such as XI, IX , etc.

From the linearly independent measurements, ρ could be obtained through simply inverting $\text{tr}(M_i M_j)$. However, this method neglects the Hermiticity and positivity properties which ρ must have. To account for this, we use the Cholesky decomposition to search for a lower triangular matrix T which can be used to parametrize any Hermitian and positive-semi definite matrix ρ as

$$\rho = \frac{T^\dagger T}{\text{tr}(T^\dagger T)}. \quad (2.39)$$

In the two qubit case, we have

$$T = \begin{pmatrix} t_1 & 0 & 0 & 0 \\ t_5 + it_6 & t_2 & 0 & 0 \\ t_{11} + it_{12} & t_7 + it_8 & t_3 & 0 \\ t_{15} + it_{16} & t_{13} + it_{14} & t_9 + it_{10} & t_4 \end{pmatrix}, \quad (2.40)$$

where the t_i can be found from Maximum Likelihood Estimation (MLE) of the likelihood function

$$\mathcal{L} = \sum_{i=1}^{16} \alpha_i (m_i - \text{tr}(M_i \rho))^2, \quad (2.41)$$

with α_i as weighting factors depending on the sensitivity of certain measurements in the

experiment [35]. We will go into more detail with respect to the merits and demerits of MLE for two-qubit state determination in chapter 8.

Now given an experimentally determined density matrix ρ , we can try to quantify how close it actually is to the ideal state we expected $|\psi\rangle$. This performance metric is known as the state fidelity \mathcal{F} , and is given by

$$\mathcal{F} = \langle \psi | \rho | \psi \rangle, \quad (2.42)$$

with values $0 \leq \mathcal{F} \leq 1$. The actual definition of fidelity varies throughout the literature, sometimes actually given by $\sqrt{\langle \psi | \rho | \psi \rangle}$ [36]. The distinction comes in as to whether the quantity desired is a probability or a probability amplitude. Nonetheless, it is important to note which of the definitions is used before comparing quoted values of the fidelity. As we will see later in this thesis, the fidelity will be an important experimental metric for determining the quality of states and we will be further discussing errors in its attainment in chapter 8.

Quantum state tomography becomes increasingly difficult with an increasing number of qubits due to the increased state matrix space. Specifically, for a system of n qubits, the number of measurements required to specify the states is $2^{2n} - 1$. As a result, for systems of three qubits or more, it can become prohibitively time-consuming to experimentally determine the entire density matrix*. Instead, it may be favorable to obtain reduced information about subsystems of the entire state, or to measure joint operators of multiple qubits, such as the parity [37, 38], as opposed to the density matrix. Furthermore, as we will see in the next section, entanglement metrics which are based upon a complete identification of ρ can be difficult to compute, and other simpler experiments for entanglement quantification will need to be developed.

2.6 Entanglement metrics

With quantum state tomography (section 2.5.2), we are able to completely reconstruct a quantum state, whether it is pure or mixed and entangled or separable. As previously introduced, a metric for quantifying the purity of experimentally produced states is $\mathcal{P} = \text{tr}(\rho^2)$. Given a d dimensional Hilbert space, we have the property $1/d \leq \mathcal{P}(\rho) \leq 1$. Another property of the purity of a quantum state is that it remains invariant under unitary transformation, such as

* The current record is 8 qubits in a trapped-ion system requiring considerable computational effort [15]

single-qubit and two-qubit operations. Experimentally, the purity can be a good indicator of the decoherence present in the quantum system.

Although \mathcal{P} and the fidelity to the targeted state \mathcal{F} (2.42) give a considerable amount of quantitative information about the quality of the states produced, we would like to have further metrics which can quantify the degree of entanglement in the system. Note that this entanglement which we wish to discuss will be bipartite entanglement, as a strict formalism beyond two qubits is still an on-going topic of theoretical research [39–41].

To characterize and quantify entanglement, we introduce the concept of an entanglement monotone $E(\rho)$. Formally, it is defined as a functional that characterizes the strength of genuinely quantum correlations with the following properties [42]

1. $E(\rho) = 0$ if ρ is a separable state.
2. $E(\rho) = 1$ if ρ describes a Bell state, which is maximally entangled.
3. $E(\rho)$ is invariant under all local unitary operations.
4. $E(\rho)$ cannot be increased by any combination of local operations with classical communication channels operating on ρ .

Given any state ρ , $E(\rho)$ will quantify the degree of entanglement between separable and maximally entangled with a monotonic mapping. Entanglement monotones theoretically only exist for bipartite entanglement[39], and so always refer to two-body density matrices. Next, we discuss a relatively well-known entanglement monotone, known as the concurrence, used as a metric across many quantum information experiments. Here, we will describe how to calculate it given the case of pure or mixed states.

2.6.1 Concurrence

The concurrence is an example of an entanglement monotone for bipartite entanglement characterization which is bounded between 0 and 1 [43]. Any pure two-qubit state $|\psi\rangle$ can be represented in terms of the computational basis states as

$$|\psi\rangle = \alpha_{00}|00\rangle + \alpha_{01}|01\rangle + \alpha_{10}|10\rangle + \alpha_{11}|11\rangle. \quad (2.43)$$

Then, the concurrence is defined as

$$C(\psi) = 2|\alpha_{00}\alpha_{11} - \alpha_{01}\alpha_{10}|. \quad (2.44)$$

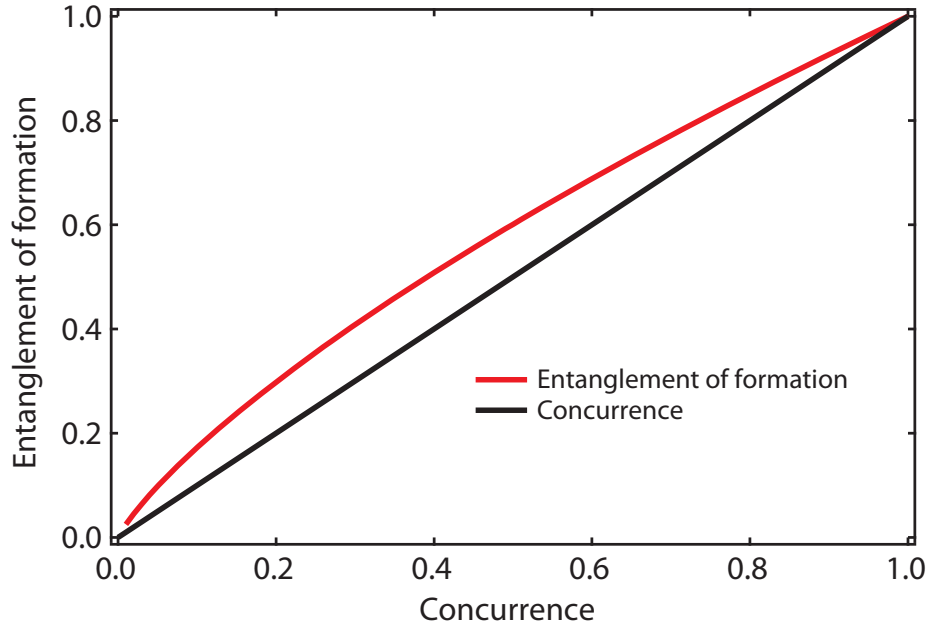


Figure 2.10: Entanglement of formation versus concurrence. All entanglement monotones for two qubits can be one-to-one mapped to each other. Here we see the relationship between the concurrence and the entanglement of formation, two commonly quoted entanglement monotones.

Another way of calculating the concurrence is from the matrix of correlations, or T matrix, given by

$$T = \left\langle \begin{pmatrix} XX & XY & XZ \\ YX & YY & YZ \\ ZX & ZY & ZZ \end{pmatrix} \right\rangle. \quad (2.45)$$

It can be shown [39, 42] that

$$C = \sqrt{\frac{\text{tr}(T^\dagger T) - 1}{2}}. \quad (2.46)$$

The concurrence is closely related with another entanglement monotone, known as the entanglement of formation [43, 44], via the relation

$$E_f(\rho) = h\left(\frac{1}{2}(1 + \sqrt{1 - C(\rho)})\right), \quad (2.47)$$

where $h(x) = -x \log_2(x) - (1-x) \log_2(1-x)$. Figure 2.10 shows the relationship between concurrence and entanglement of formation from separable to maximally entangled states.

The concurrence is an especially interesting entanglement monotone because it can be computed for mixed states as well. Given the full density matrix ρ , we first form the matrix product $R = \rho(\sigma_y \otimes \sigma_y)\rho^*(\sigma_y \otimes \sigma_y)$. Taking the eigenvalues of R and arranging them in decreasing order as $\{\lambda_1, \lambda_2, \lambda_3, \lambda_4\}$, the concurrence is then given by

$$C(\rho) \equiv \max\left(0, \sqrt{\lambda_1} - \sqrt{\lambda_2} - \sqrt{\lambda_3} - \sqrt{\lambda_4}\right). \quad (2.48)$$

Here, one of the drawbacks of C as an entanglement metric is the need to determine the full quantum state ρ . Specifically as the number of qubits coupled together grows, determining multipartite entanglement through determining the state becomes costly both in experimental terms and computational requirements. Another caveat of needing to determine ρ is the non-linear processing which is done, including maximum-likelihood estimation as well as eigenvalue decomposition, resulting in convoluted error propagation. As a result, an alternative method for quantifying entanglement can be sought, and that is to use witnesses, which will be the subject of the next section.

2.6.2 Entanglement witnesses

Entanglement witnesses are observables which give expectation values that determine whether a prepared state is entangled. It is formally defined as a Hermitian operator \mathcal{W} , such that its expectation value $\text{tr}(\rho\mathcal{W}) > 0$ for every separable state, but $\text{tr}(\rho\mathcal{W}) < 0$ for *some* entangled states. This means that any negative expectation value guarantees entanglement, *i.e.* the entanglement is ‘witnessed,’ whereas a positive value does not shed any information on the state [39, 45].

We can visualize the full state space as in figure 2.11, with a central convex set of separable states, surrounded by concentric convex sets of increasing degree of entanglement. A measurement of an entanglement witness is then given by a hyperplane slicing through the space, which gives a value $\text{tr}(\mathcal{W}\rho) = c$. All of the states which the hyperplane touches will give that value. Therefore, a witnesses \mathcal{W} can be thought of as parallel hyperplanes cutting through the space, with different measured values $c < 0$ when the state is definitely not in the separable set. When the hyperplane touches the separable state space or goes through it, then $c \geq 0$, indicating that the state is not necessarily entangled. Hyperplanes which are tangent

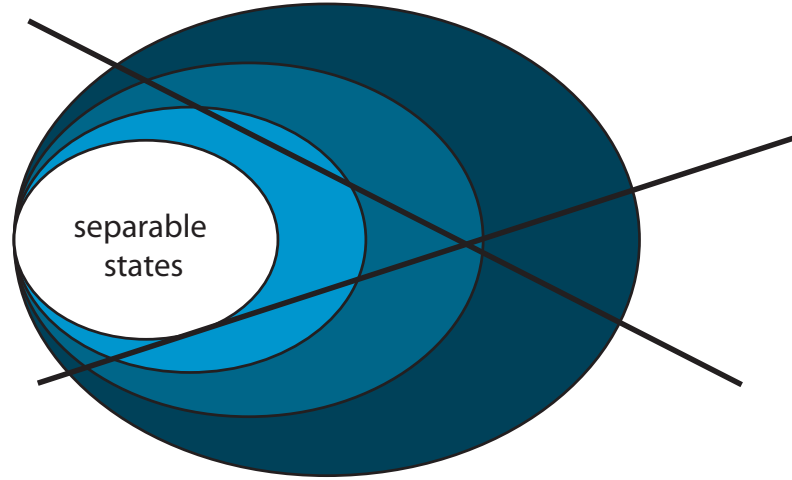


Figure 2.11: State space and entanglement witnesses. A convex set of separable states is surrounded by concentric convex sets of increasing entanglement. The measurement of an entanglement witness \mathcal{W} is represented by a straight hyperplane which cuts through the space. All states ρ along the hyperplane give a value $\text{tr}[\rho] = c$, where $c < 0$ for some entangled state. Any witness which pierces through the separable state set will give $c > 0$. (Figure used with permission from [45]. See Copyright Permissions.)

to the entangled states at the outer most edge of the entire space are optimal entanglement witnesses to those states, as c takes the minimum possible value [41].

Perhaps the most well-known maximally entangled states are the Bell states,

$$|\Psi^\pm\rangle = \frac{1}{\sqrt{2}} (|0, 0\rangle \pm |1, 1\rangle) \quad |\Phi^\pm\rangle = \frac{1}{\sqrt{2}} (|0, 1\rangle \pm |1, 0\rangle). \quad (2.49)$$

We can find a set of entanglement witnesses which, written in terms of two-qubit Pauli operators as

$$\begin{aligned} \mathcal{W}_{\Psi^\pm} &= \frac{1}{4} (II \mp XX \pm YY - ZZ), \\ \mathcal{W}_{\Phi^\pm} &= \frac{1}{4} (II \mp XX \mp YY + ZZ), \end{aligned} \quad (2.50)$$

would be optimal to these Bell states. Here, we can see that each Bell state has a unique optimal witness which corresponds to it, and gives a minimum value of -1 . These witnesses demonstrate that in order to measure the expectation values $\text{tr}(\rho\mathcal{W})$, it is in fact not necessary to have the full density matrix ρ , but just the expectation of some of the two-qubit Pauli operators, XX , YY , and ZZ .

These witnesses, although not entanglement monotones, can be used to place bounds on measures such as the concurrence. In Ref. [45], it is shown that the quantity given by

$$\mathcal{B} = -2 \operatorname{tr}(\rho \mathcal{W}) \quad (2.51)$$

is a lower bound on the concurrence of the system. Therefore, from a reduced set of measurements of the quantum system, entanglement witnesses can be measured which quantitatively restrict the degree of entanglement in the system. Furthermore, as most witnesses are simple linear combinations of measurements, errors can be easily propagated, rather than forced through layers of non-linear processing. These concepts of entanglement witnesses will be applied to experimentally generated entangled states in chapter 8.

2.7 Bell tests

Traditionally, the idea of a Bell test is to devise an experiment which attempts to validate Bell's theorem that quantum mechanics is incompatible with local realism [46]. It was Bell who showed that the presence of entanglement in quantum mechanics rules out the possibility of pre-determined physical quantities prior to measurement. The test often involves the violation of a Bell inequality, and finding a maximum value of correlation measurements for distant objects. Here, coming from a different angle, we wish to extend the previous section on entanglement witnesses and demonstrate that in fact a Bell test measurement need not be applied as a validation of quantum mechanics but instead serve as another metric of entanglement. From the point of view of quantum engineers, entanglement can be seen as a resource, and having a high degree of entanglement will lead to a violation of a Bell inequality.

2.7.1 Clauser-Horne-Shimony-Holt inequality

One of the more well-known Bell inequalities is the Clauser-Horne-Shimony-Holt (CHSH) inequality [47]. It is often the inequality of choice in experimental violations as it has well-defined classical and quantum mechanical bounds. To motivate this test, consider a source of two particles which is capable of preparing the same set of two particles repeatedly. The two particles are separated and sent to two distant parties, Alice and Bob.

Now suppose Alice and Bob can each perform two different projective measurements, $\{M_A, M'_A\}$ and $\{M_B, M'_B\}$, respectively (figure 2.12). Neither decides in advance which of

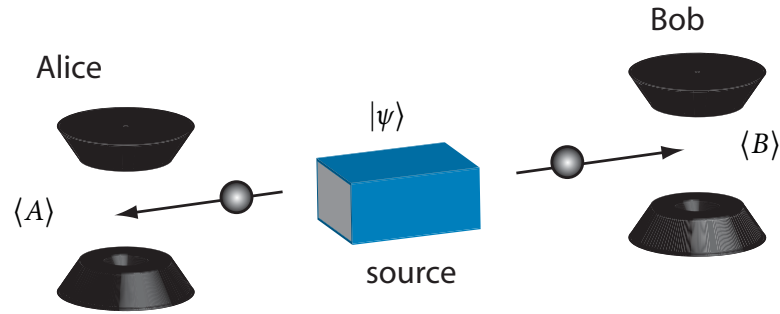


Figure 2.12: Schematic for the CHSH test. Alice and Bob each receive one of a pair of particles that have been prepared in an unknown state $|\psi\rangle$. After performing various measurements of the particles, they can compare answers and calculate the CHSH quantity given in (2.54). For two classical or completely separable particles, *i.e.* $|\psi\rangle = |\psi\rangle_A |\psi\rangle_B$, there can be no set of measurements which Alice and Bob can perform that would give a quantity larger than 2. However, if the particles are initialized in an entangled state such as a Bell state 2.49, then for a certain choice of measurement angles, they can beat the bound of 2, reaching a maximal value of $2\sqrt{2}$.

the two measurements to perform but rather chooses randomly with a probability of 0.5 for each. Upon performing a measurement simultaneously with Bob (Alice), Alice (Bob) obtains either A (B) or A' (B'), either of which can take on the outcomes $+1$ or -1 .

Now let us form the quantity $\mathbb{C} = AB + A'B + A'B' - AB'$ and investigate its properties. \mathbb{C} is often referred to as the CHSH operator, and the measurements A, A', B, B' can be thought of as different axes onto which Alice and Bob can project their state. We can re-group the terms of \mathbb{C} into

$$AB + A'B + A'B' - AB' = B(A + A') + B'(A - A'), \quad (2.52)$$

and since $A, A' = \pm 1$, one of the two terms on the right hand side must be zero. As a result, any single realization of measurements will necessarily give $AB + A'B + A'B' - AB' = \pm 2$. We can take an expectation of the quantity, which must still be bounded,

$$E(\mathbb{C}) = E(AB + A'B + A'B' - AB') \leq 2. \quad (2.53)$$

The expectation value of the \mathbb{C} can then be distributed, and then we are left with the CHSH inequality,

$$E(AB) + E(A'B) + E(A'B') - E(AB') \leq 2, \quad (2.54)$$

where the terms on the left side are found by Alice and Bob repeating the experiment multiple times and then classically multiplying their measurements.

However, if we let the particles that Alice and Bob share be quantum mechanical, now they can be initialized as a Bell state,

$$|\psi\rangle = \frac{1}{\sqrt{2}} (|01\rangle - |10\rangle), \quad (2.55)$$

before we separate the particles and send them to Alice and Bob for measurement. Now, as a result of the two particles being in an entangled state, Alice and Bob will actually violate the CHSH inequality (2.54) with an appropriate choice of measurements. Specifically, we can use the Cartesian (or Pauli) basis with Alice measuring $A \rightarrow Z^{(1)}$, $A' \rightarrow X^{(1)}$ and Bob measuring observables that are 45° rotated, $B \rightarrow (-Z^{(2)} - X^{(2)})/\sqrt{2}$, $B' \rightarrow (Z^{(2)} - X^{(2)})/\sqrt{2}$. In this case, we then find expectation values

$$\langle AB \rangle = \frac{1}{\sqrt{2}}, \quad \langle A'B \rangle = \frac{1}{\sqrt{2}}, \quad \langle A'B' \rangle = \frac{1}{\sqrt{2}}, \quad \langle AB' \rangle = -\frac{1}{\sqrt{2}}. \quad (2.56)$$

Placing these quantities into the left hand side quantity of (2.54), we then get

$$\langle AB \rangle + \langle A'B \rangle + \langle A'B' \rangle - \langle AB' \rangle = 2\sqrt{2}. \quad (2.57)$$

This is not a unique realization either, as other choices of measurements and other entangled states can be used to violate the CHSH inequality (2.54) as well. However, the example given above is the maximal violation and the value $2\sqrt{2}$ is termed Cirelson's bound [48].

Quantum mechanics thus violates the CHSH inequality (2.54). So what went *wrong* with the classical derivation? We assumed that the values A , A' , B , and B' all existed independently of measurement, suggesting pre-determined realism. We further assumed that Alice's measurement does not in any way affect Bob's measurement, suggesting locality. Therefore, violation of a Bell's inequality supports the idea that nature is non-deterministic and non-local. These aspects of Bell's tests are the focus of numerous theoretical studies, looking to reconcile quantum mechanics with non-local realism, and more recently, they are also the focus of many experimental studies [49–51] looking to close certain loopholes in tests for ruling out local hidden-variable theories, which we will not go into detail in this thesis. Instead, the measurement of the CHSH operator can be thought of in terms of the entanglement in the system.

2.7.2 CHSH entanglement witness

In the interests of building a quantum information processor, we take a less controversial point of view regarding the measurement and violation of a CHSH inequality. We can sweep foundational issues of quantum mechanics under the rug momentarily, and look at the violation of a Bell inequality not as a test of quantum mechanics, but as a measure of the degree of entanglement in the system.

Although the violation of the CHSH inequality is traditionally found for a Bell state as a 45° rotation of the measurements performed between Alice and Bob, we can instead let Alice and Bob keep their measurements 90° apart and perform a single-qubit rotation of 45° on the Bell state. So suppose we select the Cartesian axes such that $\mathbb{C} = XX - XZ + ZX + ZZ$. In fact, for this choice of measurements, the state that maximally violates the CHSH inequality with a value of $2\sqrt{2}$ is a single-qubit rotation of 45° on one of the qubits in a Bell state, or $R_y^{(1)}(-\pi/4)|\Psi_+\rangle$. In this case \mathbb{C} is actually an optimal entanglement witness [45] for this specific state.

We can therefore see that the classical threshold for $\langle \mathbb{C} \rangle = 2$ is simply an offset value of an entanglement witness: any measurement of $\langle \mathbb{C} \rangle > 2$ necessarily implies that the state prepared is entangled and not separable; any measurement $\langle \mathbb{C} \rangle < 2$ just tells us that we cannot comment on whether the state is separable or entangled. The maximal entanglement attainable is signified by a measurement of $\langle \mathbb{C} \rangle$ which approaches Cirelson's bound of $2\sqrt{2}$.

The CHSH operator is thus an extension of the entanglement witnesses discussed previously. Having the ability to measure two-qubit Pauli operators will permit the construction of \mathbb{C} and chapter 8 will demonstrate its measurement on a variety of generated separable and entangled states.

2.8 Chapter summary

The previous discussions of this chapter have been general for any qubit implementation. Building any simple quantum information processor will require single-qubit gates, an entangling two-qubit gates, and a way for reading out the quantum state. For good single-qubit control, we will want to have the ability to perform arbitrary rotations around the Bloch sphere, perhaps combining rotations around the Cartesian axes x , y , and z . We have also now seen how some two-qubit gates, such as the c -Phase and $\sqrt{i\text{SWAP}}$, can arise from two-qubit interaction Hamiltonians. These sets of gates can be a universal set for quantum computing

and at the level of two-qubits, should permit the operation of some simple algorithms, such as the Deutsch-Jozsa and four-level Grover's search. Rounding out the quantum system with a good quantum state measurement and we can be ready to develop a rudimentary two-qubit quantum processor. Therefore, we will now leave the realm of general quantum computing, and over the next few chapters motivate how we will bring some of these concepts to life in a superconducting qubit architecture.

CHAPTER 3

Superconducting Qubits and Circuit QED

PHYSICAL implementations of qubits have taken many forms: nuclear spins, trapped ions, photons, and even electrical circuits. Yet, the operating principle of the qubit is independent of its experimental formulation. The physics of the qubit *i.e.*, of a simple two level system, makes the quantum information processing described in the previous chapter (chapter 2) possible. For an experimental realization, the challenge has been to find a pair of quantum levels that can be addressed, coupled, protected from the environment, and scaled up to a large number of qubits.

Achieving these often conflicting goals in circuit-based superconducting qubits has been experimentally challenging. However, the potential of engineerable intrinsic qubit properties and eventual mass-producibility based on a circuit design employing standard lithographic fabrication techniques with all-electrical controls has driven continued progress. A particular route for quantum computing with superconducting circuits has been to implement the relatively new field of circuit quantum electrodynamics (QED) [30, 52–54], where quantum optics is brought to a solid-state chip, coupling superconducting qubits to microwave frequency photons.

This chapter will lay the foundation for superconducting circuit-based qubits and the circuit QED architecture. It will serve as important background leading into chapter 4, which will detail how circuit QED can be an excellent platform for quantum information

processing. First, section 3.1 will discuss the primary building blocks for the solid-state quantum processor of this thesis, namely superconducting charge qubits. That is followed by section 3.2 which will be an introduction to coupling multiple qubits. A review of basic cavity quantum electrodynamics in section 3.3 will serve as a springboard for the concepts that will be used in circuit QED (section 3.4), such as the strong and dispersive coupling regimes. We end the chapter with a discussion about the relevant relaxation and decoherence properties in circuit QED (section 3.5).

3.1 Superconducting qubits

Superconductivity provides an interesting foundation on which to study quantum effects. In contrast to other solid-state implementations of qubits that aim to confine a small number of microscopic quantum degrees of freedom, such as quantum dots, superconductors are composed of a large number of paired electrons, or Cooper pairs, all of which have condensed into a single ground state [55]. Quantum effects are then the result of macroscopic degrees of freedom, and circuit elements comprised of these superconductors can be constructed with tailorable interactions with other elements as well as the environment.

Ideally, non-dissipative circuit elements such as inductors and capacitors can be constructed with superconductors. However, combining these elements can only result in the harmonic oscillator, which has evenly spaced energy levels, falling short of the two-level addressability required for a qubit. Fortunately, superconductors also provide the only known simultaneously non-linear and non-dissipative circuit element, known as the Josephson junction, which will generate the necessary anharmonicity for artificial atoms. Artificial atoms possess a rich non-uniformly spaced set of quantum mechanical levels, from which two of them can be individually addressed for use as a qubit. The following sections will review the non-linear Josephson junction and its application in the charge-based Cooper-pair box and transmon qubits.

3.1.1 Josephson junction as a non-linear inductor

Physically, a Josephson junction consists of two superconducting electrodes separated by an insulating oxide. Cooper pairs can tunnel coherently across the insulating barrier, with a

supercurrent I that is given by

$$I = I_0 \sin \phi(t) \quad (3.1)$$

where I_0 is the critical current (the maximum sustainable junction supercurrent), and $\phi(t)$ is a time-dependent phase difference across the junction [55]. The phase difference evolves in time in the presence of a potential V across the junction according to

$$\hbar \frac{d\phi}{dt} = 2eV. \quad (3.2)$$

Now by taking the time-derivative of the supercurrent, we find what is commonly termed the Josephson effect,

$$\dot{I} = (I_0 \cos \phi) \dot{\phi} \quad (3.3a)$$

$$= \frac{2eVI_0}{\hbar} \cos \phi. \quad (3.3b)$$

Faraday's law gives $V = -L\dot{I}$, which lets us identify the Josephson inductance as

$$L_J = \frac{\Phi_0}{2\pi I_0 \cos \phi}, \quad (3.4)$$

where $\Phi_0 = h/e$ is the magnetic flux quantum. This non-linear inductance combined with the intrinsic capacitance of the Josephson junction, given by C_J , thus results in an anharmonic oscillator which serves as the basis for a number of superconducting qubit topologies [56].

3.1.2 The Cooper-pair box qubit

One of the simplest Josephson junction based qubit designs is the Cooper-pair box (CPB) [53, 57, 58]. This charge-based circuit is formed when a superconducting island is connected to a reservoir of Cooper pairs through a junction. The Josephson effect permits the coherent tunneling of the Cooper pairs between the island and the reservoir, while a gate voltage (V_g) can also electrostatically modulate a Coulomb blockade tunneling effect. A standard CPB geometry is shown in figure 3.1a.

Through circuit quantization [57, 59], the CPB Hamiltonian can be found to be

$$H_{\text{CPB}} = 4E_C(\hat{n} - n_g)^2 - E_J \cos \hat{\phi} \quad (3.5)$$

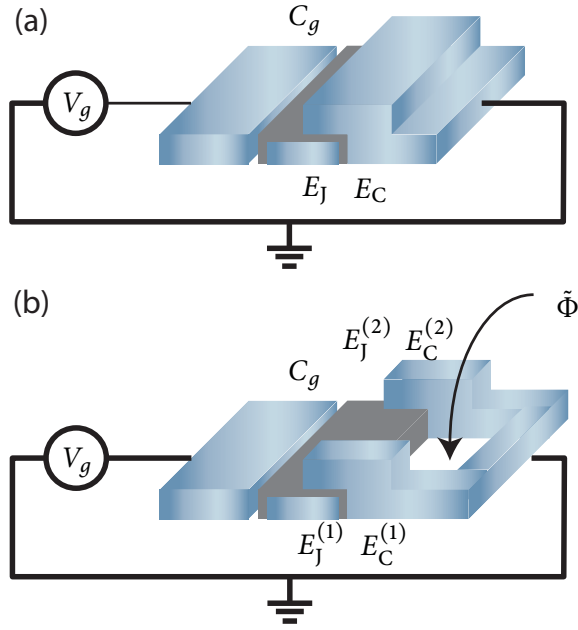


Figure 3.1: The Cooper pair box (CPB). The standard CPB (a) consists of an island connected to a superconducting reservoir through a tunnel junction and is capacitively coupled to an electrostatic voltage bias. In the split CPB (b), the island is connected to the superconducting reservoir via two split junctions, with Josephson energies $E_J^{(1)}$ and $E_J^{(2)}$. The superconducting loop gives the ability to tune the effective E_J (3.8)b by threading an external magnetic flux $\tilde{\Phi}$.

where \hat{n} is the integer-valued Cooper pair number operator, n_g is the continuously variable offset gate charge due to a dc bias, and $\hat{\phi}$ is the conjugate operator to \hat{n} , representing the Josephson phase. The first part of the Hamiltonian can be interpreted as the electrostatic charging component with the relevant charging energy scale given by $E_C = e^2/2C_\Sigma$, where $C_\Sigma = C_g + C_J$ is the total capacitance to ground of the CPB. The second term of the Hamiltonian reflects the energy across the non-linear inductor in the junction due to the Josephson effect, with a scale given by the Josephson energy $E_J \equiv I_0 \Phi_0 / 2\pi$.

The CPB is more commonly designed with a pair of junctions in parallel (figure 3.1b), forming a superconducting loop which allows the tunability of the tunneling (E_J) portion of the Hamiltonian. The split-pair of junctions forms a superconducting quantum interference device (SQUID) such that an externally applied magnetic flux $\tilde{\Phi}$ piercing the loop will control the rate at which Cooper pairs tunnel in and out of the CPB. Now including the two junctions with different Josephson energies E_{J1} , E_{J2} , we have a new Hamiltonian

$$H = E_{J1} \cos \hat{\phi} - E_{J2} \cos \left(\hat{\phi} - 2\pi \tilde{\Phi} / \Phi_0 \right). \quad (3.6)$$

This can be rewritten as [53]

$$H = (E_{J_1} + E_{J_2}) \left| \cos \left(\pi \frac{\tilde{\Phi}}{\Phi_0} \right) \right| \left(1 + d^2 \tan^2 \left(\pi \frac{\tilde{\Phi}}{\Phi_0} \right) \right)^{1/2} \cos(\hat{\phi} - \phi_0), \quad (3.7)$$

where $d = (E_{J_1} - E_{J_2}) / (E_{J_1} + E_{J_2})$ reflects differences in the junctions, and ϕ_0 is a phase offset given by $\tan(\phi_0 + \pi\tilde{\Phi}/\Phi_0) = d \tan(\pi\tilde{\Phi}/\Phi_0)$. For standard experimentally made junctions (chapter 5) that are aimed to be identical, the junction asymmetry is typically $d \sim 0.1$, small enough to give the approximate flux-tunable CPB Hamiltonian:

$$H_{\text{CPB}} = 4E_C(\hat{n} - n_g)^2 - E_J(\tilde{\Phi}) \cos(\hat{\phi} - \phi_0) \quad (3.8a)$$

$$E_J(\tilde{\Phi}) = E_J^{\text{max}} \cos(\pi\tilde{\Phi}/\Phi_0). \quad (3.8b)$$

We can explicitly write this Hamiltonian in the charge basis by using the relations

$$\hat{n} = i \frac{\partial}{\partial \phi} \quad (3.9a)$$

$$\hat{n} e^{i\hat{\phi}} = e^{i\hat{\phi}} (\hat{n} + 1) \quad (3.9b)$$

to get

$$H = 4E_C (\hat{n} - n_g)^2 - \frac{E_J}{2} \sum_n (|n\rangle \langle n+1| + |n+1\rangle \langle n|). \quad (3.10)$$

The CPB can be operated as a charge qubit in the regime where $E_J \ll 4E_C$, such that the Josephson coupling gives a small perturbation to lift the degeneracy at integer charge states. By operating the CPB at a gate charge $n_g = \pm 0.5$, the system can be reduced into a two-level qubit system with a reduced Hamiltonian given by

$$H \approx 2E_C(1 - n_g)\sigma_z - \frac{E_J(\tilde{\Phi})}{2}\sigma_x, \quad (3.11)$$

where we identify the standard spin 1/2 Pauli matrices $\sigma_z \rightarrow 2\hat{n}$ and $\sigma_x \rightarrow |n\rangle \langle n+1| + |n+1\rangle \langle n|$ in the two charge manifold. This Hamiltonian can be interpreted as a single spin in a magnetic field given by $B = E_J\hat{x} + 4E_C(1 - n_g)\hat{z}$. Here, the eigenstates are superpositions of the charge states with $n = 0, 1$, given by $(|0\rangle \pm |1\rangle) / \sqrt{2}$. Furthermore, another key aspect of the operating point with $n_g = \pm 0.5$ is the first-order insensitivity to fluctuations in n_g , as can be seen in the

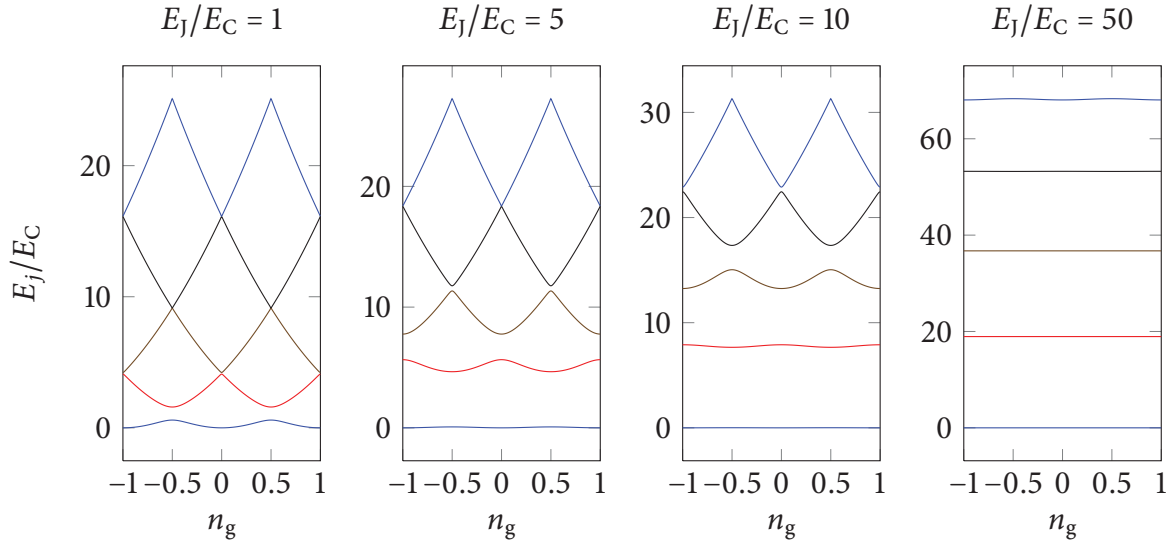


Figure 3.2: Charge dispersion. The energies of the lowest 5 levels of the charge qubit Hamiltonian (3.5), in units of the charging energy E_C . For low E_J/E_C ratio, we are in the Cooper pair box regime, and the energies are parabolic functions of the offset charge n_g , with avoided crossings. Here, operation as a qubit is performed at charge ‘sweet spots’ $n_g = \pm 0.5$ where the energy levels are first-order insensitive to charge fluctuations. As the ratio of E_J/E_C is increased the levels become exponentially flatter, as we enter the transmon regime. Figure reproduced from [61, 62].

dispersion diagram of figure 3.2. Performing experiments at this charge ‘sweet-spot’ is crucial for obtaining longer coherence times [53, 60].

3.1.3 The transmon qubit

Starting with the charge-qubit Hamiltonian of (3.5), by operating in a different regime of the ratio E_J/E_C , it is possible to have a qubit that is optimized [61, 63] with respect to $1/f$ charge noise effects [64]. Specifically, when $E_J \gg E_C$, the CPB system switches to a system that is best described as an anharmonic oscillator. In terms of physical realization, the transmon modification involves the addition of a large shunting capacitance to increase the overall capacitance to ground of the network, reducing E_C (more transmon design details are given later in this thesis in chapter 5).

To be more quantitative with regards to the dependence of the energy levels to E_J/E_C , it is useful to write out the full energy level expressions for (3.5). Switching over to the phase basis [61, 62], analytical solutions can be expressed in terms of the special Mathieu’s functions

$me_\nu(q, z)$ as,

$$\langle \phi | m \rangle = \frac{1}{\sqrt{2\pi}} \exp[in_g \phi] me_{-2(n_g+m)} \left(\frac{-E_J}{2E_C}, \frac{\phi}{2} \right) \quad (3.12)$$

and the eigenenergies are then given by

$$E_m(n_g) = E_C a_{2(n_g+k(m,n_g))}(-E_J/2E_C), \quad (3.13)$$

where $a_p(q)$ is Mathieu's characteristic value and $k(m, n_g)$ is an integer-valued function which orders the eigenvalues. The effect of increasing E_J/E_C can be seen in the level dispersion curves in figure 3.2. As the ratio increases, the levels flatten considerably and the n_g dependence of the first few levels disappears.

This flattening does not come for free, however, as another feature of the increasing E_J/E_C ratio is a reduced anharmonicity: the change in level spacing between adjacent transitions decreases. Having sufficient anharmonicity is critical for operation as a qubit, since the case of zero anharmonicity equates to a harmonic oscillator with levels that cannot be individually addressed.

The Mathieu functions can be evaluated numerically through a truncated set of charge basis states [62]. From these eigenenergies, we then define the charge dispersion,

$$\epsilon_m = E_m(n_g = 0) - E_m(n_g = 1) \quad (3.14)$$

for the m th energy band. In the CPB case with $E_J < E_C$, $\epsilon_m \approx 4E_C$. However, when $E_J/E_C \gg 1$, an exponentially reduced charge dispersion can be found from the Mathieu solutions [61],

$$\epsilon_m \simeq (-1)^m E_C \frac{2^{4m+5}}{m!} \sqrt{\frac{2}{\pi}} \left(\frac{E_J}{2E_C} \right)^{\frac{m}{2} + \frac{3}{4}} e^{-\sqrt{8E_J/E_C}}, \quad (3.15)$$

which is illustrated in figure 3.2. In practice however, determining the dispersion from the Mathieu solutions can become unwieldy and numerically intensive. Instead, we often diagonalize the full charge qubit Hamiltonian using a truncation of up to ~ 30 levels [62]. In the limit of large E_J/E_C , this treatment agrees very well with (3.15).

Now with regards to the anharmonicity, it is sufficient to use a perturbation to a harmonic oscillator, expanding the $\cos \phi$ in (3.5) to $1 - \phi^2/2 + \phi^4/24$. The Hamiltonian then takes the

form of the Duffing oscillator

$$H = \sqrt{8E_C E_J} (b^\dagger b + 1/2) - E_J - \frac{E_C}{12} (b^\dagger + b)^4, \quad (3.16)$$

where b^\dagger and b are now creation and annihilation operators for simply the harmonic oscillator portion of the $\cos \phi$ expansion. Using perturbation theory and keeping only quartic terms of the form $(b^\dagger b)^2$, the energy of the m th level can be found to be

$$E_m \simeq -E_J + \sqrt{8E_J E_C} \left(m + \frac{1}{2} \right) - \frac{E_C}{12} (6m^2 + 6m + 3). \quad (3.17)$$

The absolute anharmonicity between a transition between levels $m + 1$ and m and the next lowest transition m and $m - 1$ is given by

$$\alpha_m = E_{m+1,m} - E_{m,m-1} \simeq -E_C, \quad (3.18)$$

where $E_{mn} = E_n - E_m$. Comparing this absolute anharmonicity to the ground to first excited state transition of the transmon energy levels, $E_{01} \simeq \sqrt{8E_J E_C}$, gives the relative anharmonicity,

$$\alpha_m^r = \alpha_m / E_{01} = -(8E_J / E_C)^{-1/2}. \quad (3.19)$$

This reflects an algebraic decrease in the anharmonicity with increasing E_J / E_C . Although as $E_J / E_C \rightarrow \infty$, the anharmonicity will be reduced $\alpha_m^r \rightarrow 0$, typical transmon performance will be obtained without needing to reach this extreme. Since the charge dispersion reduces exponentially with increasing E_J / E_C , there is already sufficient band suppression before the anharmonicity becomes small enough to make two-level addressability an issue. Henceforth, we will interchange between notation in which we treat the transmon as a simple two-level system, such that its Hamiltonian is just that for a simple spin 1/2,

$$H_q = \frac{\hbar}{2} \omega_q \sigma_z, \quad (3.20)$$

and notation in which the full energy spectrum of the transmon is taken into account,

$$H_q = \hbar \sum_k \omega_k |k\rangle \langle k|, \quad (3.21)$$

where $|k\rangle$ are the exact Mathieu's solutions from (3.12) and $\omega_k = E_k / \hbar$, with E_k from (4.2.4). The higher levels of the transmon will play a critical role in some of the interactions which will be described later in this thesis.

3.2 Coupling superconducting qubits

Having introduced the charge-based superconducting qubit, we now move towards scaling up the circuit, since for quantum information processing (chapter 2), coupling *multiple* qubits is necessary. A circuit-based architecture makes this coupling an engineering challenge, and just as fabrication procedures govern the relevant parameters in the single-qubit Hamiltonian (3.5), they will also determine the strength and form of multi-qubit interactions. Furthermore, analogous to the tunability of individual qubit parameters, a circuit-based approach will permit dynamical electronic control to turn on and off interactions in-situ.

Given the circuit element nature of the qubits, the simplest way to couple them is to use another lumped circuit element, such as either a capacitor or inductor. In this section, we will discuss a few possible coupling schemes that have been suggested for charge qubits.

3.2.1 Fixed capacitive coupling

A mutual capacitance C_m can be used as in figure 3.3a to couple two charge qubits, which have Josephson energies E_{J1} and E_{J2} and charging energies E_{C1} , and E_{C2} . The resulting Hamiltonian for this two-qubit device is given by [65]

$$H = \begin{pmatrix} E_{00} & -\frac{1}{2}E_{J1} & -\frac{1}{2}E_{J2} & 0 \\ -\frac{1}{2}E_{J1} & E_{10} & 0 & -\frac{1}{2}E_{J2} \\ -\frac{1}{2}E_{J2} & 0 & E_{01} & -\frac{1}{2}E_{J1} \\ 0 & -\frac{1}{2}E_{J2} & -\frac{1}{2}E_{J1} & E_{11} \end{pmatrix}, \quad (3.22)$$

where $E_{n_1 n_2} = E_{C1}(n_{g1} - n_1)^2 + E_{C2}(n_{g2} - n_2)^2 + E_m(n_{g1} - n_1)(n_{g2} - n_2)$. Here, n_1 and n_2 are the excess Cooper pairs in the two CPBs, n_{g1} and n_{g2} are gate charges. The mutual coupling energy term is given by $E_m = 4e^2 C_m / (C_{\Sigma 1} C_{\Sigma 2} - C_m^2)$. The four computational basis states are for $|n_1, n_2\rangle$, $n_1, n_2 \in 0, 1$.

This type of shared linear capacitance interaction can be used to perform a controlled operation such as a *c*NOT (section 2.3.1). The diagonal elements of (3.22) point to the presence of a gate-controlled *ZZ*-interaction. The off-diagonal Josephson energy terms result in avoided crossings at the charge degeneracy points $n_{g1} = n_{g2} = 0.5$, split by E_{J1} and E_{J2} between the symmetric and anti-symmetric charge states $|0\rangle \pm |1\rangle$ of each qubit. A controlled operation is possible through applying a gate pulse that would take $|0, 0\rangle$ to $|0, 1\rangle$, but would

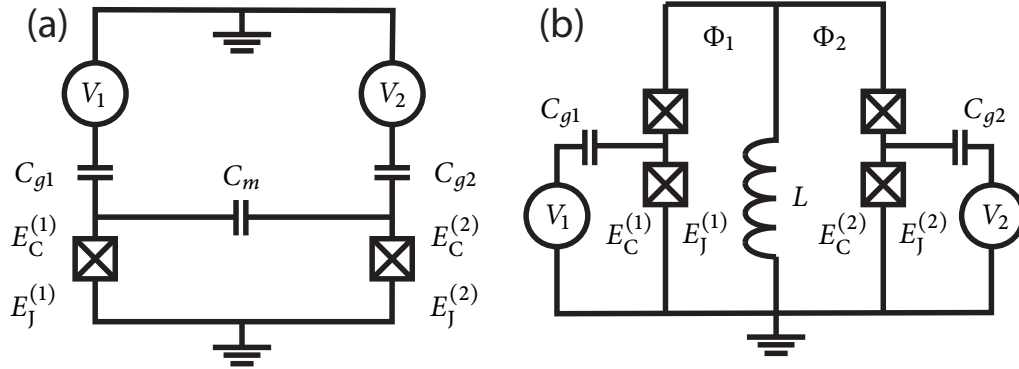


Figure 3.3: Superconducting charge qubit coupling schemes. (a) Fixed capacitive coupling. A mutual capacitance C_m connects two CPB circuits, resulting in an always-on interaction. (b) Tunable inductive coupling. Two split-CPB circuits are joined by a mutual inductance L , which allows independently tunable loops via external magnetic fluxes Φ_1 and Φ_2 .

not be commensurate with the gate pulse frequency necessary to take $|1, 0\rangle$ to $|1, 1\rangle$ (More details on actual operation can be found in [66]).

The direct capacitive coupling scheme has the topological advantage of requiring no additional control lines for the two-qubit coupling. However, the capacitive interaction E_m is fixed and always on. Although the effective strength of the coupling is tunable via changing the qubit frequencies, the gate charge modulation will necessarily move the qubits away from their optimal charge gate bias points, resulting in significant coherence time degradation. Furthermore, this scheme is limited in its scope and error performance as the number of qubits scales up since it only couples nearest neighbors, making operations between far apart qubits in a chain of multiple qubits (figure 3.4a) costly in terms of resources.

Nonetheless, such fixed capacitive coupling has resulted in the first superconducting qubit coherent dynamics experiments [65], as well as the first demonstration of a c NOT in a solid-state system [66]. Similarly, fixed capacitive coupling has been implemented with Josephson phase qubits, with the generation and state tomography of entangled states [67].

3.2.2 Tunable inductive coupling

Another choice for coupling is to share a common inductance between multiple Josephson charge qubits. The shared inductor L combined with the capacitance of the charge qubits will form an LC -oscillator mode for the coupling. Such a scheme [68, 69] lends itself towards a more scaleable architecture, as it is not limited to just nearest-neighbor qubit coupling. Figure 3.3b shows such a circuit where now the interbit coupling strength is flux-controllable.

By tuning the gate voltage and threaded flux of each CPB, it is possible to turn on either a single-qubit or a two-qubit interaction regime. By setting the flux through the second qubit (one on right hand side) loop to $\Phi_2 = \Phi_0/2$ and the gate voltage to $V_2 = (2n_{g2} + 1)e/C_{g2}$, qubit 1 (one on left hand side) in the lowest two charge states $|0\rangle$ and $|1\rangle$ is individually addressable with a Hamiltonian given by

$$H = \frac{1}{2}E_{C1}(1 - n_{g1})\sigma_z^{(1)} - E_{J1}(\Phi_1, \tilde{\Phi}, L)\sigma_x^{(1)} \quad (3.23)$$

where $n_{g1} = C_{g1}V_{g1}/e$ and the Josephson energy scale is tunable by both the external flux through the common inductance $\tilde{\Phi}$ as well as the local flux Φ_1 . At any flux bias which is not $\Phi_0/2$ in both loops there is a separate two-qubit interaction which is due to the persistent current $I = I_1 + I_2$ circulating through the common inductance. The two-qubit coupling Hamiltonian is then given by

$$H_{int} = \frac{1}{2}L(I_1 + I_2)^2, \quad (3.24)$$

where the current through each CPB loop is given by

$$I_{1(2)} = 2I_{c1(2)} \cos \phi_{1(2)} \sin \left(\pi \frac{\Phi_1 + \Phi_2 + L(I_1 + I_2)}{\Phi_0} \right) \quad (3.25)$$

In the first two charge level basis, this can be simplified into an XX interaction term, which is similar to a ZZ interaction (section 2.3.2), but with a re-labeling of states.

By tuning the gate charge such that the first two charge levels are degenerate at $n_{g1} = n_{g2} = 1/2$ for each qubit, the σ_z terms can be turned off, and the reduced Ising-like Hamiltonian of the system is then

$$H = -E_{J1}\sigma_x^1 - E_{J2}\sigma_x^2 + \Pi\sigma_x^1\sigma_x^2, \quad (3.26)$$

where Π encapsulates the coupling (details given in [69]). The eigenstates of this Hamiltonian are $|+, +\rangle, |+, -\rangle, |-, +\rangle, |-, -\rangle$ where $|\pm\rangle = (|0\rangle \mp |1\rangle)/\sqrt{2}$, representing having rotated to the basis of the XX interaction. In this four level manifold, it is then possible to produce a conditional phase gate by tuning all of the energies to be the same, $E_{J1} = E_{J2} = \Pi = -\pi\hbar/4\tau$ for a fixed amount of time τ , where the two-bit states $|+, +\rangle, |+, -\rangle, |-, +\rangle$ are left the same, but $|-, -\rangle \rightarrow -|-, -\rangle$.

It is important to note the fundamental difference of this scheme having a switchable coupling (without needing to move the qubit frequencies) as opposed to the effective tunable

coupling in the capacitive case (via detuning the qubits from the interaction point). Similar mutual inductance schemes with tunable coupling have been implemented in flux qubits, where the shared inductance is further enhanced with the addition of a Josephson junction in series [70–72]. In such systems, the coupling occurs through a magnetic-dipole interaction and can be relatively stronger than in charge qubits.

3.2.3 Quantum bus coupling

The previously discussed qubit coupling schemes deal with using explicit lumped elements in the circuits, using either a capacitor or an inductor. Experimentally controlling fixed coupling designs such as the capacitor have been challenging due to electrostatic cross-talk between different parts of the coupled circuit, while the inductive coupling can result in many mutual qubit couplings requiring more complicated pulsing schemes for turning on and off specific interactions. The coupling via the shared inductor circuit as discussed in the previous section is actually an interesting direction, as it uses the idea of coupling to an electromagnetic mode of the induced LC -oscillator. One can take this idea a step further to achieve the coupling through the distribution of quantum information over an entirely separate quantum degree of freedom. In such a scheme, multiple qubits would be coupled to a shared *quantum bus*, in analogy to classical bits of information transmitted along a data bus in a classical processor. Multi-quanta interactions can then be non-local, permitting operations over an arbitrary pair of qubits.

A bus coupling differs from the linear, or nearest-neighbor arrangement of qubits (figure 3.4a), in which performing a two-qubit interaction between non-connected qubits requires multiple pair-wise operations. This direct coupling can result in a rapid build-up of errors due to the large number of gates required to communicate between distant qubits, or by analogy to classical computers, an increased number of clock cycles per operation. The bus coupling also differs from a full mutually coupled network of qubits, as depicted in figure 3.4b. In such a scheme, every single qubit is coupled to every other qubit, forming a matrix of interactions. This makes the ability to simply address a single qubit difficult, and requires a switchable coupling to turn on and off interactions between qubits.

So how could one physically realize a quantum bus? There has been pioneering work with a quantum bus coupling of trapped-ion qubits, where the quantized motion of the ions as phonons serve as the bus. The phonon quantum bus has led to the ability to perform universal quantum operations as well as quantum algorithms in ion qubits [73]. Another

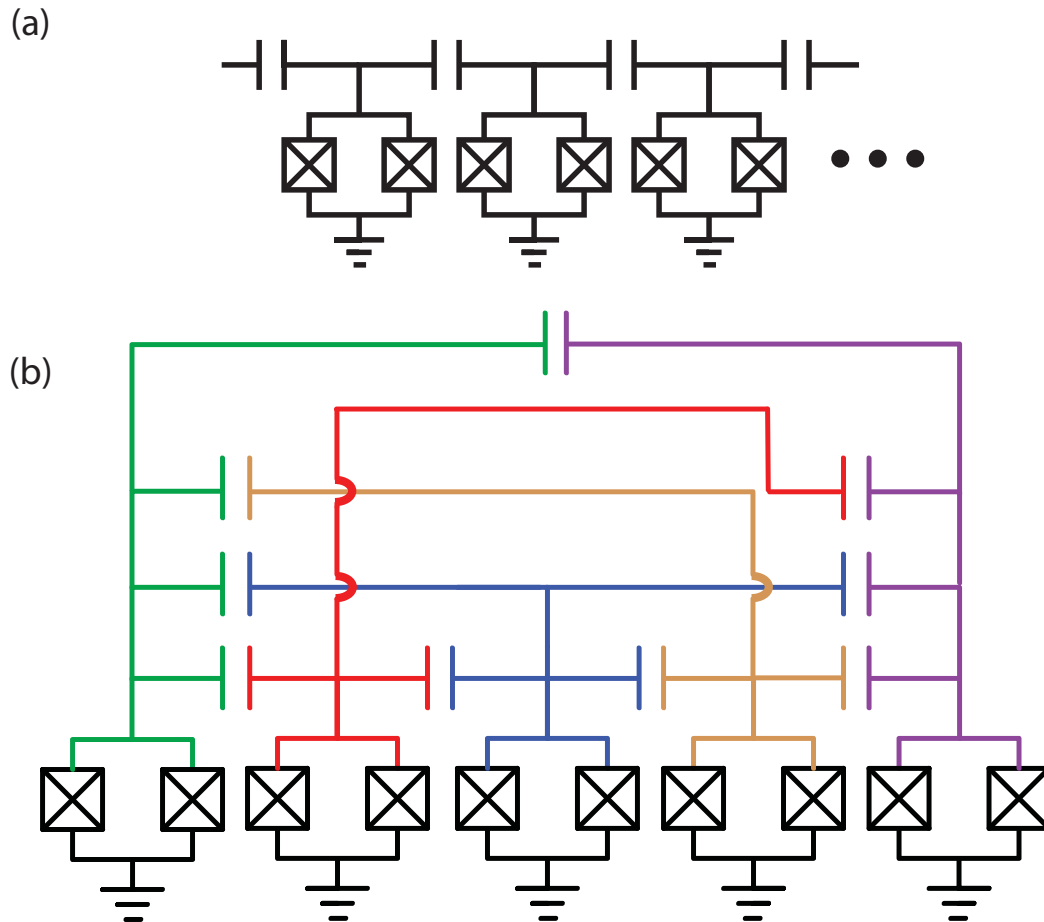


Figure 3.4: Charge-qubit coupling networks. (a) As the coupling between two charge qubits can be achieved through a discrete lumped element, such as a capacitor or an inductor, the simplest scheme for scaling up to more elements is to chain up more discrete lumped elements between each charge qubit. (b) One of the situations which can arise from attempting to couple charge qubits on a circuit with capacitances is the possibility of mutual couplings between all pairs of charge qubits. This makes the network of coupled charge qubits very large, and to address only a single qubit can become quite difficult.

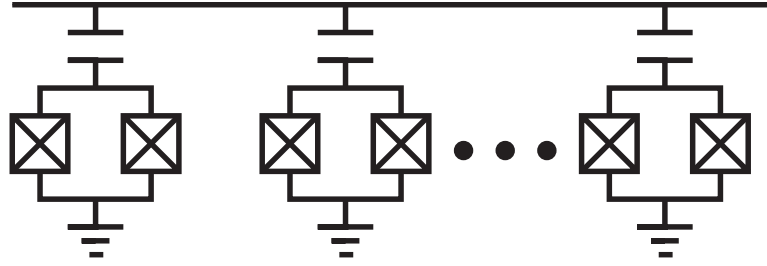


Figure 3.5: Quantum bus coupling cartoon. A quantum bus coupling attempts to use a separate quantum degree of freedom. Schematically, it has its analog in a classical instruction bus, with multiple bits locked into the same bus. Here, we can imagine the capacitive coupling of multiple charge qubits to a some feedline which will contain the quantum bus.

natural candidate for carrying quantum information is the photon. Photons can be highly coherent and interact with objects over distances greater than their wavelengths. To have increased interaction strength with a photon bus, we can employ the techniques of cavity quantum electrodynamics (QED) [74, 75], in which a single atom is coupled to a single cavity mode.

For the purposes of quantum computing with a quantum bus in superconducting qubits, cavity QED [74, 75] has been adapted into circuit quantum electrodynamics [30, 52, 53], where the photon bus is realized as a microwave frequency on-chip resonator and the atoms are replaced with superconducting qubits, such as Cooper pair boxes or transmons. It is with this architecture that we have realized a full two-qubit solid-state quantum processor. However, to motivate the quantum bus coupling in circuit QED, it is thus important to first review the key aspects of atomic cavity QED.

3.3 Cavity quantum electrodynamics

In cavity QED, individual atoms are passed through a Fabry-Perot cavity and interact coherently with the harmonic oscillator excitations, which are optical [76] or microwave [77] photons. Figure 3.6 illustrates the atom-photon field interaction. The full coupled photon-atom system is described by the Jaynes-Cummings (JC) Hamiltonian

$$H = \hbar\omega_C \left(a^\dagger a + \frac{1}{2} \right) + \frac{\hbar\omega_a}{2} \sigma_z + \hbar g (a^\dagger \sigma_- + a \sigma_+) \quad (3.27)$$

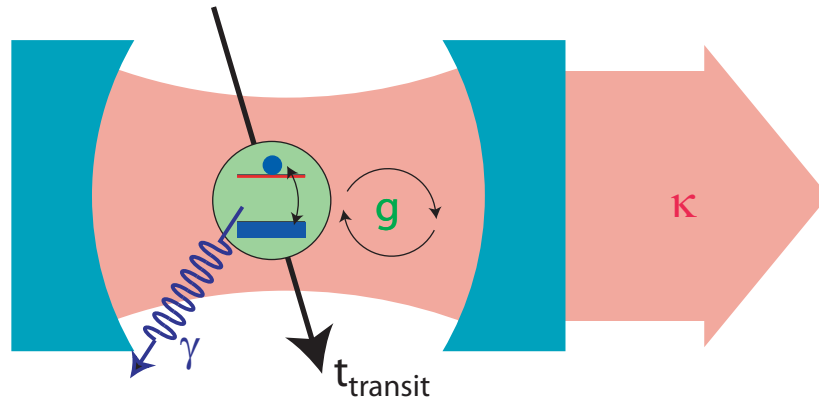


Figure 3.6: Illustration of cavity QED. A two-level atom passes through a Fabry-Perot cavity over a transit time t , during which the atom undergoes a coherent interaction with photons contained in the cavity with a strength g . Photons can leave the cavity at a rate κ and the atom decays via non-cavity modes at a rate γ .

where the first term corresponds to photons with excitation $\hbar\omega_C$ comprising the electromagnetic energy of the cavity, the second term represents the individual spin-1/2 atom with transition energy ω_a , and the third term represents a dipole interaction between the cavity and the atom within the rotating wave approximation (RWA). The interaction term, commonly known as the vacuum Rabi coupling, is the result of the quantization of the electric dipole coupling, and corresponds to coherent absorption ($\sigma_+ a$) / emission ($\sigma_- a^\dagger$) of a photon from/to the electromagnetic field at a rate g .

Although the Jaynes-Cummings Hamiltonian only describes a general two-body interaction between an atom and photon-field, a real quantum system inevitably couples to objects in the classical environment. Some of these incoherent processes in the cavity QED system include photon leakage and absorption, given by a rate κ which is often encapsulated by the transparency of the mirrors. This photon decay is actually paramount for probing the system, as photons which enter and transmit through the cavity reveal the internal dynamics of the system. The atom can also be subject to decay, either through a radiative decay via a coherent interaction with the cavity photons, or through interaction with modes outside of the Jaynes-Cummings realm. We can denote the decay of the atom due to all non-cavity channels as γ .

Depending on the values of the atom and photon energies, there can be different signatures of the interaction in cavity QED. Understanding these regimes will be critical to successfully operate the quantum bus for quantum information processing.

3.3.1 Strong coupling regime

The atom and cavity are in what is termed the *strong coupling* regime when the interaction g is much stronger than the atom and cavity decay rates, γ and κ , respectively. When the photons in the cavity and atom are in resonance with each other ($\omega_C = \omega_a$), the interaction fully hybridizes the energy levels of the combined atom and photon field system, resulting in dressed-state eigenstates in the one-excitation manifold as follows

$$|+\rangle = \frac{1}{\sqrt{2}} (|\uparrow, 0\rangle + |\downarrow, 1\rangle) \quad (3.28a)$$

$$|-\rangle = \frac{1}{\sqrt{2}} (|\uparrow, 0\rangle - |\downarrow, 1\rangle). \quad (3.28b)$$

These are simply the symmetric and anti-symmetric combinations of a single excitation in either the atom or the cavity. Here, the atom and photon can freely exchange a single quanta at a rate g as a vacuum Rabi oscillation. Later in this chapter, such a direct cavity swap interaction will be an important mechanism for inducing coupling between multiple quantum degrees of freedom.

In the strong coupling regime, more generally, there can be any number of excitations, resulting in a ladder of states with eigenstates in the n -excitation manifold given by

$$|+\rangle_n = \frac{1}{\sqrt{2}} (|\uparrow, n-1\rangle + |\downarrow, n\rangle) \quad (3.29a)$$

$$|-\rangle_n = \frac{1}{\sqrt{2}} (|\uparrow, n-1\rangle - |\downarrow, n\rangle) \quad (3.29b)$$

The energies of these states are split by $2g\sqrt{n}$ and demonstrate a built-in anharmonicity which can allow the strong-coupling regime of cavity QED to behave as a multi-level qubit.

3.3.2 Dispersive coupling regime

The cavity QED system can also be operated in a dispersive regime in which the atom and cavity do not directly exchange energy. This is achieved through detuning the atom from the cavity such that $\Delta = \omega_a - \omega_C \gg g$. Given this condition, this regime can be studied using a second-order perturbative expansion in g/Δ , to give the dispersive JC Hamiltonian,

$$H \approx \hbar \left[\omega_C + \frac{g^2}{\Delta} \sigma_z \right] \left(a^\dagger a + \frac{1}{2} \right) + \frac{\hbar \omega_a}{2} \sigma_z. \quad (3.30)$$

This new Hamiltonian reflects a re-diagonaliation of the full JC Hamiltonian given the dispersive condition. To second order, the eigenstates of this dispersive Hamiltonian coincide with those of the full Hamiltonian. The interaction is now transferred into an atom state dependent shift of the harmonic oscillator frequency (the first term), which can now take either of two values, $\omega'_C = \omega_C \pm g^2/\Delta$. The dispersive shift plays the central role for atom state interrogation in this regime via a quantum non-demolition (QND) measurement and will be the basis for multiple qubit readout in the framework of circuit QED to be discussed later.

Another way of interpreting the interaction is to re-order the terms in the Hamiltonian of (3.30) to be

$$H \approx \hbar\omega_C \left(a^\dagger a + \frac{1}{2} \right) + \frac{\hbar}{2} \left(\omega_a + \frac{2g^2}{\Delta} a^\dagger a + \frac{g^2}{\Delta} \right) \sigma_z. \quad (3.31)$$

With this arrangement, the interaction has now been moved to the right most term, behaving as a shift of the atom transition frequency. Specifically, the first term $2g^2/\Delta n$, where $n = a^\dagger a$, reflects a photon number-dependent Stark shift while the g^2/Δ term is a Lamb shift due to the electromagnetic vacuum [30, 78]. The Stark shift is a critical feature of the dispersive regime as it allows for an effective means to tune the atom transition frequency with microwave pulses, which will be discussed in more detail in regards to multi-qunta interactions for circuit QED later in this thesis (section 3.4.2).

3.4 Circuit QED

With some of the basic concepts of cavity QED under our belt, we can now move on to its analog with superconducting circuits and develop the framework for its use as a quantum bus architecture. Specifically, this section will deal with circuit QED using transmon charge qubits section 3.1.3 and we will revisit the strong and dispersive coupling regimes.

3.4.1 Coupling a transmon to a coplanar waveguide resonator

We can translate the cartoon of cavity QED (figure 3.6) into a circuit geometry as shown in figure 3.7. The Fabry-Perot cavity is now replaced by a microwave-frequency co-planar waveguide (CPW) transmission line resonator. The CPWs can be made out of superconducting material which can be low loss below their critical superconducting temperatures, allowing for high quality factor (Q) resonators. The gaps in the center-pin transmission line serve as the mirrors of the cavity, with microwave radiation forming standing waves within the

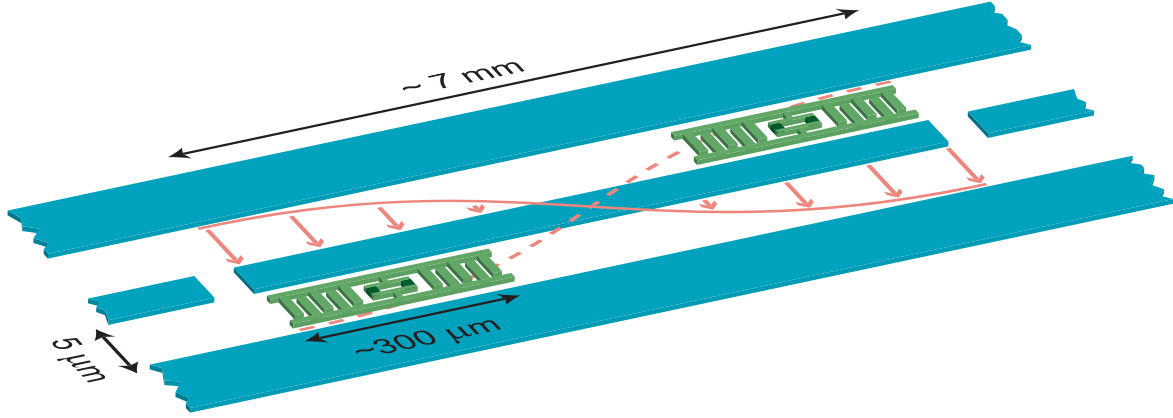


Figure 3.7: Illustration of circuit QED. A two-level atom passes through a Fabry-Perot cavity over a transit time t , during which the atom undergoes a coherent interaction with photons contained in the cavity with a strength g . Photons can leave the cavity at a rate κ and the atom decays via non-cavity modes at a rate γ .

center-stripline. Through careful engineering of these capacitive gaps and the length of the center stripline, the resonant frequency and quality factor of the resonators can be designed (chapter 5).

Following Ref. [62], the transmission line resonator circuit can be quantized. For a transmission line of length d , capacitance per unit length c , and inductance per unit length l , the Hamiltonian can be expressed as

$$H = \hbar \sum_n \omega_n \left(a_n^\dagger a_n + \frac{1}{2} \right) \quad (3.32)$$

with resonant frequencies $\omega_n = n\pi/d\sqrt{lc}$. For the purposes of the experiments discussed in this thesis, we will be working in the vicinity of just the first mode, with $n = 1$, and as a result we will write the cavity Hamiltonian with frequency $\omega_C = \pi/d\sqrt{lc}$, without the sum and subscripts.

The coupling between a transmon qubit and the transmission line resonator is an electrostatic capacitive interaction*. We can place the transmon near either end of the CPW to couple to a voltage antinode for the $n = 1$ mode ($\lambda/2$) of the resonator. The Hamiltonian for this combined system will be the sum of the transmon Hamiltonian (3.21), the transmission line resonator Hamiltonian (3.32) and a dipole interaction term from the product of the

* This is due to the physical size of the transmon being much smaller than the wavelength of the resonator, allowing a lumped element interpretation.

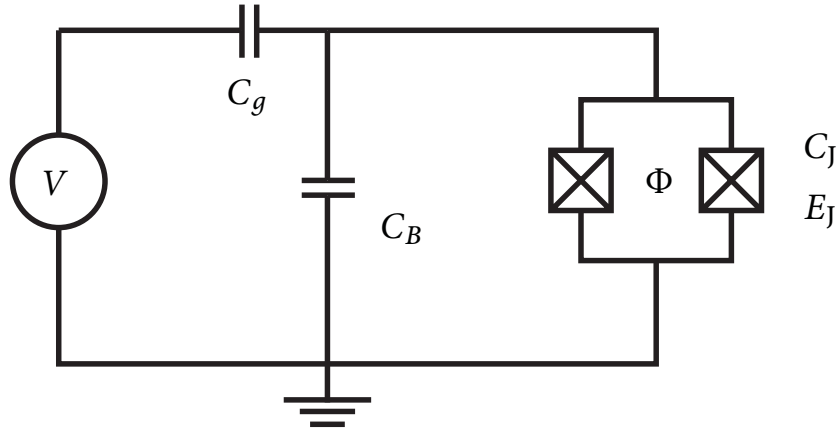


Figure 3.8: Reduced transmon coupling to CPW schematic. The transmon is coupled to the CPW transmon line via a gate capacitance C_g . A split pair of junctions with E_J and E_C are in parallel with a shunt capacitance C_B .

voltage in the cavity, $V_0(a + a^\dagger)$, where V_0 is the zero point root mean-squared voltage, with the charge of the transmon, $2ne$,

$$H = 4E_C (n - n_g)^2 - E_J \cos \phi + \hbar\omega_C a^\dagger a + 2\beta n e V_0 (a^\dagger + a). \quad (3.33)$$

Here, β is a voltage division ratio, defined by the ratio of the gate capacitance to the total capacitance. We can view the reduced capacitance network of the transmon in a CPW as shown in figure 3.8. The entire transmon coupled CPW circuit is presented in detail in chapter 5. We can express the values of the parameters of (3.33) in terms of the reduced network as,

$$E_C = \frac{e^2}{2C_\Sigma} \quad (3.34a)$$

$$V_0 = \sqrt{\frac{\hbar\omega_C}{cL}} \quad (3.34b)$$

$$\beta = \frac{C_g}{C_\Sigma} \quad (3.34c)$$

$$C_\Sigma = \frac{C_g}{C_J + C_g + C_B}, \quad (3.34d)$$

where C_B is the shunt capacitance, C_g is the gate capacitance, c is the capacitance per unit length of the resonator, and L is the length of the resonator. We can write the Hamiltonian in

the basis of the eigenstates of the transmon $|j\rangle$ as,

$$H = \hbar\omega_C a^\dagger a + \hbar \sum_j \omega_j |j\rangle \langle j| + \hbar \sum_{i,j} g_{i,j} |i\rangle \langle j| (a + a^\dagger), \quad (3.35)$$

where $\hbar g_{i,j} = 2eV_0\beta \langle i|n|j\rangle$ are dipole coupling energies which involve many charge states, as the matrix elements for different transitions will all explicitly contribute. In the asymptotic large E_J/E_C limit, the dipole coupling is given by

$$g_{ij} \approx \sqrt{2} \frac{eV_0}{\hbar} \beta \left(\frac{E_J}{8E_C} \right)^{1/4} \langle i|(c - c^\dagger)|j\rangle \quad (3.36)$$

where c and c^\dagger are lowering and raising operators for the transmon energy levels. For nearest-neighbor energy levels the coupling is given by

$$g_{j,j+1} = \frac{eV_0}{\hbar} \beta \left(\sqrt{2(j+1)} \left(\frac{E_J}{8E_C} \right)^{1/4} \right), \quad (3.37)$$

and is the dominant contribution to the coupling in the large E_J/E_C limit [61].

When there is sufficient anharmonicity such that the transmon can be operated as a qubit, we can keep just the first two levels and use the Pauli spin operator notation:

$$H = \hbar\omega_C a^\dagger a + \frac{\hbar\omega_q}{2} \sigma_z + g\sigma_x (a + a^\dagger). \quad (3.38)$$

By making the rotating wave approximation (RWA), given that $\omega_C \simeq \omega_q$ and $\omega_C \gg g$, counter-rotating terms, $a^\dagger \sigma_+$ and $a\sigma_-$ can be neglected (where $\sigma_\pm = (\sigma_x \pm i\sigma_y)/2$), so that then we recover the Jaynes-Cummings Hamiltonian as discussed in section 3.3,

$$H = \hbar\omega_C a^\dagger a + \frac{\hbar}{2} \omega_q \sigma_z + \hbar g (a\sigma_+ + a^\dagger \sigma_-). \quad (3.39)$$

More generally for the multi-level transmon, the Hamiltonian is given by

$$H = \hbar\omega_C a^\dagger a + \hbar \sum_j \omega_j |j\rangle \langle j| + \hbar \sum_j g_{j,j+1} (|j+1\rangle \langle j| a + \text{h.c.}). \quad (3.40)$$

Similar to cavity QED, we will be able to access a dispersive regime in circuit QED, described in the following section.

3.4.2 Dispersive regime of circuit QED

We have seen now that the transmon qubit can be in a strong coupling regime with a transmission line cavity. By tuning the energy levels of the transmon away from resonance with the cavity, we enter a dispersive regime (section 3.3.2) when $g_{j,j+1} \ll \omega_{j+1,j} - \omega_C$. A unitary transformation, $H \rightarrow UHU^\dagger$, similar to the one used for the simple atom case can be made, with

$$U = \exp \left[\sum_j \lambda_j |j+1\rangle \langle j| a - \text{h.c.} \right] \quad (3.41)$$

and expanding to second order in the small parameter $\lambda_j = g_{j,j+1}/(\omega_{j,j+1} - \omega_C)$. We are then left with a diagonalized Hamiltonian,

$$\begin{aligned} H/\hbar = & \sum_j \omega_j |j\rangle \langle j| + \omega_C a^\dagger a + \sum_j \chi_{j,j+1} |j+1\rangle \langle j+1| - \chi_{01} a^\dagger a |0\rangle \langle 0| \\ & + \sum_{j=1} (\chi_{j-1,j} - \chi_{j,j+1}) a^\dagger a |j\rangle \langle j| \end{aligned} \quad (3.42a)$$

with dispersive couplings χ_{ij} given by

$$\chi_{ij} = \frac{g_{ij}^2}{\omega_{ij} - \omega_C}. \quad (3.43)$$

Taking a two-level approximation for using the transmon as a qubit, the dispersive Hamiltonian then takes the form

$$H = \frac{\hbar}{2} \omega'_q \sigma_z + \hbar (\omega'_C + \chi \sigma_z) a^\dagger a, \quad (3.44)$$

where the qubit transition frequency $\omega'_q = \omega_{01} + \chi_{01}$ and the cavity frequency $\omega'_C = \omega_C - \chi_{12}/2$ are both Lamb-shifted. The dressed transitions here give a dispersive Hamiltonian similar to the one from traditional cavity QED (3.30) but with a different transmon state dependent shift given by

$$\chi = \chi_{01} - \frac{\chi_{12}}{2}. \quad (3.45)$$

Using the asymptotic expression for g_{ij} , the shift can be approximated as

$$\chi \approx -\frac{g^2}{\Delta} \frac{E_C}{\hbar \Delta - E_C}, \quad (3.46)$$

where $\Delta = \omega_{01} - \omega_C$.

3.4.3 Strong dispersive regime

The strong dispersive regime refers to the situation when the dispersive shift χ (3.45) is greater than the linewidths of the qubit, γ , and of the cavity, κ . Figure 3.9 shows both the representative spectra of the cavity and of a single qubit system (using simplified two-level transmon approximation) signifying the strong dispersive limit. With $\chi > \gamma$, the spectrum of the qubit can be resolved into individual photon number peaks. This qubit number-splitting pattern theoretically allows for the determination of the mean photon number state of the cavity. The qubit frequency peaks will be located at $\omega_n = \omega_q + 2n\chi$, and multiple peaks will be observed given a thermal or coherent distribution of photons in the cavity. For a transmon, these photon number dependent shifts will be slightly different due to the non-linearity introduced into the cavity by the relatively smaller anharmonicity [79, 80]. Nonetheless, the qubit spectrum can therefore be used to measure the photon number in the cavity.

With the cavity shift greater than the cavity linewidth, the transmission through the cavity becomes a non-linear function of the state of the qubit. The cavity transmission is Lorentzian, centered around frequency $\omega_C + \chi$ with the qubit in the ground state and centered around frequency $\omega_C - \chi$ when in the excited state. Here, the state-dependent transmission can be written as

$$T = \frac{\kappa/2}{\omega - (\omega_C \pm \chi\sigma_z) + i\kappa/2}. \quad (3.47)$$

Now, when $\chi > \kappa$, the transmission of an applied drive at $\omega_C + \chi$ will be a nonlinear function of the qubit state, which permits a projective QND readout very much in the way a Stern-Gerlach experiment can distinguish a spin polarization. This will be discussed in more detail with respect to the joint readout of a multi-qubit state in chapter 4.

3.5 Qubit decoherence

As the transmon qubits are electromagnetic circuits, there are a number of factors in their environment which can degrade their performance as quantum degrees of freedom. All qubit errors can be classified as either relaxation and dephasing.

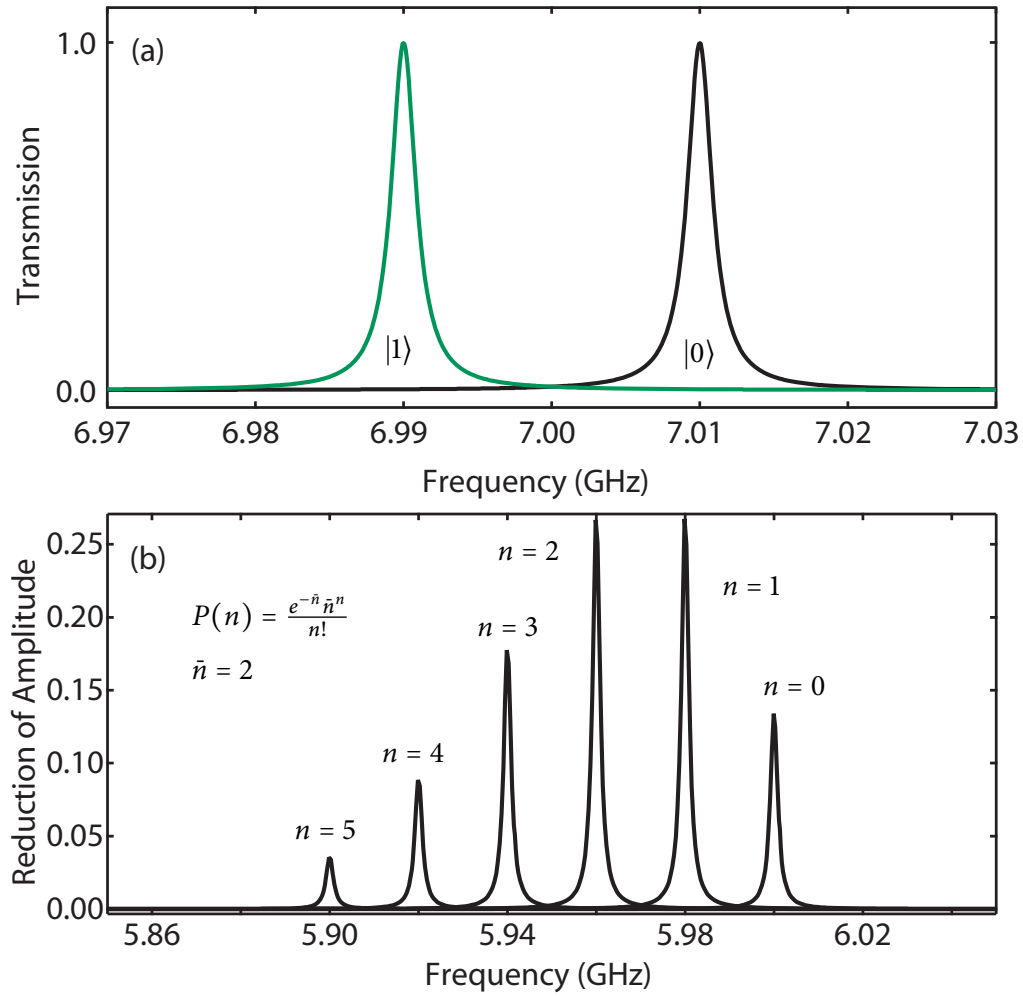


Figure 3.9: Strong dispersive regime of circuit QED. (a) Theoretical state dependent cavity transmission reveals two Lorentzian peaks for the case of $|0\rangle$ and $|1\rangle$, separated by 2χ (Here assuming $\chi/\pi = 20$ MHz). (b) Qubit spectroscopy shows multiple peaks corresponding to different cavity-photon number. The weighting of these peaks is given by a simple Poisson distribution as a function of the mean number of photons in the cavity $\bar{n} = 2$.

3.5.1 Relaxation and the Purcell effect

Relaxation and heating, are processes which result in the de-excitation and excitation of the qubit, respectively. Fluctuations in some environmental parameter M (such as the flux Φ or voltage V), can be treated as a perturbation to the qubit Hamiltonian as $\tilde{H} = \hat{\xi}M$, where $\hat{\xi}$ is an operator which couples to the qubit eigenstates. The noise that specifically results in relaxation and heating of the qubit occur at the qubit frequency ω_q . By using first-order time-dependent perturbation theory (Fermi's golden rule), transition rates between the levels can be found to be [81]

$$\Gamma_{\uparrow\downarrow} = \frac{1}{\hbar^2} \left| \langle g | \hat{\xi} | e \rangle \right|^2 S_M(\mp\omega_q), \quad (3.48)$$

where $S_M(\mp\omega_q)$ reflects the spectral density of the noise associated with environmental parameter M at the frequency of the qubit. The relaxation time is given by $T_1 = 1/(\Gamma_{\uparrow} + \Gamma_{\downarrow})$. Here, the qubit acts as a spectrometer of noise at its transition frequency [81]. Note also that the qubit will distinguish between a positive frequency component of noise, corresponding to relaxation of the qubit and excitation of the environment, and a negative frequency component, corresponding to excitation of the qubit and relaxation of the environment. To understand the qubit relaxation process thus requires investigating the environmental sources of noise at the qubit transition frequency and determining how strongly they couple to the qubit.

For a charge-based qubit, an intrinsic relaxation rate can be associated with a number of noise processes, including flux fluctuations, quasiparticle tunneling, and dipolar radiation. These are dealt with in detail for Cooper pair box qubits in Ref. [53] and for transmon qubits in Ref. [61]. However, the estimated relaxation rates due to these factors are small compared to the relaxation rate due to voltage coupling to the electromagnetic environment. Particularly, in the circuit QED setup, in which the environmental impedance is well-controlled, the qubit relaxation rate can be completely understood up to an intrinsic limit suggestive of a lossy dielectric [82].

Starting with a two-level truncation to the transmon qubit, let us formally treat the relaxation due to voltage noise. By capacitively coupling the qubit to an environmental impedance $Z(\omega)$, voltage fluctuations δv on this line couple via the charge degree of freedom \hat{n} . Here, the voltage noise coupling operator is

$$\hat{\xi} = 2e\beta\delta V \hat{n} \quad (3.49)$$

where β is the voltage division ratio, given by C_g/C_Σ . With an environmental impedance $Z(\omega)$, the zero-temperature voltage spectral density can be found from the Johnson-Nyquist formula,

$$S_V(\omega) = 2\hbar\omega\text{Re}[Z(\omega)]. \quad (3.50)$$

Then, from Fermi's golden rule (3.48), the effective decay rate Γ due to voltage coupling is then determined to be

$$\Gamma = 16\pi e^2 \beta^2 \omega_q \frac{\text{Re}[Z(\omega_q)]}{h} |\langle 0 | \hat{n} | 1 \rangle|^2. \quad (3.51)$$

For the transmon qubit, the charge matrix element between the first two levels (3.37) is [61]

$$\langle 0 | \hat{n} | 1 \rangle = \frac{1}{\sqrt{2}} \left(\frac{E_J}{8E_C} \right)^{1/4}. \quad (3.52)$$

Then, by using the expressions $E_C = e^2/2C_\Sigma$, $\omega_q = \sqrt{8E_J E_C}$, Γ can be simplified to

$$\Gamma = \frac{(\omega_q C_g)^2 \text{Re}[Z(\omega)]}{C_\Sigma}. \quad (3.53)$$

Therefore, the voltage noise effect on the relaxation rate occurs through the form of the dissipative environmental impedance $\text{Re}[Z(\omega)]$.

Interestingly enough, the above result can be found using a simple circuit model as well [82]. For the capacitive coupling circuit shown in figure 3.10, we can combine the gate capacitance C_g with the environmental impedance $Z(\omega)$ into an effective resistor given by $R = 1/\text{Re}[Y(\omega)]$ where the admittance $Y(\omega)$ is

$$Y(\omega) = \frac{\omega^2 C_g^2 Z(\omega) + i\omega C_g}{1 + \omega^2 C_g^2 Z^2(\omega)}. \quad (3.54)$$

The relaxation rate is then simply found from the decay time $1/RC_{\text{eff}}$, where $C_{\text{eff}} = C_\Sigma - C_g$, giving the effective capacitance of the transmon without the effect of the gate. Then, we find the same result as in (3.53) with this treatment.

This formalism is very powerful, as it tells us that by identifying the environmental impedance $Z(\omega)$, we are able to predict the relaxation rates of the qubit. Specifically in the case of a qubit placed within a single-mode cavity, this reproduces the well-known Purcell

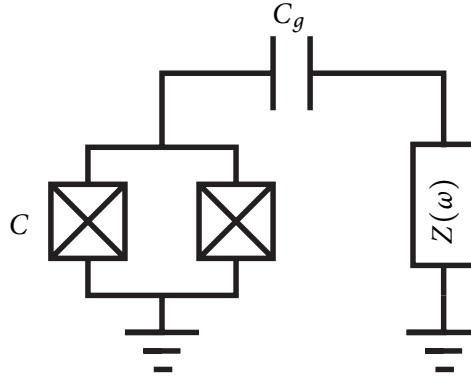


Figure 3.10: Environmental coupling of transmon. The voltage relaxation rate of the transmon qubit can be found from a simple RC decay time. The transmon capacitance C is coupled to an environmental impedance of $Z(\omega)$ through a coupling capacitor C_g .

[83] result,

$$\gamma_\kappa = \frac{g^2 \kappa}{(\omega_C - \omega_q)^2}. \quad (3.55)$$

The Purcell effect reflects the altered spontaneous emission rate due to coupling to cavity photons which decay at a rate κ . For the case of circuit QED, this simplified single-mode Purcell treatment is unfortunately inadequate as a result of strong coupling to higher modes of the transmission line cavity. Heuristically, this strong dependence on higher modes can be seen from the increasing coupling strength with mode number $g_n = g\sqrt{n+1}$ as well as the increasing decay rate of the n th harmonic, $\kappa_n = (n+1)^2\kappa$. The multi-mode cavity effects on the Jaynes-Cummings physics is still a topic of ongoing theoretical research. However, it is possible to still predict the relaxation rates due to the multi-mode Purcell effect by using the circuit formalism and considering the coupling of the qubit to a distributed transmission-line resonator. These calculations have been shown to agree strikingly well with experimental predictions, up to a global lossy limit with a $Q \sim 50,000 - 70,000$, as described in Ref. [82]. For the purposes of this thesis, the investigations of Ref. [82] demonstrate that our current T_1 is modeled and well-understood, and improvements are the subject of current research.

3.5.2 Dephasing

Dephasing is generally understood as the fluctuations of the qubit transition frequency due to coupling to the environment. Low frequency noise far below the transition frequency can cause the qubit to accumulate a random phase. Qubit relaxation will dephase the qubit at a

rate $\Gamma_{\downarrow}/2$, which can be shown from a Bloch equation treatment [62]. In addition, there can be fluctuations to the transition frequency which occur over the course of a decay lifetime, labeled with a dephasing rate of Γ_{ϕ} . We can call the total dephasing the sum of these rates $\Gamma_2 = \Gamma_{\downarrow}/2 + \Gamma_{\phi}$. In the case that $\Gamma_{\phi} = 0$, the total dephasing rate is given by $\Gamma_{\downarrow}/2$, such that the dephasing time $T_2 = 2T_1$.

Dephasing can be interpreted as the decay of off-diagonal density matrix elements. In a two-level system, given a noise power $S_M(\omega)$, this exponential decay is given by [61, 84],

$$\rho_{01}(t) = \exp\left(-\frac{1}{2} \int_{-\infty}^{\infty} \frac{d\omega}{2\pi} S_M(\omega) \frac{\sin^2(\omega t/2)}{(\omega/2)^2}\right). \quad (3.56)$$

A specific noise spectrum that can contribute to dephasing is $1/f$ noise in the parameters that determine the qubit transition frequency ω_{01} . The $1/f$ power spectrum is given by

$$S_M(\omega) = \frac{2\pi A^2}{|\omega|} \quad (3.57)$$

and is a typical noise spectrum for charge, flux, and critical current, all of which can vary ω_{01} . The parameter A determines the overall amplitude of the fluctuations and have been measured in various separate experiments [85–88]. In the case of $1/f$ noise, the limits of the integral in (3.56) are between f_{\min} and $\omega_{01}/2\pi$, where f_{\min} corresponds to a low-frequency cutoff determined by the repetition rate of an experiment [84].

A comprehensive theoretical treatment of these different noise processes which dephase charge qubits is presented in Refs. [53, 61, 64]. We will review both the charge noise and flux noise contributions for the transmon qubit. In fact, in current transmon experiments, the charge noise is sufficiently suppressed from operating in the transmon regime [63] that we find flux noise to be the dominant culprit for dephasing.

Charge noise

In the Cooper pair box, with $E_J/E_C \simeq 1$ the dephasing is primarily caused by slow fluctuations of the offset charge n_g , even while operating at the ‘sweet-spot’ [53, 60] which is first-order insensitive to charge noise. The transmon qubit operates in a different regime, with $E_J/E_C \gg 1$, resulting in the exponential suppression of the charge fluctuations. For $1/f$ charge noise, the typical amplitude is $A = 10^{-4} - 10^{-5}e$ [85]. From Ref. [61] the dephasing time dependence on

small fluctuations of the charge dispersion is given by

$$T_\phi \sim \frac{\hbar}{A} \left| \frac{\partial E_{01}}{\partial n_g} \right|^{-1} \simeq \frac{\hbar}{A\pi|\epsilon_1|} \quad (3.58)$$

where ϵ_1 is given by (3.14). Therefore, T_ϕ exponentially increases with E_J/E_C and becomes very insensitive to charge fluctuations in the transmon regime. For typical sample parameters of $E_J = 25$ GHz, $E_C = 350$ MHz, gives a dispersion $\epsilon_1 \sim 3$ kHz and using $A \sim 10^{-4}$, we find dephasing times due to charge noise to be $T_\phi \sim 170 \mu\text{s}$, far above $2T_1$.

Flux noise

Whereas charge noise is effectively removed by operating with E_J/E_C sufficiently in the transmon regime, flux noise can still be a significant dephasing mechanism. Specifically, noise in the externally applied flux can result in fluctuations of the effective Josephson coupling energy E_J . Recall the external flux-dependent functional form for $E_J(\tilde{\Phi})$ given in (3.8)b. Here, E_J is periodic in $\tilde{\Phi}$, and there are maximal values at which it becomes first-order insensitive. These applied flux bias locations are ‘sweet-spots’ in $\delta\tilde{\Phi}$.

In Ref. [61], the effect of flux noise is computed at and away from flux sweet-spots. Away from the sweet-spots, the dephasing time due to flux noise is

$$T_\phi \simeq \frac{\hbar}{A} \left| \frac{\partial E_{01}}{\partial \Phi} \right|^{-1} = \frac{\hbar}{A} \frac{\Phi_0}{\pi} \left(2E_C E_J^{\max} \left| \sin \frac{\pi\Phi}{\Phi_0} \tan \frac{\pi\Phi}{\Phi_0} \right| \right)^{-1/2}, \quad (3.59)$$

where the relevant noise parameter A has been found historically to be $10^{-5}\Phi_0$ [86]. Figure 3.11 shows the frequency, relevant frequency slope versus flux, and inferred T_ϕ for both $A = 10^{-5}\Phi_0$ and $A = 10^{-6}\Phi_0$ for $E_J = 25$ GHz and $E_C = 350$ MHz. Simply detuning to $\Phi_0/4$, results in a $T_\phi \sim 1.5 \mu\text{s}$ for the $10^{-5}\Phi_0$ case, which is now on the order of Purcell limited relaxation times. However, at the flux sweet spot, the dephasing time can be estimated with the second derivative of the transition frequency as

$$T_\phi \simeq \left| \frac{\pi^2 A^2}{\hbar} \frac{\partial^2 E_{01}}{\partial \Phi^2} \right|_{\Phi=0}^{-1} = \frac{\hbar \Phi_0^2}{A^2 \pi^2 \sqrt{2E_J E_C}} \quad (3.60)$$

and with the same parameters as above will give $T_\phi \sim 40$ ms.

Experimentally, we have found across multiple transmon qubit samples that detuning away from the flux-sweet spots results in dephasing times that are in agreement with the flux-noise treatment. We also find that the noise parameter A is in the range of $10^{-5} - 10^{-6}\Phi_0$.

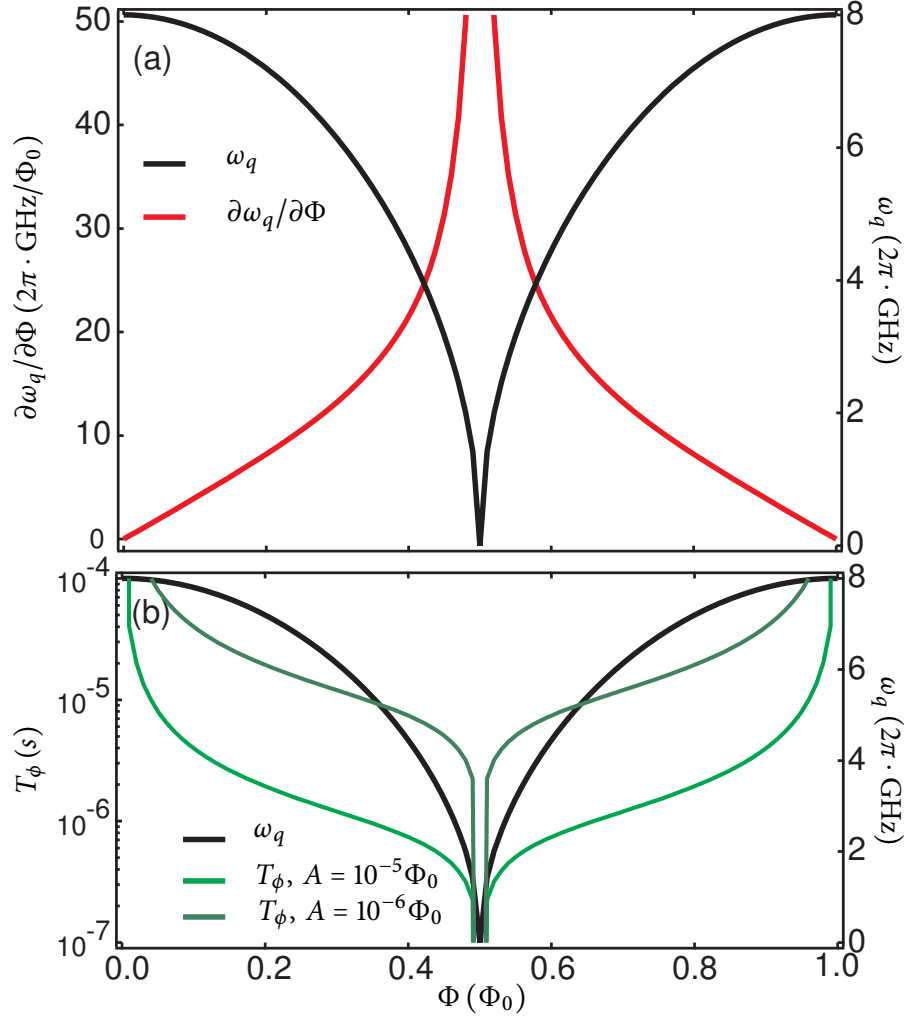


Figure 3.11: T_ϕ due to flux noise. (a) The qubit frequency ω_q (solid black) and its derivative with respect to flux $\partial\omega_q/\partial\Phi$ (solid red) are shown versus flux Φ . (b) Assuming a flux noise spectrum amplitude $A = 10^{-6}\Phi_0$, the inferred flux-dependent T_ϕ (solid green) is plotted versus Φ .

Sensitivity to changes in the external flux (moving dewars, magnetic shoes) is reduced in the experimental setup by using cryogenic magnetic shielding (detailed further in chapter 5). Most experiments currently aim to operate the qubits at their flux sweet-spots in order to reduce the effect of the flux noise. Specifically in the experiments in chapter 8 and chapter 9, the qubits are parked at their flux sweet-spots, where the coherence times are $\sim 1 - 2 \mu\text{s}$, for performing state initialization, single-qubit operations and a joint readout.

3.6 Chapter summary

In this chapter we have reviewed the superconducting charge-based transmon qubit and discussed its coupling to a microwave resonator in circuit QED. We have also introduced some of the basic regimes of circuit QED and made an association with the well-known cavity QED architecture. Thus far we have only considered circuit QED with a single transmon qubit. To build a simple quantum processor, we look to scale this up, and use the microwave resonator as a quantum bus. The next chapter continues the treatment of circuit QED, but associates the quantum information processing protocols of chapter 2 with the coupled qubit and microwave cavity system described in this chapter.

CHAPTER 4

Circuit QED: Quantum Information Processing with a Photon Bus

THE circuit QED architecture discussed in chapter 3 can be used as a quantum bus coupling scheme for multiple qubits. As previously described, transmon qubits can be coupled to a microwave coplanar waveguide resonator. We can investigate the case of having two transmons, both of which can interact with a single quantum bus by being placed at opposite ends of the microwave resonator. If we drive the $\lambda/2$ resonance, there are anti-nodes in the voltage at both ends of the resonator, which give the strong electric dipolar coupling as described in section 3.4. Therefore, we can consider a two-qubit cavity bus device, and try to understand how to perform some of the quantum information processing protocols from chapter 2.

Specifically, we will need to demonstrate a universal set of gate operations (section 2.1) as well as a full quantum-state readout (section 2.5.2). This chapter will start with a discussion about the initialization of qubits in circuit QED and the effect of residual cavity excitations on the starting state of the transmon qubits (section 4.1). Next, we will describe how we can incorporate microwave driving to implement single-qubit operations in circuit QED (section 4.2). Then, in section 4.3 we will discuss how the photon quantum bus provides a number of interactions that will be useful for implementing multi-qubit entanglement operations. These interactions can be turned on and off through fast tuning of the qubit

transition frequencies. Although we will be performing quantum logic treating the transmons as simple qubits, we will describe an interesting two-qubit interaction involving the higher excited levels (section 4.3.3). Finally, in section 4.4, we will expand on the single-qubit dispersive readout described previously (section 3.4.3) and present a joint two-qubit readout mechanism, where the same bus used for multiple qubit coupling can also be used for their multiplexed state detection.

4.1 Initialization

For the purposes of initializing a quantum register of m qubits in a circuit QED system, we require two starting conditions:

1. Qubits dispersively detuned from cavity, $|\omega_q^{(j)} - \omega_C| \gg g$, $\forall j \in m$ and qubits detuned from one another by larger than the transmon anharmonicity to the second excited state, $|\omega_q^{(j)} - \omega_q^{(i)}| \gg \alpha_1$, $\forall i, j \in m$.
2. Mean cavity photon number exceedingly small, $\bar{n} \sim 0$, and all intrinsic, non-cavity, transition processes take the qubit to the ground state.

Condition 1 imposes the dispersive regime of circuit QED, with the qubit transitions separated from one another in frequency space. Furthermore, this condition also avoids possible excitations due to virtual photon exchange with the cavity (see section 4.3.2). In addition, different qubit transition frequencies will allow independent driving of the qubits for single qubit rotations (see section 4.2). The computational basis states will then be very simple, $\{|k_1, k_2, \dots, k_m\rangle\}$, where $k_i \in \{0, 1\}$. For an m -qubit register, there are thus 2^m basis states.

Condition 2 enforces that the qubit register will start from the joint ground state, $|0, 0, \dots, 0\rangle$. The mean photon number in the cavity \bar{n} is directly related to the temperature of the bath to which it is connected. Assuming a bath temperature T , the \bar{n} at the cavity frequency is given by the Bose-Einstein distribution,

$$\bar{n} = \frac{1}{\exp(\hbar\omega_C/k_B T) - 1}. \quad (4.1)$$

For typical experimental situations, $T = 15 - 50$ mK, corresponding to dissipative 50Ω attenuators and microwave circulators anchored to the base temperature of the dilution fridge (more details of the experimental setup in chapter 5). In the case of our experiments, $\bar{n} \lesssim 0.003$ [89] (further details will be given in chapter 6).

Although this is the average excitation number for a photon only at the single cavity frequency ω_C , we also need the second part of condition 2 to hold such that the dominant excitation mechanism would be via the cavity, or that all other reservoirs to which it may decay are at the same or lower temperature than the cavity. As discussed in section 3.5.1 and in detail in Ref. [82], the relaxation of the transmon qubits can be mostly attributable to spontaneous emission through the cavity, γ_κ , via the multi-mode Purcell effect. However, also recall that there is an intrinsic loss due to a constant $Q \sim 50,000 - 70,000$ which sets in at qubit transition frequencies such that $\gamma_\kappa < \omega_q/Q$. At this time the temperature of the reservoir to which this unknown loss mechanism is connected to is neither characterized nor known. Nonetheless, what we can say is that at locations where the qubit is multi-mode Purcell limited, the qubit resets through the emission of a photon in equilibrium with a very cold reservoir characterized by $\bar{n} \lesssim 0.003$. Assuming that the qubit is only in equilibrium with this photon bath, the residual excited state polarization, P_1 , will be bounded by 0.003, giving an initial qubit polarization in the ground state, P_0 of at least 99.7%.

A strong-driving experiment while in the strong coupling regime of circuit QED can be used with precise master-equation simulations to determine the mean photon number [89]. This experimental demonstration of the initialization also provides a detailed view of Jaynes-Cummings physics and will be discussed in chapter 6. For the purposes of this chapter, from here forth we assume that our initial state will be in the mutual ground state of all the qubits, $|0, 0, \dots, 0\rangle$.

4.2 Single-qubit gates in circuit QED

In this section we will develop the groundwork for single-qubit gates, with rotations around the three Cartesian axes of the Bloch sphere (section 2.2). A simple microwave drive with controllable phase can be used for x and y rotations whereas either an off-resonant drive which induces an ac-Stark shift or fast flux tuning can be used to perform direct z rotations.

4.2.1 Introducing a drive

We can include a separate external drive term to the Jaynes-Cummings Hamiltonian of (3.40). Consider multiple classical time-dependent coherent drives with a Hamiltonian

$$H_{\text{drive}} = \sum_k (a + a^\dagger) \left(\xi_k e^{-i\omega_d^{(k)} t} + \xi_k^* e^{i\omega_d^{(k)} t} \right) \quad (4.2)$$

where ξ_k is the strength, $\omega_d^{(k)}$ is the frequency of the k th drive, and a and a^\dagger are the cavity annihilation and creation operators. When the drive strengths are weak compared to the other relevant energies (ω_C, g) the rotating-wave approximation (RWA) can be applied to give,

$$H_{\text{drive}} = \sum_k a \xi_k^* e^{i\omega_d^{(k)} t} + a^\dagger \xi_k e^{-i\omega_d^{(k)} t}. \quad (4.3)$$

For the moment, let us consider the case of just a single drive on a single qubit in circuit QED.

When combined with (3.40), we can remove the time-dependence of the full Hamiltonian by making the following unitary transformation to enter the rotating frame of the drive:

$$U(t) = \exp \left[i\omega_d t (a^\dagger a + \sum_j |j\rangle\langle j|) \right]. \quad (4.4)$$

The full Hamiltonian now takes the form

$$H = U(H + H_{\text{drive}})U^\dagger - iU\dot{U}^\dagger \quad (4.5a)$$

$$\begin{aligned} &= \hbar(\omega_C - \omega_d) a^\dagger a + \hbar \sum_j [(\omega_j - j\omega_d) |j\rangle\langle j| + g_{j,j+1} (a^\dagger |j\rangle\langle j+1| + a |j+1\rangle\langle j|)] \\ &\quad + (a\xi^* + a^\dagger\xi) \\ &= \hbar\Delta_r a^\dagger a + \hbar \sum_j \Delta_j |j\rangle\langle j| + \hbar \sum_j g_{j,j+1} (a^\dagger |j\rangle\langle j+1| + a |j+1\rangle\langle j|) \\ &\quad + (a\xi(t)^* + a^\dagger\xi(t)), \end{aligned} \quad (4.5b)$$

where we have introduced the frequency differences $\Delta_r = \omega_C - \omega_d$ and $\Delta_j = \omega_j - j\omega_d$ and allowed for the drive strength to be a slow function of time $\xi(t)$.

The drive here still reflects transitions to the cavity. We can instead enter a frame such that the drive Hamiltonian acts on transitions of the transmon by performing a Glauber displacement transformation (details in Refs. [62, 79]), with displacement operator given by

$$D(\alpha) = \exp [\alpha(t) a^\dagger - \alpha^*(t) a]. \quad (4.6)$$

By choosing $\alpha(t)$ as the solution to the differential equation

$$-i\dot{\alpha}(t) + \Delta_r \alpha(t) + \xi(t) = 0, \quad (4.7)$$

the Hamiltonian takes the simple form

$$\begin{aligned}
 H = \Delta_r a^\dagger a + \sum_j \Delta_j |j\rangle \langle j| + \sum_j g_{j,j+1} (a^\dagger |j\rangle \langle j+1| + a |j+1\rangle \langle j|) \\
 + \frac{1}{2} \sum_j (\Omega^*(t) |j\rangle \langle j+1| + \Omega(t) |j+1\rangle \langle j|),
 \end{aligned} \tag{4.8}$$

where $\Omega(t) = 2g\alpha(t)$ gives the Rabi frequency. For a time-independent drive, this Rabi frequency is given by $\Omega = 2\xi g/\Delta_r$. Here in the limit where the detuning Δ_r is large compared to the cavity half-width $\kappa/2$, we can write the average photon number $\bar{n} = (\xi/\Delta_r)^2$ such that the Rabi frequency recovers the Jaynes-Cummings form $\Omega \approx 2g\sqrt{\bar{n}}$.

Now going to the dispersive regime as described in section 3.4.2, the Hamiltonian is given by

$$\begin{aligned}
 H/\hbar = \sum_j \omega_j |j\rangle \langle j| + \omega_c a^\dagger a + \sum_j \chi_{j,j+1} |j+1\rangle \langle j+1| - \chi_{01} a^\dagger a |0\rangle \langle 0| \\
 + \sum_{j=1} (\chi_{j-1,j} - \chi_{j,j+1}) a^\dagger a |j\rangle \langle j| \\
 + \frac{1}{2} (\Omega^*(t)c + \Omega(t)c^\dagger).
 \end{aligned} \tag{4.9}$$

If we treat the transmon as just a qubit, we can write the driven dispersive JC using Pauli matrix notation,

$$H = \frac{\hbar}{2} \Delta_q \sigma_z + \hbar (\Delta_r + \chi \sigma_z) a^\dagger a + (\Omega^*(t) \sigma_- + \Omega(t) \sigma_+), \tag{4.10}$$

where we see the first term as a re-normalized qubit, the second term reflects a qubit state dependent cavity, and the third term is time-dependent raising and lowering of the qubit excitation.

4.2.2 X-Y gates for a qubit

Staying in the qubit approximation of the transmon and assuming a drive of the form

$$\Omega(t) = \begin{cases} \Omega^x(t) \cos(\omega_d t) + \Omega^y(t) \sin(\omega_d t), & 0 < t < t_g \\ 0, & \text{otherwise,} \end{cases} \tag{4.11}$$

which has two independent quadrature controls, $\Omega^x(t)$, and $\Omega^y(t)$, with t_g being the total time for a gate to take place, (4.9) can be re-written as

$$H = \frac{\hbar}{2} \Delta_q \sigma_z + \hbar (\Delta_r + \chi \sigma_z) a^\dagger a + \frac{\hbar}{2} (\Omega^x(t) \sigma_x + \Omega^y(t) \sigma_y). \quad (4.12)$$

Since we apply the drive far from the frequency band $\omega_C \pm \chi$ where the cavity population can be significant, the Lorentzian transmission damps the average photon number, giving $\langle a^\dagger a \rangle \sim 0$. Now by choosing the detuning between the drive and the qubit frequency to be 0, $\Delta_q = 0$, the above Hamiltonian generates rotations either around the x or y axes depending on the choice of $\Omega^x(t)$ and $\Omega^y(t)$. For example, choosing a drive $\Omega^x = \Omega^\pi$ and $\Omega^y = 0$, which is on for a time t_g , with $\int_0^{t_g} \Omega^\pi dt = \pi$, will be a π -pulse, or bit-flip gate σ_x , that takes the qubit population from the ground state to the excited state and vice versa. The π -pulse can similarly be performed as a y -rotation just by switching, $\Omega^y = \Omega^\pi$ and $\Omega^x = 0$. Moreover, $\pi/2$ pulses around x and y can also be performed to make superpositions of the qubit, $(|0\rangle \pm |1\rangle)/\sqrt{2}$ and $(|0\rangle \pm i|1\rangle)/\sqrt{2}$, respectively. Combinations of x and y rotations can be used to perform arbitrary rotations about any axis.

4.2.3 X-Y gates for a transmon multi-level atom

In practice, the transmon is not a simple two-level qubit, as discussed in section 3.1.3, but a rich anharmonic multilevel system. It is a generalized atom which is subject to the problem of leakage out of the qubit subspace. This is especially an issue when the bandwidth of the control is comparable to the anharmonicity. For the case of the transmon, the typical anharmonicity between the second excited state and the first excited state is

$$\alpha_1 \rightarrow -E_C \quad (4.13)$$

for large E_J/E_C . Typical design parameters result in charging energies $\sim 300 - 400$ MHz, which can be on par with the bandwidth of the shortest experimentally applied microwave control pulses ($\sim 1 - 2$ ns).

In Ref. [90], a proposal to reduce higher-level leakage due to shorter control pulses is presented in which optimized control pulses can permit high fidelity single-qubit gates. The system is described with a truncation to three levels, from which an error due to the leakage to the third level can be interpreted as a phase accumulation within the two-level qubit subspace. For simplicity, we drop the cavity and consider a single qubit with three levels and a drive

given by the Hamiltonian

$$H = \hbar \sum_{j=1,2} [\omega_j |j\rangle \langle j| + \xi(t) \lambda_j (\sigma_j^+ + \sigma_j^-)], \quad (4.14)$$

where $\sigma_j^- = |j-1\rangle \langle j|$ and $\sigma_j^+ = |j\rangle \langle j-1|$ are lowering and raising operators, $\hbar\omega_j$ denote transition energies with the ground state energy set to zero, and

$$\lambda_j = \begin{cases} 1, & j = 1 \\ \lambda, & j = 2, \end{cases} \quad (4.15)$$

is a weighting parameter on the relative strength between the 0-1 and 1-2 transitions. The anharmonicity of this reduced system α_1 is given by $\omega_2 - 2\omega_1$.

Now we allow quadrature control again over the drive, resulting in an effective driven Hamiltonian given by

$$\begin{aligned} H = \hbar \sum_{j=1,2} \Delta_j |j\rangle \langle j| + \frac{\Omega^x(t)}{2} (|0\rangle \langle 1| + |1\rangle \langle 0|) + \frac{\lambda\Omega^x(t)}{2} (|1\rangle \langle 2| + |2\rangle \langle 1|) \\ + \frac{\Omega^y(t)}{2} (|0\rangle \langle 1| + i|1\rangle \langle 0|) + \frac{\lambda\Omega^y(t)}{2} (|1\rangle \langle 2| + i|2\rangle \langle 1|). \end{aligned} \quad (4.16)$$

Ideally $\lambda = 0$, and (4.16) recovers the single-qubit driven Hamiltonian as discussed previously (4.9). However, more generally when λ is nonzero, leakage out of the qubit subspace will be dictated by the bandwidth of $\Omega^x(t)$ and $\Omega^y(t)$ in comparison to the anharmonicity α_1 . To quantify the leakage to the third level, one can apply an adiabatic transformation V ,

$$V(t) = \exp[-i\Omega^x(t)(|1\rangle \langle 0| - i|0\rangle \langle 1| + \lambda(|2\rangle \langle 1| - i|1\rangle \langle 2|))/2\alpha_1]. \quad (4.17)$$

The drive is turned on at $t = 0$ and off at $t = t_g$, such that the effect of the applied pulses are identical in both frames. By transforming the driven Hamiltonian of (4.16), we now have to

first order in the small parameter Ω^x/α_1 ,

$$\begin{aligned}
H/\hbar &= VHV^\dagger/\hbar + i\dot{V}V^\dagger \\
&\approx \frac{\Omega^x}{2} (|1\rangle\langle 0| + |0\rangle\langle 1|) + \frac{\lambda(\Omega^x)^2}{8\alpha_1} (|2\rangle\langle 0| + |2\rangle\langle 0|) + \left(\Delta_2 + \frac{(\lambda^2 + 2)(\Omega^x)^2}{4\alpha_1}\right) |2\rangle\langle 2| \\
&\quad + \left(\Delta_1 - \frac{(\lambda^2 - 4)(\Omega^x)^2}{4\alpha_1}\right) |1\rangle\langle 1| \\
&\quad + \left(\frac{\Omega^y}{2} + \frac{\dot{\Omega}^x}{2\alpha_1}\right) [(|1\rangle\langle 0| - i|0\rangle\langle 1|) + \lambda(|2\rangle\langle 1| - i|1\rangle\langle 2|)].
\end{aligned} \tag{4.18}$$

From this expression, we can see that a drive which performs a rotation around the x axis in the simple two-level picture can actually result in both a phase error via a residual y -rotation ($(|1\rangle\langle 0| - i|0\rangle\langle 1|)$ term), and a leakage to the second excited state ($\lambda(|2\rangle\langle 1| - i|1\rangle\langle 2|)$ term).

However, this effect can be adiabatically eliminated by using the other quadrature by setting

$$\Omega^y(t) = -\frac{\dot{\Omega}^x}{\alpha_1} \tag{4.19}$$

and furthermore, a phase shift error to the first excited state is removed by detuning the drive such that

$$\Delta_1 = \frac{(\lambda^2 - 4)(\Omega^x(t))^2}{4\alpha_1}. \tag{4.20}$$

Further corrections can be found by taking the transformation out to higher order. These other terms are detailed in Ref. [90]. For the purposes of this thesis, we will be discussing in chapter 6 the experimental implementation of this first-order correction by applying the derivative of the drive on the quadrature during the pulse. This technique has been denoted *DRAG* for Derivative Removal by Adiabatic Gate.

Experimentally, it has been common practice to shape the pulses with truncated Gaussian (Ω_G) envelopes,

$$\Omega_G(t) = A \exp\left[-\frac{(t - t_g/2)^2}{2\sigma^2}\right] [\Theta(t) - \Theta(t - t_g)] \tag{4.21}$$

where σ is the standard deviation for the Gaussian, A is determined by the amount of rotation desired, and $\Theta(t)$ is the Heaviside function to indicate the truncation at $t = 0$ and $t = t_g$. The

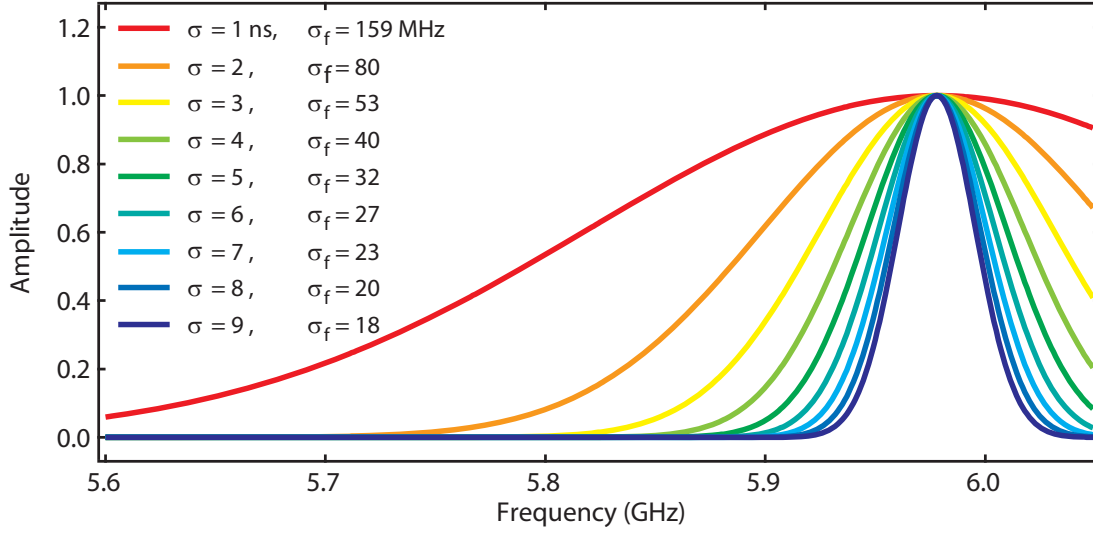


Figure 4.1: Frequency bandwidth of Gaussian pulse shapes. For the Gaussian pulse shapes given in (4.21), the fourier transform can be taken to determine the frequency extent. Given a Gaussian with standard deviation σ given in time, the equivalent frequency Gaussian standard deviation is given by $\sigma_f = (2\pi\sigma)^{-1}$. Here in this figure we can see that for $\sigma = 1$ ns, there can be a significant $\sigma_f = 159$ MHz which can cause unwanted errors via higher-order transmon excitations.

Gaussian pulse-shape has been chosen as opposed to simple square pulses due to its small frequency response bandwidth, minimizing the excitations at the transition frequency of the second excited state. Figure 4.1 shows the bandwidth of the Gaussians for different pulse lengths. We can see that for longer pulses, the frequency bandwidth can be much smaller than the anharmonicity of the third level, which in standard practice is $\sim 300 - 450$ MHz. Nonetheless, at the shortest pulse lengths, such as $\sigma = 1 - 2$ ns the third-level effects can become significant, as we will detail in chapter 6.

We can characterize the quality of a gate using the single-qubit *gate fidelity*, which is defined as [90]

$$F_g = \frac{1}{6} \sum_{j=\pm x, \pm y, \pm z} \text{Tr}[U_{\text{ideal}} \rho_j U_{\text{ideal}}^\dagger \chi(\rho_j)], \quad (4.22)$$

where U_{ideal} is the unitary transformation in the three-dimensional Hilbert space corresponding to the idealized gate, ρ_j are the six axial states of the qubit Bloch sphere, and $\chi(\rho_j)$ is the actual experimental process. More details about determining the process matrix will be given later in this thesis in chapter 6 in regards to gate characterization protocols.

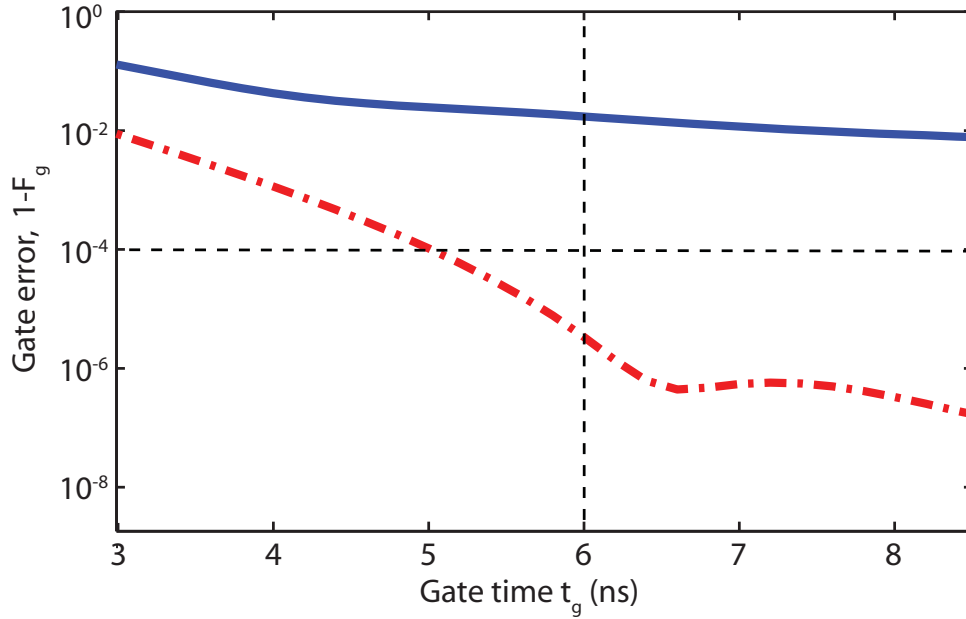


Figure 4.2: Error per gate with and without DRAG. Standard Gaussian pulses with standard deviation σ , and total gate time $t_g = 2\sigma$, result in an error per gate (blue solid line) which increases with decreasing gate time (neglecting relaxation processes) due to leakage to the second excited state of the anharmonic qubit spectrum. DRAG pulses result in an error per gate which decreases (red dashed line) down to a minimum value of $\sim 10^{-6}$, well at the fault tolerant threshold. Simulation is performed assuming a drive coupling strength to the second excited state of $\lambda = \sqrt{2}$ and anharmonicity $\alpha_1 = 2\pi(-400 \text{ MHz})$ and no decoherence properties. (Figure used with permission from [90]. See Copyright Permissions.)

Based off of Ref. [90], we can simulate the effect of the pulse shaping. Specifically, by assuming no relaxation processes (for the purposes of seeing the effect of the shaping), drive coupling strength $\lambda = \sqrt{2}$, and third level anharmonicity given by $\alpha_1 = 2\pi(-400) \text{ MHz}$, F_g is limited to 99% when the total gate time t_g is 6 ns and using standard Gaussian pulse shaping. Figure 4.2 shows in blue the error per gate, defined as $1 - F_g$ for Gaussian pulses with a standard deviation chosen to be $0.5t_g$. However, by using DRAG for the pulse shaping, $1 - F_g$ can be reduced to the curve in red, achieving a minimum gate error of $\sim 10^{-6}$. An experimental implementation of derivative pulse-shaping for single-qubit gates based on DRAG will be discussed in chapter 6, which will show a similar improvement in gate fidelity.

4.2.4 Z (phase) gates

Although concatenations of arbitrary x and y rotations are sufficient for traversing the entire single-qubit Bloch sphere, it can also be useful to directly perform rotations about the z axis. This is especially the case when the ratio of coherence times (T_1, T_2) to the gate time (t_g) is not very large, such that having full control over the three axes allows for an optimized gate sequence which takes up less time.

ac-Stark gate

One option for performing a direct rotation on the z axis is by employing the off-resonant ac-Stark shift effect. A drive which is sufficiently detuned from the qubit to not induce direct transitions via the σ_x term (Rabi frequency is small $\omega_d - \omega_q \gg 2\Omega$) will shift the qubit transition frequency due to virtual photon transitions. Starting with the driven transmon circuit QED Hamiltonian of (4.8), we can obtain an effective Hamiltonian which removes the effect of direct transitions via the drive by using the unitary transformation

$$U = \exp \left[\sum_j \beta_j (|j+1\rangle \langle j| - |j\rangle \langle j+1|) \right] \quad (4.23)$$

where $\beta_j = \Omega(t)/2\Delta_j$. This effective Hamiltonian to second order in β_j is then given by

$$H = UH_0U^\dagger \quad (4.24a)$$

$$\begin{aligned} &= \Delta_r a^\dagger a + (\Delta_0 + \eta_0) |0\rangle \langle 0| + \sum_{j=1} (\Delta_j + \eta_{j,j-1}) |j\rangle \langle j| \\ &\quad + \sum_j \tilde{g}_{j,j+1} (a |j+1\rangle \langle j| + a^\dagger |j\rangle \langle j+1|), \end{aligned} \quad (4.24b)$$

with

$$\eta_0 = \frac{\Omega^2(2\Delta_0 + \Delta_1)}{4\Delta_0^2} \quad (4.25a)$$

$$\eta_j = \frac{\Omega^2(2\Delta_j + \Delta_{j+1})}{4\Delta_j^2} - \frac{\Omega^2(4\Delta_{j-1} + \Delta_j)}{4\Delta_{j-1}^2} \quad (4.25b)$$

$$\tilde{g}_{j,j+1} = g_j \left(1 - \frac{\Omega^2}{4\Delta_j^2} - \frac{\Omega^2}{8\Delta_{j+1}^2} + \frac{\Omega^2}{4\Delta_j\Delta_{j+1}} \frac{g_{j+1}}{g_j} \right). \quad (4.25c)$$

Next, we can follow this with another dispersive transform to second order, and we are left with the Hamiltonian

$$H \approx \tilde{\Delta}_r a^\dagger a + \sum_j |j\rangle \langle j| (\Delta_j + \eta_j) + \sum_j \tilde{\chi}_{j,j+1} |j+1\rangle \langle j+1| - \tilde{\chi}_{01} a^\dagger a |0\rangle \langle 0| + \sum_{j=1} (\tilde{\chi}_{j-1,j} - \tilde{\chi}_{j,j+1}) a^\dagger a |j\rangle \langle j| \quad (4.26a)$$

where the $\tilde{\chi}_{ij}$ are now calculated using \tilde{g}_{ij} . Therefore, for the transmon, operating with an off-resonant drive, the 0-1 transition frequency can be ac-Stark shifted by an amount $\eta_1 - \eta_0$. When taking just a two-level truncation of the transmon, the effective Hamiltonian is then

$$H \approx \Delta_r a^\dagger a + \frac{1}{2} \left(\Delta_q + \chi + \frac{1}{2} \frac{\Omega^2}{\Delta_q} \right) \sigma_z \quad (4.27)$$

and the last term can be used to produce controlled rotations about the z axis. Although this is a useful procedure for shifting the phase of a single-qubit, note that when multiple qubits are coupled to the same bus, each qubit will suffer a frequency shift even when the other qubits are driven. Furthermore, for the transmon qubits, coupling to the higher levels cannot necessarily be ignored, and the Stark shift can become non-linear with respect to power of the drive due to different Stark shifts of the higher levels [79].

Flux gate

Another method for direct z rotations is to use the non-linear dependence of the qubit transition frequency on the applied flux to shift the qubit transition frequency by a controlled amount. Recall that the transmon Hamiltonian is given by

$$H = \hbar \sum_j \omega_j |j\rangle \langle j| \quad (4.28)$$

where the ω_j are given in . However, in the transmon limit, where $E_j \gg E_C$ and for a two-level truncation, the qubit Hamiltonian is simply

$$H_q = \hbar \sqrt{8E_J^{\max} |\cos(\pi\Phi/\Phi_0)|} E_C \sigma_z. \quad (4.29)$$

In the dispersive regime the full Hamiltonian is still flux-tunable, and a controlled amount of z -phase θ_z can be obtained by controlling Φ over a gate period t_g such that,

$$\theta_z = \int_0^{t_g} dt \sqrt{8E_J^{\max} |\cos(\pi\Phi(t)/\Phi_0)|}. \quad (4.30)$$

In chapter 8, these flux-based z rotations will be an important part of tuning large amounts of dynamical phase which are accumulated during a separate flux excursion used for a two-qubit c -Phase gate.

4.3 Two-qubit gates in circuit QED

We now switch our attention to two qubits in a circuit QED system and focus on how to realize entangling gates (section 2.3) to complete the suite of gates necessary for universal quantum computing (section 2.1). A full treatment of two qubit gates is given in Ref. [91]. In this section we will only highlight one of those gates, the virtual swap interaction (section 4.3.2). Besides the virtual swap, there can also be an indirect swap between qubits by tuning into direct interaction with the resonator, experimentally implemented in phase qubits [92, 93]. In circuit QED, it is also possible to use sideband transitions to perform two-qubit gates, in a scheme similar to the coupling of trapped-ion qubits, and experimentally investigated for generating Bell states [94], as well as multiple fixed off-resonant drives in a scheme called FLICFORQ [95]. However, even with the numerous two-qubit entangling gates for circuit QED described in Ref. [91], the other gate which we describe in section 4.3.3 is a completely different approach that relies on the multi-level structure of transmon qubits. Later in this thesis in chapter 8, we will demonstrate the experimental implementation of this two-qubit gate and generate highly-entangled states.

4.3.1 Two-qubits in the dispersive regime

With two transmons, the standard Jaynes-Cummings Hamiltonian is modified to include the strong coupling of the photon field with both transmons,

$$\begin{aligned}
H_{JC} = & \omega_C a^\dagger a + \sum_j \omega_j^{(1)} |j\rangle_1 \langle j|_1 + \sum_i \omega_i^{(2)} |i\rangle_2 \langle i|_2 \\
& + \sum_j g_{j,j+1}^{(1)} (a^\dagger |j\rangle_1 \langle j+1|_1 + a |j+1\rangle_1 \langle j|_1) \\
& + \sum_i g_{i,i+1}^{(2)} (a^\dagger |i\rangle_2 \langle i+1|_2 + a |i+1\rangle_2 \langle i|_2).
\end{aligned} \tag{4.31}$$

To get to the dispersive regime, the resonant Jaynes-Cummings interaction is eliminated using the transformation

$$U = \exp \left[\sum_j \lambda_j^{(1)} (a^\dagger |j\rangle_1 \langle j+1|_1 - \text{h.c.}) + \sum_i \lambda_i^{(2)} (a^\dagger |i\rangle_2 \langle i+1|_2 - \text{h.c.}) \right] \tag{4.32}$$

where $\lambda_j^{(k)} = g_{j,j+1}^{(k)} / (\omega_{j+1,j}^{(k)} - \omega_C) = g_{j,j+1}^{(k)} / \Delta_j^{(k)} \ll 1$. To second-order in $\lambda^{(k)}$, the two transmon dispersive Hamiltonian is then given by

$$\begin{aligned}
H/\hbar = & \omega_C a^\dagger a + \sum_j \left(\omega_j^{(1)} |j\rangle_1 \langle j|_1 + \chi_{j,j+1}^{(1)} |j+1\rangle_1 \langle j+1|_1 \right) \\
& + \sum_i \left(\omega_i^{(2)} |i\rangle_2 \langle i|_2 + \chi_{i,i+1}^{(2)} |i+1\rangle_2 \langle i+1|_2 \right) \\
& - a^\dagger a \left(\chi_{01}^{(1)} |0\rangle_1 \langle 0|_1 + \chi_{01}^{(2)} |0\rangle_2 \langle 0|_2 \right) \\
& + a^\dagger a \left[\sum_{j=1} \left(\chi_{j-1,j}^{(1)} - \chi_{j,j+1}^{(1)} \right) |j\rangle_1 \langle j|_1 + \sum_{i=1} \left(\chi_{i-1,i}^{(2)} - \chi_{i,i+1}^{(2)} \right) |i\rangle_2 \langle i|_2 \right] \\
& + \sum_{ji} \frac{g_{j,j+1}^{(1)} g_{i,i+1}^{(2)} (\Delta_j^{(1)} + \Delta_i^{(2)})}{2(\Delta_j^{(1)} \Delta_i^{(2)})} [|j\rangle_1 \langle j+1|_1 \otimes |i+1\rangle_2 \langle i|_2 + |j+1\rangle_1 \langle j|_1 \otimes |i\rangle_2 \langle i+1|_2].
\end{aligned} \tag{4.33a}$$

If we consider both transmons as only qubits, the effective dispersive Hamiltonian is then simplified to

$$\begin{aligned}
H/\hbar = & \left(\omega_C + \chi_1 \sigma_z^{(1)} + \chi_2 \sigma_z^{(2)} \right) a^\dagger a + \frac{1}{2} \omega_1 \sigma_z^{(1)} + \frac{1}{2} \omega_2 \sigma_z^{(2)} \\
& + \frac{g_1 g_2 (\Delta_1 + \Delta_2)}{2\Delta_1 \Delta_2} \left(\sigma_+^{(1)} \sigma_-^{(2)} + \sigma_-^{(1)} \sigma_+^{(2)} \right),
\end{aligned}$$

where the first term is the cavity dispersively shifted by both qubits, the second and third terms are the bare qubit Hamiltonians, and the final term is a two-qubit swap which occurs via virtual interaction with the cavity.

4.3.2 Virtual qubit-qubit interaction

Working within the two-qubit subspace with four independent levels, $|0, 0\rangle$, $|0, 1\rangle$, $|1, 0\rangle$, and $|1, 1\rangle$, we can see that the virtual swap interaction of the dispersive Hamiltonian is of the form described in section 2.3.3 such that we can realize an entangling $\sqrt{i\text{SWAP}}$ gate. We introduce the parameter J to represent the strength of the swap interaction,

$$J = \frac{g_1 g_2 (\Delta_1 + \Delta_2)}{2\Delta_1 \Delta_2}. \quad (4.34)$$

Now by operating in the dispersive regime, the cavity population can be small so $\langle a^\dagger a \rangle \sim 0$. We now have a two-qubit unitary with the following time evolution,

$$U_{2q}(t) = \exp\left[\frac{-it}{2} \left(\omega_1 \sigma_z^{(1)} \otimes \mathbb{1}^{(2)} + \omega_2 \mathbb{1}^{(1)} \otimes \sigma_z^{(2)} \right)\right] \\ \times \begin{pmatrix} 1 & 0 & 0 & 0 \\ 0 & \cos(Jt) & i \sin(Jt) & 0 \\ 0 & i \sin(Jt) & \cos(Jt) & 0 \\ 0 & 0 & 0 & 1 \end{pmatrix}. \quad (4.35)$$

The first piece is simply made up of single-qubit phases which are removable via the appropriate single-qubit rotations while the second piece in the large parantheses corresponds to the $\sqrt{i\text{SWAP}}$ logical operation at $t = \pi/(4J)$. The level diagram in figure 4.3 visually depicts the virtual photon exchange with the cavity, from which we can see the cavity only acting as a spectator to the interaction, never being actually populated with a photon.

Since the value of J governs the time for performing the entangling gate, the detuning between the two qubits plays a critical role for the swap interaction. As the interaction term $\sigma_+^{(1)} \sigma_-^{(2)} + \sigma_-^{(1)} \sigma_+^{(2)}$ is energy swapping, we can see that when the qubits are not near resonance but far detuned, the swap will be suppressed. The maximal interaction occurs with the qubits tuned into resonance with one another, such that $\Delta_1 = \Delta_2 = \Delta$ and $J = g_1 g_2 / \Delta$. The ability for this interaction to be strong and weak depending on the qubit detuning provides a recipe for operating a full set of universal qubit gates. One can detune the qubits for performing single-qubit logical operations where the interaction is effectively off. Then, to perform the

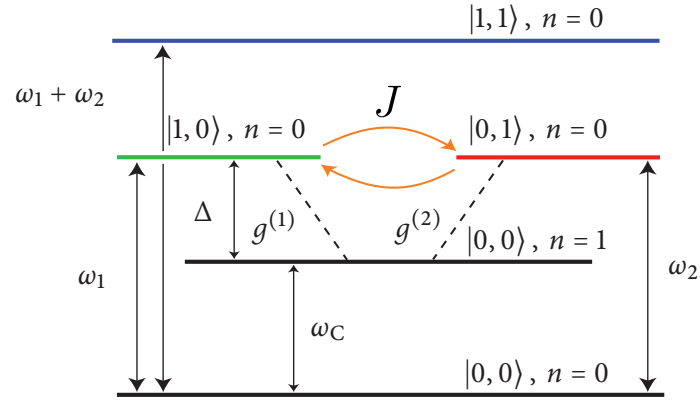


Figure 4.3: Scheme of the virtual photon swap interaction. When the qubits are detuned from the cavity ($|\Delta^{(1),(2)}| \gg g^{(1),(2)}$) the qubits both dispersively shift the cavity. The excited state in the left qubit $|1, 0\rangle \otimes |n = 0\rangle$ interacts with the excited state in the right qubit $|0, 1\rangle \otimes |n = 0\rangle$ via the exchange of a virtual photon $|0, 0\rangle \otimes |n = 1\rangle$ in the cavity.

two-qubit logic gates, the qubits are tuned into resonance with one another for the appropriate amount of time to realize the $\sqrt{i\text{SWAP}}$.

To use the $\sqrt{i\text{SWAP}}$ gate as an two-qubit entangling gate reduces to being able to change the detuning between the qubits on fast time-scales. The circuit QED architecture with transmon qubits fortunately provides this tunability through either an off-resonant ac-Stark shift or a fast dc-flux tuning.

Two-qubit ac-Stark swap gate

The off-resonant ac-Stark shift, which was introduced as a generator of rotations about the z -axis in section 4.2.4, can also be used to tune the qubits in and out of resonance with one another to effectively turn the swap interaction on and off. The treatment is similar to the case of including an off-resonant drive, except now there are two transmons which each can be Stark shifted differently due to their different interaction strengths and detunings.

The effect of applying a drive will be to shift the qubit transition frequencies for both of the transmon qubits to

$$\tilde{\omega}_q^{(k)} = \omega_q^{(k)} + \frac{\Omega^2}{2\Delta_q} + \tilde{\chi}^{(k)}, \quad (4.36)$$

where $\tilde{\chi} = \tilde{\chi}_{01} - \tilde{\chi}_{12}/2$. The Stark swap gate can be performed by starting with the qubits effectively uncoupled from one another, such that $|\omega_q^{(1)} - \omega_q^{(2)}| \gg J$, and then to turn on the appropriate amplitude drive at a frequency ω_d such that $\tilde{\omega}_q^{(1)} = \tilde{\omega}_q^{(2)}$, turning on the J

interaction. Although in the simplest two-level picture, the value of the Stark shift has a simple relationship with the detuning of the drive from the qubit frequency, for transmon qubits, higher-level couplings contribute to the Stark shift, especially at large drive powers resulting in non-linear frequency shifts.

The operation of the Stark swap gate also relies on a low enough drive power that direct transitions of the cavity do not occur, which would otherwise result in heating of the cavity and an enhancement of decoherence. Another possible error is for the Stark shift to cause direct transitions of the qubit due to insufficient detuning. The effective Rabi frequency of a detuned drive is given by $\Omega'_R = \sqrt{\Omega_R^2 + \Delta^2}$, where Ω_R is the Rabi frequency corresponding to the applied drive power if it were on resonance with the qubit, $\omega_d = \omega_q$.

Furthermore, although the Stark effect can be an effective method for turning on a two-qubit interaction, if the system expanded to more than two, there could be even higher-order Stark shifts which can make the tunability unwieldy. An experimental implementation of this Stark gate with two-qubits is described in chapter 7.

Fast flux swap gate

Another option for turning on the virtual flip-flop interaction is to directly tune the qubit frequencies into resonance with one another using independent flux control on each of the qubits. As described in section 4.2.4 in regards to the single-qubit phase gate via flux-tuning, similarly the two qubits transition frequencies,

$$\omega_{01}^{(i)}(t) = \sqrt{8(E_J^{\max,(i)} |\cos(\pi\Phi^{(i)}(t)/\Phi_0)| E_C^{(i)} - E_C^{(i)}),} \quad (4.37)$$

can be tuned with a flux pulse such that at $t = 0$ with $\omega_{01}^{(1)}(0) \neq \omega_{01}^{(2)}(0)$ and at some later time t' they are tuned to be equal, $\omega_{01}^{(1)}(t') = \omega_{01}^{(2)}(t')$. The flux pulse rise-time needs to be faster than the swap rate, but still adiabatic with respect to the qubit transition frequencies. Of course the ability for this gate to be used relies also on pre-determined device parameters, such as the charging energies and maximum Josephson energies of both qubits. Nonetheless, with fast independently tunable flux, this is a candidate for realizing the two-qubit entangling swap gate, and can be extended to systems with more qubits. In chapter 8 we will show an implementation of the swap using fast flux tuning.

4.3.3 $\sigma_z \otimes \sigma_z$ higher level transmon interaction

The swap interaction discussed in the previous sections arises from the second order expansion of the Jaynes-Cummings Hamiltonian in the dispersive regime (4.3.1). By taking the dispersive approximation to higher orders in $\lambda_j = g_{j,j+1}/(\omega_{j,j+1} - \omega_C)$, there are other two-qubit interactions which emerge.

For example, we can consider the case of going to fourth order for a two-level approximation of both qubits. This can be done by using fourth-order perturbation theory. Although all of the two-qubit interactions arising from this further expansion are much weaker than the swap interaction, one which is of particular interest is a $\sigma_z^{(1)} \otimes \sigma_z^{(2)}$ term, an interaction which can be used to generate a c-Phase gate (section 2.3.2). The coupling strength of this two-qubit interaction is given by ζ , involving a two-excitation process such that

$$\zeta = \frac{g_1^2 g_2^2 (\Delta_1 + \Delta_2)}{\Delta_1^2 \Delta_2^2}. \quad (4.38)$$

We can easily see that this coupling is smaller than J , by a factor of $g_1 g_2 / \Delta_1 \Delta_2$. The relative weakness of this interaction to the swap-interaction thus makes such a $\sigma_z^{(1)} \otimes \sigma_z^{(2)}$ interaction not very useful for performing a two-qubit gate. However, this situation changes significantly when considering multiple levels in the transmons.

For a transmon qubit, the presence of higher levels can actually boost up the strength of this interaction. Since the ζ is a result of a two-excitation process, specifically the second excited state of the transmon qubit can also interact. Consider a set of two transmons, which have a negative anharmonicity, arranged such that their single excitation transition energies do not coincide, or $\omega_{10} \neq \omega_{01}$. We will use the notation here that ω_{ij} corresponds to the transition energy for the two transmon state with the first transmon in state $|i\rangle$ and the second transmon in state $|j\rangle$. Now, suppose $\omega_{01} > \omega_{10}$. Then, by varying the applied flux on the qubit with the higher single-excitation transition energy will generate an interaction in the two excitation manifold, as shown in figure 4.4.

This interaction can be calculated using fourth order perturbation theory for a pair of qutrits coupled to a cavity, and now takes a very different form from the simple two-level

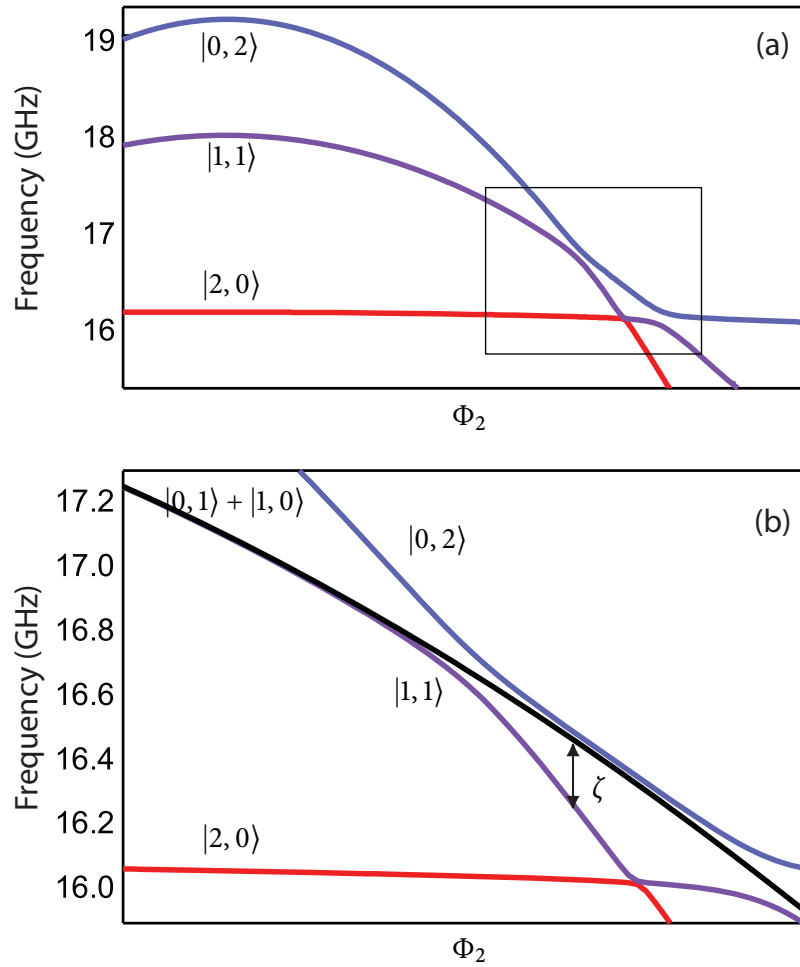


Figure 4.4: Two excitation manifold. (a) By varying Φ_2 , the external flux on the transmon with the higher E_J , the transition energy level corresponding to $|0, 2\rangle$ can be tuned into an avoided crossing with $|1, 1\rangle$, where both transmons are in the first excited states. (b) Zoom-in of the avoided crossing region shows the deviation of the transition energy of $|1, 1\rangle$ (solid purple) from the sum of the transition energies of $|0, 1\rangle$ and $|1, 0\rangle$ (solid black). This interaction strength of ζ is the generator of a two-qubit conditional phase interaction. These simulations are performed via numerical diagonalization of a Jaynes-Cummings model with two transmons, assuming $E_{J1} = 28$ GHz, $E_{J2} = 42$ GHz, $E_{C1} = 320$ MHz, $E_{C2} = 300$ MHz, $\omega_C = 7$, GHz, and $\kappa = 1$ MHz.

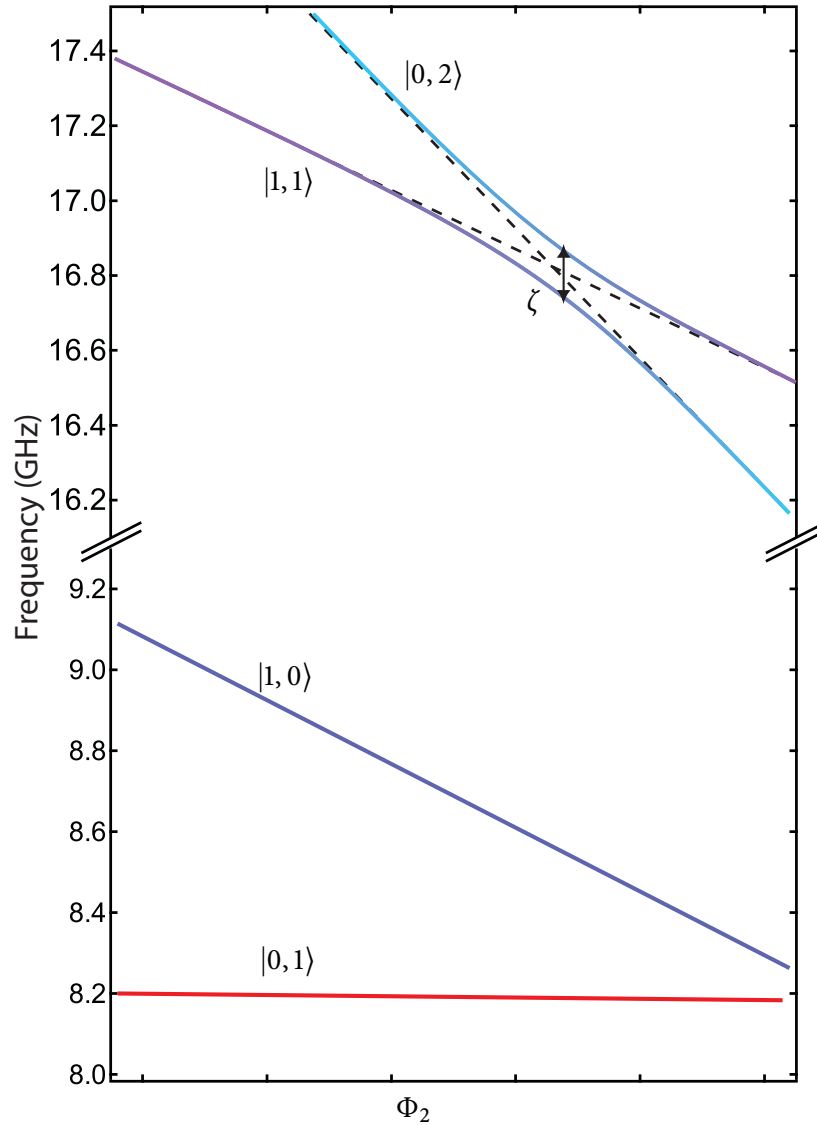


Figure 4.5: Level scheme for c-Phase. Theoretical level scheme shows that by varying the magnetic flux Φ_2 , it is possible to vary the single-qubit phase of the right qubit, θ_z^{01} . Similarly, varying the magnetic flux Φ_1 can be used to change θ_z^{10} . Due to the presence of $|0, 2\rangle$ interacting with $|1, 1\rangle$, changing Φ_2 can thus vary the phase on $|1, 1\rangle$ in a way differently than from $|0, 1\rangle$. As a result, $\theta_z^{11} \neq \theta_z^{01} + \theta_z^{10}$, and unitary operations such as the c-Phase gate are possible. These simulations are again performed via numerical diagonalization of a Jaynes-Cummings model with two transmons, assuming $E_{J1} = 28$ GHz, $E_{J2} = 42$ GHz, $E_{C1} = 320$ MHz, $E_{C2} = 300$ MHz, $\omega_C = 7$, GHz, and $\kappa = 1$ MHz.

case,

$$\zeta = -2g_1^2 g_2^2 \left(\frac{1}{(\omega_{01}^{(2)} - \omega_{12}^{(1)})(\omega_{01}^{(1)} - \omega_C)^2} + \frac{1}{(\omega_{01}^{(1)} - \omega_{12}^{(R)})(\omega_{01}^{(2)} - \omega_C)^2} + \frac{1}{(\omega_{01}^{(1)} - \omega_C)(\omega_{01}^{(2)} - \omega_C)^2} + \frac{1}{(\omega_{01}^{(2)} - \omega_C)(\omega_{01}^{(1)} - \omega_C)^2} \right). \quad (4.39)$$

This expression, we can see, diverges when the transition between the 0 and 1 levels of one transmon aligns with the 1 and 2 levels of the second transmon. Therefore, a resonance in the two excitation manifold can result in a much stronger $\sigma_z^{(1)} \otimes \sigma_z^{(2)}$ interaction.

This interaction results in an avoided crossing between the $|1, 1\rangle$ and $|0, 2\rangle$ two-transmon states. In terms of the qubit computational basis states, $\{|0, 0\rangle, |0, 1\rangle, |1, 0\rangle, |1, 1\rangle\}$ the frequency shift is completely on the $|1, 1\rangle$ state, such that the interaction strength can be expressed as

$$\zeta = \omega_{11} - \omega_{01} - \omega_{10}. \quad (4.40)$$

The action of the shift can be directly used to alter the phase (figure 4.5) of the computational basis state $|1, 1\rangle$. As discussed in section 4.2.4, a fast flux pulse can be used to change the frequency of the transmon transition frequency, resulting in a phase θ_z given by (4.30). In the case of two transmons, flux pulses can be used to modulate the phase of all the computational basis states, giving access to a unitary transformation of the form,

$$U = \begin{pmatrix} 1 & 0 & 0 & 0 \\ 0 & e^{i\theta_z^{01}} & 0 & 0 \\ 0 & 0 & e^{i\theta_z^{10}} & 0 \\ 0 & 0 & 0 & e^{i\theta_z^{11}} \end{pmatrix}, \quad (4.41)$$

where the dynamical phase shifts are given by

$$\theta_z^{ij} = \int \delta\omega_{ij}(t) dt. \quad (4.42)$$

Now suppose a square shaped flux pulse is turned for time t_f on one of the transmons such that the interaction between the $|1, 1\rangle$ and $|0, 2\rangle$ gives

$$\int_0^{t_f} \zeta(t) dt = (2n + 1)\pi, \quad (4.43)$$

where n is an integer. As a result of (4.40), the phase shift of the $|1,1\rangle$ state can now be expressed as

$$\theta_z^{11} = \theta_z^{01} + \theta_z^{10} - (2n + 1)\pi, \quad (4.44)$$

resulting in a total two-qubit phase unitary given by

$$U = \begin{pmatrix} 1 & 0 & 0 & 0 \\ 0 & e^{i\theta_z^{01}} & 0 & 0 \\ 0 & 0 & e^{i\theta_z^{10}} & 0 \\ 0 & 0 & 0 & -e^{i(\theta_z^{01} + \theta_z^{10})} \end{pmatrix}. \quad (4.45)$$

Now by simply tuning individual qubit phases with small frequency excursions using each qubit's independent flux bias, the other phases can be tuned such that $\theta_z^{01} = \theta_z^{10} = 0$, and we are left with a two-qubit c-Phase (section 2.3.2) entangling gate,

$$U = \begin{pmatrix} 1 & 0 & 0 & 0 \\ 0 & 1 & 0 & 0 \\ 0 & 0 & 1 & 0 \\ 0 & 0 & 0 & -1 \end{pmatrix}. \quad (4.46)$$

However, it is important to stress again that this $\sigma_z^{(1)} \otimes \sigma_z^{(2)}$ interaction for the c-Phase gate is only possible as a result of the avoided crossing between computational with non-computational states. It is a technique that cannot work in simple two-level systems but is accessible in any qubit implementation with finite anharmonicity, such as transmons or phase qubits [96]. This permits the ζ to be much larger than the case of just a simple two-level system, as previously noted in (4.38). Note also that it is the negative anharmonicity of the transmons which permits this interaction to occur before the onset of the swap interaction J by simply tuning the flux bias of one of the transmons.

One of the more subtle features of using this higher-level transmon interaction for generating an entanglement gate is the adiabatic flux tuning. Whereas the transverse swap coupling discussed previously requires a fast-tuning of the qubit transition frequencies directly into the avoided crossing, the $\sigma_z^{(1)} \otimes \sigma_z^{(2)}$ interaction requires only a slow tuning, acquiring phase throughout the adiabatic frequency shift. For experimental purposes, an adiabatic pulse can be simpler to implement than a very fast and sudden pulse. Typical control pulse rise times are on the order of 1 to 2 ns. Swap interactions which are $J/2\pi \sim 100$ MHz have a period of

1 ~ 2 ns, such that pulses do not necessarily turn on fast with respect to J . However, the pulses need not be fast for the ζ interaction.

As discussed in chapter 2, the c-Phase gate combined with single qubit rotations form a universal set (section 2.1) of gates for quantum computing protocols. Also recall that the c-Phase gate is easily converted into to the more traditionally studied cNOT gate section 2.3.2. Experimental implementation of the entanglement gate for producing Bell states and quantum algorithms will be presented later in this thesis in chapters 8 and 9.

4.4 Multiplexed joint qubit readout

In section 3.4.2 we introduced the strong dispersive regime of circuit QED as a feature for qubit-state determination via transmission through the cavity. By applying to the cavity a microwave field close to its resonance frequency, the transmitted amplitude is a non-linear function of the cavity pull resulting in a projective QND readout. The state dependent shift is governed by χ , as a result of the dispersive ac Stark effect. If we extend the strong dispersive regime to multiple qubits, the cavity Hamiltonian is now given by

$$H_{cav} = a^\dagger a \left(\omega_C + \sum_k \chi^{(k)} \sigma_z^{(k)} \right) \quad (4.47)$$

with k indexing the qubit number in an n -qubit register. If all of dispersive frequency pulls are large with respect to κ and different from one another, then each of the 2^n qubit computational basis states $\{|000\dots 0\rangle, |100\dots 0\rangle, |010\dots 0\rangle, \dots, |111\dots 1\rangle\}$ will have a different transmission frequency.

4.4.1 Deriving the measurement operator

For simplicity of notation, we can deal with just two qubits, although note that the treatment can be extended for an arbitrary number of qubits. Two qubits in the strong dispersive regime will have cavity peaks at the four peaks $\omega_C + \chi_1 + \chi_2$, $\omega_C + \chi_1 - \chi_2$, $\omega_C - \chi_1 + \chi_2$, and $\omega_C - \chi_1 - \chi_2$, corresponding to the states $|0, 0\rangle$, $|0, 1\rangle$, $|1, 0\rangle$, and $|1, 1\rangle$ respectively (figure 4.6). Now applying a drive would query for a joint property of the entire two-qubit state. For example, by driving at the frequency corresponding to $\omega_C + \chi_1 + \chi_2$ with the qubits in their ground state $|0, 0\rangle$ interrogates the system, by detecting a transmitted signal only if *both* qubits are in the ground state.

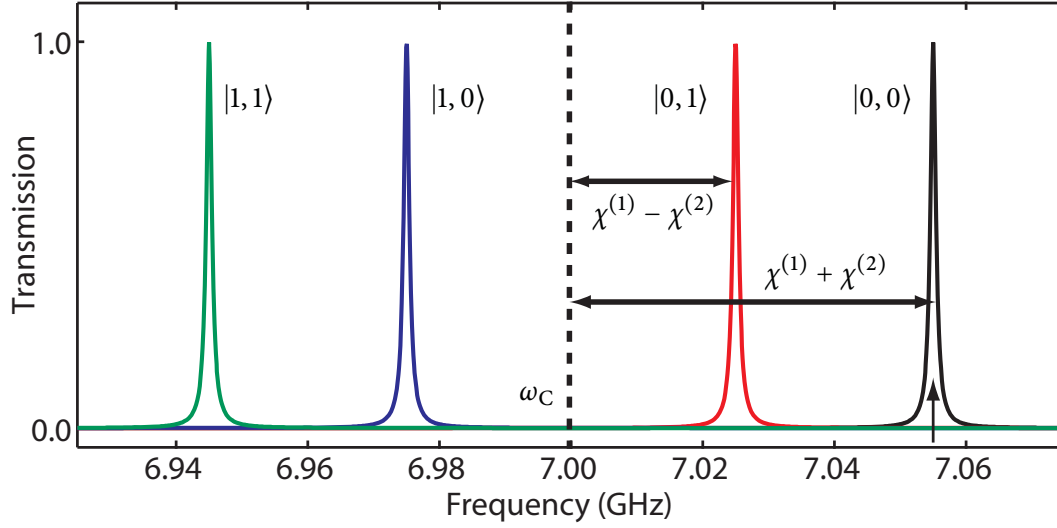


Figure 4.6: Transmission in strong dispersive regime for two qubits. The four dispersive shifted cavity transmission peaks for a two-qubit and cavity system with a bare transmission frequency of 7 GHz, and qubits with dispersive shifts $\chi^{(1)}/2\pi = 40$ MHz and $\chi^{(2)}/2\pi = 15$ MHz.

A query of the cavity at the peak for $|0, 0\rangle$ then gives rise to a measurement operator that is a projector on the two-qubit ground state,

$$M = |0, 0\rangle \langle 0, 0|. \quad (4.48)$$

This can be expressed in terms of the Pauli matrices for the two qubits as

$$M = \sigma_z^{(1)} + \sigma_z^{(2)} + \sigma_z^{(1)} \otimes \sigma_z^{(2)}. \quad (4.49)$$

In practice however, dynamics of the qubits and the cavity during measurement give a more generalized averaged measured observable given by

$$\langle M \rangle = \beta_1 \langle \sigma_z^{(1)} \rangle + \beta_2 \langle \sigma_z^{(2)} \rangle + \beta_{12} \langle \sigma_z^{(1)} \otimes \sigma_z^{(2)} \rangle, \quad (4.50)$$

where β_1 , β_2 , and β_{12} are all ≤ 1 and reflect the sensitivity of the measurement to each of three Pauli operators. We adopt a simpler notation when discussing the measurement of two-qubit operators by identifying $\sigma_z^{(1)} \otimes \mathbb{1}^{(2)} \rightarrow ZI$, $\mathbb{1}^{(1)} \otimes \sigma_z^{(2)} \rightarrow IZ$, $\sigma_z^{(1)} \otimes \sigma_z^{(2)} \rightarrow ZZ$, and similarly for all other Pauli operators.

To understand why our measurement operator is given by (4.50), we start with the cavity observables which correspond to our measurement, $I = a^\dagger + a$ and $Q = i(a^\dagger - a)$. If we

include a single drive, our Hamiltonian is

$$H/\hbar = \chi a^\dagger a + \frac{1}{2} \sum_{j=1,2} (\omega_q^{(j)} + \chi_j) \sigma_z^{(j)} + \epsilon(t) (a^\dagger + a) \quad (4.51)$$

where $\epsilon(t)$ is the measurement amplitude and $\chi = \omega_C - \omega_d + \sum_j \chi_j \sigma_z^{(j)}$. Our measurement records ensemble averages of the quadrature voltage amplitudes, given by

$$\langle I \rangle(t) = \text{Tr}[\rho(t) (a^\dagger + a)] \quad (4.52a)$$

$$\langle Q \rangle(t) = \text{Tr}[i\rho(t) (a^\dagger - a)]. \quad (4.52b)$$

From the Heisenberg dynamics and input-output theory [34, 97], the time-dependence of the cavity annihilation operator can be found to be

$$\dot{a} = -i\chi a - i\epsilon - \kappa a/2 - \sqrt{\kappa} b_{in} \quad (4.53)$$

where b_{in} describes the photon bath field annihilation operator connected to the input of the cavity. The solution to this expression is given by

$$a(t) = a(0) e^{[-(\frac{\kappa}{2} + i\chi)t]} - \epsilon \frac{(1 - e^{[-(\frac{\kappa}{2} + i\chi)t]})}{\chi - i\kappa/2}. \quad (4.54)$$

We can now evaluate the expressions for the measured quadrature voltage operators by assuming an initially separable state between the qubits and resonator, e.g. $\rho(0) = |0\rangle\langle 0| \otimes \rho_q(0)$ where the resonator is in the ground state $|0\rangle$ and the qubit density matrix for an arbitrary state can be written as

$$\rho_q(0) = \sum_{i,j,i',j'=0,1} p_{ij i' j'} |ij\rangle\langle i' j'|. \quad (4.55)$$

Putting these expressions together, we can write the average values of the field quadratures as

$$\langle I \rangle(t) = \left\langle \frac{\epsilon}{\chi^2 + \kappa^2/4} \left[-2\chi + e^{-\kappa t/2} (2\chi \cos[\chi t] + \kappa \sin[\chi t]) \right] \right\rangle \quad (4.56a)$$

$$\langle Q \rangle(t) = \left\langle \frac{\epsilon}{\chi^2 + \kappa^2/4} \left[-\kappa - e^{-\kappa t/2} (2\chi \sin[\chi t] - \kappa \cos[\chi t]) \right] \right\rangle, \quad (4.56b)$$

which in the steady state are given by

$$\langle I \rangle(t) = \left\langle \frac{-2\chi\epsilon}{\chi^2 + \kappa^2/4} \right\rangle \quad (4.57a)$$

$$\langle Q \rangle(t) = \left\langle \frac{-\chi\epsilon}{\chi^2 + \kappa^2/4} \right\rangle. \quad (4.57b)$$

This result recovers the standard Lorentzian behavior of the power transmitted, however, as a non-linear function of the two-qubit state-dependent cavity pull,

$$\langle M \rangle = I^2 + Q^2 = \frac{\epsilon^2}{\chi^2 + \kappa^2/4} = \frac{\epsilon^2}{\left(\omega_C - \omega_d + \chi_1\sigma_z^{(1)} + \chi_2\sigma_z^{(2)}\right)^2 + \kappa^2/4}. \quad (4.58)$$

The ensembled measurement operator can then be decomposed in the two-qubit Pauli basis set as

$$\langle M \rangle = \beta_0\langle II \rangle + \beta_1\langle ZI \rangle + \beta_2\langle IZ \rangle + \beta_{12}\langle ZZ \rangle, \quad (4.59)$$

where the coefficients can be found from partial traces, e.g. $\beta_{ZI} = \text{Tr}[M(t)ZI]$. The coefficients β will depend on the drive frequency. In figure 4.7, we plot the coefficients for the two quadratures I and Q as a function of $\Delta_C = \omega_C - \omega_d$ for a cavity with linewidth κ , $\chi^{(1)} = 10\kappa$ and $\chi^{(2)} = 2\kappa$. We can see that by applying a drive at the bare resonator frequency, all of the β coefficients are small, giving very little information about the ZZ correlator. However, driving at the frequency corresponding to the ground state peak $|0, 0\rangle$ will actually give maximal values for all the β , particularly in the Q channel. As a result, direct access to two-qubit correlations are attainable depending on the choice of drive. One point to note, however, is that the treatment presented here does not take into account the decoherence effects of the qubits during the drive for measurement. As the qubit relaxation rates are on the order of the cavity decay, any pulsed interrogation drive will experience a bias of the qubit state towards the ground state $|0, 0\rangle$. Such an effect results in simply a re-normalization of the β values, with the largest signal-to-noise in β obtained with a drive which is at the $|0, 0\rangle$ measurement peak. In chapter 8, we will see this in an experiment which characterizes this joint readout and the dispersive shifts associated with a two qubit circuit QED device.

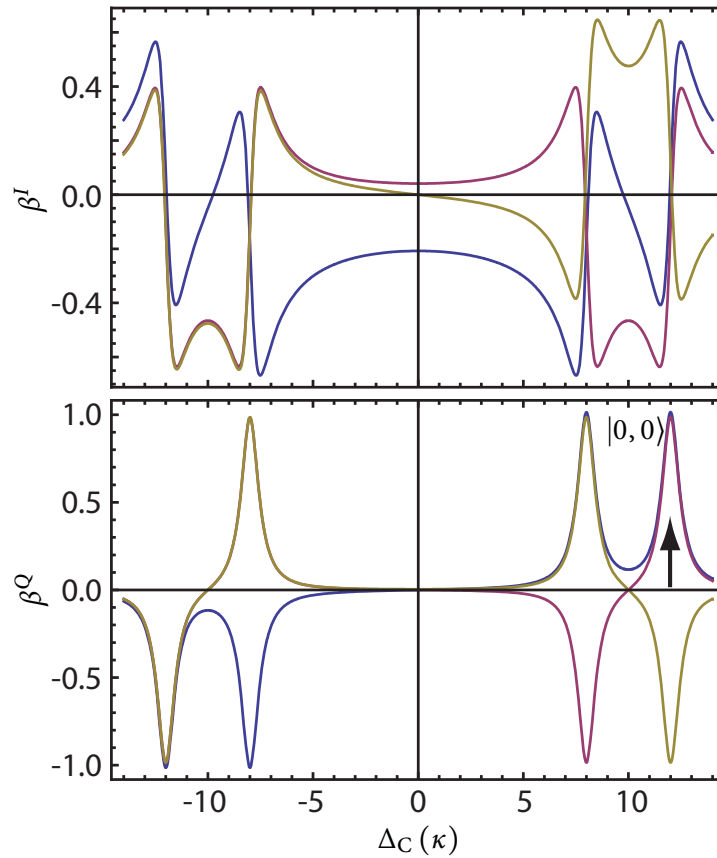


Figure 4.7: Measurement model coefficients versus drive frequency. The measurement model coefficients for ZI (blue), IZ (purple), and ZZ (gold) as a function of detuning Δ_C from the bare cavity frequency. Here the measurement model is broken down into the two cavity quadratures, I and Q . The cavity is assumed to have a linewidth κ , and the simulation is performed assuming $\chi^{(1)} = 10\kappa$ and $\chi^{(2)} = 2\kappa$.

4.4.2 State tomography in circuit QED

As discussed in chapter 2, quantum state tomography (section 2.5.2) is the technique by which the density matrix ρ of an arbitrary quantum state can be estimated. Finding this density matrix is critical in any quantum computing architecture for determining how good the quantum states are, and for the quantification of entanglement for entangled states.

The full determination of the state is traditionally performed by counting coincidences between multiple individual qubit readouts [11, 15, 67, 98]. Often these individual readouts will give ‘clicks’ corresponding to a single Pauli operator, e.g. σ_z . However, measurements of the two-qubit state need to be performed in the combined bases of the two qubits, such that there are nine combinations of the three Cartesian directions (x, y, z) for each qubit.

Single-qubit rotations such as $R_y(\pi/2)$ and $R_x(\pi/2)$ can be performed prior to readout of each qubit in order to rotate the measurement basis from σ_z to σ_x or σ_y , respectively. Hence, two-qubit correlations are actually obtained through simultaneously recorded events on each individual qubit readout combined with a classical product. However, such a readout scheme is subject to scrutiny when readout fidelity is low, making the probability of incorrect counts much higher. Another issue is the presence of crosstalk between readouts. Although this is not a serious problem in quantum systems such as photons and trapped-ions, in which the individual detectors are simply photodiodes that can be spatially separated and uncorrelated, for superconducting architectures, crosstalk can be quite impactful due to stray electromagnetic coupling on a lithographically defined chip [67, 99].

Similar to the individual readouts, the joint readout discussed in this chapter can also be used for full quantum state tomography. Since the ensembled measurement from (4.59) is a function of not only individual qubit polarizations but also two-qubit correlations, by combining a set of measurements involving single-qubit rotations before the joint measurement, the state ρ can be reconstructed. Of course, this relies on a believable characterization of the joint readout and the underlying measurement operator M . To satisfy this, the coefficients β can be determined and calibrated by simple Rabi driving of the qubits between the different computational basis states. This experiment will be described in detail in chapter 8.

Nonetheless, with the coefficients β determined, ensembles of all the two-qubit Pauli operators can be found by applying the appropriate pre-rotations (chosen from $R_y(\pm\pi/2)$, $R_x(\pm\pi/2)$, $R_{x,y}(\pi)$, $\mathbb{1}$) on both qubits. We can drop β_0 as an overall offset constant. As an example, we can get the ensemble average $\langle IZ \rangle$ by combining the measurements where we apply $\mathbb{1}^{(1)} \otimes \mathbb{1}^{(2)}$ with the measurement where we apply $R_x^{(1)}(\pi) \otimes \mathbb{1}^{(2)}$:

$$\langle M \rangle_1 = \beta_1 \langle ZI \rangle + \beta_2 \langle IZ \rangle + \beta_{12} \langle ZZ \rangle \quad (4.60a)$$

$$\langle M \rangle_2 = -\beta_1 \langle ZI \rangle + \beta_2 \langle IZ \rangle - \beta_{12} \langle ZZ \rangle. \quad (4.60b)$$

And similarly, a set of fifteen two-qubit Pauli expectation values can be obtained to reconstruct the full density matrix of the two-qubit state. Details of the full estimation and experimental state tomography will be given in chapter 8.

The joint readout method for state estimation is fundamentally different from individual qubit readouts, as the issues of poor single-shot readout fidelity and measurement crosstalk are essentially circumvented. The single-shot readout fidelity for joint readout enters statistically when it is poor and dominated by amplifier noise. Then, the ensemble averaged measurement

operator is subject to classical Gaussian fluctuations in the voltage, δv , and given by

$$\langle M \rangle = \beta_1 \langle ZI \rangle + \beta_2 \langle IZ \rangle + \beta_{12} \langle ZZ \rangle + \delta v. \quad (4.61)$$

Through multiple repetitions of obtaining M , it is thus possible to repeat and average to abate the effect of reduced measurement fidelity and fully calibrate the joint readout. As for crosstalk, the joint readout employs a single physical line, and to some degree the crosstalk between the states of the two-qubits is built into the measurement operator with the β_{12} term. We call the ratio of this to the single-qubit polarizations, $\beta_{12}/\beta_{1,2}$ the *jointness*, reflecting the two-qubit state sensitivity of the measurement operator. Therefore, with a joint readout, instead of striving to reduce the crosstalk, it is simply an inherent part of the measurement to be calibrated and taken advantage of for full state detection.

4.4.3 Entanglement by joint measurement

A further facet of the joint readout is the ability to induce conditional entanglement through the act of measurement. This situation arises in the special case when the cavity pulls of two qubits are equal, such that $\chi^{(1)} = \chi^{(2)} = \chi$ (figure 4.8). In this case, the dispersive Hamiltonian can be written as

$$H = \left[\omega_C + \chi \left(\sigma_z^{(1)} + \sigma_z^{(2)} \right) \right] a^\dagger a + \sum_{j=1,2} \frac{1}{2} (\omega^{(j)} + \chi) \sigma_z^{(j)} + \chi \left(\sigma_+^{(1)} \sigma_-^{(2)} + \sigma_-^{(1)} \sigma_+^{(2)} \right). \quad (4.62)$$

This Hamiltonian can allow a QND measurement of $(\sigma_z^{(1)} + \sigma_z^{(2)})$, as it commutes with the Hamiltonian. Since the states $|01\rangle$ and $|10\rangle$ will have the same cavity pull, the cavity is in fact un-shifted from its bare frequency when the system is in either state and the either state cannot be distinguished from the other through a measurement of $(\sigma_z^{(1)} + \sigma_z^{(2)})$.

This degeneracy in the measurement signal in regards to the state $|0, 1\rangle$ or $|1, 0\rangle$ can be a way of generating entangled Bell states. The recipe is to first create a maximally superposed state, $[(|g\rangle_1 + |e\rangle_1) \otimes (|g\rangle_2 + |e\rangle_2)]/2$ with $R_x^{(1)}(\pi/2) \otimes R_x^{(2)}(\pi/2)$, and then to perform the measurement by interrogating at the bare cavity resonance, corresponding to $\{|0, 1\rangle, |1, 0\rangle\}$. The measurement operator would then be a projector on the Bell states, $|\psi_\pm\rangle = (|0, 0\rangle \pm |1, 1\rangle)/\sqrt{2}$,

$$M = |\psi_+\rangle \langle \psi_+| + |\psi_-\rangle \langle \psi_-|. \quad (4.63)$$

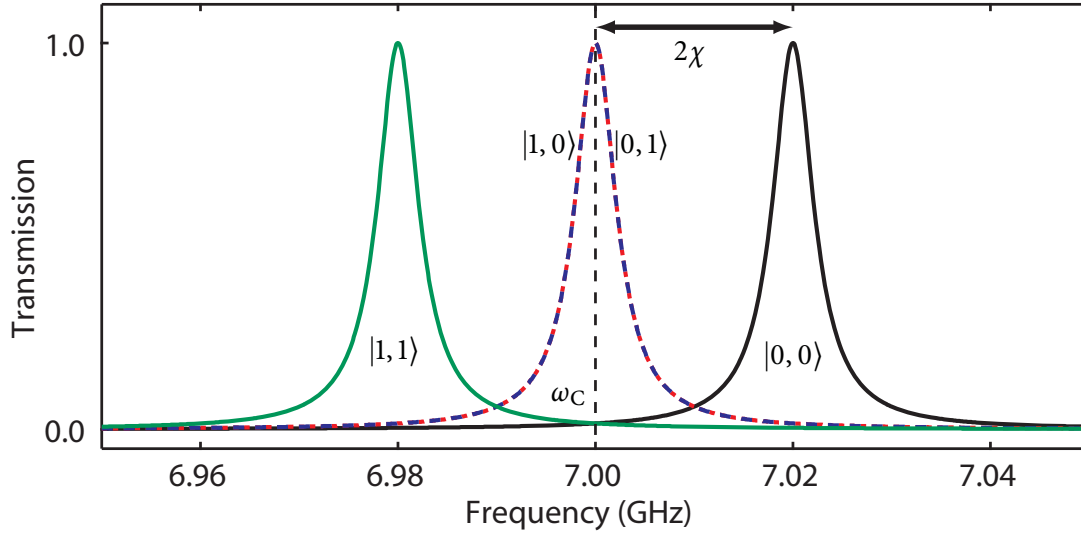


Figure 4.8: Dispersive peaks for generating Bell states by measurement. When the two qubits have equal dispersive shifts χ , the cavity transmission peaks corresponding to $|01\rangle$ and $|10\rangle$ overlap. Then a measurement tone on this cavity peak would project onto a Bell state.

The act of measurement would leave the maximally superposed state in a Bell state. This is generally known as entanglement generation conditioned upon the measurement of no cavity-pull.

4.5 Chapter summary

In this chapter, we have developed some of the basic ideas for quantum information processing in a circuit QED system. Microwave frequency pulses and fast flux bias pulses can be used to perform single-qubit rotations. Furthermore, the interaction with the photon bus allows for a number of two-qubit interactions which we may use to generate an entangling gate. Specifically, by using the virtual photon interaction, we can realize the $\sqrt{i\text{SWAP}}$, and by using higher-excitation interactions of the transmon, we can realize a c-Phase gate. Furthermore, we have introduced a joint qubit readout scheme built into the circuit QED architecture. We will need to experimentally verify and calibrate this measurement model and use it for state tomography. The remaining part of the thesis will detail our experimental implementation of the features presented in this chapter.

CHAPTER 5

Experimental Setup and Details

WE now shift our focus towards experiments and lay some groundwork for the primary results presented in this thesis. This chapter will give a brief discussion of the test samples and hardware setup used for the experiments which will be described in detail in the chapters to follow (chapters 6 to 9). This chapter will serve as a good background for understanding how the different experiments came about and what specific investigations could be performed.

First, we will identify the three experimental test samples (section 5.1) used for the experiments. Then, we give a brief review of the basic fabrication techniques (section 5.2 and section 5.3) involving optical and electron-beam lithography. We will also detail a number of design considerations for the different transmon qubits tested in this work. Specifically, we will discuss how we incorporate local flux-bias lines onto one of the samples for in-situ fast qubit frequency tuning (section 5.3.3). Next, in section 5.4, the copper boxes and printed circuit boards (PCBs) which shield, hold, and thermally anchor the transmon circuit QED test samples are described, including introducing improvements which remove spurious microwave resonances across the relevant bandwidth of our experiments. Then, we describe the cryogenic circuitry for all the coaxial lines which allow us to address and readout our samples in section 5.5. Finally, we review our room temperature control scheme (section 5.6

and section 5.7) and how we perform experiments both in the frequency domain and time domain.

5.1 Experimental test samples

The results that are presented in this thesis in chapters 6 to 9 to follow are based on experiments using three test samples, cQED187, cQED157, and cQED222. Though these three samples have been the primary focus of the coupling qubits work in the past few years, many other samples have passed through without achieving similar glory. In those samples, qubit frequencies might not have been in the appropriate range for the experiments presented here, or they might have been sacrificed over the course of incorporating the flux-bias line architecture. Nonetheless, the description about the fabrication process will be presented with regards to the development of the three specific samples.

cQED187 was used for the vacuum Rabi and single-qubit benchmarking experiments (chapter 6). cQED157 was used for demonstrating a cavity bus and virtual swap interaction with two qubits (chapter 7). cQED222 was used for generation and joint detection of highly entangled qubit states, violation of a Bell inequality (chapter 8), and demonstration of two-qubit algorithms (chapter 9).

In all cases the overall fabrication methods, from optical to electron-beam lithography, are relatively straightforward, with the only major differences in the actual designs of the transmon qubits germane to the different experiments tested.

5.2 Resonator Fabrication

A more detailed description of the resonator fabrication techniques and characterization is given in Ref. [100] and Ref. [53]. Here in this section, we will focus on the optical design considerations and standard optical lithography protocols in regards to the three samples used for the experiments presented in this thesis. This stage of the fabrication process benefitted enormously from working together with Luigi Frunzio and graduate student Joseph Schreier.

5.2.1 Resonator parameters

The resonators in all three samples are of the coplanar waveguide (CPW) geometry (figure 5.1) defined using optical lithography. The resonator frequencies are defined by the length l of

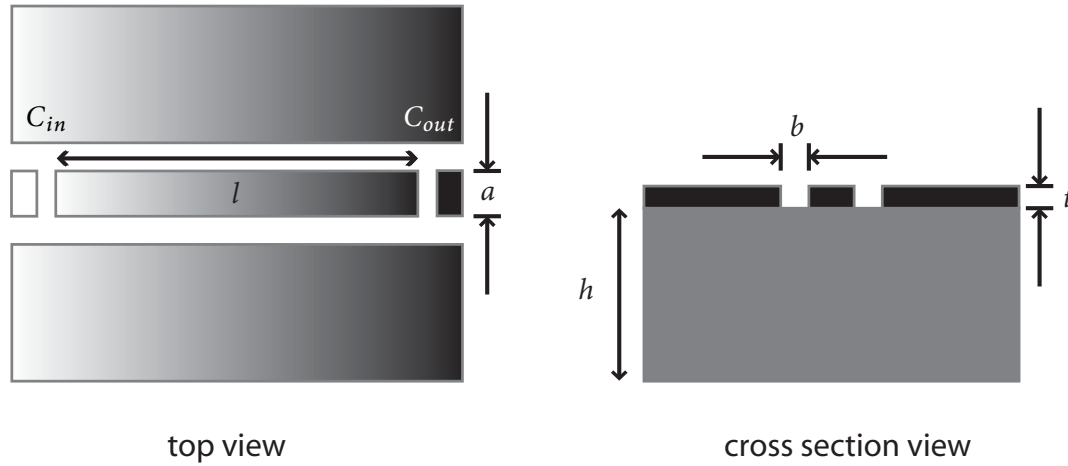


Figure 5.1: Coplanar waveguide geometry. The frequency of the CPW resonator is defined by the length of the center pin between the gap capacitors at each end. The center pin width is given by a and the gap between the center pin and ground planes is b . The ground planes are designed to be much wider than b in order to be effectively infinite.

the center conductor and the dielectric ϵ_{eff} of the underlying substrate and the vacuum above the chip, via the formula [101]

$$\omega_C = \frac{c\pi}{l\sqrt{\epsilon_{\text{eff}}}}. \quad (5.1)$$

The CPW, with center pin width a , gap between center pin and ground planes b , is designed based to have a characteristic impedance $Z_0 = 50 \Omega$. Although there are analytical expressions which give Z_0 for the CPW geometry [101], the determination of the designed a and b is aided by the microwave simulation software TXLINE, part of the AWR Microwave Office package. The quality factor is determined by the size of the gap coupling capacitors,

$$Q = \frac{\pi}{2} \frac{1}{\omega_{\lambda/2}^2 Z_0^2 (C_{\text{in}}^2 + C_{\text{out}}^2)}, \quad (5.2)$$

where $\omega_{\lambda/2}$ is the frequency of the fundamental $\lambda/2$ resonance. The CPWs can be defined to be either symmetric $C_{\text{in}} = C_{\text{out}}$ or asymmetric $C_{\text{in}} \neq C_{\text{out}}$. Asymmetric coupling capacitors can be used for increased collection efficiency, as a stronger output coupling capacitor would give the microwave photons a preferred path for leaving the cavity. cQED157 and cQED187 are both asymmetric cavities, with a Q dominated by the output capacitor, whereas cQED222 is a symmetric cavity.

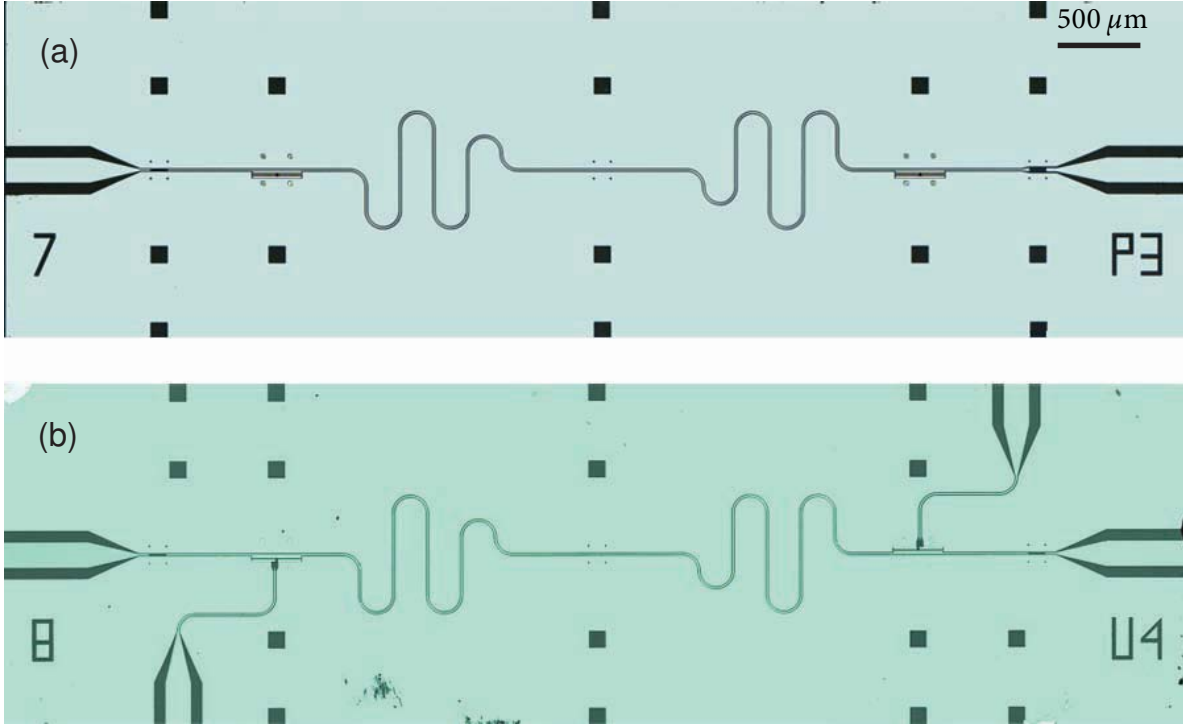


Figure 5.2: Optical images of resonator topologies. (a) Two-port resonator device as used for cQED157 and cQED187. Two transmons are defined on the same side of the center pin, but located at opposite ends near the input and output coupling capacitors. (b) Four-port resonator device as used for cQED222. The two additional ports which enter from the top and bottom sides are for the on-chip flux-bias lines. The ground plane is broken up into 4 distinct pieces. The two transmon qubits are now located on opposite sides of the center pin, and still on opposite ends of the cavity near the input and output coupling capacitors.

5.2.2 Optical lithography

cQED187 and cQED222 are defined using niobium on corundum (sapphire). The corundum is 430 μm single crystal *R*-plane and a 200 nm thick layer of niobium is dc-magnetron sputtered. After coating with S1808 resist, an optical mask with UV exposure defines the coplanar waveguide for an etch. Reactive-ion etching is performed using SF_6 as the primary agent, followed by liftoff in acetone. The resonator frequencies for both samples are designed to nominally give 7 GHz $\lambda/2$ resonance. The quality factors for cQED187 and cQED222 are designed to be 20,000 and 10,000, respectively. cQED187 employs a single finger capacitor on each of the input and output ports, but with different finger lengths of 30 μm and 100 μm. These designs give rise to simulated capacitance values of about 2 fF and 5 fF, respectively. cQED222 uses the same 100 μm finger, but on both input and output ports.

cQED₁₅₇ is made out of aluminum on silicon dioxide/silicon. The substrate is 500 μm thick silicon with a thermally grown cap layer of 220 nm thick silicon dioxide. After coating with LOR5A and S1808 resist, an optical mask with UV exposure defines the CPW for a positive deposition step. 180 nm of aluminum is deposited followed by liftoff in NMP. The $\lambda/2$ resonator frequency is designed with a center frequency of 6 GHz. The quality factor is designed to be ~ 300 , with asymmetric input and output capacitors given by approximately 4 fF for a single finger design and 54 fF for an eight finger design.

A critical change in the design of the samples is the switch from a 6 GHz resonator (cQED₁₅₇) with a $Q = 300$ to a 7 GHz resonator with a $Q = 10,000 \sim 20,000$ (cQED₁₈₇ and cQED₂₂₂). Chronologically, cQED₁₈₇ and cQED₂₂₂ were fabricated after cQED₁₅₇, reflecting our new understanding with respect to the multi-mode Purcell effect (section 3.5.1). We changed the design to push the dip in the real part of the admittance between the fundamental and first harmonic frequencies higher up and away from the band in which we operate our qubits (typically $\sim 4 - 8\text{GHz}$).

Also note the difference in the ground plane for cQED₂₂₂ in figure 5.2, permitting additional CPW traces for the on-chip flux bias controls. Incorporating these flux bias lines breaks the ground plane into 4 distinct pieces rather than 2. As we will discuss later in this chapter in section 5.3.3, on-chip wire bonds or air-bridges can be used to connect all of the ground planes into a single piece. This will play a role in the coupling of the qubits to non-CPW modes on the chip, which otherwise would adversely affect qubit coherence properties.

5.3 Transmon fabrication

All three samples are fabricated with two transmons on each, located on opposite ends of the cavity, near the input and output capacitors. The two transmons on each sample are defined in a single electron-beam lithography step. A bilayer resist system is used, with a top 100 nm thick layer of 950K PMMA A3, on top of a copolymer 550 nm thick layer of MMA(8.5)-MAA EL13. The bottom layer is more sensitive to electrons than the top, resulting in a natural undercut of ~ 80 nm during electron beam writing. The undercut is a necessary feature for achieving good clean liftoff with aluminum. The full lithography recipes follow those outlined in Ref. [53] and were performed with Luigi Frunzio, graduate student Blake Johnson, and postdoc Leonardo DiCarlo.

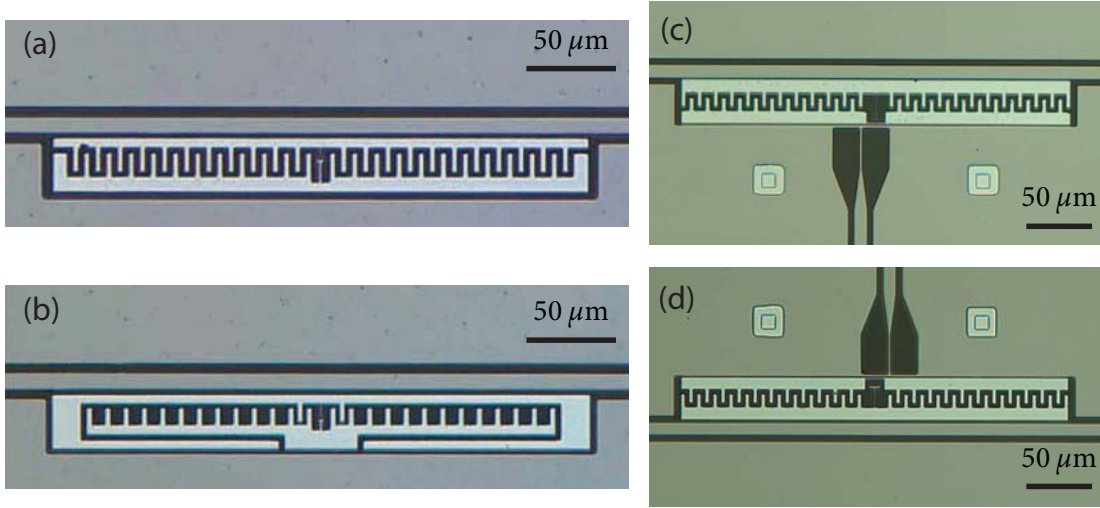


Figure 5.3: Optical images of different transmon designs. (a) Standard transmon design employed in cQED₁₅₇ and on one of the qubits in cQED₁₈₇. (b) Balanced transmon design used in one of the qubits in cQED₁₈₇. (c) and (d) Transmon designs incorporating flux bias lines. A slightly different transmon SQUID loop design is necessary to accommodate the flux bias lines entering from the (c) bottom of the chip or from the (d) top of the chip, while preserving the same double-angle evaporation procedure.

For each sample, the junctions in both transmon qubits are designed in a single step. The Dolan bridge technique which is described in Ref. [53] is used for fabricating the junctions. This method is especially useful for making small junctions, as for the transmon qubits used here, the areas are typically 150 nm by 250 nm.

The similarities between the three samples ends at the level of junction fabrication however. The sizes of the SQUID loops and the values of the relevant capacitances are important design considerations for each of the test samples, and permit them to be used for specific sets of experiment. The most traditional transmon (section 5.3.1) design is described in detail in Ref. [53]. However, here we present two additional designs, the balanced transmon (section 5.3.2) and the flux-bias transmon (section 5.3.3).

5.3.1 ‘Traditional’ transmon

A cartoon of all of the relevant pieces of metal which must be considered for the transmon design is shown here in figure 5.4. The charging energy E_C and the voltage division ratio β are defined in terms of all of the capacitances between pieces of the circuit figure 5.4. With regards to describing the fabrication and design considerations, we can be more specific about which of the different pieces in the circuit of figure 5.4 affect the transmon and cavity

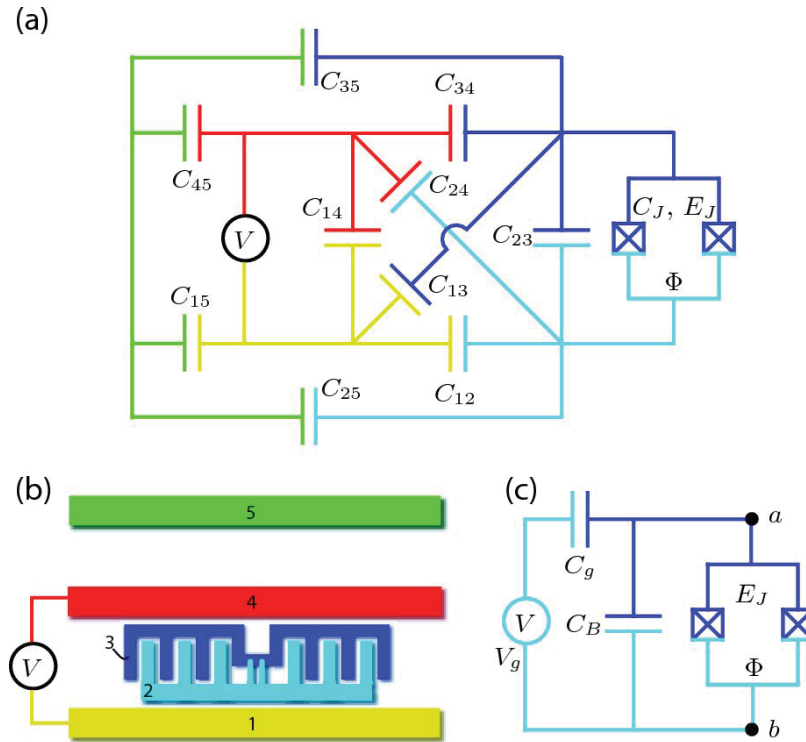


Figure 5.4: The capacitance network for the transmon in a coplanar waveguide resonator. **a** The complete circuit diagram, showing all the capacitances, designed and parasitic, between the 5 metallic areas of the transmon-cavity circuit, shown in **b** (not to scale). **c** The simplified equivalent circuit which can be found by using the electrical engineer's rules for series and parallel capacitors. (Figure used with permission from [61]. See Copyright Permissions.)

coupling parameters. Piece 1 refers to the lower ground plane (yellow); piece 4 is the CPW center pin (red); piece 5 is the upper ground plane (green); piece 2 is the lower transmon island (cyan); piece 3 is the upper transmon island (blue).

All samples employ a pocket size of $300 \mu\text{m}$ by $30 \mu\text{m}$ cut out of the lower CPW ground plane, in which the transmon islands can be defined. In the traditional transmon design, as shown in figure 5.3a, we get typically $E_C = 300 \sim 400 \text{ MHz}$ with $\beta \sim 0.10 - 12$, which yields $g_{01}/\pi = 150 \sim 250 \text{ MHz}$. The best way to adjust E_C is through changing the capacitance between the islands, C_{23} . The coupling capacitance C_g , is primarily determined by the length of piece 3, typically $290 - 300 \mu\text{m}$, and the gap between piece 3 and piece 4, typically $3 - 5 \mu\text{m}$. The standard transmon design gives simulated values of $C_{34} \approx C_{23} = 24 \text{ fF}$. SQUID loops are typically designed with dimensions in the range of $2 - 3 \mu\text{m} \times 2 - 3 \mu\text{m}$.

5.3.2 Balanced design

As a result of the location of the transmon between the center pin and one of the ground planes of the CPW, it is possible for the transmon to couple to a slotline mode [102] of the resonator where the top and bottom ground planes oscillate out of phase. The balanced transmon is the result of an attempt to balance the asymmetry between the top and the bottom line using a Wheatstone bridge technique (to be discussed in more detail in Ref. [103]). It was proposed [61] that coupling to such a slotline mode could cause a Purcell-like spontaneous decay, and lead to shorter qubit relaxation times.

Although the balanced design was originally intended to make the effective coupling to a slotline mode minimal, one of the byproducts of the design was actually a much smaller g_{01} due to a reduced voltage division ratio $\beta \sim 0.08$. Whereas most traditional transmons have coupling strengths in the 200 – 300 MHz range, these balanced transmons are on the order of 50 – 100 MHz. Figure 5.3b shows one such balanced design, employed in cQED187. The diminished coupling is primarily due to the reduced length of piece 3, resulting in a smaller direct capacitance to the center pin C_{34} . The balancing is achieved through increasing C_{31} , C_{24} , and C_{25} .

In the experiments presented in this thesis, the intended effect of the balancing in regards to slotline mode coupling is not tested. However, the smaller g_{01} side-effect is critical for the strongly-driven vacuum Rabi experiments, permitting us to see higher order photon interactions in the Jaynes-Cummings ladder (section 6.1.1) for characterizing our state initialization (section 6.1).

5.3.3 Flux-bias transmon design

cQED222 employs a different transmon style which permits on-chip flux tunability. The design of not only the qubit (two designs shown in figure 5.3c–d), but the entire chip (figure 5.2c) is modified. The transmon SQUID loop and flux-bias line traces are designed to achieve enough coupling for sufficient qubit transition frequency tuning.

Flux coupling

Together with former postdoc Johannes Majer, we designed the flux-bias line (FBL) to be itself a 50Ω coplanar waveguide which runs perpendicular to the CPW resonator on the chip towards the transmon pocket. At the pocket, the FBL is terminated in a short circuit to

the ground planes. An optical zoom-in image on the flux-bias line termination is shown in figure 5.5a. The CPW which feeds the FBL tapers down to $2\ \mu\text{m}$ before being short-circuited near the pocket for the transmon with a width of $2\ \mu\text{m}$ and length of $10\ \mu\text{m}$ on each side. By placing the loop off center, as shown in the optical image figure 5.5a, and right up against the split inductive short permits one arm of the inductive short to couple more strongly than the other, such that a non-zero flux is threaded through the loop. Although the mutual inductance between the FBL and the loop can be calculated from simple electrostatics and simulations, the presence of superconductor around the actual FBL and qubit loop can result in flux focusing via the Meissner effect, which significantly increases the magnetic field coupling by a factor of 2-3. From initial experiments on FBL qubits, we have found it takes $\sim 6 - 10\ \text{mA}$ at the sample to tune half a Φ_0 for SQUID loop sizes of $8 - 10\ \mu\text{m} \times 5 - 7\ \mu\text{m}$. With regards to the entire FBL circuitry up to room temperature ($\sim 300\ \text{K}$), the amount of current applied to the external line will be determined by the total attenuation and filtering of the line used for thermalization (section 5.5). Therefore, it is also important to pay attention to the thermal heat load on the line to not swamp the cooling power of the cryostat. In practice, transmon tunability using a current range at the sample of $\pm 10\ \text{mA}$ can be afforded without significantly affecting the base temperature ($+ \sim 5 - 10\ \text{mK}$).

Relaxation of the flux-bias transmon

While the flux-bias lines provide enough magnetic coupling to sufficiently tune the qubit transition energies, it is an additional connection which can also electrostatically connect the qubit to the $50\ \Omega$ environment. As discussed in section 3.5.1, the key quantity to consider for qubit relaxation is the real part of the total impedance seen by the qubit. In the standard transmon design, the impedance which we find to be the primary culprit is that of the transmission line resonator, resulting in the multi-mode Purcell effect.

However, separate characterization experiments that first implemented FBL transmons demonstrated qubit relaxation rates that did not follow just the simple multi-mode Purcell effect [82] compounded with the intrinsic $Q \sim 70,000$. Instead, in these samples, which had a cavity frequency of $7\ \text{GHz}$, measured relaxation times at frequencies above $7\ \text{GHz}$ would fall off very precipitously and at much lower frequencies than would be predicted due to the λ mode of the transmission line cavity. As a result, together with postdoc Leonardo DiCarlo, we moved towards performing simple simulations based on the FBLs using both Microwave Office and a high frequency electromagnetic simulation software named Sonnet.

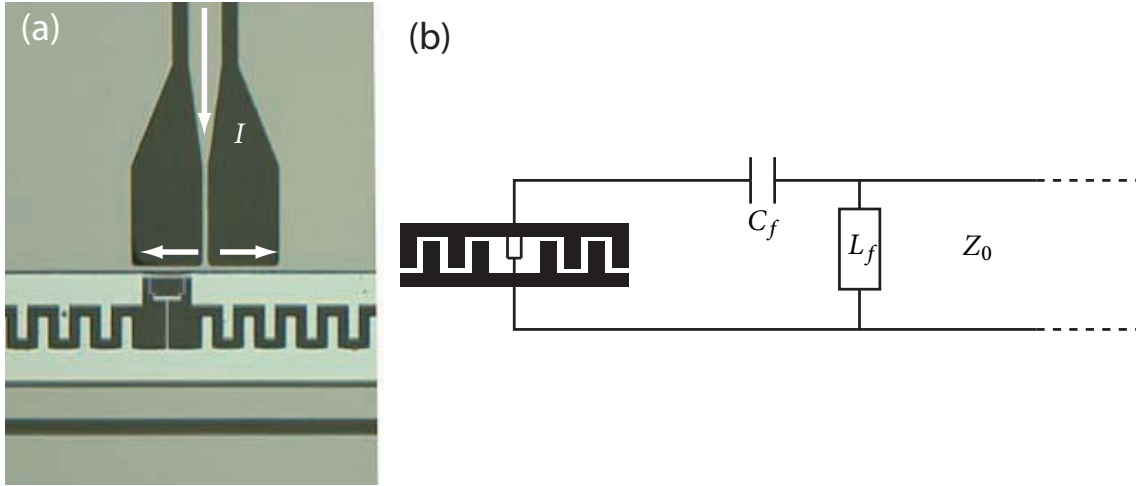


Figure 5.5: The flux-bias line. (a) Optical image of the flux-bias line short-circuited termination near the SQUID loop of the transmon qubit. (b) Modeling the flux-bias line as a circuit-decomposition, with a capacitance in series C_f with the transmon, and a shunt inductance L_f . The inductance is accounted for by the $2\ \mu\text{m}$ by $20\ \mu\text{m}$ short-circuited termination to ground.

For the Microwave Office simulations, we can model the circuit with the FBLs using a capacitance C_f in series with the transmon and a shunt inductance L_f , as shown in figure 5.5c. The capacitance can be estimated to be $\sim 3\ \text{fF}$ and the inductance to be $\sim 20\ \text{pH}$ (from electrostatic simulations). For this simple model, the real part of the admittance can be found to be

$$\text{Re}[Y] = \frac{1}{Z_0} \left(\frac{\omega}{\omega_0} \right)^4, \quad (5.3)$$

where $\omega_0 = 1/\sqrt{L_f C_f}$. This reflects a much steeper fall-off of the T_1 with respect to frequency than is generally the case without the FBLs. However, it does not explain the sharp drop off immediately above the fundamental CPW mode.

Sonnet provides a different method of simulation by giving high frequency electromagnetic field calculations based on 2D geometries. The full resonator with two FBLs can actually be designed in the software and the real part of the admittance seen from the location of the qubit, labeled port 1 in figure 5.6, can be determined. Assuming a qubit coupling capacitance of $C_g = 15\ \text{fF}$, a relaxation time, or T_1 , curve due to the entire flux bias line coplanar waveguide resonator is found and plotted in figure 5.7. The overall asymptotic behavior agrees with the simple $1/\omega^4$ model from the simple Microwave Office simulation. However, the Sonnet simulations tell us a lot more information about the resonant structure of the full chip.

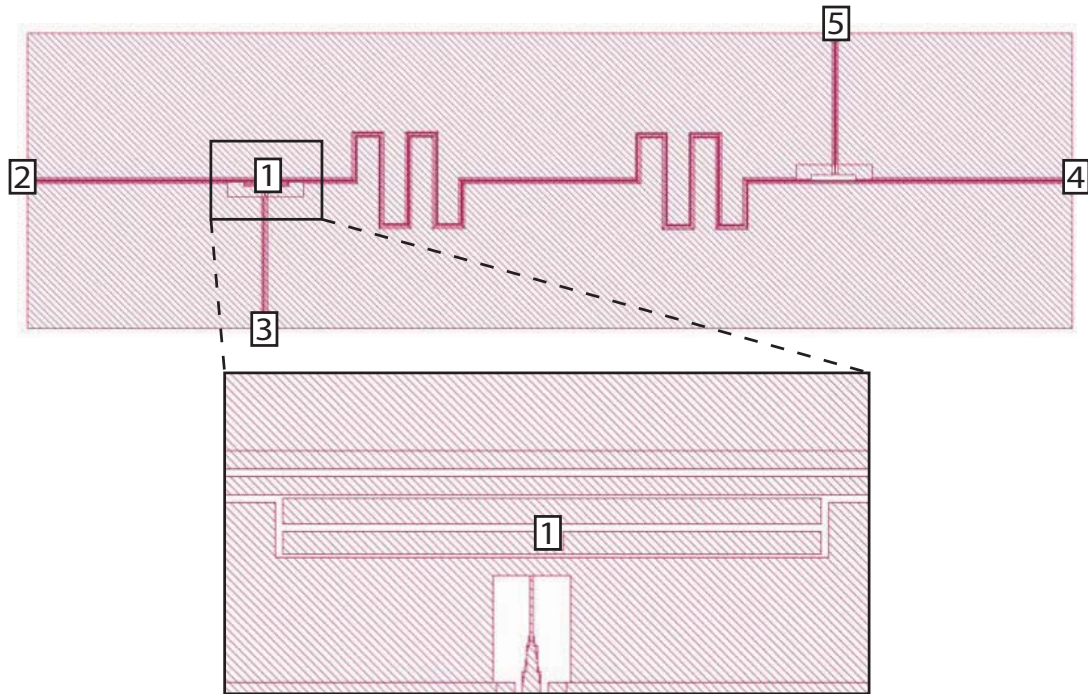


Figure 5.6: FBL schematic for Sonnet simulations. For performing the Sonnet simulations, a simplified chip and transmon design is used. We label 5 ports, and find the total admittance referenced to port 1, where the transmon qubit is located.

Specifically, besides the presence of the two resonances due to the $\lambda/2$ and λ CPW modes at $f_0 = 6.45$ GHz and $f_1 = 12.8$ GHz, a third mode is found at $f_s = 11.65$ GHz.

The location of this third mode in between the two standard CPW modes agrees qualitatively with the experimental drop off in the relaxation times at frequencies directly above the $\lambda/2$ resonance. We can identify this mode with a slotline, or ‘wiggle-waggle,’ mode which is due to an odd transmission line mode between the lower and upper ground planes of the CPW. This is the same mode to which the modified transmon balanced design (section 5.3.2) attempts to decrease the coupling to. In the standard CPW with transmon designs, the presence of this mode has not been detected in T_1 versus transition frequency measurements. However, in the case of the CPW with flux bias line transmons, the flux bias lines provide a path of coupling the environment to such a mode. This is best seen by using Sonnet to view the current density over the entire chip as a function of frequency, as shown in figure 5.8. We find that at the fundamental and first harmonic frequencies of the CPW resonator, the current density is primarily distributed over the center pin and concentrated around the gap capacitors which define the cavity. This reflects a preferred loss path for photons in the cavity

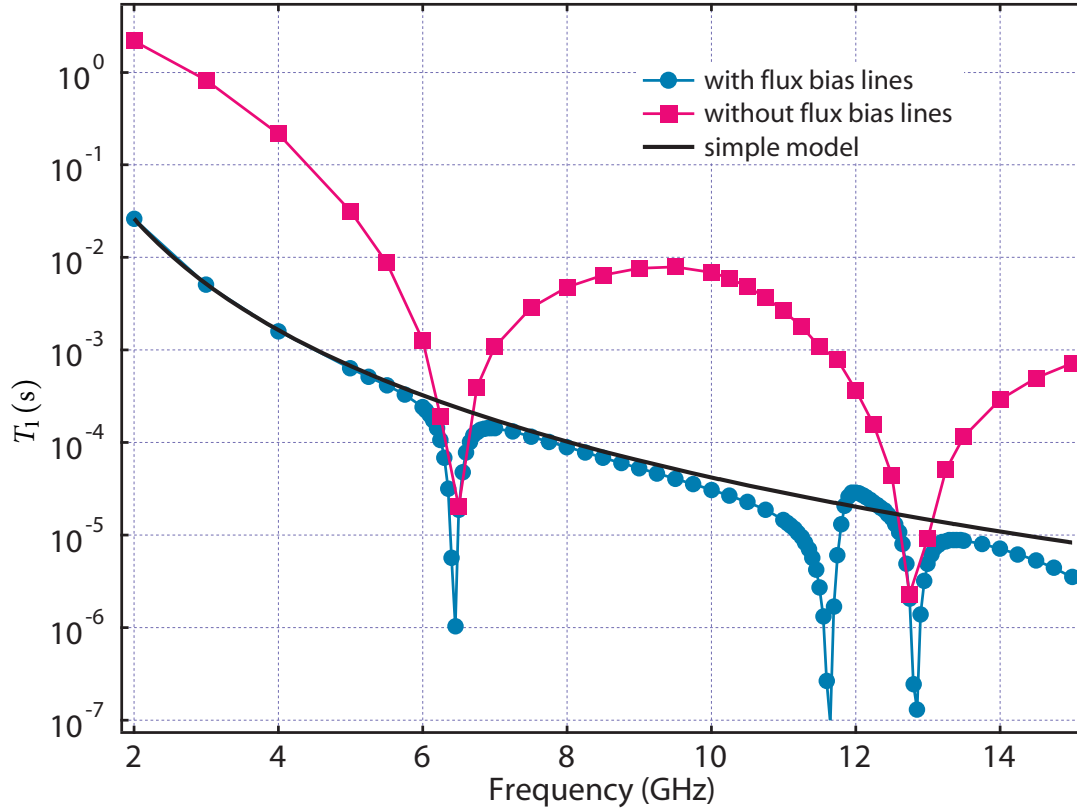


Figure 5.7: T_1 Simulations of resonators with and without FBLs. The simulation software returns the $\text{Re}[Y]$, from which we calculate T_1 . Without the presence of the FBLs, we find the standard multi-mode Purcell curve (magenta squares), with two dips corresponding to the $\lambda/2$ and λ CPW resonances. With the presence of the FBLs (blue circles), we see an extra dip, at 11.65 GHz. The overall behavior of the FBL case also agrees over the frequency range according to the simple $1/\omega^4$ model.

out through the capacitors, which is the expected Purcell effect for spontaneous emission (section 3.5.1). However, at f_s corresponding to the wiggle-waggle mode, current becomes concentrated over the flux bias line ports, resulting in a different path for spontaneous emission. Therefore, whereas the wiggle-waggle mode may not have been a serious problem for previous transmon designs, for the flux-bias line sample it poses a significant obstacle to operating with qubit transition frequencies above the fundamental CPW mode.

On-chip wirebonds

It is possible to employ some on-chip engineering to abate the issue with the wiggle-waggle mode. Specifically, by connecting the upper and lower ground planes via an air-bridge in the middle of the center-pin line, as shown in figure 5.9a, we can actually move the frequency of

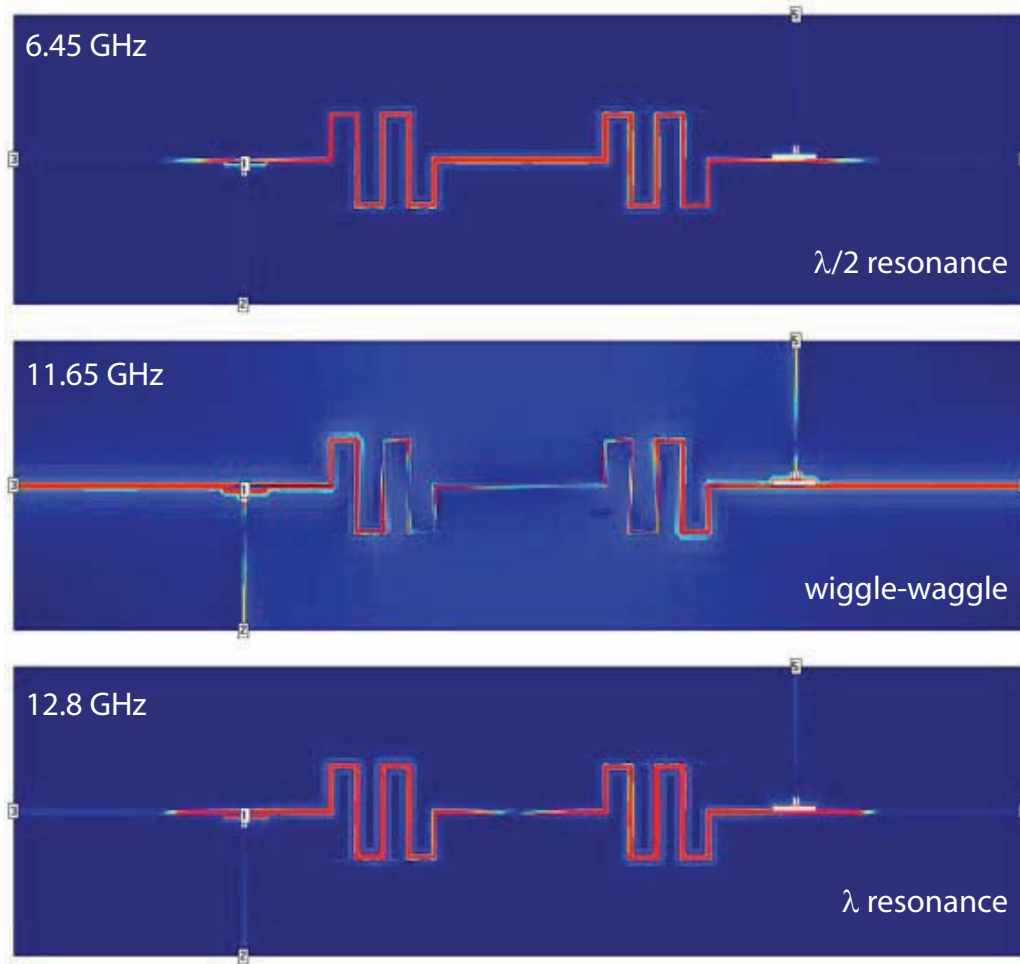


Figure 5.8: Current density simulations of resonators with FBLs. Color scale shows the current density across the chip. Blue represents no current and red represents high current. For the $\lambda/2$ and λ resonances, we can see the radiation along the center pin and, coupled through only the input and output capacitances on each end. However, for the wiggle-waggle resonance, there are high current paths along the flux-bias lines and all along the center-pin.

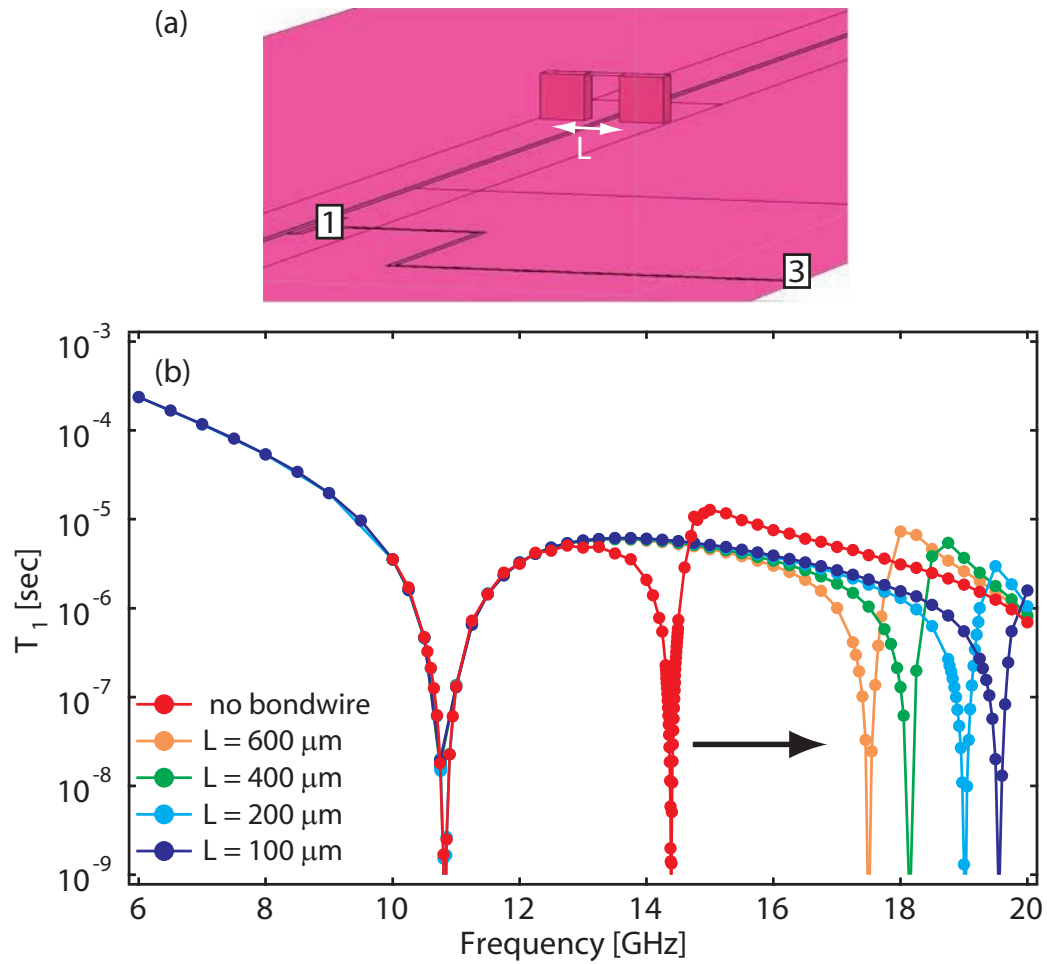


Figure 5.9: Pushing up the wiggle-waggle with bondwires. (a) Schematic for Sonnet simulation incorporating an on-chip air-bridge for connecting the upper and lower ground planes at the center of the CPW. L is the length of such a bridge. (b) Simulated T_1 curves for resonator with FBLs and on-chip air-bridge with varying L from $600 \mu\text{m}$ to $100 \mu\text{m}$. With decreasing L , the wiggle-waggle resonance is pushed up in frequency.

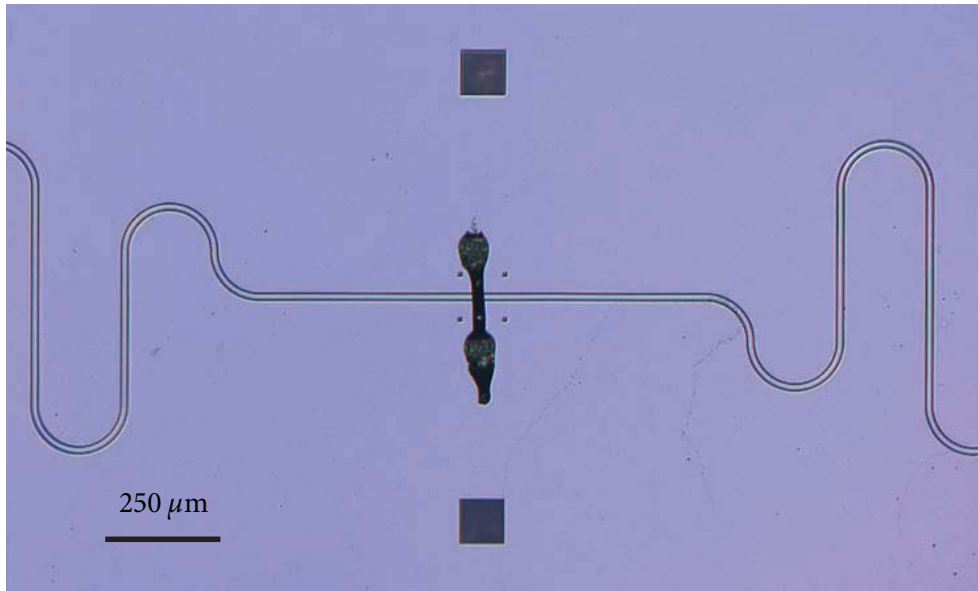


Figure 5.10: Optical image of an on-chip wirebond. Wirebonds across the center pin are generally 200 – 300 μm long. In standard practice, we place 3 wirebonds in parallel.

the wiggle-waggle mode. By including such an airbridge in our Sonnet simulations, we find that the wiggle-waggle mode can be pushed past the λ CPW resonance and away from the standard qubit operating regime. Figure 5.9b shows that varying the distance L between the location of the air-bridge and the center pin changes where the position in frequency of the wiggle-waggle resonance.

In experimental practice, this air-bridge can be achieved by placing on-chip wirebonds which go over the center pin but connect the lower and upper ground planes. Figure 5.10 shows an optical image where one such wirebond is placed across the center pin in the center of the CPW line. We can perform simple 4 K transmission experiments with Nb resonators to demonstrate the effect of the wirebonding. Figure 5.11a shows the transmission measurements of a 7 GHz Nb resonator, with a $Q = 100$, and having performed no modifications to the chip or sample holder (described in section 5.4). S_{21} reflects the standard input-output CPW transmission path. S_{2L} (S_{2R}) reflects applying the drive to the left (right) flux-bias line port and transmitting out the output path.

Besides the $\lambda/2$ and λ resonances, a peak in the transmission in all three measurements is seen around 11 GHz. By adding on-chip wirebonds at the center of the sample and repeating the measurements, we find the transmission spectrum given by figure 5.11b, where the struc-

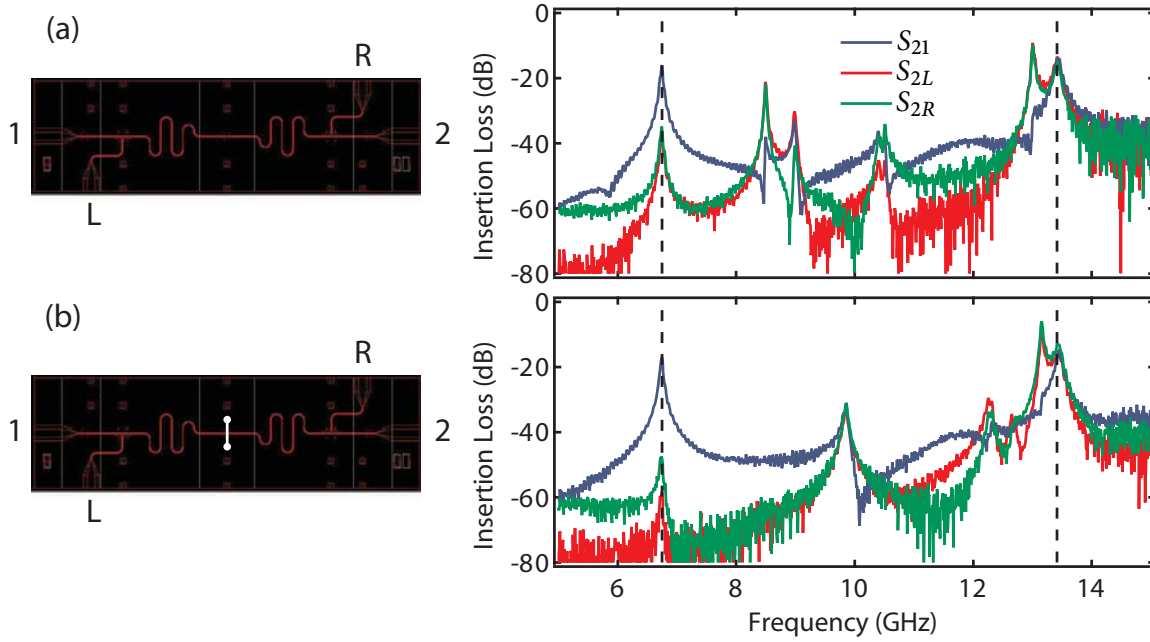


Figure 5.11: Experiment showing transmission spectrum with and without wirebond. (a) Transmission experiments are performed in a 4 K dunk test set-up. We measure the standard CPW transmission S_{21} (blue), the transmission from the left FBL to the output S_{2L} (red), and the transmission from the right FBL to the output S_{2R} . The black dashed lines indicate the location of the CPW $\lambda/2$ and λ resonances. The wiggle-waggle mode can be seen at around 11 GHz. (b) After re-dunking having added on-chip wirebonds to the center of the chip, the spectrum is improved considerably, with the wiggle-waggle resonance previously seen in S_{2L} and S_{2R} now pushed up near 13 GHz.

ture at 11 GHz is no longer there. Other resonances are due to copper traces on the sample board holder as well as the sample box, which will be the subject of the next section.

The flux-bias line sample studied in this thesis, cQED222, employs such a set of three wirebonds over the center pin to suppress this wiggle-waggle mode and all flux-bias line samples now employ this same technique.

5.4 Sample boards and holders

Having described the samples at the chip-level, we now proceed up through the experimental setup onto the sample boards and sample boxes. We need both a sample holder and box which suppress parasitic resonances and can be easy to use and convert into microwave coaxial cable lines for input and output through the cryostat. cQED187 and cQED157 each have only two ports each, and we use a simple design known as the ‘coffin’ class (section 5.4.1)

of sample holders. However, cQED222 is a bit more complicated, with 4 ports, an input, output, and two connections for flux bias line control. In that case we employ the ‘octobox’ class (section 5.4.2) of sample holders.

5.4.1 Coffin design

The coffin design consists of two ports, an input and an output, for drive and readout lines to a CPW resonator. The printed circuit board (PCB) is copper plated on the top and bottom of an Arlon AD1000 ($\epsilon_r = 10$) dielectric with a single milled out slot to the bottom copper plane. There are locations for two Rosenberger SMP connectors for the input and output ports. A 50Ω CPW line is etched into the copper, with a center pin width of $150 \mu\text{m}$ and gap to ground plane of $90 \mu\text{m}$. The upper and bottom ground planes are connected by copper coated vias (12 mil hole size) which are drilled throughout. These vias reduce the parasitic modes which can arise due to imbalances in the top and bottom copper ground planes. A $2 \text{ mm} \times 7 \text{ mm}$ chip can be mounted into the slot. Many wirebonds are used to attach ground planes of PCB to ground planes of chip and three wirebonds are used for connecting the ground planes across the center of the chip. A picture of the coffin PCB is shown in figure 5.12a.

The coffin PCB is mounted onto a copper plate which is then covered by a rectangular copper box, with two output ports which mate to an SMA terminated coaxial cable. Rosenberger SMP connectors are soldered onto the slots of the board, and SMP bullets connect the board to the SMA terminated coaxial cable. The full set-up is shown in figure 5.12b.

5.4.2 Octobox design

The octobox design, shown in figure 5.13, expands the number of connections from 2 to 8, allowing for geometries with two chips, each with an input and output, or for a single chip with multiple connections for extra control lines of multiple qubits on a sample. In the case of cQED187, the octobox is used, but for the simplest experiment of just two lines, with an input and an output. For cQED222, we use 4 ports of the octobox, input, output, and a line for each qubit’s fast flux bias line.

Whereas the coffin design has a relatively clean microwave spectrum between 2 to 12 GHz, the octobox and its corresponding PCB actually suffer from quite a number of resonances. Figure 5.14a shows the transmission of a simple bare 7 GHz resonator with on-chip flux-bias lines and on-chip wirebonds as discussed earlier, mounted on an octobox PCB with 8 connections to the single chip and placed in the copper octobox. Although the on-chip

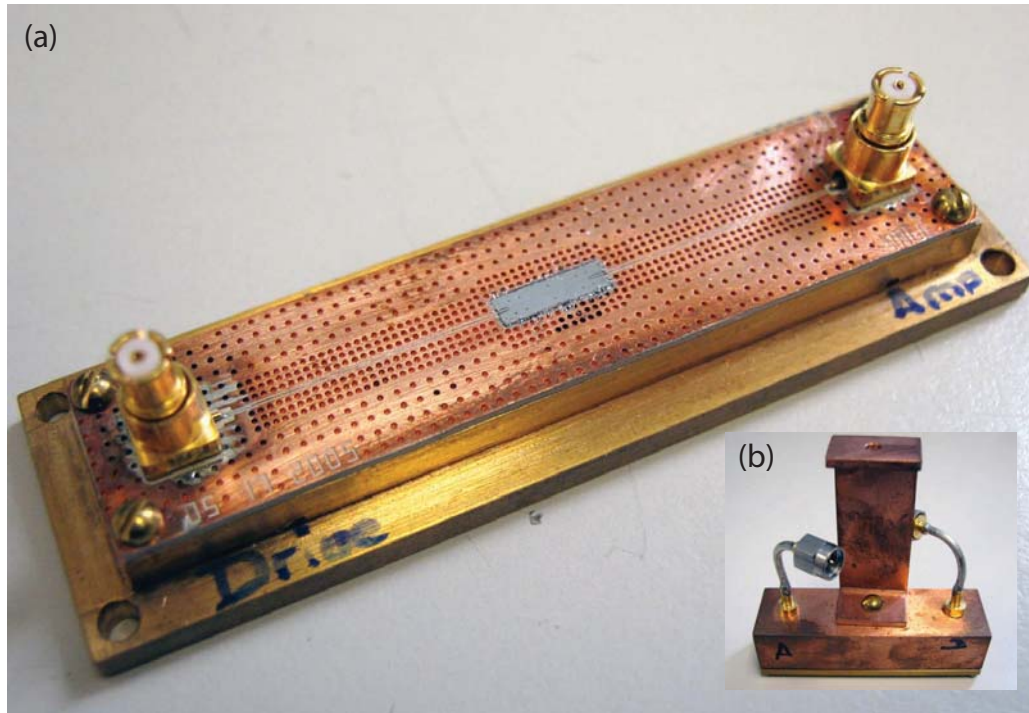


Figure 5.12: Coffin box holder. (a) The sample is placed into a 2 mm by 7 mm pocket located in the center of the PCB. The PCB connects to semirigid coaxial cables via SMP surface mount connectors using a bullet. Vias are drilled into the PCB and copper plated to connect the top and bottom ground planes. (b) Inset shows the entire rectangular coffin box with SMA to SMP jumpers.

wirebonds removed the structure at 11 GHz, there are still many other resonances throughout, including a very strong one at 10 GHz. This resonance corresponds to a whispering gallery mode of the box, removable by filling up the three-dimensional cavity within the sample holder.

A lot of the structure is actually removed from the system by modifying the octobox with a flip-chip combined with a larger copper back plate. The flip-chip is simply another PCB, or thin copper plate, with the appropriate holes cut into it sitting on top of the standard PCB, effectively placing another ground plane right on top of the CPW traces, as shown in figure 5.13. This makes the geometry more symmetric and limits any modes which may arise due to differences in the dielectric on top and below the copper traces. The larger copper back plate serves to fill up most of the volume within the box, removing whispering gallery and other 3D resonator modes. Together, these effectively eliminate any parasitic box modes,

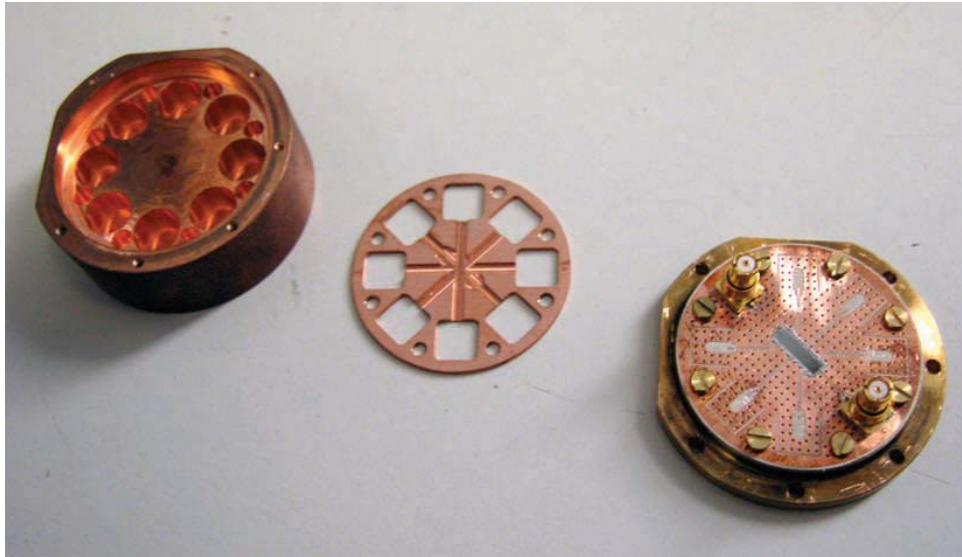


Figure 5.13: Octobox holder. The far left is the copper octobox which permits 8 connections to a sample. This particular copper octobox is designed to fill up the entire space in between the box and the sample lid. The piece in the middle is the “flip-chip” which is similar in size to a PCB, but made out of copper with traces milled out to avoid shorting to transmission lines on the PCB. The piece on the right is the lid with 8-port PCB but only a two-port sample attached.

and the difference is night and day as shown in the transmission spectrum before and after the changes of figure 5.14b.

The development of this flip-chip and reduced mode volume is now incorporated into all of our experiments.

5.5 Cryogenic setup

The experiments were performed using a Cryoconcept $200\mu\text{W}@100\text{ mK}$ dilution cryostat, capable of attaining base temperatures 10 – 15 mK, with the samples at temperatures 15 ~ 20 mK. The key details of the cryogenic setup pertain to the reduction of heat and noise that can reach the sample from room temperature or microwave cryogenic amplifiers. A schematic of the cryogenic circuitry is shown in figure 5.15.

For samples cQED187 and cQED157, the only pathways to the sample are the RF drive and the RF output. Johnson noise from room temperature on the RF drive line is attenuated with 20 dB at the 4 K stage, followed by 30 dB at the 15-20 mK base temperature plate (figure 5.15). The long cryogenic lines give an additional ~ 10 dB resulting in a total line attenuation of 60 dB. We can permit this level of attenuation and still be able to perform on-resonant measurement

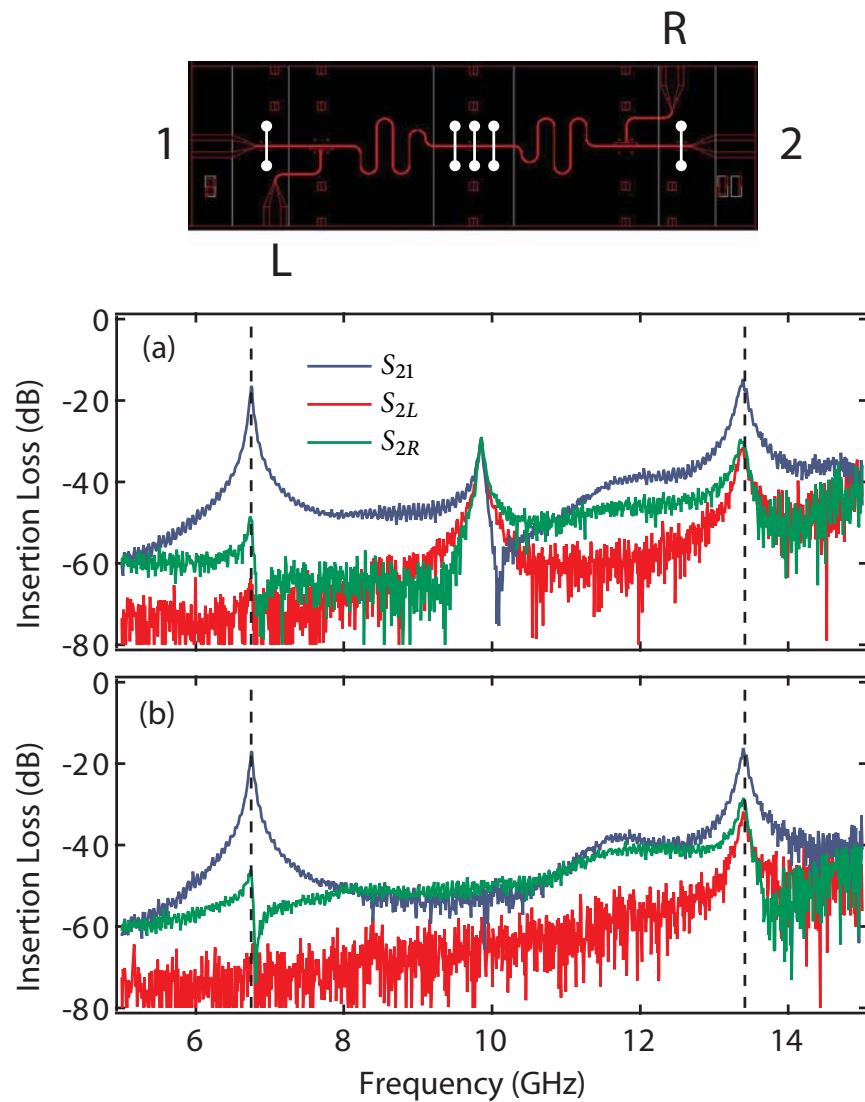


Figure 5.14: Resonator with FBL in octobox. With additional wirebonds, the transmission spectrum is further improved to (a). However, there is still a strong resonance in all 3 measurements at ~ 10 GHz, corresponding to a 3 dimensional cavity mode. This is suppressed with the use of the flip-chip and filled octobox design, with which we measure the transmission spectra shown in (b).

of the cavity (~ -80 dBm) as well as off-resonant drive of the qubits (~ -20 dBm), without significantly heating the attenuators at the cold stage. All attenuators in the cryogenic samples are made by XMA.

On the RF output line, the primary noise source is in fact the cryogenic amplifier at 4 K. These amplifiers have typical noise temperatures $T_N = 5$ K. It is not advisable here to use attenuation between the output port of the cavity and the amplifier as the whole point of the amplifier is to increase the amount of signal. However, a microwave circulator allows for the signal to pass through to the amplifier without being attenuated, while taking all the reflected noise off of the amplifier and dumping it in a 50Ω termination instead of reaching the sample. In our experiments, we used high-electron mobility transistor (HEMT) amplifiers, made by Caltech Radiometer Group, Model Numbers LNA93D and LNA95D, with low temperature gain of $\sim 33 - 36$ dB.

The location of the microwave circulator can affect the mean photon number in the cavity. For cQED187, experiments were performed in two cryogenic configurations, with two circulators at the 100 mK plate of the cryostat, and with an additional third circulator at the 20 mK base plate. As we will show in section 6.1.1, in fact, this simple change means a difference in the number of photons going from 0.018 down to 0.003. The mean photon number was extracted using fits to strongly driven vacuum Rabi spectra [89]. For cQED157, the experiments were actually performed before adding the third circulator. Then, finally for cQED222, there were two broadband (4–12 GHz isolators (circulators with built-in 50Ω terminations, Pamtech Model No. CWJ1019), thermally anchored to the base temperature plate.

The flux bias line sample cQED222 actually requires a bit more of care in terms of the cryogenic thermalization, because in addition to the RF drive and output, there are two additional lines for each qubit flux-bias. The primary requirements of such a line are the ability to tune through at least a single flux quantum on the SQUID of each qubit as well as the ability to allow enough bandwidth for tuning of the qubits on fast nanosecond timescales.

The flux bias lines are first attenuated with 20 dB at 4 K. Then at base temperature, the lines pass through first a Mini-Circuits VLFX-1050, 1 GHz low-pass filter, followed by a “chocolate” powder or eccosorb powder filter (figure 5.15). These dissipative powder filters have the characteristic of allowing through DC-300 MHz, followed by a sharp exponential roll-off of the transmission for higher frequencies. The 20 dB at 4 K is chosen to afford enough current for biasing the transmon across a single Φ_0 . The technique of using the powder filters for

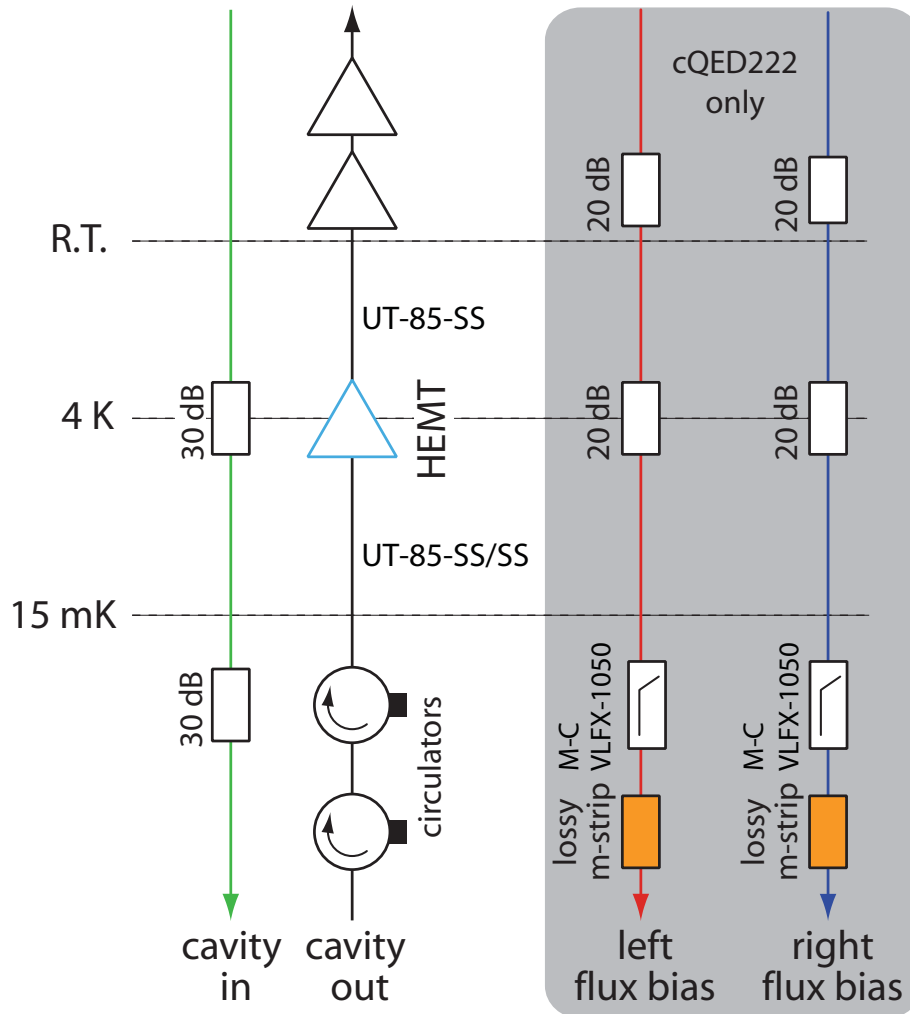


Figure 5.15: Schematic of cryogenic circuitry. There are a total of four cryogenic lines: input, output, left flux-bias and right flux-bias. The experiments for cQED157 and cQED187 do not employ the FBLs.

thermalization is very analogous to that used for DC gate control lines in Cooper-pair box circuit QED experiments [53].

5.6 Room temperature control

Outside of the cryostat, we have all of the control components which allow us to apply microwave signals to address the cavity and the qubits, as well as the components necessary for readout of the output line. For the cavity, an Agilent microwave signal generator E8257D is used to address either the 5 GHz or 7 GHz cavity. A built-in pulse modulation feature allows for shaping of measurement pulses with a bandwidth of ~ 10 MHz. The qubits are also addressed using Agilent microwave signal generators. Normally, the qubit frequencies are detuned from the cavity frequency, and hence the qubit drives are off-resonant and need to be higher in power. All of the signals are added using microwave power splitters (Mini-Circuits ZFSC-2-10G) used in reverse. Pulse-shaping of the qubit signals is done using IQ modulation, which is another feature built into Agilent IQ microwave generators E8267C/E8267D. A detailed schematic is given in figure 5.16.

For cQED187 and cQED157, the qubit transition frequencies are tuned via an external flux produced by the superconducting coil within the body of the Cryoconcept dilution cryostat. This superconducting coil produces 335 gauss per ampere. By biasing either a 10 k Ω or 1 k Ω resistor with a Yokogawa DC voltage source, we are able to tune across many Φ_0 for each qubit.

cQED222, with its built-in on-chip FBLs, obviates the use of an external magnetic field. Instead, each qubit FBL is connected to its own Yokogawa voltage source, driving a 20 dB attenuator at room temperature, for DC tuning. For fast tuning (up to bandwidth of ~ 300 MHz, each FBL is connected to a channel of a Tektronix AWG5014 arbitrary waveform generator (figure 5.16).

The output line is further amplified outside of the cryostat with a pair of amplifiers, Miteq ULN-10 and ULN-35, with quoted max noise figures of $F = 1$ and $F = 3.5$ and a gain of 33 and 23 dB, respectively, over a bandwidth of 3 to 8 GHz.

Since the state of the qubits are encoded in the phase and amplitude of the transmitted cavity signal, we can use an IQ demodulation technique in either homodyne or heterodyne [53]. In the heterodyne detection scheme, an IQ mixer (Marki Microwave IQ0307MXP) is used to mix down, as a demodulator, such that the output signal enters through the RF port, and a microwave tone which is 1 \sim 10 MHz detuned from the cavity signal is applied to the

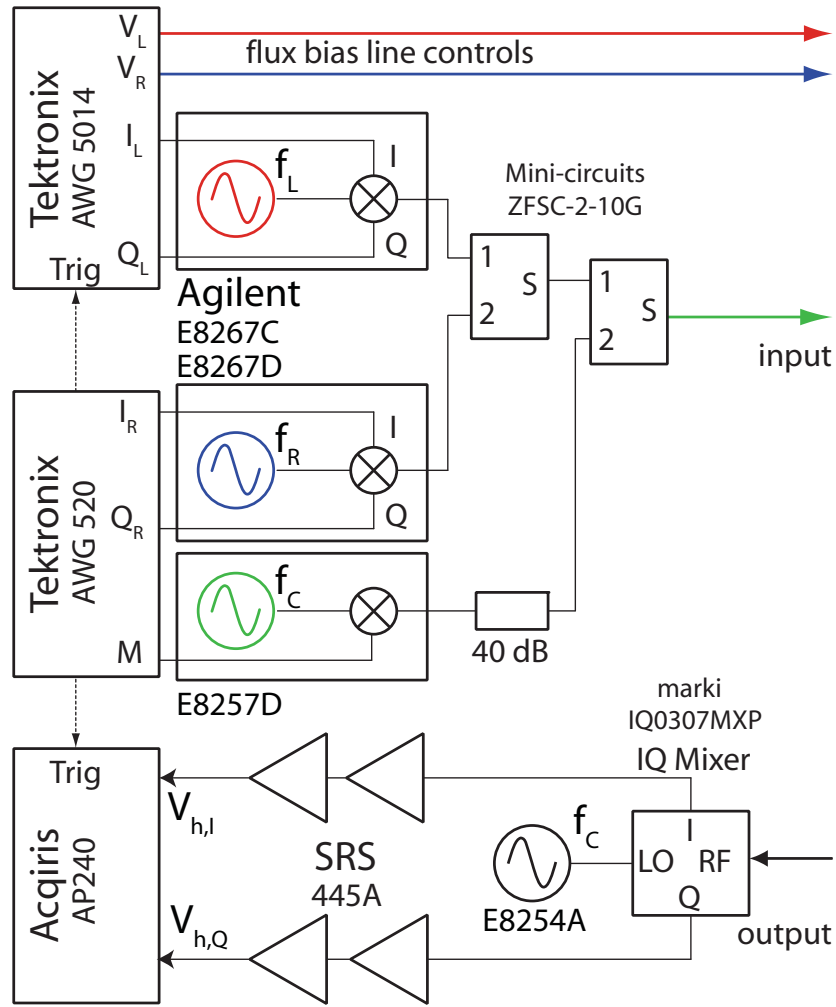


Figure 5.16: Room temperature control schematic.

LO port. The IQ demodulator gives two outputs, one in-phase and one 90° out-of phase at an IF frequency equal to the detuning between the LO frequency and the applied drive at the RF port. Homodyne detection refers to using an IF frequency of 0, such that the final signals on both channels are simply DC and correspond to two signals that correspond to I and Q quadratures of the cavity signal.

The two IF signals go through a final stage of low-bandwidth amplification using an Stanford Research Systems 350 MHz (Model No. SR445A) preamplifier, before finally entering two channels of a 1 GS/s Acqiris AP240 acquisition board. When performing heterodyne detection, a further digital demodulation is performed known as digital homodyne. Here, only a single output of the IQ demodulator is kept and a sine and cosine at the IF frequency

is digitally multiplied to the signal. The outputs are then a digital I and a digital Q , which can then be combined to give an amplitude $A = \sqrt{I^2 + Q^2}$ or a phase $\phi = \tan^{-1}(I/Q)$. All components are locked in phase via a common SRS 10 MHz rubidium frequency standard.

5.7 Pulse control and modulation

Qubit control pulse generation is performed via an Agilent vector IQ microwave frequency generator (E8267C/E8267D). Although such a piece of hardware is not the only way of producing good dual-quadrature control pulses, it is very reliable in terms of timing, bandwidth, and linearity. To control each qubit, we are looking for microwave carrier frequencies in the 3 ~ 10 GHz range, while shaped with pulses that have nano-second resolution, at a bandwidth of 30 ~ 300 MHz.

The pulses are programmed in either Labview or Mathematica, and then imported into either a Tektronix 4-channel AWG5014 or 2-channel AWG520 arbitrary waveform generator. Both generators provide at least 1 GS/s and a voltage amplitude of 2 V peak-to-peak for driving the vector generator's internal IQ mixer. The vector control of the pulses allows us to apply signals either in-phase, or 90° out-of-phase for rotations along the x and y directions of the qubit's Bloch sphere. Each quadrature corresponds uses up one channel of the AWG, such that controlling the x and y rotations of a single-qubit requires two channels.

Current investigations are being performed to build a piece of hardware that takes a single carrier frequency, splits it into two signals in quadrature, and mixes in a modulated pulse shape. The resulting waveform is mixed down to the appropriate qubit frequency. This technique of single-sideband modulation will allow us to remove reliance on the expensive IQ generators provided by Agilent.

5.8 Chapter summary

In this chapter, we have reviewed the basics of circuit QED sample fabrication, and touched upon the design considerations of the three samples investigated in this thesis. Overall, the fabrication techniques are quite simple and reliable to within ~ 10% of all parameters. Currently the biggest variation which exists is still in hitting targeted E_J values. This is most likely due to slight differences in the conditions during the electron-beam lithography step for writing the Josephson junctions. Most of the other design parameters, including the charging energy E_C , cavity-qubit coupling g , cavity frequency ω_C , cavity quality factor Q , are

Table 5.1: Summary of measured sample parameters.

Qubit/Sample ID	$\omega_C/2\pi$ (GHz)	$\kappa/2\pi$ (MHz)	g/π	E_J^{\max}/h (GHz)	E_C/h (MHz)
cQED157 qubit 1	5.22	33	105	14.9	420
cQED157 qubit 2	5.22	33	105	18.9	440
cQED187 qubit 1	6.920	0.3	347	18.0	400
cQED187 qubit 2	6.920	0.3	94.4	22.6	340
cQED222 qubit 1	6.902	1.0	199	28.48	320
cQED222 qubit 2	6.902	1.0	183	42.34	300

found in experiments to agree well with targeted specifications. Table 5.1 summarizes the three samples discussed in this chapter in terms of experimentally measured parameters.

This chapter has also reviewed the experimental setups both inside of the cryostat and outside. The cryogenic circuitry is very important for the system to behave as qubits in their ground state coupled to a cavity. Next in the chapters to follow, we will investigate how we use the room temperature control apparatus to perform basic aspects of quantum information processing.

Initialization and Benchmarking of Single-Qubit Gates

THE success of any computational architecture depends on the ability to perform a large number of gates, and gate errors meeting a fault-tolerant threshold. The most advanced classical computers today can perform up to 10^{15} operations without the need for error correction. For a quantum computer, in order to maintain coherence throughout a long string of operations, quantum error correction is a proposed necessity. Surprisingly, the most conservative estimates place the required gate errors thresholds to be on the order of 10^{-4} [26, 104] for quantum error correcting codes to function. Yet, thus far such control of quantum systems has been difficult to attain in experimental quantum systems.

For an experimental quantum computing system to be considered viable for quantum error correction, the gate error rates must be characterized and understood. Here, we benchmark the single qubit error rates for transmon qubits in a circuit QED system. Although photons and trapped-ion systems remain the paragon for single qubit gate fidelity, reaching upwards of 99.9%, solid-state systems are making rapid progress, and the full characterization of single-qubit operations here demonstrate that the road ahead for superconducting qubits is promising.

Of course to be able to perform single-qubit operations, it is critical for the qubit to also start in a well-defined pure state. Although many qubit systems employ active cooling techniques [105, 106] to initialize a ground state, most circuit QED architectures simply rely

on external thermal cooling of the sample*. In this chapter, we will first present in section 6.1 a sensitive measurement of the cavity temperature to which the transmon qubits couple using the nonlinear vacuum Rabi spectrum (as published in Ref. [89]), from which we can estimate the polarization of the initial qubit state. Then, section 6.2 will discuss multiple techniques for characterizing single-qubit operations in circuit QED, as based on Ref. [108]. Finally, we will introduce some new qubit control techniques for further improving single-qubit gate fidelities in the cavity coupled transmon system (section 6.4).

6.1 Initializing pure states

In circuit QED, where the qubit and cavity excitations are in the microwave frequency regime, a pure ground state initialization of the qubit is strongly dependent on the thermal bath into which the qubit decays. When the qubit is Purcell limited such that the primary decay channel is via spontaneous emission through the cavity, the temperature of the cavity will determine the equilibrium polarization of the qubit. The temperature of the cavity is directly reflected as a thermal population of photons, as given in section 4.1 by (4.1). For our experiments performed at cryogenic dilution refrigerator temperatures, with a base temperature of 20 mK, this would ideally correspond to $\langle n \rangle \sim 10^{-7}$ photons for a 7 GHz cavity.

Despite the nominally ~ 20 mK base temperature, it is still important to be able to experimentally verify the mean number of photons in the cavity, as the experimental setup can result in elevated thermal noise and also non-equilibrium excitations. Although the sample itself is thermally anchored to the base temperature, the control lines can still serve as noise sources. For example, warm attenuators can be black body sources of radiation. Another major source of noise is the cryogenic HEMT amplifier on the output port of the sample. With a noise temperature of 5 K, a direct connection to the output port of the cavity would be detrimental. As mentioned in section 5.5 however, we employ a microwave frequency circulator in between the output port of the sample and the cryogenic amplifier to combat this effect. Nonetheless, the reflected noise radiated from the amplifier is still dissipated in a 50Ω termination connected to the circulator, which could be a source of elevated mean photon numbers in the cavity.

So what are some of the ways to experimentally detect the mean photon number in the circuit QED system? One method is the ac Stark shift previously discussed in section 4.2.4.

* Active cooling may be helpful for the new *fluxonium* qubit design [107].

By directly increasing the number of photons in the cavity through a coherent drive, the ac Stark effect (4.27), results in a linear shift of the qubit transition frequency (as long as the ac Stark drive is not too strong). Another option is if the qubit and cavity are in the number-splitting regime (section 3.4.3), then by driving the cavity with a coherent state and observing the number-split spectrum of the qubit, it is possible to fit to a combined thermal and Poisson-distributed spectrum, from which a mean photon number could be extracted. Though both of these methods are sensitive to the level of ~ 0.1 photon in the cavity [109, 110], current signal-to-noise ratios in the detection of the qubit spectrum prevent them from being sensitive to even lower photon numbers.

However, an interesting regime of circuit QED which actually provides a very sensitive photon number meter is the strongly driven regime [62, 89]. The strong driving regime goes beyond simple linear response theory of a driven qubit-cavity system, and in fact allows testing of the Jaynes-Cummings spectrum. We will describe how the experiment provides a remarkably excellent understanding of the Hamiltonian and circuit QED system in general. The extraction of a limit on the cavity population is a nice extra result from this work. This experiment is termed the nonlinear vacuum Rabi, and it will be described in detail here.

6.1.1 Nonlinear vacuum Rabi

In standard cavity QED experiments, the signature feature of the Jaynes-Cummings interaction,

$$H = \hbar\omega_C \left(a^\dagger a + \frac{1}{2} \right) + \frac{\hbar\omega_a}{2} \sigma_z + \hbar g (a^\dagger \sigma_- + a \sigma_+) \quad (6.1)$$

is the vacuum Rabi splitting, as shown in figure 6.1. Vacuum Rabi peaks refer to the split structure of the cavity transmission line when the atom is resonant with the cavity. The degree of splitting is twice the coupling strength, $2g$, and is often termed the vacuum Rabi frequency. Experimental observation of the splitting is dependent on the separation between the peaks being much greater than the linewidth of the peaks.

The Jaynes Cummings interaction is not simply a single excitation construct, but in fact describes an entire ladder of eigenstates, as shown in figure 6.2. By compounding a number of resonant excitation pulses, it is possible to climb up the ladder and observe the $2g\sqrt{n}$ spacing between the levels, as previously discussed in section 3.3.1. The \sqrt{n} splittings have been observed in other circuit QED experiments as well [111], even allowing for the generation of Fock states and other non-classical states of light [112, 113].

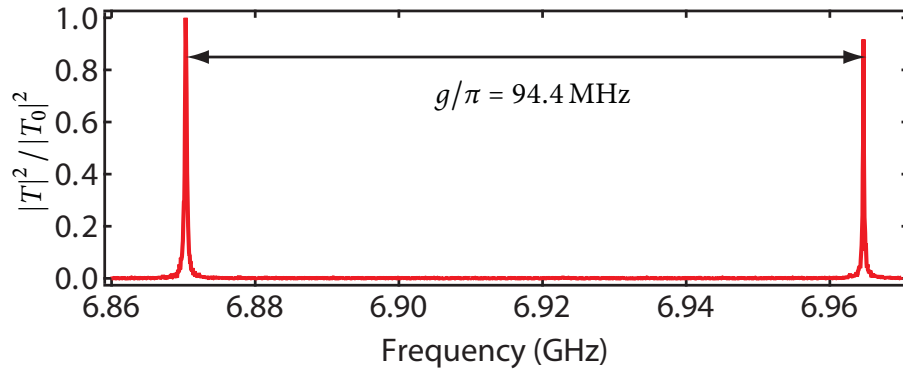


Figure 6.1: Vacuum Rabi splitting. When the qubit is in strong coupling with the cavity, the cavity transmission undergoes a splitting into two peaks, separated in frequency by g/π . Shown here is the normalized transmitted homodyne amplitude as a function of applied frequency, with the vacuum Rabi peaks split by 94.4 MHz. This splitting is associated with one of the qubits in sample cQED187.

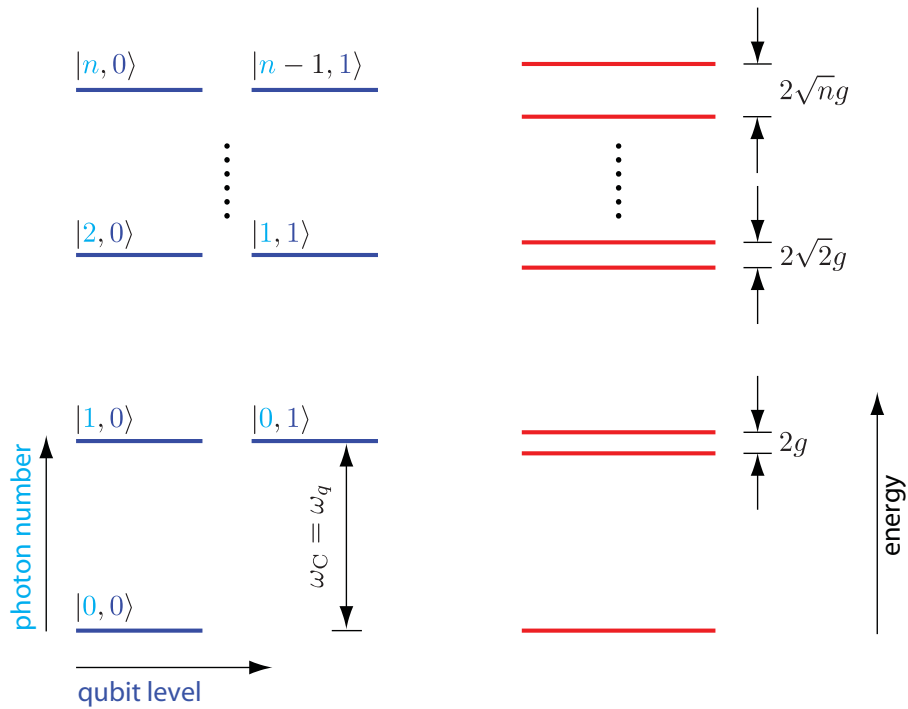


Figure 6.2: Jaynes-Cummings ladder. The energy levels of the qubit-cavity coupled system can be shown in this ladder diagram. On the left in blue are the energy levels corresponding to the coupling turned off, with two ladders of increasing photon number with the qubit in either state, $|n, 0\rangle$ and $|n, 1\rangle$. The red ladder of energy levels on the right reflect the strong coupling interaction g , resulting in a splitting of the resonant doublets $|n, 0\rangle$ and $|n-1, 1\rangle$ by $2g\sqrt{n}$.

However, in the nonlinear vacuum Rabi experiment, we are able to investigate the Jaynes-Cummings ladder with a different approach. Instead of multiple time-synchronized pulses which allow one to climb up to any level while starting in the ground state with no excitations $|n = 0\rangle$, we use a continuous strong driving technique which performs an n -excitation virtual transition up to the n th Jaynes-Cummings state.

Experimental procedure

The sample used for this experiment is cQED187. The fabrication and details of the sample are previously discussed in chapter 5. Here, we simply re-state a few of the salient characteristics necessary for understanding the strong driving experiment. The cavity has a $\lambda/2$ resonant frequency of 6.92 GHz with a photon decay rate of $\kappa/2\pi = 300$ kHz. Although the sample contains two qubits, we will only be studying the balanced transmon (section 5.3.2), corresponding to $g/\pi = 94.4$ MHz and charging energy $E_C/2\pi = 340$ MHz.

Time domain measurements of the balanced transmon show that T_1 is limited by the multimode Purcell effect and completely homogeneously broadened ($T_2 = 2T_1$) at the flux sweet spot, where the maximal transition frequency is $f_{\max} = 7.48$ GHz. The experiment investigates the vacuum Rabi splitting, where the qubit is tuned into resonance with the cavity. When the qubit is tuned slightly below the cavity frequency, at around 6 GHz, the measured coherence times are $T_1 = 1.7 \mu\text{s}$ and $T_2 = 0.7 \mu\text{s}$.

The experiment is performed via a heterodyne detection scheme [53]. An RF drive tone is applied into the input side of the cavity. The frequency and power of this RF drive are controllable at room temperature. The transmitted RF voltage signal from the cavity is amplified both cryogenically and at room temperature before being mixed down to a 1 MHz IF signal. The in-phase and quadrature components of the IF signal are extracted digitally. These components are then combined as a heterodyne amplitude.

To accurately find the vacuum Rabi splitting, large transmission maps are taken as a function of changing the applied transmission frequency and varying the external magnetic field. Figure 6.3 gives a coarse location of splittings in the full two-qubit system, and provides a way of finding the range of magnetic fields in which the vacuum Rabi splitting occurs.

Strong driving vacuum Rabi spectrum

When the qubit and cavity are exactly resonant, the cavity transmission peak is split into two peaks with equal maximum transmitted homodyne amplitude, as shown in figure 6.1.

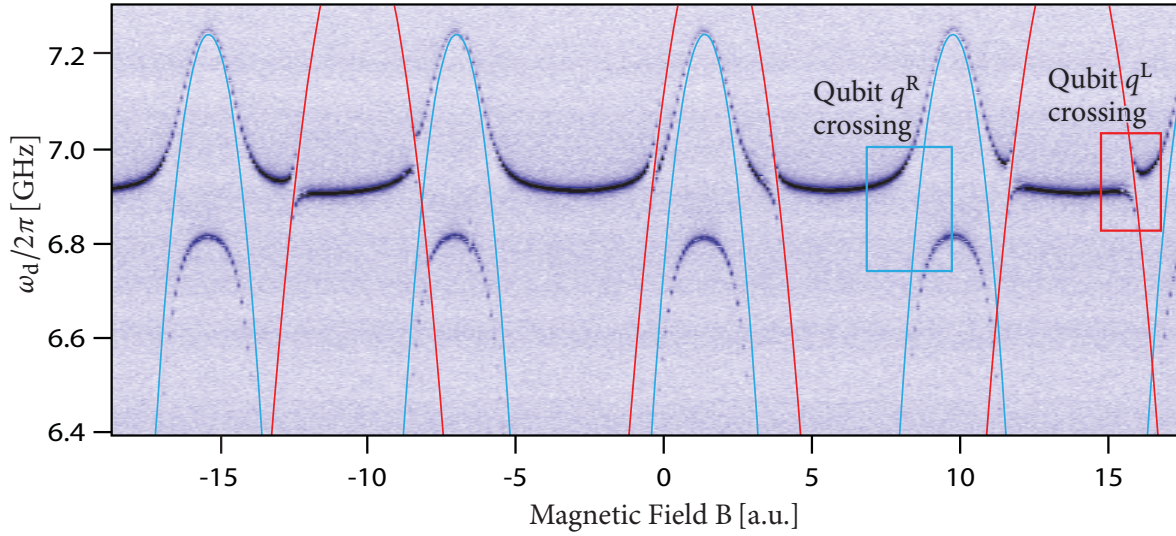


Figure 6.3: Transmission versus magnetic field and drive frequency. Although the sample cQED187 is a two transmon device, the strong driving vacuum Rabi experiment is performed on only one of the transmons, specifically investigating the splitting shown in the red box, around magnetic field $B = 15$.

However, upon turning up the power of the applied drive, the measured spectrum changes into a more complicated structure. Figure 6.4 shows the emergence of other peaks in addition to the original two in the vacuum Rabi splitting. Refs. [62, 89] describe this strong driving effect and the supersplitting of the vacuum Rabi peak in greater detail.

Figure 6.4 also shows three slices through the power map, with each dip corresponding to higher order photon transitions up the Jaynes-Cummings ladder. Solid lines in figure 6.4c-d represent theory lines going directly through the experimental data. We will use these theory fits to understand the full Jaynes-Cummings spectrum as well as infer a temperature of the system.

Modeling the bath and multi-dimensional fit

To understand the measurement, we use input-output theory. Let the output bath mode be described by the annihilation operator b_{out} [97]. This bath mode can then be related to the photons inside of the cavity by

$$b_{out} = \sqrt{\kappa}a, \quad (6.2)$$

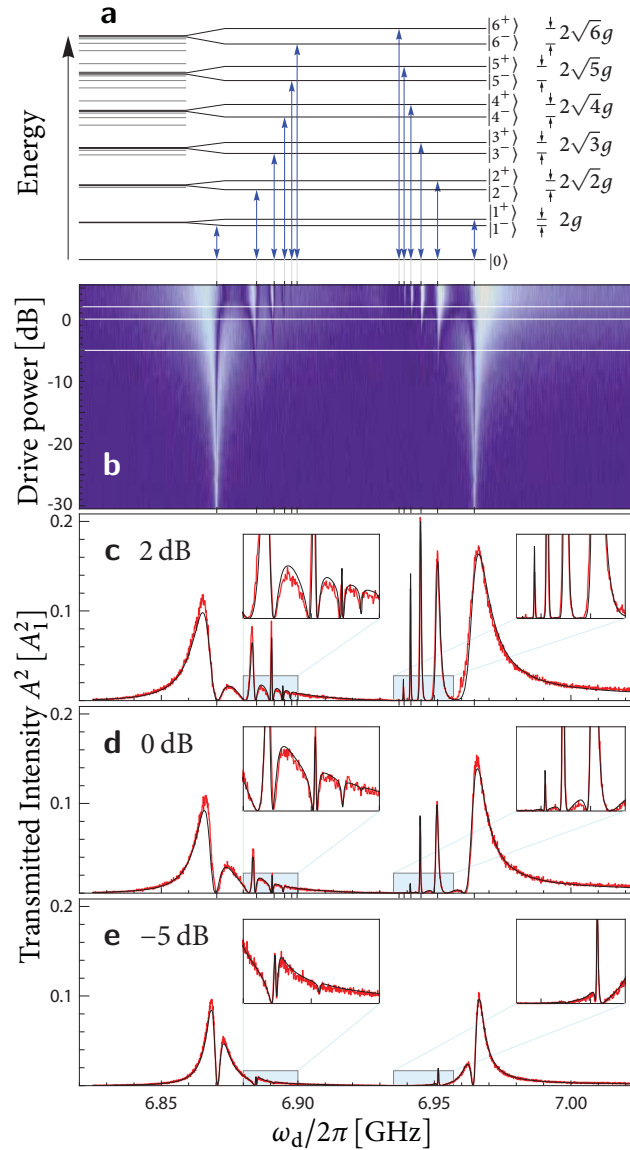


Figure 6.4: Emergence of \sqrt{n} peaks under strong driving of the vacuum Rabi transition. (a) The extended Jaynes–Cummings energy spectrum. All levels are shown to scale in the left part of the diagram: black lines represent levels $|n, \pm\rangle \simeq (|n, 0\rangle \pm |n-1, 1\rangle)/\sqrt{2}$ with only small contributions from higher ($j > 1$) transmon states; grey lines represent levels with large contributions from higher transmon states. In the right part of the diagram, the \sqrt{n} scaling of the splitting between the $|n, \pm\rangle$ states is exaggerated for clarity, and the transitions observed in plots (b–e) are indicated at the x -coordinate $E_{n\pm}/2\pi n$ of their n -photon transition frequency from the ground state. (b) Measured intensity (A^2 , heterodyne amplitude squared) in color scale as a function of drive frequency and power. The multiphoton transitions shown in (a) are observed at their calculated positions. (c–e), Examples of cuts for constant power, at the values indicated in (b) (results from a master equation in black; experimental results in red), demonstrating excellent agreement between theory and experiment, which is reinforced in the enlarged insets. Good agreement is found over the full range in drive power from -45 dB to $+3$ dB, for a single set of parameters. Figure reproduced from [62].

where we have dropped the reflected wave b_{in} because the quantum noise contributes negligibly to the classical noise due to the HEMT amplifier [62]. The measured output voltage can be written in terms of the bath operators as $V_H = \langle b_{out} + b_{out}^\dagger \rangle$. After being amplified with gain α , the voltage wave is mixed with a local oscillator of frequency ω_{LO} , resulting in a mixer output of

$$V_m = \alpha \langle b_{out} + b_{out}^\dagger \rangle^\dagger \cos \omega_{LO} t \quad (6.3a)$$

$$= \alpha \sqrt{\kappa} \langle a e^{-i\omega_d t} + a^\dagger e^{i\omega_d t} \rangle \cos \omega_{LO} t \quad (6.3b)$$

$$= \frac{\alpha \sqrt{\kappa}}{2}. \quad (6.3c)$$

The final output is given at the intermediate frequency $\omega_{IF} = \omega_d - \omega_{LO}$, which in the experiments we choose to be 1 MHz. Low pass filtering removes the fast oscillating terms, and then we can extract the quadrature measurements

$$\begin{aligned} I &= V_0 \langle a + a^\dagger \rangle \\ Q &= V_0 \langle i a^\dagger - i a \rangle, \end{aligned} \quad (6.4)$$

where V_0 is the voltage related to the gain of the entire experimental amplification chain. In these experiments, the phase relation between the LO and the RF drive is not maintained while sweeping the drive frequency. As a result, our detection scheme deals with the transmission amplitude, given by

$$A = \sqrt{I^2 + Q^2} = 2V_0 |\langle a \rangle| = 2V_0 |\text{tr}(a\rho_s)|, \quad (6.5)$$

where ρ_s is the steady-state density matrix of the system.

The actual experiment can be better modeled by using

$$A^2 = |2V_0 \text{tr}(a\rho_s) + b\xi|^2 + 2\sigma_n^2, \quad (6.6)$$

with $b \in \mathbb{C}$ describing the amplitude and phase of a direct leakage channel for the drive to bypass the cavity, and σ_n is measurement noise in each of the I and Q channels. The steady-state density matrix ρ_s is obtained from solving the master equation of the system numerically. Details of the full master equation will not be given here and can be found in [62]. Although the set of fit parameters is large, including V_0 , b , E_C , E_J^{\max} , ω_C , T , $\tilde{\Phi}$, ω_d , ξ , κ , γ_1 , γ_ϕ , most of the fit parameters can be measured to some degree in separate experiments, and only slight adjustments are necessary here. The fits are obtained by minimizing the mean

squared deviation between the experiment and the model over the entire power range and frequency range, with the only unconstrained fit parameters being b and two scaling factors which describe the attenuation and amplification on the input and output signals. These fits are shown in the solid-lines of the slices in figure 6.4.

6.1.2 Cavity temperature

The system temperature is related to the fitted values of κ_+ and γ_+ , both of which are consistent with zero. The key figure of merit is the ratio $r = \kappa_+/\kappa_- = \gamma_+/\gamma_-$. In the data from figure 6.4, the largest value of r placed into the fits which is still consistent is approximately 0.003, associated with an upper bound on the reservoir temperature of ~ 55 mK. This is higher than the base temperature of the fridge, but it is still the most stringent bound on the temperature of any circuit QED sample performed thus far.

To recognize the sensitivity to temperature which this technique provides, we can investigate strong driving with an elevated temperature. The same experiment as is shown in figure 6.4 is performed, but with the circulator on the output of the cavity thermalized to the ‘100 mK stage’ of the fridge, instead of the base plate. The actual temperature of this plate is often in the 90–110 mK range. Now, a representative measurement is shown in figure 6.5, where the primary new feature is the pair of broad peaks in between all of the multiphoton peaks. We find good agreement with the theory when using an effective temperature of 130 mK. The fits get worse for larger drive powers due to the truncation of the Hilbert space used in the master equation simulations.

The extra thermal peaks are due to overlapping transitions between very highly excited states. With a high enough temperature, the strong driving thus causes a bistable situation, where in one case we probe the anharmonic Jaynes-Cummings ladder, and in another case where the system fluctuates into a sufficiently excited state that the anharmonicity is reduced causing the strong driving to generate states comparable to coherent states. We can think of the second case as a cascade effect, where strongly driving a small starting thermal population can result in a highly excited state of the cavity. This effect makes this strongly driven vacuum Rabi technique a particularly sensitive meter for the temperature of the cavity.

6.1.3 Vacuum Rabi summary

From the strong driving vacuum Rabi experiments, we can confidently say that our circuit QED system operates with $\langle n \rangle \lesssim 0.003$. This implies that the qubits, which are detuned

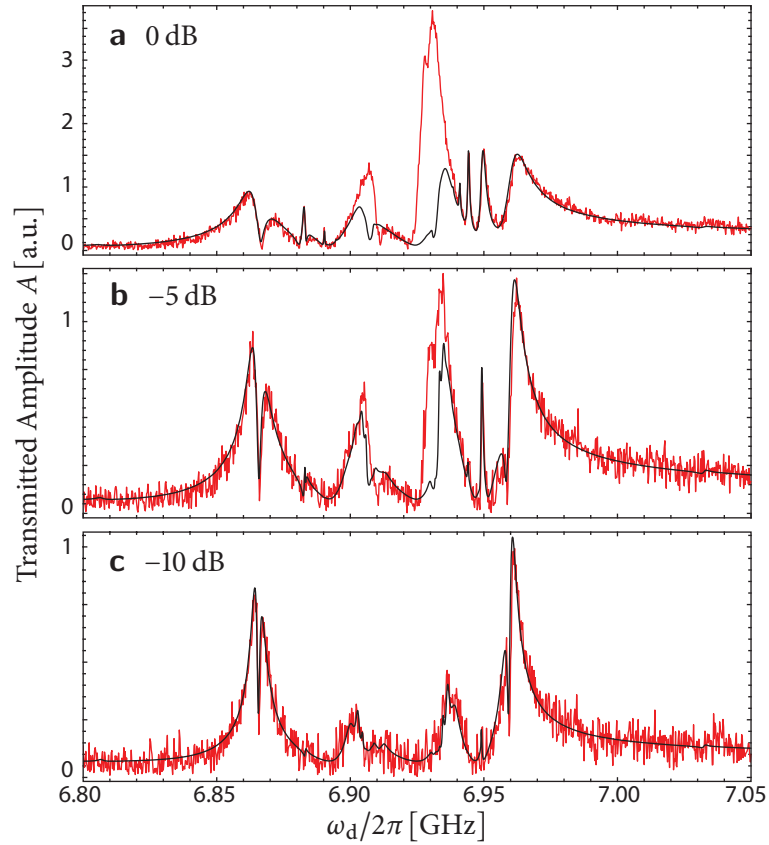


Figure 6.5: Strongly-driven vacuum Rabi response at elevated temperature. For this run of the experiment, the $50\ \Omega$ termination on the circulator at the output port of the sample was kept at a temperature of $\sim 110\ \text{mK}$. The theoretical response (black) was calculated for an effective temperature of $130\ \text{mK}$, showing good agreement with moderate driving, (c). For the stronger driving of (a) and (b), the theory and experiment disagree due to the truncated Hilbert space used in the simulations. Figure reproduced from [62].

from the cavity, should effectively start from a pure ground state $|0\rangle$, so long as the qubits are Purcell limited and thus coupled to the “cold” cavity bath. This is the case because the temperature, which goes as γ_+/γ_- does not change with the qubits detuned from the qubit. Although both the rates γ_+ and γ_- decrease as g^2/Δ^2 (assuming a naive two-level qubit case), the overall ratio, and hence the temperature stay the same.

Of course, there are situations where the qubit might be more strongly coupled to some other loss mechanism (such as the intrinsic $Q \sim 50,000 - 70,000$ discussed previously in section 3.5.1) than the microwave resonator, in which case we would not be able to definitively comment on the qubit starting state.

Nonetheless, in the multi-mode Purcell limit, we have then an upper bound on the

number of photons in the cavity of 0.003 giving also an upper bound on the excited state population $P_1 \sim 0.003$. This corresponds thus to a steady-state ground state population of $P_0 = 0.997$.

The quality of our ground states will be investigated in a different way later in this thesis, when we perform state tomography on two qubit states in chapter 8. However, next in this chapter, we will work with a single-qubit again, and benchmark the single-qubit gate fidelity.

6.2 Characterizing single-qubit gates

Gate fidelity, previously defined in (4.22), is the standard measure of agreement between an ideal operation and its experimental realization. Beyond the gate fidelity, identifying the nature of the dominant errors in a specific architecture is particularly important for improving performance. While NMR, linear optics, and trapped ion systems are primarily limited by systematic errors such as spatial inhomogeneities and imperfect calibration [35, 114, 115], for solid-state systems decoherence is generally the limiting factor. It is thus crucial to employ experimental tests of qubit operations which either distinguish between various error mechanisms, or average over all the errors such as not to give a biased result. This question of how to measure average gate errors or distinguish between various error mechanisms has produced different experimental protocols for measuring gate fidelity, such as the double π metric employed in superconducting qubits [116], process tomography as demonstrated in trapped ions, NMR, and superconducting systems [35, 114, 115, 117], and randomized benchmarking, as performed in trapped ions and NMR [118, 119].

The double π metric ($\pi - \pi$) is one of the simplest gate fidelity metrics, as it consists of applying only two π pulses in succession. This should ideally correspond to the identity operation $\mathbb{1}$. The aim of π - π is to determine the deviations from $\mathbb{1}$ by measuring the residual population of the excited state following the pulses. Despite its simplicity, this metric captures the effects of qubit relaxation and the existence of levels beyond a two-level Hilbert space. However, in general, it is merely a rough estimate of the actual gate fidelity as it does not contain information about all possible errors. In particular, errors that affect only eigenstates of σ_x or σ_y and deviations of the rotation angle from π are not well captured by this measure.

A second metric that, in principle, completely reveals the nature of all deviations from the ideal gate operation is Quantum Process Tomography (QPT) [120]. Ideally, QPT makes it possible to associate deviations with specific error sources, such as decoherence effects or non-ideal gate pulse calibration. However, in systems where the “preparation,” “process,” and

“measurement” all involve the same single-qubit rotations, it is difficult to assign the results from QPT to a single gate error. Moreover, the number of measurements that are necessary for QPT scales exponentially with the number of qubits.

While QPT provides information about a single gate, randomized benchmarking (RB) [118, 121] gives a measure of the accumulated error over a long sequence of gates. This metric hypothesizes that with a sequence of randomly chosen Clifford group generators ($R_u = e^{\pm i\sigma_u\pi/4}$, $u = x, y$) the noise can behave as a depolarizing channel where all error mechanisms are weighted equally, and an average gate fidelity can be obtained. In contrast to both $\pi - \pi$ and QPT, RB is approximately independent of errors in the state preparation and measurement. Also, while the other metrics measure a single operation and extrapolate the performance of a real quantum computation, RB tests the concatenation of many operations (here up to ~ 200), just as would be required in a real quantum algorithm.

In the rest of the chapter, we present measurements of single-qubit gate fidelities where the three metrics mentioned above are implemented in our circuit QED system with a transmon qubit. We find single-qubit gate errors at the 1 \sim 2% level consistently among all metrics. These low gate errors reflect the good coherence times [63, 82], systematic microwave pulse calibration, and accurate determination of gate errors despite limited measurement fidelity. Specifically, in circuit QED, measurement fidelity can be as high as 70%, though in this experiment it is $\sim 5\%$, as readout is not optimized. Although the experiments are performed in a solid-state qubit implementation, the theory and discussion about the gate errors in this chapter extend generally to all qubit systems including ions and spins. Before going into details on each of the metrics, let us first describe some basic experimental information about the sample and pulse calibration.

6.3 Single-qubit gate error experiments

The gate error protocols are performed on cQED₁₈₇, which is described in detail in chapter 5. Although the sample consists of two transmon qubits coupled to a coplanar waveguide resonator, we investigate the gate fidelity of only the balanced transmon, with the other unbalanced transmon tuned away from any interaction. Experimentally measured parameters include the qubit-cavity coupling strength given by $g_0/\pi = 94.4$ MHz, the resonator frequency $\omega_r/2\pi = 6.92$ GHz, photon decay rate of $\kappa/2\pi = 300$ kHz, and qubit charging energy $E_C/2\pi = 340$ MHz. The qubit is detuned from its flux sweet spot by ~ 1.5 GHz with a resonant frequency of $\omega_{01}/2\pi = 5.96$ GHz, and coherence times of $T_1 = 2.2 \mu\text{s}$ and $T_2^* = 1.3 \mu\text{s}$.

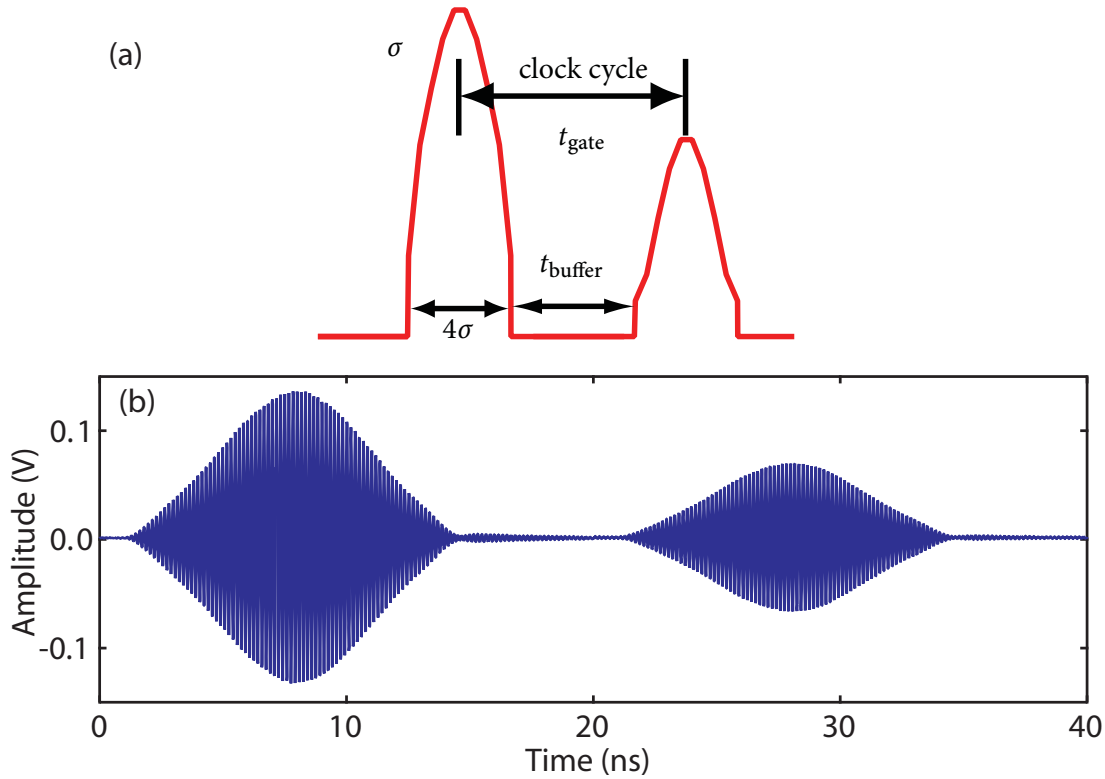


Figure 6.6: Microwave pulse shapes. The applied pulse shapes (a) are Gaussians, with standard deviation given by σ , and truncated on each side to take up a total time of 4σ . In the experiments, σ is typically between 1–12 ns. A delay of t_{buffer} , typically 5–8 ns is included at the end of each truncated pulse shape to allow for complete turn off, as the generated pulse shapes in the AWG result in a spurious tail on the falling edge. One clock cycle corresponds to the total gate time t_g . (b) Measured pulses with $\sigma = 3$ ns on a fast-sampling scope after modulation with a microwave frequency signal at 5 GHz. The residual incomplete pulse turn-off can be seen after the falling edge of each pulse.

6.3.1 Microwave pulse shaping

As previously discussed in section 4.2, microwave frequency with quadrature control can be used to perform rotations about the x and y axes of a single-qubit. Rotations about any axis of the Bloch sphere can be generated from combinations of rotations around x and y . The carrier frequency of the microwaves need to be resonant with the qubit transition frequency and the pulse amplitudes and phases define the rotation angle and axis orientation, respectively. In all experiments, the pulse-shape is Gaussian with standard deviation σ that we vary between 1 and 12 ns. The pulses are truncated at 2σ on each side and a constant buffer time of 8 ns is inserted after each pulse to ensure complete separation of the pulses. The Gaussian pulse envelopes are generated with a 10-bit Tektronix AWG520 arbitrary waveform

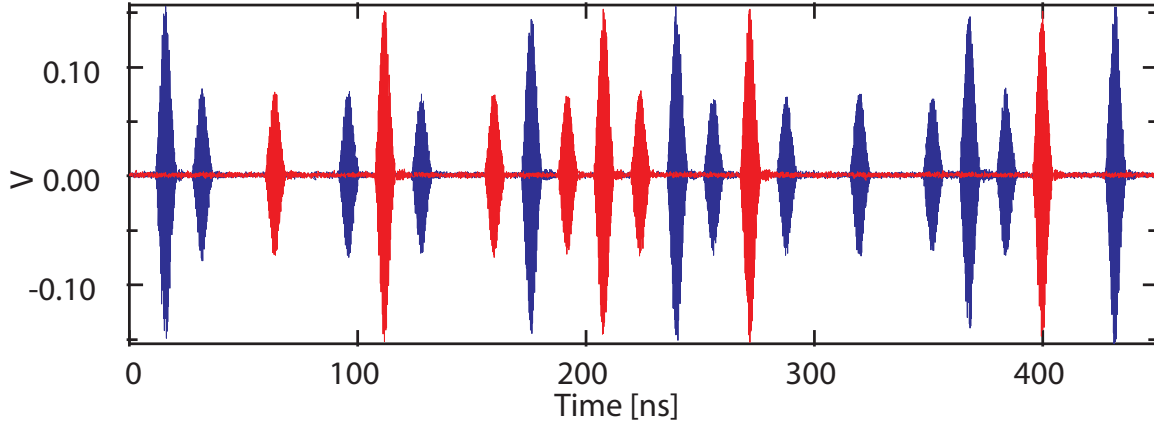


Figure 6.7: Sample sequence of concatenated pulses. Example of a sequence of concatenated pulses for randomized benchmarking section 6.3.6. Blue (red) pulses are x (y) gates of either π or $\pi/2$ rotations. The longest applied sequences consist of ~ 200 gates.

generator with 1 ns resolution. The pulse shapes are mixed with sine and cosine waves at the qubit transition frequency of 5.95 GHz using an Agilent E8267C Vector Signal generator. It is thus possible to produce pulses phase-shifted by 90° for qubit rotations around x and y . Figure 6.6 shows two sample pulses which we program into the AWG and the microwave modulated single-qubit pulses used in our experiments.

When experimentally observing each pulse with a fast oscilloscope, it becomes clear that each pulse turns on much quicker than it turns off, with a residual tail that which takes up around $\sim 4 - 8$ ns. The inclusion of the relatively long buffer time of 8 ns at the end of each pulse is to ensure that a single microwave pulse is completely turned off before the next one is applied. The gate characterization experiments can involve sequences of up to ~ 200 concatenated pulses, such that avoiding residual pulse overlap becomes very important. Figure 6.7 is a sample sequence showing a train of concatenated pulses measured on the fast-sampling scope. The gate sequence corresponds to applying $R_y(\pi)R_y(-\pi/2)R_z(-\pi)R_x(\pi/2)\dots R_y(-\pi/2)R_x(\pi)R_z(\pi)R_y(-\pi)$.

Rotations about the z axis are performed with a rotation of the reference frame with an accompanying delay equivalent to the time required for x and y pulses, see Ref. [118]. For example, the sequence $R_x(\pi)R_z(\pi)R_y(\pi)$ becomes $R_x(\pi)\mathbb{1}R_y(-\pi)$. Although this is permissible for single-qubit experiments, for multiple qubits, a simple rotation of the frame is not enough, and explicit z -operations can be performed by modulating each qubit's transition frequency, either by ac-Stark shift or flux bias.

6.3.2 Calibration of single-qubit gates

In order to obtain the best gate fidelity, accurate pulse amplitude calibration is necessary. We use tune-up sequences similar to those used in NMR experiments [122], which involve applying repeated pulses such that small systematic errors accumulate to produce a large signal which may then be nulled out. The rotations $R_x(\pm\pi/2)$, $R_y(\pm\pi/2)$, $R_x(\pm\pi)$, $R_y(\pm\pi)$ are each calibrated independently.

To calibrate the $\pi/2$ rotation around the x axis, we apply sequences consisting of an odd number n of the pulses, $[R_x(\pi/2)]^n$, and subsequently measure $\langle\sigma_z\rangle$. Performing this for several n , we calibrate the pulse amplitude by comparing the measured values with the ideal outcomes, which generally should look identical, half way between the signal of performing $\mathbb{1}$ and $R_x(\pi)$. A slight over-rotation in the $\pi/2$ rotations results in a zig-zag looking pattern, and the calibration experiment is tuned until this pattern becomes flattened. The other $\pi/2$ pulses are calibrated similarly.

Once all $\pi/2$ pulses are calibrated, the π pulses are calibrated with a slightly different scheme. To calibrate a π pulse around the x -axis, we first apply a single calibrated $R_x(\pi/2)$ pulse followed by an integer number m of the π pulses, $R_x(\pi/2)[R_x(\pi)]^m$. Again, the measured values of $\langle\sigma_z\rangle$ for different m are compared with simulation to calibrate the amplitude of the $R_x(\pi)$ pulse. The prepended $\pi/2$ pulse has the effect of rendering the scheme to be first-order sensitive to deviations in the π pulse amplitude. The scheme is repeated *mutatis mutandis* for the other π pulses.

6.3.3 Single qubit readout calibration

The measurements performed for gate characterization are performed in the time-domain and employ the strong dispersive regime of circuit QED. As discussed in section 3.4.2, in this regime, we can apply microwaves at the frequency corresponding to the qubit in the ground state to obtain a projective measurement on $|0\rangle$. Here, we apply a square-pulse modulated interrogation tone at $\omega_C + \chi$, and detect both an in-phase and quadrature homodyne voltage transient. In all the time-domain experiments, all qubit operations are applied before the measurement pulse. The same gate sequence is applied repeatedly roughly 250,000 times, and the recorded measurement transients are averaged to combat the low $\sim 5\%$ readout fidelity. We then integrate the measured transient signal over a time $t \sim T_1$ after the measurement tone is turned on to obtain an average homodyne voltage response in both quadratures. These two quadrature voltages, I and Q , are combined with a quadrature sum to form an average

homodyne voltage amplitude $A_H(\rho) = \sqrt{I^2 + Q^2}$, which is a function of the single-qubit state ρ .

We calibrate the single qubit measurement by finding A_H corresponding to having prepared the states $|0\rangle$ and $|1\rangle$. State $|0\rangle$ is simple as it involves applying no microwaves to excite the qubit. A coarse calibration of the qubit pulse amplitude needed to prepare $|1\rangle$ is found by performing a Rabi oscillation in amplitude: apply a varying amplitude of a Gaussian shaped pulse at the qubit frequency and measure A_H for each amplitude. The maximum deviation of A_H from $A_H(|0\rangle\langle 0|)$ is nominally the amplitude for $|1\rangle$. Then, finer tuning is then performed through implementing the single-qubit rotation calibration sequences mentioned in the previous section. Therefore, the accurate single-qubit readout calibration and single-qubit gate calibration bootstrap off one another.

With the level of A_H defined for both $|0\rangle$ and $|1\rangle$, the population of the excited state P_1 for any prepared single-qubit state $|\psi\rangle$ is determined by a simple normalization,

$$P_1 = \frac{A_H(\rho) - A_H(|0\rangle\langle 0|)}{A_H(|1\rangle\langle 1|) - A_H(|0\rangle\langle 0|)}. \quad (6.7)$$

In all experiments, we concatenate readout calibration experiments which involve either applying no microwaves (to prepare $|0\rangle$) or $R_{x,y}(\pi)$ (to prepare $|1\rangle$) and extract P_1 . These readout calibration experiments are necessary as a result of phase drift on the homodyne detection, which can result in the overall amplitude of the homodyne voltage to change over time. The measurements in the rest of the chapter will correspond to determining either P_1 or $P_0 = 1 - P_1$.

6.3.4 Double π metric

After calibrating our single-qubit pulses, we perform the π - π experiments by applying a π pulse, waiting for a separation time t_{sep} , applying a second π pulse, and then performing the homodyne measurement described from the previous section, to find the excited state probability P_1 . Figure 6.8a shows the measured P_1 for the π - π experiment as a function of t_{sep} using $\sigma=2$ ns pulses. Due to the decay of the excited state following the first π pulse, P_1 increases as a function of t_{sep} .

The effect of the experiment can be accurately captured in simulations with a simple theoretical model consisting of the dynamics from a master equation for a driven three-level atom subject to relaxation and dephasing, with corresponding time-scales T_1 and T_ϕ . The

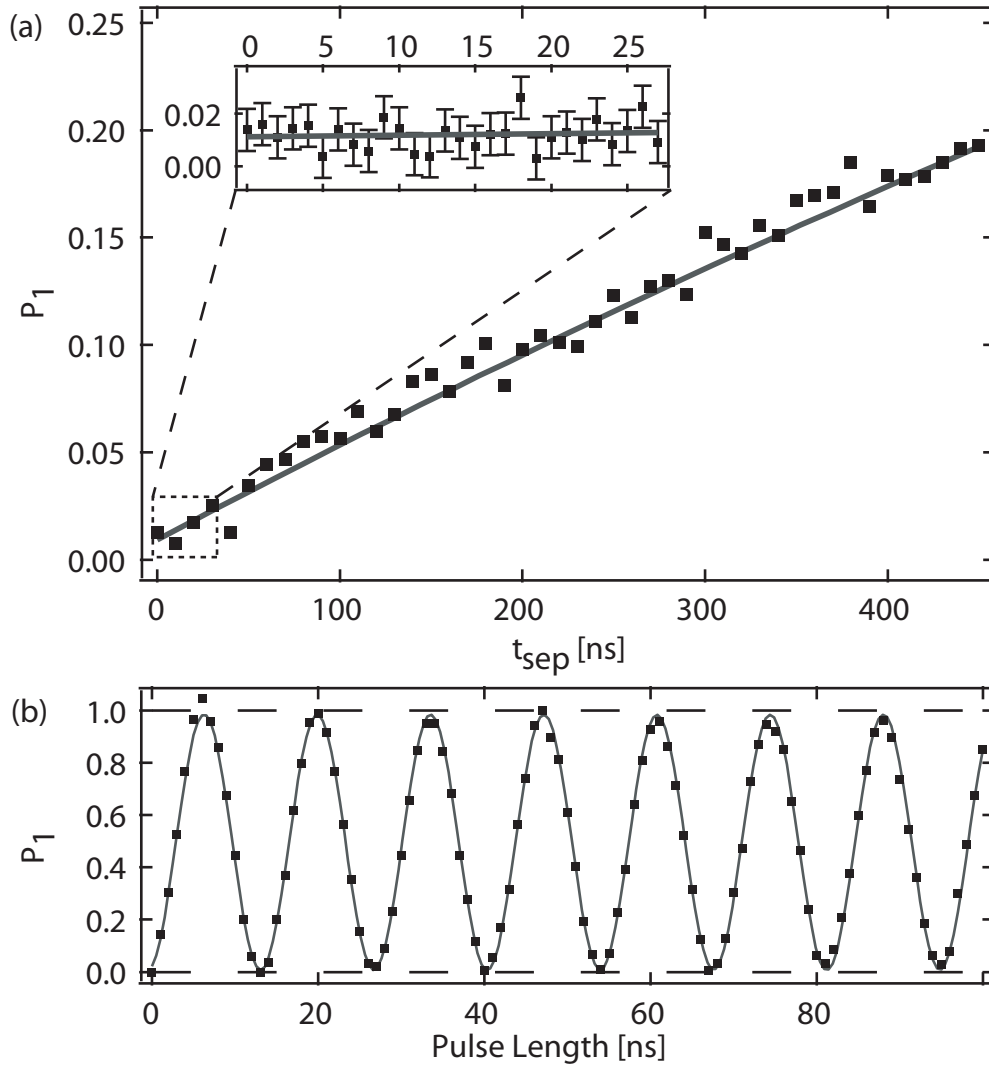


Figure 6.8: Bang-bang gate characterization and visibility. (a) Excited state qubit population P_1 vs. separation time t_{sep} between two successive π -pulses ($\sigma = 2$ ns). The data agree well with the simulation (solid line) involving relaxation and decoherence. The inset shows additional data taken for $0 \leq t_{\text{sep}} \leq 30$ ns. The residual population corresponding to the minimal separation is found to be 0.014 ± 0.008 giving a single qubit gate error of $0.7 \pm 0.4\%$. (b) Rabi oscillations show a visibility of $100.4 \pm 1.0\%$.

coherent evolution is governed by the Hamiltonian

$$H = \hbar \sum_{j=1,2} \left[\omega_{0j} \sigma_j^\dagger \sigma_j + \varepsilon_j(t) (\sigma_j^\dagger + \sigma_j) \right], \quad (6.8)$$

where $\sigma_j = |j-1\rangle\langle j|$ is the lowering operator for the multi-level atom with eigenenergies $\hbar\omega_j$. The corresponding transition energies are denoted $\hbar\omega_{ij} = \hbar(\omega_j - \omega_i)$. Drive strength and pulse-shapes are determined by

$$\varepsilon_j(t) = \frac{g_j^2}{\omega_r - \omega_{j-1,j}} [X(t) \cos(\omega_d t) + Y(t) \sin(\omega_d t)]. \quad (6.9)$$

Here, $g_j \sim \sqrt{j}g_0$ is the transmon coupling strength [61], $\omega_d/2\pi$ is the frequency of the drive, and $X(t)$ and $Y(t)$ are the pulse envelopes in the two quadratures.

The inset of figure 6.8a shows the experiment with t_{sep} varying between 0 ns and 30 ns repeated 2.5×10^6 times. We measure $P_1 = 0.014 \pm 0.008$ at $t_{\text{sep}} = 0$ ns. Dividing this probability by two as in Ref. [116] gives a single gate error of $0.7 \pm 0.4\%$.

Conceptually, the π - π measure is similar to the visibility measure used by Wallraff *et al.* in Ref. [123], corresponding to $(1 - \langle \sigma_z \rangle)/2$ after a single π pulse. Figure 6.8b shows Rabi oscillations made by increasing the length of a pulse resonant with the qubit transition frequency. The visibility is found to be $100.4 \pm 1.0\%$. This also agrees with our simple theoretical model taking into account the T_1 , T_2^* , and third-level at our specific operating point.

Although the π - π measure is relatively simple to implement, it does not sufficiently take into account errors which may manifest when the qubit state is neither $|0\rangle$ nor $|1\rangle$. For example, qubit dephasing significantly influences superposition states such as $(|0\rangle + |1\rangle)/\sqrt{2}$. However, the π - π scheme does not involve any $\pi/2$ rotations which would be required to generate such states. Furthermore, although we calibrate our π and $\pi/2$ pulses, deviations of the rotation angle only manifest as second-order errors in π pulses, as opposed to linearly in $\pi/2$ pulses. Although, there are experiments which refer to this measurement of $1 - P_1$ as a gate fidelity [116], in practice, due to the incompleteness of the protocol, we simply take the gate error result of π - π as a simple estimator, with more stringent tests necessary to fully characterize the single-qubit operations.

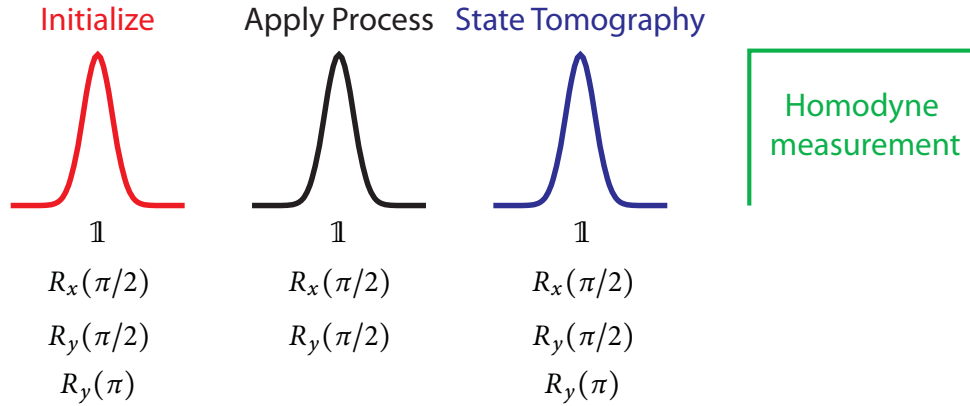


Figure 6.9: Schematic for quantum process tomography. QPT consists of three stages of gates. The initialization stage involves rotation gates which prepare the input states $|0\rangle$, $|1\rangle$ ($|0\rangle - |1\rangle$)/ $\sqrt{2}$ ($|0\rangle + i|1\rangle$)/ $\sqrt{2}$. The second stage involve applying the process to be studied, which in the experiments presented here are $\mathbb{1}$, $R_x(\pi/2)$, and $R_y(\pi/2)$. The final stage performs state tomography of the qubit system by measuring the projection along the three Cartesian axes through the application of $\mathbb{1}$, $R_x(\pi/2)$, $R_y(\pi/2)$, and $R_y(\pi)$. This is followed by the homodyne measurement described in section 6.3.3.

6.3.5 Quantum process tomography

The idea behind QPT is to determine the completely positive map \mathcal{E} , which represents the process acting on an arbitrary input state ρ . The theory is detailed in Refs. [120, 124] and can be summarized as follows. Any process for a d dimensional system can be written as

$$\mathcal{E}(\rho) = \sum_{m,n=0}^{d^2-1} \chi_{mn} B_m \rho B_n^\dagger, \tag{6.10}$$

where $\{B_n\}$ are operators which form a basis in the space of $d \times d$ matrices, and χ is the process matrix that we aim to measure. Here, any $d \times d$ matrix can be written as linear combinations of the elements of $\{B_n\}$. The process matrix χ is a positive superoperator (a linear map of a space of operators to another space of operators) which completely characterizes the process \mathcal{E} using the basis operators $\{B_n\}$. To determine χ , we prepare d^2 linearly independent input states $\{\rho_n^{\text{in}}\}$. For every input state, the output state $\rho_n^{\text{out}} = \mathcal{E}(\rho_n^{\text{in}})$ is determined by state tomography (section 2.5.2). The process matrix is then obtained by inverting Eq. (6.10), although in general this last step does not guarantee a completely positive map. To remedy this, a maximum likelihood estimation (MLE) based on Ref. [35] can be used.

In all the QPT experiments, the measurements are performed after sequences of three concatenated pulses (figure 6.9) are applied to the qubit. The first pulse, chosen from $\{\mathbb{1}$,

$R_x(\pi), R_x(\pi/2), R_y(\pi/2)\}$, prepares the four linearly independent input states $|0\rangle, |1\rangle, (|0\rangle + i|1\rangle)/\sqrt{2}$, and $(|0\rangle - |1\rangle)/\sqrt{2}$, whose projectors span the space of 2×2 density matrices ρ . The second pulse corresponds to the process for which look to determine χ , and is chosen from, $\{\mathbb{1}, R_x(\pi/2), R_y(\pi/2)\}$. A final pulse ($\{\mathbb{1}, R_x(\pi), R_x(\pi/2), R_y(\pi/2)\}$) rotates the measurement axis to perform state tomography on the state resulting from the first two pulses.

The state tomography data allows us to construct the process $\mathcal{E}(\rho)$, for one qubit ($d = 2$), and find the process matrix χ_{mn} which is defined with respect to the operator basis given by the Pauli basis $\{B_n\} = \{\mathbb{1}, \sigma_x, \sigma_y, \sigma_z\}$. By definition the χ matrix must be Hermitian. Furthermore, the completeness constraint requires that it must satisfy [120]

$$\sum_{mn} \chi_{mn} B_n^\dagger B_m = \mathbb{1}. \quad (6.11)$$

To find χ using MLE, we first write the process matrix in a Cholesky decomposition of the form

$$\chi(\vec{t}) = T^\dagger T, \quad (6.12)$$

where T is a lower triangular matrix parametrized by the vector \vec{t} . This ensures that χ be Hermitian. Next, the measured data is fit to a physical process by minimizing the function

$$f(\vec{t}) = \sum_{a,b=1}^{d^2} \left[m_{ab} - \sum_{m,n=0}^{d^2-1} \chi_{mn} \text{Tr}[M_b B_m |\phi_a\rangle \langle \phi_a| B_n^\dagger] \right]^2. \quad (6.13)$$

Here, m_{ab} is the measured data for the case where the state $|\phi_a\rangle$ was prepared and the observable M_b was measured. A Lagrange multiplier is then used to impose the completeness condition (6.11), such that we find the minimum of the function

$$f(\vec{t}) = \sum_{a,b=1}^{d^2} \left[m_{ab} - \sum_{m,n=0}^{d^2-1} \chi_{mn} \text{Tr}[M_b B_m |\phi_a\rangle \langle \phi_a| B_n^\dagger] \right]^2 + \lambda \sum_{k=0}^{d^2-1} \left[\sum_{m,n=0}^{d^2-1} \chi_{mn} \text{Tr}[B_m B_k B_n^\dagger] - \text{Tr}[B_k] \right]^2 \quad (6.14)$$

to obtain the most probable completely positive χ matrix corresponding to the measured values.

The results of QPT on the three processes $\mathbb{1}, R_x(\pi/2)$ and $R_y(\pi/2)$ are shown in figure 6.10.

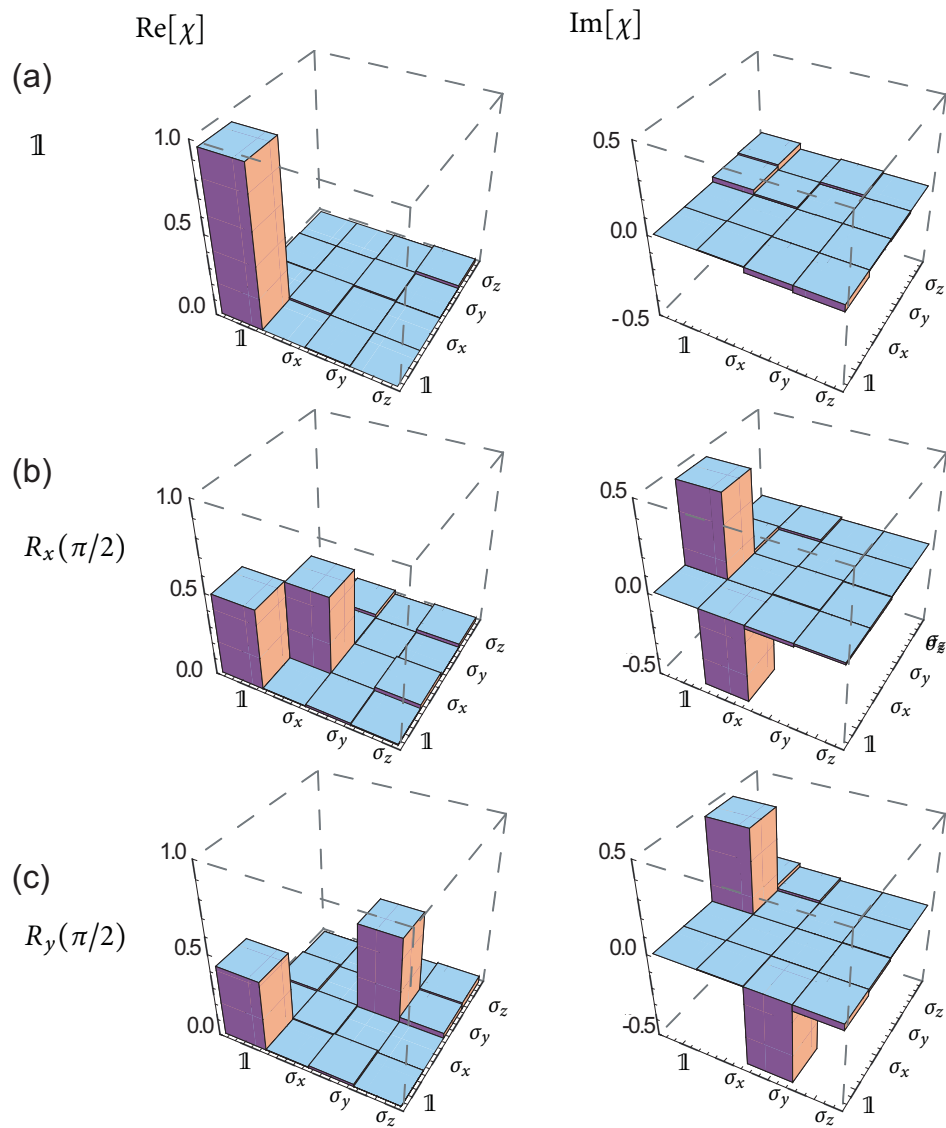


Figure 6.10: Quantum process tomography experimental results. Real and imaginary parts of the experimentally obtained process matrix χ for the three processes (a) $\mathbb{1}$, (b) $R_x(\pi/2)$, and (c) $R_y(\pi/2)$ for $\sigma = 2$ ns.

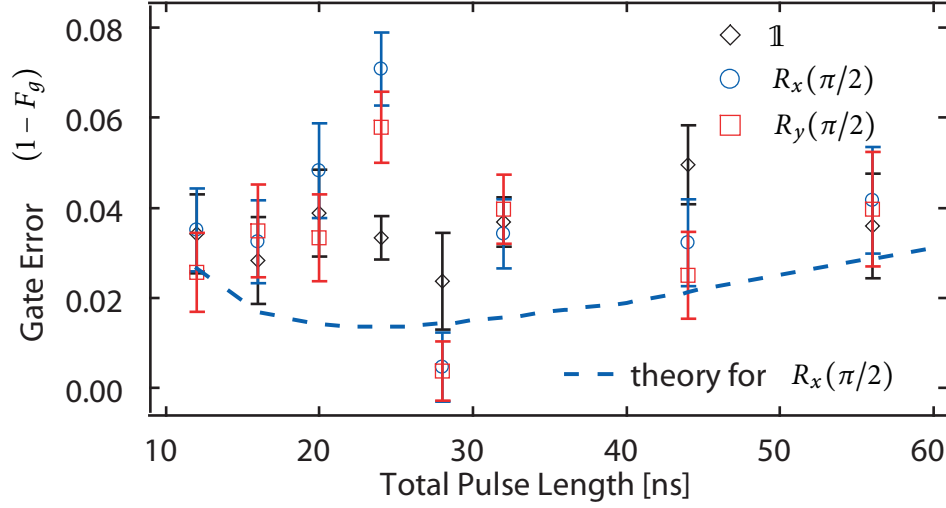


Figure 6.11: Gate errors from QPT. Gate error vs. total pulse length obtained from quantum process tomography plotted for the three processes $\mathbb{1}$, $R_x(\pi/2)$, $R_y(\pi/2)$

Here, bar plots of the real and imaginary parts of χ are shown for a pulse with $\sigma = 2$ ns in the Pauli basis $\{B_n\} = \{\mathbb{1}, \sigma_x, \sigma_y, \sigma_z\}$. We can compare our data to the ideal process matrices χ_{ideal} . For instance, for the $\mathbb{1}$ process, we expect $\chi_{\mathbb{1}\mathbb{1}} = 1$ and $\chi_{uu'} = 0$ otherwise, which is in good agreement with the measured results. Small deviations from χ_{ideal} arise from preparation and measurement errors, gate over-rotations, decoherence processes, qubit anharmonicity, etc. Calibration errors of the rotations around the x axis are seen as a non-zero $\text{Im}[\chi_{\mathbb{1}\sigma_x}]$ and a drive detuning error is exhibited in $\text{Im}[\chi_{\mathbb{1}\sigma_z}]$.

From the experimentally obtained process matrix χ and its ideal counterpart χ_{ideal} we can directly calculate the process fidelity, defined as $F_p = \text{tr}[\chi_{\text{ideal}}\chi]$, as well as the gate fidelity $F_g = \int d\psi \langle \psi | U^\dagger \mathcal{E}(\psi) U | \psi \rangle$. Here the integral uses the uniform measure $d\psi$ on the state space, normalized such that $\int d\psi = 1$. F_g can be understood as how close \mathcal{E} comes to the implementation of the unitary U when averaged over all possible input states $|\psi\rangle$. From Ref. [125], there is a simple relationship between the F_p and F_g , namely $F_g = (dF_p + 1)/(1 + d)$. For the three processes displayed in figure 6.10, F_p is 0.96, 0.95, and 0.95 ± 0.01 .

Figure 6.11 shows F_g as a function of pulse length. The error bars are standard deviations obtained by repeating the maximum-likelihood estimation for input values chosen from a distribution with mean and variance given by measurement. The large scatter in the gate error versus pulse length is primarily attributed to drift in the system which occurs over the course of the data acquisition. Such errors can be reduced via cryogenic magnetic shielding, but was not done for the experiment presented here.

Although QPT is an excellent way to establish the complete behavior of the quantum gate for certain systems where preparation and readout are near perfect and independent of the process operation, in circuit QED, it does not extricate the process errors from errors in the preparation or analysis gates. Specifically, in the experiment described above, the demonstrated gate fidelity corresponds to in each case the performance of a three gate sequence. As a result, QPT as a gate error technique to some degree gives too much information which is not simply attributable to any specific gate or syndrome. Furthermore, as the number of qubits increases, the complexity of process tomography scales exponentially due to the increased number of input states as well as basis states for the state tomography, making it a less attractive option for error determination in larger quantum systems.

Instead of trying to find out the all the details of the errors in the system via QPT, a different approach is to find an average gate fidelity. This can be done with randomized benchmarking, which we detail in the next section.

6.3.6 Randomized benchmarking

The randomized benchmarking experimental protocol, described in Knill *et al.* [118], consists of the following: (1) initialize the system in the ground state, (2) apply a sequence of randomly chosen pulses in the pattern $\prod_i C_i P_i$ where C_i are Clifford group generators $e^{\pm i \sigma_u \pi/4}$, with $u = x, y$, and P_i are Pauli rotations, i.e. $\mathbb{1}, \sigma_x, \sigma_y, \sigma_z$, (3) apply a final Clifford or Pauli pulse to return to one of the eigenstates of σ_z , (4) perform repeated measurements of σ_z , and compare to theory to obtain the sequence fidelity.

The RB sequences contain only π and $\pi/2$ rotations, which are in the Clifford group such that the single qubit state is always an eigenstate of a Pauli operator during the pulse sequence. The C_i pulses are all $\pi/2$ pulses and the P_i pulses which follow are π pulses which serve to randomize the errors. It also means that truncation of any long random sequence of such gates places the qubit in a state which is at most a single $\pi/2$ rotation away from an eigenstate of σ_z . The π pulses can be thought of as rotations which rotate the Cartesian axes of the Bloch sphere into one another.

Randomization with Clifford gates has been shown [125] to provide a depolarized noise channel. A depolarized channel is a type of quantum noise which takes the state of a qubit towards a completely mixed state with a probability d . Specifically, the new state of a qubit in

state ρ after being acted on by a depolarized noise is given by [12]

$$\rho' = d \left(\mathbb{1} \frac{1}{2} \right) + (1 - d)\rho. \quad (6.15)$$

The effect of this depolarized channel is to reduce the amplitude of the Bloch vector towards the center of the Bloch sphere [12]. Qubit noise processes such as relaxation (T_1 processes) and decoherence (T_ϕ processes) are not depolarizing, but polarizing, as it is easy to see that relaxation tends to bring the state to $|0\rangle$ and decoherence results in the state going towards either $|0\rangle$ or $|1\rangle$. However, the randomized Clifford gates rotate the qubit Bloch vector throughout the Bloch sphere, sampling different parts of the state space which can be more or less sensitive to specific forms of noise. This accumulation of different types of errors will end up giving an average effect of all the errors, and result in a depolarized noise channel. Then, the fidelity of the system will on average decay exponentially with the number of gates applied.

To see the exponential decay, we will repeat the derivation as given in Ref. [118]. Suppose we have a long randomized sequence of L combinations of randomized $P_i C_i$ and perform experiments at truncated lengths $i = 1, \dots, L$. Let p_i be the average error probability for sequences of length i and d_i be the probability that at any given step i , the qubit has depolarized. The probability of the state being depolarized at step k is given by

$$p_k = E \left(\frac{1}{2} \left[1 - \prod_{i=0}^k (1 - d_i) \right] \right), \quad (6.16)$$

where the expectation is taken over the distribution of random choices of $P_i C_i$ and the factor of $1/2$ emerges due to depolarization giving the correct state regardless $1/2$ of the time. Since all the choices of $P_i C_i$ are independently chosen except for the final pulse, we have

$$p_k = \frac{1}{2} \left[1 - (1 - d_f)(1 - d)^k \right], \quad (6.17)$$

where d is the average depolarization probability of a random choice of $P_i C_i$ and d_f is the depolarization probability of the final pulse. From this result, we see that p_k decays to $1/2$ exponentially as a function of the number of gates k and the decay constant gives d . Then, we finally have that the average gate fidelity \mathcal{F}_g is related to d via [118]

$$\mathcal{F}_g = 1 - \frac{d}{2} \quad (6.18)$$

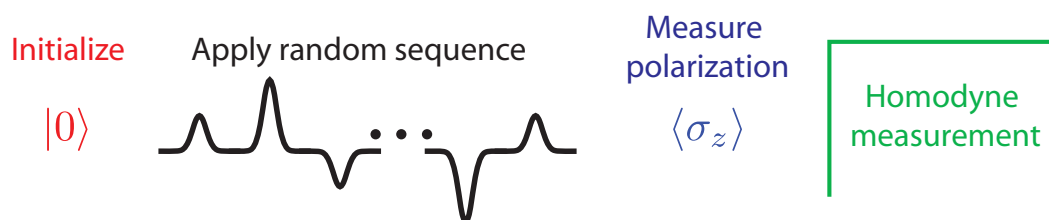


Figure 6.12: Schematic for randomized benchmarking. The randomized benchmarking scheme begins with the qubit always in the ground state $|0\rangle$. That is followed by a randomized sequence of alternating Clifford and Pauli gates. A final gate is always applied to place the final state in either $|0\rangle$ or $|1\rangle$ such that the final measurement will be on an eigenstate of σ_z . As exponential decay of the final state fidelity is found as a function of the number of gates in the central randomized sequence of Clifford and Pauli gates.

We follow the experimental recipe for the pulse sequences exactly as given in Ref. [118]. We create computational sequences 192 pulses long, with 4 different randomizations of Clifford gates C_i , and 8 different randomizations of Pauli gates P_i for 32 total unique sequences. Each sequence is then truncated to 17 different computation (where a computation consists of two gates, $P_i C_i$) lengths, $\{2, 3, 4, 5, 6, 8, 10, 12, 16, 20, 24, 32, 40, 48, 64, 80, 96\}$. This therefore results in 544 different experiments, each applied for 250,000 repeated measurements, taking a total time of about an hour.

The experimental results show the average fidelity is an exponentially decaying function with respect to the number of gates. Figure 6.13 plots the fidelity as a function of the number of computational gates for all randomized sequences with $\sigma = 3$ ns. An average error per gate of 0.011 ± 0.003 is obtained by averaging over all the randomizations and fitting to the exponential decay. The excellent fit to a single exponential indicates a constant error per gate, consistent with uncorrelated random gate errors due to T_1 , T_ϕ , and no other mechanisms significantly affecting repeated application of single-qubit gates.

The benchmarking protocol is repeated for different pulse widths σ , and the average error per gate is extracted for each. Figure 6.14 shows the average fidelity versus number of gates for a number of pulse widths. The extracted average error per gate can be plotted versus total gate length, and compared to theory, as shown in figure 6.15. For large σ , experimental results agree well with theory. In this regime, errors are dominated by relaxation and dephasing. For small σ , the gate fidelity is limited by the finite anharmonicity and the resulting occupation of the third level, although the effect is not very pronounced. We obtain error bars from standard deviations in error per gate having generated fidelity values from distributions with means and variance obtained from the experiment and theory. We observe an increase in

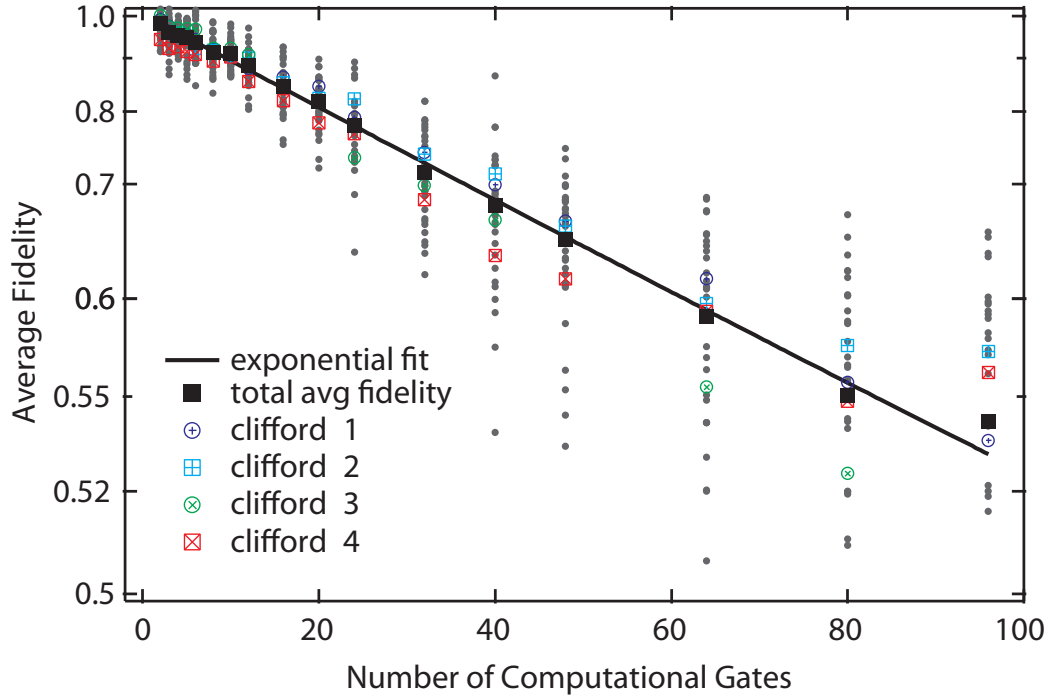


Figure 6.13: Randomized benchmarking for 3 ns pulse width. Average fidelity vs. number of applied computational gates for all 32 unique sequences are shown in the small gray points. Computational gates consist of a randomized Pauli with a randomized Clifford generator. The colored points involve averaging over the 8 Pauli randomizations. The black squares are the result of then averaging over the 4 Clifford randomizations. We can see that just the averaging over the randomized Pauli gates already gives an exponential decay. The solid black line is an exponential fit, from which we find an average gate error of 1.1%.

the standard error for $\sigma = 1$ ns. This increased variance in the experiments we attribute to the onset of the finite anharmonicity. The optimal gate length is found to be 20 ns, as shown in Fig. 4(b). The anharmonicity effect will be explored further in the next section on a different sample where the coupling and hence leakage to the second excited state is much stronger.

The reduction of the error by a factor of $\sim 1/3$ from QPT is likely due to the over-estimation of errors in QPT where gate errors cannot be isolated from measurement and preparation errors.

6.3.7 Summary of error metrics

We have thus systematically investigated gate errors in a circuit QED system by measuring gate fidelity using the $\pi - \pi$ metric, quantum process tomography, and randomized benchmarking. Table I summarizes our results and displays consistently low gate errors across all metrics.

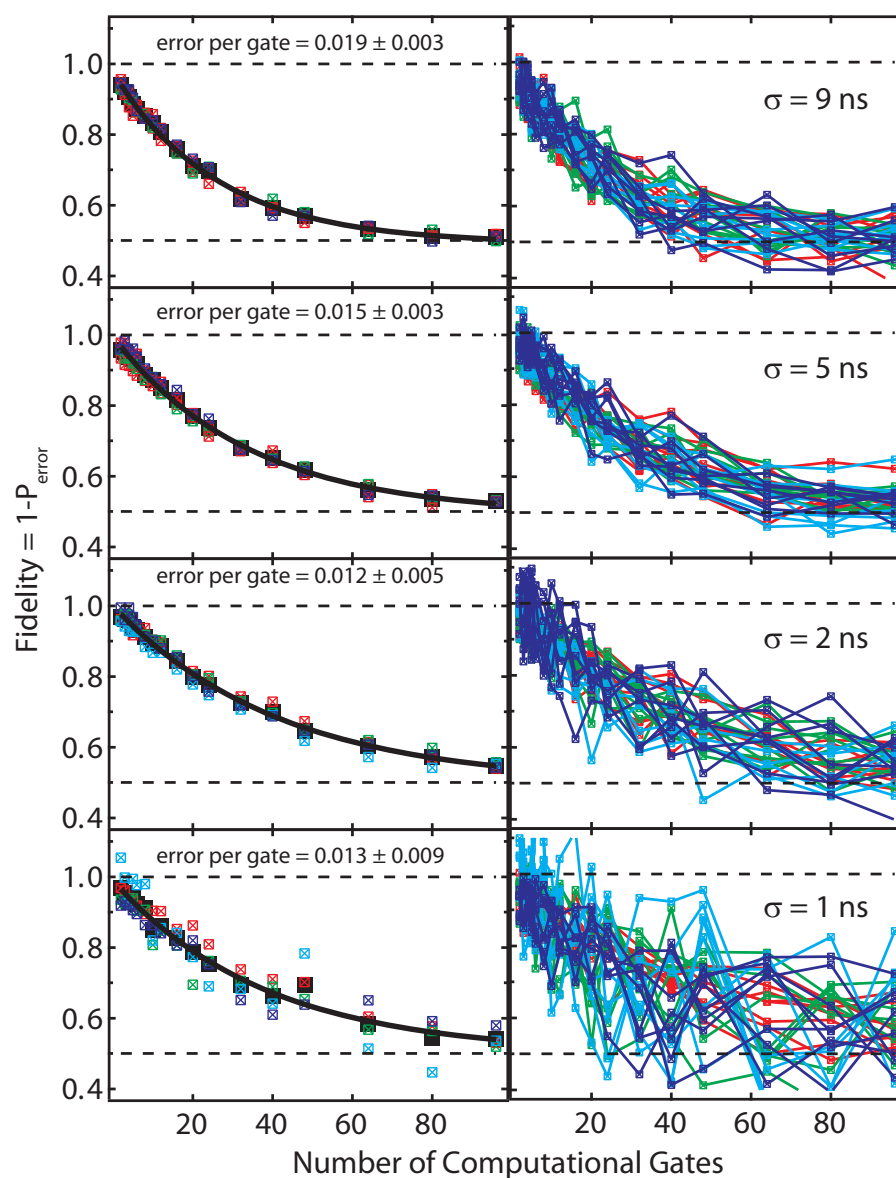


Figure 6.14: Trace by trace randomized benchmarking. The average error per gate is shown in the left panels for $\sigma = 9, 5, 2, 1$ ns. The 32 unique trace-by-trace realizations are shown for the same σ in the right panels. We can see the increase in the spread of all the traces at the shortest pulse lengths, reflected in the increase in the error bars of the extracted error per gate.

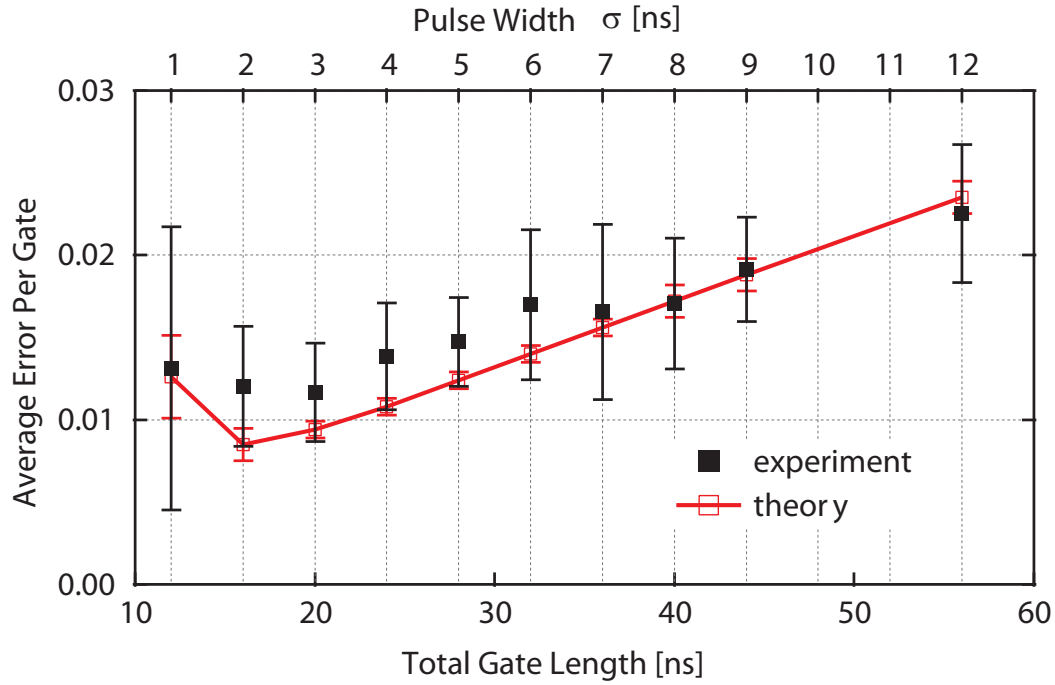


Figure 6.15: Error per gate versus pulse width. Average error per gate (experimental and theoretical) at different pulse widths. The rise for $\sigma < 2$ ns corresponds to the onset of limitation by the third level of the transmon. The increase in error per gate for $\sigma > 2$ ns is due to the limitation by relaxation..

Table 6.1: Gate errors for the three metrics. The measurements show consistently low gate errors of the order of 1 ~ 2%.

Metric	Measured error in %
π - π	0.7 ± 0.4
Process tomography: $\mathbb{1}$	2.4 ± 1.1
Process tomography: $R_x(\pi/2)$	2.6 ± 0.8
Process tomography: $R_y(\pi/2)$	2.2 ± 0.7
Randomized benchmarking	1.1 ± 0.3

From comparison with theory, we conclude that the observed magnitude of errors fully agrees with the limitations imposed by qubit decoherence and finite anharmonicity. Specifically, in the T_1 limited case and for moderate gate lengths t_g , we find that the gate error scales as $\sim t_g/T_1$. Once coherence times of superconducting qubits and pulse-shaping are improved, the aforementioned metrics will be useful tools for characterizing gate fidelities as they approach the fault-tolerant threshold.

Randomized benchmarking will be a particularly attractive option for multi-qubit systems due to its favorable scaling properties as compared to QPT. There have already been experiments in NMR which investigate randomization for two-qubit gates as well [119]. We next extend the RB single-qubit gate error characterization for a qubit which experiences a sharp increase in error for short pulse lengths.

6.4 Derivative-based pulse shaping

In the previous section, our experimental characterization of single-qubit gates revealed that the gate fidelity is limited by the coherence times of the system and how fast the gates can be performed. Certainly one limit to how fast we can perform qubit operations is the hardware used. Our current arbitrary waveform generators allow for pulses with ns resolution (section 5.7). However, as discussed in section 4.2.3, for shorter and shorter pulses, errors can also arise due to the finite and small anharmonicity of the transmon qubits.

The sample discussed in the previous section does not show a very sharp increase in the gate error at the shortest pulses because the transmon transition energy levels are located below the cavity and the coupling strength g_{01} is relatively small, both contributing to making the direct coupling to the $|2\rangle$ state negligible. However, now we present similar single-qubit gate experiments but on one of the qubits in cQED222 (chapter 5) in which this coupling is not so small, and the effect of the transmon anharmonicity becomes evident in the measured average gate errors.

6.4.1 Experimental details

Again, although cQED222 contains two qubits coupled to a coplanar waveguide cavity, here we only investigate single-qubit gates on one of the transmon qubits. The other qubit is tuned via its local flux bias line far away from both the cavity and the qubit which we will be studying. The bare cavity resonance frequency is 6.902 GHz, and the investigated transmon is tuned to a maximal frequency $\omega_{\max} = 8.18$ GHz, with corresponding coherence times of $T_1 = 1.2 \mu\text{s}$ and $T_2 = 1.5 \mu\text{s}$. The anharmonicity of the system is governed by the charging energy, measured via spectroscopic means to be $E_C/2\pi = 317$ MHz [126, 127].

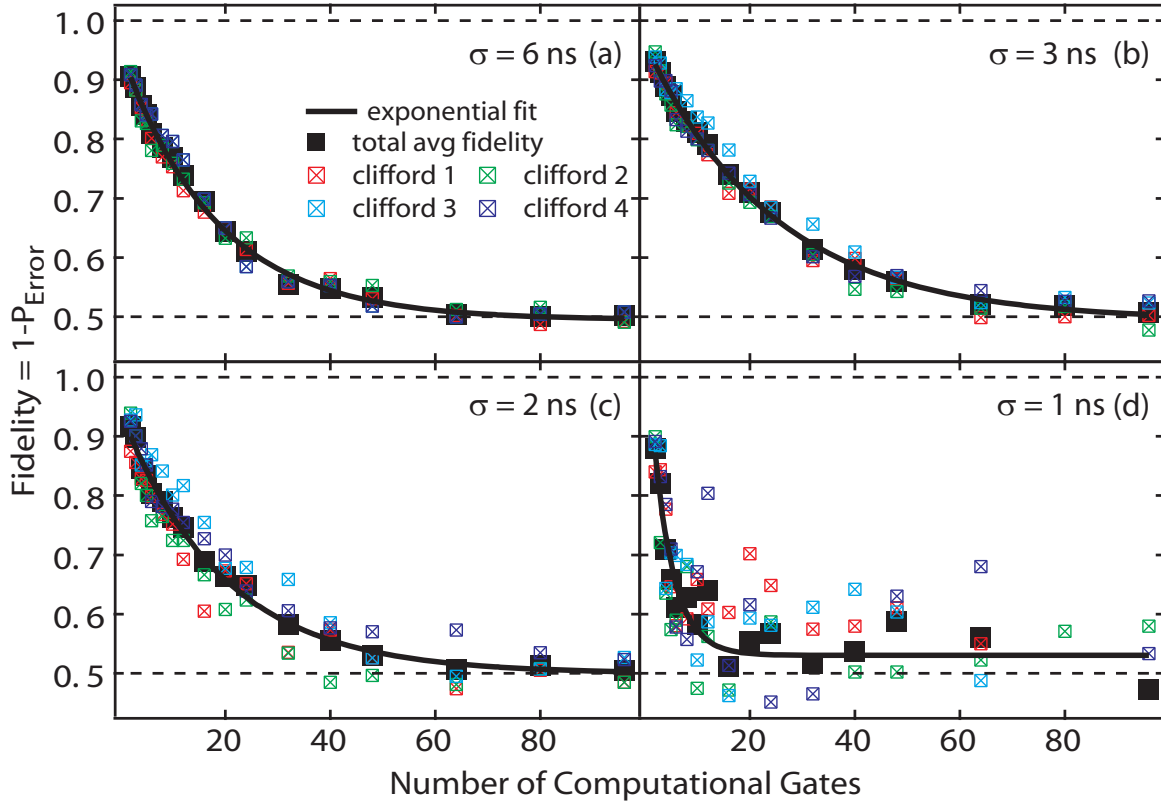


Figure 6.16: Clifford averaged RB for cQED222 with standard pulse shaping. Total average fidelity (black squares) and averaging just over the Pauli randomizations, (red, green, cyan, blue hash markers), for $\sigma = 6, 3, 2, 1$ ns. At $\sigma = 3$ ns, the error per gate already starts to increase, and at $\sigma = 1$ ns, the scatter even in the Pauli averaged traces remains large. The solid black lines are exponential fits to the total average fidelities.

6.4.2 Results with standard pulse shaping

We first repeat the randomized benchmarking experiment of section 6.3.6 using truncated Gaussian pulses of varying σ . The average fidelity is found to be an exponentially decaying function for all σ . Figure 6.16 show the 4 Clifford randomizations with the 17 different truncated lengths for $\sigma = \{6, 3, 2, 1\}$ ns. We are able to see improvement in the average fidelity measurements as σ goes from 6 ns to 3 ns (figure 6.16a–b). However, it is also obvious that for shorter pulses, $\sigma = 3 - 1$ ns, the extracted average error per gate gets progressively worse (figure 6.16b–d).

This is made more obvious by extracting the average gate fidelity from exponential fits for each of the different σ , plotted in figure 6.17. Furthermore, the calculated standard errors (shown as error bars at each point) for each σ can also be seen to get worse with shorter gate

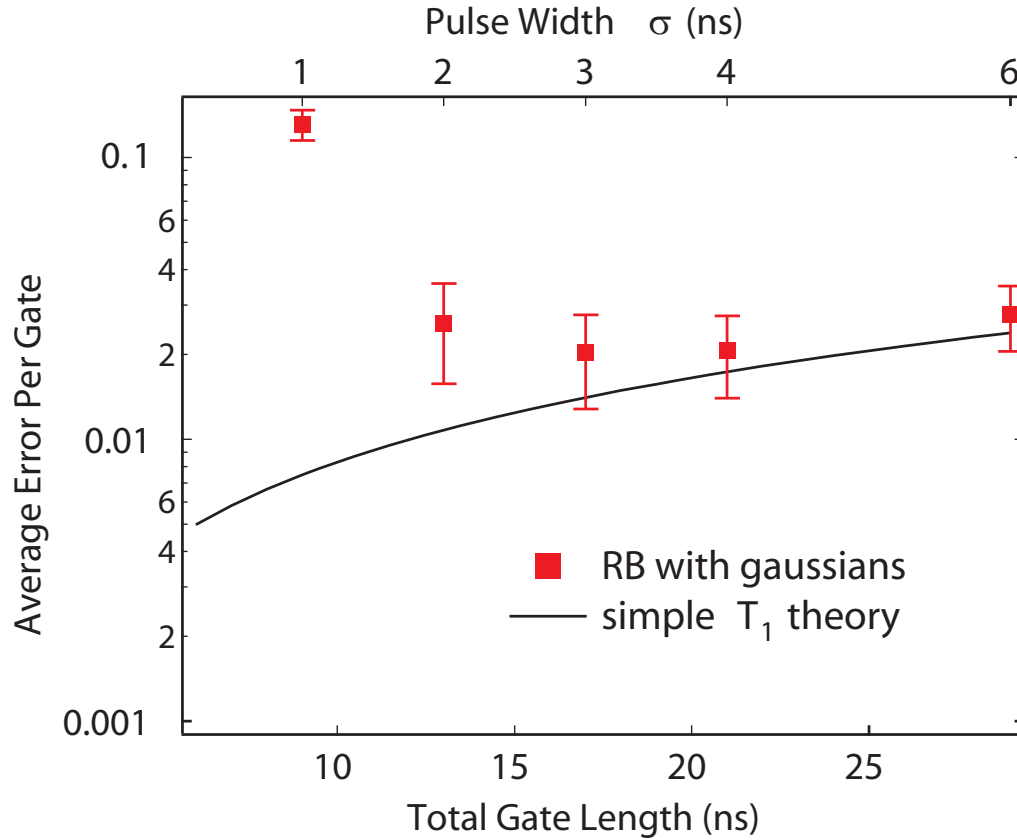


Figure 6.17: Error per gate with normal pulse shaping. Extracted error per gate versus total gate length using Gaussian pulse shapes. There is a sharp rise in the error per gate at $\sigma = 3$ ns. The solid line is a simple two-level system model taking into account the relaxation of the qubit.

lengths. We find the average gate error bottoms out at 0.020 ± 0.007 , at $\sigma = 3$ ns. However, simple theory (solid line) taking into account the T_1 and T_2^* for a two-level system suggests further improvement for shorter gate lengths and predicts an average gate error of 0.007 for $\sigma = 1$ ns.

The error mechanism for these shortest pulses can be inferred by looking at $\langle \sigma_z \rangle$ of the qubit for a certain combination of gates. Figure 6.18 shows the measurement of $\langle \sigma_z \rangle$ for all concatenations of a $\pm\pi$ rotation along either x or y with a $\pm\pi/2$ rotation along either x or y . The calibrated levels of $\langle \sigma_z \rangle = -1$ and $\langle \sigma_z \rangle = 1$ are obtained from two separate experiments where no single-qubit gate is applied and when a π pulse with $\sigma = 6$ ns is used. Here the longer π pulse is used to calibrate the scale because of the increased prevalence of errors for shorter pulses. The theoretical results of all the combinations of pulses correspond to $\langle \sigma_z \rangle \in \{-1, 0, 1\}$. However, we can see in figure 6.18 that many experiments (red-outlined

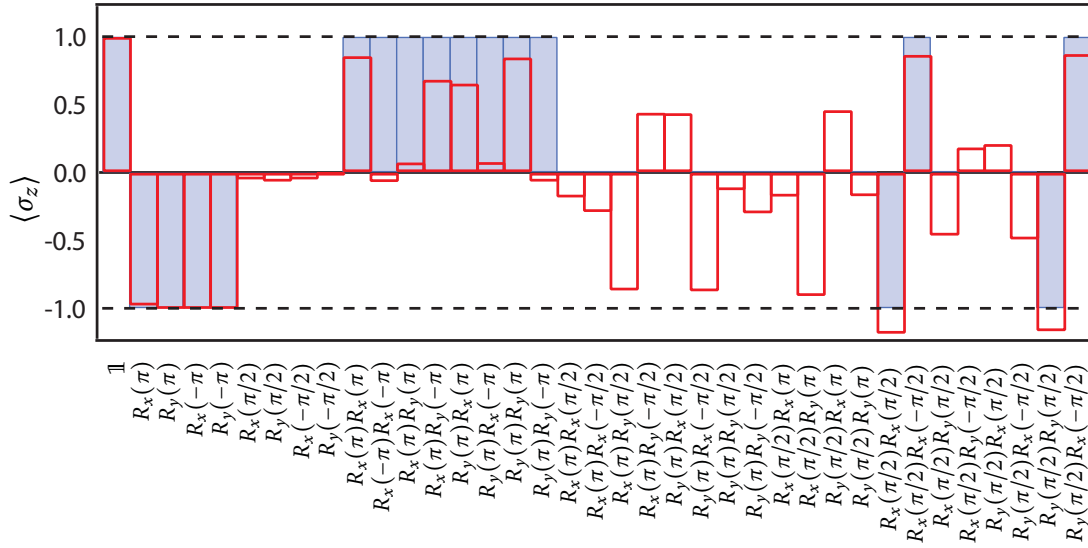


Figure 6.18: Composite x and y rotations with standard Gaussian pulse shaping. Inferred $\langle \sigma_z \rangle$ for a set of simple qubit rotation experiments. All combinations of rotations should result in the qubit giving $\langle \sigma_z \rangle = -1, 0, 1$, as indicated by the blue shaded bars. The experimentally determined values are given as the red-outlined bars. Large errors are found in composite pulse sequences involving both x and y rotations. The first five experiments are used for calibration.

bars) deviate from their theoretical expectations (solid blue bars). Specifically, the greatest errors occur for combinations of gates where the second gate is in the opposite quadrature from the first. For example, the sequence $R_x(\pi)R_y(\pi/2)$ should place the qubit in an equal superposition state of $|0\rangle$ and $|1\rangle$ such that $\langle \sigma_z \rangle = 0$. But in the experiment, we find this to give $\langle \sigma_z \rangle = -0.87$, which is almost an order unity error. The symmetry of the measured $\langle \sigma_z \rangle$ around 0 for the experiments $R_x(\pi)R_y(\pi/2)$ and $R_x(\pi)R_y(-\pi/2)$ (which gives $\langle \sigma_x \rangle = 0.44$) suggests a phase error which has resulted before the second rotation in each case, $R_y(\pm\pi/2)$. The second gate thus performs a rotation around an axis not commensurate with the one perpendicular to the x rotation axis defined by the first pulse.

6.4.3 Experimentally implementing derivative pulse shaping

The critical issue for this sample is the larger g_{01} and the fact that we operate the transmon above the cavity, with the higher order transitions actually closer to the cavity resonance in frequency than ω_{01} . The reduced detuning to the transition frequencies ω_{12} and $\omega_{02}/2$ combined with the larger coupling strength g_{01} suggest that direct coupling to the $|2\rangle$ state of the transmon might not be negligible for shorter pulses that have higher frequency bandwidth.

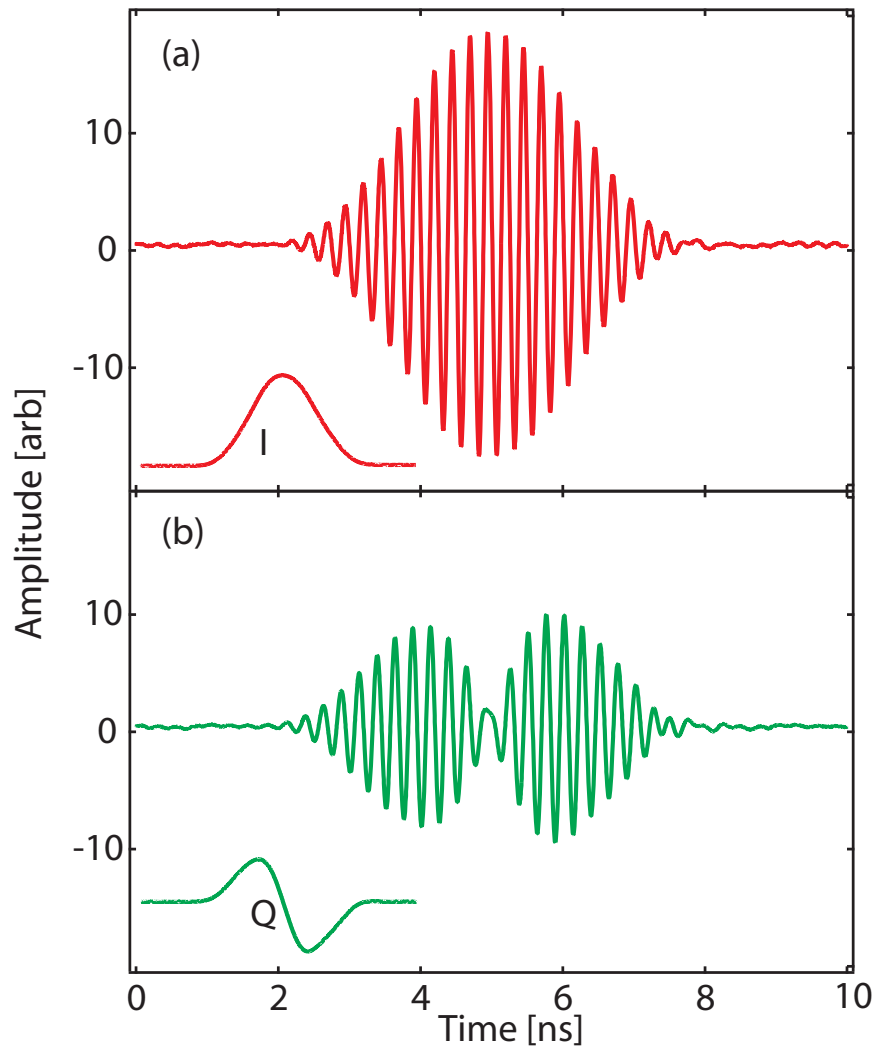


Figure 6.19: Gaussian and derivative on I and Q quadratures. (a) A standard truncated Gaussian is applied on one quadrature. (b) Frequency modulated truncated derivative of Gaussian is applied on the other quadrature. The pulse shape is shown in the lower left corner.

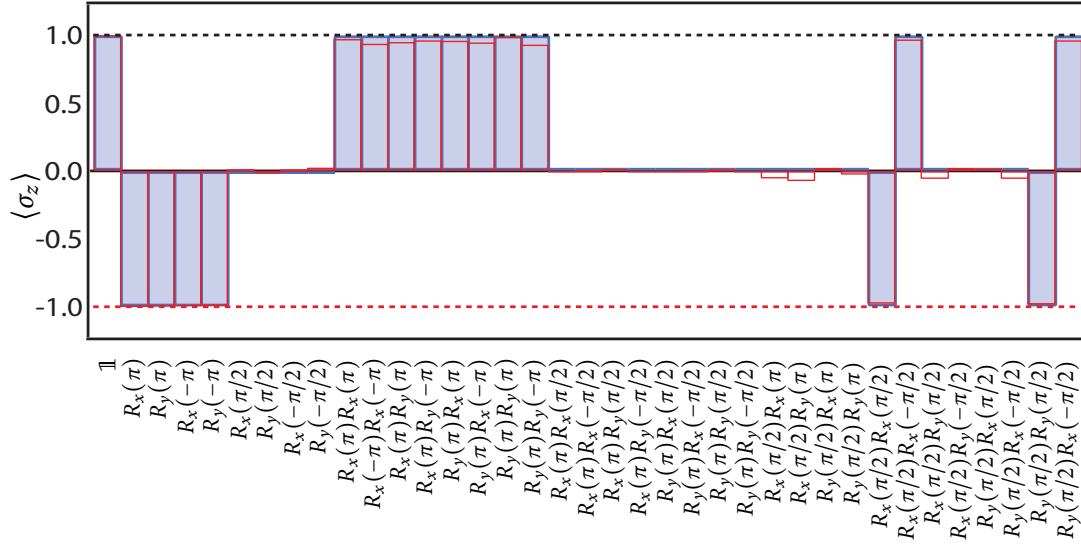


Figure 6.20: Composite x and y rotations with derivative pulse shaping. Inferred $\langle \sigma_z \rangle$ for a set of simple qubit rotation experiments. All combinations of rotations should result in the qubit giving $\langle \sigma_z \rangle = -1$, as indicated by the blue shaded bars. The first five experiments from the left are used for measurement calibration. The experimentally determined values are shown as the red-outlined bars in good agreement with the theoretical expectation.

By employing pulse shaping based on the optimal control technique of DRAG (section 4.2.3), we are able to reduce the single-qubit gate errors at lower pulse widths. To recall, the DRAG [90] technique is a protocol for pulse shaping such as to reduce the error caused by the presence of a third level.

Here, we experimentally implement derivative pulse-shaping (DPS) and show the improvement of single-qubit gate performance. In DPS, when a single-qubit rotation pulse is applied along the x axis, a derivative of the pulse is applied along the y axis to cancel out the higher level leakage, and vice versa. As before, rotations around the x and y axes are performed with in-phase and quadrature microwaves tuned to the qubit ground to first excited state frequency, and are shaped with Gaussian envelopes, truncated to two standard deviations σ on each side. After each gate, we still include a 5 ns buffer to avoid any overlap with the following gate. This makes the total gate time $t_g = 4\sigma + 5$ ns. The leakage due to an x -rotation or in-phase pulse is reduced by applying a complementary quadrature tone shaped by an amplitude scale factor D of the truncated derivative-of-Gaussian envelope. Similarly, for a y -rotation or quadrature pulse, the same scale factor D of the truncated derivative is applied on the x or in-phase channel.

We can visualize these truncated Gaussians and their corresponding derivatives in fig-

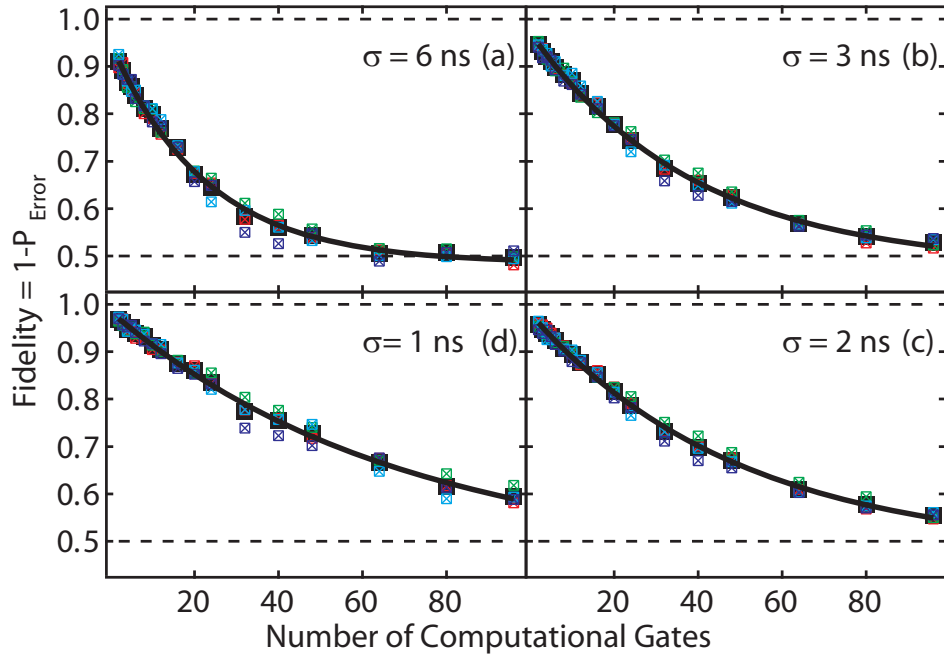


Figure 6.21: Randomized benchmarking for various pulse widths using derivative pulse shaping. Total average fidelity and averaging just over the Pauli randomizations for $\sigma = 6, 3, 2, 1$ ns having implemented derivative pulse shaping. The error per gate decreases monotonically with decreasing σ .

ure 6.19, here with the scaling parameter $D = 1$. In practice, this scale factor D is tuned via a simple calibration experiment. The calibration is an iterative procedure, starting with standard Gaussians on one quadrature and $D = 0$, and measuring the homodyne voltage for applying $\mathbb{1}$, $R_x(\pi)$, $R_x(\pi/2)$, $R_x(\pi)R_y(\pi/2)$, $R_x(\pi)R_y(-\pi/2)$. In this case, we are able to obtain the homodyne voltage levels corresponding to being in $|0\rangle$, $|1\rangle$, and the equal superposition of the two basis states. The last two experiments, as discussed previously and part of the experiment shown in figure 6.18, contain a systematic symmetric error around the result for $R_x(\pi/2)$. Next, we repeat the same experiment but program the pulses such that $D = 0.1$ and therefore microwaves are applied both to x and y . Ideally, the results of the last three pulse sequences, $R_x(\pi/2)$, $R_x(\pi)R_y(\pi/2)$, $R_x(\pi)R_y(-\pi/2)$ should be the same. As D is scaled up, the three values approach one another. If D is increased too much, the last two experiments give values which deviate from the superposition level again. Therefore, from this calibration technique the scaling of the derivative pulse on the complementary quadrature can be determined.

For the qubit discussed in this section, the level D is found to be 0.4. We can first explore

the collection of gates where we concatenate x rotations with y rotations. Figure 6.20 shows the same experiment as in figure 6.18, but having implemented the DPS on the conjugate quadrature. All of the previous errors are now removed and we have excellent agreement with theory.

What is now the effect of these pulses on the average gate fidelity? We repeat the randomized benchmarking protocols for various pulse widths σ . The fidelity as a function of number of gates averaging over the 8 different Pauli randomizations is shown in figure 6.21. The 32 individual (recall 8 Pauli and 4 Clifford randomizations) randomized traces along with the average fidelity as a function of the number of gates for a number of σ are shown in figure 6.22. The clearest and most striking improvement can be seen for $\sigma = 1, 2$ ns. The spread of the 32 unique traces, with order unity deviations for $\sigma = 1$ ns without DPS, is now improved considerably.

Next, we extract the average gate fidelity from the exponential fits and plot it against the pulse width in figure 6.23, where we have included the pre-DPS results as well as the simple decoherence theory. Using DPS, we obtain a minimum error per gate of 0.007 ± 0.006 for our shortest possible gates, with $\sigma = 1$ ns. As we can see from figure 6.23, we experience improved gate performance for $\sigma = 1 - 3$ ns which agrees remarkably well with the two-level system theory.

6.4.4 Summary of DPS

Thus, DPS allows us to improve gate performance and use shorter gate lengths. It seems as though the additional error due to the finite and small anharmonicity of the transmon can be mostly removed from the system through optimal control of the single-qubit gates. The experiment also demonstrates that our single-qubit gates are limited by their coherence times and the sensitivity of our hardware, as our current arbitrary waveform generators only provide 1 ns resolution. Additional time resolution would permit even more complicated optimal control schemes and even shorter pulses. Combined with improved coherence times, the fault-tolerant threshold of 10^{-4} error per gate can become within reach. However, the current experiment does not test explicitly whether the error mechanism is leakage to $|2\rangle$. In the future, we would like to perform experiments which characterize the population of this level as a function of shorter gate lengths, as well as implement higher-order corrections as proposed by Ref. [90] when the hardware control of our pulse-shaping can beat 1 ns resolution.

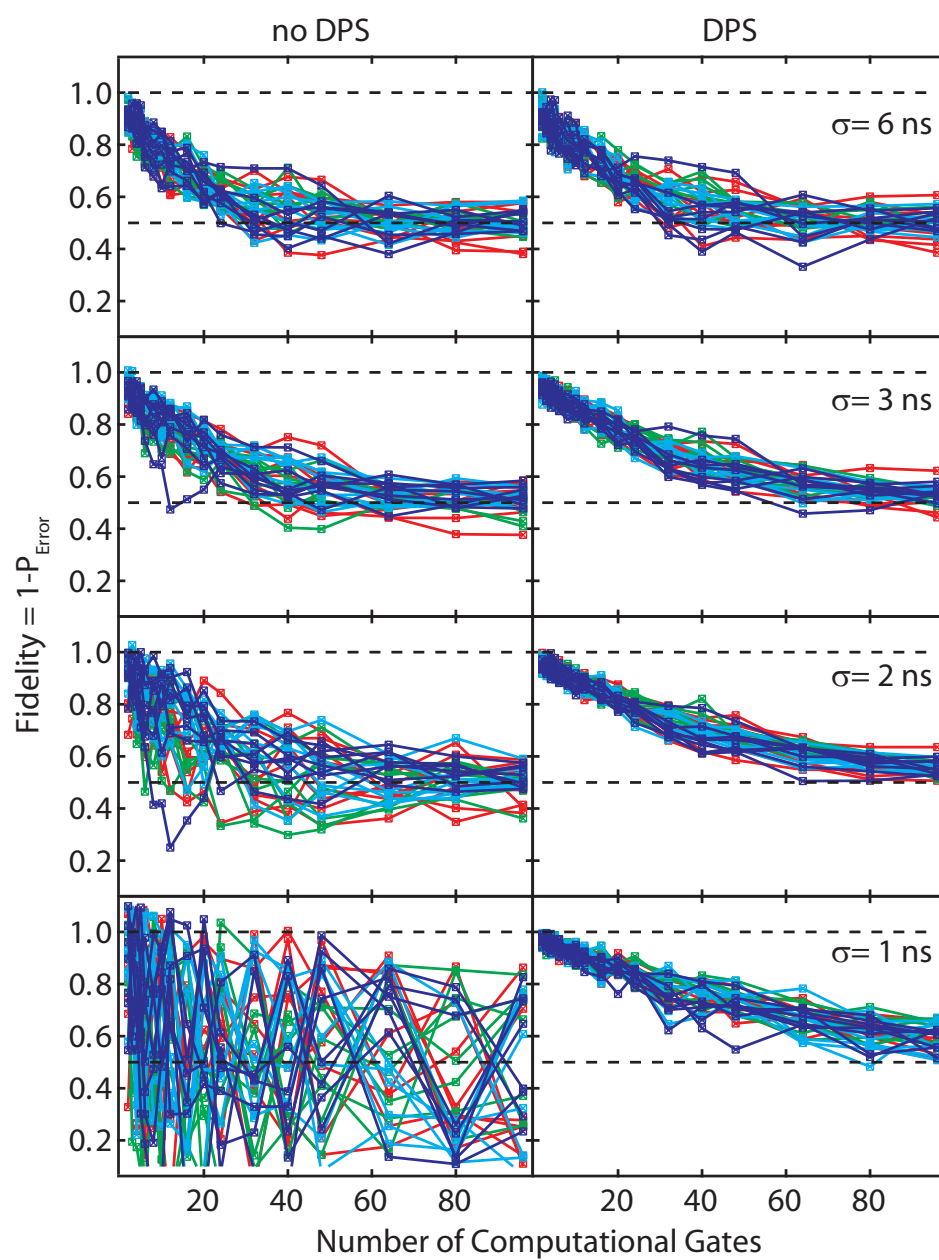


Figure 6.22: Trace by trace with and without derivative pulse shaping. All unique 32 randomized traces with and without the derivative pulse shaping for $\sigma = 6, 3, 2, 1$ ns. The spread in the traces can be seen to get visibly worse without the shaping, and visibly better with the shaping.

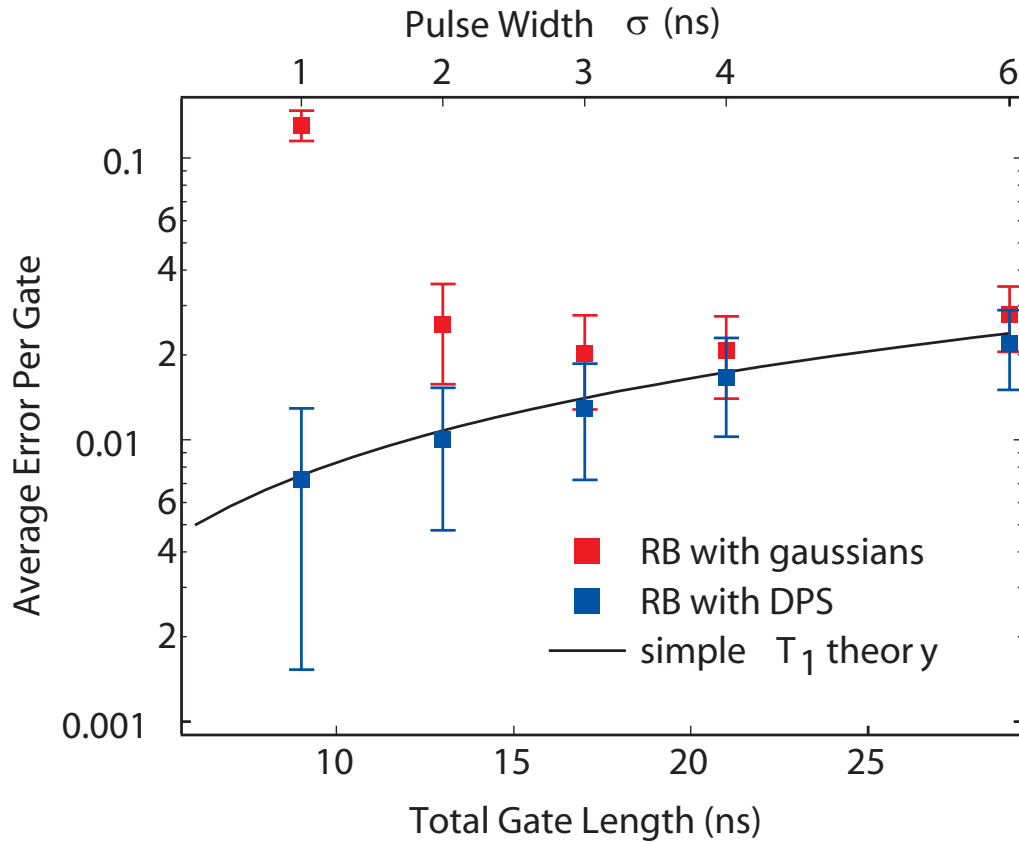


Figure 6.23: Error per gate with derivative pulse shaping. Extracted error per gate versus total gate length with (blue square markers) and without (red square markers) the derivative pulse shaping. We find that with the derivative shaping, an excellent agreement with the simple theory (black solid line). The minimum error per gate of 0.007 ± 0.006 is reached at $\sigma = 1$ ns.

6.5 Chapter summary

In this chapter, we have demonstrated the critical starting requirements for a quantum information processor. Specifically, for the circuit QED system with transmon qubits, we have observed a lower bound on the average photon number in the system of 0.003, corresponding to an initial ground state polarization of the qubit of over 0.9999. Furthermore, through various gate error characterization techniques combined with optimized pulse-shaping protocols, we have benchmarked single-qubit gates to $\sim 1\%$ errors. While initialization and single-qubit operations are necessary, they are also not sufficient for quantum computing. The next chapters will explore the expansion of the circuit QED architecture to two qubits and the prospects of the cavity bus for coupling and generating entanglement will be determined.

Two-Qubit Circuit QED: Riding the Quantum Bus

WITH universality of quantum computing (section 2.1) dictating the need for a two-qubit entangling gate, we now expand the circuit QED architecture from a robust single-qubit system to one with two qubits. Although single-qubit gates are now ubiquitous across most superconducting qubit implementations, operations on and the coupling of multiple qubits are still a subject of ongoing research. Specifically, for flux qubits, two-qubit coupling [128] and a controllable coupling mechanism have been realized [70, 72, 129]. Two phase qubits have also been successfully coupled [130] and the entanglement between them has been observed [67]. However, all of these interactions have been realized by connecting qubits via lumped circuit elements (section 3.2), with capacitive coupling (section 3.2.1) in the case of charge and phase qubits, and inductive coupling (section 3.2.2) for flux qubits. Therefore, these coupling mechanisms have been restricted to local interactions and couple only nearest neighbor qubits.

Performing gates between an arbitrary pair of distant qubits is highly desirable for a scalable quantum computer architecture. An efficient way to achieve this goal is to couple the qubits to a quantum bus (section 3.2.3), which distributes quantum information among the qubits. The primary requirement for a quantum bus architecture is to have a quantum degree of freedom which can interact strongly with independent quantum systems for storage or transfer of information. There are several physical systems in which one could realize a

quantum bus. A particular example is trapped ions [13, 14] in which a variety of quantum operations and algorithms have been performed using the quantized motion of the ions (phonons) as the bus. Photons are another natural candidate as a carrier of quantum information [131, 132], because they are highly coherent and can mediate interactions between distant objects. To create a photon bus, it is helpful to utilize the increased interaction strength provided by the techniques of cavity quantum electrodynamics (section 3.3), where an atom is coupled to a single cavity mode. In the strong coupling limit (section 3.3.1) the interaction is coherent, permitting the transfer of quantum information between the atom and the photon. Such a photon bus has led to the generation of entanglement between atoms using a Rydberg atom cavity QED [133–135] experiment.

Circuit QED as previously described (section 3.4) is a realization of the physics of cavity QED with superconducting qubits and a microwave cavity on a chip. Here in this chapter, we will show the first implementation of a quantum bus in circuit QED, using microwave photons confined in a transmission line cavity, to couple two superconducting qubits on opposite sides of a chip. Instead of providing a lumped element coupling, the cavity behaves as a distributed circuit element permitting long-range quantum interaction which need not be nearest-neighbor. Section 7.2 will detail the coupling of two qubits to the microwave cavity. A two-qubit interaction (section 7.2.1) is mediated by the exchange of virtual rather than real photons over the bus, with the added benefit of avoiding direct loss through the cavity. Then, in section 7.4 we show the ability to use an ac-Stark interaction for fast control of the qubits to switch the coupling effectively on and off. Controlling both the individual qubits independently as well as the coupling interaction, we demonstrate coherent transfer of quantum states between the qubits. The same cavity which couples the qubits is also used to perform multiplexed control and measurement of the qubit states. The experiment presented in this chapter is a more detailed description of that described in Ref. [136] and reflects the combined efforts by myself and postdoc Johannes Majer. These results represent the first step for circuit QED in the direction of generating and detecting entanglement, and will serve as a useful springboard to the experiments presented in chapters 8 and 9 to immediately follow.

7.1 Experimental details

The cavity bus described in this chapter will refer to sample cQED₁₅₇, with fabrication details given in chapter 5. The sample and basic experimental schematic are shown in figure 7.1. The two superconducting transmon qubits are 5 mm apart at opposite ends of the superconducting

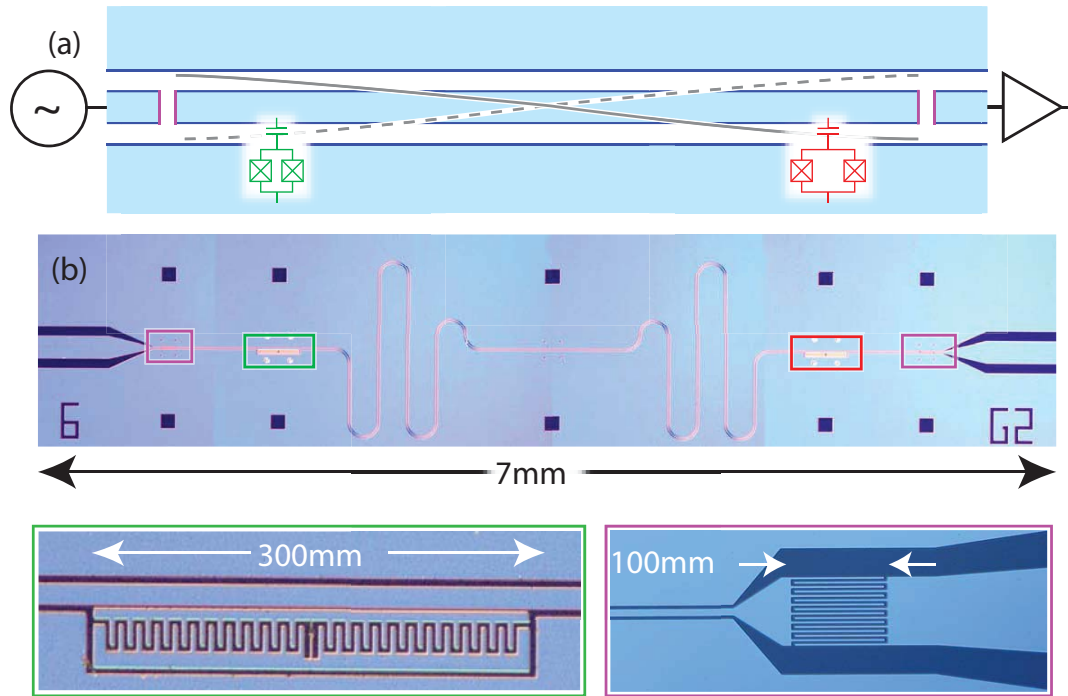


Figure 7.1: Sample and scheme used to couple two qubits to an on-chip microwave cavity. Circuit (a) and optical micrograph (b) of the sample, cQED₁₅₇, with two transmon qubits coupled by a microwave cavity. The cavity is formed by a coplanar waveguide (light blue) interrupted by two coupling capacitors (purple). The resonant frequency of the cavity is $\omega_C/2\pi = 5.22$ GHz and its width is $\kappa/2\pi = 33$ MHz. The output coupling capacitor is shown in the purple inset. The cavity is operated as a half-wave resonator ($L = \lambda/2 = 12.3$ mm) and the electric field in the cavity is indicated by the gray line. The two transmon qubits are located at opposite ends of the cavity where the electric field has an antinode. Each transmon qubit consists of two superconducting islands connected by a pair of Josephson junctions and an extra shunting capacitor (interdigitated finger structure in the green inset). The microwave signals enter the chip from the left, and the response of the cavity is amplified and measured on the right.

coplanar waveguide resonator ($\omega_C/2\pi = 5.22$ GHz, $\kappa/2\pi = 33$ MHz). Recalling the transition frequency of the transmon qubits from (3.17), the split-pair of Josephson junctions give an external flux tunable Josephson energy, $E_J = E_J^{\max} |\cos(\pi\tilde{\Phi}/\Phi_0)|$. The external magnetic flux $\tilde{\Phi}$ is applied with a superconducting magnet in the cryostat to tune both qubit transition energies. Recall that for this sample, we designed the size of the two loops to be different and incommensurate by a factor of approximately 5/8, so that control of the two transition frequencies is attainable with a certain degree of independence. The left qubit (qubit 1, color coded green) has a charging energy of $E_{C1}/h = 424$ MHz and maximum Josephson energy

of $E_{J1}^{\max}/h = 14.9$ GHz. The right qubit (qubit 2, color coded red) has a charging energy of $E_{C2}/h = 442$ MHz and maximum Josephson energy of $E_{J2}^{\max}/h = 18.9$ GHz.

7.2 Two-qubit spectroscopy

We can demonstrate strong coupling of each of the qubits separately to the cavity bus by varying the externally applied magnetic flux, until each of the two qubits are tuned into resonance with the cavity as shown in figure 7.2. This experiment involves applying a single microwave excitation tone continuously, and we monitor the transmitted homodyne voltage amplitude while sweeping the frequency of the applied tone. With both of the qubits not excited, we see only a single peak in the measured homodyne signal, following a Lorentzian lineshape centered at the cavity frequency. However, the qubit transition frequencies can be tuned into resonance with the cavity using the external magnetic flux. In figure 7.2, we observe vacuum Rabi splittings (section 3.3.1) of both qubits with the cavity, indicating that each qubit can in fact reach the strong coupling limit with the cavity. Theoretically determined frequencies for the left and right qubit are shown in the green and red dashed lines, respectively. The experimentally determined frequencies follow the theoretical flux dependence of the Josephson energy and allows us to extract the magnetic field corresponding to Φ_0 for each of the qubits. In the vacuum Rabi splitting, each of the peaks corresponds to a superposition of qubit excitation and a cavity photon in which the energy is shared between the two systems. Furthermore, from the frequency difference at the maximal splitting for each qubit, the coupling parameters $g^{(1),(2)}/\pi \approx 105$ MHz can be determined.

In the dispersive limit, both qubits are detuned from the resonator such that

$$|\Delta^{(1),(2)}| = |\omega^{(1),(2)} - \omega_C| \gg g^{(1),(2)}. \quad (7.1)$$

Recall from chapter 4, that in this limit, we can use second order perturbation theory to describe the full system with the two qubits and the cavity with the effective Hamiltonian:

$$H_{\text{eff}} = \frac{\hbar\omega^{(1)}}{2}\sigma_z^{(1)} + \frac{\hbar\omega^{(2)}}{2}\sigma_z^{(2)} + \hbar\left(\omega_C + \chi^{(1)}\sigma_z^{(1)} + \chi^{(2)}\sigma_z^{(2)}\right)a^\dagger a + \hbar J\left(\sigma_-^{(1)}\sigma_+^{(2)} + \sigma_-^{(2)}\sigma_+^{(1)}\right). \quad (7.2)$$

In this regime, no energy is exchanged with the cavity. However, the qubits and cavity are still dispersively coupled, resulting in a qubit-state-dependent shift $\pm\chi^{(1),(2)}$ of the cavity frequency

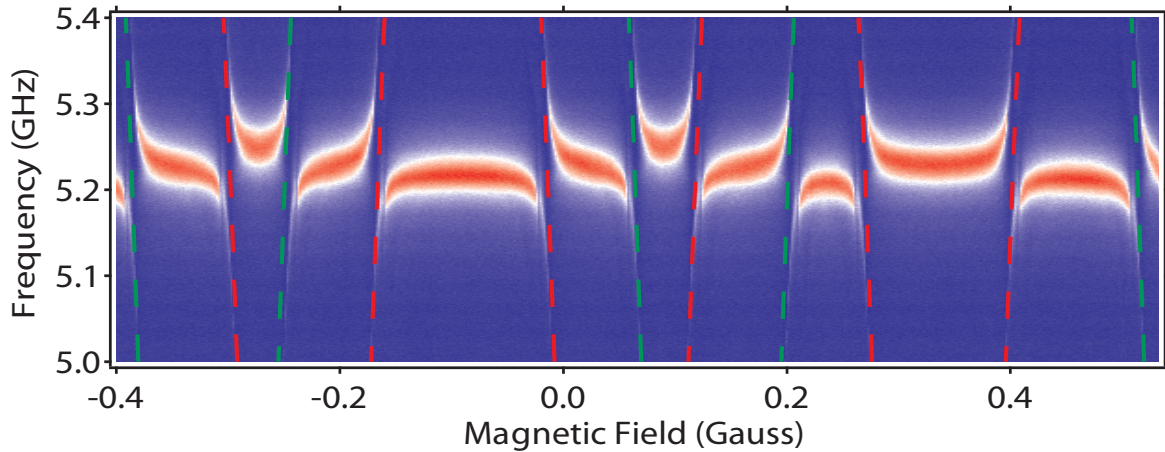


Figure 7.2: Strong coupling of two superconducting qubits. Density plots of the transmission as a function of drive frequency and magnetic field. Blue (red) indicates low (high) transmission. When the qubits are far detuned from the cavity frequency $\omega_C = 5.22$ GHz, there is a single peak in transmission, as is seen in at -0.1 Gauss. However, by tuning the global external flux, the qubit frequencies can be tuned into resonance with the cavity, and we can observe avoided crossings with the cavity. When exactly on resonance, the cavity peak is split into two vacuum Rabi peaks, from which the qubit-cavity coupling strengths are determined.

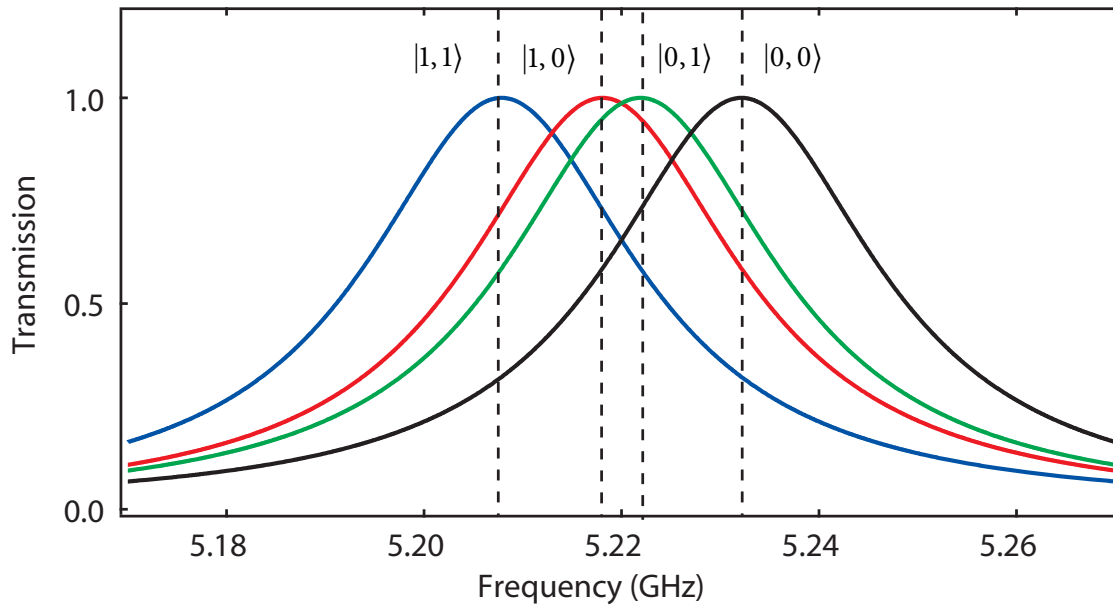


Figure 7.3: Dispersive shifts of the cavity. In the dispersive regime, the bare cavity transmission is shifted to four frequencies depending on the state of the two qubits ($|1, 1\rangle$ in blue, $|0, 1\rangle$ in red, $|1, 0\rangle$ in green, $|0, 0\rangle$ in black). Here, we show simulated Lorentzians with $\kappa/2\pi = 33$ MHz and $\chi^{(1)} = 7$ MHz and $\chi^{(2)} = 5$ MHz. Measurements are generally performed by looking at transmission corresponding to the $|0, 0\rangle$ in black.

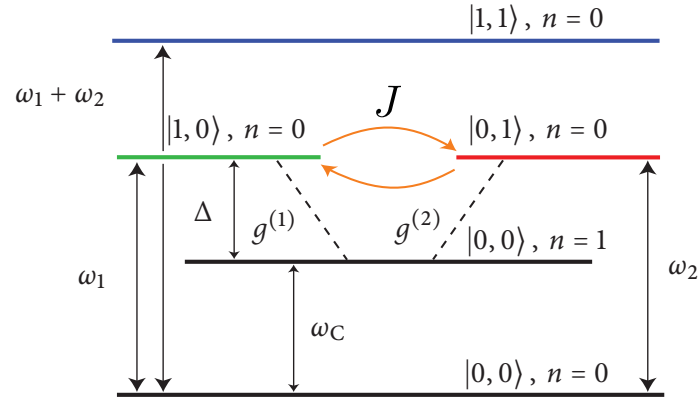


Figure 7.4: Scheme of the virtual photon swap interaction. When the qubits are detuned from the cavity ($|\Delta^{(1),(2)}| \gg g^{(1),(2)}$) the qubits both dispersively shift the cavity. The excited state in the left qubit $|10\rangle \otimes |n=0\rangle$ interacts with the excited state in the right qubit $|01\rangle \otimes |n=0\rangle$ via the exchange of a virtual photon $|00\rangle \otimes |n=1\rangle$ in the cavity.

(see figure 7.3) or equivalently an ac Stark shift of the qubit frequencies (section 4.2.4). The frequency shift $\chi^{(1),(2)}$ can be calculated from the detuning $\Delta^{(1),(2)}$ and the measured coupling strength $g^{(1),(2)}$ (3.45). The last term describes the interaction between the qubits, which is a transverse exchange interaction of strength $J = g^{(1)}g^{(2)}(1/\Delta^{(1)} + 1/\Delta^{(2)})/2$. The qubit-qubit interaction (section 4.3.2) is a result of virtual exchange of photons with the cavity. When the qubits are degenerate with each other, an excitation in one qubit can be transferred to the other qubit by virtually becoming a photon in the cavity (see figure 7.4). However, when the qubits are non-degenerate $|\omega^{(1)} - \omega^{(2)}| \gg J$ this process does not conserve energy, and therefore the interaction is effectively turned off. Thus, instead of modifying the actual coupling constant [70, 72, 129], we control the *effective* coupling strength by tuning the qubit transition frequencies. This is possible since the qubit-qubit coupling is transverse (section 2.3.3), which also distinguishes our experiment from the situation in liquid-state NMR quantum computation, where an effective switching-off can only be achieved by repeatedly applying decoupling pulses [137].

We can observe the coherent interaction between the two qubits via the cavity by performing spectroscopy of their transition frequencies (see figure 7.5). Spectroscopy is a dual microwave tone experiment. A measurement tone is applied continuously at the cavity transmission corresponding to both qubits being in their ground states, while a second tone is swept in frequency away from the cavity frequency to probe for the qubit transitions. As long as the qubit is in the dispersive regime, there is a dispersive cavity shift which depends on the state of the qubit (section 3.4.2). If the probe microwave signal is resonant with the qubit

transition, the qubit state will be driven to a mixed state of $|0\rangle$ and $|1\rangle$. This is the result of the probe signal being on continuously and the T_1 relaxation process of the qubit when it is in the excited state. Therefore, when the drive is resonant with the qubit, the transmission at the cavity transmission frequency ω_C is reduced due to the state of the qubit, shifting the transmission to the frequency $\omega_C + \chi$. This homodyne voltage is detected and can be displayed as a function of the drive frequency to produce spectroscopy maps of the qubit transition frequencies while also varying the applied external magnetic flux.

7.2.1 Qubit-qubit avoided crossing

Varying the external magnetic flux $\tilde{\Phi}$, we spectroscopically observe a map of the two qubit transitions, as shown in figure 7.5. We can overlay the theoretical calculation for the transition frequencies (3.17). By varying $\tilde{\Phi}$, we find that it is possible to tune the qubits through resonance with each other (see figure 7.5b), revealing an avoided crossing. This reflects the virtual-photon swap interaction (section 4.3.2). The magnitude of the splitting agrees well with the theoretical value $2J = 2g^{(1)}g^{(2)}/\Delta = 2\pi \cdot 26$ MHz when one takes into account that $g^{(1),(2)}$ vary with frequency for a transmon qubit [61]. The splitting is well resolved, with a magnitude J much greater than the qubit line widths, indicating both a coherent coupling and that the qubits are in the strong dispersive limit [110]. Note that although the coupling strength J is smaller than the cavity decay rate $\kappa/2\pi \sim 33$ MHz, the avoided crossing is nearly unaffected by the cavity loss. This is possible in such a large- κ cavity, required for fast measurements, because only virtual photons are exchanged; if real photons were used, the cavity induced relaxation of the qubits (see Purcell effect section 3.5.1 and [82]) would make coherent state transfer unfeasible.

7.2.2 The dark state

Another manifestation of the coherence of this interaction is the observation of a dark state. There is a disappearance of one of the spectroscopy peaks near the avoided crossing point, which is due to destructive interference associated with the fact that the qubits are separated by half a wavelength. This effect is a result of the physical location of the qubits, being on opposite ends of the $\lambda/2$ microwave cavity. Recall from that an applied microwave drive tone takes the form

$$H_{\text{drive}} = (a + a^\dagger) (\xi e^{-i\omega_{\text{dt}}} + \xi^* e^{i\omega_{\text{dt}}}), \quad (7.3)$$

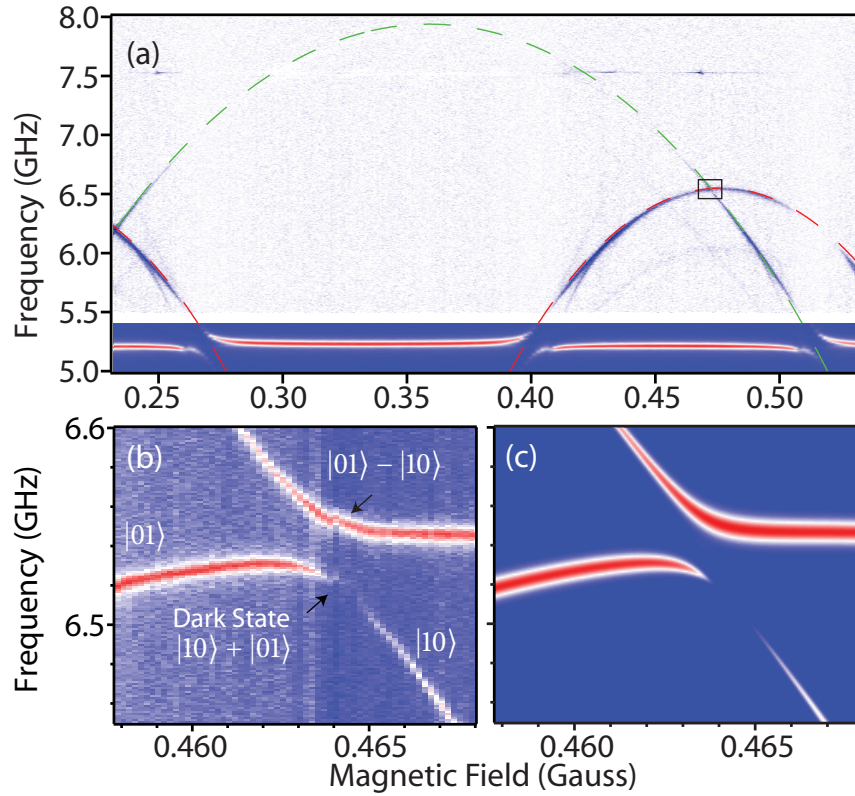


Figure 7.5: Two qubit spectroscopy. Cavity transmission and spectroscopy of single and coupled qubits. (a) The transmission through the cavity as a function of applied magnetic field is shown in the frequency range between 5 GHz and 5.4 GHz. When either of the qubits is in resonance with the cavity, the cavity transmission shows an avoided crossing due to the vacuum Rabi splitting. Above 5.5 GHz, spectroscopic measurements of the two qubit transitions is shown. The density plot reflects the change in transmission of a probe signal on resonance with the cavity transmission when both qubits are in the ground state. The dashed lines show the resonance frequencies of the two qubits, which are a function of the applied flux according to $\omega^{(1),(2)} = \omega_{\max}^{(1),(2)} \sqrt{|\cos(\pi\tilde{\Phi}/\Phi_0)|}$. The maximum transition frequency for the first qubit is $\omega_{\max}^{(1)}/2\pi = 7.8$ GHz and for the second qubit is $\omega_{\max}^{(2)}/2\pi = 6.45$ GHz. For strong drive powers, additional resonances between higher qubit levels are visible. (b) Spectroscopy of the two-qubit crossing. The qubit levels show a clear avoided crossing with a minimal distance of $2J/2\pi = 26$ MHz. At the crossing the eigenstates of the system are symmetric and anti-symmetric superpositions of the two qubit states. The spectroscopic drive is anti-symmetric and therefore unable to drive any transitions to the symmetric state, resulting in a dark state. (c) Predicted spectroscopy at the qubit-qubit crossing using a Markovian master equation that takes into account higher modes of the cavity.

where the ω_d is the drive frequency and ξ is the drive strength. Hidden in this drive Hamiltonian is the voltage of the cavity, $V_0(a + a^\dagger)$, where the V_0 has been absorbed into ξ . This is an important subtlety however, that the drive is in fact a capacitive coupling between the voltage mode of the cavity and that of a drive cavity which remains in a highly-excited coherent state [62]. For the particular arrangement of the qubits being located on opposite ends of the sample, the voltage which couples to the two qubits will be different. Specifically, since we drive the cavity with a $\lambda/2$ mode, the electric field at the different ends will have opposite signs. Therefore, the voltage seen by the left qubit near the input port will be $V_0(a + a^\dagger)$, whereas the voltage at the right qubit near the output port will be $-V_0(a + a^\dagger)$. This extra negative sign means that the drive (with similar treatment of assuming RWA and dispersive limit as in section 7.2.2) will now take the form

$$H_{\text{drive}} = \sigma_x^{(1)} \frac{2g^{(1)}\xi}{\omega^{(1)} - \omega_d} - \sigma_x^{(2)} \frac{2g^{(2)}\xi}{\omega^{(2)} - \omega_d}. \quad (7.4)$$

When performing spectroscopy, both qubits start out in the ground state, $|00\rangle$. The action of this drive on the ground state will then be

$$H_{\text{drive}} |0, 0\rangle = 2\xi \left(\frac{g^{(1)}}{\Delta_d^{(1)}} |1, 0\rangle - \frac{g^{(2)}}{\Delta_d^{(2)}} |0, 1\rangle \right), \quad (7.5)$$

where $\Delta_d^{(1),(2)}$ are the detunings for the qubits from the drive $\omega^{(1),(2)} - \omega_d$.

At the avoided crossing, the eigenstates are superpositions of the single qubit states. In particular, the state with lower frequency is the symmetric triplet state $|+\rangle = (|0, 1\rangle + |1, 0\rangle)/\sqrt{2}$ and the state at higher frequency is the antisymmetric singlet state $|-\rangle = (|0, 1\rangle - |1, 0\rangle)/\sqrt{2}$. Therefore, when tuning to the avoided crossing, we can drive the two qubits with H_{drive} and compute the overlap with $|\pm\rangle$,

$$\langle 0, 1 + 1, 0 | H_{\text{drive}} | 0, 0 \rangle = \frac{g^{(1)}}{\Delta^{(1)}} - \frac{g^{(2)}}{\Delta^{(2)}} \quad (7.6a)$$

$$\langle 0, 1 - 1, 0 | H_{\text{drive}} | 0, 0 \rangle = \frac{g^{(1)}}{\Delta^{(1)}} + \frac{g^{(2)}}{\Delta^{(2)}}. \quad (7.6b)$$

For $g^{(1)} = g^{(2)}$, the symmetric state will be ‘dark’ when the two qubits are in resonance with each other in the sense that the drive will not make real transitions to the state. Moreover, for this state to not couple to the drive, means that it is in fact protected against decay through the cavity. Conversely, the decay from the anti-symmetric state is enhanced, similar to

super-radiant effects observed in atomic physics [138, 139]. Figure 7.5c shows the simulated spectroscopy at the qubit-qubit crossing, which reproduces all qualitative features of the measured data. The simulation is performed via a Markovian master equation which takes into account higher modes of the cavity and uses parameters such as $g^{(1),(2)}$ obtained from the vacuum Rabi data, κ , and coherence times T_1 and T_2 for both qubits near the resonance point.

The presence of the dark state thus reflects a spectroscopic verification of the coherent virtual-photon coupling of the two qubits. However, it would be even better to verify the coupling through time-domain experiments and observe the coherent swapping of states between the qubits. Yet to be able to perform that experiment, we need to lay the groundwork for the qubit readout.

7.3 Multiplexed joint qubit readout

In addition to acting as a quantum bus, the same cavity is also used for multiplexed readout and control of the two qubits. Here, “multiplexed” refers to acquisition of information or control of more than one qubit via a single channel.

To address the qubits independently, the flux is tuned such that the qubit frequencies are 88 MHz apart ($\omega^{(1)} = 6.617$ GHz, $\omega^{(2)} = 6.529$ GHz), making the qubit-qubit coupling negligible. Rabi driving experiments showing individual control are performed by applying an rf-pulse at the resonant frequency of either qubit, followed by a measurement pulse at the resonator frequency. The measured homodyne amplitude response (see figure 7.6 for driving each qubit) is consistent with that of a single qubit oscillation and shows no beating, indicating that the coupling does not affect single-qubit operations and readout.

With similar measurements the relaxation times (T_1) of the two qubits are determined to be 78 ns and 120 ns, and with Ramsey fringe measurements the coherence times (T_2) are found to be 120 ns and 160 ns. The T_1 times are consistent with the Purcell effect, as the cavity is relatively fast decaying with $\kappa/2\pi = 33$ MHz.

The ability to simultaneously readout the states of both qubits using a single line is demonstrated by measuring the cavity phase shift, proportional to $\chi^{(1)}\sigma_z^{(1)} + \chi^{(2)}\sigma_z^{(2)}$, after applying a π -pulse to one or both of the qubits. Figure 7.7 shows the response of the cavity after a π -pulse has been applied on the first qubit (green points), on the second qubit (red points) or on both qubits (blue points). For comparison the response of the cavity without any pulse applied (black points) is shown. Since the cavity frequency shifts for the two qubits

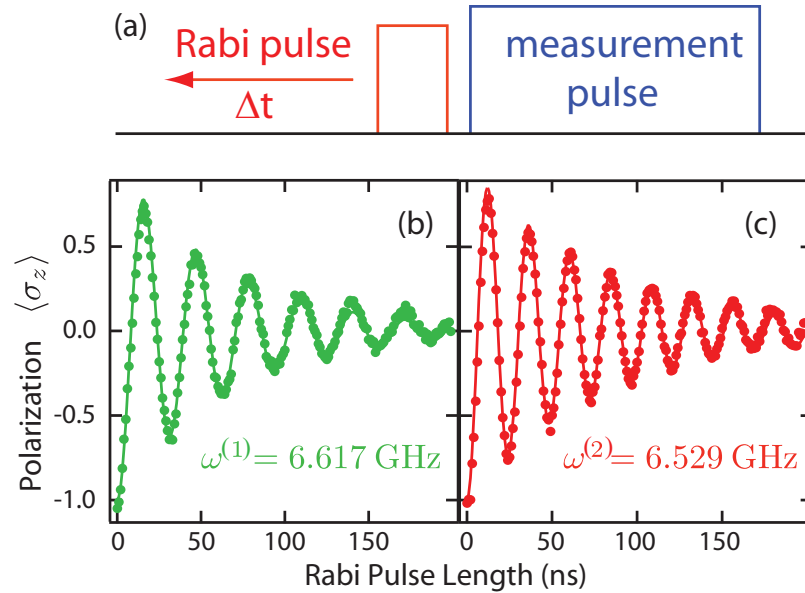


Figure 7.6: Independent Rabi driving of two qubits. (a) Pulse protocol for performing Rabi oscillations. The Rabi pulse is applied resonant to the qubit transition frequency for a varying duration of Δt . The response of the cavity transmission is measured after the pulse is turned off. Oscillations of quadrature voltages are measured for each of the qubits and mapped onto the polarization $\langle \sigma_{1,2}^z \rangle$. (b–c) Rabi oscillations of qubit 1 and qubit 2. The solid line shows results from a master equation simulation, which takes into account the full dynamics of the two qubits and the cavity. The absence of beating in both traces is a signature of the suppression of the qubit-qubit coupling at this detuning.

are different ($\chi^{(1)} \neq \chi^{(2)}$), we are able to distinguish the four states $|00\rangle$, $|01\rangle$, $|10\rangle$, and $|11\rangle$ of the qubits with a single readout line. Although not performed in this experiment due to the relaxation limited signal-to-noise ratio, the joint readout can be combined with single-qubit rotations to give a full reconstruction of the density matrix (state tomography as described in section 2.5.2).

The solid lines in figure 7.7 show the results from a theoretical calculation taking into account the full dynamics of the cavity and the two qubits, including the relaxation rates of the qubits. The agreement of the theory with the measured response shows that the measured contrast is the maximum expected. From the calculated values one can estimate the selectivity, i.e. the ability to address one qubit without affecting the other, $S = (P_a - P_u)/(P_a + P_u)$, where P_a and P_u are the maximum populations in the excited state of the addressed qubit and in the excited state of the unaddressed qubit, respectively. The selectivity for qubit 1 is 87 % and qubit 2 is 94 %, which indicates good individual control of the qubits.

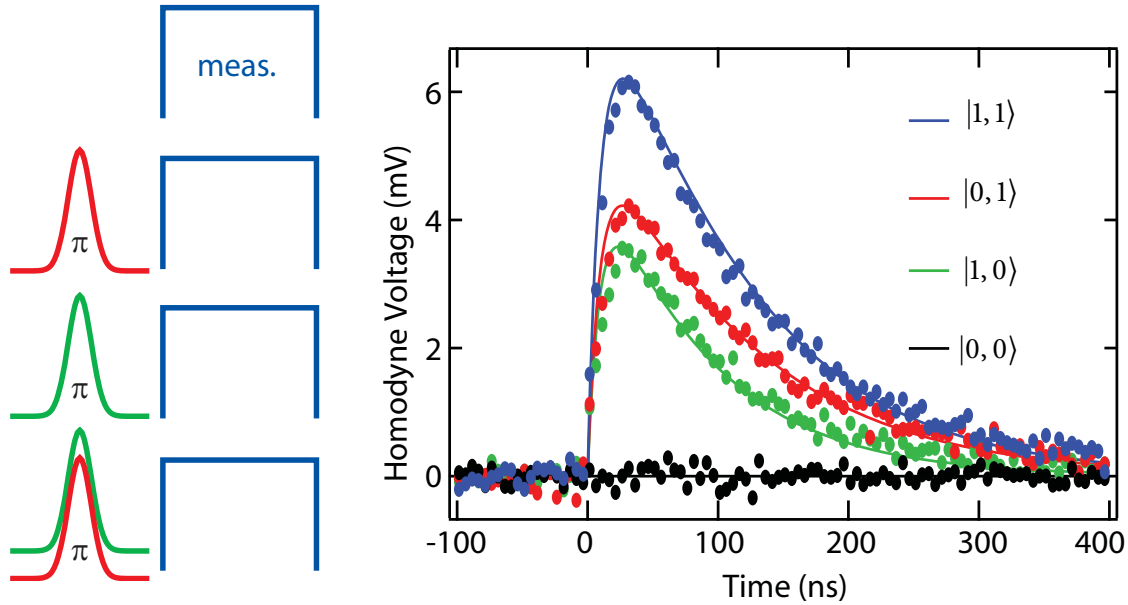


Figure 7.7: Two qubit multiplexed readout. Pulse schemes shown on the left for preparing the four different states and then performing a homodyne measurement. The homodyne response (average of 1,000,000 traces) of the cavity after a π pulse on qubit 1 (green), qubit 2 (red), and both qubits (blue). The black trace shows the level when no pulses are applied. The contrasts (i.e. the amplitude of the pulse relative to its ideal maximum value) for these pulses are 60% (green), 61% (green) and 65% (blue). The solid line shows the simulated value including the qubit relaxation and the turn-on time of the cavity. The agreement between the theoretical prediction and the data indicates the measured contrast is the maximum observable. From the theoretical calculation one can estimate the selectivity for each π -pulse to be 87% (qubit 1) and 94% (qubit 2). This figure of merit is not at all intrinsic and that it could be improved by increasing the detuning between the two qubits for instance, or using shaped excitation pulses.

7.4 Coherent state transfer: Stark swap

Although the spectroscopy (figure 7.5b) suggests a coherent qubit-qubit interaction through the avoided crossing and the presence of the dark state, we would like to observe the interaction in the time-domain. We can perform coherent state transfer, or qubit state swap, in the time-domain if we can turn the effective qubit-qubit coupling on and off, rapidly, on time-scales corresponding to the decoherence times of the two qubits.

The simplest protocol to think of is to use the external magnetic flux to pulse into the avoided crossing of figure 7.5b. However, in this implementation of the experiment, the flux tunability is achieved through ramping a common superconducting coil within the cryostat. The time-constant for ramping such a large magnet is too long to drive coherent interactions and achieve single-qubit operations before the qubits decohere.

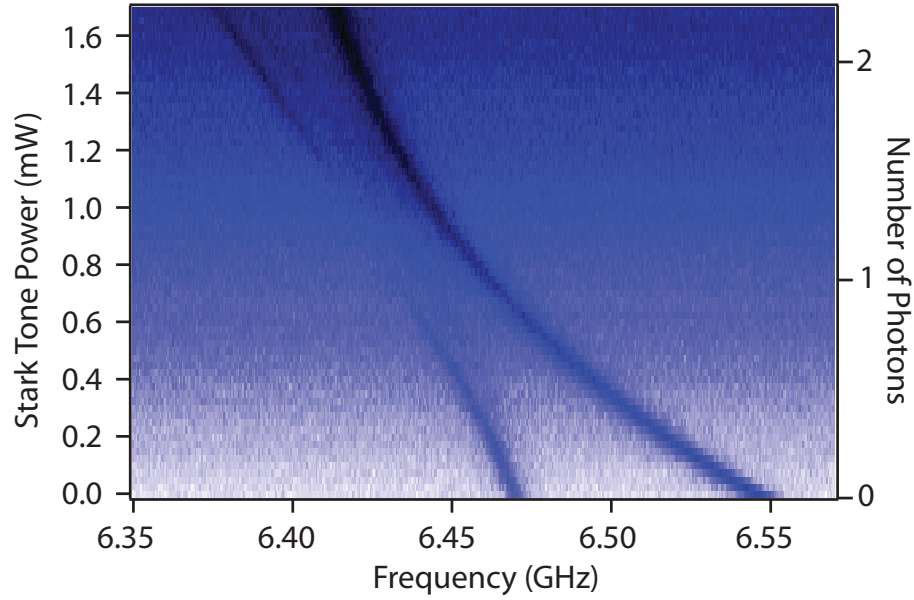


Figure 7.8: Two qubit Stark shift spectroscopy. Spectroscopy of qubits versus applied Stark tone power. Taking into account an attenuation of 67 dB before the cavity and the filtering effect of the cavity, 0.77 mW corresponds to an average of one photon in the resonator. The qubit transition frequencies (starting at $\omega^{(1)}/2\pi = 6.469$ GHz and $\omega^{(2)}/2\pi = 6.546$ GHz) are brought into resonance with a Stark pulse applied at 6.675 GHz. An avoided crossing is observed with one of the qubit transition levels becoming dark as in figure 7.5b.

As a result, rather than the slow flux tuning, we now make use of a strongly detuned rf-drive[91], which results in an off-resonant Stark shift (section 4.2.4) of the qubit frequencies on the nanosecond time scale. To see how this works, consider re-writing the dispersive two-qubit Hamiltonian as

$$H_{\text{eff}} = \frac{\hbar}{2}(\omega^{(1)} + \chi^{(1)} a^\dagger a) \sigma_z^{(1)} + \frac{\hbar}{2}(\omega^{(2)} + \chi^{(2)} a^\dagger a) \sigma_z^{(2)} + \hbar \omega_C a^\dagger a + \hbar J (\sigma_-^{(1)} \sigma_+^{(2)} + \sigma_-^{(2)} \sigma_+^{(1)}). \quad (7.7)$$

Although details of the ac Stark effect are given previously in section 4.3.2, here with a quick glance at the Hamiltonian, we see that the an applied drive changes the number of photons and thus shifts the effective qubit frequencies.

We can perform a spectroscopy experiment starting with the two qubits separated in frequency and observe the shift of the lines as a function of increasing the power of an off-resonant Stark drive. With the qubits originally tuned to 6.47 GHz and 6.55 GHz, and placing a drive tone at 6.675 GHz, we spectroscopically detect the Stark shift of both qubits

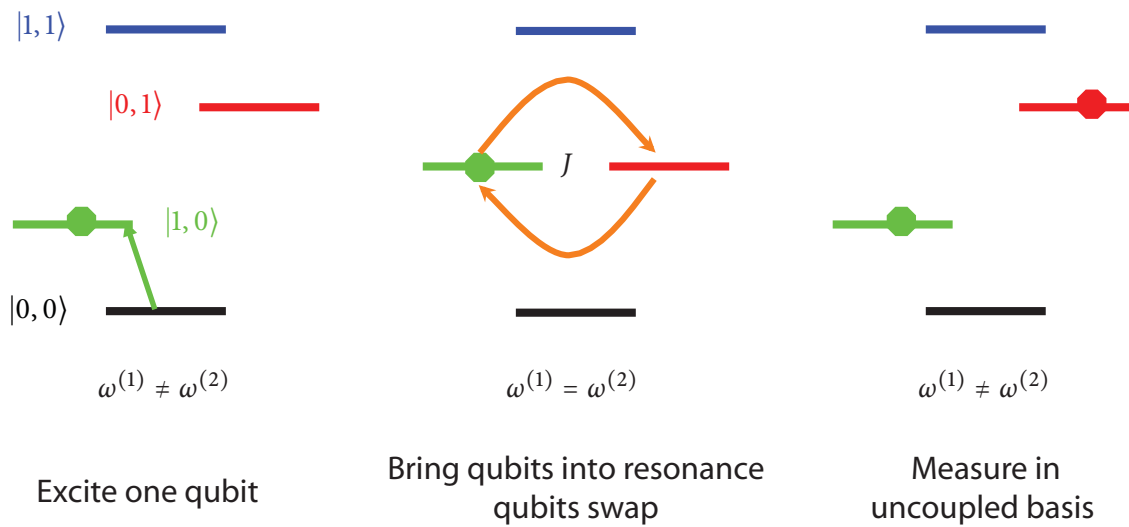


Figure 7.9: Coherent swap protocol. Three step process for performing coherent swaps.

figure 7.8. The qubit frequencies are pushed into resonance and a similar avoided crossing is observed as in figure 7.5. The avoided crossing of the two qubits is possible even though the cavity couplings of each qubit, $g^{(1)}$ and $g^{(2)}$, are equal as a result of the difference in detuning between the qubit transition frequencies from the Stark drive frequency.

With the Stark drive's ability to quickly tune the qubits into resonance, it is possible to observe coherent oscillations between the qubits, using the following protocol (see figure 7.9):

1. Initially the qubits are 80 MHz detuned from each other, where their effective coupling is small, and they are allowed to relax to the ground state $|0,0\rangle$.
2. Next, a π -pulse is applied to one of the qubits to either create the state $|1,0\rangle$ or $|0,1\rangle$.
3. Then, a Stark pulse of power P_{AC} is applied bringing the qubits into resonance for a variable time Δt . Since $|1,0\rangle$ and $|0,1\rangle$ are not eigenstates of the coupled system, oscillations between these two states occur, as shown in figure 7.10.

The power of the Stark pulse P_{AC} can be varied, mapping out the same $2J$ interaction but in a time-sensitive way. The resulting oscillations for various P_{AC} is plotted in the map shown in figure 7.10b. Figure 7.11b shows the extracted frequency of these oscillations for different powers P_{AC} of the Stark pulse, which agrees with the spectroscopy measurement of the frequency splitting observed in figure 7.8. Furthermore, we observe the anti-correlation between the swap oscillations when initially applying the π pulse on either qubit 1 or qubit 2, as evidenced by the red and green traces of figure 7.10. These data provide strong evidence

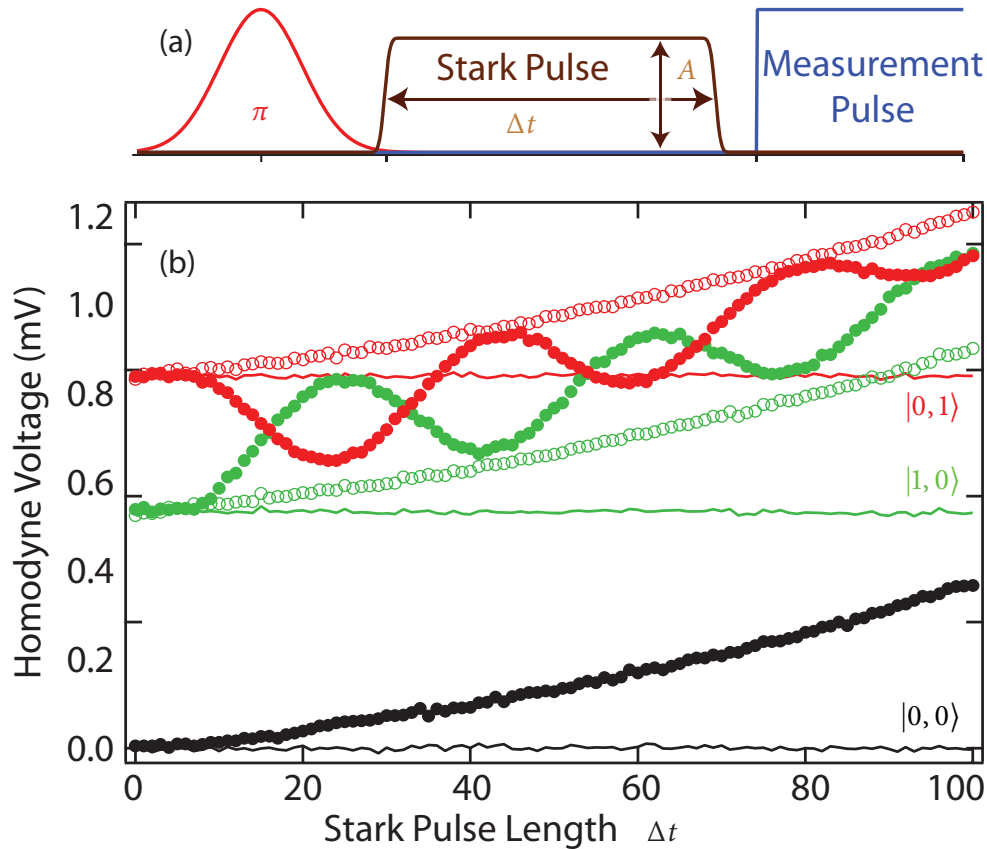


Figure 7.10: Coherent state exchange. (a) Pulse protocol for the coherent state transfer using the Stark shift. The pulse sequence consists of a Gaussian-shaped π pulse (red) on one of the qubits at its transition frequency $\omega_{1,2}$ followed by a square-shaped Stark pulse (brown) of varying duration Δt and amplitude A detuned from the qubits, and finally a square measurement pulse (blue) at the cavity frequency. The time between the π pulse and the measurement is kept fixed at 130 ns. (b) Coherent state transfer between the qubits according to the protocol above. The plot shows the measured homodyne voltage (average of 3,000,000 traces) with the π pulse applied to qubit 1 (green dots) and to qubit 2 (red dots) as a function of the Stark pulse length Δt . For reference, the black dots show the signal without any π pulse applied to either qubit. The overall increase of the signal is caused by the residual Rabi driving due to the off-resonant Stark tone, which is also reproduced by the theory. Improved designs featuring different coupling strengths for the individual qubits could easily avoid this effect. The thin solid lines show the signal in the absence of a Stark pulse. Adding the background trace (black dots) to these, we construct the curves consisting of open circles, which correctly reproduce the upper and lower limits of the oscillating signals due to coherent state transfer.

that the oscillations are due to the coupling between the qubits and that the state of the qubits is transferred from one to the other.

A quarter period of these oscillations should correspond to a $\sqrt{i\text{SWAP}}$, which would

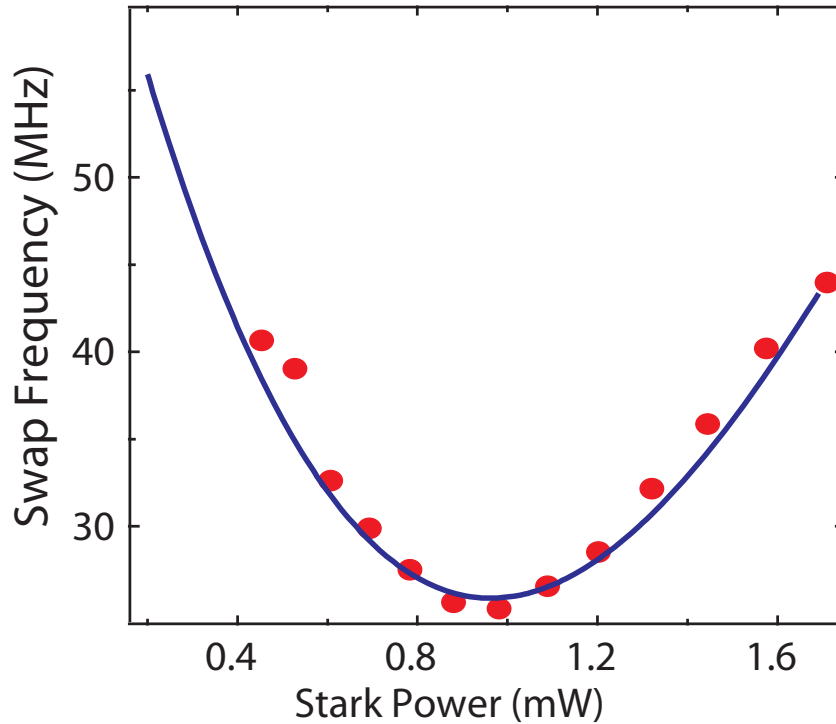


Figure 7.11: Stark swap frequency. By repeating the Stark swap protocol for various powers P_{AC} , we are able to extract the frequency of the oscillations (red points) and map out the same avoided crossing with splitting $2J$ as in figure 7.8, which is shown in the solid blue curve.

be a universal gate (section 2.3.3). However, the short coherence times of this sample make concatenation of a two-qubit $\sqrt{i\text{SWAP}}$ with single-qubit operations difficult. In order to experimentally generate entangled states and characterize an interaction gate, better qubit coherence is necessary.

One significant error which can be seen in the experiments shown in figure 7.10b is the positive slope of the oscillations. The black curve represents a control experiment in which both qubits are kept in the ground states and only the Stark pulse is turned on. The slope is evident there as well, without any oscillations. A similar effect is in fact seen in the Stark shift spectroscopy map of figure 7.8, as a gradient in the measured homodyne amplitude can be seen in the background as the Stark drive power is increased. This effect is most likely attributed to a power-dependent shift of the cavity resonance. The increased Stark drive, despite being off-resonant from the cavity, will at large enough powers begin to Stark shift the cavity frequency, such that the transmission of the measurement drive which is locked to the starting cavity frequency is reduced during the experiment.

7.5 Chapter summary

The observed qubit-qubit avoided crossing and the coherent state transfer demonstrate that the cavity in a circuit QED system can act as a coupling bus for superconducting qubits. The interaction is coherent and effectively switchable, as evidenced by the avoided crossing in spectroscopy and the ability to coherently swap in the time-domain. Furthermore, the coupling is long range and could possibly be extended to non-nearest neighbors. By operating in the dispersive regime of cavity QED, the qubit interactions are protected against loss in the bus by the use of virtual photons. The direct improvements which are necessary to take a leap ahead towards generating and detecting entangled states are improved coherence times and an improved method of turning on and off the interaction. The coherence times of the sample studied in this experiment were multi-mode Purcell limited [82]. By reducing the cavity linewidth, the loss of polarization via spontaneous emission would be reduced. Furthermore, although the Stark shift is a creative way of turning the qubit-qubit interaction on and off, a better option would be to directly tune the flux, which we can hope to achieve with high-bandwidth on-chip flux bias. The next two chapters will detail our extension of the experiment described in this chapter, implementing the two aforementioned changes, and cementing the circuit QED architecture as a simple but viable quantum information processor.



Entanglement On-Demand and Joint Readout

ENTANGLEMENT, non-classical correlations between qubits, is often seen as being a critical resource for experimental progress in quantum information science. Although its role in generating speed-up in quantum computers over classical computers is still a subject of theoretical debate, experimental verifications of its ‘spooky’ behavior over large distances certainly support its importance in transmitting and storing quantum information. In the previous chapter (chapter 7), we demonstrated the first steps towards entangling two superconducting qubits via a cavity bus. Furthermore, we could see the possibility to employ the same bus which provides the interaction to act as a multiplexed readout of the two qubit quantum state. Here, through the implementation of on-chip fast flux bias lines and improved qubit coherence times, we are able to take both of those experimental concepts of the circuit QED architecture a step further. First, in section 8.3 we present a new two-qubit interaction, tunable in strength by two orders of magnitude on nanosecond time scales, which is mediated by the cavity bus and relies on the higher excitation manifolds of the transmon qubits. Such an interaction leads to the generation of maximally entangled states, *i.e.* the four canonical Bell states (section 8.3.2).

However, the accurate and reliable detection of such quantum states and their degree of entanglement is itself a major necessity and nontrivial problem for quantum information systems. In any experiment one obtains information about the quantum system only through

the observation of the output from a detector, whose classical imperfections can introduce bias and noise. As a result, to make precise statements about intrinsic properties of quantum states, such as entanglement or purity (section 2.6), it is imperative to have a full understanding of the measurement process. In traditional quantum information processing architectures, such as those employing photons or trapped ions, the relationship between a quantum state and the quantities measured has been well established. In addition, the fidelity of single-shot measurements can in such cases be very high ($\sim 99.99\%$ for ions [140]). Consequently, the difficulties of calibration are minimized and the paradigm for correlation measurements [15, 16] is to record coincidences between individual detector ‘clicks’ and build statistics through repetition.

However, in the context of solid-state systems, the details of the measurement process itself are not fully understood and are an area of active research and recent progress. Single-shot individual qubit measurements have been technically challenging, and the readout fidelity is not yet as high as the fidelity of qubit operations ($\sim 98 - 99\%$ for single-qubit gates [108, 116]). Each individual readout channel can provide an additional path for decoherence and must also be calibrated. An example of the need for calibration is measurement cross-talk, which can be significant in circuit-based architectures [99], but has now been suppressed to the 0.5% level using an on-chip cavity as a filter [51]. Recently, the single-shot fidelity of independent readouts of superconducting qubits has also been improved [51, 141] to $\sim 95\%$.

Alluded to previously, our circuit QED architecture provides access to an intriguingly simple quadratic, or joint detector, where the measurement operator itself includes multi-qubit correlations. In the last chapter (chapter 7) we observed the first steps towards using the cavity as a joint qubit state detector. The coherence times in that experiment were unfortunately too low for the generating high purity separable and entangled states. In this chapter, we will show the full calibration and characterization of our joint detector and place bounds of 2% on systematic deviations from the ideal joint measurement (section 8.4). This is similar to determining the systematic errors, such as cross-talk [67], in individual readouts. We then employ the joint detector for two qubits to perform quantum state tomography for both separable states as well as highly entangled states, generated using the cavity bus two transmon interaction (section 8.6). Furthermore, we demonstrate a high degree of entanglement by measuring a large violation of a Clauser-Horne-Shimony-Holt inequality [47] in a solid-state system, with a value of 2.61 ± 0.04 , without optimizing for the target state (section 8.7). Although not a strict test of local-hidden variable theories, our CHSH

experiment serves as an entanglement witness and reflects the quality of both the separable and entangled states generated in our system.

8.1 Experimental setup

The experiments presented in this chapter all involve the sample cQED222, reflecting an improved design (chapter 5) of our standard multi-qubit circuit QED system. Although still containing two transmon qubits, cQED222 also has on-chip independent transmon flux tunability (section 5.3.3). This can be seen as an immediate improvement on the sample cQED157, described in the cavity bus experiments presented in chapter 7.

The sample, as shown in figure 8.1, is a 4-port superconducting device comprising two transmon qubits [61, 63] (which we will call Q_L , color-coded red, and Q_R , color-coded blue) inside a microwave cavity bus, and flux-bias lines proximal to each qubit. The cavity, normally off-resonance with the qubit transition frequencies f_L and f_R , couples the qubits by virtual photon exchange and shields them from the electromagnetic continuum. As previously discussed in chapter 7, microwave pulses resonant with f_L or f_R applied to the cavity input port provide frequency-multiplexed single-qubit x - and y -rotations with high fidelity [108] and selectivity [136]. Pulsed measurement of the homodyne voltage V_H on the cavity output port provides the joint qubit readout to be discussed later. The remaining two ports create local magnetic fields that tune the qubit transition frequencies. Each qubit has a split-pair of Josephson junctions, so its frequency is flux-tunable. By employing short-circuited transmission lines with a bandwidth from dc to 2 GHz, we can tune f_L and f_R by many GHz using room temperature voltages V_L and V_R (section 5.3.3).

Static tuning of qubit transitions using the flux-bias lines is demonstrated in figure 8.2. This spectrum of single excitations shows the essential features of the cavity-coupled two-qubit Hamiltonian and allows determination of relevant system parameters. Recall that the Jaynes-Cummings Hamiltonian generalized (section 4.3.1) to multi-level transmon qubits is

$$H = \omega_C a^\dagger a + \sum_{q \in \{L, R\}} \left(\sum_{j=0}^N \omega_{0j}^q |j\rangle_q \langle j|_q + (a + a^\dagger) \sum_{j,k=0}^N g_{jk}^q |j\rangle_q \langle k|_q \right). \quad (8.1)$$

Here, ω_C is the bare cavity frequency, $\omega_{0j}^q = \omega_{0j}(E_{Cq}, E_{Jq})$ is the transition frequency for qubit q from ground to excited state j , and $g_{jk}^q = g_q n_{jk}(E_{Cq}, E_{Jq})$, with g_q a bare qubit-cavity coupling and n_{jk} a level-dependent coupling matrix element. These parameters will depend on the qubit charging energy E_{Cq} and Josephson energy E_{Jq} . The flux control enters

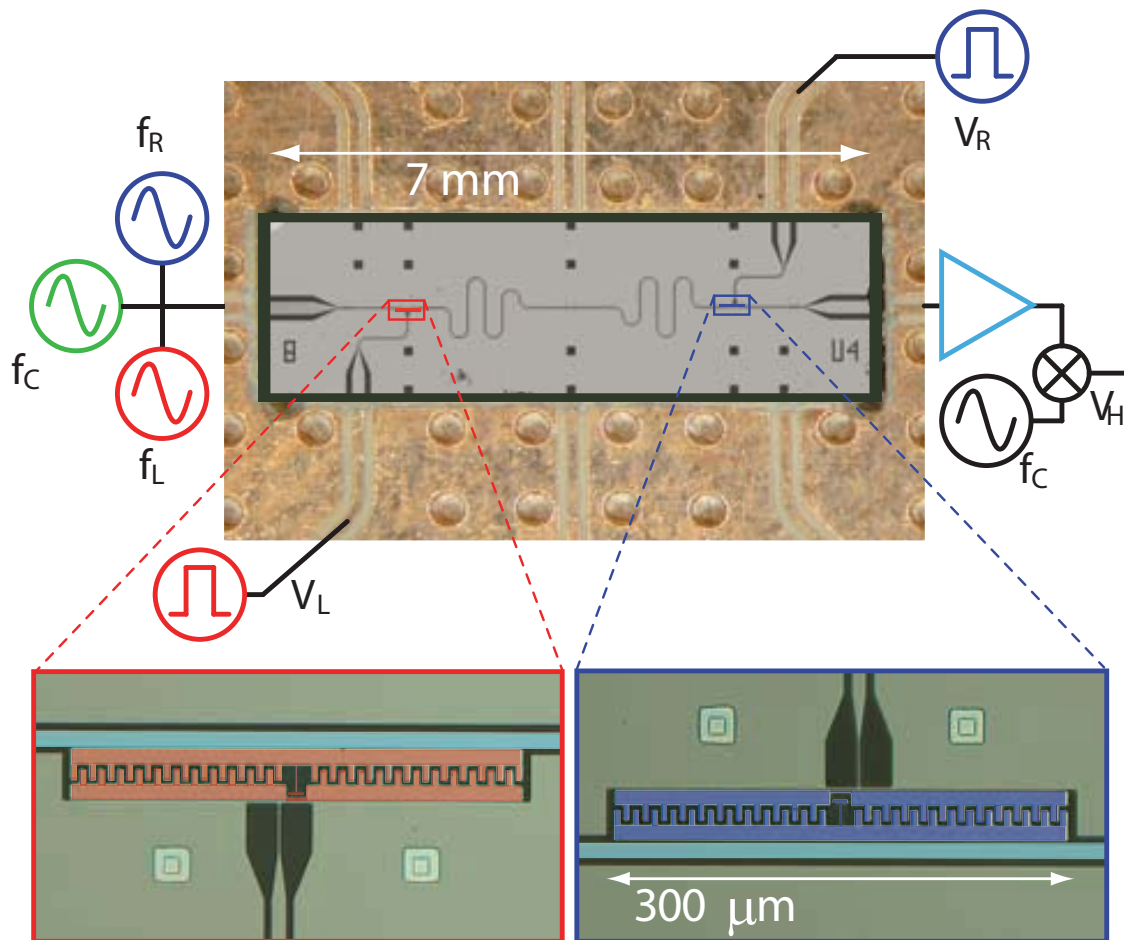


Figure 8.1: Schematic for two-qubit quantum bus with on-chip flux bias lines. Optical micrograph of 4-port device with a coplanar waveguide cavity bus coupling two transmon qubits (insets), and local flux-bias lines providing fast qubit tuning. Microwave pulses at the qubit transition frequencies f_L and f_R drive single-qubit rotations, and a pulsed measurement of the cavity homodyne voltage V_H (at frequency f_C) provides two-qubit readout. The flux-bias lines (bottom-left and top-right ports) are coplanar waveguides with short-circuit termination next to their target qubit. The termination geometry allows current on the line to couple flux through the split junctions.

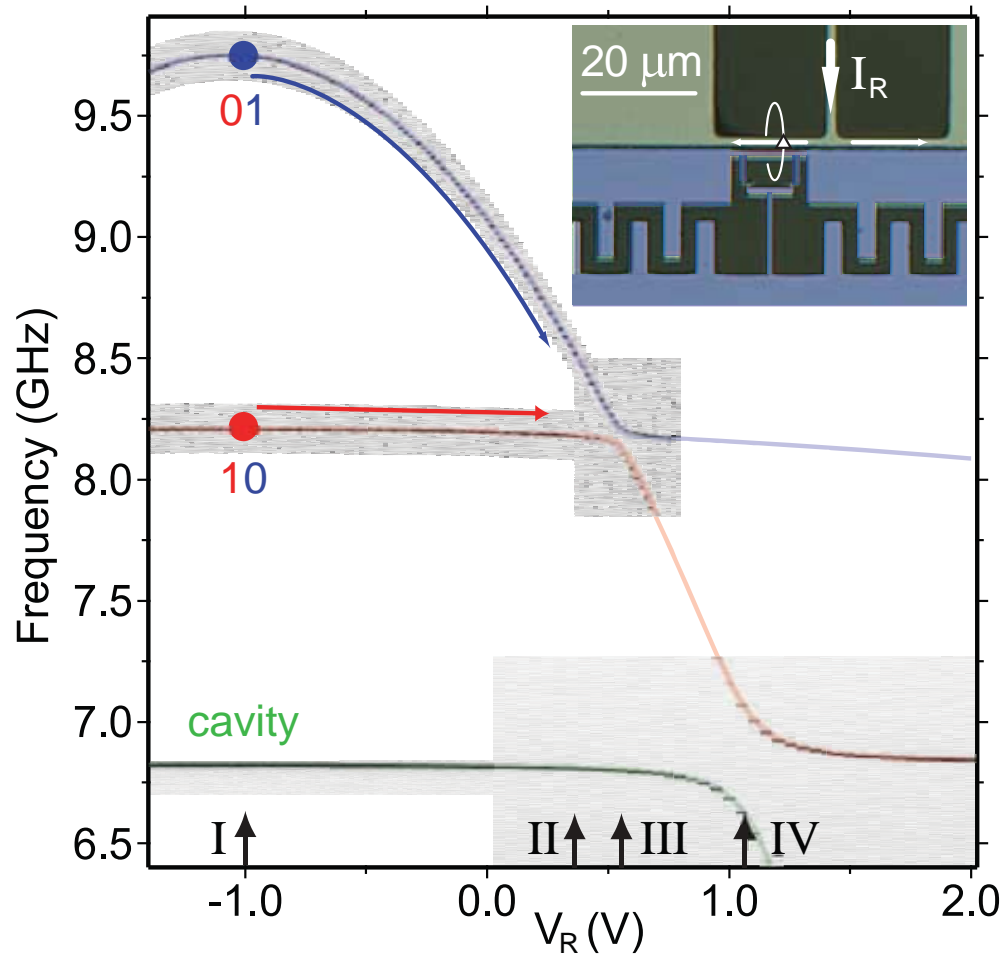


Figure 8.2: Single excitation spectroscopy. Grey scale images of cavity transmission and of qubit spectroscopy as a function of V_R , showing local tuning of Q_R across the avoided crossing with Q_L (point III) and across the vacuum Rabi splitting with the cavity (point IV). Semi-transparent lines are theoretical best fits obtained from numerical diagonalization of a generalized Jaynes–Cummings Hamiltonian. Preparation, single-qubit operations and measurements are performed at point I, and a c -Phase gate for generating two-qubit entanglement is achieved by pulsing into point II.

through $E_{Jq} = E_{Jq}^{\max} |\cos(\pi\Phi_q/\Phi_0)|$, with Φ_q the flux through the qubit loop, and a linear flux-voltage relation $\Phi_q = \alpha_{qL} V_L + \alpha_{qR} V_R + \Phi_{q,0}$, accounting for current crosstalk and offsets. (Crosstalk, $\sim 30\%$, likely results from spatial distribution of flux-bias return currents on the ground plane.) The above parameters are tightly constrained by the spectroscopy and transmission data shown (figure 8.2) and other transmission data for the Q_L -cavity vacuum Rabi splitting. Simultaneously fitting the spectra given by numerical diagonalization of the Hamiltonian (truncated to $N = 5$ qubit levels and 5 cavity photons) to these data gives $E_{JL(R)}^{\max}/h = 28.48$ (42.34) GHz, $E_{CL(R)}/h = 317$ (297) MHz, $g_{L(R)}/2\pi = 199$ (183) MHz. Cavity parameters are $\omega_C/2\pi = 6.902$ GHz and linewidth $\kappa/2\pi = 1$ MHz.

When the qubits are tuned to their maximum frequencies, point I in figure 8.2, they are far detuned from the cavity and from each other, so that interactions are small. This point is used for state preparation, single-qubit rotations and the joint measurement, in the computational basis $|0, 0\rangle$, $|0, 1\rangle$, $|1, 0\rangle$, and $|1, 1\rangle$, where $|l, r\rangle$ denotes excitation level l (r) for Q_L (Q_R). Operation at this point is also desirable because it is a flux sweet spot [63] for both qubits, providing long coherence, with relaxation and dephasing times $T_{1,L(R)} = 1.3$ (0.79) μs and $T_{2,L(R)}^* = 1.8$ (1.15) μs , respectively. The coherence times are measured in the standard way using a sliding π pulse protocol for the T_1 determination and a Ramsey fringe interference experiment for T_2 .

Tuning Q_R into resonance with the cavity, point IV, reveals a vacuum Rabi splitting [52] from which the qubit-cavity interaction strength is extracted. Tuning Q_R into resonance with Q_L , point III, shows an avoided crossing resulting from a cavity-mediated, qubit-qubit transverse interaction [91] as discussed in section 4.3.2 and experimentally investigated in section 7.4. One might expect, given the emphasis on the swap oscillations from before, that this would be the location for implementing a two-qubit entangling gate. However, we will actually find that another interaction works better and will be the subject of the work in this and chapter 9. Nonetheless, we can still characterize this transverse interaction region.

8.2 Virtual swap interaction via flux bias

The coupling strength between the two-qubits is found to be $J/\pi = 105$ MHz and can be seen in the spectroscopy map at point III in figure 8.2. Whereas previously to turn on a qubit-qubit swap, we were limited to using the ac-Stark interaction (section 7.4), here with the presence of on-chip fast flux bias lines, it is possible to tune the swap interaction by simply modulating the flux on one of the qubits.

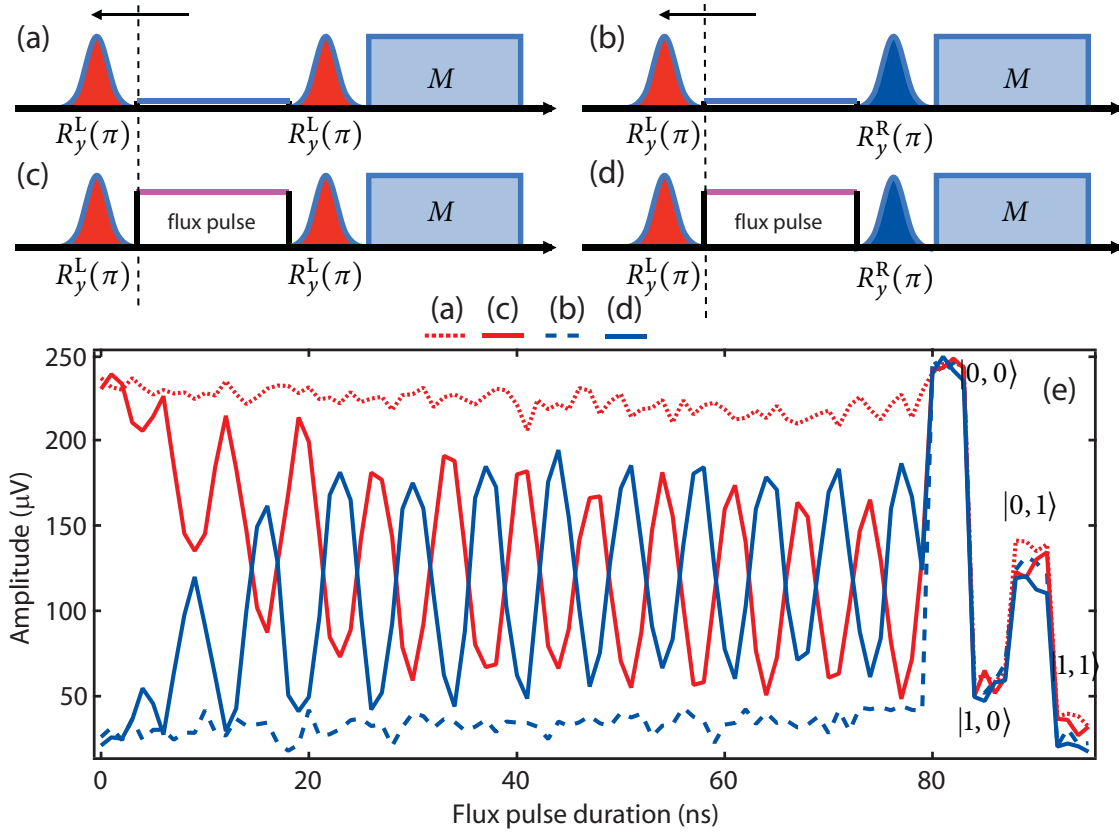


Figure 8.3: Flux bias swap experiments. (a)–(d) Protocols for flux-based swap oscillations. In (a), the experiment is a sliding π - π on the left qubit, resulting in a finite population of $|1,0\rangle$ with increasing time between the pulses [shown in (e) dotted red trace]. In (b), the experiment is a π on the left qubit followed by a variable delay and then π on the right qubit. The resulting state ends up being near the $|1,1\rangle$ level [in (e) dashed blue trace]. Swap oscillations [solid red and blue in (e)] can be seen when the flux pulse is turned on, for gate sequences (c) and for (d), and out of phase from one another.

We can perform a protocol similar to that given in figure 7.9, except with the ac-Stark pulse replaced by a flux pulse. Flux pulses are implemented on each of the lines (L and R) using two channels of a Tektronix AWG 5014. The flux pulses are programmed to have a rise time of 1 ns. The length of the flux pulse can be varied just as the Stark pulse length and coherent swap oscillations can be seen, as shown in figure 8.3.

Due to the improved coherence times, these swaps can go on for much longer with higher contrast. Furthermore, the slope in the swap oscillations which were observed with the Stark swap are no longer present. We can also observe the anti-correlations between the oscillations depending on applying the final π rotation on either the left qubit (figure 8.3c) or the right qubit (figure 8.3d).

However, upon trying to use the flux swaps for performing a $\sqrt{i\text{SWAP}}$ gate in this system proves to be difficult. The primary issue is that we cannot turn the swap interaction on fast enough to perform the $\sqrt{i\text{SWAP}}$. The ns-resolution of the flux pulses results is too short compared to the swap frequency J/π , making an adiabatic state transfer more likely than the swap. Fortunately, we can exploit the two-transmon $\sigma_z \otimes \sigma_z$ interaction described in chapter 4, which does not require very fast tuning, but employ a slower, adiabatic flux control.

8.3 Higher-level transmon interaction

Looking back at the single excitation spectroscopy map of figure 8.2, the V_R bias point at which we we perform two-qubit interactions is at point II. At this voltage, which comes slightly before the virtual qubit-qubit swap interaction, there are in fact no interactions which are immediately apparent on examining the one-excitation manifold.

However, a useful two-qubit interaction is revealed in the two-excitation spectrum, figure 8.4a. As V_R is swept away from point I, the non-computational higher-level transmon excitation $|0, 2\rangle$ (left transmon in ground state, right transmon in second excited state), decreases more rapidly than the computational state $|1, 1\rangle$ (both transmons in their first excited states). These two states in fact can be tuned into degeneracy at point II. However, as shown in figure 8.4b, there is actually a large (160 MHz) cavity-mediated interaction between these levels, resulting in a frequency shift $\zeta/2\pi$ of the lower branch with respect to the sum $f_L + f_R$, in good agreement with a numerical diagonalization of the generalized Jaynes–Cummings Hamiltonian. This avoided crossing causes the transition frequency to $|1, 1\rangle$ to deviate from the sum of the transition frequencies to $|0, 1\rangle$ and $|1, 0\rangle$.

The two-excitation spectroscopy is performed using a pump and probe two-tone technique: one microwave excitation pulse is applied to the single-excitation transition frequencies, f_{01} or f_{10} , before a second probe pulse is swept as a function of frequency, and the change in homodyne transmission through the cavity is measured.

The shift of the transition frequency to $|1, 1\rangle$ is the mechanism of an entangling conditional phase (c-Phase) gate (section 2.3.2 and section 4.3.3). Recall that flux pulses, adiabatic with

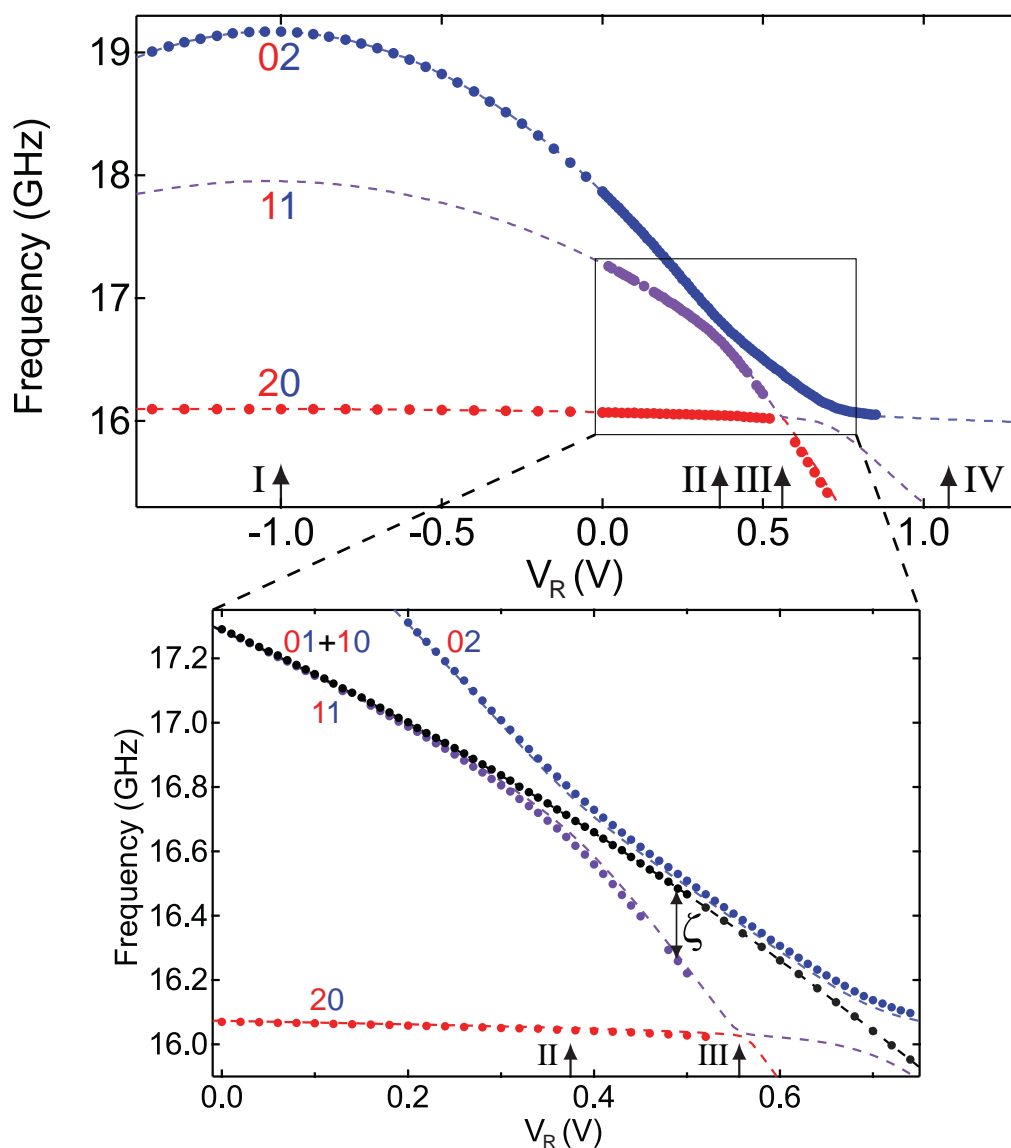


Figure 8.4: Two excitation spectroscopy. (a) Flux dependence of transition frequencies from the ground state $|0,0\rangle$ to the two-excitation manifold. Two-tone spectroscopy measurements (points) show an avoided crossing between the computational state $|1,1\rangle$ and the non-computational state $|0,2\rangle$ at point II, in good agreement with numerical diagonalization of the Hamiltonian (dashed curves). (b) Zoom-in on the avoided crossing, where we see that the transition frequency to $|1,1\rangle$ deviates from the sum of the transition frequencies to $|0,1\rangle$ and $|1,0\rangle$.

respect to the $|1, 1\rangle \leftrightarrow |0, 2\rangle$ avoided crossing, produce phase gates

$$U = \begin{pmatrix} 1 & 0 & 0 & 0 \\ 0 & e^{i\theta_z^{01}} & 0 & 0 \\ 0 & 0 & e^{i\theta_z^{10}} & 0 \\ 0 & 0 & 0 & e^{i\theta_z^{11}} \end{pmatrix} \quad (8.2)$$

in the computational Hilbert space. Here, $\theta_z^{lr} = 2\pi \int \delta f_{lr}(t) dt$ is the dynamical phase acquired by $|l, r\rangle$, and δf_{lr} is the deviation of f_{lr} from its value at point I. A V_R pulse into point II such that $\int \zeta(t) dt = (2n + 1)\pi$ with integer n implements a c-Phase, because $\theta_z^{11} = \theta_z^{01} + \theta_z^{10} - \int \zeta(t) dt$. This method of realizing a c-Phase by adiabatically using the avoided crossing between computational and non-computational states is generally applicable to qubit implementations with finite anharmonicity, such as transmons [63] or phase qubits [116]. A similar approach involving higher excitation levels with non-adiabatic pulses was previously proposed [96]. The negative anharmonicity permits the phase gate at point II to occur before the onset of transverse coupling at point III.

Control of ζ by two orders of magnitude provides an excellent on-off ratio for the c-Phase gate. Measurements of ζ obtained from spectroscopy and from time-domain experiments show very good agreement as shown in figure 8.5. The time-domain method measures the difference in the precession frequency of Q_L in two Ramsey-style experiments where a V_R -pulse of varying duration (0–100 ns) is inserted between $\pi/2$ rotations of Q_L , with Q_R either in the ground state $|0\rangle$ or excited into state $|1\rangle$. Using the time-domain approach, we measure a residual $\zeta/2\pi \approx 1.2$ MHz at point I (indicated in figure 8.5 by the star). The theoretical ζ obtained by numerical diagonalization shows reasonable agreement with the data, except for a scale factor that is likely due to higher modes of the cavity, not included in the calculation.

8.3.1 Tuning up a c-Phase gate

We employ a protocol to tune up the c-Phase gates which is quite similar to a Ramsey fringe experiment. As first alluded to in the previous section, the c-Phase is dependent upon $\zeta(t)$ as well as the individual qubit dynamical phases θ_z^{01} and θ_z^{10} . Whereas the $\zeta(t)$ interaction needs to be an adiabatic pulse with a large enough amplitude to enter the $|0, 2\rangle \leftrightarrow |1, 1\rangle$ interaction region, the individual qubit dynamical phases can be achieved with small flux excursions which shift the qubit frequencies f_{01} and f_{10} via a z -rotation (section 8.6). Therefore, in our

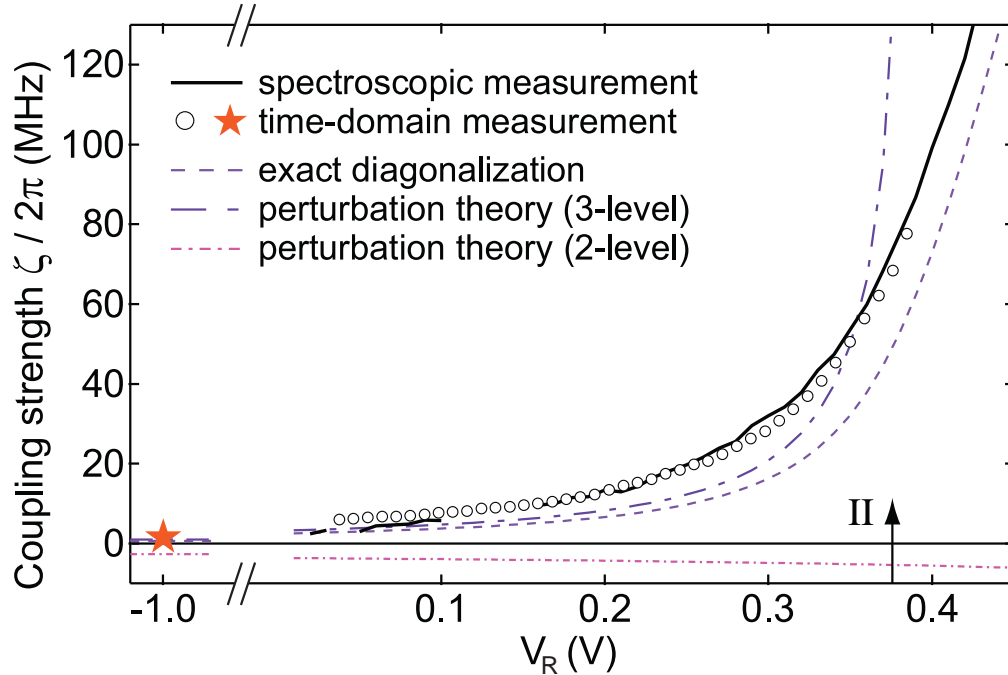


Figure 8.5: Agreement of the splitting between experiment and theory. The coupling strength $\zeta/2\pi = f_{01} + f_{10} - f_{11}$ of the effective $\sigma_z^L \otimes \sigma_z^R$ interaction, obtained both from spectroscopy (solid curve) and from time-domain experiments (points) (see text for details). Numerical diagonalization and perturbation theory for 3-level transmons agree reasonably with data. The perturbation calculation diverges at the avoided crossing. Perturbation theory for 2-level qubits gives the wrong magnitude and sign for ζ , and demonstrates that the higher transmon excitations are necessary for the interaction. Time-domain measurement and theory both give $\zeta/2\pi \simeq 1.2$ MHz at point I. The tunability of ζ over two orders of magnitude provides an excellent on-off ratio for the two-qubit c-Phase gate.

implementation, to tune up a c-Phase gate, we have to combine a strong flux pulse on the right qubit FBL with weaker flux pulses on both the right and left FBLs.

Since the qubits start from being at point I for the single-qubit operations, the flux bias lines are both originally set to nominal DC voltages which tune to this location, which we can call V_L^0 and V_R^0 . The four different c-Phase gates differ by whether θ_z^{01} and θ_z^{10} are even or odd multiples of π : we fine tune θ_z^{01} with small adjustments to the rising and falling edges of the V_R -pulse, and θ_z^{10} with the amplitude of a simultaneous weak V_L -pulse as shown in figure 8.6. The pulse onto the right flux bias line is essentially a bi-level pulse, with the larger amplitude ΔV_R^ζ sufficient to tune into the conditional phase interaction $\zeta(t)$ and the lower amplitude ΔV_R^0 at the start and end to tune the dynamical z -phase on the right qubit. The left

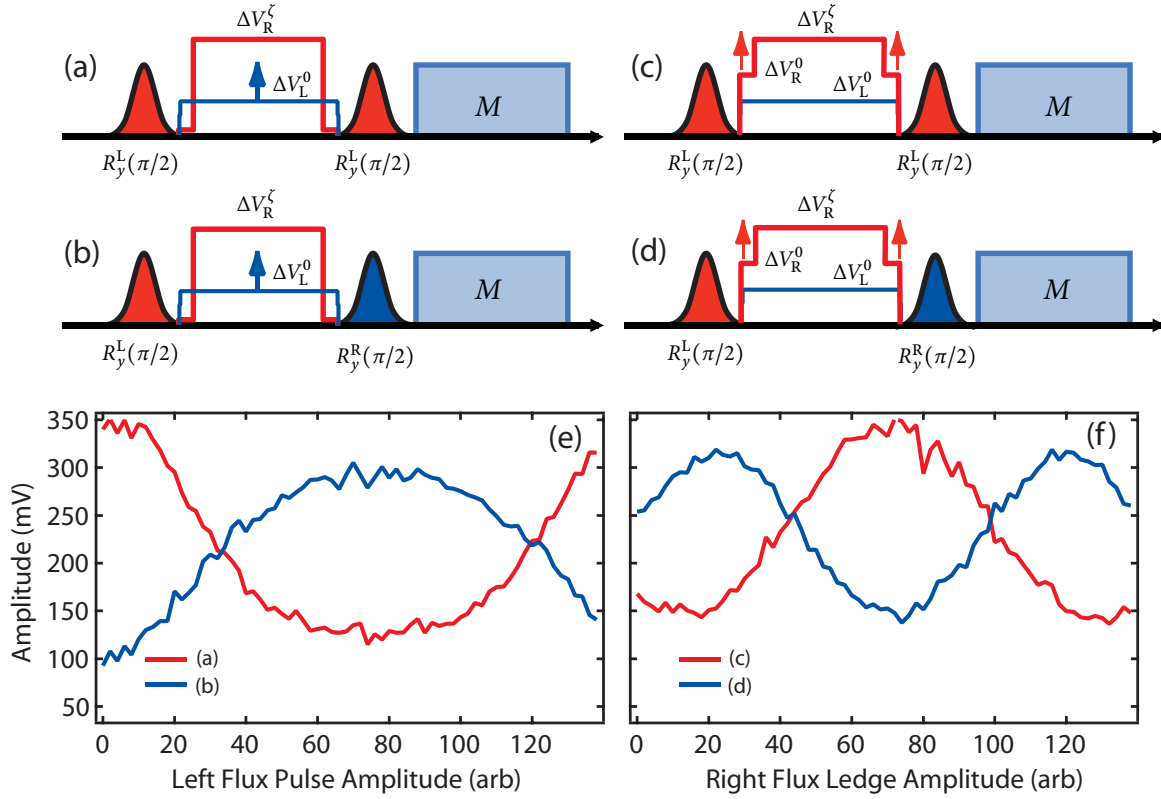


Figure 8.6: Conditional phase gate tune-up sequences. Two sets of experiments are used to tune up the flux pulses for the conditional phase gates. (a) and (b) involve first applying a $\pi/2$ pulse on the left qubit, followed by a fixed flux pulse of ΔV_R^ζ on the right FBL combined with a left FBL pulse with a varying amplitude ΔV_L^0 , and then a final $\pi/2$ pulse on either the left or right qubit. The second set (c) and (d) uses a similar pulse sequence, but with varying the ledge amplitude, ΔV_R^0 , on the rising and falling edges of the pulse on the right FBL. The measured homodyne responses are shown in (e) and (f). In (e), the ΔV_L^0 is set such that the solid red and blue curves are exactly out of phase, here at ~ 79 . Then, in (f), depending on tuning ΔV_R^0 to ~ 20 or ~ 70 will define the c-Phase gate corresponding to cU_{01} or cU_{11} .

qubit pulse is simply a square pulse with a single amplitude level ΔV_L^0 used to tune the left qubit dynamical phase.

We employ two experiments in a two-step procedure for tuning the flux bias line levels for the c-Phase gates. The first experiment is built up of two sequences: in the first we apply a $R_y(\pi/2)$ pulse to the left qubit, turn on a large right FBL pulse ΔV_R^ζ to get into the c-Phase interaction region, while also turning on a left FBL pulse of varying amplitude ΔV_L^0 , followed by a final pulse on the left qubit which is again a $R_y(\pi/2)$; the second sequence is identical to the first except at the last stage we also add an additional $R_y(\pi)$ to the right qubit. We expect to see oscillations in each case, and look for the appropriate ΔV_R^ζ and ΔV_L^0 such that

the oscillations in the two traces are out-of-phase. In the second sequence, the different state of the right qubit affects the phase of the oscillations. Therefore, we are probing the amount of phase necessary on the left qubit in order to realize the conditional-phase flip. The protocol and a sample experimental output is shown in figure 8.6a.

The second step is again built up of two sequences, and aims to unwrap the dynamical phase on the right qubit: for the first sequence, (1) apply $R_y(\pi/2)$ on to the right qubit; (2) turn on the large right FBL pulse of amplitude ΔV_R^ζ and left FBL pulse of amplitude ΔV_L^0 (both determined from the first step) while sweeping the offset voltage on the right FBL ΔV_R^0 ; (3) apply $R_y(\pi/2)$ on to the right qubit; for the second sequence, same as the first except steps (1) and (3) apply $R_y(\pi)$ onto the left qubit as well. Again, we expect to see oscillations depending on the amplitude of the right FBL offset voltage. Depending on the selection of ΔV_R^0 will allow us to tune-up any of the four cU_{ij} conditional phase gates (see figure 8.6b).

8.3.2 Generating Bell states

With access to the four different c -Phase gates (cU_{ij}) as well as single-qubit rotations, it is then possible to generate maximally entangled states, such as the four Bell states,

$$|\Psi^\pm\rangle = \frac{1}{\sqrt{2}} (|0, 0\rangle \pm |1, 1\rangle) \quad |\Phi^\pm\rangle = \frac{1}{\sqrt{2}} (|0, 1\rangle \pm |1, 0\rangle). \quad (8.3)$$

The pulse protocols for their generation are summarized in figure 8.7. In each case, the scheme involves first to place both qubits in a superposition state using individual single-qubit $\pi/2$ rotations. That is followed by the application of any of the 4 different c -Phase gates. At this point the two qubits are in fact already in an entangled state. To make this more evident, a single-qubit rotation of $\pi/2$ on one of the qubits will result in one of the four Bell states.

Simply the ability to generate entangled states is not enough however, as it is imperative to be able to readout the state and figure out exactly how accurately are the experimentally created states from what is theoretically expected. Therefore, we next build upon the ideas of using the cavity as a joint readout and state tomography discussed in section 4.4.2 and apply it to both separable and entangled states.

8.4 Joint readout of two qubits

To accurately and precisely detect two-qubit states with our cavity bus, we first seek a complete physical model and calibration of the joint readout. The physical mechanism enabling the

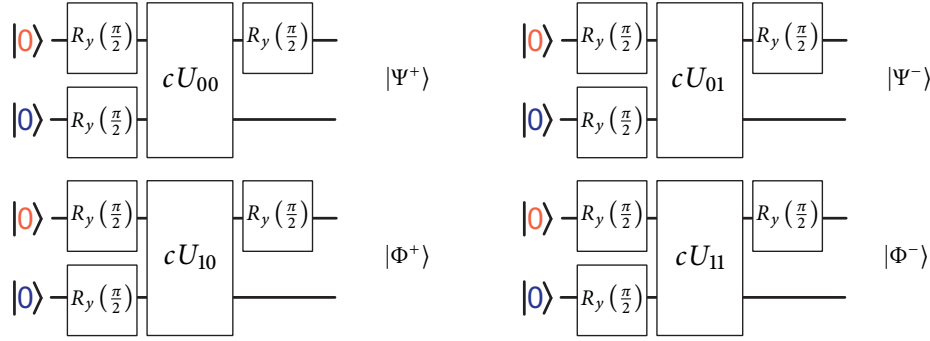


Figure 8.7: Experimental protocols for generating Bell states. Gate sequence generating two-qubit entanglement. Starting from $|0, 0\rangle$, simultaneous $\pi/2$ rotations on both qubits create an equal superposition of the four computational states. A c -Phase cU_{ij} then phase shifts $|i, j\rangle$ in the superposition and produces entanglement. A final $\pi/2$ rotation on Q_L evolves the entangled state into one of the four Bell states depending on the cU_{ij} applied.

joint readout is a qubit-state-dependent dispersive cavity shift that is large relative to the cavity linewidth $\kappa/2\pi = 1$ MHz. In this ‘strong dispersive’ regime [110], recall that the system is described by a dispersive Jaynes-Cummings Hamiltonian

$$H_{JC}/\hbar = (\omega_C + \chi^L ZI + \chi^R IZ) a^\dagger a - \frac{\omega^L}{2} ZI - \frac{\omega^R}{2} IZ, \quad (8.4)$$

where ω_C is the bare resonator frequency, $\omega^{L(R)}$ is the first excited state transition frequency for the left (right) qubit, and $\chi^{L(R)}$ is the left (right) qubit-state dependent cavity shift. Note that we have assumed that the qubits are also far enough detuned from one another that we drop the virtual-swap interaction term. The cavity shifts $\chi^{L,R}$ are determined by a pulsed measurement of the transmitted homodyne voltage V_H , having prepared each of the four computational basis states ($|0, 0\rangle, |0, 1\rangle, |1, 0\rangle, |1, 1\rangle$) using single-qubit gates. Figure 8.8a–d show the transient in $\langle V_H \rangle$ as a function of drive frequency ω_{RF} (ensemble average of 600,000 repetitions). On time scales shorter than the qubit relaxation times, $t \lesssim T_1^{L(R)} = 1.2(0.9) \mu s$, the largest transmission occurs at distinct frequencies (Fig. 1f shows a time-averaged voltage $\bar{V}_H = \langle \int_0^{\Delta t} V_H dt \rangle / \Delta t$ with $\Delta t = 0.5 \mu s$), from which we estimate $\chi^{L(R)}/2\pi = 13(4)$ MHz.

When the shifts are many linewidths, $\chi^L, \chi^R \gg \kappa$, and qubit relaxation during measurement is negligible, $\Delta t \ll T_1$, driving with a tone at the cavity frequency corresponding to $|0, 0\rangle$ would query the joint property that *both qubits are in the ground state*: transmission is high when the state is projected onto $|0, 0\rangle$ and zero otherwise. In this ideal scenario, $\bar{V}_H = \text{Tr}(\rho M)$, where ρ is the two-qubit density matrix and $M \propto |0, 0\rangle \langle 0, 0| = (I + ZI + IZ + ZZ)/4$ is the measurement operator. However, qubit relaxation during the measurement and partial over-

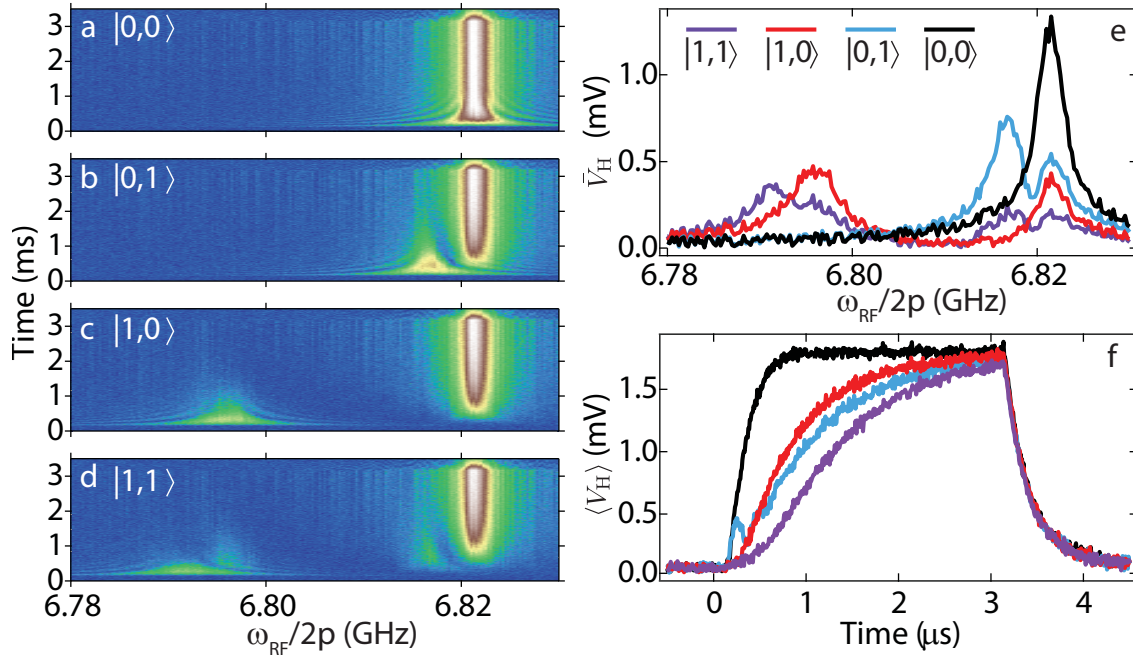


Figure 8.8: Measurement transients for joint readout. Transmitted V_H amplitude as a function of time and cavity drive frequency ω_{RF} , for computational basis states (a) $|0,0\rangle$, (b) $|0,1\rangle$, (c) $|1,0\rangle$, and (d) $|1,1\rangle$. (e) Time average of the V_H transients in (a–d) over the first 500 ns. (f) Transients of V_H for ω_{RF} at the cavity frequency corresponding to $|0,0\rangle$.

lap of the dispersive peaks, evident in figure 8.8e, make the measurement operator take the more general form

$$M = \beta_{II}II + \beta_{ZI}ZI + \beta_{IZ}IZ + \beta_{ZZ}ZZ, \quad (8.5)$$

where β_{LR} are real calibration constants that must be determined.

8.5 Calibrating the measurement model

A comprehensive test of this measurement model is performed with a sequence of Rabi-flopping experiments. Figure 8.9a–b show \bar{V}_H as a function of the duration of an applied drive at ω^L and ω^R , respectively. In each case the drive induces a Rabi oscillation of the addressed qubit around the y axis of its Bloch sphere. A third experiment figure 8.9c measures \bar{V}_H in response to simultaneous driving of both qubits. The observed oscillations show frequency components at the individual qubit Rabi frequencies, Ω^L , Ω^R , but also at the sum and

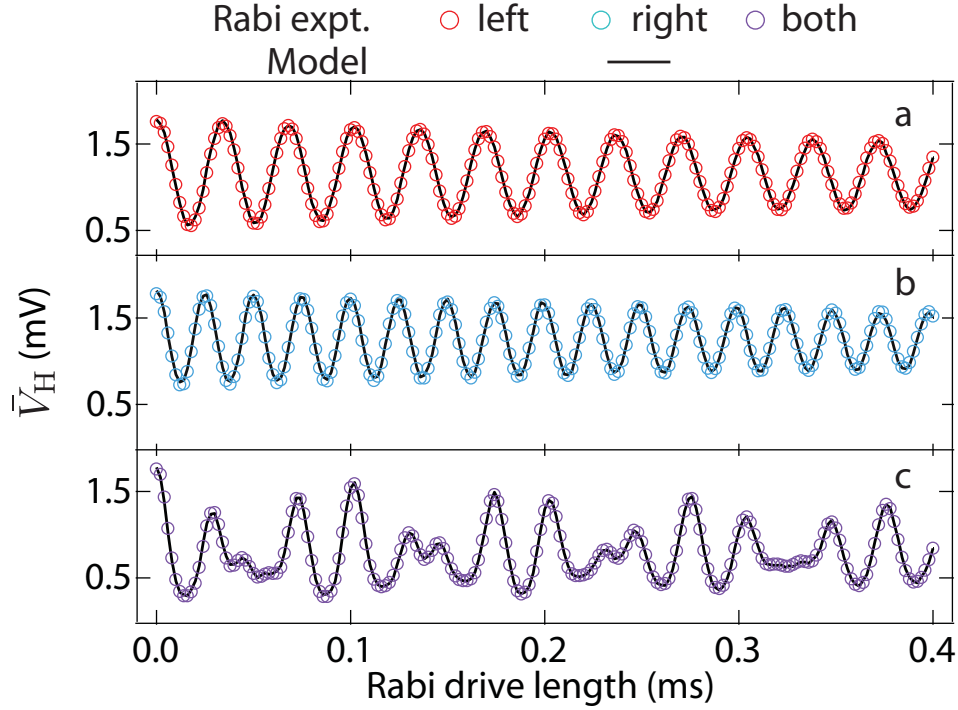


Figure 8.9: Rabi experiments for readout characterization. Rabi oscillations on the (a) left qubit, (b) right qubit, and (c) simultaneously on both. Solid lines are fits to the model in (8.5).

difference due to the ZZ term in Eq. (2). This is clearly revealed in the Fourier transform of the oscillations shown in figure 8.10.

We these oscillations with the most general two-qubit measurement operator

$$M = \sum_{L,R \in \{I,X,Y,Z\}} \beta_{LR} LR, \quad (8.6)$$

using theoretical expressions for $\langle Z \rangle$ and $\langle X \rangle$ assuming independently driven qubits. Because in these tests each qubit is driven around the y axis of its Bloch sphere, all terms involving Y^L and Y^R in (8.6) would not contribute to \bar{V}_H . The presence of such terms can be tested by rotating each or both qubits around their x axis instead. We do not find any significant differences in such experiments from the ones presented in the text, and the results here can be generalized for both quadratures X and Y .

In our experiment the detuning ~ 1.5 GHz between the two qubits is large compared to the Rabi-flopping rates, and we can assume a simple model of independent qubit driving. For a qubit driven at a rate Ω around its y axis starting from the ground state, the theoretical

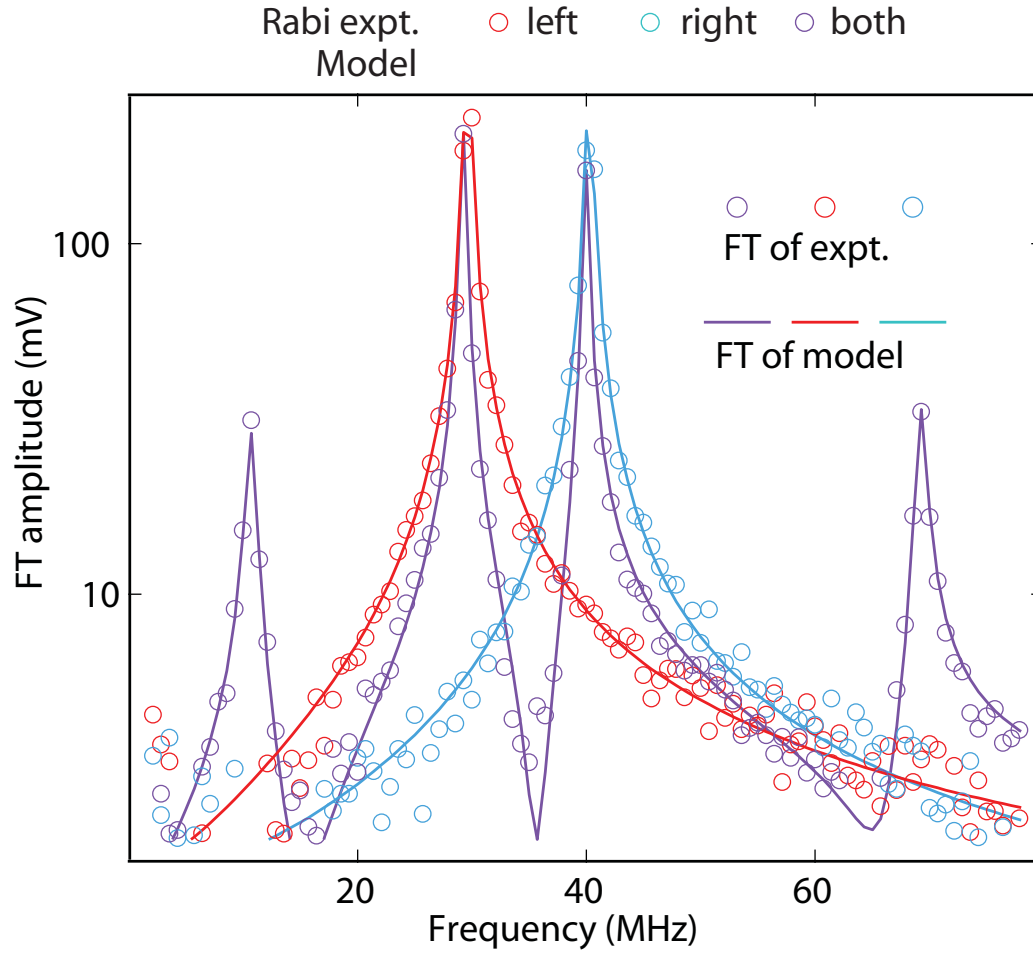


Figure 8.10: Fourier transforms of Rabi oscillations. Fourier transform (FT) of the three Rabi experiments (circles) and of best fits (lines). While the red (blue) traces show one main peak at the Rabi frequency $\Omega^{L(R)}$, the purple traces reveal peaks at Ω^L , Ω^R , $\Omega^L + \Omega^R$, and $\Omega^L - \Omega^R$, demonstrating the mixing property that makes the joint measurement sensitive to qubit-qubit correlations.

time evolution of $\langle Z \rangle$ and $\langle X \rangle$ is given by

$$\langle Z \rangle(t) = \frac{\gamma_1 \gamma_2}{\gamma_1 \gamma_2 + \Omega^2} + \frac{e^{-t/\tau_R} \Omega^2}{\gamma_1 \gamma_2 + \Omega^2} \left(\cos(\tilde{\Omega} t) + \frac{\sin(\tilde{\Omega} t)}{\tau_R \tilde{\Omega}} \right), \quad (8.7a)$$

$$\langle X \rangle(t) = \frac{\gamma_1 \Omega}{\gamma_1 \gamma_2 + \Omega^2} - \frac{e^{-t/\tau_R} \Omega}{\gamma_1 \gamma_2 + \Omega^2} \left(\gamma_1 \cos(\tilde{\Omega} t) - \frac{[2\Omega^2 + \gamma_1(\gamma_2 - \gamma_1)] \sin(\tilde{\Omega} t)}{2\tilde{\Omega}} \right). \quad (8.7b)$$

Here, $\tilde{\Omega} = \sqrt{\Omega^2 - (1/\tau_R)^2}$ is an effective oscillation rate, $\gamma_1 = 1/T_1$ is the relaxation rate, $\gamma_2 = \gamma_1/2 + \gamma_\phi$ is the dephasing rate, and $\tau_R = 2/(\gamma_1 + \gamma_2)$ is the Rabi decay time.

The best fits to the oscillations place bounds on deviations from the measurement model of (8.5). Using these expressions in the full model, (8.6), and fitting to the three experiments, we estimate the coefficients β_{LR} . For single-qubit driving (figure 8.9a–b), the right (left) qubit is always in the ground state, and only terms $\langle ZI \rangle$, $\langle XI \rangle$, $\langle XZ \rangle$ and $\langle ZZ \rangle$ ($\langle IZ \rangle$, $\langle IX \rangle$, $\langle ZX \rangle$, and $\langle ZZ \rangle$) contribute to the \bar{V}_H oscillation. Using the form

$$\bar{V}_H^a = W_0 + W_1 \langle ZI \rangle + W_2 \langle XI \rangle, \quad (8.8a)$$

$$\bar{V}_H^b = W_0 + W_1 \langle IZ \rangle + W_2 \langle IX \rangle, \quad (8.8b)$$

with W_0 , W_1 , W_2 , $\Omega^{L(R)}$, $\gamma_1^{L(R)}$, and $\gamma_2^{L(R)}$ as free parameters gives an excellent fit. In both cases, the best-fit W_2 , corresponding to $\beta_{XI(IX)} + \beta_{XZ(ZX)}$, is less than 2% of the full range of \bar{V}_H , $\sim 2\beta_{IZ} + 2\beta_{ZI}$. For the doubly-driven case (figure 8.9c), the fit function used is

$$\begin{aligned} \bar{V}_H^c = & \beta_{II} + \beta_{XI} \langle XI \rangle + \beta_{ZI} \langle ZI \rangle + \beta_{IX} \langle IX \rangle + \beta_{IZ} \langle IZ \rangle \\ & + \beta_{XX} \langle XX \rangle + \beta_{XZ} \langle XZ \rangle + \beta_{ZX} \langle ZX \rangle + \beta_{ZZ} \langle ZZ \rangle, \end{aligned} \quad (8.9a)$$

with β_{ij} , Ω^L , Ω^R , γ_j^L , and γ_j^R as fit parameters. The best-fit coefficients captured in (8.5) are $(\beta_{II}, \beta_{IZ}, \beta_{ZI}, \beta_{ZZ}) = (800, 380, 380, 200) \mu V$. Best-fit values of the remaining coefficients are each less than 2% of the full range of \bar{V}_H .

These Rabi experiments thus corroborate (8.5) and give the calibration $(\beta_{II}, \beta_{IZ}, \beta_{ZI}, \beta_{ZZ}) = (800, 380, 380, 200) \mu V$. The jointness, defined as $\beta_{ZZ}/\beta_{IZ(ZI)}$, is 0.6, indicating the high sensitivity of the readout to qubit-qubit correlations. This high relative sensitivity to two-qubit correlations in the measurement operator, or *jointness*, makes the joint readout as efficient for measuring qubit correlations as for single-qubit polarizations. Since the correlation is performed before averaging, the classical amplifier noise that limits the single-shot readout fidelity enters only as a statistical error, and can be largely eliminated with sufficient repetition. Therefore, this fully-characterized joint readout will be sufficient to perform full two-qubit state tomography.

8.6 Quantum state tomography and the Pauli set

Having characterized the joint readout, we can now perform quantum state tomography of separable and entangled two-qubit states generated using the C-phase gate. We extend ref. 4, where two-qubit state tomography with a joint readout was first demonstrated, by obtaining an overcomplete set of 30 measurements through applying different pairs of simultaneous

single-qubit rotations prior to detection as shown in table 8.1. These measurements involve applying different simultaneous rotations on the qubits. The 15 measurements labeled M_i involve positive rotations chosen from $\{I, R_x^{+\pi}, R_x^{+\pi/2}, R_y^{+\pi/2}\}$. The remaining 15, labeled N_i , involve negative rotations chosen from $\{I, R_x^{-\pi}, R_x^{-\pi/2}, R_y^{-\pi/2}\}$. Ensemble averages of M_i and N_i are obtained by repeating state preparation, analysis rotation, and measurement 600,000 times. Although just 15 linearly independent measurements (such as either all M_i or all N_i) is sufficient for state tomography, using all of these rotations and least-squares estimation reduces the statistical and systematic error in the final extraction of either the density matrix ρ or the Pauli set \vec{P} discussed in the next two sections.

8.6.1 The density matrix representation

The set of measurements described above can be used to estimate the density matrix ρ for describing the quantum mechanical state using the prescription described in section 2.5.2. Recall that for any two-qubit quantum state we can choose a set of 16 linearly independent operators $\{M_i\}$ such that ρ can be decomposed as

$$\rho = \sum_{i=1}^{16} c_i M_i,$$

where the set $\{c_i\}$ are the 16 parameters to be estimated. If the operators are observables, then the 16 expectation values $m_i = \text{Tr}[M_i \rho]$ determine c_j by

$$m_i = \sum_{j=1}^{16} \text{Tr}[M_i M_j] c_j.$$

Only 15 independent (either all the positive, or all the negative) measurements are needed to determine ρ because of the constraint of trace normalization, $\text{tr } \rho = 1$ (equivalently we choose $M_{16} = I$, which always gives $m_{16} = 1$). While ideally ρ could be obtained from the experimental m_i by inversion of $\text{Tr}[M_i M_j]$, this method pays no attention to the properties ρ must have: Hermiticity and positive semi-definiteness (trace normalization is included by the choice of decomposition). However, by following the Maximum Likelihood Estimation (MLE) technique from section 2.5.2, it is possible to obtain estimates to the density matrices.

The inferred density matrices ρ_{ml} for the four Bell states are shown in figure 8.11. We characterize the quality of these states through metrics which are computable from ρ_{ml} : purity (section 2.6) given by $P(\rho) = \text{tr}(\rho^2)$, fidelity to the target state $|\psi\rangle$ given by $F(\rho, \psi) = \langle \psi | \rho | \psi \rangle$,

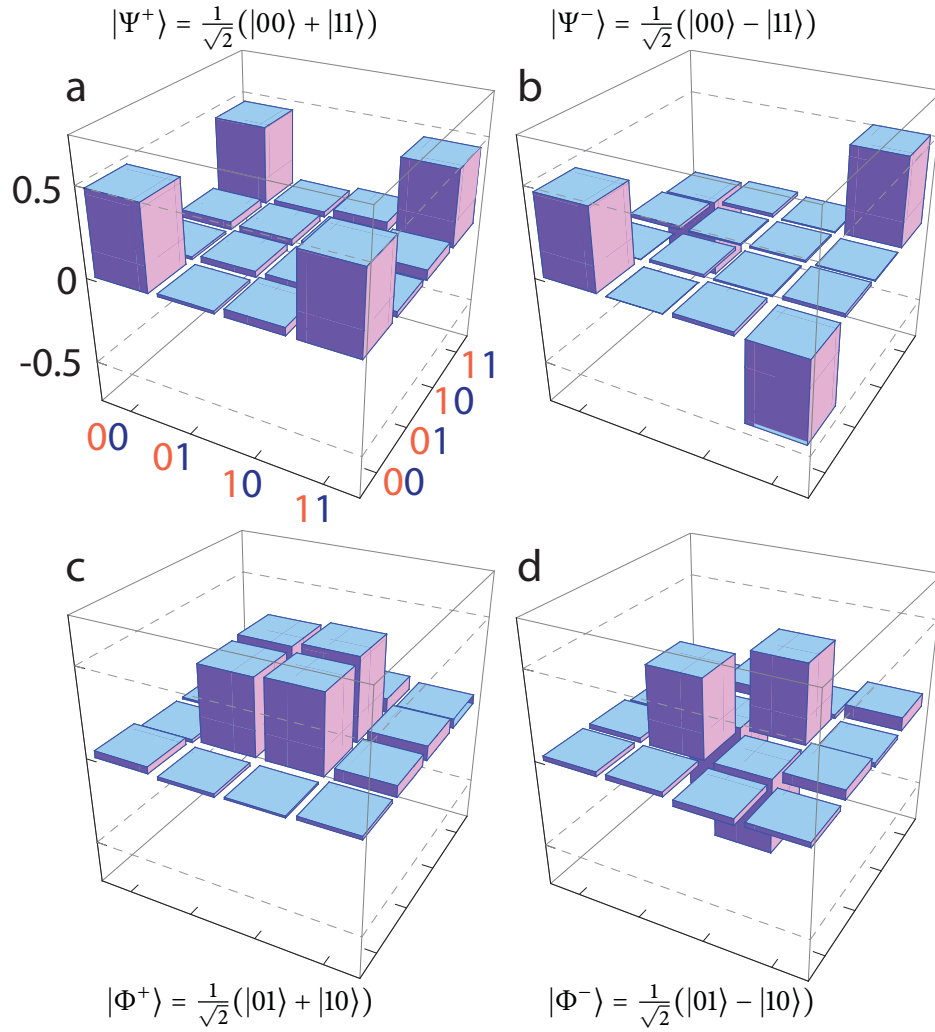


Figure 8.11: Density matrix representation of Bell states. Real part of maximum-likelihood density matrix ρ_{ml} of the entangler output for cU_{10} , cU_{00} , cU_{11} , and cU_{01} , respectively (imaginary elements of ρ_{ml} are less than 0.03, 0.02, 0.07, 0.08). Extracted metrics for the four entangler outputs include purity $P = 0.87 \pm 0.02, 0.92 \pm 0.02, 0.88 \pm 0.02, 0.79 \pm 0.03$, fidelity to the ideal Bell state $F = 0.91 \pm 0.01, 0.94 \pm 0.01, 0.90 \pm 0.01, 0.87 \pm 0.02$ and concurrence $C = 0.88 \pm 0.02, 0.94 \pm 0.01, 0.86 \pm 0.02, 0.81 \pm 0.04$. The uncertainties correspond to the standard deviation in 16 repetitions of generation-tomography for each entangler.

Table 8.1: The 30 raw measurements.

	Pre-rotation	Measurement operator
M_{01}	$I \otimes I$	$+\beta_{ZI}ZI + \beta_{IZ}IZ + \beta_{ZZ}ZZ$
M_{02}	$R_x^\pi \otimes I$	$-\beta_{ZI}ZI + \beta_{IZ}IZ - \beta_{ZZ}ZZ$
M_{03}	$I \otimes R_x^\pi$	$+\beta_{ZI}ZI - \beta_{IZ}IZ - \beta_{ZZ}ZZ$
M_{04}	$R_x^{\pi/2} \otimes I$	$+\beta_{ZI}YI + \beta_{IZ}IZ + \beta_{ZZ}YZ$
M_{05}	$R_x^{\pi/2} \otimes R_x^{\pi/2}$	$+\beta_{ZI}YI + \beta_{IZ}IY + \beta_{ZZ}YY$
M_{06}	$R_x^{\pi/2} \otimes R_y^{\pi/2}$	$+\beta_{ZI}YI - \beta_{IZ}IX - \beta_{ZZ}YX$
M_{07}	$R_x^{\pi/2} \otimes R_x^\pi$	$+\beta_{ZI}YI - \beta_{IZ}IZ - \beta_{ZZ}YZ$
M_{08}	$R_y^{\pi/2} \otimes I$	$-\beta_{ZI}XI + \beta_{IZ}IZ - \beta_{ZZ}XZ$
M_{09}	$R_y^{\pi/2} \otimes R_x^{\pi/2}$	$-\beta_{ZI}XI + \beta_{IZ}IY - \beta_{ZZ}XY$
M_{10}	$R_y^{\pi/2} \otimes R_y^{\pi/2}$	$-\beta_{ZI}XI - \beta_{IZ}IX + \beta_{ZZ}XX$
M_{11}	$R_y^{\pi/2} \otimes R_x^\pi$	$-\beta_{ZI}XI - \beta_{IZ}IZ + \beta_{ZZ}XZ$
M_{12}	$I \otimes R_x^{\pi/2}$	$+\beta_{ZI}ZI + \beta_{IZ}IY + \beta_{ZZ}ZY$
M_{13}	$R_x^\pi \otimes R_x^{\pi/2}$	$-\beta_{ZI}ZI + \beta_{IZ}IY - \beta_{ZZ}ZY$
M_{14}	$I \otimes R_y^{\pi/2}$	$+\beta_{ZI}ZI - \beta_{IZ}IX - \beta_{ZZ}ZX$
M_{15}	$R_x^\pi \otimes R_y^{\pi/2}$	$-\beta_{ZI}ZI - \beta_{IZ}IX + \beta_{ZZ}ZX$
N_{01}	$I \otimes I$	$+\beta_{ZI}ZI + \beta_{IZ}IZ + \beta_{ZZ}ZZ$
N_{02}	$R_x^{-\pi} \otimes I$	$-\beta_{ZI}ZI + \beta_{IZ}IZ - \beta_{ZZ}ZZ$
N_{03}	$I \otimes R_x^{-\pi}$	$+\beta_{ZI}ZI - \beta_{IZ}IZ - \beta_{ZZ}ZZ$
N_{04}	$R_x^{-\pi/2} \otimes I$	$-\beta_{ZI}YI + \beta_{IZ}IZ - \beta_{ZZ}YZ$
N_{05}	$R_x^{-\pi/2} \otimes R_x^{-\pi/2}$	$-\beta_{ZI}YI - \beta_{IZ}IY + \beta_{ZZ}YY$
N_{06}	$R_x^{-\pi/2} \otimes R_y^{-\pi/2}$	$-\beta_{ZI}YI + \beta_{IZ}IX - \beta_{ZZ}YX$
N_{07}	$R_x^{-\pi/2} \otimes R_x^{-\pi}$	$-\beta_{ZI}YI - \beta_{IZ}IZ + \beta_{ZZ}YZ$
N_{08}	$R_y^{-\pi/2} \otimes I$	$+\beta_{ZI}XI + \beta_{IZ}IZ + \beta_{ZZ}XZ$
N_{09}	$R_y^{-\pi/2} \otimes R_x^{-\pi/2}$	$+\beta_{ZI}XI - \beta_{IZ}IY - \beta_{ZZ}XY$
N_{10}	$R_y^{-\pi/2} \otimes R_y^{-\pi/2}$	$+\beta_{ZI}XI + \beta_{IZ}IX + \beta_{ZZ}XX$
N_{11}	$R_y^{-\pi/2} \otimes R_x^{-\pi}$	$+\beta_{ZI}XI - \beta_{IZ}IZ - \beta_{ZZ}XZ$
N_{12}	$I \otimes R_x^{-\pi/2}$	$+\beta_{ZI}ZI - \beta_{IZ}IY - \beta_{ZZ}ZY$
N_{13}	$R_x^{-\pi} \otimes R_x^{-\pi/2}$	$-\beta_{ZI}ZI - \beta_{IZ}IY + \beta_{ZZ}ZY$
N_{14}	$I \otimes R_y^{-\pi/2}$	$+\beta_{ZI}ZI + \beta_{IZ}IX + \beta_{ZZ}ZX$
N_{15}	$R_x^{-\pi} \otimes R_y^{-\pi/2}$	$-\beta_{ZI}ZI + \beta_{IZ}IX - \beta_{ZZ}ZX$

and concurrence (section 2.6.1) C . Note that there are several common definitions of fidelity in the literature. Our definition is the square of the fidelity used in [67] and [142]. The extracted metrics for the four separate Bell state cases are $P = 0.87 \pm 0.02, 0.92 \pm 0.02, 0.88 \pm 0.02, 0.79 \pm 0.03$, fidelity to the ideal Bell state $F = 0.91 \pm 0.01, 0.94 \pm 0.01, 0.90 \pm 0.01, 0.87 \pm 0.02$ and concurrence $C = 0.88 \pm 0.02, 0.94 \pm 0.01, 0.86 \pm 0.02, 0.81 \pm 0.04$. The uncertainties correspond to the standard deviation in 16 repetitions of generation and state tomography

for each sequences. These values significantly extend the state of the art for solid-state entanglement [67], and provide evidence that we have a high-fidelity universal set of two-qubit gates.

8.6.2 Biasing of metrics by maximum-likelihood estimation

Although the density matrix representation is the more common method of depicting quantum state tomography, the maximum-likelihood estimation often associated with the density matrix determination can become biased if the true mean lies close to a boundary of the allowed parameter space [143]. Specifically, as the fidelity of the states become closer and closer to ideal, a biased estimation via maximum-likelihood becomes more probable.

In order to quantify the importance of this effect on the estimation of lower bounds on concurrence C given by entanglement witnesses (discussed in the next section), we can perform Monte-Carlo simulations for nearly-pure Werner states [39],

$$\rho_W(\lambda) = \lambda |\psi^-\rangle \langle \psi^-| + (1 - \lambda)I/4, \quad (8.10)$$

with Werner parameter $\lambda \in [0.8, 1]$. We can create 100 sets of simulated raw measurements for each λ by assuming Gaussian amplifier noise consistent with our experiments. Figure 8.12 shows a lower bound on the concurrence C_{bound} as a function of the true C of the Werner state, obtained with and without MLE processing of the simulated noisy data. We find that while the mean of C_{bound} estimated directly from the raw data is unbiased, the mean of the concurrence bound obtained with MLE becomes increasingly biased the more pure the Werner state, i.e., the closer λ is to unity. MLE underestimates the bound by 1% at $C = 0.85$, and by 4% at $C = 1$.

Therefore, although using MLE for obtaining a density matrix can be a very useful technique to get at a real physical state, it can also be a highly non-linear process which can result in the incorrect estimation of certain metrics associated with the states themselves. Furthermore, while errors on the individual measurements are Gaussian, the propagation of such errors through the estimation process of the density matrix is not very straightforward. The best technique is to Monte Carlo simulate the noise on the extraction of the density matrix given the raw experimental measurements and their associated Gaussian noise variance. However, we can attempt to process and visualize the measurements in an alternative way that will allow linear propagation of errors while avoiding MLE.

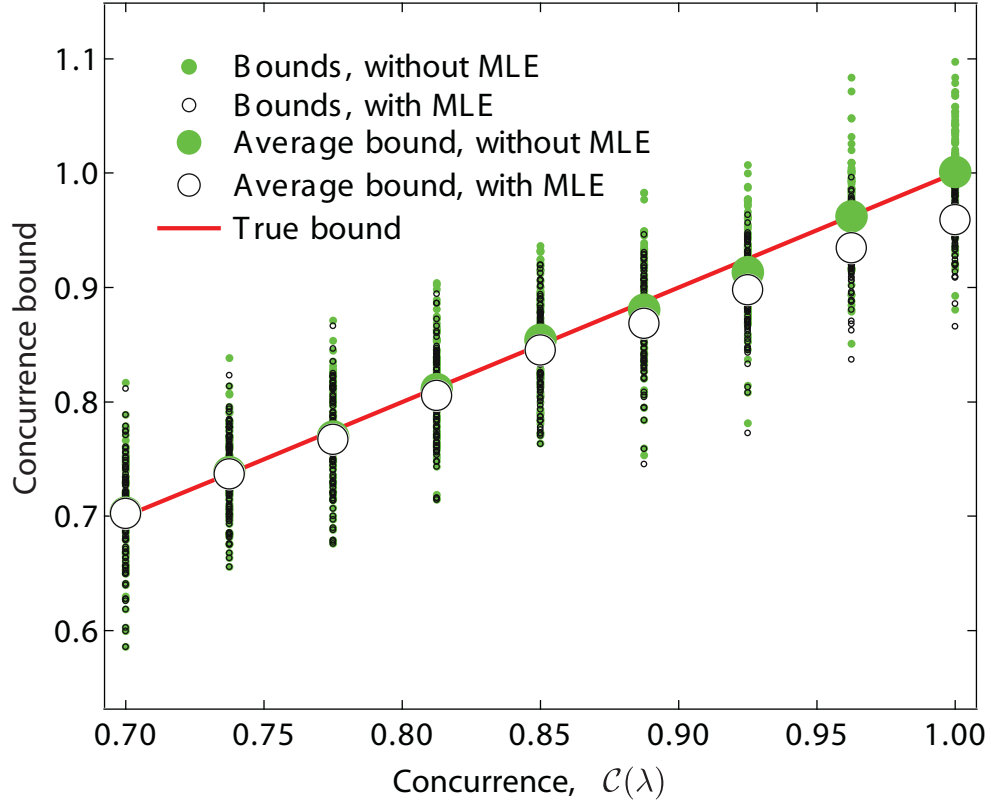


Figure 8.12: Bias of entanglement metrics from MLE. Comparison of the lower bound C_{bound} on concurrence C computed from simulated noisy raw data with and without use of MLE. The bound computed using MLE systematically underestimates the true bound (in this case, always equal to the true concurrence C , red line), while the bound computed directly from the simulated raw data remains faithful even as the Werner state approaches the Bell state $|\Psi^-\rangle$, i.e., as $\lambda \rightarrow 1$. For $|\Psi^-\rangle$, the MLE-computed bound underestimates the true bound by 4%.

8.6.3 The Pauli set representation

The Pauli set \vec{P} is another representation of the full quantum state which can be a handy tool for visualization, systematic errors determination, and statistical error propagation. A linear least-squares estimator can be used to extract the Pauli set \vec{P} , whose 16 elements are the expectation values of the two-qubit Pauli operators, $\langle LR \rangle$, where $L, R \in \{I, X, Y, Z\}$. The Pauli set is related to the raw measurements as given in table 8.1. The two-qubit density matrix (without MLE) is linearly related to the elements of \vec{P} by $\rho = \sum_{L,R} LR \langle LR \rangle / 4$.

An advantage of examining the set \vec{P} is that it is a simple visual tool to distinguish separable from entangled states. In figure 8.13, we show two separable (a-b) and two entangled (c-d) states. For pure states, \vec{P} ideally contains three non-zero bars, all of unit magnitude. \vec{P} can

be divided into three sections: the single-qubit polarization vectors, $\vec{P}^L = \{XI, YI, ZI\}$ (red) and $\vec{P}^R = \{IX, IY, IZ\}$ (blue), and the vector of two-qubit correlations $\vec{Q} = \{\langle XY \rangle, \dots, \langle ZZ \rangle\}$ (purple). For the separable states, we observe near unity components in the three sections. In contrast, for the entangled states, only \vec{Q} has components with near-unity magnitude. The presence of strong correlations and vanishing qubit polarization is a signature of a high degree of entanglement.

To test for systematic errors we measure \vec{P} for a collection of states that differ only by a single-qubit rotation prior to measurement. These errors in detection could appear as offsets or amplitudes that exceed the ± 1 range of the elements of \vec{P} . Two such experiments involving a rotation θ of the left qubit about its y axis having prepared the separable state $|0, 0\rangle$ (experiment I) and the entangled state $(|0, 0\rangle + |0, 1\rangle - |1, 0\rangle + |1, 1\rangle)/2$ (experiment II) are shown in figure 8.14a–b, respectively. In experiment I, $\langle XI \rangle$, $\langle ZI \rangle$, $\langle XZ \rangle$, and $\langle ZZ \rangle$ oscillate with an average visibility of $97.6 \pm 0.3\%$. Moreover, the measured amplitude of all the ideally-zero bars is less than 0.1. In experiment II, the dominant oscillating components are all in \vec{Q} , indicating that the state remains entangled throughout. In this case, we find a visibility of $91.5 \pm 0.3\%$, in good agreement with a master equation simulation incorporating qubit relaxation and dephasing. An oscillation amplitude of ~ 0.1 is observed in $\langle XI \rangle$ and $\langle ZI \rangle$, a factor ~ 2 larger than expected from theory. This discrepancy can arise from a combination of small calibration errors in single-qubit rotations and various residual higher order couplings. For example, the discrepancies between the experiment and master equation simulation can arise from a systematic under-rotation of both qubits by only 1%. There are also higher order couplings that are relevant at this level. The first is the finite strength of the two-qubit ZZ entangling interaction [126] even in the off state ($\zeta/2\pi \sim 1.2$ MHz). This residual coupling leads to errors in some of the two-qubit correlations on the order of $\zeta/\Omega^{L(R)} \sim 2\%$. A second is the presence of a residual qubit-qubit interaction [136], as discussed in section 4.3.2, ($J/2\pi \sim 60$ MHz), that can lead to errors of order $J/(\omega^L - \omega^R) \sim 4\%$. Another effect is the qubit-state dependent filtering of the drive applied to a qubit, which is expected to be on the order of $\chi^{R(L)}/(\omega^{L(R)} - \omega_C) \sim 2\%$. The effect of these couplings can be mitigated by implementing appropriate composite pulse schemes [144] and will be explored in the future.

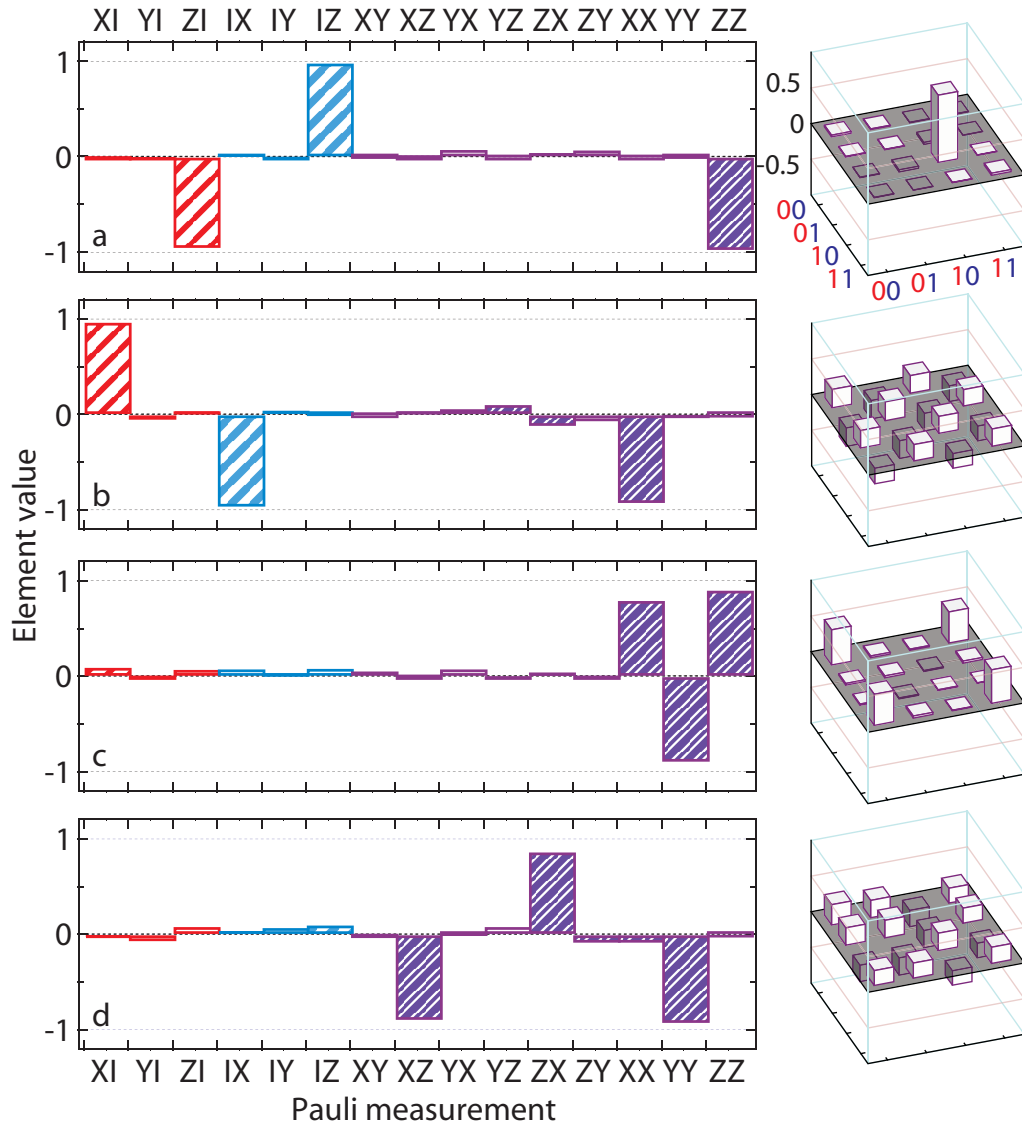


Figure 8.13: Pauli set representation of two-qubit states. Experimental Pauli set (with trivial $\langle II \rangle = 1$ not shown), for separable states **a** $|1, 0\rangle$ and **b** $(|0, 0\rangle - |0, 1\rangle + |1, 0\rangle - |1, 1\rangle)/2$ and entangled states **c** $|\Psi_+\rangle$ and **d** $(|0, 0\rangle + |0, 1\rangle - |1, 0\rangle + |1, 1\rangle)/2$. Red (blue) bars correspond to left (right) single-qubit Pauli operators. Purple bars are the qubit-qubit correlations. The fidelities to the four targeted states are $\mathcal{F} = 98.2 \pm 0.4\%$, $96.8 \pm 0.4\%$, $90.0 \pm 0.6\%$, and $92.5 \pm 0.7\%$. The real part of the density matrix obtained using constrained maximum-likelihood estimation on the same raw measurements is shown in the three-dimensional plot to the right of each Pauli set.

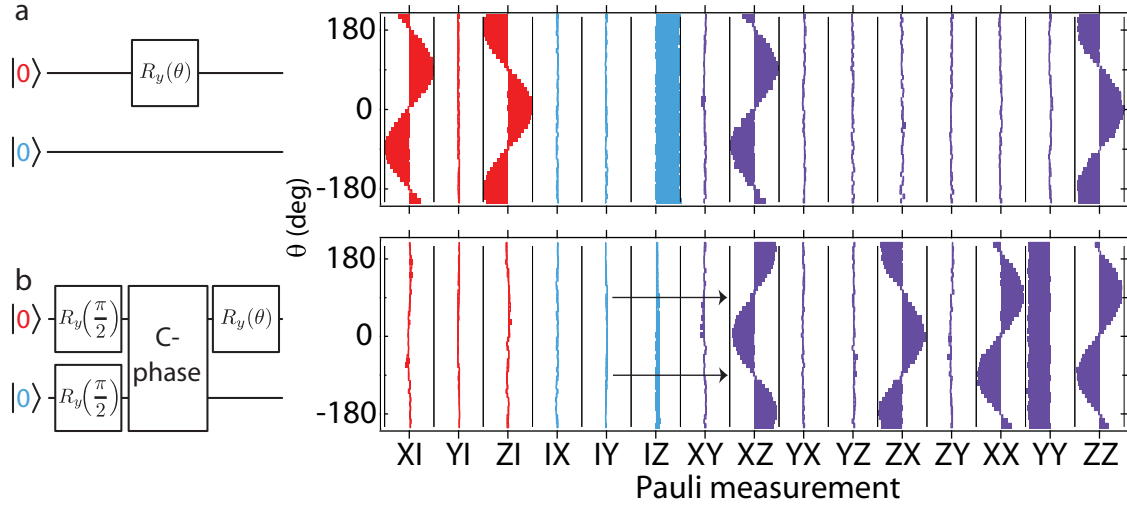


Figure 8.14: Pauli set for separable and entangled states differing only by a single-qubit rotation. Gate sequences and measured \vec{P} , having subjected a (experiment I) the separable state $|0, 0\rangle$ and b (experiment II) the entangled state $(|0, 0\rangle + |0, 1\rangle - |1, 0\rangle + |1, 1\rangle)/2$ to a rotation $R_y(\theta)$ on the left qubit, $-210^\circ \leq \theta \leq 210^\circ$. In experiment I, the left qubit polarization rotates along the x - z plane, while the right qubit remains fully-polarized along z . In experiment II, both qubit polarizations vanish, with the only nonzero and oscillating Pauli operators being qubit-qubit correlators (purple bars). Arrows at $\theta = -90(+90)^\circ$ indicate when the ideal two-qubit state is the Bell state $|\Phi_-\rangle$ ($|\Psi_+\rangle$).

8.7 Characterizing the quantum states

Although we have mentioned a few metrics which characterize the state and entanglement using the full density matrix, we can now work with another set of metrics that use the Pauli set of measurements, and permit the linear propagation of statistical measurement errors.

8.7.1 Fidelity to targeted states

In section 2.5.2, we introduced the fidelity (2.42), $\mathcal{F} = \langle \psi | \rho | \psi \rangle$ to a targeted state $|\psi\rangle$ quantifies the control over two-qubit states, and is given by

$$\mathcal{F} = \frac{1}{4} \vec{P} \cdot \vec{P}_{\text{target}}. \quad (8.11)$$

For experiment I and II, we find $\mathcal{F} = 98.8 \pm 1.0\%$ and $93.4 \pm 1.5\%$ (averaged over θ), respectively. We find excellent agreement between experiment (black circles) and simulation (solid), demonstrating the accuracy of both the state preparation and the measurement (Figs. 4c–d).

8.7.2 Entanglement witnesses

Measures beyond fidelity are necessary to quantify the degree of two-qubit entanglement. Often, entanglement monotones such as concurrence [39] C are obtained using non-linear estimators. As previously mentioned, it is standard practice to first perform maximum-likelihood estimation [145] to generate a positive ρ despite statistical or systematic errors in the measurements, and to then calculate these metrics from the eigenvalue spectrum of related matrices [39]. This non-linear process complicates the propagation of any statistical and systematic errors in the measurements. It can also bias the estimation of metrics such as C when the purity of the two-qubit state is high compared to the readout fidelity [146, 147], as is typically the case with superconducting qubits.

Although not entanglement monotones, entanglement witnesses [39, 45] do allow us to make quantitative statements about entanglement while using only linear operations on measurements. To review, an entanglement witness \mathcal{W} is a unity-trace observable with a positive expectation value for all separable states, such that $\text{tr}(\rho\mathcal{W}) < 0$ guarantees entanglement. Furthermore, $\mathcal{B} = -2 \text{tr}(\rho\mathcal{W})$ gives a lower bound [45] on C . The optimal witnesses (strictest lower bound) for the Bell states are

$$\mathcal{W}_{\Psi_{\pm}} = \frac{1}{4}(II \mp XX \pm YY - ZZ), \quad (8.12a)$$

$$\mathcal{W}_{\Phi_{\pm}} = \frac{1}{4}(II \mp XX \mp YY + ZZ). \quad (8.12b)$$

We return to the experiments described above *I* and *II* of the measured Pauli sets for the separable and entangled states. The measured bounds on concurrence for experiment I (II) are shown in figure 8.15 (figure 8.16). In experiment I, the four bounds are non-positive for all θ to within measurement error, indicating that entanglement is not witnessed. This is expected, since single-qubit rotations should not produce any entanglement. In figure 8.16 in contrast, bounds $\mathcal{B}_{\Psi_{+}}$ and $\mathcal{B}_{\Phi_{-}}$ extend into the positive region, reaching $85.9 \pm 1.5\%$ and $88.1 \pm 1.5\%$ at $\theta = -90^{\circ}$ and 90° , respectively. There is at least one positive bound for most θ (excluding $\pm 180^{\circ}$ and 0°), indicating that the two qubits are entangled. Agreement with the master equation simulation (solid lines) in figure 8.15 and figure 8.16 shows the accuracy of the entanglement witnesses and the small residuals $\sim 2\%$ demonstrate the precision of measurement by joint readout.

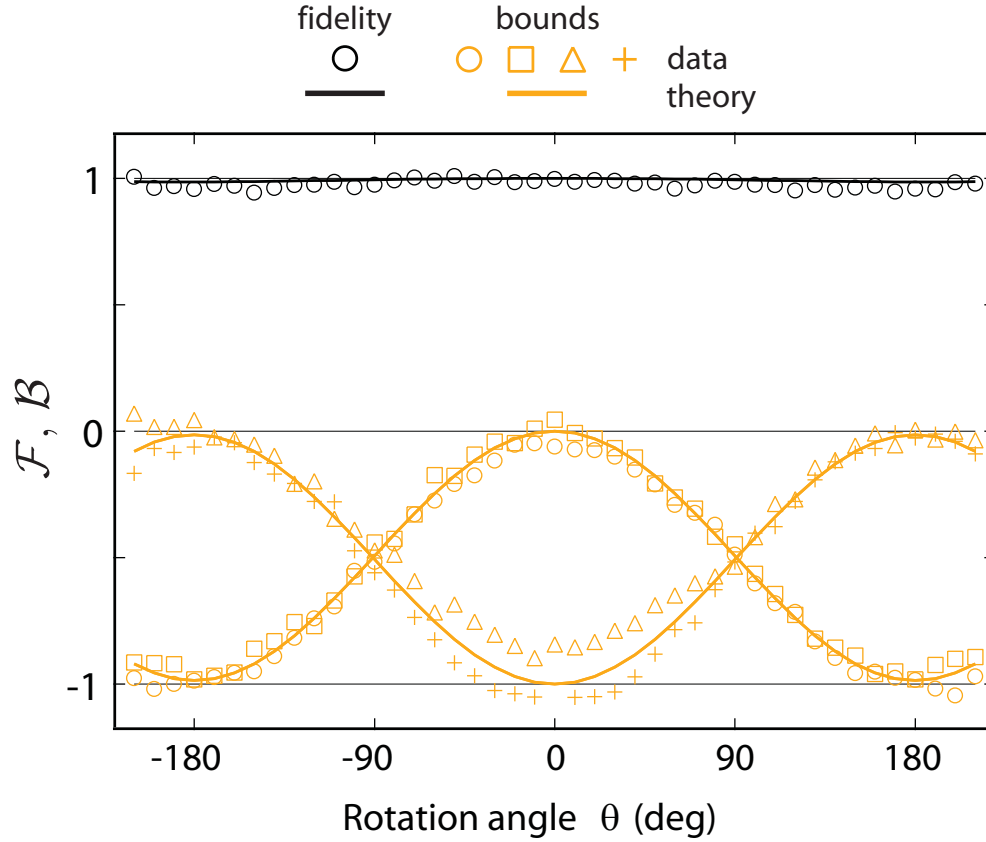


Figure 8.15: Entanglement witness for separable states. Experimental lower bounds \mathcal{B}_i (orange) on concurrence given by the optimal witnesses for Bell states \mathcal{W}_{Ψ_+} (circles), \mathcal{W}_{Ψ_-} (squares), \mathcal{W}_{Φ_+} (triangles), and \mathcal{W}_{Φ_-} (crosses), and fidelity \mathcal{F} to the ideal state (black circles) for experiment I. Solid curves are results of master equation simulations.

8.7.3 Clauser-Horne-Shimony-Holt inequality violation

A related entanglement measure is the Clauser-Horne-Shimony-Holt (CHSH) operator, often used to test quantum mechanics against local-hidden variable (LHV) theories. A CHSH operator [47] is defined as

$$\mathbb{C}_{L,R,L',R'} = LR + LR' + L'R - L'R', \quad (8.13)$$

with $\{L, L'\}$ and $\{R, R'\}$ being pairs of single-qubit Pauli operators along any two axes of the left and right qubits, respectively. With a general choice of axes, for separable states, $|\langle \mathbb{C} \rangle| \leq 2$, coinciding with the LHV bound. For the specific choice $L \perp L'$ and $R \perp R'$, the separable bound is tighter, $|\langle \mathbb{C} \rangle| \leq \sqrt{2}$.

From a subset of the measured \vec{P} in Experiment I and II, we obtain expectation values

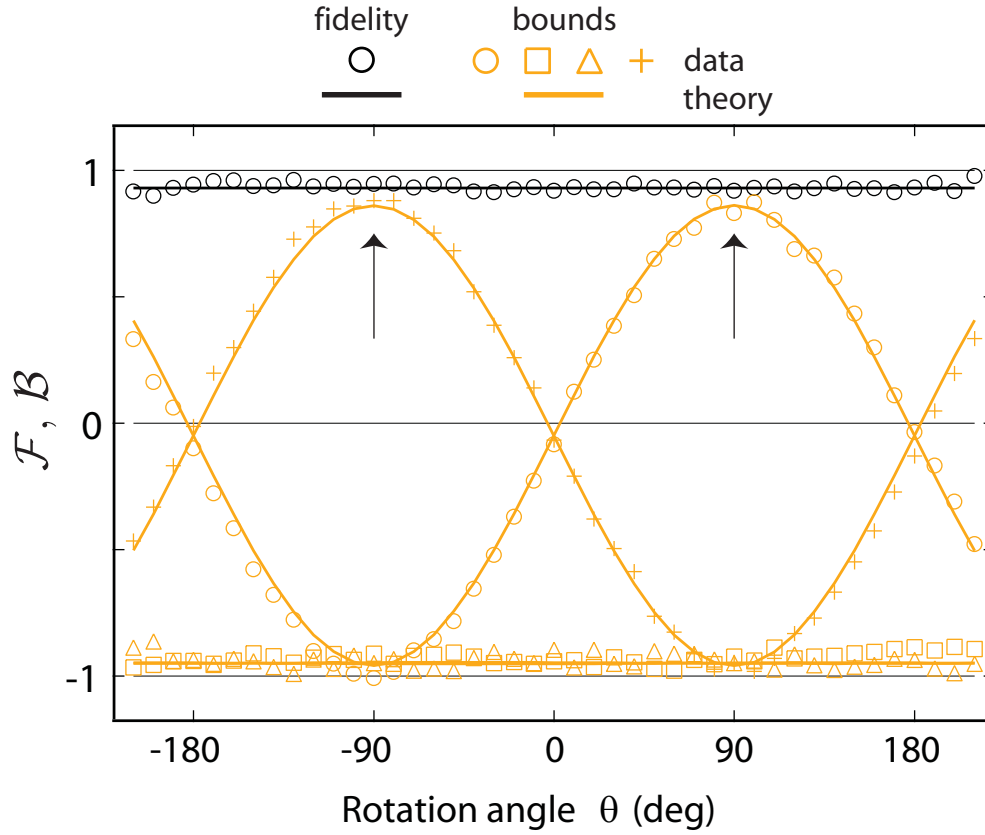


Figure 8.16: Entanglement witness for entangled states. Experimental lower bounds \mathcal{B}_i (orange) on concurrence given by the optimal witnesses for Bell states \mathcal{W}_{Ψ_+} (circles), \mathcal{W}_{Ψ_-} (squares), \mathcal{W}_{Φ_+} (triangles), and \mathcal{W}_{Φ_-} (crosses), and fidelity \mathcal{F} to the ideal state (black circles) for experiment II. A maximum lower bound is reached by \mathcal{B}_{Φ_-} (\mathcal{B}_{Ψ_+}) at $\theta = -90(+90)^\circ$. Solid curves are results of master equation simulations.

of four CHSH operators with $L, L' \in \{X^L, Z^L\}$ and $R, R' \in \{X^R, Z^R\}$. For experiment I (figure 8.17), we find to within statistical error that $\langle \mathcal{C}_{ZXZX} \rangle = \langle XX \rangle - \langle XZ \rangle + \langle ZX \rangle + \langle ZZ \rangle$ (squares) and $\langle \mathcal{C}_{ZXZX} \rangle = \langle XX \rangle + \langle XZ \rangle - \langle ZX \rangle + \langle ZZ \rangle$ (triangles) remain within one standard deviation of the separable bound for all θ . Conversely, for the entangled states prepared in experiment II (figure 8.18), $\langle \mathcal{C} \rangle$ clearly oscillates well past the separable bounds. At $\theta = \pm 45^\circ$, a maximum value $|\langle \mathcal{C} \rangle| = 2.61 \pm 0.04$ is reached. The agreement with theory and proximity of this maximum $|\langle \mathcal{C} \rangle|$ to the $2\sqrt{2}$ upper bound [39] further demonstrate the highly entangled states produced, and the ability of the joint measurement to determine the degree of entanglement precisely. Here, $|\langle \mathcal{C} \rangle|$ exceeds the separable state bound of $\sqrt{2}$ by ~ 30 standard deviations. Furthermore, it also violates a Bell inequality by exceeding the classical bound of 2 by ~ 15 standard deviations. Locality and detection loopholes present

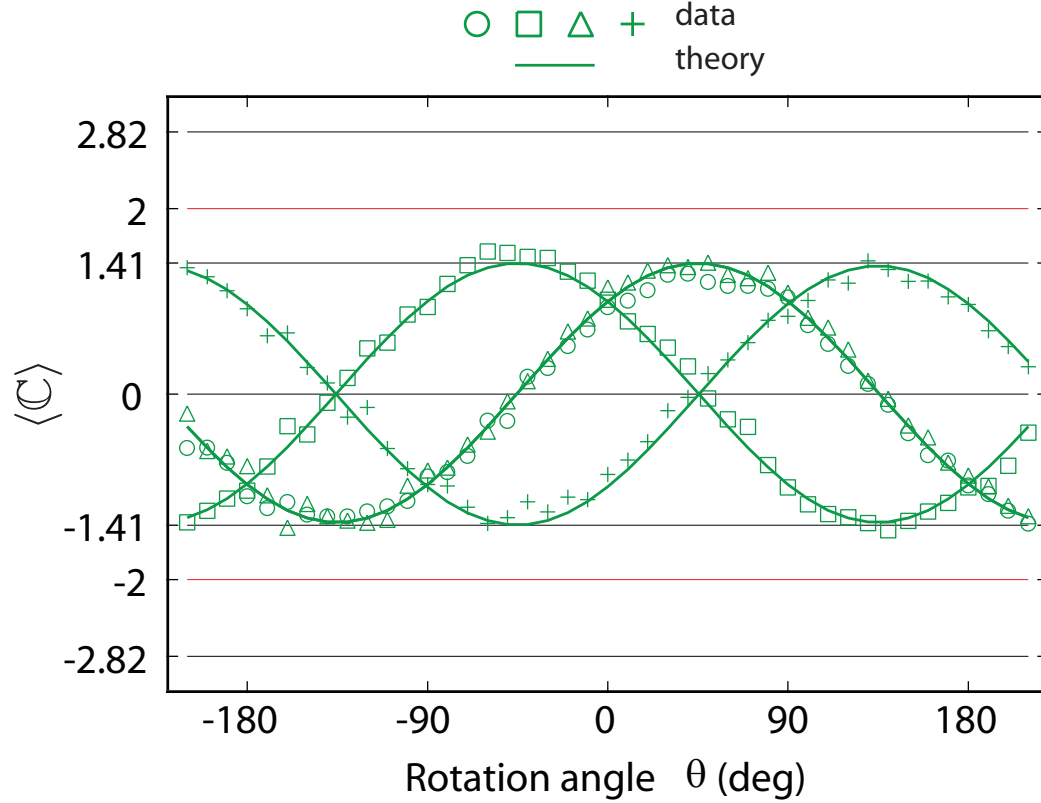


Figure 8.17: CHSH for separable states. Experimental average value of CHSH operators C_{ZZXX} (circles), C_{ZXXZ} (squares), C_{ZXZX} (triangles), C_{XXZZ} (crosses). For experiment I all $\langle C \rangle$ values stay within the separable state bounds $\pm\sqrt{2}$ up to measurement noise (~ 0.04). Solid curves are results of master equation simulations.

in our system preclude a fundamental test disproving LHV. For Josephson phase qubits, the detection loophole has recently been closed using the more traditional technique of single-shot independent readouts [51]. We emphasize that we calibrate the measurement and the gates but we do not specifically optimize for a maximum $\langle C \rangle$ value.

8.8 Chapter summary

In this chapter, we have extended two-qubit circuit QED using on-chip flux control. Using the flux-bias lines, we are able to turn on a two-qubit $\sigma_z \otimes \sigma_z$ interaction which functions via a coupling in the two-excitation manifold of the transmons. This permits the construction of entangling c-Phase gates, which can be used to generate highly-entangled states such as the Bell states. Furthermore, we have demonstrated a joint readout of superconducting

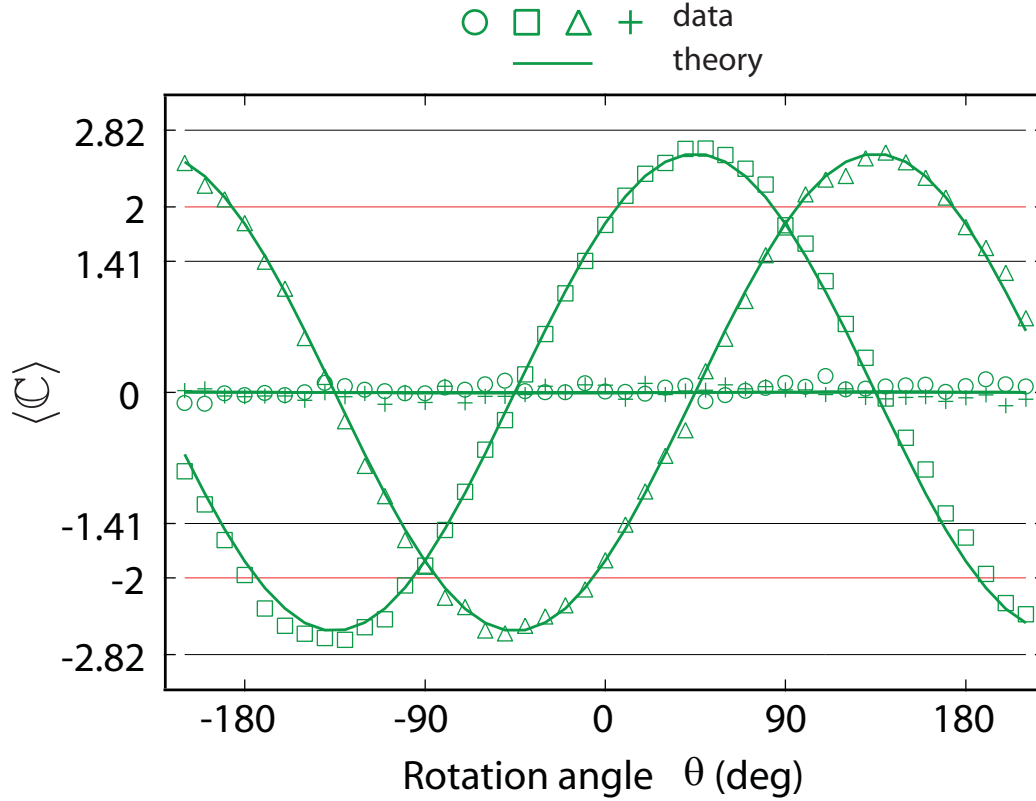


Figure 8.18: CHSH violation with entangled states. Experimental average value of CHSH operators \mathbb{C}_{ZZXX} (circles), \mathbb{C}_{ZXXZ} (squares), \mathbb{C}_{ZXXZ} (triangles), \mathbb{C}_{XXZZ} (crosses). For experiment II, $\max |\langle C \rangle| = 2.61 \pm 0.04$. Solid curves are results of master equation simulations.

qubits using the microwave cavity as a single measurement channel to gives direct access to qubit correlations. This readout is advantageous because it introduces the minimal number of channels for qubit decoherence and is easy to model and calibrate accurately. The joint readout represents a different strategy from that of individual qubit readouts, but is shown to be a viable approach for precisely characterizing entangled states. In its present form, this joint readout has the resolution to detect future improvements in two-qubit gates and will be extendable to systems of three or four qubits. Applying this readout to analyze highly-entangled states, we report the largest violation of CHSH inequalities in a solid-state system. These results represent an advance in the ability to quantify the entanglement between superconducting qubits. Furthermore, the possibility to measure multi-qubit parity operators could be useful for quantum error correction, generating entanglement by post-selection [148, 149] or fundamental tests of quantum contextuality [150, 151].

Next, in chapter 9 we put together all of the components we have discussed thus far, the

high-fidelity single-qubit gates from chapter 6 with the two-qubit c -Phase gate and joint readout described in this chapter, to operate simple quantum algorithms. Specifically, we will deal with the two-qubit Deutsch-Jozsa and Grover's search algorithms, demonstrating the ability of our circuit QED system to behave as a quantum processor.

CHAPTER 9

Two-Qubit Algorithms

By harnessing superposition and entanglement of physical states, it has been proposed that quantum computers could outperform their classical counterparts in solving problems of technological impact, such as factoring large numbers and searching databases [12, 23]. A quantum processor executes algorithms by applying a programmable sequence of gates to an initialized register of qubits, which coherently evolves into a final state containing the result of the computation. Simultaneously meeting the conflicting requirements of long coherence, state preparation, universal gate operations, and qubit readout makes physical realizations of quantum processors challenging.

Although few-qubit processors have already been demonstrated in nuclear magnetic resonance [8–10], cold ion trap [152, 153] and optical [154] systems, a solid-state realization has remained an outstanding challenge. Yet, over the last decade, superconducting circuits have made considerable progress on all the requirements necessary for an electrically-controlled, solid-state quantum computer. In the work for this chapter, we employ superconducting qubits which have coherence times that have risen by three orders of magnitude to $\sim 1 \mu\text{s}$, and combine it with excellent state preparation and single-qubit gates as discussed in chapter 6 to reach error rates [108, 116] of 1%. Furthermore, we have also demonstrated an engineered two-qubit interaction tunable by two orders of magnitude on nanosecond time scales, capable of generating entanglement to violate a CHSH inequality (chapter 8). Finally, we have also

shown that the microwave cavity can serve as a joint qubit readout, which exploits our excellent single-qubit gates and circumvents poor readout fidelity (chapter 8).

In this chapter, we combine all of these achievements and demonstrate a two-qubit superconducting processor capable of implementing the Deutsch–Jozsa (section 2.4.2) and the Grover’s search (section 2.4.3) quantum algorithms. The quantum bus architecture combined with the on-chip flux-bias lines provide the ability to couple, control, and measure the qubits. By pulsing the qubit frequencies to an avoided crossing where a $\sigma_z \otimes \sigma_z$ interaction turns on (section 4.3.3), we realize the two-qubit conditional phase (c-Phase) gate, theoretically treated in section 2.3.2 and experimentally shown in section 8.3.1. Operation in the strong-dispersive regime (section 3.4.3) [110] of cQED allows joint readout [127, 142] and detection of two-qubit correlations through a single line (section 8.4). We will review the basics of the experimental setup (section 9.1), although the algorithms are performed on the same sample cQED₂₂₂ described in chapter 8. In section 9.2 we discuss the implementation of the Deutsch-Jozsa algorithm for two superconducting qubits and in section 9.3 we demonstrate the simple four-level Grover’s search.

9.1 Experimental details

The experimental sample and setup for implementing these algorithms are exactly the same as those in the previous chapter. However, to understand the operation of our two-qubit processor, it will be useful to recall the single excitations spectrum of figure 8.2. Again, the two operation points will be locations I and II. Single-qubit gates and the joint readout will be performed at location I while the two-qubit c-Phase gate will be implemented by flux-pulsing into location II.

We have single-qubit rotations around the x and y axes of each qubit ($\{R_x(\theta), R_y(\theta)\}$), via shaped microwave excitations, at our disposal, as well as the four different c-Phase gates (cU_{ij}) described previously. The pulse sequences for the algorithms are defined in Mathematica and programmed into six channels across two arbitrary waveform generators (Tektronix AWG 520 and AWG 5014). We next review the two simple quantum algorithms (Deutsch-Jozsa and Grover’s) and describe how we implement them in our circuit QED processor.

9.2 Deutsch-Jozsa algorithm

The Deutsch–Jozsa (DJ) algorithm (section 2.4.2) is one of the simplest quantum algorithms to implement and one of the quintessential examples of using quantum mechanics to determine a quantity using fewer operations than a classical algorithm. It also represents a class of deterministic quantum algorithms which provide an exponential speedup over classical algorithms. The advantage of the DJ algorithm is explicitly described earlier in this thesis in section 2.4.2. Here, we review a few of the basic concepts to understand how to implement it in our two-qubit superconducting quantum processor.

To motivate the use of the DJ algorithm, recall the problem of finding out whether a coin is fair, with heads on one side and tails on the other, or biased, with heads on both or tails on both. The classical method for determining the answer requires that each side of the coin be examined. However, this classical solution in fact gives too much information, as we not only find out whether the coin is fair or not, but also exactly which sides are heads or tails. We can instead employ the DJ algorithm on a register of two qubits and determine *only* information about the nature of the coin in *one* examination step.

We can represent the four possible coins with four functions f that map one input bit, $x = 0, 1$, representing the two sides of the coin, onto a single output bit, $f(x) = 0, 1$, representing either heads or tails. There are only four such functions which take a single bit to another single bit. Two of these functions are constant, or independent of the input bit x , $f_0(x) = 0$, $f_1(x) = 1$, representing the fake coins. The other two functions are balanced, $f_2(x) = x$, $f_3(x) = 1 - x$, representing the fair coins. The DJ algorithm functions by performing a bitwise addition of the functions evaluated on one of the qubits with the other qubit. Specifically, as previously described in section 2.4.2, the operation of the function on one of the qubits can result in a quantum phase kickback onto the state of the other qubit which then permits determination of the quantity $f(0) \oplus f(1)$.

9.2.1 Breaking down the algorithm

The DJ algorithm programmed in our system is schematically represented in figure 9.1. We identify the left qubit as the control qubit and the right qubit as the target qubit. Both qubits in the register start off in the ground states, such that $|\psi\rangle_0 = |0, 0\rangle$. The algorithm consists of three main parts. The first block is simply a simultaneous single-qubit rotation on both

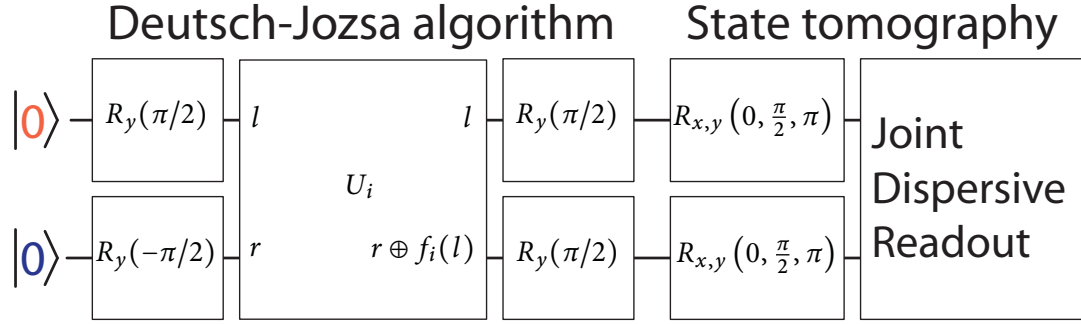


Figure 9.1: Quantum circuit for DJ algorithm. The DJ algorithm is comprised of two stages of single-qubit operations surrounding a two-qubit unitary U_i . The two-qubit gates U_i encode the four functions of one bit to one bit, $f_0(x) = 0$, $f_1(x) = 1$, $f_2(x) = x$, and $f_3(x) = 1 - x$, as the transformations $|l, r\rangle \rightarrow |l, r \oplus f_i(l)\rangle$ (\oplus denotes addition modulo 2). The encoding unitaries are $U_0 = I \otimes I$, $U_1 = I \otimes R_x^\pi$, $U_2 = (I \otimes R_y^{\pi/2} R_x^\pi) cU_{00} (I \otimes R_y^{\pi/2})$, and $U_3 = (I \otimes R_y^{-\pi/2} R_x^\pi) cU_{11} (I \otimes R_y^{-\pi/2})$, respectively. The final state tomography step involves 15 combinations of single-qubit rotations for determination of ρ .

qubits to get into the superposition state

$$|\psi\rangle_1 = \frac{1}{2} (|0, 0\rangle - |0, 1\rangle + |1, 0\rangle - |1, 1\rangle). \quad (9.1)$$

The next step involves applying the unitary transformation which will perform the bit-wise addition, $|lr\rangle \rightarrow |l(r \oplus f_i(l))\rangle$, for the four different functions f_i . With single-qubit rotations and two-qubit c -phase gates (cU_{ij}) at our disposal, we can identify the four unitary transformations U_i which engender the properties of the four possible functions f_i :

$$U_0 = \mathbb{1} \otimes \mathbb{1} \quad (9.2a)$$

$$U_1 = \mathbb{1} \otimes R_x(\pi) \quad (9.2b)$$

$$U_2 = [\mathbb{1} \otimes R_y(\pi/2)] cU_{00} [\mathbb{1} \otimes R_y(\pi/2)] \quad (9.2c)$$

$$U_3 = [\mathbb{1} \otimes R_y(-\pi/2)] cU_{11} [\mathbb{1} \otimes R_y(-\pi/2)]. \quad (9.2d)$$

It is easy to understand U_0 and U_1 , as they are simply the identity, and a bit-flip of the target qubit, respectively. These both do nothing to the state of the control qubit, and hence at the end of the final step, where another $\pi/2$ rotation is applied, the state is measured as $|1, 0\rangle$. Note that the target qubit is unaffected by U_0 and U_1 because the first $-\pi/2$ rotation has placed it into an eigenstate of each unitary, with eigenvalue equal to 1.

In the case of the balanced unitaries, U_2 and U_3 , correspond to applying c NOT and $z - c$ NOT. It is trivial to build these gates from our c -Phase gates, requiring only single-qubit

rotations on the target qubit in each case. Although neither U_2 nor U_3 directly alters the state of the control qubit, a phase of -1 is attained as a result of its operation on the target qubit superposition state. This phase in effect flips the superposition of the control qubit, such that the final $\pi/2$ rotation in the last step takes the final state to $|0, 0\rangle$.

9.2.2 Deutsch–Jozsa results

In our experiment, we run the algorithm for all four possible functions f and then perform quantum state tomography on the two-qubit register. Although the operation of the algorithm requires only the measurement of the control qubit (with the state $|1\rangle$ corresponding to constant and $|0\rangle$ for balanced), state tomography permits us to observe the state of the target qubit as well as any errors which may arise.

The two-qubit state tomography is performed as described in section 8.6. We also follow the same prescription given earlier (section 8.6.1) for obtaining a density matrix through maximum-likelihood estimation, ρ_{ML} . Figure 9.2 shows the real part of the inferred ρ_{ML} for the four cases. All elements of the imaginary part of ρ_{ML} are less than ~ 0.05 . For constant functions f_0 and f_1 , shown in figure 9.2a–b, we find the final state $|1, 0\rangle$ with a fidelity (as given by Eq. (8.11)) of 0.94 and 0.95, respectively. For the balanced functions f_0 and f_1 (figure 9.2c–d), we measure the state $|0, 0\rangle$ with fidelities of 0.92 and 0.85.

The fidelities to the constant functions are slightly higher than those of the balanced functions due to shorter length of pulse sequences. In the case of the constant functions, there are only single-qubit operations, with each gate taking 8 ns and separated by 5 ns buffering time, for a total of 34 ns. On the other hand, for the balanced functions, the unitary step which implements f_2 and f_3 itself consists of 2 single-qubit rotations and a two-qubit gate which takes 30 ns. Therefore, there are a total of 4 single-qubit rotations, the two-qubit gate, and 5 ns buffer between all pulses resulting in a total algorithm time of 82 ns. The lower fidelity for the balanced cases can be seen when repeating the algorithm multiple times. We obtain statistics from 8 measurements of the four cases, finding fidelities to the ideal final states of 0.93 ± 0.01 , 0.93 ± 0.01 , 0.909 ± 0.006 , 0.841 ± 0.009 .

Although the reduced fidelity for f_2 and f_3 are roughly consistent with the time it takes to perform the algorithm and the coherence times of the system, a full characterization of the unitary gates which generate the functions should be performed to understand the nature of the errors. This work is left for the future.

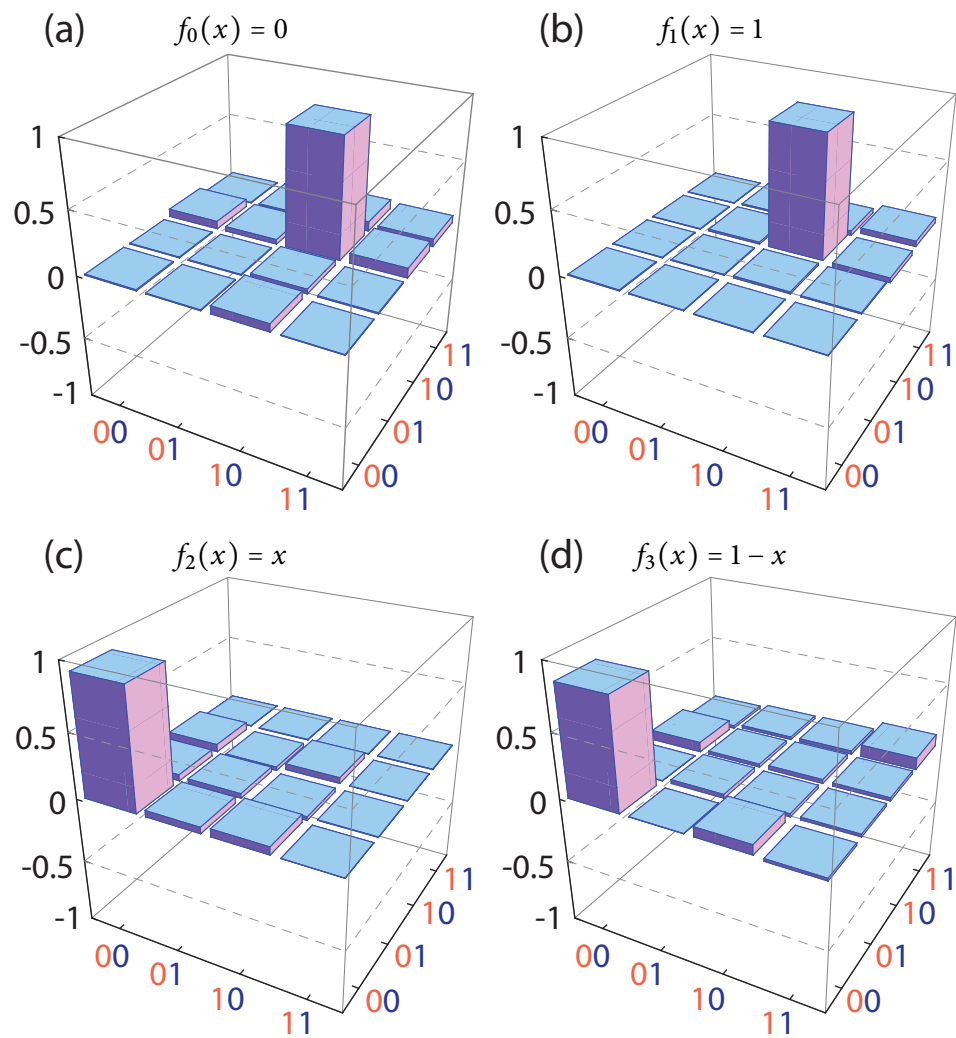


Figure 9.2: Results for four cases in DJ algorithm. Real part of the inferred density matrix ρ_{ml} of the algorithm output in the four cases (imaginary elements of ρ_{ml} are less than 0.05, 0.03, 0.05, 0.06, respectively). For the constant (balanced) functions f_0 and f_1 (f_2 and f_3), ρ_{ml} shows a high fidelity to $|1, 0\rangle$ ($|0, 0\rangle$), as expected. For the density matrices shown, the fidelities to the ideal output states are $\mathcal{F} = 0.94, 0.95, 0.92,$ and 0.85 .

9.3 Grover search algorithm

The other quantum algorithm which we implement in our two-qubit processor is the Grover search algorithm. It reflects a separate class of quantum algorithms which is probabilistic in nature—the correct solution can be found with high probability—and not deterministic like the Deutsch-Jozsa algorithm which always gives the correct answer. We describe Grover’s search algorithm in detail earlier in this thesis in section 2.4.3. Here we simply recall the basic concepts behind the algorithm and discuss it in regards to our two-qubit implementation.

A classical search for a particular entry in an unordered list of N elements requires linear time, or $O(N)$ queries to the list. We can think of the problem as searching for a phone number in a telephone book, and the classical search involves randomly choosing a name from the list for the search. Grover’s algorithm, however, provides a method for search faster than the classical case, and in the best case allows a quadratic speedup, or $O(\sqrt{N})$ time.

With two qubits, it is possible to implement a Grover’s search with $N = 4$. Let the four entries be represented by the set $x = \{0, 1, 2, 3\}$ and there is a function $f(x)$ which returns the value 0 for all x except for x_0 , where $f(x_0) = 1$. Classically searching for x_0 would require on average 2.25 evaluations of the function f . However, using Grover’s algorithm, we can simply use a single evaluation.

9.3.1 The oracle

In our implementation, we can identify the two-bit set as $x \in \{00, 01, 10, 11\}$, being the labels of our four computational basis states. Grover’s algorithm allows us to determine the x_0 at which $f(x_0) = 1$ through a single call to an oracle O which has encoded $f(x)$ into a quantum phase,

$$O|x\rangle = (-1)^{f(x)}|x\rangle. \quad (9.3)$$

Hence, for all $x \neq x_0$, we simply return the same state, whereas for the target x_0 , we pick up a -1 phase difference. An oracle which realizes the relation of Eq. (9.3) is the c-Phase gate (section 2.3.2 and section 8.3.1). Specifically, for finding any of the 4 $x = ij$, the oracle to be used is then $O = cU_{ij}$.

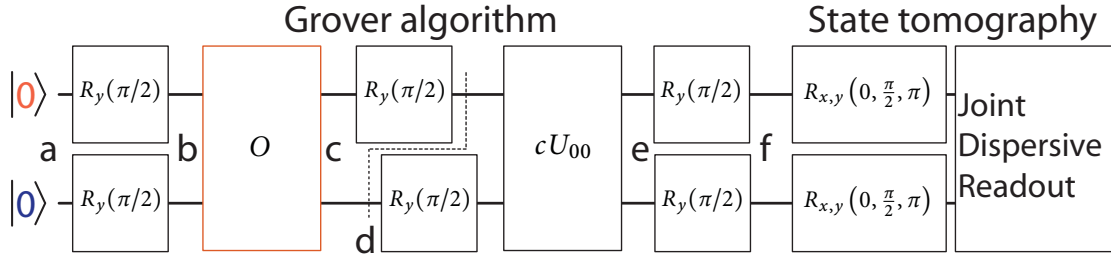


Figure 9.3: $N=4$ Two-qubit Grover algorithm schematic. Concatenation of single-qubit and c -Phase gates implementing one iteration of Grover searching. Without loss of generality, we have replaced the Walsh–Hadamard transformations $W = R_x^\pi R_y^{\pi/2}$ in the usual description of the algorithm [12, 23] with $R_y^{\pi/2}$ rotations in order to eliminate 6 single-qubit rotations and complete the sequence in 104 ns. The orange box is the oracle $O = cU_{ij}$ that encodes the solution $x_0 = ij$ to the search problem in a quantum phase. Note that the first half of the algorithm is identical to the entangling sequence in figure 8.7 for generating Bell states, while the second half is essentially its mirror image.

9.3.2 Breaking down the algorithm

The basic Grover’s algorithm consists of three main parts (section 2.4.3): superposition state initialization, oracle call to mark the targeted state with a phase, conditional phase to amplify the amplitude of the targeted state. Whereas an N -entry Grover’s search can require multiple iterations of the last two parts, in our 4 state case, we will only need to run each step once. Our sequence for implementing Grover’s algorithm is schematically illustrated in figure 9.3.

Both qubits start off in the ground state, $|\psi\rangle_0 = |0, 0\rangle$. The algorithm begins with the initialization of a superposition of all 4 possible elements in the set is performed using simultaneous single-qubit $\pi/2$ rotations on both the left and right qubit, $R = R_y^L(\pi/2) \otimes R_y^R(\pi/2)$. This results in the maximal superposition state

$$|\psi\rangle_1 = \frac{1}{2} (|0, 0\rangle + |0, 1\rangle + |1, 0\rangle + |1, 1\rangle). \quad (9.4)$$

Next, the oracle operator is applied, which in our case is any one of the four c -Phase gates, cU_{ij} , depending on which of the four entries we would like to search for. For illustrative

purposes, let us search for the third entry $ij = 10$, so that we apply

$$O = cU_{10} = \begin{pmatrix} 1 & 0 & 0 & 0 \\ 0 & 1 & 0 & 0 \\ 0 & 0 & -1 & 0 \\ 0 & 0 & 0 & 1 \end{pmatrix}. \quad (9.5)$$

After this step, the state of the two-qubit register is then

$$|\psi\rangle_2 = \frac{1}{2} (|0, 0\rangle + |0, 1\rangle - |1, 0\rangle + |1, 1\rangle), \quad (9.6)$$

where the oracle has done its job to mark the solution with a phase in front of the relevant searched entry, $|1, 0\rangle$.

At this point of the algorithm, the solution has already been encoded into the quantum register. However, to be able to determine the solution, a deterministic measurement on the qubits will need to be performed. A measurement at this stage would simply give a probabilistic result of one of the four computational basis states. The nature of the third part of the algorithm is to increase the probability that the measurement will return the targeted entry. This is performed by applying the combination of another set of simultaneous single-qubit $\pi/2$ rotations, R , with a conditional phase gate cU_{00} , followed by R again. We can see that after the first RcU_{00} , we are then in the state

$$|\psi\rangle_3 = \frac{1}{2} (|0, 0\rangle - |0, 1\rangle + |1, 0\rangle - |1, 1\rangle). \quad (9.7)$$

These two pulses combined apply a phase shift of -1 to all states which are orthogonal to the state $|0, 0\rangle$. The resulting state is simply a separable state, and the final application of R , in fact leaves us in the targeted state $|1, 0\rangle$. The combination of $RcU_{00}R$ in effect inverts the state around the mean and has transferred the phase in front of the $|1, 0\rangle$ in $|\psi\rangle_2$ into an amplitude which can be detected in a computational basis state measurement.

9.3.3 Grover results and debugger

Experimentally, we simply concatenate our single-qubit and two-qubit gates as prescribed in the schematic figure 9.3. The single-qubit gates used here have $\sigma = 2$ ns with a total width of 4σ . A buffer time of 5 ns is left in between all stages of pulses to ensure complete turn-off. The first applied conditional phase gate which serves as the oracle is tuned up as prescribed

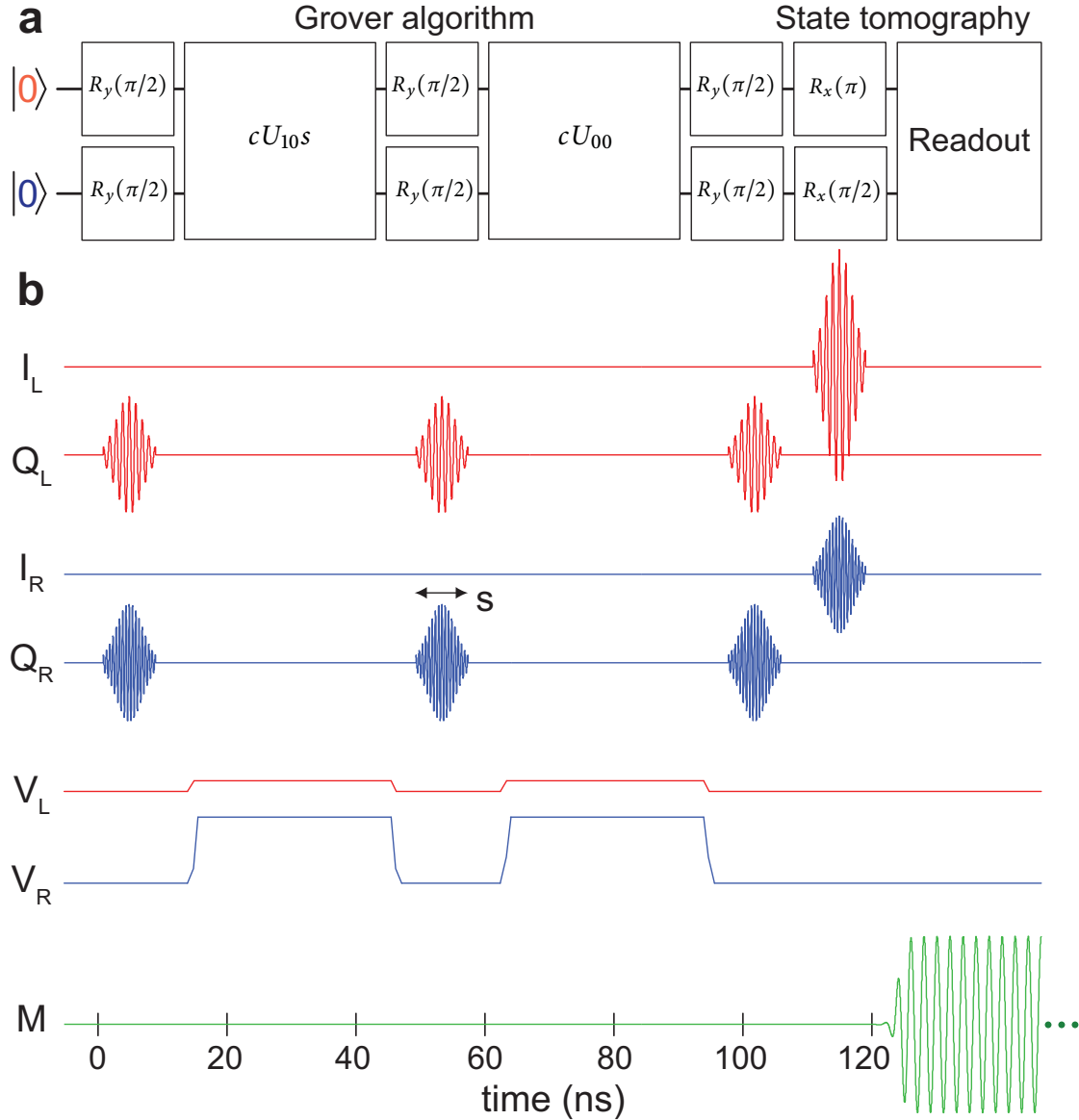


Figure 9.4: Microwave and flux pulses for Grover algorithm. (a) An example sequence, executing the Grover search algorithm with oracle $O = cU_{10}$ and measuring $M_{13} = -\beta_1\sigma_z^L + \beta_2\sigma_y^R - \beta_{12}\sigma_z^L \otimes \sigma_y^R$. (b) Illustration of the microwave and flux pulses realizing the operations directly above. All microwave pulses implementing the x - and y -rotations have Gaussian envelopes, with standard deviation $\sigma = 2$ ns, truncated at $\pm 2\sigma$. The rotation axis is set using I-Q (vector) modulation (chapter 5) and the rotation angle is controlled by pulse amplitude. Flux pulses implementing c -Phase gates have three tuning parameters: the amplitude A of V_R , the amplitude B of 1 ns ledges at the beginning and end of the V_R -pulse, and the amplitude C of V_L (section 8.3.1). The flux pulse duration is fixed at 30 ns.

in section 8.3.1. The voltage levels of the flux bias pulses on both the left and right flux bias lines are found for each of the four different conditional phase gates.

The second applied conditional phase gate, however, does not behave the same way as the first conditional phase gate. When concatenating flux pulses, there tends to be a ‘memory’ effect which causes a phase shift on the qubits due to the first pulse. The second pulse is affected in the same way by any of the flux pulses used for the first c-Phase, so fortunately it does not affect the performance of the algorithm. Rather, the voltage levels of the second c-Phase needs to be tuned independently of the first. We employ experiments much like the tune-up of the first c-Phase, but include a flux pulse with a duration and amplitude equal to that of the first c-Phase.

Therefore, when we run the algorithm according to the prescription, the second c-Phase gate uses a different set of flux bias voltages from the first. Nonetheless, the algorithm still functions as it should, and we can investigate its action every step of the way. We employ a debugging technique by interrupting the algorithm after each step and performing state tomography. Figure 9.5 shows the step-by-step breakdown of our Grover’s search algorithm. We perform two-qubit state tomography (section 8.6) using our joint readout (section 8.4) at 6 different stages of the algorithm, and map out the behavior of the two qubits along the way. Maximum-likelihood estimation is used to obtain the density matrix ρ_{ml} , which we plot in the standard computational basis.

The first density matrix figure 9.5a shows the initialization of the two-qubits in the ground state $|0, 0\rangle$. Here, the fidelity is 0.99 to the ideal ground state. Next, the single-qubit $\pi/2$ rotations place us in the maximal superposition state (9.4), signified in the density matrix with all the bars raised to a value ~ 0.25 , figure 9.5b. This preparation gives a fidelity to the ideal state of 0.99. Then, the oracle is applied with flux pulses, here chosen to be $O = cU_{10}$, and leaving us in the entangled state (9.6). This density matrix figure 9.5c looks similar to the previous one, except the searched entry $ij = 10$ is now marked with all the non-diagonal bars along the 10 row and column being negative (fidelity is 0.83). We can see that this is maximally entangled state as we can perform a single-qubit operation ($R_y(\pi/2)$) on the left qubit, and end up with figure 9.5d, which is the Bell state $|\Psi^+\rangle$. The fidelity to this Bell state is 0.88. Next, a single-qubit gate is applied to the right qubit, followed by the second c-Phase (cU_{00}), resulting in the state given in (9.7). This second c-Phase has taken the phase from the oracle and re-distributed it into a unique separable state (fidelity is 0.91), figure 9.5e, which can be transformed with the simultaneous single-qubit rotation R into the final solution state $|1, 0\rangle$, shown in figure 9.5f. The fidelity to the final state is found to be 0.82.

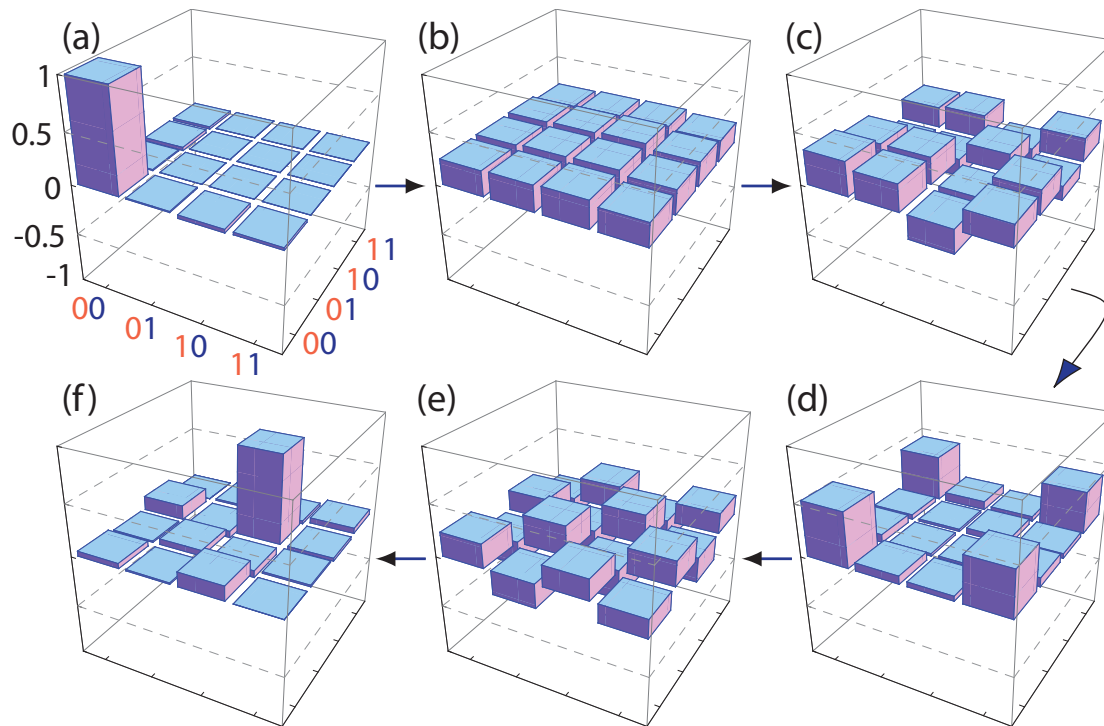


Figure 9.5: Implementing Grover's algorithm. Real part of ρ_{ml} obtained by state tomography after each step of the algorithm with oracle $O = cU_{10}$. Starting from $|0, 0\rangle$ (a), the qubits are simultaneously rotated into a maximal superposition state (b). The oracle then marks the solution, $|1, 0\rangle$, by inverting its phase (c). The $R_y^{\pi/2}$ rotation on Q_L turns the state into the Bell state $|\Psi^+\rangle$, demonstrating that the state is highly entangled at this stage (d). The $R_y^{\pi/2}$ rotation on Q_R produces a state identical to (c) (data not shown). The application of cU_{00} undoes the entanglement, producing a maximal superposition state (e). The final rotations yield an output state (f) with fidelity $\mathcal{F} = 82\%$ to the correct answer, $|1, 0\rangle$.

Similar performance is obtained for the other three oracles and shown in figure 9.6. The reduction in fidelity of $\sim 15 - 20\%$ is consistent with the coherence times of the two qubits and the 104 ns it takes to perform the entire algorithm and measurement sequence (3 single-qubit rotations, 2 c-Phase gates, another single-qubit rotation for state tomography).

However, the issue with needing to re-tune the second c-Phase gate makes the current implementation difficult to scale up to more and more complex algorithms. Investigations are presently being carried out to ascertain the nature of the flux pulse memory and creative pulse shaping schemes for combatting it are being developed. Also, the fidelity to the states at different points of the Grover debugger is not a simple monotonic function of the total gate time. Rather, there is some variation with respect to the fidelities after specific stages. We do

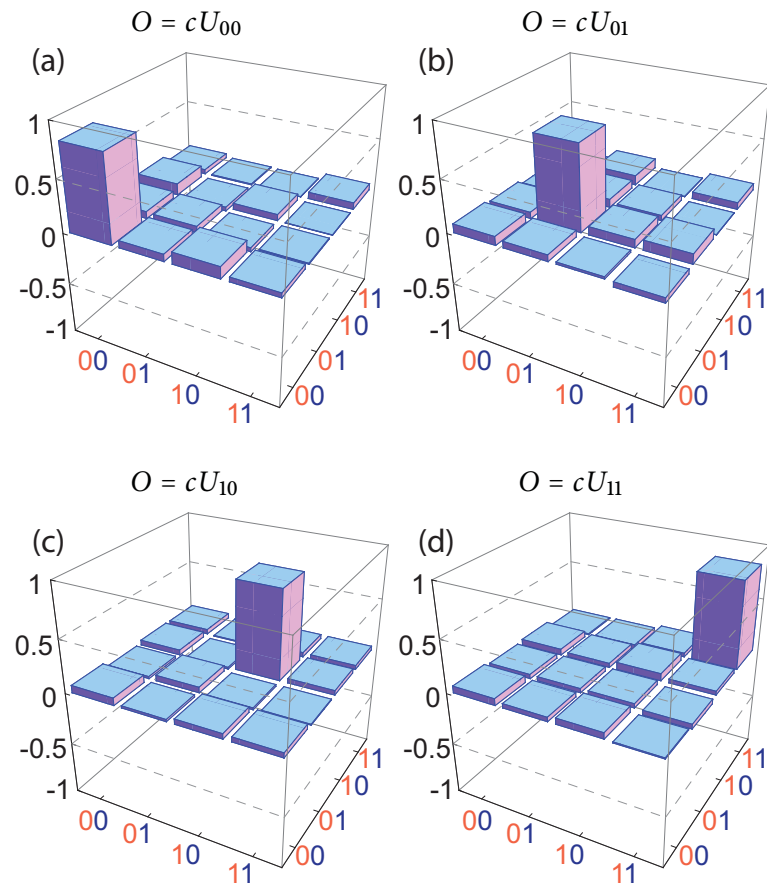


Figure 9.6: Grover fidelity for all choice of oracles. The Grover’s algorithm is run for all four choices of oracles $O = cU_{00}$, cU_{01} , cU_{10} , cU_{11} , finding fidelities of 0.81, 0.80, 0.82, 0.81, respectively.

not yet understand the reason for this, but further characterization of the two-qubit gate and combinations of two-qubit and single-qubit gates via process tomography or randomized benchmarking techniques could clarify the picture greatly. This work is left for the future.

9.4 Chapter summary

In summary, we have demonstrated two-qubit quantum algorithms using a superconducting circuit. The incorporation of local flux control and joint-dispersive readout into cQED, together with a tenfold increase in qubit coherence over previous two-qubit devices, has enabled on-demand generation and detection of entanglement and the implementation of the Grover and Deutsch–Jozsa algorithms. As the first demonstration of such quantum algorithms in a solid-state system, we can look towards more interesting and complex quantum information

processing using circuit QED. Specifically, the present architecture can be immediately expanded to several qubits with controllable $\sigma_z \otimes \sigma_z$ interactions between nearest-frequency neighbors, placing within reach the generation of Greenberger–Horne–Zeilinger states and the exploration of basic concepts of quantum error correction [12, 23]. The final chapter of this thesis will suggest some more future directions for our quantum information processor and provide a little broader perspective on quantum computing as a burgeoning field of research.

CHAPTER 10

Conclusions and Future Work

THE rudimentary superconducting quantum processor presented in this thesis represents a major first step towards the achievement of a larger scale quantum computer. Over the past ten years superconducting circuit-based quantum computing has gone from a few Rabi oscillations that lasted just nanoseconds to the programming of simple quantum algorithms. Yet, moving forward, there is still a formidable challenge of how to build on what has been demonstrated to push the envelope both on the technological aspects of a quantum computer as well as the physics of quantum information processing. The rapid progress of superconducting qubit based quantum computing has been due in large part to the already well-developed protocols for NMR, photon, and trapped-ion quantum computing systems. The immediate task at hand of scaling the superconducting system to more than two qubits will most likely be no different, as it takes merely minutes to scour through the literature to find three and four qubit experiments already implemented to build a list that will take more than two years of work to accomplish. Regardless, these are necessary steps for demonstrating that the superconducting-circuit based quantum computing system is viable and possibly a more attractive option further down the road.

Here, some reflections on extending the work presented in this thesis are given, broken down into ideas for improving the control over single and two-qubit operations (section 10.1) and a few proposed experiments for expanding past two qubits (section 10.2). Finally, an

outlook for the longer term prospects of scaling quantum information systems is given (section 10.3).

10.1 Improving one and two-qubit operations

As mentioned previously in this thesis (chapter 6), the ultimate goal of a fault-tolerant quantum computer will require considerably lower error rates ($10^{-4} - 10^{-5}$) than the 10^{-2} achievable at this time. Furthermore, the current two-qubit *c*-Phase gate lags even further behind with the generated entangled states achieving state fidelities $\sim 90\%$. There is certainly a lot of room for improvement and working towards the fault-tolerant threshold is an important direction. Here, we highlight a few possible directions.

10.1.1 Longer coherence times

Perhaps the most critical component towards improving both single and two qubit operations is obtaining longer coherence times. It is safe to say that all the gate fidelities would improve significantly with another order of magnitude of improvement from our current $1 - 2 \mu\text{s}$ range. As briefly discussed in section 3.5.1, the transmon qubits currently have relaxation times which are well-understood through the multi-mode Purcell effect up to the limit of an intrinsic $Q \sim 50,000 - 70,000$. At this stage, it is unclear as to what is the direct cause of this intrinsic limit, which is seen not only with the transmon qubits used in our circuit QED architecture, but in other superconducting qubit experiments as well [155, 156].

There have been a number of proposed loss mechanisms, including decaying into two-level systems on the surfaces of the superconductor [157], dissipation into the dielectric substrate [155], trapped surface vortices, and decay into non-equilibrium quasiparticles near the Josephson junctions. Which, if any, of these are the reason for the intrinsic loss is currently under investigation. Specifically, there are current efforts in our group to examine the quality factors of substrate materials (such as sapphire, or silicon-dioxide). This can be investigated by making a very good high-Q factor single-photon cavity, and finding out whether it can be spoiled by including dielectric slabs. Another avenue is to specially engineer the superconducting films around the Josephson-junctions of the superconducting qubits in order to reduce stray non-equilibrium quasiparticles from interacting with the junctions.

Outside of the intrinsic loss, in the circuit QED system, the qubit relaxation times are governed by the multi-mode Purcell effect. In terms of T_1 of the qubit, it would seem like

the best result is to use narrower cavities, and decreasing the spontaneous emission decay. However, this is not optimal for readout, as it can result in a very poor signal-to-noise ratio due to fewer signal photons being collected during a qubit T_1 [53]. A solution to avoid the Purcell-limited qubit decay is to employ a carefully microwave-engineered addition to the cavity which changes the real part of the impedance at a specific frequency [82]. This idea of a “Purcell filter” would then allow a qubit to have longer relaxation times while also maintaining a fast readout.

10.1.2 Better qubit operations

Although improved coherence times would undoubtedly make single-qubit gates better, we can also build on the work in section 6.4, where we employ derivative-pulse shaping to improve the gate fidelity. As discussed in section 4.2.3, the anharmonic spectrum of the transmon qubit can result in leakage out of the computational basis at shorter gate lengths. Pulse shaping techniques can be used to mitigate this effect. Although the experimental work in section 6.4 does not prove that the error mechanism is due to leakage to the second excited state, the pulse-shaping does drastically improve the gate fidelity for shorter gate lengths. A true test of whether the error mechanism is the anharmonicity would be to test for the population of the $|2\rangle$ state.

Nonetheless, as we start to add more and more qubits, the Hilbert space becomes quite large and even weak residual cavity-mediated interactions can be a source of error. It is thus important to actually determine whether a single-qubit is behaving as an uncoupled single-qubit should. A novel way to test this would be to use the randomized benchmarking technique to extract the average gate fidelity of a single-qubit, but while a residual coupling to another qubit is still on. We can see from section 8.3 that even when the qubits in that experiment were detuned by over ~ 2 GHz, a residual $\sigma_z \otimes \sigma_z$ interaction still persisted on the order of $\sim 1 - 2$ MHz. An experiment which attempts randomized benchmarking on one qubit, while performing arbitrary operations on the other qubit, would be a good metric for how the average fidelity degrades due to the presence of this always-on interaction. To advance this even further, one could imagine repeating the same experiment but for different pulse-shapes to see if the effect of the coupling could be minimized through optimal control techniques.

Other improvements in single-qubit operations could be sought through using techniques such as optimized dynamical decoupling [158] to suppress specific forms of error. These

techniques have already begun to be used in trapped-ion [159] and electron spin systems [160]. However, the extension of such protocols to improve the performance of arbitrary gate sequences is still a topic of ongoing theoretical research.

Whereas in this thesis we have detailed the importance of single-qubit gate characterization (chapter 6), we have yet to accomplish the same level of rigor with the two-qubit entangling gate demonstrated in chapter 8. Specifically, we may ask the same questions as in the single-qubit gate case: what are the gate fidelity and process fidelity associated with the *c*-Phase?

To characterize two-qubit gates, we may again consider two techniques used with single-qubit gates, namely process tomography and randomized benchmarking. As discussed in chapter 6, process tomography can theoretically give a lot of information about the underlying gate, and would result, in the two-qubit case, with a 16×16 process matrix χ . The protocol would be very similar to that given in figure 6.9, with the preparation of at least 16 starting states to span the two-qubit Hilbert space, followed by the action of the two-qubit gate, and then ending with state tomography for all 16 cases. However, the same caveats for QPT being a good gate metric in the single-qubit case arise for the two-qubit case as well. Specifically, generating the starting states and the state tomography steps both involve single-qubit rotations, which themselves will introduce errors. However, QPT could still be useful for determining certain systematic errors in the single or two-qubit gates applied on the system, and it reflects an important step for comparison purposes with other quantum computing systems, such as NMR, trapped-ions, and photons, in which the protocol has already been achieved and two-qubit gate benchmarks show fidelities of $\sim 90 - 95\%$ [35, 114, 115].

Randomized benchmarking can be extended to the two-qubit system as well, to obtain an average estimate of the gate fidelity. Details for how to implement RB including two-qubit gates are given in Ref. [119], where RB is used on an NMR system. One main difference from the single qubit case is the inclusion of the *c*NOT gate, which is itself in the set of two-qubit Clifford group generators and can give a fully depolarized noise channel [161]. Similar to the single-qubit case, the extracted average gate errors could be compared with theory taking into account the relevant time-scales of the system. It would also open up the possibility of testing optimal control pulse shaping on the two-qubit gates, just as we have begun to do with the derivative pulse-shaping technique on single-qubit gates (section 6.4).

One more intriguing idea within two-qubit experiments is to characterize the two-qubit entangled state space. Numerous experiments have now been carried out detailing the single-qubit Hilbert space quite well, from measuring the relaxation and coherence times to

determining gate and state fidelities. However, it would be interesting to obtain similar metrics, but for the Hilbert space spanned by two entangled states. For example, in section 8.6.3, we were able to rotate a single-qubit after preparing an entangled state. This action did not change the entanglement of the state, but did perform rotations within a pseudo-Bloch sphere where the poles are two of the Bell states. It is fair to then ask what the decoherence and relaxation properties are in this Bell basis. For example, we can imagine a ‘hyper-Ramsey’ experiment, by generating a superposition state of two Bell states (*i.e.* by applying a $\pi/2$ pulse in the Bell basis), and allowing the state to undergo free precession, before undoing the superposition to determine the decoherence time. A further motivation for understanding this sub-qubit within two entangled qubits is the dark state, as discussed in section 7.2.2. Recall that the Bell state $|\Phi^+\rangle = (|0,1\rangle + |1,0\rangle)/\sqrt{2}$ could not be directly driven through the microwave cavity, and hence does not couple to the environment through the cavity. Therefore, that state could possibly be part of a ‘decoherence free sub-space’ (DFS) [162], with many further applications for errorless quantum computing. Nonetheless, understanding the dynamics of the dark state or the super-radiant state would be critical for determining if indeed there is an accessible DFS.

10.2 More qubits in circuit QED

The list for experiments with only two-qubits could probably go on, but alas to build a quantum computer scaling past two is a necessity. Fortunately, the current circuit QED design is not limited to just 2 qubits coupled to a single microwave CPW resonator. Even by continuing to drive the $\lambda/2$ resonance, it is possible to place up to 4 qubits, as shown in figure 10.1. Each qubit is independently flux tunable via its own flux line. Such samples have already been made and are now in the process of being tested and characterized by Leonardo DiCarlo and Matt Reed.

With the independent flux tuning, it will be simpler to use only three out of the four qubits first, and detune one of the qubits far away from any interactions with the cavity or with the other qubits. The simplest experiments to aim for are to repeat the characterization of the joint readout, but now for a three-qubit system. Operating in the strong dispersive regime of 3 qubits, there would now be 8 different cavity shifted frequencies. Similar protocols to those presented in this thesis involving pre-rotations could be used to construct the three-qubit Pauli set \vec{P} or the density matrix ρ .

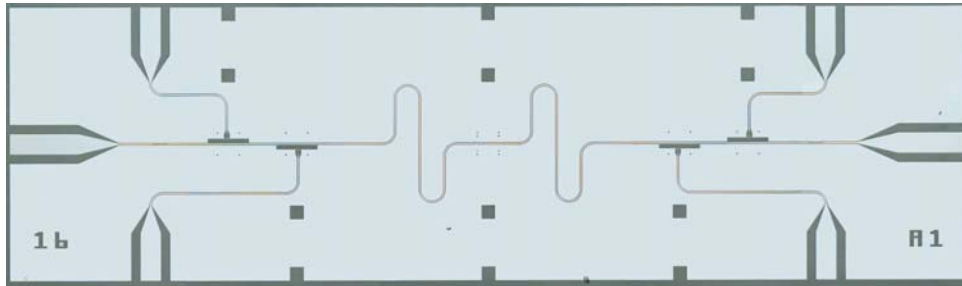


Figure 10.1: Four qubit circuit QED sample. New four qubit circuit QED samples places two qubits on each end of the resonator. The device is now a 6 port device, as there are now 4 flux-bias lines for each of the qubits, in addition to the input and output ports of the resonator.

Generating two-qubit entangled states will be done in exactly the same way. Recall that the controlled z interaction used to generate the c -Phase gate (section 4.3.3) functions by adiabatically pulsing into an interaction between the $|1, 1\rangle$ and $|0, 2\rangle$ states. For this to occur, the two transmon ground to first excited state have to be nearest neighbors in frequency space*. Therefore, if we imagine starting with three qubits such that $\omega^{(1)} > \omega^{(2)} > \omega^{(3)}$, we would like to have access to a c -Phase gate between qubits 1 and 2, and another gate between 2 and 3. In that situation, the protocol for generating a maximally entangled three-qubit state, such as the GHZ state given by $|GHZ\rangle = (|000\rangle + |111\rangle)/\sqrt{2}$, is quite simple and shown schematically in figure 10.2a.

Now having access to three qubit entanglement opens up a wealth of possible experiments. One interesting path is to implement simple quantum error correcting codes. Quantum error correction is an important step for quantum computing, as it can be used to protect the information stored in qubits from errors such as decoherence or systematic gate errors [12]. Most quantum error correcting codes involve spreading out the information of a single-qubit across the entangled state of a register of qubits. One of the simplest codes employs 3 qubits, and can be used to correct for dephasing errors [163]. It was first experimentally demonstrated in NMR [164] and trapped ions [165]. Recently, the protocol has been proposed for implementation in superconducting qubits [166], employing exactly the same conditional phase gates which we have access to in our current setup. A schematic of the required gate sequence is shown in figure 10.2b. One important thing to note is the final step requires either

* Optimized pulse-shaping of the flux could possibly allow a Landau-Zener type transition across qubit transition frequencies.

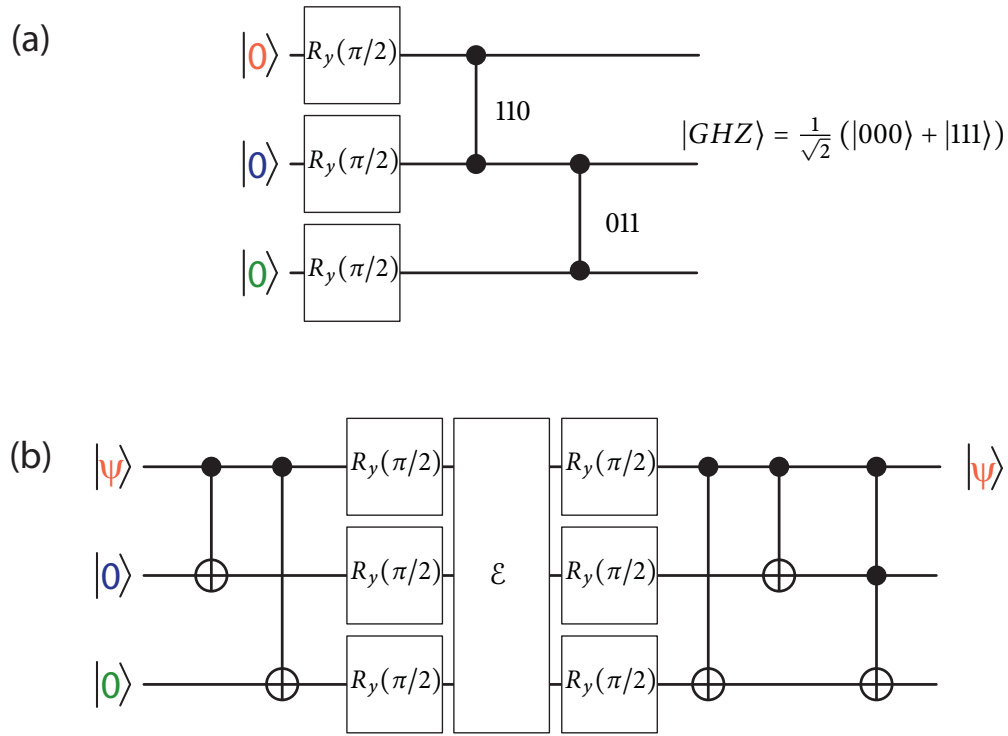


Figure 10.2: Protocols for GHZ and 3-qubit code. (a) The GHZ state is generated by first applying $\pi/2$ rotations onto each of the three qubits, generating a maximal superposition state. Then, that is followed by two successive c-Phase gates, first between the first two qubits, and then between the second and third qubits. (b) The three-bit code allows for the correction of the state on one qubit. First a set of cNOT gates are used to encode the state of the qubit into the three qubit register. That is followed by single-qubit $\pi/2$ rotations and then the error process \mathcal{E} . The state of the qubit is de-encoded and a final Toffoli gate is used to leave the corrected qubit in its initial state.

performing a Toffoli gate [25] or a final single-qubit rotation conditioned on the measurement of two of the qubits.

The experimental demonstration of the Toffoli gate would be a key hallmark to achieve in itself, as it is an archetypal three-qubit gate, valuable in many more complex quantum algorithms. It can be especially useful if it achieves a task with using fewer resources than the equivalent one and two-qubit gate decomposition. Although certainly it could be built from one and two-qubit gates, a novel direction with transmon qubits in circuit QED is to dive into the spaghetti of energy levels and search for a three-qubit interaction along the lines of the $\sigma_z \otimes \sigma_z$ interaction which we used to generate our c-Phase gate.

Here again, the list of experiments can go on and on, but hopefully this has provided some perspective for interesting three qubit experiments. Scaling past 3 and 4, there are even

more error correcting codes to attempt such as the Steane code with 7 qubits [163], as well as quantum teleportation experiments [167–170] and even quantum simulation of Hamiltonians [171, 172].

10.3 Quantum information outlook

For a view towards the future of superconducting qubits, it is important to recognize the rapid progress over the past ten years, getting from coherence times of just a few nanoseconds, to being able to perform hundreds of operations and even implementing basic quantum algorithms. To strike an analogy with the classical computer which we started this thesis discussing, the current development of our two-qubit superconducting quantum processor at Yale could be akin to the four-bit Intel 4004 microprocessor in 1971. Subsequently, it took about ten years to transition to IBM's PC in the 1980s, implementing the 16-bit Intel 8088 microprocessor. By 1982-83, the IBM personal computer became an industry standard and almost all leading manufacturers switched into making products that would be compatible with IBM's computer. At Yale, we are now progressing to 3 and 4 superconducting quantum processors and it would be interesting to see how far we can get in the next ten years.

Suppose the experiments outlined here go according to plan: superconducting coherence times increase by another two orders of magnitude; gate operations reach the fault-tolerant threshold; more complex quantum algorithms and error correcting codes are implemented. Then what? From a quantum engineering point of view, that would represent a shift away from understanding just simple quantum information processing very well, towards scaling the system up and making a quantum computer that might be useful for practical purposes. In reference to the classical computers, the problem becomes one of engineering the *quantum integrated circuit* for scalability. At that point, progress could be as precipitous as the subsequent development of computing from the 8088 microprocessor.

How might we envision this quantum computer in terms of superconducting qubits in the circuit QED architecture? First, we would have to think about how to interconnect ever more qubits. With error correcting codes requiring $\sim 5-7$ qubits to give a single fault-tolerant qubit, we could envision that one microwave resonator with these $5-7$ qubits coupled to it would be used as a single logical qubit. From there, a new challenge emerges in terms of how to couple this cluster of qubits to another similar cluster of qubits. Perhaps a more complicated architecture involving coupling between multiple resonators is necessary. Furthermore, an actual implementation would probably require operations to be run massively in parallel on

many qubits at once, and then to have interactions and information transfers switchable to communicate between different clusters. The hardware to control such a behemoth operation would need to be very well-developed and planned as well.

For now, we should be excited about our two-qubit processor and immediate next set of experiments. Though there are still numerous hurdles to get over before being able to scale towards a large quantum computer, the ever-growing research emphasis on superconducting qubits and the rapid progress over the past decade might not make the wildest quantum computing dreams that far out of reach.





Bibliography

1. J. B. Copeland, *Colossus: The Secrets of Bletchley Park's Codebreaking Computers*. Oxford University Press, 2006. Cited on page 1.
2. D. C. Brock, ed., *Understanding Moore's Law: Four Decades of Innovation*. Chemical Heritage Press, 2006. Cited on page 2.
3. R. Feynman, "Simulating physics with computers," *International Journal of Theoretical Physics* **21**, 467–488 (1982). Cited on pages 2 & 9.
4. D. Deutsch, "Quantum theory, the church-turing principle and the universal quantum computer," *Proceedings of the Royal Society of London A* **400**, 99–117 (1985). Cited on pages 2, 3 & 23.
5. P. W. Shor, "Algorithms for quantum computation: discrete logarithms and factoring," *Foundations of Computer Science, 1994 Proceedings., 35th Annual Symposium* 124–134 (1994). Cited on page 3.
6. R. Rivest, A. Shamir, and L. Adleman, "A method for obtaining digital signatures and public-key cryptosystems," *Communications of the ACM* **21**, 120–126 (1978). Cited on page 3.
7. C. H. Bennett, F. Bessette, G. Brassard, L. Salvail, and J. Smolin, "Experimental quantum cryptography," *Journal of Cryptology* **5**, 3–28 (1992). Cited on page 3.
8. I. L. Chuang, N. Gershenfeld, and M. Kubinec, "Experimental implementation of fast quantum searching," *Phys. Rev. Lett.* **80**, (1998). Cited on pages 4 & 219.
9. I. L. Chuang, L. M. K. Vandersypen, X. Zhou, D. W. Leung, and S. Lloyd, "Experimental realization of a quantum algorithm," *Nature* **393**, 143–146 (1998). Cited on pages 4 & 219.

10. J. A. Jones, M. Mosca, and R. H. Hansen, "Implementation of a quantum search algorithm on a quantum computer," *Nature* **393**, 344–346 (1998). Cited on pages 4 & 219.
11. L. M. K. Vandersypen, M. Steffen, G. Breyta, C. S. Yannoni, M. H. Sherwood, and I. L. Chuang, "Experimental realization of Shor's quantum factoring algorithm using nuclear magnetic resonance," *Nature* **414**, 883–887 (2001). Cited on pages 4 & 101.
12. M. A. Nielsen and I. L. Chuang, *Quantum Computation and Quantum Information*. Cambridge University Press, Cambridge, 2000. Cited on pages 4, 9, 10, 11, 14, 29, 30, 33, 154, 219, 226, 232 & 238.
13. J. I. Cirac and P. Zoller, "Quantum computations with cold trapped ions," *Phys. Rev. Lett.* **74**, (1995). Cited on pages 4 & 170.
14. D. Leibfried, R. Blatt, C. Monroe, and D. Wineland, "Quantum dynamics of single trapped ions," *Rev. Mod. Phys.* **75**, (2003). Cited on pages 5 & 170.
15. H. Häffner, W. Hänsel, C. F. Roos, J. Benhelm, D. Chek-Al-Kar, M. Chwalla, T. Körber, U. D. Rapol, M. Riebe, P. O. Schmidt, C. Becher, O. Guhne, W. Dür, and R. Blatt, "Scalable multiparticle entanglement of trapped ions," *Nature* **438**, 643–646 (2005). Cited on pages 5, 35, 101 & 188.
16. D. Leibfried, E. Knill, S. Seidelin, J. Britton, R. B. Blakestad, J. Chiaverini, D. B. Hume, W. M. Itano, J. D. Jost, C. Langer, R. Ozeri, R. Reichle, and D. J. Wineland, "Creation of a six-atom 'Schrödinger cat' state," *Nature* **438**, 639–642 (2005). Cited on pages 5 & 188.
17. D. Loss and D. P. DiVincenzo, "Quantum computation with quantum dots," *Phys. Rev. A* **57**, 120 (1998). Cited on pages 5 & 18.
18. F. Jelezko, T. Gaebel, I. Popa, A. Gruber, and J. Wrachtrup, "Observation of coherent oscillations in a single electron spin," *Phys. Rev. Lett.* **92**, (2004). Cited on page 5.
19. M. V. G. Dutt, L. Childress, L. Jiang, E. Togan, J. Maze, F. Jelezko, A. S. Zibrov, P. R. Hemmer, and M. D. Lukin, "Quantum register based on individual electronic and nuclear spin qubits in diamond," *Science* **316**, 1312–1316 (2007). Cited on page 5.
20. B. E. Kane, "A silicon-based nuclear spin quantum computer," *Nature* **393**, 133–137 (1998). Cited on page 5.
21. Y. Nakamura, Y. A. Pashkin, and J. S. Tsai, "Coherent control of macroscopic quantum states in a single-Cooper-pair box," *Nature* **398**, 786 (1999). Cited on page 5.
22. N. D. Mermin, *Quantum Computer Science*. Cambridge University Press, Cambridge, 2007. Cited on pages 9, 14, 18 & 29.

23. P. Kaye, R. Laflamme, and M. Mosca, *An Introduction to Quantum Computing*. Oxford University Press, 2007. Cited on pages 9, 14, 29, 219, 226 & 232.
24. D. P. DiVincenzo, "Two-bit gates are universal for quantum computation," *Phys. Rev. A* **51**, (1995). Cited on page 10.
25. T. Toffoli, "Reversible computing," *Technical Report MIT/LCS/TM-151* (1980). Cited on pages 11 & 239.
26. D. Gottesman, *Stabilizer Codes and Quantum Error Correction*. PhD thesis, California Institute of Technology, Pasadena, 1997. Cited on pages 14 & 131.
27. T. P. Orlando, J. E. Mooij, L. Tian, C. H. van der Wal, L. S. Levitov, S. Lloyd, and J. J. Mazo, "Superconducting persistent-current qubit," *Phys. Rev. B* **60**, (1999). Cited on page 16.
28. Y. Makhlin, G. Scöhn, and A. Shnirman, "Josephson-junction qubits with controlled couplings," *Nature* **398**, 305–307 (1999). Cited on page 16.
29. D. Mozyrsky, V. Privman, and M. L. Glasser, "Indirect interaction of solid-state qubits via two-dimensional electron gas," *Phys. Rev. Lett.* **86**, (2001). Cited on page 18.
30. A. Blais, R.-S. Huang, A. Wallraff, S. M. Girvin, and R. J. Schoelkopf, "Cavity quantum electrodynamics for superconducting electrical circuits: an architecture for quantum computation," *Phys. Rev. A* **69**, 062320 (2004). Cited on pages 18, 45, 58 & 61.
31. D. Deutsch and R. Jozsa, "Rapid solution of problems by quantum computation," *Proc. R. Soc. London A* **439**, 553 (1992). Cited on page 23.
32. L. K. Grover, "Quantum mechanics helps in searching for a needle in a haystack," *Phys. Rev. Lett.* **79**, 325 (1997). Cited on page 25.
33. A. Einstein, B. Podolsky, and N. Rosen, "Can quantum-mechanical description of physical reality be considered complete?," *Phys. Rev.* **47**, 777–780 (1935). Cited on page 30.
34. D. Walls and G. Milburn, *Quantum Optics*. Springer, 1st ed. 1994. 2nd printing ed., Feb., 1995. Cited on pages 31 & 99.
35. J. L. O'Brien, G. J. Pryde, A. Gilchrist, D. F. V. James, N. K. Langford, T. C. Ralph, and A. G. White, "Quantum process tomography of a controlled-not gate," *Phys. Rev. Lett.* **93**, 080502 (2004). Cited on pages 35, 141, 149 & 236.
36. R. Jozsa, "Fidelity for mixed quantum states," *Journal of Modern Optics* **41**, 2315–2323 (1994). Cited on page 35.

37. B. Trauzettel, A. N. Jordan, C. W. J. Beenakker, and M. Büttiker, “Parity meter for charge qubits: An efficient quantum entangler,” *Phys. Rev. B* **73**, 235331 (2006). Cited on page 35.
38. J. Benhelm, G. Kirchmair, C. F. Roos, and R. Blatt, “Towards fault-tolerant quantum computing with trapped ions,” *Nature Physics* **4**, 463–466 (2008). Cited on page 35.
39. R. Horodecki, P. Horodecki, M. Horodecki, and K. Horodecki, “Quantum entanglement,” *Rev. Mod. Phys.* **81**, 865 (2009). Cited on pages 36, 37, 38, 208, 213 & 215.
40. M. Lewenstein, B. Kraus, J. I. Cirac, and P. Horodecki, “Optimization of entanglement witnesses,” *Phys. Rev. A* **62**, (2000). Cited on page 36.
41. P. Hyllus, O. Gühne, D. Brufl, and M. Lewenstein, “Relations between entanglement witnesses and Bell inequalities,” *Phys. Rev. A* **72**, (2005). Cited on pages 36 & 39.
42. G. Jaeger, *Quantum Information*. Springer, 2007. Cited on pages 36 & 37.
43. S. Hill and W. K. Wootters, “Entanglement of a pair of quantum bits,” *Phys. Rev. Lett.* **78**, (1997). Cited on pages 36 & 37.
44. W. K. Wootters, “Entanglement of formation of an arbitrary state of two qubits,” *Phys. Rev. Lett.* **80**, (1998). Cited on page 37.
45. J. Eisert, F. G. S. L. Brandao, and K. M. R. Audenaert, “Quantitative entanglement witnesses,” *New J. Phys.* **9**, 46 (2007). Cited on pages 38, 39, 40, 43 & 213.
46. J. S. Bell, *Speakable and Unspeakable in Quantum Mechanics*. Cambridge University Press, 1987. Cited on page 40.
47. J. F. Clauser, M. A. Horne, A. Shimony, and R. A. Holt, “Proposed experiment to test local hidden-variable theories,” *Phys. Rev. Lett.* **23**, 880–884 (1969). Cited on pages 40, 188 & 214.
48. B. S. Cirel’son, “Quantum generalizations of Bell’s inequality,” *Lett. Math. Phys.* **4**, 93–100 (1980). Cited on page 42.
49. A. Aspect, J. Dalibard, and G. Roger, “Experimental Test of Bell’s Inequalities Using Time-Varying Analyzers,” *Phys. Rev. Lett.* **49**, 1804–1807 (1982). Cited on page 42.
50. G. Weihs, T. Jennewein, C. Simon, H. Weinfurter, and A. Zeilinger, “Violation of Bell’s Inequality under Strict Einstein Locality Conditions,” *Phys. Rev. Lett.* **81**, 5039–5043 (1998). Cited on page 42.

51. M. Ansmann, H. Wang, R. C. Bialczak, M. Hofheinz, E. Lucero, M. Neeley, A. D. O'Connell, D. Sank, M. Weides, J. Wenner, A. N. Cleland, and J. M. Martinis, "Violation of Bell's inequality in Josephson phase qubits," *Nature* **461**, 504–506 (2009). Cited on pages 42, 188 & 216.
52. A. Wallraff, D. I. Schuster, A. Blais, L. Frunzio, R. S. Huang, J. Majer, S. Kumar, S. M. Girvin, and R. J. Schoelkopf, "Strong coupling of a single photon to a superconducting qubit using circuit quantum electrodynamics," *Nature* **431**, 162–167 (2004). Cited on pages 45, 58 & 192.
53. D. I. Schuster, *Circuit quantum electrodynamics*. PhD thesis, Yale University, 2007. UMI No. 3267357. Cited on pages 45, 47, 49, 50, 58, 68, 71, 106, 109, 110, 127, 135 & 235.
54. R. J. Schoelkopf and S. M. Girvin, "Wiring up quantum systems," *Nature* **451**, 664–669 (2008). Cited on page 45.
55. M. Tinkham, *Introduction to Superconductivity*. Courier Dover Publications, second edition ed., 2004. Cited on pages 46 & 47.
56. J. Clarke and F. K. Wilhelm, "Superconducting quantum bits," *Nature* **453**, 1031–1042 (2008). Cited on page 47.
57. M. H. Devoret, *Quantum Fluctuations in Electrical Circuits*. Elsevier, 1997. Cited on page 47.
58. V. Bouchiat, D. Vion, P. Joyez, D. Esteve, and M. H. Devoret, "Quantum Coherence with a Single Cooper Pair," *Physica Scripta* **T76**, 165 (1998). Cited on page 47.
59. A. Cottet, *Implementation of a Quantum Bit in a Superconducting Circuit*. PhD thesis, Universite Paris VI, 2002. Cited on page 47.
60. D. Vion, A. Aassime, A. Cottet, P. Joyez, H. Pothier, C. Urbina, D. Esteve, and M. H. Devoret, "Manipulating the quantum state of an electrical circuit," *Science* **296**, 886 (2002). Cited on pages 50 & 71.
61. J. Koch, T. M. Yu, J. Gambetta, A. A. Houck, D. I. Schuster, J. Majer, A. Blais, M. H. Devoret, S. M. Girvin, and R. J. Schoelkopf, "Charge-insensitive qubit design derived from the Cooper pair box," *Phys. Rev. A* **76**, 042319 (2007). Cited on pages 50, 51, 64, 68, 69, 71, 72, 111, 112, 148, 175 & 189.
62. L. S. Bishop, *Circuit quantum electrodynamics*. PhD thesis, Yale University, 2010. Cited on pages 50, 51, 62, 71, 78, 133, 136, 137, 138, 140 & 177.

63. J. A. Schreier, A. A. Houck, J. Koch, D. I. Schuster, B. R. Johnson, J. M. Chow, J. M. Gambetta, J. Majer, L. Frunzio, M. H. Devoret, S. M. Girvin, and R. J. Schoelkopf, "Suppressing charge noise decoherence in superconducting charge qubits," *Phys. Rev. B* **77**, 180502(R) (2008). Cited on pages 50, 71, 142, 189, 192 & 196.
64. G. Ithier, E. Collin, P. Joyez, P. J. Meeson, D. Vion, D. Esteve, F. Chiarello, A. Shnirman, Y. Makhlin, J. Schrieffer, and G. Schön, "Decoherence in a superconducting quantum bit circuit," *Phys. Rev. B* **72**, 134519 (2005). Cited on pages 50 & 71.
65. Y. A. Pashkin, T. Yamamoto, O. Astafiev, Y. Nakamura, D. V. Averin, and J. S. Tsai, "Quantum oscillations in two coupled charge qubits," *Nature* **421**, 823–826 (2003). Cited on pages 53 & 54.
66. T. Yamamoto, Y. A. Pashkin, O. Astafiev, Y. Nakamura, and J. S. Tsai, "Demonstration of conditional gate operation using superconducting charge qubits," *Nature* **425**, 941–944 (2003). Cited on page 54.
67. M. Steffen, M. Ansmann, R. C. Bialczak, N. Katz, E. Lucero, R. McDermott, M. Neeley, E. M. Weig, A. N. Cleland, and J. M. Martinis, "Measurement of the entanglement of two superconducting qubits via state tomography," *Science* **313**, 1423–1425 (2006). Cited on pages 54, 101, 102, 169, 188, 207 & 208.
68. A. Shnirman, G. Schön, and Z. Hermon, "Quantum Manipulations of Small Josephson Junctions," *Phys. Rev. Lett.* **79**, (1997). Cited on page 54.
69. J. Q. You, J. S. Tsai, and F. Nori, "Scalable quantum computing with josephson charge qubits," *Phys. Rev. Lett.* **89**, (2002). Cited on pages 54 & 55.
70. T. Hime, P. A. Reichardt, B. L. T. Plourde, T. L. Robertson, C. E. Wu, A. V. Ustinov, and J. Clarke, "Solid-state qubits with current-controlled coupling," *Science* **314**, 1427–1429 (2006). Cited on pages 56, 169 & 174.
71. X.-L. He, J. Q. You, Y.-x. Liu, L. F. Wei, and F. Nori, "Switchable coupling between charge and flux qubits," *Phys. Rev. B* **76**, (2007). Cited on page 56.
72. A. O. Niskanen, K. Harrabi, F. Yoshihara, Y. Nakamura, S. Lloyd, and J. S. Tsai, "Quantum coherent tunable coupling of superconducting qubits," *Science* **316**, 723–726 (2007). Cited on pages 56, 169 & 174.
73. R. Blatt and D. Wineland, "Entangled states of trapped atomic ions," *Nature* **453**, 1008–1015 (2008). Cited on page 56.
74. J. M. Raimond, M. Brune, and S. Haroche, "Manipulating quantum entanglement with atoms and photons in a cavity," *Rev. Mod. Phys.* **73**, (2001). Cited on page 58.

75. S. Haroche and J.-M. Raimond, *Exploring the Quantum*. Oxford University Press, 2006. Cited on page 58.
76. R. J. Thompson, G. Rempe, and H. J. Kimble, "Observation of normal-mode splitting for an atom in an optical cavity," *Phys. Rev. Lett.* **68**, 1132 (1992). Cited on page 58.
77. M. Brune, F. Schmidt-Kaler, A. Maali, J. Dreyer, E. Hagley, J. M. Raimond, and S. Haroche, "Quantum Rabi Oscillation: A Direct Test of Field Quantization in a Cavity," *Phys. Rev. Lett.* **76**, 1800 (1996). Cited on page 58.
78. J. M. Gambetta, A. Blais, D. I. Schuster, A. Wallraff, L. Frunzio, J. Majer, M. H. Devoret, S. M. Girvin, and R. J. Schoelkopf, "Qubit-photon interactions in a cavity: Measurement-induced dephasing and number splitting," *Phys. Rev. A* **74**, 042318–14 (2006). Cited on page 61.
79. J. M. Gambetta, A. Blais, D. I. Schuster, A. Wallraff, L. Frunzio, J. Majer, M. H. Devoret, S. M. Girvin, and R. J. Schoelkopf, "Qubit-photon interactions in a cavity: Measurement induced dephasing and number splitting," *Phys. Rev. A* **74**, 042318 (2006). Cited on pages 66, 78 & 86.
80. M. Boissonneault, J. M. Gambetta, and A. Blais, "Dispersive regime of circuit QED: Photon-dependent qubit dephasing and relaxation rates," *Phys. Rev. A* **79**, (2009). Cited on page 66.
81. R. J. Schoelkopf, A. A. Clerk, S. M. Girvin, K. W. Lehnert, and M. H. Devoret, "Qubits as spectrometers of quantum noise," in *Quantum noise in mesoscopic physics*, Y. V. Nazarov, ed., p. 175. Springer, 2003. cond-mat/0210247. Cited on page 68.
82. A. A. Houck, J. A. Schreier, B. R. Johnson, J. M. Chow, J. Koch, J. M. Gambetta, D. I. Schuster, L. Frunzio, M. H. Devoret, S. M. Girvin, and R. J. Schoelkopf, "Controlling the spontaneous emission of a superconducting transmon qubit," *Phys. Rev. Lett.* **101**, 080502 (2008). Cited on pages 68, 69, 70, 77, 113, 142, 175, 185 & 235.
83. E. M. Purcell, "Proceedings of the American Physical Society," *Phys. Rev.* **69**, 681 (1946). Cited on page 70.
84. J. M. Martinis, S. Nam, J. Aumentado, K. M. Lang, and C. Urbina, "Decoherence of a superconducting qubit due to bias noise," *Phys. Rev. B* **67**, (2003). Cited on page 71.
85. A. B. Zorin, F.-J. Ahlers, J. Niemeyer, T. Weimann, and H. Wolf, "Background charge noise in metallic single-electron tunneling devices," *Phys. Rev. B* **53**, 13682 (1996). Cited on page 71.
86. F. C. Wellstood, C. Urbina, and J. Clarke, "Low-frequency noise in dc superconducting quantum interference devices below 1k," *Appl. Phys. Lett.* **50**, 772 (1987). Cited on pages 71 & 72.

87. D. J. V. Harlingen, T. L. Robertson, B. L. T. Plourde, P. A. Reichardt, T. A. Crane, and J. Clarke, “Decoherence in Josephson-junction qubits due to critical-current fluctuations,” *Phys. Rev. B* **70**, 064517 (2004). Cited on page 71.
88. F. Yoshihara, K. Harrabi, A. O. Niskanen, Y. Nakamura, and J. S. Tsai, “Decoherence of flux qubits due to $1/f$ flux noise,” *Phys. Rev. Lett.* **97**, 16001 (2006). Cited on page 71.
89. L. S. Bishop, J. M. Chow, J. Koch, A. A. Houck, M. H. Devoret, E. Thuneberg, S. M. Girvin, and R. J. Schoelkopf, “Nonlinear response of the vacuum Rabi resonance,” *Nature Physics* **5**, 105–109 (2009). Cited on pages 76, 77, 125, 132, 133 & 136.
90. F. Motzoi, J. M. Gambetta, P. Rebentrost, and F. K. Wilhelm, “Simple pulses for elimination of leakage in weakly nonlinear qubits,” *Phys. Rev. Lett.* **103**, 110501 (2009). Cited on pages 80, 82, 83, 84, 164 & 166.
91. A. Blais, J. Gambetta, A. Wallraff, D. I. Schuster, S. M. Girvin, M. H. Devoret, and R. J. Schoelkopf, “Quantum-information processing with circuit quantum electrodynamics,” *Physical Review A* **75**, 032329–21 (2007). Cited on pages 87, 181 & 192.
92. M. A. Sillanpää, J. I. Park, and R. W. Simmonds, “Coherent quantum state storage and transfer between two phase qubits via a resonant cavity,” *Nature* **449**, 438–442 (2007). Cited on page 87.
93. R. C. Bialczak, M. Ansmann, M. Hofheinz, E. Lucero, M. Neeley, A. O’Connell, D. Sank, H. Wang, J. Wenner, M. Steffen, A. Cleland, and J. Martinis, “Quantum Process Tomography of a Universal Entangling Gate Implemented with Josephson Phase Qubits,” arXiv:0910.1118 [quant-ph]. Cited on page 87.
94. P. J. Leek, S. Filipp, P. Maurer, M. Baur, R. Bianchetti, J. M. Fink, M. G. Epppl, L. Steffen, and A. Wallraff, “Using sideband transitions for two-qubit operations in superconducting circuits,” *Phys. Rev. B* **79**, (2009). Cited on page 87.
95. C. Rigetti, A. Blais, and M. Devoret, “Protocol for universal gates in optimally biased superconducting qubits,” *Phys. Rev. Lett.* **94**, (2005). Cited on page 87.
96. F. W. Strauch, P. R. Johnson, A. J. Dragt, C. J. Lobb, J. R. Anderson, and F. C. Wellstood, “Quantum logic gates for coupled superconducting phase qubits,” *Phys. Rev. Lett.* **91**, (2003). Cited on pages 96 & 196.
97. A. A. Clerk, M. H. Devoret, S. M. Girvin, F. Marquardt, and R. J. Schoelkopf, “Introduction to quantum noise, measurement and amplification,” arXiv:0810.4729 [cond-mat]. Cited on pages 99 & 136.
98. J. B. Altepeter, E. R. Jeffrey, P. G. Kwiat, S. Tanzilli, N. Gisin, and A. Acín, “Experimental methods for detecting entanglement,” *Phys. Rev. Lett.* **95**, 033601 (2005). Cited on page 101.

99. R. McDermott, R. W. Simmonds, M. Steffen, K. B. Cooper, K. Cicak, K. D. Osborn, S. Oh, D. P. Pappas, and J. M. Martinis, “Simultaneous state measurement of coupled Josephson phase qubits,” *Science* **307**, 1299–1302 (2005). Cited on pages 102 & 188.
100. L. Frunzio, A. Wallraff, D. Schuster, J. Majer, and R. Schoelkopf, “Fabrication and Characterization of Superconducting Circuit QED Devices for Quantum Computation,” *IEEE Trans. Appl. Supercond.* **15**, 860 (2005). Cited on page 106.
101. R. N. Simons, *Coplanar Waveguide Circuits Components & Systems*. Wiley-IEEE Press, 2002. Cited on page 107.
102. D. M. Pozar, *Microwave Engineering*. John Wiley & Sons, 3rd ed., 2005. Cited on page 112.
103. B. R. Johnson, *In Preparation*. PhD thesis, Yale University, 2010. Cited on page 112.
104. E. Knill, “Quantum computing with realistically noisy devices,” *Nature* **434**, 39–44 (2005). Cited on page 131.
105. S. O. Valenzuela, W. D. Oliver, D. M. Berns, K. K. Berggren, L. S. Levitov, and T. P. Orlando, “Microwave-induced cooling of a superconducting qubit,” *Science* **314**, 1589–1592 (2006). Cited on page 131.
106. M. Grajcar, S. H. W. van der Ploeg, A. Izmailkov, E. Il’ichev, H. G. Meyer, A. Fedorov, A. Shnirman, and G. Schön, “Sisyphus cooling and amplification by a superconducting qubit,” *Nature Physics* **4**, 612–616 (2008). Cited on page 131.
107. V. E. Manucharyan, J. Koch, L. I. Glazman, and M. H. Devoret, “Fluxonium: Single Cooper-Pair Circuit Free of Charge Offsets,” *Science* **326**, 113–116 (2009). Cited on page 132.
108. J. M. Chow, J. M. Gambetta, L. Tornberg, J. Koch, L. S. Bishop, A. A. Houck, B. R. Johnson, L. Frunzio, S. M. Girvin, and R. J. Schoelkopf, “Randomized benchmarking and process tomography for gate errors in a solid-state qubit,” *Phys. Rev. Lett.* **102**, 090502 (2009). Cited on pages 132, 188, 189 & 219.
109. D. I. Schuster, A. Wallraff, A. Blais, L. Frunzio, R.-S. Huang, J. Majer, S. M. Girvin, and R. J. Schoelkopf, “ac Stark Shift and Dephasing of a Superconducting Qubit Strongly Coupled to a Cavity Field,” *Phys. Rev. Lett.* **94**, 123602 (2005). Cited on page 133.
110. D. I. Schuster, A. A. Houck, J. A. Schreier, A. Wallraff, J. M. Gambetta, A. Blais, L. Frunzio, B. Johnson, M. H. Devoret, S. M. Girvin, and R. J. Schoelkopf, “Resolving photon number states in a superconducting circuit,” *Nature* **445**, 515 (2007). Cited on pages 133, 175, 200 & 220.

111. J. M. Fink, M. Goppl, M. Baur, R. Bianchetti, P. J. Leek, A. Blais, and A. Wallraff, “Climbing the Jaynes-Cummings ladder and observing its nonlinearity in a cavity QED system,” *Nature* **454**, 315–318 (2008). Cited on page 133.
112. M. Hofheinz, E. M. Weig, M. Ansmann, R. C. Bialczak, E. Lucero, M. Neeley, A. D. O’Connell, H. Wang, J. M. Martinis, and A. N. Cleland, “Generation of Fock states in a superconducting quantum circuit,” *Nature* **454**, 310–314 (2008). Cited on page 133.
113. M. Hofheinz, H. Wang, M. Ansmann, R. C. Bialczak, E. Lucero, M. Neeley, A. D. O’Connell, D. Sank, J. Wenner, J. M. Martinis, and A. N. Cleland, “Synthesizing arbitrary quantum states in a superconducting resonator,” *Nature* **459**, 546–549 (2009). Cited on page 133.
114. A. M. Childs, I. L. Chuang, and D. W. Leung, “Realization of quantum process tomography in NMR,” *Phys. Rev. A* **64**, 012314 (2001). Cited on pages 141 & 236.
115. M. Riebe, K. Kim, P. Schindler, T. Monz, P. O. Schmidt, T. K. Korber, W. Hansel, H. Haffner, C. F. Roos, and R. Blatt, “Process tomography of ion trap quantum gates,” *Phys. Rev. Lett.* **97**, 220407 (2006). Cited on pages 141 & 236.
116. E. Lucero, M. Hofheinz, M. Ansmann, R. C. Bialczak, N. Katz, M. Neeley, A. D. O’Connell, H. Wang, A. N. Cleland, and J. M. Martinis, “High-fidelity gates in a single Josephson qubit,” *Phys. Rev. Lett.* **100**, 247001 (2008). Cited on pages 141, 148, 188, 196 & 219.
117. M. Neeley, M. Ansmann, R. C. Bialczak, M. Hofheinz, N. Katz, E. Lucero, A. O’Connell, H. Wang, A. N. Cleland, and J. M. Martinis, “Process tomography of quantum memory in a Josephson-phase qubit coupled to a two-level state,” *Nature Physics* **4**, 523–526 (2008). Cited on page 141.
118. E. Knill, D. Leibfried, R. Reichle, J. Britton, R. B. Blakestad, J. D. Jost, C. Langer, R. Ozeri, S. Seidelin, and D. J. Wineland, “Randomized benchmarking of quantum gates,” *Phys. Rev. A* **77**, 012307–7 (2008). Cited on pages 141, 142, 144, 153, 154 & 155.
119. C. A. Ryan, M. Laforest, and R. Laflamme, “Randomized benchmarking of single- and multi-qubit control in liquid-state NMR quantum information processing,” *New J. Phys.* **11**, (2009). Cited on pages 141, 159 & 236.
120. I. L. Chuang and M. Nielsen, “Prescription for experimental determination of the dynamics of a quantum black box,” *Journal of Modern Optics* **44**, 2455–2467 (1997). Cited on pages 141, 149 & 150.
121. J. Emerson, M. Silva, O. Moussa, C. Ryan, M. Laforest, J. Baugh, D. G. Cory, and R. Laflamme, “Symmetrized characterization of noisy quantum processes,” *Science* **317**, 1893–1896 (2007). Cited on page 142.

122. R. W. Vaughan, D. D. Elleman, L. M. Stacey, W.-K. Rhim, and J. W. Lee, “A Simple, Low Power, Multiple Pulse NMR Spectrometer,” *Review of Scientific Instruments* **43**, 1356–1364 (1972). Cited on page 145.
123. A. Wallraff, D. I. Schuster, A. Blais, L. Frunzio, J. Majer, M. Devoret, S. M. Girvin, and R. J. Schoelkopf, “Approaching unit visibility for control of a superconducting qubit with dispersive readout,” *Phys. Rev. Lett.* **95**, 060501 (2005). Cited on page 148.
124. J. F. Poyatos, J. I. Cirac, and P. Zoller, “Complete characterization of a quantum process: The two-bit quantum gate,” *Phys. Rev. Lett.* **78**, 390–393 (1997). Cited on page 149.
125. M. A. Nielsen, “A simple formula for the average gate fidelity of a quantum dynamical operation,” *Phys. Lett. A* **303**, 249–252 (2002). Cited on pages 152 & 153.
126. L. DiCarlo, J. M. Chow, J. M. Gambetta, L. S. Bishop, B. R. Johnson, D. I. Schuster, J. Majer, A. Blais, L. Frunzio, S. M. Girvin, and R. J. Schoelkopf, “Demonstration of two-qubit algorithms with a superconducting quantum processor,” *Nature* **460**, 240–244 (2009). Cited on pages 159 & 210.
127. J. M. Chow, L. DiCarlo, J. M. Gambetta, A. Nunnenkamp, L. S. Bishop, L. Frunzio, M. H. Devoret, S. M. Girvin, and R. J. Schoelkopf, “Entanglement metrology using a joint readout of superconducting qubits,” arXiv:0908.1955 [cond-mat]. Cited on pages 159 & 220.
128. J. B. Majer, F. G. Paauw, A. C. J. ter Haar, C. J. P. M. Harmans, and J. E. Mooij, “Spectroscopy on two coupled superconducting flux qubits,” *Phys. Rev. Lett.* **94**, (2005). Cited on page 169.
129. S. H. W. van der Ploeg, A. Izmailkov, A. M. van den Brink, U. Hübner, M. Grajcar, E. Il’ichev, H. G. Meyer, and A. M. Zagoskin, “Controllable Coupling of Superconducting Flux Qubits,” *Phys. Rev. Lett.* **98**, (2007). Cited on pages 169 & 174.
130. A. J. Berkley, H. Xu, R. C. Ramos, M. A. Gubrud, F. W. Strauch, P. R. Johnson, J. R. Anderson, A. J. Dragt, C. J. Lobb, and F. C. Wellstood, “Entangled macroscopic quantum states in two superconducting qubits,” *Science* **300**, 1548–1550 (2003). Cited on page 169.
131. L. M. Duan, M. D. Lukin, J. I. Cirac, and P. Zoller, “Long-distance quantum communication with atomic ensembles and linear optics,” *Nature* **414**, 413–418 (2001). Cited on page 170.
132. C.-W. Chou, J. Laurat, H. Deng, K. S. Choi, H. de Riedmatten, D. Felinto, and H. J. Kimble, “Functional quantum nodes for entanglement distribution over scalable quantum networks,” *Science* **316**, 1316–1320 (2007). Cited on page 170.

133. E. Hagley, X. Maître, G. Nogues, C. Wunderlich, M. Brune, J. M. Raimond, and S. Haroche, “Generation of Einstein-Podolsky-Rosen Pairs of Atoms,” *Phys. Rev. Lett.* **79**, (1997). Cited on page 170.
134. S.-B. Zheng and G.-C. Guo, “Efficient scheme for two-atom entanglement and quantum information processing in cavity qed,” *Phys. Rev. Lett.* **85**, (2000). Cited on page 170.
135. S. Osnaghi, P. Bertet, A. Auffeves, P. Maioli, M. Brune, J. M. Raimond, and S. Haroche, “Coherent control of an atomic collision in a cavity,” *Phys. Rev. Lett.* **87**, (2001). Cited on page 170.
136. J. Majer, J. M. Chow, J. M. Gambetta, J. Koch, B. R. Johnson, J. A. Schreier, L. Frunzio, D. I. Schuster, A. A. Houck, A. Wallraff, A. Blais, M. H. Devoret, S. M. Girvin, and R. J. Schoelkopf, “Coupling superconducting qubits via a cavity bus,” *Nature* **449**, 443–447 (2007). Cited on pages 170, 189 & 210.
137. N. A. Gershenfeld and I. L. Chuang, “Bulk spin-resonance quantum computation,” *Science* **275**, 350–356 (1997). Cited on page 174.
138. P. Grangier, A. Aspect, and J. Vigue, “Quantum interference effect for two atoms radiating a single photon,” *Phys. Rev. Lett.* **54**, (1985). Cited on page 178.
139. W. M. Itano, J. C. Bergquist, J. J. Bollinger, D. J. Wineland, U. Eichmann, and M. G. Raizen, “Complementarity and Young’s interference fringes from two atoms,” *Phys. Rev. A* **57**, (1998). Cited on page 178.
140. A. H. Myerson, D. J. Szwer, S. C. Webster, D. T. C. Allcock, M. J. Curtis, G. Imreh, J. A. Sherman, D. N. Stacey, A. M. Steane, and D. M. Lucas, “High-fidelity readout of trapped-ion qubits,” *Phys. Rev. Lett.* **100**, 200502 (2008). Cited on page 188.
141. F. Mallet, F. R. Ong, A. Palacios-Laloy, F. Nguyen, P. Bertet, D. Vion, and D. Esteve, “Single-shot qubit readout in circuit quantum electrodynamics,” *Nature Physics* **5**, 791–795 (2009). Cited on page 188.
142. S. Filipp, P. Maurer, P. J. Leek, M. Baur, R. Bianchetti, J. M. Fink, M. Goppl, L. Steffen, J. M. Gambetta, A. Blais, and A. Wallraff, “Two-qubit state tomography using a joint dispersive readout,” *Phys. Rev. Lett.* **102**, 200402 (2009). Cited on pages 207 & 220.
143. E. Lehmann and G. Casella, *The theory of point estimation*. Springer, 2nd ed., 2003. Cited on page 208.
144. H. K. Cummins, G. Llewellyn, and J. A. Jones, “Tackling systematic errors in quantum logic gates with composite rotations,” *Phys. Rev. A* **67**, 042308 (2003). Cited on page 210.

145. D. F. V. James, P. G. Kwiat, W. J. Munro, and A. G. White, "Measurement of qubits," *Phys. Rev. A* **64**, 052312 (2001). Cited on page 213.
146. R. Blume-Kohout, "Optimal, reliable estimation of quantum states," arXiv:0611080 [quant-ph]. Cited on page 213.
147. J. P. Home, D. Hanneke, J. D. Jost, J. M. Amini, D. Leibfried, and D. J. Wineland, "Complete methods set for scalable ion trap quantum information processing," *Science* **325**, 1227–1230 (2009). Cited on page 213.
148. C. L. Hutchison, J. M. Gambetta, A. Blais, and F. Wilhelm, "Quantum trajectory equation for multiple qubits in circuit QED: Generating entanglement by measurement," *Can. J. Phys.* **87**, 225–231 (2009). Cited on page 217.
149. L. S. Bishop, L. Tornberg, D. Price, E. Ginossar, A. Nunnenkamp, A. A. Houck, J. M. Gambetta, J. Koch, G. Johansson, S. M. Girvin, and R. J. Schoelkopf, "Proposal for generating and detecting multi-qubit GHZ states in circuit QED," *New J. Phys.* **11**, 073040 (2009). Cited on page 217.
150. S. Kochen and E. P. Specker, "The problem of hidden variables in quantum mechanics," *J. Math. Mech.* **17**, 59–87 (1967). Cited on page 217.
151. G. Kirchmair, F. Zahringer, R. Gerritsma, M. Kleinmann, O. Guhne, A. Cabello, R. Blatt, and C. F. Roos, "State-independent experimental test of quantum contextuality," *Nature* **460**, 494–497 (2009). Cited on page 217.
152. S. Gulde, M. Riebe, G. P. T. Lancaster, C. Becher, J. Eschner, H. Haffner, F. Schmidt-Kaler, I. L. Chuang, and R. Blatt, "Implementation of the Deutsch-Jozsa algorithm on an ion-trap quantum computer," *Nature* **421**, 48–50 (2003). Cited on page 219.
153. K. A. Brickman, P. C. Haljan, P. J. Lee, M. Acton, L. Deslauriers, and C. Monroe, "Implementation of Grover's quantum search algorithm in a scalable system," *Phys. Rev. A* **72**, (2005). Cited on page 219.
154. P. G. Kwiat, J. R. Mitchell, P. D. D. Schwindt, and A. G. White, "Grover's search algorithm: An optical approach," *Journal of Modern Optics* **47**, 257–266 (2000). Cited on page 219.
155. J. M. Martinis, K. Cooper, R. McDermott, M. Steffen, M. Ansmann, K. Osborn, K. Cicak, S. Oh, D. Pappas, R. Simmonds, and C. C. Yu, "Decoherence in Josephson Qubits from Dielectric Loss," *Phys. Rev. Lett.* **95**, 210503 (2005). Cited on page 234.
156. A. D. O'Connell, M. Ansmann, R. C. Bialczak, M. Hofheinz, N. Katz, E. Lucero, C. McKenney, M. Neeley, H. Wang, E. M. Weig, A. N. Cleland, and J. M. Martinis, "Microwave dielectric loss at single photon energies and millikelvin temperatures," *Appl. Phys. Lett.* **92**, 112903–3 (2008). Cited on page 234.

157. H. Wang, M. Hofheinz, J. Wenner, M. Ansmann, R. C. Bialczak, M. Lenander, E. Lucero, M. Neeley, A. D. O'Connell, D. Sank, M. Weides, A. N. Cleland, and J. M. Martinis, "Improving the coherence time of superconducting coplanar resonators," arXiv:0909.0547 [cond-mat]. Cited on page 234.
158. L. Viola, E. Knill, and S. Lloyd, "Dynamical decoupling of open quantum systems," *Phys. Rev. Lett.* **82**, (1999). Cited on page 235.
159. M. J. Biercuk, H. Uys, A. P. VanDevender, N. Shiga, W. M. Itano, and J. J. Bollinger, "Optimized dynamical decoupling in a model quantum memory," *Nature* **458**, 996–1000 (2009). Cited on page 236.
160. J. Du, X. Rong, N. Zhao, Y. Wang, J. Yang, and R. B. Liu, "Preserving electron spin coherence in solids by optimal dynamical decoupling," *Nature* **461**, 1265–1268 (2009). Cited on page 236.
161. C. Dankert, R. Cleve, J. Emerson, and E. Livine, "Exact and approximate unitary 2-designs and their application to fidelity estimation," *Phys. Rev. A* **80**, (2009). Cited on page 236.
162. D. A. Lidar, I. L. Chuang, and K. B. Whaley, "Decoherence-free subspaces for quantum computation," *Phys. Rev. Lett.* **81**, (1998). Cited on page 237.
163. A. Steane, "Multiple-particle interference and quantum error correction," *Proceedings of the Royal Society of London. Series A: Mathematical, Physical and Engineering Sciences* **452**, 2551–2577 (1996). Cited on pages 238 & 240.
164. D. G. Cory, M. D. Price, W. Maas, E. Knill, R. Laflamme, W. H. Zurek, T. F. Havel, and S. S. Somaroo, "Experimental quantum error correction," *Phys. Rev. Lett.* **81**, (1998). Cited on page 238.
165. J. Chiaverini, D. Leibfried, T. Schaetz, M. D. Barrett, R. B. Blakestad, J. Britton, W. M. Itano, J. D. Jost, E. Knill, C. Langer, R. Ozeri, and D. J. Wineland, "Realization of quantum error correction," *Nature* **432**, 602–605 (2004). Cited on page 238.
166. L. Tornberg, M. Wallquist, G. Johansson, V. S. Shumeiko, and G. Wendin, "Implementation of the three-qubit phase-flip error correction code with superconducting qubits," *Phys. Rev. B* **77**, (2008). Cited on page 238.
167. G. Rigolin, "Quantum teleportation of an arbitrary two-qubit state and its relation to multipartite entanglement," *Phys. Rev. A* **71**, (2005). Cited on page 240.
168. D. Bouwmeester, J.-W. Pan, K. Mattle, M. Eibl, H. Weinfurter, and A. Zeilinger, "Experimental quantum teleportation," *Nature* **390**, 575–579 (1997). Cited on page 240.

169. M. D. Barrett, J. Chiaverini, T. Schaetz, J. Britton, W. M. Itano, J. D. Jost, E. Knill, C. Langer, D. Leibfried, R. Ozeri, and D. J. Wineland, “Deterministic quantum teleportation of atomic qubits,” *Nature* **429**, 737–739 (2004). Cited on page 240.
170. M. Riebe, H. Haffner, C. F. Roos, W. Hansel, J. Benhelm, G. P. T. Lancaster, T. W. Korber, C. Becher, F. Schmidt-Kaler, D. F. V. James, and R. Blatt, “Deterministic quantum teleportation with atoms,” *Nature* **429**, 734–737 (2004). Cited on page 240.
171. G. Passante, O. Moussa, C. A. Ryan, and R. Laflamme, “Experimental Approximation of the Jones Polynomial with One Quantum Bit,” *Phys. Rev. Lett.* **103**, (2009). Cited on page 240.
172. R. Gerritsma, G. Kirchmair, F. Zahringer, E. Solano, R. Blatt, and C. F. Roos, “Quantum simulation of the Dirac equation,” *Nature* **463**, 68–71 (2010). Cited on page 240.



APPENDIX A

Mathematica code for microwave pulse generation

CODE for generating pulse sequences for the various experiments of chapters 6 to 9. The pulse sequences are generated as .pat files, which are uploaded into the arbitrary wave form generators, either the AWG520 or the AWG5014. Each experiment corresponds to running a sequence of many different .pat files. Generating the .pat files is done in Mathematica; pulse shapes are defined using various functions (gaussian, square, hyperbolic tangent, etc.). The DAC levels of the AWG are governed by calibration experiments. The first section of the code defines the names of the various types of pulses, whether they be for qubit drive or flux-bias, as well as the relevant timings and delays. The function `PulseIdentify[]` serves as a look-up table for all of the different drive and flux pulses which we use. Then, we give various pulse shape functions, as well as a function, `GetNewSeq[]`, for concatenating many different pulse types. The section ‘Calibration Sequences’ gives a number of experiments for tuning-up qubit drive pulses and flux pulses. Then, we also provide the code for generating randomized benchmarking sequences, single-qubit process tomography, and two-qubit state tomography.

Pulse Parameters and Names

■ Define variables for pulses

```
(* DAC Offsets for defining zero*)
(* QUBIT 1*)
DACOffsetLX = 512; DACOffsetLY = 512; DACOffsetLZ = 0;
(*QUBIT 2 *)
DACOffsetRX = 512; DACOffsetRY = 512; DACOffsetRZ = 0;
(*Define the amplitudes for all  $\pi/2$  pulses (X,Y,+,-)*)
(* QUBIT 1*)
ampLX90m = 342; ampLY90m = 342; ampLX90p = 682; ampLY90p = 682;
(* QUBIT 2*)
ampRX90m = 342; ampRY90m = 342; ampRX90p = 682; ampRY90p = 682;
(*Define the amplitudes for all  $\pi$  pulses*)
(*QUBIT 1*)
ampLXm = 172; ampLYm = 172; ampLXp = 852; ampLYp = 852;
(*QUBIT 2*)
ampRXm = 172; ampRYm = 172; ampRXp = 852; ampRYp = 852;

(*Flux pulse default widths*)
fwidthL = 0; fwidthR = 0;
(*Flux pulse default amplitudes, Step 1 of Grover*)
ampCOL = 0; ampC1L = 0; ampC2L = 0; ampC3L = 0;
ampCOR = 0; ampC1R = 0; ampC2R = 0; ampC3R = 0;
(*Flux pulse default offsets, Step 1 of Grover*)
offsetCOL = 0; offsetC1L = 0; offsetC2L = 0; offsetC3L = 0;
offsetCOR = 0; offsetC1R = 0; offsetC2R = 0; offsetC3R = 0;
(*Flux pulse default amplitudes, Step 2 of Grover*)
ampCOLb = 0; ampC1Lb = 0; ampC2Lb = 0; ampC3Lb = 0;
ampCORb = 0; ampC1Rb = 0; ampC2Rb = 0; ampC3Rb = 0;
(*Flux pulse default offsets, Step 2 of Grover*)
offsetCOLb = 0; offsetC1Lb = 0; offsetC2Lb = 0; offsetC3Lb = 0;
offsetCORb = 0; offsetC1Rb = 0; offsetC2Rb = 0; offsetC3Rb = 0;

(* Global pattern times *) (* in ns*)
fixedPointCh1 = 5000; cycleLength = 9000; MeasPulseLength = 3000;
(*Delays*) (* in ns*)
SpecPulseDelay = 0; MeasPulseDelay = -40;
FluxPulseDelay = 20; SpecBufferDelay = -65;
AWG520Delay = 468; triggerWidth = 100; delay = 5; fluxdelay = 5;
(* Pulse buffer times *)
bufferS = 5; bufferF = 5;
bufferSS = 3; (*spec followed by spec*)
bufferSF = 3; (*spec followed by flux*)
bufferFS = 3; (*flux followed by spec*)
bufferFF = 0; (*flux followed by flux*)
(*Default Spec pulse parameters *)
GaussWidth = 3; numSigmas = 4;
SpecPulseLength = GaussWidth
(* Actual pulse length is numSigmas*GaussWidth *)
SpecBufferMargin = 10;
```

■ Pulse sequence parse function

The following function is used as a lookup table of different kinds of pulses, which can be π or $\pi/2$ pulses on either qubit, as well as flux pulses for z-rotations. Depending on the pulse, it assigns certain amplitudes and offsets.

```

PulseIdentify[test1_] := Module[{phaseL, ampL, phaseR, ampR, ampLZ,
  widthLZ, offsetLZ, ampRZ, widthRZ, offsetRZ, spec, flux, Ssigma},
  (* Set default values *)
  phaseL = 0; (* 0 for X,  $\pi/2$  for Y*)
  ampL = DACoffsetLX; phaseR = 0; ampR = DACoffsetRX;
  ampLZ = DACoffsetLZ; widthLZ = 0; offsetLZ = 0;
  ampRZ = DACoffsetRZ; widthRZ = 0; offsetRZ = 0;
  spec = 1; flux = 0;
  Ssigma = SpecPulseLength;
  (*Default pulse case will return Identity, Id*)
  (* Single Qubit L Pulses *)
  If[test1 == LX90p, {phaseL = 0, ampL = ampLX90p}];
  If[test1 == LX90m, {phaseL = 0, ampL = ampLX90m}];
  If[test1 == LY90p, {phaseL =  $\pi/2$ , ampL = ampLY90p}];
  If[test1 == LY90m, {phaseL =  $\pi/2$ , ampL = ampLY90m}];
  If[test1 == LXp, {phaseL = 0, ampL = ampLXp}];
  If[test1 == LXm, {phaseL = 0, ampL = ampLXm}];
  If[test1 == LYp, {phaseL =  $\pi/2$ , ampL = ampLYp}];
  If[test1 == LYm, {phaseL =  $\pi/2$ , ampL = ampLYm}];
  (* Single Qubit R Pulses *)
  If[test1 == RX90p, {phaseR = 0, ampR = ampRX90p}];
  If[test1 == RX90m, {phaseR = 0, ampR = ampRX90m}];
  If[test1 == RY90p, {phaseR =  $\pi/2$ , ampR = ampRY90p}];
  If[test1 == RY90m, {phaseR =  $\pi/2$ , ampR = ampRY90m}];
  If[test1 == RXp, {phaseR = 0, ampR = ampRXp}];
  If[test1 == RXm, {phaseR = 0, ampR = ampRXm}];
  If[test1 == RYp, {phaseR =  $\pi/2$ , ampR = ampRYp}];
  If[test1 == RYm, {phaseR =  $\pi/2$ , ampR = ampRYm}];
  (* Composite Single Qubit LR Pulses *)
  If[test1 == LX90pRX90p,
    {phaseL = 0, ampL = ampLX90p, phaseR = 0, ampR = ampRX90p}];
  If[test1 == LX90mRX90p, {phaseL = 0, ampL = ampLX90m,
    phaseR = 0, ampR = ampRX90p}];
  If[test1 == LY90pRX90p, {phaseL =  $\pi/2$ , ampL = ampLY90p,
    phaseR = 0, ampR = ampRX90p}];
  If[test1 == LY90mRX90p, {phaseL =  $\pi/2$ , ampL = ampLY90m,
    phaseR = 0, ampR = ampRX90p}];
  If[test1 == LXpRX90p, {phaseL = 0, ampL = ampLXp, phaseR = 0, ampR = ampRX90p}];
  If[test1 == LXmRX90p, {phaseL = 0, ampL = ampLXm, phaseR = 0, ampR = ampRX90p}];
  If[test1 == LYpRX90p,
    {phaseL =  $\pi/2$ , ampL = ampLYp, phaseR = 0, ampR = ampRX90p}];
  If[test1 == LYmRX90p, {phaseL =  $\pi/2$ , ampL = ampLYm,
    phaseR = 0, ampR = ampRX90p}];
  If[test1 == LX90pRX90m, {phaseL = 0, ampL = ampLX90p,
    phaseR = 0, ampR = ampRX90m}];
  If[test1 == LX90mRX90m, {phaseL = 0, ampL = ampLX90m,
    phaseR = 0, ampR = ampRX90m}];
  If[test1 == LY90pRX90m, {phaseL =  $\pi/2$ , ampL = ampLY90p,
    phaseR = 0, ampR = ampRX90m}];
  If[test1 == LY90mRX90m, {phaseL =  $\pi/2$ , ampL = ampLY90m,
    phaseR = 0, ampR = ampRX90m}];
  If[test1 == LXpRX90m, {phaseL = 0, ampL = ampLXp, phaseR = 0, ampR = ampRX90m}];
  If[test1 == LXmRX90m, {phaseL = 0, ampL = ampLXm, phaseR = 0, ampR = ampRX90m}];
  If[test1 == LYpRX90m,

```

```

{phaseL =  $\pi/2$ , ampL = ampLYp, phaseR = 0, ampR = ampRX90m}];
If[test1 == LYmRX90m, {phaseL =  $\pi/2$ , ampL = ampLYm,
  phaseR = 0, ampR = ampRX90m}];
If[test1 == LX90pRY90p, {phaseL = 0, ampL = ampLX90p,
  phaseR =  $\pi/2$ , ampR = ampRY90p}];
If[test1 == LX90mRY90p, {phaseL = 0, ampL = ampLX90m,
  phaseR =  $\pi/2$ , ampR = ampRY90p}];
If[test1 == LY90pRY90p, {phaseL =  $\pi/2$ , ampL = ampLY90p,
  phaseR =  $\pi/2$ , ampR = ampRY90p}];
If[test1 == LY90mRY90p, {phaseL =  $\pi/2$ , ampL = ampLY90m,
  phaseR =  $\pi/2$ , ampR = ampRY90p}];
If[test1 == LXpRY90p, {phaseL = 0, ampL = ampLXp,
  phaseR =  $\pi/2$ , ampR = ampRY90p}];
If[test1 == LXmRY90p, {phaseL = 0, ampL = ampLXm,
  phaseR =  $\pi/2$ , ampR = ampRY90p}];
If[test1 == LYpRY90p, {phaseL =  $\pi/2$ , ampL = ampLYp,
  phaseR =  $\pi/2$ , ampR = ampRY90p}];
If[test1 == LYmRY90p, {phaseL =  $\pi/2$ , ampL = ampLYm,
  phaseR =  $\pi/2$ , ampR = ampRY90p}];
If[test1 == LX90pRY90m, {phaseL = 0, ampL = ampLX90p,
  phaseR =  $\pi/2$ , ampR = ampRY90m}];
If[test1 == LX90mRY90m, {phaseL = 0, ampL = ampLX90m,
  phaseR =  $\pi/2$ , ampR = ampRY90m}];
If[test1 == LY90pRY90m, {phaseL =  $\pi/2$ , ampL = ampLY90p,
  phaseR =  $\pi/2$ , ampR = ampRY90m}];
If[test1 == LY90mRY90m, {phaseL =  $\pi/2$ , ampL = ampLY90m,
  phaseR =  $\pi/2$ , ampR = ampRY90m}];
If[test1 == LXpRY90m, {phaseL = 0, ampL = ampLXp,
  phaseR =  $\pi/2$ , ampR = ampRY90m}];
If[test1 == LXmRY90m, {phaseL = 0, ampL = ampLXm,
  phaseR =  $\pi/2$ , ampR = ampRY90m}];
If[test1 == LYpRY90m, {phaseL =  $\pi/2$ , ampL = ampLYp,
  phaseR =  $\pi/2$ , ampR = ampRY90m}];
If[test1 == LYmRY90m, {phaseL =  $\pi/2$ , ampL = ampLYm,
  phaseR =  $\pi/2$ , ampR = ampRY90m}];
If[test1 == LX90pRXp, {phaseL = 0, ampL = ampLX90p, phaseR = 0, ampR = ampRXp}];
If[test1 == LX90mRXp, {phaseL = 0, ampL = ampLX90m, phaseR = 0, ampR = ampRXp}];
If[test1 == LY90pRXp,
  {phaseL =  $\pi/2$ , ampL = ampLY90p, phaseR = 0, ampR = ampRXp}];
If[test1 == LY90mRXp, {phaseL =  $\pi/2$ , ampL = ampLY90m,
  phaseR = 0, ampR = ampRXp}];
If[test1 == LXpRXp, {phaseL = 0, ampL = ampLXp, phaseR = 0, ampR = ampRXp}];
If[test1 == LXmRXp, {phaseL = 0, ampL = ampLXm, phaseR = 0, ampR = ampRXp}];
If[test1 == LYpRXp, {phaseL =  $\pi/2$ , ampL = ampLYp, phaseR = 0, ampR = ampRXp}];
If[test1 == LYmRXp, {phaseL =  $\pi/2$ , ampL = ampLYm, phaseR = 0, ampR = ampRXp}];
If[test1 == LX90pRXm, {phaseL = 0, ampL = ampLX90p, phaseR = 0, ampR = ampRXm}];
If[test1 == LX90mRXm, {phaseL = 0, ampL = ampLX90m, phaseR = 0, ampR = ampRXm}];
If[test1 == LY90pRXm,
  {phaseL =  $\pi/2$ , ampL = ampLY90p, phaseR = 0, ampR = ampRXm}];
If[test1 == LY90mRXm, {phaseL =  $\pi/2$ , ampL = ampLY90m,
  phaseR = 0, ampR = ampRXm}];
If[test1 == LXpRXm, {phaseL = 0, ampL = ampLXp, phaseR = 0, ampR = ampRXm}];
If[test1 == LXmRXm, {phaseL = 0, ampL = ampLXm, phaseR = 0, ampR = ampRXm}];
If[test1 == LYpRXm, {phaseL =  $\pi/2$ , ampL = ampLYp, phaseR = 0, ampR = ampRXm}];
If[test1 == LYmRXm, {phaseL =  $\pi/2$ , ampL = ampLYm, phaseR = 0, ampR = ampRXm}];
If[test1 == LX90pRYp,
  {phaseL = 0, ampL = ampLX90p, phaseR =  $\pi/2$ , ampR = ampRYp}];
If[test1 == LX90mRYp, {phaseL = 0, ampL = ampLX90m,
  phaseR =  $\pi/2$ , ampR = ampRYp}];
If[test1 == LY90pRYp, {phaseL =  $\pi/2$ , ampL = ampLY90p,
  phaseR =  $\pi/2$ , ampR = ampRYp}];
If[test1 == LY90mRYp, {phaseL =  $\pi/2$ , ampL = ampLY90m,

```

```

    phaseR =  $\pi/2$ , ampR = ampRYp]];
If[test1 == LXpRYp, {phaseL = 0, ampL = ampLXp, phaseR =  $\pi/2$ , ampR = ampRYp}]];
If[test1 == LXmRYp, {phaseL = 0, ampL = ampLXm, phaseR =  $\pi/2$ , ampR = ampRYp}]];
If[test1 == LYpRYp,
  {phaseL =  $\pi/2$ , ampL = ampLYp, phaseR =  $\pi/2$ , ampR = ampRYp}]];
If[test1 == LYmRYp, {phaseL =  $\pi/2$ , ampL = ampLYm,
  phaseR =  $\pi/2$ , ampR = ampRYp}]];
If[test1 == LX9OpRYm, {phaseL = 0, ampL = ampLX9Op,
  phaseR =  $\pi/2$ , ampR = ampRYm}]];
If[test1 == LX9OmRYm, {phaseL = 0, ampL = ampLX9Om,
  phaseR =  $\pi/2$ , ampR = ampRYm}]];
If[test1 == LY9OpRYm, {phaseL =  $\pi/2$ , ampL = ampLY9Op,
  phaseR =  $\pi/2$ , ampR = ampRYm}]];
If[test1 == LY9OmRYm, {phaseL =  $\pi/2$ , ampL = ampLY9Om,
  phaseR =  $\pi/2$ , ampR = ampRYm}]];
If[test1 == LXpRYm, {phaseL = 0, ampL = ampLXp, phaseR =  $\pi/2$ , ampR = ampRYm}]];
If[test1 == LXmRYm, {phaseL = 0, ampL = ampLXm, phaseR =  $\pi/2$ , ampR = ampRYm}]];
If[test1 == LYpRYm,
  {phaseL =  $\pi/2$ , ampL = ampLYp, phaseR =  $\pi/2$ , ampR = ampRYm}]];
If[test1 == LYmRYm, {phaseL =  $\pi/2$ , ampL = ampLYm,
  phaseR =  $\pi/2$ , ampR = ampRYm}]];
(* Single Qubit Arbitrary Rotation Pulses with Arbitrary Sigma *)
If[test1 == LX $\theta$ , {phaseL = 0, ampL = 2000, Ssigma = 2000}]];
If[test1 == LY $\theta$ , {phaseL =  $\pi/2$ , ampL = 2000, Ssigma = 2000}]];
If[test1 == RX $\theta$ , {phaseR = 0, ampR = 2000, Ssigma = 2000}]];
If[test1 == RY $\theta$ , {phaseR =  $\pi/2$ , ampR = 2000, Ssigma = 2000}]];
If[test1 == LX $\theta$ RX $\theta$ ,
  {phaseL = 0, ampL = 2000, phaseR = 0, ampR = 2000, Ssigma = 2000}]];
If[test1 == LX $\theta$ RY $\theta$ , {phaseL = 0, ampL = 2000,
  phaseR =  $\pi/2$ , ampR = 2000, Ssigma = 2000}]];
If[test1 == LY $\theta$ RX $\theta$ , {phaseL =  $\pi/2$ , ampL = 2000, phaseR = 0,
  ampR = 2000, Ssigma = 2000}]];
If[test1 == LY $\theta$ RY $\theta$ , {phaseL =  $\pi/2$ , ampL = 2000,
  phaseR =  $\pi/2$ , ampR = 2000, Ssigma = 2000}]];
(* Single Qubit Z-Pulses *)
If[test1 == LZf, {ampLZ = 2000, widthLZ = cycleLength, spec = 0, flux = 1}]];
If[test1 == RZf, {ampRZ = 2000, widthRZ = cycleLength, spec = 0, flux = 1}]];
If[test1 == LZfRZf, {ampLZ = 2000, ampRZ = 2000,
  widthLZ = cycleLength, widthRZ = cycleLength, spec = 0, flux = 1}]];
(* Two Qubit C-Phases Type a *)
If[test1 == C0,
  {ampLZ = ampCOL, ampRZ = ampCOR, widthLZ = fwidthL, widthRZ = fwidthR,
  offsetLZ = offsetCOL, offsetRZ = offsetCOR, spec = 0, flux = 1}]];
If[test1 == C1, {ampLZ = ampC1L, ampRZ = ampC1R, widthLZ = fwidthL, widthRZ =
  fwidthR, offsetLZ = offsetC1L, offsetRZ = offsetC1R, spec = 0, flux = 1}]];
If[test1 == C2, {ampLZ = ampC2L, ampRZ = ampC2R, widthLZ = fwidthL, widthRZ =
  fwidthR, offsetLZ = offsetC2L, offsetRZ = offsetC2R, spec = 0, flux = 1}]];
If[test1 == C3, {ampLZ = ampC3L, ampRZ = ampC3R, widthLZ = fwidthL, widthRZ =
  fwidthR, offsetLZ = offsetC3L, offsetRZ = offsetC3R, spec = 0, flux = 1}]];
(* Two Qubit C-Phases Type b, when following a C-Phase type a*)
If[test1 == C0b,
  {ampLZ = ampCOLb, ampRZ = ampCORb, widthLZ = fwidthL, widthRZ = fwidthR,
  offsetLZ = offsetCOLb, offsetRZ = offsetCORb, spec = 0, flux = 1}]];
If[test1 == C1b, {ampLZ = ampC1Lb, ampRZ = ampC1Rb, widthLZ = fwidthL, widthRZ =
  fwidthR, offsetLZ = offsetC1Lb, offsetRZ = offsetC1Rb, spec = 0, flux = 1}]];
If[test1 == C2b, {ampLZ = ampC2Lb, ampRZ = ampC2Rb, widthLZ = fwidthL, widthRZ =
  fwidthR, offsetLZ = offsetC2Lb, offsetRZ = offsetC2Rb, spec = 0, flux = 1}]];
If[test1 == C3b, {ampLZ = ampC3Lb, ampRZ = ampC3Rb, widthLZ = fwidthL, widthRZ =
  fwidthR, offsetLZ = offsetC3Lb, offsetRZ = offsetC3Rb, spec = 0, flux = 1}]];
{phaseL, ampL, phaseR, ampR, ampLZ, widthLZ, offsetLZ,
  ampRZ, widthRZ, offsetRZ, spec, flux, Ssigma}]];

```

Rabi angle to AWG DAC value function

```
AngletoDAC[Angle_, mPiDAC_, zeroDAC_] :=
Module[{DACLevel}, DACLevel = Round[mPiDAC +  $\frac{\text{zeroDAC} - \text{mPiDAC}}{180.} (\text{Angle} + 180)$ ];
{DACLevel}];
```

Pulse Functions

■ Various Gaussian and tangent hyperbolic spec pulse functions

```
DerivGaussianPulse[amp_, n_,  $\sigma$ _] := Module[{midpoint}, midpoint = (n + 1) / 2;
Round [Table[- amp  $\frac{(x - \text{midpoint})}{\sigma^2}$  Exp[-  $\frac{(x - \text{midpoint})^2}{2 \sigma^2}$ ], {x, 1, n}]]]
```

```
GaussianPulseSubOff[amp_, n_,  $\sigma$ _] := Module[{midpoint}, midpoint = (n + 1) / 2;
Round [Table[amp  $\frac{(\text{Exp}[-\frac{(x - \text{midpoint})^2}{2 \sigma^2}] - \text{Exp}[-\frac{(\text{midpoint})^2}{2 \sigma^2}])}{1 - \text{Exp}[-\frac{(\text{midpoint})^2}{2 \sigma^2}]}$ , {x, 1, n}]]]
```

```
DerivGaussianPulseSubOff[amp_, n_,  $\sigma$ _] :=
Module[{midpoint}, midpoint = (n + 1) / 2;
Round [Table[- amp  $\frac{(x - \text{midpoint})}{\sigma^2}$ 
 $\frac{(\text{Exp}[-\frac{(x - \text{midpoint})^2}{2 \sigma^2}] - \text{Exp}[-\frac{(\text{midpoint})^2}{2 \sigma^2}])}{1 - \text{Exp}[-\frac{(\text{midpoint})^2}{2 \sigma^2}]}$ , {x, 1, n}]]]
```

```
SquareGaussPow[amp_, n_, m_,  $\sigma$ _, p_] := Module[{t0, t1},
(* amp is the max amplitude,
n is the total length, m is the number of sigmas for truncation,
 $\sigma$  is the std. dev, p is the root of gaussian to take*)
t0 = (m  $\sigma$  + 1) / 2;
t1 = n - (m  $\sigma$  + 1) / 2;
Round [Table [ amp / 2 HeavisideTheta[t0 - t]
 $\left( \text{Exp} \left[ -\frac{(t - t0)^2}{2 \sigma^2} \right] \right)^{1/p}$  + amp ((HeavisideTheta[t - t0] + HeavisideTheta[t1 - t]) / 2)
amp / 2 HeavisideTheta[t - t1]  $\left( \text{Exp} \left[ -\frac{(t - t1)^2}{2 \sigma^2} \right] \right)^{1/p}$ , {t, 1, n}]]]
```

```
TanhPulse[amp_,  $\sigma$ _, length_] := Module[{t0, t1},
  t0 = 4  $\sigma$ ;
  t1 = 4  $\sigma$  + length;
  Round[Table[
    amp (Tanh[(t - t0) /  $\sigma$ ] + Tanh[-(t - t1) /  $\sigma$ ]) / 2, {t, 0, Round[length + 8  $\sigma$ ]}]]
];

TanhPulseOffset[amp_,  $\sigma$ _, length_, offset_] := Module[{t0, t1},
  t0 = 4  $\sigma$ ;
  t1 = 4  $\sigma$  + length;
  Round[Table[amp (Tanh[(t - t0) /  $\sigma$ ] + Tanh[-(t - t1) /  $\sigma$ ]) / 2 +
    offset * (KroneckerDelta[t, t0] + KroneckerDelta[t, t1]),
    {t, 0, Round[length + 8  $\sigma$ ]}]]
];

GaussPulseOffset[amp_, numSigmas_, length_, offset_] := Module[{trueoffset},
  trueoffset = {Round[offset / 100 * amp * Exp[-(numSigmas / 2) ^ 2 / 2]}}];
  Join[trueoffset,
    GaussianPulse[amp, (length - 2), (length - 2) / numSigmas, trueoffset]];
];
```

■ Building up spectroscopy and flux pulses

```
(* Flux pulse with rounded top *)
FluxPulse[amp_, numSigmas_, length_,
  offset_, fixedPoint_, cycleLength_, FluxDelay_] :=
  MakePattern[GaussPulsewOffset[amp, numSigmas, length, offset],
    fixedPoint + FluxDelay, {}, cycleLength];
(* DPS scale factor D *)
DerivAmpScaleL = 0.5;
DerivAmpScaleR = 0.2;
(* Spectroscopy pulse with option for using DPS,
gaussian, square, or tanh *)
FullSpecPulse[amp_, SpecPulseLength_,
  fixedPoint_, cycleLength_, SpecDelay_, type_] :=
  MakePattern[Which[type == 0, GaussianPulseSubOff[amp,
    numSigmas * SpecPulseLength, SpecPulseLength],
    type == 1, SquarePulse[amp,
    numSigmas * SpecPulseLength],
    type == 2, TanhPulse[amp, tanhSigma,
    numSigmas * SpecPulseLength - 8 * tanhSigma],
    type == 3, InputPulse[amp,
    SpecPulseLength, SpecPulseLength, SpecPointsI],
    type == 4, InputPulse[amp,
    SpecPulseLength, SpecPulseLength, SpecPointsQ],
    type == 6, DerivGaussianPulseSubOff[
    amp, numSigmas * SpecPulseLength, SpecPulseLength]
  ], fixedPoint + SpecDelay, {}, cycleLength];
(* Single spectroscopy pulse, used for Rabi,
T1 and as bulding block for Ramsey *)
SpecPulse[amp_, SpecPulseLength_, fixedPoint_, cycleLength_, SpecDelay_] :=
  MakePattern[GaussianPulse[amp, numSigmas * SpecPulseLength, SpecPulseLength],
    fixedPoint + SpecDelay, {}, cycleLength];
(* Measurement Pulse *)
MeasPulse[MeasPulseLength_, fixedPoint_, cycleLength_] :=
  MakePattern[{}, fixedPoint, SquarePulse[1, MeasPulseLength], cycleLength];
MeasPulseArray[n_, MeasPulseLength_, fixedPoint_, cycleLength_] :=
  Join@@Table[MeasPulse[MeasPulseLength, fixedPoint, cycleLength], {n}];
(* Blank out Pulse *)
BlankPulse[BlankPulseLength_, fixedPoint_, cycleLength_] :=
  MakePattern[{}, fixedPoint, SquarePulse[0, BlankPulseLength], cycleLength];
BlankPulseArray[n_, BlankPulseLength_, fixedPoint_, cycleLength_] :=
  Join@@Table[BlankPulse[BlankPulseLength, fixedPoint, cycleLength], {n}];
(* Buffer pulse *)
SpecBufferPulse[specBufferLength_, endPoint_, cycleLength_,
  SpecBufferDelay_] := MakePattern[SquarePulse[1, specBufferLength],
  endPoint + SpecBufferDelay, {}, cycleLength];
```

Pattern Functions

The following function parses through sequences of many pulses, comprised of both qubit driving pulses and flux pulses. It calls `PulseIdentify[-]` to assign the appropriate times, delays, amplitudes, and offsets.

```
GetNewSeq[seq_, SpecAmpL_, SpecAmpR_, numSigmasfL_, numSigmasfR_,
  fampL_, fampR_, widthfL_, widthfR_, specType_, sigma_, awgType_] :=
  Module[{seqLX, seqLY, aL, L, seqRX, seqRY, aR, R, seqLZ, aLZ, wLZ,
    oLZ, seqRZ, aRZ, wRZ, oRZ, s, f, widthF, widthSL, widthSR, bufferL,
    bufferR, Ssigma, typeI, typeQ, typeIpQ, input, quadspec,
```

```

cLength, fPoint, AWGDelay, sigma7102, bufferSL, bufferSR},

(* Default values *)
seqLX = 0; seqLY = 0; seqRX = 0; seqRY = 0; seqLZ = 0; seqRZ = 0;
aL = DACoffsetLX;
aR = DACoffsetRX;
widthF = 0; widthSL = 0; widthSR = 0; bufferL = 0; bufferR = 0;
input = 0;
quadspec = 0;
cLength = cycleLength;
fPoint = fixedPointCh1;
AWGDelay = AWG520Delay;
bufferSL = bufferS; bufferSR = bufferS;
For[j = Length[seq], j ≥ 1, j--, {
  {L, aL, R, aR, aLZ, wLZ, oLZ, aRZ, wRZ, oRZ, s, f, Ssigma} =
  PulseIdentify[seq[[j]]];
  typeI = specType;
  typeQ = specType;
  typeIpQ = 0;
  If[specType == 6, {quadspec = 1, typeI = 0, typeQ = 0, typeIpQ = 6}];
  If[seq[[j]] == LXi,
    {typeI = 3, typeQ = 4, input = 1, s = 0, aL = SpecAmpL, L = 0, Ssigma = sigma}];
  If[seq[[j]] == LYi, {typeI = 4, typeQ = 3, input = 1,
    s = 0, aL = SpecAmpL, L = 0, Ssigma = sigma}];
  If[seq[[j]] == RXi, {typeI = 3, typeQ = 4, input = 1, s = 0,
    aR = SpecAmpR, R = 0, Ssigma = sigma}];
  If[seq[[j]] == RYi, {typeI = 4, typeQ = 3, input = 1, s = 0,
    aR = SpecAmpR, R = 0, Ssigma = sigma}];
  (* For arbitrary flux amplitude pulses *)
  If[aL == 2000, {aL = SpecAmpL}];
  If[aR == 2000, {aR = SpecAmpR}];
  If[aLZ == 2000, aLZ = fampL];
  If[aRZ == 2000, aRZ = fampR];
  If[wLZ == cycleLength, wLZ = widthfL];
  If[wRZ == cycleLength, wRZ = widthfR];
  If[Ssigma == 2000, Ssigma = sigma];

  seqLX += Cos[L] FullSpecPulse[aL - DACoffsetLX, Ssigma,
    fPoint - bufferL - widthF - widthSL, cLength, SpecPulseDelay, typeI] +
    input * Sin[L] FullSpecPulse[aL - DACoffsetLX, Ssigma,
    fPoint - bufferL - widthF - widthSL, cLength, SpecPulseDelay, typeI] +
    (*quadspec * Sin[L] FullSpecPulse[aL - DACoffsetLX, Ssigma,
    fPoint - bufferL - widthF - widthSL, cLength, SpecPulseDelay, typeIpQ];*)
    quadspec * Sin[L] FullSpecPulse[DerivAmpScaleL (aL - DACoffsetLX),
    sigma7102, fPoint - bufferL - widthF - widthSL,
    cLength, SpecPulseDelay, 6];
  seqLY += Sin[L] FullSpecPulse[aL - DACoffsetLY, Ssigma,
    fPoint - bufferL - widthF - widthSL, cLength, SpecPulseDelay, typeQ] +
    input * Cos[L] FullSpecPulse[aL - DACoffsetLY, Ssigma,
    fPoint - bufferL - widthF - widthSL, cLength, SpecPulseDelay, typeQ] -
    (*quadspec * Cos[L] FullSpecPulse[aL - DACoffsetLX, Ssigma,
    fPoint - bufferL - widthF - widthSL, cLength, SpecPulseDelay, typeIpQ];*)
    quadspec * Cos[L] FullSpecPulse[DerivAmpScaleL (aL - DACoffsetLX),
    sigma7102, fPoint - bufferL - widthF - widthSL,
    cLength, SpecPulseDelay, 6];
  seqRX += Cos[R] FullSpecPulse[aR - DACoffsetRX, Ssigma,
    fixedPointCh1 - bufferR - widthF - widthSR, cycleLength,
    SpecPulseDelay + AWGDelay, typeI] + input * Sin[R]
    FullSpecPulse[aR - DACoffsetRX, Ssigma, fixedPointCh1 - bufferR -
    widthF - widthSR, cycleLength, SpecPulseDelay + AWGDelay, typeI] +
    quadspec * Sin[R] FullSpecPulse[DerivAmpScaleR (aR - DACoffsetRX),
    Ssigma, fixedPointCh1 - bufferR - widthF - widthSR,

```

```

    cycleLength, SpecPulseDelay + AWGDelay, 6] ;
seqRY += Sin[R] FullSpecPulse[aR - DACoffsetRY, Ssigma,
    fixedPointCh1 - bufferR - widthF - widthSR, cycleLength,
    SpecPulseDelay + AWGDelay, typeQ] + input * Cos[R]
FullSpecPulse[aR - DACoffsetLY, Ssigma, fixedPointCh1 - bufferR -
    widthF - widthSR, cycleLength, SpecPulseDelay + AWGDelay, typeQ] -
quadspec * Cos[R] FullSpecPulse[DerivAmpScaler (aR - DACoffsetLX),
    Ssigma, fixedPointCh1 - bufferR - widthF - widthSR,
    cycleLength, SpecPulseDelay + AWGDelay, 6] ;
seqLZ += FluxPulse[aLZ - DACoffsetLZ, numSigmasfL, wLZ, oLZ,
    fixedPointCh1 - bufferR - widthF - widthSR, cycleLength, FluxPulseDelay];
seqRZ += FluxPulse[aRZ - DACoffsetLZ, numSigmasfL, wRZ, oRZ,
    fixedPointCh1 - bufferR - widthF - widthSR, cycleLength, FluxPulseDelay];

widthF += Max[wLZ, wRZ] * f;
widthSL += numSigmas * Ssigma * s + Length[SpecPointsI] * input;
widthSR += numSigmas * Ssigma * s + Length[SpecPointsI] * input;
bufferL += bufferSL * (input + s) + bufferF * f;
bufferR += bufferSL * (input + s) + bufferF * f;

}];
Round /@ {Clip[seqLX + DACoffsetLX, {0, 1023}],
    Clip[seqLY + DACoffsetLY, {0, 1023}], Clip[seqRX + DACoffsetRX, {0, 1023}],
    Clip[seqRY + DACoffsetRY, {0, 1023}],
    Clip[seqLZ + DACoffsetLZ, {0, 1023}], Clip[seqRZ + DACoffsetRZ, {0, 1023}],
    widthF, widthSL, widthSR, bufferL, bufferR}];

```

Calibration Sequences

The calibration sequences here refer to tuning up the DAC levels for π and $\pi/2$ pulses based on Rabi driving, the drive detuning based off of Ramsey fringe experiments, the level of DPS to use based on the ALLXY sequences consisting of pairs of X and Y pulses, as well as the conditional phase flux pulse amplitudes and offsets. All of these routines involve:

1. Defining the pulse sequences
2. Generating the pattern files for each AWG channel
3. Generating the marker pattern files for measurement, spectroscopy buffering, and acquisition card triggering
4. Exporting the files

Each section below will only give the steps 1 and 2, defining the pulse sequences and pattern files. Subsequently, steps 3 to 4 are the same for all cases and are given at the end.

Amplitude Rabi

■ Define pulse sequences and file directories

```

basename = "ARabi";
datapathAWG5014 = RootAWG5014 <> basename <> "_5014\\";
datapathAWG520 = RootAWG520 <> basename <> "_520\\";
CreateDirectory[datapathAWG5014];
CreateDirectory[datapathAWG520];
filePrefix5014 = basename <> "_5014";
filePrefix520 = basename <> "_520";
numstepsExp = 80;
ExpSeq = Table[{LXØRXØ}, {k, 1, numstepsExp}];
numsteps = Length[ExpSeq];

```

■ Generate pulse patterns

```

(* Initialization *)
patTableCh1 =
  patTableCh2 = patTableCh3 = patTableCh4 = patTableCh5 = patTableCh6 = {};
SpecBufferWidthPointsL = {}; SpecBufferWidthPointsR = {};
RabiCenter = 0; RabiStep = 17;
RabiPointsL = DACoffsetLX +
  Table[RabiCenter + (ii - numstepsExp/2) * RabiStep, {ii, 0, numsteps - 1}];
RabiPointsR = DACoffsetRX + Table[RabiCenter + (ii - numstepsExp/2) * RabiStep,
  {ii, 0, numsteps - 1}];

Monitor[Do[
  ampL = RabiPointsL[[ii]]; ampR = RabiPointsR[[ii]];
  numSigmasFL = 0.000001; numSigmasFR = 0.000001;
  widthFL = 0; widthFR = 0;
  ampFL = DACoffsetLZ; ampFR = DACoffsetRZ;
  {patLX, patLY, patRX, patRY, patLZ,
   patRZ, widthF, widthSL, widthSR, bufferL, bufferR} =
   GetNewSeq[ExpSeq[[ii]], RabiPointsL[[ii]], RabiPointsR[[ii]], numSigmasFL,
   numSigmasFR, ampFL, ampFR, widthFL, widthFR, 0, SpecPulseLength, 7];
  patTableCh1 = Append[patTableCh1, patLX];
  patTableCh2 = Append[patTableCh2, patLY];
  patTableCh3 = Append[patTableCh3, patLZ];
  patTableCh4 = Append[patTableCh4, patRZ];
  patTableCh5 = Append[patTableCh5, patRX];
  patTableCh6 = Append[patTableCh6, patRY];
  totalTimeL = widthSL + widthF + bufferL;
  totalTimeR = widthSR + widthF + bufferR;
  SpecBufferWidthPointsL =
    Append[SpecBufferWidthPointsL, totalTimeL + 2 * SpecBufferMargin7102];
  SpecBufferWidthPointsR = Append[SpecBufferWidthPointsR,
    totalTimeR + 2 * SpecBufferMargin];
, {ii, 1, numsteps}], ii];

```

Ramsey

■ Define pulse sequences

```
basename = "Ram";
numstepsExp = 80;
ExpSeq = Table[{LX90pRX90p, LZfRZf, LX90pRX90p}, {k, 1, numstepsExp}];
numsteps = Length[ExpSeq];
```

■ Generate pulse patterns

```
(* Initialization *)
patTableCh1 =
  patTableCh2 = patTableCh3 = patTableCh4 = patTableCh5 = patTableCh6 = {};
SpecBufferWidthPointsL = {}; SpecBufferWidthPointsR = {};
RamseyStart = 0; RamseyStepR = 20; RamseyStepL = 200; (* in ns *)
RamseyPointsR = Table[RamseyStart + ii RamseyStepR, {ii, 0, numsteps - 1}];
RamseyPointsL = Table[RamseyStart + ii RamseyStepL, {ii, 0, numsteps - 1}];
Monitor[Do[
  ampL = DACoffsetLX; ampR = DACoffsetRX;
  numSigmasFL = 0.000001; numSigmasFR = 0.000001;
  widthFL = RamseyPointsL[[ii]]; widthFR = RamseyPointsR[[ii]];
  ampFL = DACoffsetLZ; ampFR = DACoffsetRZ;
  {patLX, patLY, patRX, patRY, patLZ, patRZ, widthF, widthSL, widthSR,
   bufferL, bufferR} = GetNewSeq[ExpSeq[[ii]], ampL, ampR, numSigmasFL,
   numSigmasFR, ampFL, ampFR, widthFL, widthFR, 11, SpecPulseLength, 7];
  patTableCh1 = Append[patTableCh1, patLX];
  patTableCh2 = Append[patTableCh2, patLY];
  patTableCh3 = Append[patTableCh3, patLZ];
  patTableCh4 = Append[patTableCh4, patRZ];
  patTableCh5 = Append[patTableCh5, patRX];
  patTableCh6 = Append[patTableCh6, patRY];
  totalTimeL = widthSL + widthF + bufferL;
  totalTimeR = widthSR + widthF + bufferR;
  SpecBufferWidthPointsL =
    Append[SpecBufferWidthPointsL, totalTimeL + 2 * SpecBufferMargin7102];
  SpecBufferWidthPointsR = Append[SpecBufferWidthPointsR,
    totalTimeR + 2 * SpecBufferMargin];
  , {ii, 1, numsteps}], ii];
```

All XY

■ Define pulse sequences

```
runType = 0;
basename = Which[runType == 0, "ALLXY_L", runType == 1, "AllXY_R"];
```

```

ExpSeq = Which[runType == 0,
  {{Id}, {Id}, {LXp}, {LXp}, {LYp}, {LYp}, {LX90p}, {LX90p}, {LY90p}, {LY90p},
  {LXp, LXp}, {LXp, LXp}, {LXp, LYp}, {LXp, LYp},
  {LYp, LXp}, {LYp, LXp}, {LYp, LYp}, {LYp, LYp},
  {LXp, LX90p}, {LXp, LX90p}, {LXp, LY90p}, {LXp, LY90p}, {LYp, LX90p},
  {LYp, LX90p}, {LYp, LY90p}, {LYp, LY90p}, {LX90p, LXp}, {LX90p, LXp},
  {LX90p, LYp}, {LX90p, LYp}, {LY90p, LXp}, {LY90p, LXp},
  {LY90p, LYp}, {LY90p, LYp}, {LX90p, LX90p}, {LX90p, LX90p},
  {LX90p, LY90p}, {LX90p, LY90p}, {LY90p, LX90p},
  {LY90p, LX90p}, {LY90p, LY90p}, {LY90p, LY90p}},
runType == 1,
  {{Id}, {Id}, {RXp}, {RXp}, {RYp}, {RYp}, {RX90p}, {RX90p},
  {RY90p}, {RY90p}, {RXp, RXp}, {RXp, RXp}, {RXp, RYp}, {RXp, RYp},
  {RYp, RXp}, {RYp, RXp}, {RYp, RYp}, {RYp, RYp}, {RXp, RX90p},
  {RXp, RX90p}, {RXp, RY90p}, {RXp, RY90p}, {RYp, RX90p}, {RYp, RX90p},
  {RYp, RY90p}, {RYp, RY90p}, {RX90p, RXp}, {RX90p, RXp}, {RX90p, RYp},
  {RX90p, RYp}, {RY90p, RXp}, {RY90p, RXp}, {RY90p, RYp}, {RY90p, RYp},
  {RX90p, RX90p}, {RX90p, RX90p}, {RX90p, RY90p}, {RX90p, RY90p},
  {RY90p, RX90p}, {RY90p, RX90p}, {RY90p, RY90p}, {RY90p, RY90p}},
];
numsteps = Length[ExpSeq]

```

■ Generate pulse patterns

```

(* Initialization *)
patTableCh1 =
  patTableCh2 = patTableCh3 = patTableCh4 = patTableCh5 = patTableCh6 = {};
SpecBufferWidthPointsL = {};
SpecBufferWidthPointsR = {};
RabiCenter = 0; RabiStep = 16;
RabiPointsL = DACoffsetLX +
  Table[RabiCenter + (ii - numsteps/2) * RabiStep, {ii, 0, numsteps - 1}];
RabiPointsR = RabiPointsL;
Monitor[Do[
  ampL = RabiPointsL[[ii]];
  ampR = RabiPointsR[[ii]];
  numSigmasFL = 0.000001;
  numSigmasFR = 0.000001;
  widthFL = 0;
  widthFR = 0;
  ampFL = DACoffsetLZ;
  ampFR = DACoffsetRZ;
  {patLX, patLY, patRX, patRY, patLZ, patRZ, widthF, widthSL,
  widthSR, bufferL, bufferR} = GetNewSeq[ExpSeq[[ii]], ampL, ampR,
  numSigmasFL, numSigmasFR, ampFL, ampFR, widthFL, widthFR, 11, 1, 7];
  patTableCh1 = Append[patTableCh1, patLX];
  patTableCh2 = Append[patTableCh2, patLY];
  patTableCh3 = Append[patTableCh3, patLZ];
  patTableCh4 = Append[patTableCh4, patRZ];
  patTableCh5 = Append[patTableCh5, patRX];
  patTableCh6 = Append[patTableCh6, patRY];
  totalTimeL = widthSL + widthF + bufferL;
  totalTimeR = widthSR + widthF + bufferR;
  SpecBufferWidthPointsL =
  Append[SpecBufferWidthPointsL, totalTimeL + 2 * SpecBufferMargin];
  SpecBufferWidthPointsR = Append[SpecBufferWidthPointsR,
  totalTimeR + 2 * SpecBufferMargin];
  , {ii, 1, numsteps}], ii];

```

Conditional Phase Tune-Up

■ Define pulse sequences

```
runType = 2; (* 0 instructs to sweep pulse width,  
1 instructs to sweep left dynamic phase,  
2 instructs to sweep right dynamic phase *)  
basename = Which[runType == 0, "CPHL_vW",  
runType == 1, "CPHL_vDL", runType == 2, "CPHR_vDR"]  
SeqEx1 = Table[Which[runType == 0, {LY90p, LZfRZf, LY90p},  
runType == 1, {LY90p, LZfRZf, LY90p},  
runType == 2, {RY90p, LZfRZf, RY90p}], {k, 1, 101}];  
SeqEx2 = Table[Which[runType == 0, {LY90pRYp, LZfRZf, LY90pRYp},  
runType == 1, {LY90pRYp, LZfRZf, LY90pRYp},  
runType == 2, {LYpRY90p, LZfRZf, LYpRY90p}], {k, 1, 101}];  
IdSeq = Table[{Id}, {k, 1, 5}];  
LXpSeq = Table[{LXp}, {k, 1, 5}];  
RXpSeq = Table[{RXp}, {k, 1, 5}];  
LXpRXpSeq = Table[{LXpRXp}, {k, 1, 5}];  
SeqEx1 = Join[SeqEx1, IdSeq, LXpSeq, RXpSeq, LXpRXpSeq];  
SeqEx2 = Join[SeqEx2, IdSeq, LXpSeq, RXpSeq, LXpRXpSeq];  
numsteps = Length[SeqEx1]
```

■ Generate pattern files

```
(* Initialization *)
patTableCh1Ex1 = {}; patTableCh2Ex1 = {}; patTableCh3Ex1 = {};
patTableCh4Ex1 = {}; patTableCh5Ex1 = {}; patTableCh6Ex1 = {};
patTableCh1Ex2 = {}; patTableCh2Ex2 = {}; patTableCh3Ex2 = {};
patTableCh4Ex2 = {}; patTableCh5Ex2 = {}; patTableCh6Ex2 = {};
SpecBufferWidthPointsEx1 = {}; SpecBufferWidthPointsEx2 = {};

FluxPulseAmpLStart = Which[ runType == 0,
  DACOffsetLZ, runType == 1, DACOffsetLZ, runType == 2, 660];
FluxPulseAmpLStep = Which[ runType == 0,
  runType == 1, 10, runType == 2, 0];
FluxPulseAmpRStart = Which[ runType == 0,
  0, runType == 1, 1000, runType == 2, 1000];
FluxPulseAmpRStep = Which[ runType == 0,
  0, runType == 1, 0, runType == 2, 0];
FluxPulseOffsetLStart = Which[ runType == 0,
  0, runType == 1, 0, runType == 2, 0];
FluxPulseOffsetLStep = Which[ runType == 0,
  0, runType == 1, 0, runType == 2, 0];
FluxPulseOffsetRStart = Which[ runType == 0,
  0, runType == 1, 0, runType == 2, 0];
FluxPulseOffsetRStep = Which[ runType == 0,
  0, runType == 1, 0, runType == 2, 1];
FluxPulseWidthStart = Which[ runType == 0, 0,
  runType == 1, 30, runType == 2, 30];
FluxPulseWidthStep = Which[ runType == 0, 1,
  runType == 1, 0, runType == 2, 0];
FluxPulseOffsetLPoints = Table[FluxPulseOffsetLStart + ii FluxPulseOffsetLStep,
  {ii, 0, numsteps - 1}];
FluxPulseOffsetRPoints = Table[FluxPulseOffsetRStart + ii FluxPulseOffsetRStep,
  {ii, 0, numsteps - 1}];
FluxPulseAmpLPoints = Table[FluxPulseAmpLStart + ii FluxPulseAmpLStep,
  {ii, 0, numsteps - 1}];
FluxPulseAmpRPoints = Table[FluxPulseAmpRStart + ii FluxPulseAmpRStep,
  {ii, 0, numsteps - 1}];
FluxPulseWidthPoints = Table[FluxPulseWidthStart + ii FluxPulseWidthStep,
  {ii, 0, numsteps - 1}];
numSigmasFL = 0.000001;
numSigmasFR = 0.000001;

Monitor[Do[
  ampFL = {FluxPulseAmpLPoints[[ii]], FluxPulseAmpLPoints[[ii]]};
  ampFR = {FluxPulseAmpRPoints[[ii]], FluxPulseAmpRPoints[[ii]]};
  offsetFL = {FluxPulseOffsetLPoints[[ii]], FluxPulseOffsetLPoints[[ii]]};
  offsetFR = {FluxPulseOffsetRPoints[[ii]], FluxPulseOffsetRPoints[[ii]]};
  widthFL = {FluxPulseWidthPoints[[ii]], FluxPulseWidthPoints[[ii]]};
  widthFR = {FluxPulseWidthPoints[[ii]], FluxPulseWidthPoints[[ii]]};

  {patLX, patLY, patRX, patRY, patLZ, patRZ, widthF, currdelay, widthS} =
  GetSeqXYZFluxGauss[SeqEx1[[ii]], ampFL, ampFR, widthFL,
  widthFR, offsetFL, offsetFR, numSigmasFL, numSigmasFR];
  patTableCh1Ex1 = Append[patTableCh1Ex1, patLX];
  patTableCh2Ex1 = Append[patTableCh2Ex1, patLY];
  patTableCh3Ex1 = Append[patTableCh3Ex1, patLZ];
  patTableCh4Ex1 = Append[patTableCh4Ex1, patRZ];
  patTableCh5Ex1 = Append[patTableCh5Ex1, patRX];
  patTableCh6Ex1 = Append[patTableCh6Ex1, patRY];
  totalTime = widthS + widthF + currdelay;
  SpecBufferWidthPointsEx1 =
```

```

    Append[SpecBufferWidthPointsEx1, totalTime + 2 * SpecBufferMargin];
    , {ii, 1, numsteps}], ii];

Monitor[Do[
  ampFL = {FluxPulseAmpLPoints[[ii]], FluxPulseAmpLPoints[[ii]]};
  ampFR = {FluxPulseAmpRPoints[[ii]], FluxPulseAmpRPoints[[ii]]};
  offsetFL = {FluxPulseOffsetLPoints[[ii]], FluxPulseOffsetLPoints[[ii]]};
  offsetFR = {FluxPulseOffsetRPoints[[ii]], FluxPulseOffsetRPoints[[ii]]};
  widthFL = {FluxPulseWidthPoints[[ii]], FluxPulseWidthPoints[[ii]]};
  widthFR = {FluxPulseWidthPoints[[ii]], FluxPulseWidthPoints[[ii]]};

  {patLX, patLY, patRX, patRY, patLZ, patRZ, widthF, currdelay, widthS} =
  GetSeqXYZFluxGauss[SeqEx2[[ii]], ampFL, ampFR, widthFL,
    widthFR, offsetFL, offsetFR, numSigmasFL, numSigmasFR];
  patTableCh1Ex2 = Append[patTableCh1Ex2, patLX];
  patTableCh2Ex2 = Append[patTableCh2Ex2, patLY];
  patTableCh3Ex2 = Append[patTableCh3Ex2, patLZ];
  patTableCh4Ex2 = Append[patTableCh4Ex2, patRZ];
  patTableCh5Ex2 = Append[patTableCh5Ex2, patRX];
  patTableCh6Ex2 = Append[patTableCh6Ex2, patRY];
  totalTime = widthS + widthF + currdelay;
  SpecBufferWidthPointsEx2 =
  Append[SpecBufferWidthPointsEx2, totalTime + 2 * SpecBufferMargin];
  , {ii, 1, numsteps}], ii];
(* Join the two experiments *)
patTableCh1 =
  Table[Join[patTableCh1Ex1[[ii]], patTableCh1Ex2[[ii]], {ii, numsteps}];
patTableCh2 = Table[Join[patTableCh2Ex1[[ii]], patTableCh2Ex2[[ii]],
  {ii, numsteps}];
patTableCh3 = Table[Join[patTableCh3Ex1[[ii]], patTableCh3Ex2[[ii]],
  {ii, numsteps}];
patTableCh4 = Table[Join[patTableCh4Ex1[[ii]], patTableCh4Ex2[[ii]],
  {ii, numsteps}];
patTableCh5 = Table[Join[patTableCh5Ex1[[ii]], patTableCh5Ex2[[ii]],
  {ii, numsteps}];
patTableCh6 = Table[Join[patTableCh6Ex1[[ii]], patTableCh6Ex2[[ii]],
  {ii, numsteps}];

```

Define AWG marker patterns

```

(*AWG5014 Qubit 1 Markers*)
markerTable1 = Table[
  PadRight[Join[Delay[1], SquarePulse[1, triggerWidth]], cycleLength],
  {ii, numsteps}]; (* Marker 1 is a trigger *)
markerTable2 = Table[
  SpecBufferPulse[SpecBufferWidthPointsR[[ii]], fixedPointCh1 +
  SpecBufferMargin, cycleLength, SpecBufferDelay], {ii, numsteps}];
(* Marker 2 is the spec buffer for Qubit 1 Channels *)
markerTable3 = Table[
  PadRight[Join[Delay[1], SquarePulse[1, triggerWidth]], 1 * cycleLength],
  {ii, numsteps}]; (* Marker 3 is a trigger *)
markerTable4 = markerTable2; (* Marker 4 is the spec
buffer for Qubit 1 Channels *)
(*AWG5014 FBL Markers*)
markerTable5 = Table[
  PadRight[Join[Delay[1], SquarePulse[1, triggerWidth]], 1 * cycleLength],
  {ii, numsteps}]; (* Marker 5 is a trigger *)
markerTable6 = Table[
  MeasPulseArray[1, MeasPulseLength, fixedPointCh1 + MeasPulseDelay,
  cycleLength], {ii, numsteps}]; (* Marker 6 is a measurement pulse *)
markerTable7 = Table[
  PadRight[Join[Delay[1], SquarePulse[1, triggerWidth]], 1 * cycleLength],
  {ii, numsteps}]; (* Marker 7 is a trigger *)
markerTable8 = Table[
  MeasPulseArray[1, MeasPulseLength,
  fixedPointCh1 + MeasPulseDelay, cycleLength], {ii, numsteps}];
(* Marker 8 is a measurement pulse *)
(*AWG520 QR Markers*)
markerTable9 = Table[
  PadRight[Join[Delay[1], SquarePulse[1, triggerWidth]], 1 * cycleLength],
  {ii, numsteps}]; (* Marker 9 is a trigger *)
markerTable10 = Table[
  SpecBufferPulse[SpecBufferWidthPointsR[[ii]],
  fixedPointCh1 + SpecBufferMargin, cycleLength,
  SpecBufferDelay + AWG520Delay], {ii, numsteps}];
(* Marker 10 is the spec buffer for Qubit 2 Channels *)
markerTable11 = Table[
  PadRight[Join[Delay[1], SquarePulse[1, triggerWidth]], 1 * cycleLength],
  {ii, numsteps}]; (* Marker 11 is a trigger *)
markerTable12 = Table[
  MeasPulseArray[1, MeasPulseLength,
  fixedPointCh1 + MeasPulseDelay + AWG520Delay, cycleLength], {ii, numsteps}];
(* Marker 12 is a measurement pulse *)

```

Export pulse pattern files

```

(* Export pulses *)
steps = Range[numsteps];
ExportTekPatternsAWG5014[datapathAWG5014, filePrefix5014,
patTableCh1, markerTable1, markerTable2, patTableCh2, markerTable3,
markerTable4, patTableCh3, markerTable5, markerTable6,
patTableCh4, markerTable7, markerTable8, steps, parameterList]
ExportTekPatternsAWG520[datapathAWG520, filePrefix520,
patTableCh5, markerTable9, markerTable10, patTableCh6,
markerTable11, markerTable12, steps, parameterList]

```

1-Qubit Benchmarking

Pulse sequences and functions for single-qubit randomized benchmarking (pattern generation, marker generation, and file exporting omitted)

■ Tools

Pauli and the Clifford generators

```
Pauli = {{Idp, Idm}, {Xp, Xm}, {Yp, Ym}, {Zp, Zm}};
Clifford = {{X90p, X90m}, {Y90p, Y90m}};
Undo = {{Idp, Idm}, {X90p, X90m}, {Y90p, Y90m}};
```

Getting the generating function

```
Gates[NumberOfGates_] := Module[{gates, cgate, pgate,
  signc, signp, undo, undotemp, zswap, signtemp}, gates = {};
  cgate = CallClifford[[1]];
  pgate = CallPauli[[1]];
  zswap = 1;
  If[pgate == 4, {zswap = -zswap, pgate = 1}];
  signtemp = CallSignC[[1]];
  signc = If[zswap == -1, Mod[signtemp, 2] + 1, signtemp];
  signtemp = CallSignP[[1]];
  signp = If[zswap == -1, Mod[signtemp, 2] + 1, signtemp];
  undotemp = cgate;
  undo = undotemp;
  gates = Append[gates, Pauli[[pgate, signp]]];
  gates = Append[gates, Clifford[[cgate, signc]]];
  For[i = 1, i < NumberOfGates, {
    cgate = CallClifford[[i]];
    pgate = CallPauli[[i]];
    If[pgate == 4, {zswap = -zswap, pgate = 1}];
    signtemp = CallSignC[[i]];
    signc = If[zswap == -1, Mod[signtemp, 2] + 1, signtemp];
    signtemp = CallSignP[[i]];
    signp = If[zswap == -1, Mod[signtemp, 2] + 1, signtemp];
    If[undo == 0, undotemp = cgate];
    If[undo == cgate, undotemp = 0];
    undo = undotemp;
    gates = Append[gates, Pauli[[pgate, signp]]];
    gates = Append[gates, Clifford[[cgate, signc]]], i++];
  pgate = CallPauli[[i + 1]];
  If[pgate == 4, {zswap = -zswap, pgate = 1}];
  signtemp = CallSignP[[i + 1]];
  signp = If[zswap == -1, Mod[signtemp, 2] + 1, signtemp];
  gates = Append[gates, Pauli[[pgate, signp]]];
  gates = Append[gates, Undo[[undo + 1, Random[Integer, 1] + 1]];
  pgate = CallPauli[[i + 2]];
  If[pgate == 4, {zswap = -zswap, pgate = 1}];
  signtemp = CallSignP[[i + 2]];
  signp = If[zswap == -1, Mod[signtemp, 2] + 1, signtemp];
  gates = Append[gates, Pauli[[pgate, signp]]];
```

Standard commands to define a lowering operator, identity and dagger

```

ident[dim_] := SparseArray[{{Poutine$_, Poutine$_} -> 1}, {dim, dim}];
destroy[dim_] :=
  SparseArray[{{Poutine$_, Maudite$_} //; Poutine$ + 1 == Maudite$ ->  $\sqrt{\text{Poutine\$}}$ ,
    {dim, dim}];
dagger[a_] := Transpose[Conjugate[a]];
qbasis[dim_, n_] := Flatten[SparseArray[{{n + 1, 1} -> 1}, {dim, 1}]];

```

The SU 2 operators

```

 $\sigma_+$  = destroy[2];
 $\sigma_-$  = dagger[ $\sigma_+$ ];
 $\sigma_x$  =  $\sigma_- + \sigma_+$ ;
 $\sigma_y$  =  $i \sigma_- - i \sigma_+$ ;
 $\sigma_z$  = -  $\sigma_- \cdot \sigma_+ + \sigma_+ \cdot \sigma_-$ ;

```

Rotations

```

X[ $\theta$ ] = MatrixExp[- $i \sigma_x \theta / 2$ ] // Normal;
Y[ $\theta$ ] = MatrixExp[- $i \sigma_y \theta / 2$ ] // Normal;
Z[ $\theta$ ] = MatrixExp[- $i \sigma_z \theta / 2$ ] // Normal;
II = ident[2] // Normal;

```

Numerical replacements

```

NRep = {X90p -> X[ $\frac{\pi}{2}$ ], X90m -> X[- $\frac{\pi}{2}$ ], Y90p -> Y[ $\frac{\pi}{2}$ ], Y90m -> Y[- $\frac{\pi}{2}$ ],
  Idp -> II, Idm -> II, Xp -> X[ $\pi$ ], Xm -> X[- $\pi$ ], Yp -> Y[ $\pi$ ], Ym -> Y[- $\pi$ ]};

NumericalCheck1[seq_] := Module[{ans, temp, test}, temp = seq /. NRep;
  test = temp[[1]];
  For[i = 1, i <= Length[temp] - 1, {
    test = test.temp[[i]], i++;
  }];
  ans = test.{0, 1}; If[ans[[1]] == 0, "ground", "excited"];

NumericalCheck2[seq_] := Module[{temp, test}, temp = seq /. NRep;
  test = temp[[1]];
  For[i = 1, i <= Length[temp] - 1, {
    test = test.temp[[i]], i++;
  }];
  test.{0, 1};

```

■ Pulse generation sequences for single qubit randomized benchmarking

```

NG = 4;
NP = 8;
lengths = {2, 3, 4, 5, 6, 8, 10, 12, 16, 20, 24, 32, 40, 48, 64, 80, 96};
NL = Length[lengths];

expinfo = {};
expsequences = {};

```

```

exp = 0;
For[ng = 0, ng < NG, {
  CallClifford = Table[Random[Integer, 1] + 1, {i, 1, 100}];
  CallSignC = Table[Random[Integer, 1] + 1, {i, 1, 100}]; For[np = 0, np < NP, {
    CallPauli = Table[Random[Integer, 3] + 1, {i, 1, 100 + 2}];
    CallSignP = Table[Random[Integer, 1] + 1, {i, 1, 100 + 2}];
    For[nl = 0, nl < NL, {
      numGates = lengths[[nl]];
      seq = Gates[numGates];
      exp += 1;
      expinfo = Append[expinfo, {exp, ng, np, nl, NumericalCheck1[seq]}];
      expsequences = Append[expsequences, seq];
      (*Print["Exp",exp,":", " ng=",ng, " np=",np, " nl=" ,
        nl, " Result= ",NumericalCheck1[seq], "\n", " seq=",seq];*)
    }, nl++]
  }, np++]
}, ng++]

```

1-Qubit Process Tomography

Pulse generation sequences for single qubit process tomography (pattern generation, marker generation, and file exporting omitted)

```

runType = 5;
qubit = L;
(*choose the process to be investigated *)
basename = Which[ runType == 0, "Id",
  runType == 1, "LX90p",
  runType == 2, "LX90m",
  runType == 3, "LY90p",
  runType == 4, "LY90m",
  runType == 5, "LXp",
  runType == 6, "LYp",
  runType == 7, "RX90p",
  runType == 8, "RX90m",
  runType == 9, "RY90p",
  runType == 10, "RY90m",
  runType == 11, "RXp",
  runType == 12, "RYp"
];

```

```

ProcTomoloQSeq[Proc_, Qubit_, m_, n_] :=
Module[{LUnitaries, RUnitaries, Prep, Meas},
  LUnitaries = {Id, LXp, LYp, LX90p, LY90m};
  RUnitaries = {Id, RXp, RYp, RX90p, RY90m};
  If[Qubit == L, {Prep = LUnitaries[[m]], Meas = LUnitaries[[n]]}];
  If[Qubit == R, {Prep = RUnitaries[[m]], Meas = RUnitaries[[n]]}];
  {Prep, Proc, Meas}];
BuildProcTomoloQ[Proc_, Qubit_] := Module[{TomoSequences},
  TomoSequences = {};
  For[m = 1, m ≤ 5, m++, {
    For[n = 1, n ≤ 5, n++, {TomoSequences =
      Append[TomoSequences, ProcTomoloQSeq[Proc, Qubit, m, n]]}}];
  TomoSequences];
CalSeq = Which[ToString[qubit] == "L", {
  {Id}, {Id}, {Id}, {Id}, {Id},
  {LXp}, {LXp}, {LXp}, {LXp}, {LXp},
  {LXm}, {LXm}, {LXm}, {LXm}, {LXm},
  {LYp}, {LYp}, {LYp}, {LYp}, {LYp},
  {LYm}, {LYm}, {LYm}, {LYm}, {LYm}
},
  ToString[qubit] == "R", {
  {Id}, {Id}, {Id}, {Id}, {Id},
  {RXp}, {RXp}, {RXp}, {RXp}, {RXp},
  {RXm}, {RXm}, {RXm}, {RXm}, {RXm},
  {RYp}, {RYp}, {RYp}, {RYp}, {RYp},
  {RYm}, {RYm}, {RYm}, {RYm}, {RYm}}];
ProcTomographySeq = BuildProcTomoloQ[
  Which[ runType == 0,      Id,
        runType == 1,      LX90p,
        runType == 2,      LX90m,
        runType == 3,      LY90p,
        runType == 4,      LY90m,
        runType == 5,      LXp,
        runType == 6,      LYp,
        runType == 7,      RX90p,
        runType == 8,      RX90m,
        runType == 9,      RY90p,
        runType == 10,     RY90m,
        runType == 11,     RXp,
        runType == 12,     RYp
  ], qubit];
ProcTomographySeq = Join[CalSeq, ProcTomographySeq];

```

2-Qubit State Tomography

Pulse generation sequences for two qubit state tomography (pattern generation, marker generation, and file exporting omitted)

```

(*Choose the state desired *)
runType = 8;
basename = Which[ runType == 0, "B0",
                 runType == 1, "B1",
                 runType == 2, "B2",
                 runType == 3, "B3",
                 runType == 4, "Id",
                 runType == 5, "YY",
                 runType == 6, "RXp",
                 runType == 7, "LXp",
                 runType == 8, "LXpRXp",
                 runType == 9, "RY90m",

```

```

runType == 10, "B0a",
runType == 11, "B1a",
runType == 12, "B2a",
runType == 13, "B3a",
runType == 14, "B0p0",
runType == 15, "B0p1",
runType == 16, "B0p2",
runType == 17, "B0p3"]
ampFL = DACoffsetLZ; ampFR = DACoffsetRZ;
widthFL = 0; widthFR = 0;
numSigmasFL = 0.000001; numSigmasFR = 0.000001;
OneStateTomo2QSeq[Proc_, m_, opcode_] :=
Module[{Unitaries, numUnitaries, Meas},
Unitaries = {Id,
LXp,
RXp,
LX90p,
LX90pRX90p, LX90pRX90p, LX90pRX90p, LX90pRX90p,
LX90pRY90p, LX90pRY90p, LX90pRY90p, LX90pRY90p,
LX90pRXp,
LY90p,
LY90pRX90p, LY90pRX90p, LY90pRX90p, LY90pRX90p,
LY90pRY90p, LY90pRY90p, LY90pRY90p, LY90pRY90p,
LY90pRXp,
RX90p,
LXpRX90p,
RY90p,
LXpRY90p};
numUnitaries = Length[Unitaries];
Meas = Unitaries[[m]];
Flatten[{Proc, Meas}];
BuildStateTomo2QSeq[Proc_, numReps_] :=
Module[{TomoSequences, numSequences},
TomoSequences = {};
numSequences = 27;
For[m = 1, m ≤ numSequences, m++, {
For[n = 1, n ≤ numReps, n++, {
TomoSequences =
Append[TomoSequences, OneStateTomo2QSeq[Proc, m, 1]]}}];
TomoSequences];
AllStateTomo2QSeq = {
{Id}, {Id}, {Id}, {Id}, {Id},
{LXp}, {LXp}, {LXp}, {LXp}, {LXp},
{RXp}, {RXp}, {RXp}, {RXp}, {RXp},
{LXpRXp}, {LXpRXp}, {LXpRXp}, {LXpRXp}, {LXpRXp}};
AllStateTomo2QSeq = Join[AllStateTomo2QSeq, BuildStateTomo2QSeq[
Which[ runType ≤ 3, {LY90pRY90p, LZfRZf, LY90p},
runType == 4, Id,
runType == 5, LY90pRY90p
(*LY90pRY90p*), (*LY90mRY90m, LY90pRY90m, LY90mRY90p*)
runType == 6, RXp,
runType == 7, LXp,
runType == 8, LXpRXp,
runType == 9, RY90m,
runType == 20, {LXp, RXp},
runType == 10, {LY90pRY90m, LZfRZf, LY90p},
runType == 11, {LY90pRY90p, LZfRZf, LY90p},
runType == 12, {LY90mRY90m, LZfRZf, LY90p},
runType == 13, {LY90mRY90p, LZfRZf, LY90p},
runType == 14 || runType == 15 || runType == 16 || runType == 17,
{LZfRZf, LY90pRY90p, LZfRZf, LY90p}], 2]]

```

APPENDIX B

Mathematica code for tomography

CODE for analyzing the raw measurements for two-qubit state tomography as well as single-qubit process tomography. The Mathematica code is adapted from that written and developed by postdoc Jay Gambetta. In the ‘2 qubit state tomography’ section, we define a function `Likely[]` which generates a likelihood function with built in physicality constraints and with inputs that are the raw measurements described in section 8.4. The density matrix is then reconstructed and can be compared to theory. In ‘1 qubit process tomography experiment’ a similar `Likely[]` function is used, and the χ matrix, as described in section 6.3.5 can be obtained from a maximization of the likelihood function.

Initialization

```
Needs["BarCharts`"]
Needs["ErrorBarPlots`"]

ident[dim_] := SparseArray[{{Poutine$_, Poutine$_} -> 1}, {dim, dim}];
destroy[dim_] := SparseArray[{{Poutine$_, Maudite$_} /;
  Poutine$ + 1 == Maudite$ -> Sqrt[Poutine$]}, {dim, dim}];
dagger[a_] := Transpose[Conjugate[a]];
TensorProduct[a_, b_] := SparseArray[KroneckerProduct[a, b]];
flat[ρ_] := Flatten[Transpose[ρ]]
unflat[ρ_, dim_] := Transpose[Partition[ρ, dim]]
LowerDiagonalMatrix[f_, n_Integer?NonNegative] :=
  Array[If[# > #2, ToExpression["tt" <> ToString[(n (# - 1) + #2)]] +
    i ToExpression["tt" <> ToString[(n (#2 - 1) + #)]]], 0] &, {n, n}] +
  Array[If[# == #2, ToExpression["tt" <> ToString[(n (# - 1) + #2)]]], 0] &, {n, n}]
psitorho[ψ_] := Outer[Times, ψ, Conjugate[ψ]];
```

2 qubit state tomography

■ Operations

This section defines the Pauli algebra as well as the Likely function, with inputs from the raw measurements, for maximization subjected to constraints.

```
σp = destroy[2];
σm = dagger[σp];
σx = σp + σm;
σy = -i σp + i σm;
σz = -σm.σp + σp.σm;
σi = ident[2];
σii = TensorProduct[σi, σi];
σxi = TensorProduct[σx, σi];
σyi = TensorProduct[σy, σi];
σzi = TensorProduct[σz, σi];
σix = TensorProduct[σi, σx];
σxx = TensorProduct[σx, σx];
σyx = TensorProduct[σy, σx];
σzx = TensorProduct[σz, σx];
σiy = TensorProduct[σi, σy];
σxy = TensorProduct[σx, σy];
σyy = TensorProduct[σy, σy];
σzy = TensorProduct[σz, σy];
σiz = TensorProduct[σi, σz];
σxz = TensorProduct[σx, σz];
σyz = TensorProduct[σy, σz];
σzz = TensorProduct[σz, σz];

U[θ_, σ_] := MatrixExp[-i  $\frac{\theta}{2}$  Normal[σ]];

ListPauli[rho_] := {{Tr[σii.rho], Tr[σix.rho], Tr[σiy.rho], Tr[σiz.rho]},
  {Tr[σxi.rho], Tr[σxx.rho], Tr[σxy.rho], Tr[σxz.rho]},
  {Tr[σyi.rho], Tr[σyx.rho], Tr[σyy.rho], Tr[σyz.rho]},
  {Tr[σzi.rho], Tr[σzx.rho], Tr[σzy.rho], Tr[σzz.rho]}} / 2;

Rho[t1_, t2_, t3_, t4_, t5_, t6_, t7_, t8_,
```

```
t9_, t10_, t11_, t12_, t13_, t14_, t15_, t16_] := Simplify[
dagger[{{t1, 0, 0, 0}, {t5 + i t6, t2, 0, 0}, {t11 + i t12, t7 + i t8, t3, 0},
{t15 + i t16, t13 + i t14, t9 + i t10, t4}}].{{t1, 0, 0, 0}, {t5 + i t6, t2, 0,
0}, {t11 + i t12, t7 + i t8, t3, 0}, {t15 + i t16, t13 + i t14, t9 + i t10, t4}} /
Tr[dagger[{{t1, 0, 0, 0}, {t5 + i t6, t2, 0, 0}, {t11 + i t12, t7 + i t8, t3, 0},
{t15 + i t16, t13 + i t14, t9 + i t10, t4}}].{{t1, 0, 0, 0}, {t5 + i t6, t2, 0,
0}, {t11 + i t12, t7 + i t8, t3, 0}, {t15 + i t16, t13 + i t14, t9 + i t10, t4}}],
Assumptions -> {{t1, t2, t3, t4, t5, t6, t7, t8, t9, t10, t11,
t12, t13, t14, t15, t16} ∈ Reals}];
```

```
Likely[t1_, t2_, t3_, t4_, t5_, t6_, t7_, t8_, t9_, t10_, t11_,
t12_, t13_, t14_, t15_, t16_, r1_, r2_, r3_, r4_, r5_, r6_, r7_, r8_,
r9_, r10_, r11_, r12_, r13_, r14_, r15_, r16_, β1_, β2_, β12_] :=
(-1 + r16)^2 + (-r12 (t1^2 + t10^2 + t11^2 + t12^2 + t13^2 + t14^2 + t15^2 + t16^2 + t2^2 +
t3^2 + t4^2 + t5^2 + t6^2 + t7^2 + t8^2 + t9^2) + t1^2 β1 - t10^2 β1 + t11^2 β1 +
t12^2 β1 + t13^2 β1 + t14^2 β1 + t15^2 β1 + t16^2 β1 + t2^2 β1 - t3^2 β1 - t4^2 β1 +
t5^2 β1 + t6^2 β1 + t7^2 β1 + t8^2 β1 - t9^2 β1 - 2 t14 t15 β12 + 2 t13 t16 β12 -
2 t10 t4 β12 + 2 t2 t6 β12 + 2 t12 t7 β12 - 2 t11 t8 β12 - 2 t14 t15 β2 +
2 t13 t16 β2 + 2 t10 t4 β2 + 2 t2 t6 β2 + 2 t12 t7 β2 - 2 t11 t8 β2)^2 /
(t1^2 + t10^2 + t11^2 + t12^2 + t13^2 + t14^2 + t15^2 + t16^2 + t2^2 + t3^2 +
t4^2 + t5^2 + t6^2 + t7^2 + t8^2 + t9^2)^2 +
(r13 (t1^2 + t10^2 + t11^2 + t12^2 + t13^2 + t14^2 + t15^2 + t16^2 + t2^2 + t3^2 + t4^2 +
t5^2 + t6^2 + t7^2 + t8^2 + t9^2) + t1^2 β1 - t10^2 β1 + t11^2 β1 + t12^2 β1 +
t13^2 β1 + t14^2 β1 + t15^2 β1 + t16^2 β1 + t2^2 β1 - t3^2 β1 - t4^2 β1 + t5^2 β1 +
t6^2 β1 + t7^2 β1 + t8^2 β1 - t9^2 β1 - 2 t14 t15 β12 + 2 t13 t16 β12 -
2 t10 t4 β12 + 2 t2 t6 β12 + 2 t12 t7 β12 - 2 t11 t8 β12 + 2 t14 t15 β2 -
2 t13 t16 β2 - 2 t10 t4 β2 - 2 t2 t6 β2 - 2 t12 t7 β2 + 2 t11 t8 β2)^2 /
(t1^2 + t10^2 + t11^2 + t12^2 + t13^2 + t14^2 + t15^2 + t16^2 + t2^2 + t3^2 +
t4^2 + t5^2 + t6^2 + t7^2 + t8^2 + t9^2)^2 +
(-r14 (t1^2 + t10^2 + t11^2 + t12^2 + t13^2 + t14^2 + t15^2 + t16^2 + t2^2 + t3^2 + t4^2 +
t5^2 + t6^2 + t7^2 + t8^2 + t9^2) + t1^2 β1 - t10^2 β1 + t11^2 β1 + t12^2 β1 +
t13^2 β1 + t14^2 β1 + t15^2 β1 + t16^2 β1 + t2^2 β1 - t3^2 β1 - t4^2 β1 + t5^2 β1 +
t6^2 β1 + t7^2 β1 + t8^2 β1 - t9^2 β1 - 2 t13 t15 β12 - 2 t14 t16 β12 -
2 t2 t5 β12 - 2 t11 t7 β12 - 2 t12 t8 β12 + 2 t4 t9 β12 - 2 t13 t15 β2 -
2 t14 t16 β2 - 2 t2 t5 β2 - 2 t11 t7 β2 - 2 t12 t8 β2 - 2 t4 t9 β2)^2 /
(t1^2 + t10^2 + t11^2 + t12^2 + t13^2 + t14^2 + t15^2 + t16^2 + t2^2 + t3^2 +
t4^2 + t5^2 + t6^2 + t7^2 + t8^2 + t9^2)^2 +
(r15 (t1^2 + t10^2 + t11^2 + t12^2 + t13^2 + t14^2 + t15^2 + t16^2 + t2^2 + t3^2 + t4^2 +
t5^2 + t6^2 + t7^2 + t8^2 + t9^2) + t1^2 β1 - t10^2 β1 + t11^2 β1 + t12^2 β1 +
t13^2 β1 + t14^2 β1 + t15^2 β1 + t16^2 β1 + t2^2 β1 - t3^2 β1 - t4^2 β1 + t5^2 β1 +
t6^2 β1 + t7^2 β1 + t8^2 β1 - t9^2 β1 - 2 t13 t15 β12 - 2 t14 t16 β12 -
2 t2 t5 β12 - 2 t11 t7 β12 - 2 t12 t8 β12 + 2 t4 t9 β12 + 2 t13 t15 β2 +
2 t14 t16 β2 + 2 t2 t5 β2 + 2 t11 t7 β2 + 2 t12 t8 β2 + 2 t4 t9 β2)^2 /
(t1^2 + t10^2 + t11^2 + t12^2 + t13^2 + t14^2 + t15^2 + t16^2 + t2^2 + t3^2 +
t4^2 + t5^2 + t6^2 + t7^2 + t8^2 + t9^2)^2 +
(r11 (t1^2 + t10^2 + t11^2 + t12^2 + t13^2 + t14^2 + t15^2 + t16^2 + t2^2 + t3^2 + t4^2 +
t5^2 + t6^2 + t7^2 + t8^2 + t9^2) + 2 t11 t3 β1 + 2 t13 t4 β1 + 2 t15 t9 β1 +
```


$$\begin{aligned}
 & (r2 - (t4^2 (\beta1 - \beta12 - \beta2)) / (t1^2 + t10^2 + t11^2 + t12^2 + t13^2 + t14^2 + t15^2 + \\
 & \quad t16^2 + t2^2 + t3^2 + t4^2 + t5^2 + t6^2 + t7^2 + t8^2 + t9^2) + \\
 & \quad ((t1^2 + t11^2 + t12^2 + t15^2 + t16^2 + t5^2 + t6^2) (\beta1 + \beta12 - \beta2)) / (t1^2 + t10^2 + t11^2 + \\
 & \quad t12^2 + t13^2 + t14^2 + t15^2 + t16^2 + t2^2 + t3^2 + t4^2 + t5^2 + t6^2 + t7^2 + t8^2 + t9^2) + \\
 & \quad ((t13^2 + t14^2 + t2^2 + t7^2 + t8^2) (\beta1 - \beta12 + \beta2)) / (t1^2 + t10^2 + t11^2 + t12^2 + \\
 & \quad t13^2 + t14^2 + t15^2 + t16^2 + t2^2 + t3^2 + t4^2 + t5^2 + t6^2 + t7^2 + t8^2 + t9^2) - \\
 & \quad ((t10^2 + t3^2 + t9^2) (\beta1 + \beta12 + \beta2)) / (t1^2 + t10^2 + t11^2 + t12^2 + t13^2 + \\
 & \quad t14^2 + t15^2 + t16^2 + t2^2 + t3^2 + t4^2 + t5^2 + t6^2 + t7^2 + t8^2 + t9^2))^2 + \\
 & (r10 (t1^2 + t10^2 + t11^2 + t12^2 + t13^2 + t14^2 + t15^2 + t16^2 + t2^2 + t3^2 + t4^2 + \\
 & \quad t5^2 + t6^2 + t7^2 + t8^2 + t9^2) + 2 (t10 t16 \beta1 + t11 t3 \beta1 + t13 t4 \beta1 + \\
 & \quad t15 t9 \beta1 - t10 t14 \beta12 - t15 t4 \beta12 - t3 t7 \beta12 - t13 t9 \beta12 + \\
 & \quad t13 t15 \beta2 + t14 t16 \beta2 + t2 t5 \beta2 + t11 t7 \beta2 + t12 t8 \beta2 + t4 t9 \beta2))^2 / \\
 & (t1^2 + t10^2 + t11^2 + t12^2 + t13^2 + t14^2 + t15^2 + t16^2 + t2^2 + t3^2 + t4^2 + \\
 & \quad t5^2 + t6^2 + t7^2 + t8^2 + t9^2)^2 + \\
 & (r6 (t1^2 + t10^2 + t11^2 + t12^2 + t13^2 + t14^2 + t15^2 + t16^2 + t2^2 + t3^2 + t4^2 + \\
 & \quad t5^2 + t6^2 + t7^2 + t8^2 + t9^2) + 2 (t10 t15 \beta1 - t12 t3 \beta1 - t14 t4 \beta1 - \\
 & \quad t16 t9 \beta1 - t10 t13 \beta12 + t16 t4 \beta12 + t3 t8 \beta12 + t14 t9 \beta12 + \\
 & \quad t13 t15 \beta2 + t14 t16 \beta2 + t2 t5 \beta2 + t11 t7 \beta2 + t12 t8 \beta2 + t4 t9 \beta2))^2 / \\
 & (t1^2 + t10^2 + t11^2 + t12^2 + t13^2 + t14^2 + t15^2 + t16^2 + t2^2 + t3^2 + t4^2 + \\
 & \quad t5^2 + t6^2 + t7^2 + t8^2 + t9^2)^2 + \\
 & (r9 (t1^2 + t10^2 + t11^2 + t12^2 + t13^2 + t14^2 + t15^2 + t16^2 + t2^2 + t3^2 + t4^2 + \\
 & \quad t5^2 + t6^2 + t7^2 + t8^2 + t9^2) + 2 (t11 t3 \beta1 + t13 t4 \beta1 + t15 t9 \beta1 + \\
 & \quad t16 t4 \beta12 - t3 t8 \beta12 - t14 t9 \beta12 + t14 t15 \beta2 - t13 t16 \beta2 - \\
 & \quad t2 t6 \beta2 - t12 t7 \beta2 + t11 t8 \beta2 + t10 (t16 \beta1 + t13 \beta12 - t4 \beta2)))^2 / \\
 & (t1^2 + t10^2 + t11^2 + t12^2 + t13^2 + t14^2 + t15^2 + t16^2 + t2^2 + t3^2 + t4^2 + \\
 & \quad t5^2 + t6^2 + t7^2 + t8^2 + t9^2)^2 + \\
 & (r5 (t1^2 + t10^2 + t11^2 + t12^2 + t13^2 + t14^2 + t15^2 + t16^2 + t2^2 + t3^2 + t4^2 + \\
 & \quad t5^2 + t6^2 + t7^2 + t8^2 + t9^2) - 2 (t12 t3 \beta1 + t14 t4 \beta1 + t16 t9 \beta1 - \\
 & \quad t15 t4 \beta12 + t3 t7 \beta12 + t13 t9 \beta12 - t14 t15 \beta2 + t13 t16 \beta2 + \\
 & \quad t2 t6 \beta2 + t12 t7 \beta2 - t11 t8 \beta2 + t10 (-t15 \beta1 + t14 \beta12 + t4 \beta2)))^2 / \\
 & (t1^2 + t10^2 + t11^2 + t12^2 + t13^2 + t14^2 + t15^2 + t16^2 + t2^2 + t3^2 + t4^2 + \\
 & \quad t5^2 + t6^2 + t7^2 + t8^2 + t9^2)^2
 \end{aligned}$$

Define the theoretical measurements, given experimental amplitudes that describe the joint measurement

```

Clear[β1, β2, β12];
Clear[α1, α2, α12];
M = (β1 σzi + β2 σiz + β12 σzz);
m1 = M;
m2 = dagger[U[π, σxi]] . M . U[π, σxi];
m3 = dagger[U[π, σix]] . M . U[π, σix];
m4 = dagger[U[π/2, σxi]] . M . U[π/2, σxi];
m5 = dagger[U[π/2, σxi + σix]] . M . U[π/2, σxi + σix];

```

```

m6 = dagger[U[ $\frac{\pi}{2}$ ,  $\sigma_{xi} + \sigma_{iy}$ ]].M.U[ $\frac{\pi}{2}$ ,  $\sigma_{xi} + \sigma_{iy}$ ];
m7 = dagger[U[ $\frac{\pi}{2}$ ,  $\sigma_{xi} + 2 \sigma_{ix}$ ]].M.U[ $\frac{\pi}{2}$ ,  $\sigma_{xi} + 2 \sigma_{ix}$ ];
m8 = dagger[U[ $\frac{\pi}{2}$ ,  $\sigma_{yi}$ ]].M.U[ $\frac{\pi}{2}$ ,  $\sigma_{yi}$ ];
m9 = dagger[U[ $\frac{\pi}{2}$ ,  $\sigma_{yi} + \sigma_{ix}$ ]].M.U[ $\frac{\pi}{2}$ ,  $\sigma_{yi} + \sigma_{ix}$ ];
m10 = dagger[U[ $\frac{\pi}{2}$ ,  $\sigma_{yi} + \sigma_{iy}$ ]].M.U[ $\frac{\pi}{2}$ ,  $\sigma_{yi} + \sigma_{iy}$ ];
m11 = dagger[U[ $\frac{\pi}{2}$ ,  $\sigma_{yi} + 2 \sigma_{ix}$ ]].M.U[ $\frac{\pi}{2}$ ,  $\sigma_{yi} + 2 \sigma_{ix}$ ];
m12 = dagger[U[ $\frac{\pi}{2}$ ,  $\sigma_{ix}$ ]].M.U[ $\frac{\pi}{2}$ ,  $\sigma_{ix}$ ];
m13 = dagger[U[ $\frac{\pi}{2}$ ,  $\sigma_{ix} + 2 \sigma_{xi}$ ]].M.U[ $\frac{\pi}{2}$ ,  $\sigma_{ix} + 2 \sigma_{xi}$ ];
m14 = dagger[U[ $\frac{\pi}{2}$ ,  $\sigma_{iy}$ ]].M.U[ $\frac{\pi}{2}$ ,  $\sigma_{iy}$ ];
m15 = dagger[U[ $\frac{\pi}{2}$ ,  $\sigma_{iy} + 2 \sigma_{xi}$ ]].M.U[ $\frac{\pi}{2}$ ,  $\sigma_{iy} + 2 \sigma_{xi}$ ];
m16 =  $\sigma_{ii}$ ;

P = ( $\alpha_1 \sigma_{zi} + \alpha_2 \sigma_{iz} + \alpha_{12} \sigma_{zz}$ );
p1 = P;
p2 = dagger[U[ $\pi$ ,  $\sigma_{xi}$ ]].P.U[ $\pi$ ,  $\sigma_{xi}$ ];
p3 = dagger[U[ $\pi$ ,  $\sigma_{ix}$ ]].P.U[ $\pi$ ,  $\sigma_{ix}$ ];
p4 = dagger[U[ $\frac{\pi}{2}$ ,  $\sigma_{xi}$ ]].P.U[ $\frac{\pi}{2}$ ,  $\sigma_{xi}$ ];
p5 = dagger[U[ $\frac{\pi}{2}$ ,  $\sigma_{xi} + \sigma_{ix}$ ]].P.U[ $\frac{\pi}{2}$ ,  $\sigma_{xi} + \sigma_{ix}$ ];
p6 = dagger[U[ $\frac{\pi}{2}$ ,  $\sigma_{xi} + \sigma_{iy}$ ]].P.U[ $\frac{\pi}{2}$ ,  $\sigma_{xi} + \sigma_{iy}$ ];
p7 = dagger[U[ $\frac{\pi}{2}$ ,  $\sigma_{xi} + 2 \sigma_{ix}$ ]].P.U[ $\frac{\pi}{2}$ ,  $\sigma_{xi} + 2 \sigma_{ix}$ ];
p8 = dagger[U[ $\frac{\pi}{2}$ ,  $\sigma_{yi}$ ]].P.U[ $\frac{\pi}{2}$ ,  $\sigma_{yi}$ ];
p9 = dagger[U[ $\frac{\pi}{2}$ ,  $\sigma_{yi} + \sigma_{ix}$ ]].P.U[ $\frac{\pi}{2}$ ,  $\sigma_{yi} + \sigma_{ix}$ ];
p10 = dagger[U[ $\frac{\pi}{2}$ ,  $\sigma_{yi} + \sigma_{iy}$ ]].P.U[ $\frac{\pi}{2}$ ,  $\sigma_{yi} + \sigma_{iy}$ ];
p11 = dagger[U[ $\frac{\pi}{2}$ ,  $\sigma_{yi} + 2 \sigma_{ix}$ ]].P.U[ $\frac{\pi}{2}$ ,  $\sigma_{yi} + 2 \sigma_{ix}$ ];
p12 = dagger[U[ $\frac{\pi}{2}$ ,  $\sigma_{ix}$ ]].P.U[ $\frac{\pi}{2}$ ,  $\sigma_{ix}$ ];
p13 = dagger[U[ $\frac{\pi}{2}$ ,  $\sigma_{ix} + 2 \sigma_{xi}$ ]].P.U[ $\frac{\pi}{2}$ ,  $\sigma_{ix} + 2 \sigma_{xi}$ ];
p14 = dagger[U[ $\frac{\pi}{2}$ ,  $\sigma_{iy}$ ]].P.U[ $\frac{\pi}{2}$ ,  $\sigma_{iy}$ ];
p15 = dagger[U[ $\frac{\pi}{2}$ ,  $\sigma_{iy} + 2 \sigma_{xi}$ ]].P.U[ $\frac{\pi}{2}$ ,  $\sigma_{iy} + 2 \sigma_{xi}$ ];
p16 =  $\sigma_{ii}$ ;

```

```

RowAforI[m1_] :=  $\frac{1}{4}$  {Tr[m1.σii], Tr[m1.σxi], Tr[m1.σyi], Tr[m1.σzi], Tr[m1.σix],
  Tr[m1.σxx], Tr[m1.σyx], Tr[m1.σzx], Tr[m1.σiy], Tr[m1.σxy], Tr[m1.σyy],
  Tr[m1.σzy], Tr[m1.σiz], Tr[m1.σxz], Tr[m1.σyz], Tr[m1.σzz]};
AforI = Table[FullSimplify[RowAforI[ToExpression["m" <> ToString[ i]]]],
  {i, 1, 16}];
AiforI = Inverse[AforI];
RowAforQ[p1_] :=
 $\frac{1}{4}$  {Tr[p1.σii], Tr[p1.σxi], Tr[p1.σyi], Tr[p1.σzi], Tr[p1.σix],
  Tr[p1.σxx], Tr[p1.σyx], Tr[p1.σzx], Tr[p1.σiy], Tr[p1.σxy], Tr[p1.σyy],
  Tr[p1.σzy], Tr[p1.σiz], Tr[p1.σxz], Tr[p1.σyz], Tr[p1.σzz]};
AforQ = Table[FullSimplify[RowAforQ[ToExpression["p" <> ToString[ i]]]],
  {i, 1, 16}];
AiforQ = Inverse[AforQ];
MatrixRank[{Flatten[m1], Flatten[m2], Flatten[m3],
  Flatten[m4], Flatten[m5], Flatten[m6], Flatten[m7], Flatten[m8],
  Flatten[m9], Flatten[m10], Flatten[m11], Flatten[m12],
  Flatten[m13], Flatten[m14], Flatten[m15], Flatten[m16]}]
MatrixRank[{Flatten[m1], Flatten[m2], Flatten[m3], Flatten[m4],
  Flatten[m5], Flatten[m6], Flatten[m7], Flatten[m8], Flatten[m9],
  Flatten[m10], Flatten[m11], Flatten[m12], Flatten[m13],
  Flatten[m14], Flatten[m15], Flatten[m16]} /. β12 → 0]

```

Define some metrics, including concurrence, entanglement of formation, and fidelity to the targeted state.

```

Con[ρ_] := Module[{λ}, λ =
  Chop[Sort[√Eigenvalues[(ρ.σyy.Conjugate[ρ].σyy)], Re[#1] > Re[#2] &], 10-7];
  Max[0, λ[[1]] - λ[[2]] - λ[[3]] - λ[[4]]];
Ef[c_] := - $\frac{1 + \sqrt{1 - c^2}}{2}$  Log[2,  $\frac{1 + \sqrt{1 - c^2}}{2}$ ] -
   $\left(1 - \frac{1 + \sqrt{1 - c^2}}{2}\right)$  Log[2,  $1 - \frac{1 + \sqrt{1 - c^2}}{2}$ ];
Fidelity[ρ1_, ρ2_] := Chop[
  Re[Tr[MatrixPower[MatrixPower[ρ1,  $\frac{1}{2}$ ].ρ2.MatrixPower[ρ1,  $\frac{1}{2}$ ],  $\frac{1}{2}$ ]]2, 10-8];

```

■ 2 Qubit state tomography from experimental data - 2 Input sets

After inputting the raw measurements in both the I and Q quadratures, we reconstruct the physical density matrix with a constrained maximization of the Likely function.

```

datapath = "C:\\Experiments\\LatestTomography\\";
thisNum = 0;

suffix = Which[thisNum == 0, "", thisNum > 0, "_" <> ToString[thisNum]];

ST2QvecI1 = Import[datapath <> "ST2QvecI" <> suffix <> ".txt", "Table"];
ST2QvecQ1 = Import[datapath <> "ST2QvecQ" <> suffix <> ".txt", "Table"];
ST2QvecI = Flatten[ST2QvecQ1];
ST2QvecQ = Flatten[ST2QvecQ1];

```

```

β1 = ST2QvecI[[1]]; β2 = ST2QvecI[[2]]; β12 = ST2QvecI[[3]];
α1 = ST2QvecQ[[1]]; α2 = ST2QvecQ[[2]]; α12 = ST2QvecQ[[3]];
m1i = ST2QvecI[[4]]; m2i = ST2QvecI[[5]];
m3i = ST2QvecI[[6]]; m4i = ST2QvecI[[7]];
m5i = ST2QvecI[[8]]; m6i = ST2QvecI[[9]];
m7i = ST2QvecI[[10]]; m8i = ST2QvecI[[11]];
m9i = ST2QvecI[[12]]; m10i = ST2QvecI[[13]];
m11i = ST2QvecI[[14]]; m12i = ST2QvecI[[15]];
m13i = ST2QvecI[[16]]; m14i = ST2QvecI[[17]];
m15i = ST2QvecI[[18]]; m16i = ST2QvecI[[19]];
m1q = ST2QvecQ[[4]]; m2q = ST2QvecQ[[5]];
m3q = ST2QvecQ[[6]]; m4q = ST2QvecQ[[7]];
m5q = ST2QvecQ[[8]]; m6q = ST2QvecQ[[9]];
m7q = ST2QvecQ[[10]]; m8q = ST2QvecQ[[11]];
m9q = ST2QvecQ[[12]]; m10q = ST2QvecQ[[13]];
m11q = ST2QvecQ[[14]]; m12q = ST2QvecQ[[15]];
m13q = ST2QvecQ[[16]]; m14q = ST2QvecQ[[17]];
m15q = ST2QvecQ[[18]]; m16q = ST2QvecQ[[19]];

q2 = 1; j = 1;
epsL = -0.0;
epsR = -0.00;
ψTheo = Bell12[0, 0, 0, 0];
RhoTheo = psitorho[ψTheo];
M = (β1 σzi + β2 σiz + β12 σzz);
n1 = M;
n2 = dagger[U[π, (1 + epsL) σxi]] . M . U[π, (1 + epsL) σxi];
n3 = dagger[U[π, q2 (1 + epsR) σix]] . M . U[π, q2 (1 + epsR) σix];
n4 = dagger[U[π/2, (1 + epsL) σxi]] . M . U[π/2, (1 + epsL) σxi];
n5 = dagger[U[π/2, (1 + epsL) σxi + q2 (1 + epsR) σix]] .
M . U[π/2, (1 + epsL) σxi + q2 (1 + epsR) σix];
n6 = dagger[U[π/2, (1 + epsL) σxi + j q2 (1 + epsR) σiy]] . M .
U[π/2, (1 + epsL) σxi + j q2 (1 + epsR) σiy];
n7 = dagger[U[π/2, (1 + epsL) σxi + 2 q2 (1 + epsR) σix]] . M .
U[π/2, (1 + epsL) σxi + 2 q2 (1 + epsR) σix];
n8 = dagger[U[π/2, j (1 + epsL) σyi]] . M . U[π/2, j (1 + epsL) σyi];
n9 = dagger[U[π/2, j (1 + epsL) σyi + q2 (1 + epsR) σix]] .
M . U[π/2, j (1 + epsL) σyi + q2 (1 + epsR) σix];
n10 = dagger[U[π/2, j (1 + epsL) σyi + j q2 (1 + epsR) σiy]] .
M . U[π/2, j (1 + epsL) σyi + j q2 (1 + epsR) σiy];
n11 = dagger[U[π/2, j (1 + epsL) σyi + 2 q2 (1 + epsR) σix]] .
M . U[π/2, j (1 + epsL) σyi + 2 q2 (1 + epsR) σix];

```

```

n12 = dagger[U[ $\frac{\pi}{2}$ , q2 (1 + epsR)  $\sigma_{ix}$ ]].M.U[ $\frac{\pi}{2}$ , q2 (1 + epsR)  $\sigma_{ix}$ ];
n13 = dagger[U[ $\frac{\pi}{2}$ , q2 (1 + epsR)  $\sigma_{ix} + 2 (1 + epsL) \sigma_{xi}$ ]].
    M.U[ $\frac{\pi}{2}$ , q2 (1 + epsR)  $\sigma_{ix} + (1 + epsL) 2 \sigma_{xi}$ ];
n14 = dagger[U[ $\frac{\pi}{2}$ , j q2 (1 + epsR)  $\sigma_{iy}$ ]].M.U[ $\frac{\pi}{2}$ , j q2 (1 + epsR)  $\sigma_{iy}$ ];
n15 = dagger[U[ $\frac{\pi}{2}$ , j q2 (1 + epsR)  $\sigma_{iy} + 2 (1 + epsL) \sigma_{xi}$ ]].
    M.U[ $\frac{\pi}{2}$ , j q2 (1 + epsR)  $\sigma_{iy} + (1 + epsL) 2 \sigma_{xi}$ ];
n16 =  $\sigma_{ii}$ ;

P = ( $\alpha_1 \sigma_{zi} + \alpha_2 \sigma_{iz} + \alpha_{12} \sigma_{zz}$ );
p1 = P;
p2 = dagger[U[ $\pi$ , (1 + epsL)  $\sigma_{xi}$ ]].P.U[ $\pi$ , (1 + epsL)  $\sigma_{xi}$ ];
p3 = dagger[U[ $\pi$ , q2 (1 + epsR)  $\sigma_{ix}$ ]].P.U[ $\pi$ , q2 (1 + epsR)  $\sigma_{ix}$ ];
p4 = dagger[U[ $\frac{\pi}{2}$ , (1 + epsL)  $\sigma_{xi}$ ]].P.U[ $\frac{\pi}{2}$ , (1 + epsL)  $\sigma_{xi}$ ];
p5 = dagger[U[ $\frac{\pi}{2}$ , (1 + epsL)  $\sigma_{xi} + q2 (1 + epsR) \sigma_{ix}$ ]].
    P.U[ $\frac{\pi}{2}$ , (1 + epsL)  $\sigma_{xi} + q2 (1 + epsR) \sigma_{ix}$ ];
p6 = dagger[U[ $\frac{\pi}{2}$ , (1 + epsL)  $\sigma_{xi} + j q2 (1 + epsR) \sigma_{iy}$ ]].P.
    U[ $\frac{\pi}{2}$ , (1 + epsL)  $\sigma_{xi} + j q2 (1 + epsR) \sigma_{iy}$ ];
p7 = dagger[U[ $\frac{\pi}{2}$ , (1 + epsL)  $\sigma_{xi} + 2 q2 (1 + epsR) \sigma_{ix}$ ]].P.
    U[ $\frac{\pi}{2}$ , (1 + epsL)  $\sigma_{xi} + 2 q2 (1 + epsR) \sigma_{ix}$ ];
p8 = dagger[U[ $\frac{\pi}{2}$ , j (1 + epsL)  $\sigma_{yi}$ ]].P.U[ $\frac{\pi}{2}$ , j (1 + epsL)  $\sigma_{yi}$ ];
p9 = dagger[U[ $\frac{\pi}{2}$ , j (1 + epsL)  $\sigma_{yi} + q2 (1 + epsR) \sigma_{ix}$ ]].
    P.U[ $\frac{\pi}{2}$ , j (1 + epsL)  $\sigma_{yi} + q2 (1 + epsR) \sigma_{ix}$ ];
p10 = dagger[U[ $\frac{\pi}{2}$ , j (1 + epsL)  $\sigma_{yi} + j q2 (1 + epsR) \sigma_{iy}$ ]].
    P.U[ $\frac{\pi}{2}$ , j (1 + epsL)  $\sigma_{yi} + j q2 (1 + epsR) \sigma_{iy}$ ];
p11 = dagger[U[ $\frac{\pi}{2}$ , j (1 + epsL)  $\sigma_{yi} + 2 q2 (1 + epsR) \sigma_{ix}$ ]].
    P.U[ $\frac{\pi}{2}$ , j (1 + epsL)  $\sigma_{yi} + 2 q2 (1 + epsR) \sigma_{ix}$ ];
p12 = dagger[U[ $\frac{\pi}{2}$ , q2 (1 + epsR)  $\sigma_{ix}$ ]].P.U[ $\frac{\pi}{2}$ , q2 (1 + epsR)  $\sigma_{ix}$ ];
p13 = dagger[U[ $\frac{\pi}{2}$ , q2 (1 + epsR)  $\sigma_{ix} + 2 (1 + epsL) \sigma_{xi}$ ]].
    P.U[ $\frac{\pi}{2}$ , q2 (1 + epsR)  $\sigma_{ix} + (1 + epsL) 2 \sigma_{xi}$ ];

```

```

p14 = dagger[U[ $\frac{\pi}{2}$ , j q2 (1 + epsR)  $\sigma_{iy}$ ]].P.U[ $\frac{\pi}{2}$ , j q2 (1 + epsR)  $\sigma_{iy}$ ];
p15 = dagger[U[ $\frac{\pi}{2}$ , j q2 (1 + epsR)  $\sigma_{iy}$  + 2 (1 + epsL)  $\sigma_{xi}$ ]].
P.U[ $\frac{\pi}{2}$ , j q2 (1 + epsR)  $\sigma_{iy}$  + (1 + epsL) 2  $\sigma_{xi}$ ];
p16 =  $\sigma_{ii}$ ;

(* Simulated measurement results *)
t1i1 = Re[Tr[n1.RhoTheo]]; t2i1 = Re[Tr[n2.RhoTheo]];
t3i1 = Re[Tr[n3.RhoTheo]]; t4i1 = Re[Tr[n4.RhoTheo]];
t5i1 = Re[Tr[n5.RhoTheo]]; t6i1 = Re[Tr[n6.RhoTheo]];
t7i1 = Re[Tr[n7.RhoTheo]]; t8i1 = Re[Tr[n8.RhoTheo]];
t9i1 = Re[Tr[n9.RhoTheo]]; t10i1 = Re[Tr[n10.RhoTheo]];
t11i1 = Re[Tr[n11.RhoTheo]]; t12i1 = Re[Tr[n12.RhoTheo]];
t13i1 = Re[Tr[n13.RhoTheo]]; t14i1 = Re[Tr[n14.RhoTheo]];
t15i1 = Re[Tr[n15.RhoTheo]]; t16i1 = Re[Tr[n16.RhoTheo]];

t1q1 = Re[Tr[p1.RhoTheo]]; t2q1 = Re[Tr[p2.RhoTheo]];
t3q1 = Re[Tr[p3.RhoTheo]]; t4q1 = Re[Tr[p4.RhoTheo]];
t5q1 = Re[Tr[p5.RhoTheo]]; t6q1 = Re[Tr[p6.RhoTheo]];
t7q1 = Re[Tr[p7.RhoTheo]]; t8q1 = Re[Tr[p8.RhoTheo]];
t9q1 = Re[Tr[p9.RhoTheo]]; t10q1 = Re[Tr[p10.RhoTheo]];
t11q1 = Re[Tr[p11.RhoTheo]]; t12q1 = Re[Tr[p12.RhoTheo]];
t13q1 = Re[Tr[p13.RhoTheo]]; t14q1 = Re[Tr[p14.RhoTheo]];
t15q1 = Re[Tr[p15.RhoTheo]]; t16q1 = Re[Tr[p16.RhoTheo]];

ExpVecI = {m1i, m2i, m3i, m4i, m5i, m6i,
m7i, m8i, m9i, m10i, m11i, m12i, m13i, m14i, m15i, m16i};
ExpVecQ = {m1q, m2q, m3q, m4q, m5q, m6q, m7q, m8q, m9q,
m10q, m11q, m12q, m13q, m14q, m15q, m16q};
TheoryVecI = {t1i1, t2i1, t3i1, t4i1, t5i1, t6i1, t7i1, t8i1,
t9i1, t10i1, t11i1, t12i1, t13i1, t14i1, t15i1, t16i1};
TheoryVecQ = {t1q1, t2q1, t3q1, t4q1, t5q1, t6q1, t7q1, t8q1,
t9q1, t10q1, t11q1, t12q1, t13q1, t14q1, t15q1, t16q1};

solExp = NMinimize[
Chop[
Likely[t1, t2, t3, t4, t5, t6, t7, t8, t9, t10, t11, t12, t13, t14, t15, t16,
m1i, m2i, m3i, m4i, m5i, m6i, m7i, m8i,
m9i, m10i, m11i, m12i, m13i, m14i, m15i, m16i,  $\beta_1$ ,  $\beta_2$ ,  $\beta_{12}$ ] +
Likely[t1, t2, t3, t4, t5, t6, t7, t8, t9, t10, t11, t12, t13, t14, t15, t16,
m1q, m2q, m3q, m4q, m5q, m6q, m7q, m8q,
m9q, m10q, m11q, m12q, m13q, m14q, m15q, m16q,  $\alpha_1$ ,  $\alpha_2$ ,  $\alpha_{12}$ ]],
{t1, t2, t3, t4, t5, t6, t7, t8, t9, t10, t11, t12, t13, t14, t15, t16}];

RhoExp = Rho[t1, t2, t3, t4, t5, t6, t7,
t8, t9, t10, t11, t12, t13, t14, t15, t16] /. solExp[[2]];

solTheo = NMinimize[
Chop[
Likely[t1, t2, t3, t4, t5, t6, t7, t8, t9, t10, t11, t12, t13, t14, t15, t16,
t1i1, t2i1, t3i1, t4i1, t5i1, t6i1, t7i1, t8i1, t9i1,
t10i1, t11i1, t12i1, t13i1, t14i1, t15i1, t16i1,  $\beta_1$ ,  $\beta_2$ ,  $\beta_{12}$ ] +
Likely[t1, t2, t3, t4, t5, t6, t7, t8, t9, t10, t11, t12, t13, t14, t15, t16,
t1q1, t2q1, t3q1, t4q1, t5q1, t6q1, t7q1, t8q1, t9q1,
t10q1, t11q1, t12q1, t13q1, t14q1, t15q1, t16q1,  $\alpha_1$ ,  $\alpha_2$ ,  $\alpha_{12}$ ]],
{t1, t2, t3, t4, t5, t6, t7, t8, t9, t10, t11, t12, t13, t14, t15, t16}];

RhoTheo2 = Rho[t1, t2, t3, t4, t5, t6, t7,
t8, t9, t10, t11, t12, t13, t14, t15, t16] /. solTheo[[2]];

```

```

(* reconstructing the state *)
{Chop[Tr[RhoExp]], Chop[Tr[RhoExp.RhoExp]]}
{Con[RhoExp], Ef[Con[RhoExp]]}
Fidelity[RhoExp, RhoTheo2]
(* Fidelity of state to |10> and to |01> *)
ψ = {1, 0, 0, 0}; RhoT1 = psitorho[ψ];
ψ = {0, 1, 0, 0}; RhoT2 = psitorho[ψ];
ψ = {0, 0, 1, 0}; RhoT3 = psitorho[ψ];
ψ = {0, 0, 0, 1}; RhoT4 = psitorho[ψ];
{Fidelity[RhoExp, RhoT1], Fidelity[RhoExp, RhoT2],
 Fidelity[RhoExp, RhoT3], Fidelity[RhoExp, RhoT4] }
{{Chop[Tr[RhoExp]]}, {Chop[Tr[RhoExp.RhoExp]]},
 {Con[RhoExp]}, {Ef[Con[RhoExp]]}, {Fidelity[RhoExp, RhoTheo]}};

(* Simulated measurement results *)
t1i2 = Re[Tr[n1.RhoExp]];
t2i2 = Re[Tr[n2.RhoExp]];
t3i2 = Re[Tr[n3.RhoExp]];
t4i2 = Re[Tr[n4.RhoExp]];
t5i2 = Re[Tr[n5.RhoExp]];
t6i2 = Re[Tr[n6.RhoExp]];
t7i2 = Re[Tr[n7.RhoExp]];
t8i2 = Re[Tr[n8.RhoExp]];
t9i2 = Re[Tr[n9.RhoExp]];
t10i2 = Re[Tr[n10.RhoExp]];
t11i2 = Re[Tr[n11.RhoExp]];
t12i2 = Re[Tr[n12.RhoExp]];
t13i2 = Re[Tr[n13.RhoExp]];
t14i2 = Re[Tr[n14.RhoExp]];
t15i2 = Re[Tr[n15.RhoExp]];
t16i2 = Re[Tr[n16.RhoExp]];

(* Simulated measurement results *)
t1q2 = Re[Tr[p1.RhoExp]];
t2q2 = Re[Tr[p2.RhoExp]];
t3q2 = Re[Tr[p3.RhoExp]];
t4q2 = Re[Tr[p4.RhoExp]];
t5q2 = Re[Tr[p5.RhoExp]];
t6q2 = Re[Tr[p6.RhoExp]];
t7q2 = Re[Tr[p7.RhoExp]];
t8q2 = Re[Tr[p8.RhoExp]];
t9q2 = Re[Tr[p9.RhoExp]];
t10q2 = Re[Tr[p10.RhoExp]];
t11q2 = Re[Tr[p11.RhoExp]];
t12q2 = Re[Tr[p12.RhoExp]];
t13q2 = Re[Tr[p13.RhoExp]];
t14q2 = Re[Tr[p14.RhoExp]];
t15q2 = Re[Tr[p15.RhoExp]];
t16q2 = Re[Tr[p16.RhoExp]];

TheoryVecI2 = {t1i2, t2i2, t3i2, t4i2, t5i2, t6i2, t7i2,
 t8i2, t9i2, t10i2, t11i2, t12i2, t13i2, t14i2, t15i2, t16i2};
TheoryVecQ2 = {t1q2, t2q2, t3q2, t4q2, t5q2, t6q2, t7q2, t8q2,
 t9q2, t10q2, t11q2, t12q2, t13q2, t14q2, t15q2, t16q2};

PlotMax = Max[Abs[β1] + Abs[β2] + Abs[β12], Abs[α1] + Abs[α2] + Abs[α12]];
PlotMin = -PlotMax;
ListPlot[{ExpVecI, TheoryVecI, ExpVecQ, TheoryVecQ}, PlotStyle →
 {RGBColor[1, 0, 0], RGBColor[0, 1, 0], RGBColor[1, 0, 0], RGBColor[0, 0, 1]},
 PlotJoined → True, PlotRange → {PlotMin, PlotMax}, GridLines → Automatic,

```

```

Frame → True, FrameLabel → {"Measurement number", "Amplitude"}]

GraphicsRow[{
  BarChart3D[Re[RhoExp], PlotRange -> {All, All, {-1, 1}},
    BarStyle → Directive[Glow[Blue], Opacity[0.9]], BarEdgeStyle → Blue,
    BarSpacing → .15, BarEdges → True, Boxed → True],
  BarChart3D[Im[RhoExp], PlotRange -> {All, All, {-1, 1}},
    BarStyle → Directive[Glow[Blue], Opacity[0.9]], BarEdgeStyle → Blue,
    BarSpacing → .15, BarEdges → True, Boxed → True]
}];

GraphicsRow[{
  BarChart3D[Re[RhoExp], PlotRange -> {All, All, {-1, 1}}],
  BarChart3D[Im[RhoExp], PlotRange -> {All, All, {-1, 1}}]
}]

GraphicsRow[{
  BarChart3D[Re[RhoTheo2], PlotRange -> {All, All, {-1, 1}}],
  BarChart3D[Im[RhoTheo2], PlotRange -> {All, All, {-1, 1}}]
}]

GraphicsRow[{
  BarChart3D[Re[RhoExp], PlotRange -> {All, All, {-1, 1}},
    BarStyle → Directive[Glow[Blue], Opacity[0.7]], BarEdgeStyle → Blue,
    BarSpacing → .15, BarEdges → True, Boxed → True,
    Ticks → {{1, 2, 3, 4}, {1, 2, 3, 4}, {-1, -0.5, 0, 0.5, 1}},
    ViewPoint → {1.3, -2.4, 1.5},
    FaceGrids → { { {0, -1, 0}, {}, {{-0.5, Dashed}, {0.5, Dashed}} },
      { {0, 1, 0}, {}, {{-0.5, Dashed}, {0.5, Dashed}} },
      { {1, 0, 0}, {}, {{-0.5, Dashed}, {0.5, Dashed}} },
      { {-1, 0, 0}, {}, {{-0.5, Dashed}, {0.5, Dashed}} } },
    FaceGridsStyle → Directive[Thin, Gray]],
  BarChart3D[Im[RhoExp], PlotRange -> {All, All, {-1, 1}},
    BarStyle → Directive[Glow[Blue], Opacity[0.7]], BarEdgeStyle → Blue,
    BarSpacing → .15, BarEdges → True, Boxed → True,
    Ticks → {{1, 2, 3, 4}, {1, 2, 3, 4}, {-1, -0.5, 0, 0.5, 1}},
    ViewPoint → {1.3, -2.4, 1.5},
    FaceGrids → { { {0, -1, 0}, {}, {{-0.5, Dashed}, {0.5, Dashed}} },
      { {0, 1, 0}, {}, {{-0.5, Dashed}, {0.5, Dashed}} },
      { {1, 0, 0}, {}, {{-0.5, Dashed}, {0.5, Dashed}} },
      { {-1, 0, 0}, {}, {{-0.5, Dashed}, {0.5, Dashed}} } },
    FaceGridsStyle → Directive[Thin, Gray]]
}];

```

1 qubit process tomography experiment

This section shows the maximum-likelihood estimation of the χ matrix for a single-qubit quantum process tomography experiment.

■ Operations for QPT

```

Rho[t1_, t2_, t3_, t4_] :=
Simplify[
$$\frac{\text{dagger}[\{\{t1, 0\}, \{t3 + i t4, t2\}\}].\{\{t1, 0\}, \{t3 + i t4, t2\}\}}{\text{Tr}[\text{dagger}[\{\{t1, 0\}, \{t3 + i t4, t2\}\}].\{\{t1, 0\}, \{t3 + i t4, t2\}\}]}$$
,
Assumptions → { {t1, t2, t3, t4} ∈ Reals}]

```

```

op = destroy[2];
om = dagger[op];
ox = op + om;
oy = -i op + i om;
oz = -om.op + op.om;
oi = ident[2];

U[θ_, σ_] := MatrixExp[-i  $\frac{\theta}{2}$  Normal[σ]];

(* the basis of physical measurements states *)
rj1 = {{0, 0}, {0, 1}};
rj2 = U[π, ox].rj1.dagger[U[π, ox]]
rj3 = U[ $\frac{\pi}{2}$ , ox].rj1.dagger[U[ $\frac{\pi}{2}$ , ox]]

rj4 = U[ $\frac{\pi}{2}$ , oy].rj1.dagger[U[ $\frac{\pi}{2}$ , oy]]

rj5 = U[ $\frac{-\pi}{2}$ , ox].rj1.dagger[U[ $\frac{-\pi}{2}$ , ox]]

rj6 = U[ $\frac{-\pi}{2}$ , oy].rj1.dagger[U[ $\frac{-\pi}{2}$ , oy]]

Likely[t1_, t2_, t3_, t4_, pg_, pe_, py_, px_, V_] :=

$$\frac{1}{2V} \left( \frac{3}{2} + (-2 + pe) pe + pg^2 + (-1 + px) px + (-1 + py) py + \right.$$


$$\left. \frac{-t1^2 t2^2 + t2^4}{(t1^2 + t2^2 + t3^2 + t4^2)^2} + \frac{t2 ((-1 + 2 pe - 2 pg) t2 + (-1 + 2 px) t3 + t4 - 2 py t4)}{t1^2 + t2^2 + t3^2 + t4^2} \right)$$


MLE[xm_, ym_, zm_, im_, V_] := Module[{t1, t2, t3, t4, sol},
sol = NMinimize[Likely[t1, t2, t3, t4, xm, ym, zm, im, V], {t1, t2, t3, t4}];
flat[Rho[t1, t2, t3, t4] /. sol[[2]]]]

AMat [rjm1_, rjm2_, rjm3_, rjm4_] :=
Module[{rjmtemp, rktemp}, rjmtemp = {rjm1, rjm2, rjm3, rjm4};
rktemp = { $\frac{\text{flat}[\sigma_i]}{\sqrt{2}}$ ,  $\frac{\text{flat}[\sigma_x]}{\sqrt{2}}$ ,  $\frac{\text{flat}[\sigma_y]}{\sqrt{2}}$ ,  $\frac{\text{flat}[\sigma_z]}{\sqrt{2}}$ };
Table[Conjugate[rktemp[[k]].rjmtemp[[j]], {k, 1, 4}, {j, 1, 4}]]

BMat[rj1_, rj2_, rj3_, rj4_] :=
Module[{rjtemp, rktemp, S}, rjtemp = {rj1, rj2, rj3, rj4};
rktemp = { $\frac{\text{flat}[\sigma_i]}{\sqrt{2}}$ ,  $\frac{\text{flat}[\sigma_x]}{\sqrt{2}}$ ,  $\frac{\text{flat}[\sigma_y]}{\sqrt{2}}$ ,  $\frac{\text{flat}[\sigma_z]}{\sqrt{2}}$ }; S = {σi, σx, σy, σz};
Table[Flatten[Table[Conjugate[rktemp[[Mod[p - 1, 4] + 1]]].
flat[S[[m]].rjtemp[[Floor[(p - 1) / 4 + 1]]].S[[n]]],
{m, 1, 4}, {n, 1, 4}]], {p, 1, 16}]]];

```

```

ChiMat[rjm1_, rjm2_, rjm3_, rjm4_, rj1_, rj2_, rj3_, rj4_] :=
Module[{rjtemp, rjmtemp, rktemp, S, λ, β}, rjtemp = {rj1, rj2, rj3, rj4};
rktemp = {

$$\frac{\text{flat}[\sigma_i]}{\sqrt{2}}, \frac{\text{flat}[\sigma_x]}{\sqrt{2}}, \frac{\text{flat}[\sigma_y]}{\sqrt{2}}, \frac{\text{flat}[\sigma_z]}{\sqrt{2}}$$

};
S = {σi, σx, σy, σz}; rjmtemp = {rjm1, rjm2, rjm3, rjm4};
λ = flat[Table[Conjugate[rktemp[[k]].rjmtemp[[j]], {j, 1, 4}, {k, 1, 4}]];
β = Table[flat[Table[Conjugate[rktemp[[Floor[(p - 1) / 4 + 1]]]],
flat[S[[m]].rjtemp[[Mod[p - 1, 4] + 1]].S[[n]]], {m, 1, 4}, {n, 1, 4}],
{p, 1, 16}]; unflat[Chop[Inverse[β].λ], 4]

ChiT[t1_, t2_, t3_, t4_, t5_, t6_, t7_,
t8_, t9_, t10_, t11_, t12_, t13_, t14_, t15_, t16_] :=
Simplify[dagger[{{t1, 0, 0, 0}, {t5 + i t6, t2, 0, 0}, {t11 + i t12, t7 + i t8, t3, 0},
{t15 + i t16, t13 + i t14, t9 + i t10, t4}}].{{t1, 0, 0, 0}, {t5 + i t6, t2, 0, 0},
{t11 + i t12, t7 + i t8, t3, 0}, {t15 + i t16, t13 + i t14, t9 + i t10, t4}},
Assumptions → {t1, t2, t3, t4, t5, t6, t7, t8, t9, t10,
t11, t12, t13, t14, t15, t16} ∈ Reals]

Clear[λ]

```

```

ProcessMin2[t1_, t2_, t3_, t4_, t5_, t6_, t7_, t8_, t9_, t10_, t11_, t12_,
t13_, t14_, t15_, t16_, p1m1_, p1m2_, p1m3_, p1m4_, p2m1_, p2m2_, p2m3_,
p2m4_, p3m1_, p3m2_, p3m3_, p3m4_, p4m1_, p4m2_, p4m3_, p4m4_, λ_] :=
1/4 (4 (-p1m1 + t12 + t112 + t122 + t162 + (t15 - t4)2 + t52 + t62)2 +
4 (-p2m2 + t12 + t112 + t122 + t162 + (t15 + t4)2 + t52 + t62)2 +
4 (-p4m4 + t12 + (t13 - t15)2 + (t14 - t16)2 + (t2 - t5)2 + t62 + (t11 - t7)2 +
(t12 - t8)2)2 + 4 (-p2m1 + (t10 + t13)2 + t22 + t72 + (t3 - t8)2 + (t14 - t9)2)2 +
(-2 p3m1 + t12 + (t10 + t13 + t16)2 + t52 + (t2 + t6)2 + (t12 + t7)2 +
(t11 + t3 - t8)2 + (t14 - t15 + t4 - t9)2)2 +
4 (-p1m2 + (t10 - t13)2 + t22 + t72 + (t3 + t8)2 + (t14 + t9)2)2 +
4 (-p3m3 + t12 + t122 + (t10 + t16)2 + (t11 + t3)2 + t52 + t62 + (t15 + t9)2)2 +
(-2 p3m4 + t12 + (t10 - t14 + t16 - t4)2 + (t2 - t5)2 + t62 +
(t11 + t3 - t7)2 + (t12 - t8)2 + (-t13 + t15 + t9)2)2 +
(-2 p4m3 + t12 + (t10 - t14 + t16 + t4)2 + (t2 - t5)2 + t62 + (t11 + t3 - t7)2 +
(t12 - t8)2 + (-t13 + t15 + t9)2)2 + (-2 p1m4 + t12 + (t10 - t13 + t15 - t4)2 +
(t2 - t5)2 + t62 + (t11 - t7)2 + (-t12 + t3 + t8)2 + (t14 - t16 + t9)2)2 +
(-2 p4m2 + t12 + (t10 - t13 + t15 + t4)2 + (t2 - t5)2 + t62 + (t11 - t7)2 +
(-t12 + t3 + t8)2 + (t14 - t16 + t9)2)2 + (-2 p2m4 + t12 + (t10 + t13 - t15 - t4)2 +
(t2 - t5)2 + t62 + (t11 - t7)2 + (t12 + t3 - t8)2 + (-t14 + t16 + t9)2)2 +
(-2 p4m1 + t12 + (t10 + t13 - t15 + t4)2 + (t2 - t5)2 + t62 + (t11 - t7)2 +
(t12 + t3 - t8)2 + (-t14 + t16 + t9)2)2 + (-2 p1m3 + t12 + (t10 - t13 + t16)2 +
t52 + (t2 - t6)2 + (t12 - t7)2 + (t11 + t3 + t8)2 + (t14 + t15 - t4 + t9)2)2 +
(-2 p2m3 + t12 + (t10 + t13 + t16)2 + t52 + (t2 + t6)2 + (t12 + t7)2 +
(t11 + t3 - t8)2 + (-t14 + t15 + t4 + t9)2)2 +
(-2 p3m2 + t12 + (t10 - t13 + t16)2 + t52 + (t2 - t6)2 + (t12 - t7)2 +
(t11 + t3 + t8)2 + (t14 + t15 + t4 + t9)2)2) +
λ 4 (4 (t13 t15 + t14 t16 - t10 t4 + t2 t5 + t11 t7 + t12 t8)2 +
4 (t10 t13 + t15 t4 - t3 t8 - t14 t9)2 + 4 (t10 t16 + t11 t3 + t14 t4 + t15 t9)2 +
(-1 + t12 + t102 + t112 + t122 + t132 + t142 + t152 +
t162 + t22 + t32 + t42 + t52 + t62 + t72 + t82 + t92)2)
MLEP2[p1m1_, p1m2_, p1m3_, p1m4_, p2m1_, p2m2_, p2m3_, p2m4_,
p3m1_, p3m2_, p3m3_, p3m4_, p4m1_, p4m2_, p4m3_, p4m4_, λ_] := Module[
{t1, t2, t3, t4, t5, t6, t7, t8, t9, t10, t11, t12, t13, t14, t15, t16, sol},
sol = NMinimize[ProcessMin2[t1, t2, t3, t4, t5, t6, t7, t8, t9, t10,
t11, t12, t13, t14, t15, t16, p1m1, p1m2, p1m3, p1m4, p2m1, p2m2,
p2m3, p2m4, p3m1, p3m2, p3m3, p3m4, p4m1, p4m2, p4m3, p4m4, λ],
{t1, t2, t3, t4, t5, t6, t7, t8, t9, t10, t11, t12, t13, t14, t15, t16},
MaxIterations -> 10 000]; ChiT[t1, t2, t3, t4, t5, t6, t7,
t8, t9, t10, t11, t12, t13, t14, t15, t16] /. sol[[2]]]

```

Copyright Permissions

- Figures 6.2 to 6.4 reproduced with permission from :
Lev S. Bishop, J. M. Chow, Jens Koch, A. A. Houck, M. H. Devoret, E. Thuneberg, S. M. Girvin, and R. J. Schoelkopf, *Nature Phys.* **5**, 105–109 (2009).
Copyright © 2009, Nature Publishing Group.
- Figure 5.4 reproduced with permission from:
Jens Koch, Terri M. Yu, Jay Gambetta, A. A. Houck, D. I. Schuster, J. Majer, Alexandre Blais, M. H. Devoret, S. M. Girvin, and R. J. Schoelkopf, *Phys. Rev. A* **76**, 042319 (2007).
Copyright (2007) by the American Physical Society.
- Figure 4.2 reproduced with permission from :
F. Motzoi, J. M. Gambetta, P. Rebentrost, and F. K. Wilhelm, *Phys. Rev. Lett.* **103**, 110501 (2009).
Copyright (2009) by the American Physical Society.
- Figures 6.8, 6.10, 6.11, 6.13 and 6.15 reproduced with permission from :
J. M. Chow, J. M. Gambetta, L. Tornberg, Jens Koch, Lev S. Bishop, A. A. Houck, B. R. Johnson, L. Frunzio, S. M. Girvin, and R. J. Schoelkopf, *Phys. Rev. Lett.* **102**, 090502 (2009).
Copyright (2009) by the American Physical Society.
- Figures 7.1, 7.4 to 7.8, 7.10 and 7.11 reproduced with permission from :
J. Majer, J. M. Chow, J. M. Gambetta, Jens Koch, B. R. Johnson, J. A. Schreier, L. Frunzio, D. I. Schuster, A. A. Houck, A. Wallraff, A. Blais, M. H. Devoret, S. M. Girvin, and R. J. Schoelkopf, *Nature* **449**, 443–447 (2007).
Copyright © 2007, Nature Publishing Group.

- Figures 8.1, 8.2, 8.4, 8.5, 8.11, 9.2, 9.4 and 9.5 reproduced with permission from :
L. DiCarlo, J. M. Chow, J. M. Gambetta, Lev S. Bishop, B. R. Johnson, D. I. Schuster,
J. Majer, A. Blais, L. Frunzio, S. M. Girvin, and R. J. Schoelkopf, *Nature* **460**, 240–
244 (2009).
Copyright © 2009, Nature Publishing Group.